City Research Online

City, University of London Institutional Repository

THE CHARACTERISATION OF THE INTERNAL DIESEL FLOW AND THE EXTERNAL SPRAY STRUCTURE USING LASER DIAGNOSTICS

Kassandra Makri

This thesis is submitted in fulfilment of the requirements for the degree of

Doctor of Philosophy

City, University of London, School of Mathematics, Computer Science and

Engineering, Department of Mechanical Engineering

May 2018

Table of Contents

Table of figures

List of Tables

Acknowledgements

First of all, I would like to thank my supervisor Dr Russel Lockett who gave me the opportunity to work on such a challenging and interesting project. This dissertation would not have been possible without his guidance, support and advice. I would also wish to thank Shell Global Solutions for funding this project.

I would like to acknowledge the technicians of City, University of London: Mr Rob Cherry, Mr Grant Clow and Mr Jim Ford, who delivered complicated requests and were always willing to help me in resolving problems during the execution of my experiments. I would also like to thank Professor John Carlton and Professor Jamshid Nouri for giving me permission to use their equipment and providing me with useful tips. Lastly, I would like to acknowledge Dr Olawole Kuti 's contribution who inspired me to compose my first publication and shared useful tips and material with me.

I owe a debt of gratitude to my colleagues Alberto and Zeeshan, who have become my closest friends during this journey at City. Their moral support and useful conversations cheered me up when I needed it the most. I would also like to mention all my friends and colleagues with whom I shared the PhD office and lunch times: Yannis, Elina, Kostas, Antonio, Eleni, Saeed, Dimitris and Israt. Lastly, I genuinely thank all my friends Nancy, Palmyra, Agni, George, Stavros, Athina and Elena who bore with me patiently during all this time and supported me in any possible way.

Finally, I could not forget to thank all my family back home who kept supporting and encouraging me during this tough, but also challenging and rewarding period of my life.

Abstract

The advances in Fuel Injection Equipment have increased the injection and combustion efficiency, but have also increased the possibility of failure. Recent studies have identified various types of deposits of different components, such as fuel filters, injector nozzles etc. In this regard, white light scattered from the internal flow structures along with both elastic (Mie signal) and inelastic light (fluorescence) from the external sprays were synchronously captured by two separate high-speed cameras. The part of the present work was based on the experiments conducted by Jeshani Mahesh and post-processed by the author of this dissertation. The analysis performed suggested potential deposit formation mechanisms inside diesel injector nozzles considering the operating conditions of the injection system and the physical properties of the fuels. The observed circumferential bubble motion at the late stages of the needle return and post-injection, has been proven to generate low and high-pressure gradients which govern the bubble movement inside the nozzle passages. In engine conditions, the inward bubble movement inside the passages is believed to be the mechanism for the admission of hot combustion gases inside the nozzle geometry. The reaction of these hot gases with the liquid fuels is believed to produce deposits inside the FIE. The LIF-Mie obtained ratios provided an insight into the external spray drop-sizing and atomisation characteristics. The undertaken analysis revealed a strong link between the spray drop size and the physical properties of the fuels. It was also shown that both the needle lift and the operating conditions played a decisive role in the atomisation process and that an increase in rail pressure led to the formation of smaller droplets, while an increase in viscosity and surface tension led to larger droplets. The size of the spray droplets during the early and late stages of the needle lift was larger in relation to the maximum needle lift, due to the synergy of flow chocking and various types of cavitation (needle cavitation, string cavitation). The final section of this analysis involves the phenomenological study of the emerging sprays based on the LIF spray data. This study that the liquid core of the sprays was destroyed either inside the nozzle passage or in the vicinity of the nozzle exit. The obtained results referred to the LVF of different regions of the sprays as a function fuels' properties, needle lift and rail pressure.

A similar analysis was based on data obtained from an improved experimental setup. The white light scattering was replaced by LIF to enable a quantitative analysis in terms of Liquid Volume fraction inside the nozzle passage. To the best of the author's knowledge, such measurements were attempted for the first time and there are no similar results in the available literature. The spray results obtained came to an agreement with the afore-mentioned findings, validating the experimental and processing methodologies. The inelastic scattered light captured from the structures were formed inside a real-size nozzle passage reflected the effects of the fuels' physical properties, needle lift and rail pressure. The results obtained referred to the relative LVF of the flow inside the nozzle passage. An increase in rail pressure led to lower relative LVF or SFLVF (term introduced for the purposes of the present work), as a result of enhanced cavitation phenomena. Additionally, the SFVLF of lighter fuels was lower compared to heavier fuels, due to intensive cavitation, which reduced the amount of liquid fuel in the hole. The obtained results also confirmed the argument suggesting the spray asymmetry to be associated to the geometric cavitation formed in the vicinity of the nozzle entrance.

Abbreviations

ac: Amplitude of modulated light

ASTM: American Society for Testing   Materials

CCD: Charge Coupled Device

C$_d$: Discharge coefficient

CN: Cetane Number

CO: Carbon monoxide

CO$_2$: Carbon Dioxide

CFR: Cooperative Fuel Research

CR: Common Rail

dc: Amplitude of non-modulated light

DCA: Deposit Control Additives

DDSA: Dodecenyl Succinic Acid

DI: Direct Injection

ECC: Enhanced Correlation Coefficient

EDS: Energy Dispersive X-Ray Spectroscopy

EM: Electro-Magnetic

FAME: Fatty Acid Methyl Esters

FIE: Fuel Injection Equipment.

FTIR: Fourier Transform Infrared Spectroscopy

FWHM: Full Width Half Maximum

GTL: Gas To Liquid

HC: HydroCarbons

HDSA: Hexadecenyl Succinic Acid

HOMO: Highest Occupied Molecule Orbitals

HPLC: High Performance Liquid
   Chromatography

IDI: Indirect Injection

IID: Internal Injector Deposits

INF: INternal Flow

l$_c$: Length of the spray liquid core

LC: Liquid Chromatography

LDA: Laser Doppler Anemometry

LDV: Laser Doppler Velocimetry

LIF: Laser Induced Fluorescence

LSD: Laser Sheet Drop-sizing

LUMO: Lowest Unoccupied Molecule nOrbitals

LVF: Liquid Volume Fraction

MS: Mass Spectroscopy

NaOH: Sodium hydroxide

NI: National Instruments

NO$_x$: Nitrogen Oxide

NR: Needle Return

OD: Optical Density

Oh: Ohresorge

PAH: Polycyclic Aromatic Hydrocarbons

PIBSA: Polyisobutylene anhydrite

PIBSI: Polyisobutylene succinimide

RhB: Rhodamine B

SEM: Scanning Electron Microscopy

SFLVF: Scattered Fluorescence Liquid Volume
   Fraction

SIC: Single Ion Chromatographs

SLIPI: Structured Laser Illumination Planar
   Imaging

SMD: Sauter Mean Diameter

SNR: Signal to Noise Ratio

SoI: Start of Injection

STD: Standard deviation

VCO: Valve Covered Orifice

We: Weber number

σ$_v$: Cavitation number

Chapter 1

Introduction

The increasing demand of energy and mobility in contrast to the limited resources of fossil fuels and the environmental concerns with regards to global warming and air pollution have led to the development of new, cleaner and more efficient technologies for energy production. In the past decades, the research community has focused its attention on the development of new propulsion systems including advanced processes and highly efficient, environmental friendly fuels. In this regard, significant efforts have been made on the sufficient understanding the fundamental physics of major processes (i.e. combustion, atomisation) taking place in diesel engines. One of the biggest advances of the modern diesel engines is the introduction of efficient high-pressure common rail injection systems, which provide great flexibility in terms of engine control and management over a wide spectrum of operating conditions and fuels.

The employment aim of such systems is the enhancement of the atomisation process and the delivery of accurate, precise and optimal air-fuel mixtures to the combustion chamber. It has been suggested[1] that there is a strong correlation amongst the atomised diesel fuels, the combustion and thermal efficiency and the engine-out emissions. Therefore, a thorough study of the atomisation process is essential to obtain a suitable optimal range of the parameters capable of improving the fuel-air mixing process and subsequently resulting in reduced emissions. However, the scientific and industrial interest in spray characterisation barely existed a few decades ago, due to its complexity and lack of suitable facilities and experimental techniques. Nowadays, the development of technology (i.e. high-speed cameras, lasers etc) together with the many applications of sprays to various industries (i.e. aviation, agricultural, automotive) have promoted the development of suitable optical diagnostics for spray characterisation.

The most significant example of spray application concerns the injection of liquid fuel into pistons through multiple multi-hole diesel injector nozzles. During the injection process, the fuel is subjected

Introduction

to large pressure gradients, which in turn cause local boiling conditions. This is likely to occur when the pressure drops below the saturated vapour pressure of the fuel. Under such conditions, the fuel state changes into vapour creating local vapour cavities. This phenomenon is known as cavitation. A cavitating flow has been suggested to affect the structure of the emerging sprays, the atomisation process and the lifetime of the FIE[2,3]. It has also been shown experimentally that cavitation modifies significantly the injector surfaces, possibly due to hydro-erosion and hydro-grinding[4]. Additionally, cavitation is believed to be dependent on the physical properties of the fuels. Several researchers[4,5] have reported that fuel samples containing Fatty Acid Methyl Esters (FAME) have the tendency to cavitate less in relation to the conventional diesel.

The demand for better combustion and atomisation efficiency has led the FIE industry to develop systems that operate at extreme pressure conditions. World leading injector manufacturers such as Bosch, Denso have reported the development of common rail injection systems capable of achieving pressures of up to 3,000bar[6,7]. The extreme temperature and pressure conditions generated together with the small dimensions of the nozzle passages create conditions that are able to support the formation of injector deposits via pyrolysis reactions, chemical re-arrangement or the fuel decomposition. These may lead to nozzle blockage or even failure. The synergy of the extreme operating conditions together with the introduction of new fuel blends (low sulphur content fuels blended with a wide range of additives and biofuels) has led to an increase in the incidents of injector fouling. Indeed, several authors [8–12] have reported the existence of deposits at various points of the injector geometry such as hole entrance, needle, nozzle sac etc., while others have made attempts to suggest potential mechanisms for deposit formation[8,13]. However, the results and the models developed so far are not conclusive. It has been suggested that atomisation and internal flow are greatly affected by the presence of deposits, which can potentially lead to increased fuel consumption, power loss and equipment failure[15]. The effect of cavitation in deposit formation appeared to be beneficial for the removal of deposits from diesel injectors.

Apart from the impact of the fuel's physical properties on cavitation, it has been experimentally observed that they significantly affect the atomisation process and the spray characteristics such as

droplet size, spray cone angle etc.[14,15]. In practice, atomisation is the result of the dominant effects of the internal or external forces over the stabilizing effects of the viscosity and surface tension of the fuel. Some of the most significant parameters contributing to the atomisation process are cavitation, flow turbulence and fuel properties. Depending on the stage of the liquid disintegration and droplet stability, atomisation can be classified into primary and secondary atomisation. In most cases, the liquid break-up is an unstable and complex physical process, which is difficult to control and investigate. The first approach in investigating such complex systems was the primary identification of the spray properties (i.e. droplet size, spray cone angle, spray penetration length etc) under a range of different operating conditions.

In the last few decades, the spray characterisation was initially achieved using mechanical or electrical devices, but more recently optical techniques have become the methods of choice, due to their remote sensing, non-intrusive nature and the availability of a wide variety of instruments suitable for spray measurements. However, each of these optical diagnostics serve a different purpose and provide specific and/or local information. Some of them provide general information with regards to the structure and geometry of the spray, while some others to the size, velocity, temperature of the spray droplets. Additionally, some other techniques are employed to investigate the spray break-up mechanisms (primary and secondary break-up mechanisms) and atomisation. In many cases, the combination of more than one method is usually required for a complete spray characterisation. On the other hand, despite the profound advantages of these techniques, there are cases, such as dense spray regions, where their application and performance are doubtful.

The present work involved experimental data obtained from two individual experiments. The first set of experiments was executed by Jeshani[16] and the second set by the author of this dissertation. The data processing was based on Jeshani's work, but it has been further developed and improved by this thesis's author.

The objective of this work was to comprehensively investigate the external structure of the atomising sprays emerging from a custom manufactured, real-sized, 6-hole, optically accessible mini-sac type nozzle together with the internal flow phenomena occurring in the nozzle during and post injection

using optical diagnostics. The analysis performed on Jeshani's data was focused on the investigation of the external spray droplet size and phenomenology using Laser Sheet Drop-sizing and Laser Induced Fluorescence techniques respectively. It was also attempted to suggest potential deposit formation mechanism based on the post-injection phenomena occurring in the sac and the nozzle holes. The experimental method used for the identification of internal flow features was white light scattering (elastic scattering).

The analysis based on the experimental work of this thesis's author attempted to primarily improve the previous experiment by replacing white light scattering with Laser Induced Fluorescence (LIF) technique. This method is capable of providing quantitative measurements of the liquid volume faction inside the nozzle passage during the injection process and to identify flow features, such as geometric cavitation. Similarly to Jeshani's data, the spray characterisation was achieved using Laser Sheet Drop-sizing technique, providing the opportunity to evaluate the results obtained by comparison. To the best of the author's knowledge, the application of LIF in real-sized, mini-sac nozzles was attempted for the first time, therefore this work could be considered original and novel.

A key aspect of this investigation was the identification of the correlation amongst the internal flow, the external sprays and the physical properties of the fuels, as a function of the transient movement of the injector needle and the operating conditions (the experiments were performed at 250bar and 350bar). Jeshani's results were obtained from five diesel fuel samples, while the second set of results from four diesel samples. The majority of the fuels used had similarities in terms of their physical properties (i.e. distillation profile, viscosity etc). All fuel samples were provided by Shell Global Solutions.

The work presented in this dissertation was distributed into 7 Chapters. A brief summary of the content of each Chapter individually is listed below.

Chapter 2 provides a detailed literature review of the fields related to this work. Initially, it provides a quick overview over the fundamentals of diesel fuels and injection systems. It describes the fundamentals of cavitation and atomisation processes and the optical diagnostics suitable for their investigation. Lastly, a brief summary of the types of deposits found in FIE was also presented. The

experimental setup, apparatus, high speed acquisition setup and timing, laser sheet drop-sizing setup, experimental and calibration methodologies were described in Chapter 3. Chapter 4 involved the detailed description of the internal flow data obtained from both white light and fluorescence scattering experiments respectively. The results from both experiments were presented and discussed in detail.

Chapter 5 and 6 referred to the characterisation of the diesel sprays in terms of the droplet size and liquid volume fraction using the Laser Sheet Drop-sizing and Laser Induced Fluorescence experimental data. It involved the detailed description of the processing methodologies used and the discussion of the results obtained from both experiments, which highlighted the dependence of the droplets size on the physical properties of the fuels, the transient movement of the needle and the injection pressure.

Lastly, Chapter 7 provided an overview of the conclusions drawn from the analyses together with the future work and suggestions.

Chapter 2

Literature review

This section was devoted to the reviews of the fundamentals of diesel fuels, diesel injection systems, cavitation, atomisation and deposit formation processes together with a detailed description of the optical techniques widely used for internal flow and spray characterisation. The aim was to familiarise the reader with the most dominant processes and terms elaborated in this work.

2.1 Diesel fuel background

Diesel fuel is one of the most common fossil fuels utilised for industrial, domestic and agricultural purposes. The combustion produces sufficient chemical energy which in turn is converted into mechanical energy. In this section the production, composition and performance parameters of diesel fuels and diesel engines were discussed. The literature review was mostly based on Srivastava, Hancsó[17] and other technical reports found online. The description of the fuel refinement processes was also presented in order to highlight the main production processes and therefore, provide an insight of the fuel composition and properties. The understanding of the physical properties of the fuels was essential for this work, as they related to the work presented in later chapters. Additionally, the effects of the performance parameters on the fuel properties and their impact on various processes (i.e. cavitation, atomisation, combustion) taking place in Fuel Injection Equipment (FIE) were also reported. Ultimately, the discussion of currently used alternative fuels and fuel additives was presented at the end of this chapter to provide information about fuel's performance.

<u>Refinery process of crude oil and diesel fuel composition.</u>

Diesel fuel comes from the refinement of crude oil. Crude oil is mainly composed of carbon (83-87% w/w), hydrogen (11-14% w/w) and small traces of other elements (e.g. sulphur). It varies from thin, light coloured, brownish or greenish crude oils (low density, high gravity) to thick, black oils (high density, low gravity). The petroleum crude oil is refined to produce various fuels such as diesel, gasoline, kerosene etc. The main processes of the refining process are separation, upgrading and

conversion processes. The first two stages refer to processes that do not change the chemical structure of the crude oil, while the last one significantly changes its molecular structure. A simple schematic of a crude oil refinery plant is shown in Figure 2.1

Figure 2.1:Basic schematic of a crude oil refinery system[18].

Initially, crude oil undergoes a separation process which is based on the nature of the hydrocarbons in terms of their physical properties (i.e. volatility). The most common separation process is distillation, and in the refinery industry it can be processed at either atmospheric pressure or vacuum. In the case of atmospheric distillation process, crude oil is separated into a wide range of products with narrow boiling point ranges. The operating principles behind this process are fairly simple. Firstly, the crude oil is

heated into a heat exchange train, it then enters the distillation column as a gas-liquid mixture. The more volatile, light components rise upwards, while the heavier compounds are being condensed by the cold down flow of liquid fuel. These light components exit the column at the top, where they are subjected to condensation such that light gases (C1-C4) and light naptha are obtained. The purity of these light products is later improved in other units of the refinery plant, employing several methods (i.e. stripping). The rest of the hydrocarbon mixture has higher boiling point and does not reach the top of the column. In particular, gasoline is drawn off from the side of the column while kerosene and diesel (higher boiling points relative to gasoline) are drawn off successively lower from the distillation column. The oil residue is in liquid phase and consists of the heaviest components; therefore; it exits the column at the bottom.

This primary separation process is then followed by several upgrading processes which aim to improve the quality of the distillates by removing undesirable compounds present into the fuels. The most common upgrading process is hydro-treating, which is employed to a) remove oxygen and sulphur compounds via chemical reactions involving hydrogen and b) to saturate aromatic rings and to eliminate the amount of nitrogen and sulphur compounds left in the distillates. After the upgrade processes, the fuel is subjected to conversion processes which are utilised to perform changes in the chemical structure of the hydrocarbons and eventually to meet the desired requirements in terms of fuel quality. This conversion involves methods which either alter the number of the carbon molecules in the hydrocarbons or produce molecules of more useful hydrocarbon molecules. Some of the most common processes related to conversion of hydrocarbon without any changes in the carbon molecule population are de-sulfurization and skeletal isomerization. On the other hand, the methods utilised for the conversion of hydrocarbon structures into compounds of higher or lower number of carbon molecules are oligomerization or several types of cracking respectively (i.e. catalytic cracking, thermal cracking etc.).

In this work, the focus is on middle distillate products whose distillate profiles are similar to diesel fuel. In general, diesel fuels are mixtures of crude oil derived and alternative blending components. Such blends offer high energy content and high cetane number. However, due to strict legislation, diesel fuels

have to comply with very specific requirements; therefore, it is essential to employ certain refinery technologies along with a carefully selected range of additives and complex processing methods.

<u>Composition and properties of diesel fuel</u>

Diesel fuel is a mixture of thousands of hydrocarbons obtained through the fractional distillation of petroleum fuel oil, with a boiling point in the range of 175-350°C. Due to its complexity, diesel oil cannot be characterised by a single well-defined boiling point, but by a boiling point range and by temperature values related to the distilled fraction. A typical distillation curve of a diesel sample is shown in Figure 2.2.
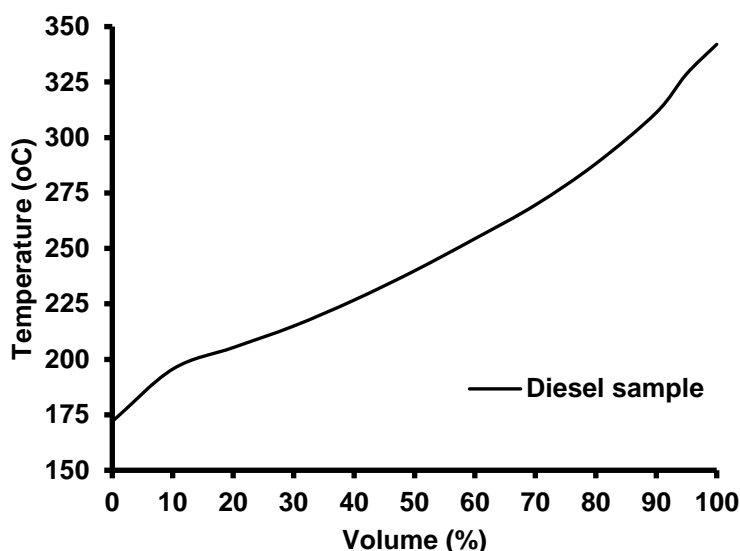
Figure 2.2:Typical distillation curve of diesel sample

Crude oil derived diesel fuels have a composition of approximately 75% aliphatic hydrocarbons and 25% aromatic hydrocarbons. The most common hydrocarbon classes found in such fuels are paraffins, olefins, napthenes and aromatic rings. Each class of hydrocarbons has different physical and chemical properties; hence each blend of diesel fuel is different from other blends due to each having different proportions of these classes. The most important fuel properties are the distillation curve, density, surface tension, cetane number and viscosity, which vary depending on their relative proportions of classes of hydrocarbons[19].

Literature review

A fundamental parameter of fuels is the distillation curve (boiling point curve) which is experimentally determined using ASTM-D86 method. By increasing the temperature, more volatile components may be reduced, while the heavier may be caught by the lighter ones. The range of boiling point for diesel fuels is quite wide and significantly affects properties such as viscosity, density, ignition delay and flashpoint. It also determines the applicability and the behaviour of fuels in the engine. Deposit built-up in engines is influenced by excessive amounts of high-boiling point compounds. Thus, limitations are set on carbon residue and the distillation product at 90% evaporated temperature[20].

Cetane Number (CN) defines the quality of the fuel in terms of its ignition. In other words, it is a measure to quantify the propensity of the fuels to burn under diesel engine conditions. The cetane number also offers an estimate with regards to the ignition delay period, namely the time period between the start of the injection and the first moment where the combustion pressure developed in the combustion chamber becomes noticeable. A rapid increase of the pressure, as a result of the rapid heat release due to combustion, is responsible for the characteristic combustion occurring after the initial delay. Therefore, fuels with high cetane number ignite shortly after the fuel injection into the cylinder resulting in a smooth, quiet engine run, but it is not necessarily more efficient. On the other hand, fuels with relatively low CN resist auto-ignition and present a longer ignition delay period. The latter is a very important parameter that required careful adjustment. In the case of a very long ignition delay, the combustion of the fuels occurs violently while in case of a short ignition delay, the fuel ignites before achieving adequate mixing and consequently the amount of the emitted gases increases. Lastly, CN is a valid ignition delay measure only in cases of a single cylinder engines. The most widely methods used for the determination of Cetane number is the traditional ASTM D613 and the ASTM D6890 methods[21]. The traditional ASTM D613 method evaluates the ignition quality of diesel samples. The fuel samples are inserted into a variable volume combustion chamber of a Cooperative Fuel Research (CFR) engine where the compression ratio is regulated to produce a standard ignition delay of 13° after the top dead centre (farthest piston position from the crankshaft). Lastly, the determination of the fuel quality is achieved by comparing the corresponding ignition delay to the reference fuel

On the other hand, the ASTM D6890 method provides a more modern approach in evaluating the ignition quality of the fuel samples. Instead of a variable volume chamber, ASTM D6890 method

employs a fixed combustion chamber to measure the ignition delay. Then the measured values are substituted into correlation equations to obtain the derived cetane number. The experimental apparatus used for the execution of this method is called Diesel Fuel Ignition Quality Tester. Both methods provide comparable results; the latter is capable of evaluating fuels that the traditional method cannot measure.

Therefore, in case of tests in real engines, two other methods are utilised to serve this purpose: The Cetane Index(CI)Reference 22 and the Diesel Index (DI) methods.

The Cetane Index (CI) provides an estimate of the ASTM cetane number (D613) of distillate fuels utilising density and distillation recovery temperature measurements[23]. It is a supplementary tool for estimating the cetane number when a test engine is not applicable and if a cetane improver is not used. CI is not valid in cases of pure hydrocarbon mixtures, residual fuels, synthetic fuels or coal tar products. The calculation of the CI can be achieved using Equation 1.1.

$$CI = 45.2 + 0.0892\left(T_{10} - 215\right) + 0.131\left(T_{50} - 260\right) + 0.05823\left(T_{90} - 310\right) + 0.901B\left(T_{50} - 260\right)$$

$$-0.420B\left(T_{90} - 310\right) + 0.0049\left(T_{10} - 215\right)^2 - 0.0049\left(T_{90} - 310\right)^2 + 107B + 60B^2 \qquad 2.1$$

Where $B = e^{[-3.5(D-0.85)]}$, D: the specific gravity at 15°C and T_x: x% distillation temperatures.

The Diesel Index (DI) is a measure of the ignition quality of a diesel fuel calculated from a formula involving the gravity of the fuel and its aniline point. Its mathematical approach is shown in Equation 2.2.

$$DI = \frac{aniline\,point * gravity}{100}$$

Equation 2.2

The aniline point is the minimum temperature of complete miscibility of an equal volume of aniline and a test sample. The higher the aniline point is the higher paraffinic content or lower the aromatic content of the fuel.

Volatility is the tendency of a substance to vaporize and is directly related to fuel's saturated vapour pressure. It is expressed in terms of the temperature (T_{95}) at which 95% of the sample is evaporated and presents a measure of the least volatile component present in the fuel sample[24]. At a given temperature, a fuel with a higher saturated vapour pressure vaporizes easier than a fuel with a lower saturated vapour

pressure. Therefore, in case of a highly volatile fuel, the transition from the liquid to the vapour state could take place at any time inside the fuel delivery system and subsequently result in vapour lock phenomenon and possibly in lower flash point. The flash point of a volatile material is the lowest temperature at which it can vaporize to form an ignitable mixture in air. Hence, fuels with a low flash point have shown an adverse effect on safety in handling and storage, while high flash point fuels seem to have an increased propensity to form deposits and smoke and cause wear in various parts of the equipment. It is evident that volatility is an important parameter which greatly affects the engine emissions. In particular, when reducing the T_{95}, the amount of the NO_x emissions is decreased, while the amounts of the emitted hydrocarbons and CO are increased. However, the proportion of the emitted PMs seems to be independent from such a reduction[20].

The density of a substance is defined as the fraction of its mass per volume unit. The density of diesel fuels directly influences the volumetric energy content (lower heating value), which in turn influences the driving moment as a function of the revolution. With higher density and same injection volume, engines provide higher performance as a result of the higher energy content; hence, with increasing density the acceleration of the vehicle will be higher. On the other hand, a reduction in fuel density leads to less NO_x emissions in Indirect Injection (IDI) diesel engines; however, emissions obtained from modern Direct Injection (DI) diesel engines do not seem to be sensitive to density changes[20,22].

In principle, the viscosity of a fluid is defined as a measure to quantify its resistance to the gradual deformation by shear stress or tensile stress. In fuels particular, it is primarily related to molecular weight and not so much to the hydrocarbon class. It also plays an important role in achieving good performance of the fuel injection system, in terms of fine atomisation and good lubrication of the fuel supply system. High viscosity fuels cause wear in the fuel injection pump, reduced atomization and vaporization of fuel, while fuels with lower viscosity decrease the velocity gradients developed inside the nozzle geometry[17] and also they may lead to less intensive cavitation phenomena and consequently to poorer atomisation. Finally, the viscosity determines the size of the droplets and the penetration of the diesel spray[5].

Surface tension has been reported[25] to be one of the most important parameters in the atomization process and subsequently in engine performance. By definition, surface tension is the elastic tendency

of a fluid to occupy the least area possible. It is sensitive to both pressure and temperature variations; surface tension linearly decreases with increasing pressure and temperature, with the latter exhibiting a greater impact on the reduction observed[26]. Fuels with high surface tension tend to oppose droplet formation processes[25], an observation which may explain the formation of fewer and finer droplets in the case of light fuels[14,27]. However, the optimization of the atomisation process is a result of the synergy between the physical properties of the fuels, such as viscosity, surface tension and density.

2.1.1 Fundamentals of fuel injection systems

A diesel engine is an internal combustion engine, meaning that the combustion of the fuels takes place within the cylinders. The main components of a diesel engine are fairly similar to those of a gasoline engine, but they are manufactured from stronger, more resilient materials which are able to withstand the intense dynamic forces developed as a result of high combustion pressure. The combustion pressure is strongly related to the compression ratio used by the diesel engine. The compression ratio is defined as the ratio of the maximum cylinder volume (when the piston is at its maximum position) over the minimum cylinder volume (when the piston is at its innermost position). In other words, it is a measure of how much the engine compresses the gasses inside the combustion cylinders. Typical compression ratios in diesel engines range between 14:1 and 24:1[28].

Nowadays, diesel engines are direct injection systems; the fuel is injected directly into the combustion cylinder via multi-hole injector nozzles. The processes taking place in the engines (i.e. atomisation, evaporation, mixing formation) occur in very fast succession and they are strongly dependent on fuel or/and injection system type and diesel engine characteristics[29].

Figure2.3 summarises the six main categories of diesel engine characteristics. In modern diesel engines, the injection system employed consist of mainly an injector and an electronic control system (i.e. common rail systems). Its operating principle is similar to the mechanically controlled injection system, but its timing is controlled by the engine control unit. The advantages of such systems rely upon their capability to obtain maximum horsepower without violating the emission tier, minimum emissions or fuel consumption at the expense of slightly increased fuel consumption/emissions and optimum performance.
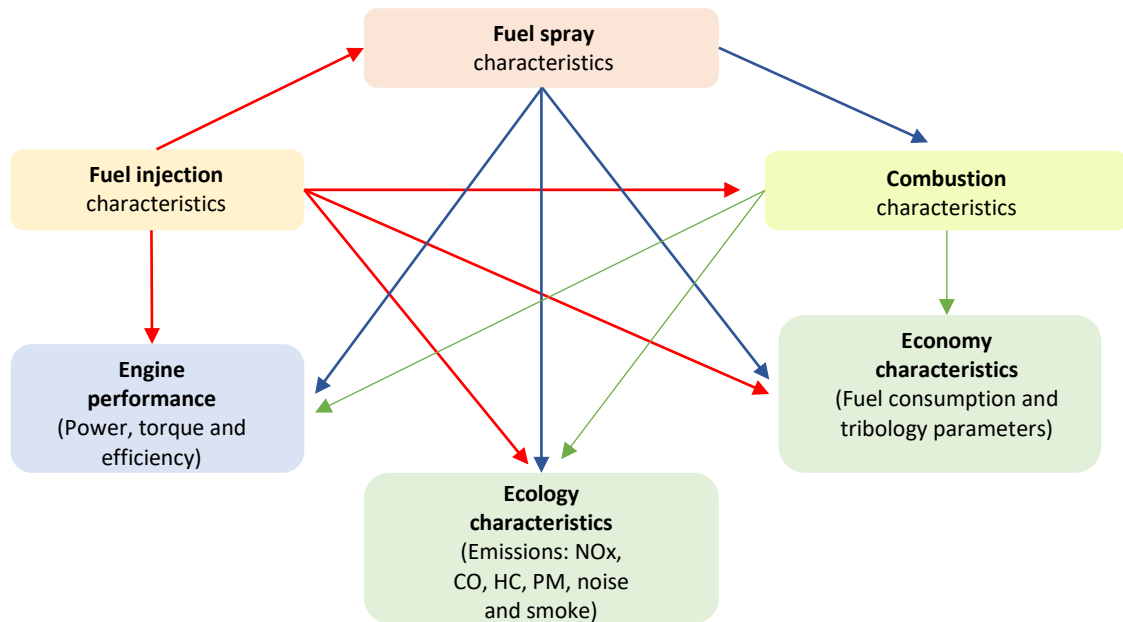
Figure2.3: Diesel engine characteristics

A widely used electronically controlled injection system is the common rail system. It employs a pump to supply fuel inside the engine, a common rail to maintain the fuel in high pressure and lastly an injector controlling the injection process. The injection operation involves three main phases a) no injection, b) start of injection and c) end of injection.

The first phase describes the case where the solenoid coil is not energised and consequently the valve body along with the ball valve are pushed by the valve spring restricting the fuel flow through the orifice plate. Hence, the pressure developed inside the control chamber increases while at the same time equivalent pressure develops on the needle shoulder. The combined effect of the fuel pressure applied to the top of the nozzle spring and to the control chamber cannot be overcome by the pressure onto the needle nozzle thus the needle remains seated.

However, when the solenoid coil is energised, the valve body moves upwards allowing the fuel to pass through the opened ball valve and eventually to reach the fuel tank. Therefore, the control chamber pressure drops below the pressure applied to the needle shoulder and the needle starts moving upwards. The fuel enters the nozzle and is injected into the cylinder via the nozzle passages (usually 4-6 holes).

Lastly, the end of the injection is a result of the ceased electromagnetic force applied to the solenoid coil. Consequently, the valve body and ball back are being pushed down and the pressure inside the control chamber rises again. This pressure increase leads to the needle returning to its initial position and subsequently to the end of the injection [30].
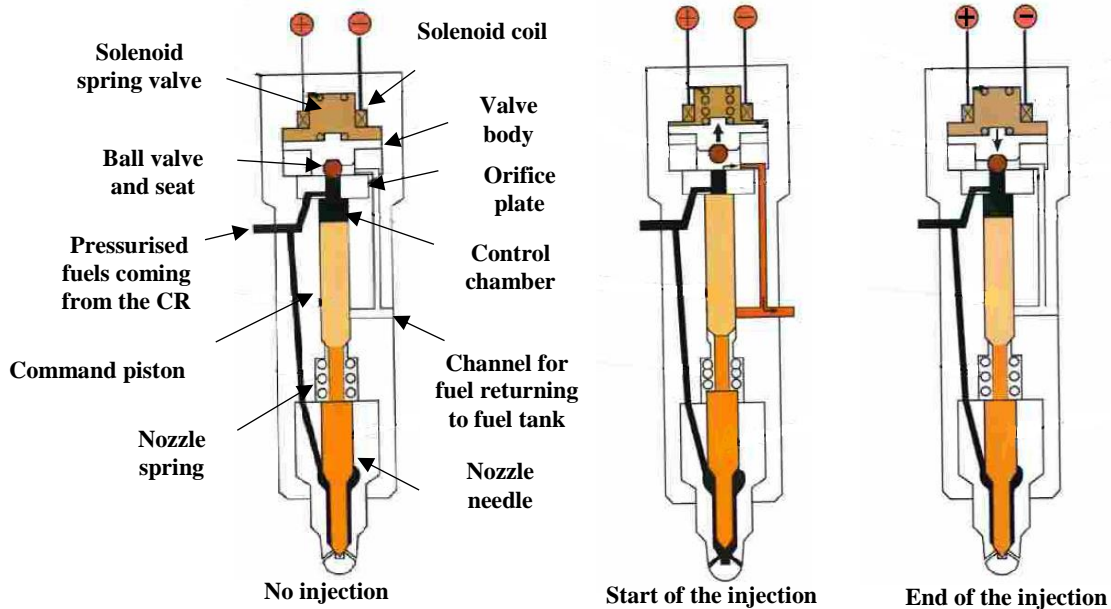
Figure 2.4: Schematic diagram of CR injection showing no injection, start of injection and end of injection stages[30].

2.1.2 Alternative fuels

Environmental problems such as global warming and air pollution have led to stricter regulations with regards to engine emissions and fuel sustainability. Therefore, fuel industry companies have been keen on finding alternative energy sources which potentially can substitute the conventional fossil fuels. Biodiesel and GTL have been proven to be two very promising potential substitutes, considering the similarities in physical properties relative to conventional diesel. In later chapters, blends of conventional diesel with the former fuels are investigated in terms of the performance of atomisation and of the internal flow phenomena.

Biodiesel

Biodiesel is an alternative fuel similar to conventional or 'fossil' diesel. Biodiesel can be produced from vegetable oil, animal oil/fats, tallow and waste cooking oil. The process used to convert these oils to

biodiesel is called transesterification. Almost all biodiesel is produced using base catalysed transesterification as it is the most economical process, requiring only low temperatures and pressures producing a 98% conversion yield. Biodiesel can be produced by either edible (sunflower oil, peanut oil, coconut oil etc.) or non-edible (jatropha oil, mahua oil) feedstocks; the resultant biofuels are classified in first-generation and second-generation biofuels respectively. Recently, microalgae biodiesel has captured industry's attention as a clean renewable fuel due to its promising characteristics such as high productivity and its ability to convert CO into CO_2[41]. Biodiesels also have low sulphur content and relatively high cetane numbers and they can be directly blended with conventional fuels[31]. They are rapidly biodegradable and completely non-toxic, meaning spillages represent far less of a risk than those of fossil diesel. Biodiesel has a higher flash point than fossil diesel and so is safer in the event of a crash.

Blends of biodiesel and conventional hydrocarbon-based diesel are products which are most commonly distributed for use in the retail diesel fuel marketplace. Much of the world uses a system known as the "B" factor to state the amount of biodiesel in any fuel mix, e.g. 100% biodiesel is denoted as B100. There is a general agreement in the literature[31–36] that the performance and operability benefits of biodiesel include reduced HC, CO and CO2 emissions and lower visible smoke. The first two findings can be attributed to the high oxygen content in biodiesel, which promotes the further oxidation of HC and CO which subsequently leads to slightly increased CO2 levels. The reduced amount of HC is a consequence of better combustion efficiency (higher energy output) due to the presence of oxygen and higher cetane number which reduces the ignition delay and subsequently the amount of unburnt HC[34]. The results obtained with regards to the NOx emissions produced by the biodiesel combustion process are not conclusive. It has been suggested that the NOx emissions can be either reduced[31,34,37] or increased[33,36,38] depending on the nature of the raw oil material used for the production of biodiesel (i.e. neem oil, palm oil, microalgae, tallow), on the complement of additives (i.e. ethanol, cetane number improvers, oxygenated additives) and on the operating conditions (i.e. low/high engine load, exhaust temperature) of the diesel engine.

Lastly, apart from the beneficial effects of the physical properties of biodiesel apart from the beneficial effects on the diesel engines (good lubrication, lower emissions etc.) on the diesel engines there are also some drawbacks. The most important is the propensity of biodiesel to cavitate less[4,5] due to reduced velocity gradients in the injector body. There are also concerns that the addition of biodiesel may lead to increased water content and microbial contamination, altered oxidation and oxidative stability and often to filter plugging[39].

Gas-To-Liquid (GTL)

GTL is a synthetic fuel which was introduced to the market in the 1970's and it is being used widely in transportation fuels, motor oils. GTL products are produced by the Fisher-Tropsch process which includes three main stages. The first stage involves the production of synthetic gas by the partial oxidation of natural gas and the removal of any impurities present in the syngas. Secondly, the processed syngas is then converted into liquid hydrocarbons using a catalyst to maximise the rate of conversion. Lastly, the third stage involves cracking and isomerisation processes, which alter the molecule chains of the products giving the desired properties. The final products are high-quality liquids such as diesel, kerosene and lubricant oils.

Such liquids contain paraffins without any aromatic compounds and they are free of sulphur and nitrogen. Due to the significantly higher paraffinic content of GTL relative to conventional diesel, the cetane number of the former is much higher. Studies on the effect of GTL diesel fuels on emissions and engine performance[40,41] have shown that the amount of the HC, CO, NOx and PM emissions is considerably reduced as a consequence of the higher cetane number and lower aromatic content after testing the engines at both low and high loads. The lower smoke and soot emissions facilitate NOx reductions and it has also has been observed that the levels of CO_2 are increased, therefore the combustion of GTL may contribute to global warming. Lastly, Maly[41] has reported an increased fuel consumption of 5% in the case of cold and hot test of a Mercedes Benz E 220 CDI limousine 2003 engine on a chassis dynamometer. However, in terms of energy, the efficiency of GTL was improved by 2-3%.

Fuel additives

Literature review

The growing demand of the consumers for better fuel efficiency and engine performance along with the stricter environmental regulations have led to the development of effective fuels additives. There are numerous additives designed to meet, maintain and improve the fuel properties. Cetane improvers are used to increase the cetane number of the fuels and to improve the ignition quality. It is known that fuels with high cetane numbers produce lower emissions, reduce the amount of white smoke and noise during engine start up and enhance the ease of starting the engine in cold environments[22]. Lubricity additives are added to the fuels to compensate for the low lubricity of the hydro treated and low sulphur content diesel fuels. Such additives usually contain polar groups which facilitate the formation of a thin layer of lubricant on metal surfaces preventing equipment wear. A solution to the severe problem of deposit formation in FIE is the usage of detergents and dispersants. They contain both polar and non-polar groups which can prevent deposit formation and also clean up existing deposits. Such capabilities rely upon the ability of the polar group to adhere to the deposits and deposit precursors and of the non-polar group to dissolve them in the fuel. Several types of additives can be used to inhibit oxidation, thereby reducing formation of gums and precipitates. This extends the storage life of the fuel. Such additives are antioxidants, stabilizers and metal deactivators. Biocides are used in the prevention of fuel filter blockages by reducing the formation of bacteria and fungi. In colder temperatures, low temperature operability additives may be added to lower the cloud point or the pour point or to improve the cold flow properties of the fuel. The beneficial effects of such additives include the temperature reduction at which paraffins solidify and form waxes, the prevention of the freezing of the fuel lines and lastly to the improvement of the low temperature operability and cold flow properties[20]. Other vehicle performance related additives include smoke suppressants which enhance the combustion quality, resulting in reduced smoke levels; emulsifiers and dehazers, which facilitate the water separation from the fuels. Anti-foam agents are added to the fuels to prevent foam formation during pumping process. The foaming interferes with the complete filling of the tank and/or results in fuel spill. Lastly, the addition of dyes serves the grade identification of the fuels for regulatory purposes[22,39]. Examples of additives, which are not related to vehicle performance, include conductivity improvers and anti-drag agents. Conductivity improvers are utilised to improve the conductivity of the fuel. Fuels with low conductivity exhibit higher fire risk, as the fuel can possibly act as an insulator facilitating the

charge accumulation, the discharge of which could potentially initiate a fire. Lastly, anti-drag agents are utilised to improve the pipeline flow rates. Typically, such agents are polymers of high molecular weight capable of altering the turbulent flow characteristics. However, they do not affect the fuel performance as they break down into smaller molecules after pumping process.

2.2 Cavitation- Bubble nucleation, growth and collapse dynamics

2.2.1 Cavitation phenomenon

Cavitation is a phenomenon frequently observed in various industrial configurations such as rotating machinery, injectors etc. In principle, cavitation occurs when the local fluid pressure drops below the vapour pressure, giving rise to the formation of vapour cavities. In the case of injection systems, the fuel is injected into the cylinder under high pressure through the nozzle passages. The large pressure gradients formed in the nozzles usually lead to local boiling and eventually to the formation of vapour cavities in the liquid fuel. Cavitation phenomenon can be classified into four different types according to the nature of the provoking source of cavitation. The four types of cavitation along with their main features are summarised in Table 2.1.

Table 2.1: Types of cavitation and their main features[42].

Cavitation Type	Disturbance Source	Brief Description
Acoustic	Sound waves	Sound waves cause pressure variations
Hydrodynamic	Geometric configuration	Geometric configuration creates velocity variations which cause pressure changes
Optic	Photons of high intensity light	Photons rupture the liquid continuum
Particle	Beam of elementary particles	Beam ruptures the liquid continuum

Acoustic cavitation

Acoustic cavitation is caused by sound waves, which in turn give rise to pressure variations. The fluid elements of the cavitating medium start vibrating and the incident sound waves are superimposed upon the existing pressure of the liquid. In the case of large pressure gradients applied to the liquid continuum, the distance between the molecules becomes greater relative to the distance required to keep the

molecules of the liquid together; therefore, the liquid breaks down resulting in the formation of vapour cavities. The created nuclei will grow until the negative pressure reaches its minimum value. The bubble growth is then followed by the sound wave compression cycle during which the cavitation bubbles are forced to decrease their size and possibly to collapse[43]. The relationship between the change of the bubble size and the generated pressure variations is not linear. Additionally, the energy content of the bubble during the compression cycle of the sound wave is very large, resulting in elevated temperature and pressures developing inside the bubble volume. Such conditions can potentially initiate chemical reactions and consequently cause erosion on various parts of the equipment[44].

Hydrodynamic cavitation

Hydrodynamic cavitation occurs as a result of a local pressure drop to below the saturated vapour pressure of the liquid, occurring as a result of abrupt changes in the velocity of the flowing liquid, due to geometrical features (i.e. sharp nozzle inlet). For instance, in the case of a liquid flowing in an orifice, the reduction in the cross-section gives rise to the velocity, while the pressure decreases. The flow re-expansion is then followed by the separation of the flow in the vicinity of the lower end of the orifice promoting the generation of eddies. At this point, the pressure drops as a consequence of the intensive turbulence and large friction losses. When the flow reaches a critical velocity, the pressure may fall below the saturated vapour pressure of the fluid, leading to the formation of cavitation structures. A subsequent consequence of the pressure drop is the release of gas from the cavitation bubble into the surrounding liquid[43].

Optic cavitation and particle cavitation

In principle, optic cavitation is the rupture of the liquid continuum using photons of high intensity[42]. The liquid break-down is believed to be accompanied by the emission of shock waves. Lauterborn[52] has reported the formation of a jet as a result of low liquid viscosity, which seems to play a significant role in the cavitation bubble lifetime. As soon as the intensity of the beam reaches high levels, the liquid breaks down at the locations where the laser is incident and initiating the bubble formation process. Such observations suggest that the location and the moment of the bubble generation can be known a

priori. Lastly, the cavitation phenomena caused by the liquid rupture due to its interference with a beam of elementary particles is called particle cavitation. The dynamics describing this phenomenon are very similar to the ones reported in the instance of optic cavitation[42].

In general, in any type of cavitating flow it is essential to distinguish four different stages in the evolution of the cavitation phenomenon. Figure 2.5 shows a schematic of the four stages of cavitation development.
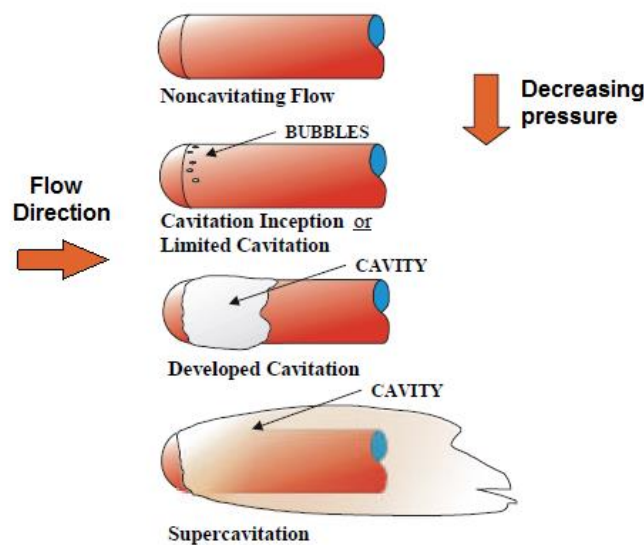
Figure 2.5: Schematic of the four stages of the cavitation evolution.[44]

The first stage refers to the non-cavitation flow, where the pressure levels are quite high suppressing bubble formation. The stage allowing the observation of the first appearance of cavitation is known as incipient cavitation. With decreasing pressure, the intensity of cavitation increases resulting in the formation of vapour pockets extending over a significant fraction of the nozzle body length. Such a phenomenon is known as developed cavitation. The enhancement of this phenomena results in the stage of supercavitation where, the vapour pockets cover the whole length of the nozzle body[45]. Usually, such events lead to equipment fouling or even failure.

Cavitation flows are usually described by a dimensionless parameter called cavitation number (σ_v). It refers to the dynamic rather than geometric parameters and it is applicable only to multiphase flows[45]. The general expression of the cavitation number is described by

$$\sigma_v = \frac{P_r - P_v}{\Delta P} \qquad\qquad \text{Equation 2.3}$$

Where P_r is the pressure at a conventional reference point (i.e. injection pressure), P_v is the saturated vapour pressure of the liquid and ΔP is the pressure difference associated with the system under examination. Depending on the application, the cavitation number obtains different forms[44,45]. For example, in case of a gate σ_v is expressed by

$$\sigma_v = \frac{P_r - P_v}{\frac{1}{2}\rho V^2} \qquad\qquad \text{Equation 2.4}$$

Of particular importance in the study of cavitation phenomena is number σ_{vi}. This parameter corresponds to a cavitation inception at any point of the system and depends on the flow geometry, the properties of the fluid, the turbulence levels etc. Any reduction in the cavitation number below this threshold leads to intensive cavitation phenomena, namely the number and the extent of the vapour bubbles significantly increase. In many occasions, the σ_{vi} number is considered to be equal to the minimum pressure coefficient (Equation 1.5), assuming that cavitation occurs at the regions of minimum pressure and the pressure threshold is the saturated vapour pressure of the liquid[44,45].

$$\sigma_v = cp_{min} = \frac{P_r - P_v}{\Delta P} = \frac{P_r - P_v}{\frac{1}{2}\rho V^2} \qquad\qquad \text{Equation 2.5}$$

2.2.2 Cavitation bubble dynamics- Nucleation, Growth, Collapse

The first investigation into the cavitation problem and bubble dynamics was undertaken by Rayleigh[46], who solved the problem of the collapse of an empty cavity in a liquid ignoring the effects of liquid compressibility, viscosity and surface tension. The derivation of the momentum equation leads to that describes the bubble boundary R(t).

$$R\ddot{R}+\frac{3}{2}\left(\dot{R}\right)^{2}=\frac{p(R)-p_{\infty}}{\rho} \qquad\qquad \text{Equation 2.6}$$

In 1944, Plesset and Prosperetti[47] further implemented Equation 2.6 including the effects of surface tension, viscosity and they concluded in the generalized Rayleigh equation (Equation 2.7) which, describes the bubble dynamics, namely thr bubble nucleation, growth and implosion.

$$R\ddot{R}+\frac{3}{2}\left(\dot{R}\right)^{2}=\frac{1}{\rho}\left[p(R)-p_{\infty}-\frac{2\sigma}{R}-\frac{4\mu}{R}\dot{R}\right] \qquad\qquad \text{Equation 2.7}$$

Cavitation is often dependent on the existence of nucleation sites. Nucleation is the formation process of small voids/bubbles in the bulk liquid. The existence of such bubbles in the liquid continuum is believed to act as the starting points for the liquid break-down[45,48]. These voids, when connected to regions of low pressure, grow rapidly to macroscopic size and eventually collapse as they reach regions of higher pressure. In general, the nucleation process is very complex and depends on various parameters such as saturated vapour pressure, contamination levels, temperature etc.[49] Depending on the nature of the nucleation sites, the nucleation process can be categorized as homogeneous or heterogeneous.

The homogeneous nucleation refers to the formation of small voids in a liquid phase without prior presence of additional phases[50]. The formation of cavitation nuclei is a consequence of thermal effects applied to the molecules comprising a volume of liquid. If the energy of a group of molecules exceeds a threshold, then this group forms to a gas-vapour pocket in the liquid continuum. The generated cavitation nuclei are unstable, as a result of the non-uniform energy distribution. Therefore, in order for these cavities to serve as cavitation nuclei, their size should not exceed a critical size (preventing the bubble rising to the liquid surface) and at the same time they should be large enough to grow when they connect with low pressure regions. Any free microbubbles present in the liquid bulk prior to the nucleation process, could potentially initiate bubble formation. However, the void fraction resulting from the presence of free nuclei is extremely small and can be considered negligible[45]. In most engineering systems, the flow is contaminated by solid particles or dissolved gases, which in turn can

be considered potential nucleation sites. In such cases, the nucleation process is called heterogeneous[48,50].

Once the cavitation nuclei are formed inside the liquid, they undergo processes which are responsible for their growth and eventually their collapse. Such processes are mainly affected by inertial, thermal, mass diffusion and liquid compressibility effects. During the early stages of the bubble growth, the bubble size increase is inhibited as a consequence of surface tension effects. After this initial 'delay period', the bubble size increases mostly due to inertial effects and pressure difference developed between the pressure inside the cavitation bubble and the ambient fluid pressure. Thermal effects are considered negligible for the whole duration of the early stages of the bubble growth. The significance of thermal effects in the bubble growth process becomes evident after the first critical time period[48] (Equation 2.8).

$$t_{c1} = \frac{P_v - P}{\rho_L} \frac{1}{\Sigma^2}$$

Equation 2.8

where P_v is the saturated vapour pressure of the liquid, P is the ambient pressure, ρ_L is the density of the liquid and Σ is a thermodynamic parameter, sensitive in temperature variations.

It is believed that prior to this critical moment, the bubble growth is mainly governed by inertial effects (inertially controlled bubble growth), whereas when this time threshold is exceeded, the significance of thermal effects becomes important. In more detail as the bubble grows, the temperature at its interface decreases. The temperature difference between the bubble interface and its surroundings generates a temperature gradient in the vicinity of the bubble volume, which is responsible for the induction of heat from the surroundings to the bubble. Consequently, the increased temperature inside the bubble volume creates favourable conditions in terms of bubble growth.[45,48] Another important mechanism involved in the bubble growth process is mass diffusion. The partial pressure of the gaseous content of the bubble is given by Henry 's law (Equation 2.9).

$$P_{GE} = Hc_{g,sat}$$

Equation 2.9

Where P_{GE} is the partial pressure of the gas inside the bubble, H is a constant and $c_{g,sat}$ is the concentration of the saturated gas in the liquid.

According to Henry's law, when the pressure of the gas inside the bubble drops, the concentration of the gas dissolved in the liquid decreases. Therefore, gas diffusion phenomena from the liquid to the bubble volume are permitted, resulting in bubble size increase. Such bubbles are believed to be unstable. However, in case of a static bubble relative to its surrounding liquid, the bubble releases gas into the liquid due to achieved equilibrium. On the other hand, in the case of flowing liquid, the gas supply from the liquid to the bubble is considered indefinite, and thus the bubble continues to grow. If the ambient pressure is greater than the partial pressure of the gas inside the bubble, the bubble should dissolve away completely. However, it has been observed that the cavitation nuclei persist indefinitely. This can be attributed to the preservation of the bubble interface, occurring as a consequence of surface contamination effects and bubble entrapment in solid particles suspended in the liquid continuum[45,48,50]. Finally, in ambient pressure oscillations, mass diffusion effects may lead to significant nonlinearities which are responsible for the observed bubble oscillation and subsequently bubble growth, even in a sub-saturated liquid environment.

Bubble collapse is an issue of particular importance, due to its consequences regarding the noise and the possible damage caused to the equipment as a result of the extreme pressure and temperature conditions occurring during the collapse. The observed violent behaviour of bubble collapse can be attributed to the pressure of the bubble. This however, does not oppose the motion of the liquid; the property of liquid volume conservation tends to concentrate the energy of the moving liquid in an increasing smaller volume. After the characteristic collapse time or Rayleigh time, a cavitation bubble obtains its maximum radius in an environment of higher pressure. The partial pressure of the gas inside the bubble becomes very small and the bubble collapse begins (Rayleigh collapse)[48] . As a result, the pressure and temperature inside the bubble volume increase. Gas diffusion from the liquid into the bubble along with liquid compressibility effects may restrict the resulting increase in temperature and pressure. However, these effects do not imply that the generation of extreme conditions or shock waves can be avoided. Moreover, high gas pressure is not actually achieved due to the non-spherical bubbles

during the collapse process. The bubble surface is deformed during the compression cycle of the bubble. At rebound, a pressure wave forms and propagates outwards at approximately the velocity of sound. Its fronts gradually steepen and the maximum pressure decreases as 1/r [45,51]. In general, the propagation of shock waves can be generated either from bubble collapse or successive bubble oscillations.

On the other hand, when the bubble collapse occurs in the vicinity of a rigid boundary, fluid motion is directed towards the wall, following a perpendicular velocity component and simultaneously gaining momentum. Since the size of the bubble under collapse decreases, the velocity developing at the centre of the bubble increases. This velocity increase leads to large pressure differences which cannot be balanced by the forces generated by the uniform gas pressure and the surface tension effects acting on the bubble. Thus, the bubble surface is subjected to involution which results in the formation of a microjet in the vicinity of the wall. The velocity of the generated microjet is high enough to cause severe damages to the wall material.[51]

2.2.3 Internal cavitation flow inside diesel injectors

The significance of the investigation of the internal flow inside diesel injectors relied upon its effects on the atomisation and combustion efficiency and its implications for deposit formation. The dynamics of diesel injector flow are very complex involving turbulent phenomena, high velocities and multi-phase structures. Additionally, the transient nature of the phenomena taking place along with the very small dimensions of the nozzle geometry add another level of complexity. However, the research community has focused its attention on the study of the internal flow, attempting to identify the flow dynamics and the multi-phase structures observed, as a function of the operating conditions, the nozzle geometry and the physical properties of diesel fuel.

The multiphase flow occurring inside the nozzle body is believed to be cavitating flow. This has been observed and reported by numerous computational and experimental studies, which have argued the presence of two distinct types of cavitation, geometrically induced cavitation, commonly appearing at the upper corner at the entrance of the nozzle passages[52–55] and string cavitation, occurring either along the central axis of the nozzle passages or inside the nozzle sac volume[56–58].

Literature review

The cavitation phenomena can be characterised by three dimensionless parameters; cavitation number (CN), Reynolds number (Re) and discharge coefficient (C_d). The cavitation number describes the nature of the flow, or in other words it expresses the intensity of the cavitation phenomena occurring inside an orifice. This number can obtain several forms and for the purposes of the present analysis it is expressed by

$$CN = \frac{P_{inj} - P_{back}}{P_{back} - P_v}$$

Equation 2.10

Reynolds number is strongly related to turbulence and it is defined as the ratio of the inertial forces to viscous forces.

$$Re = \frac{\rho U d}{\mu}$$

Equation 2.11

Above a specific threshold (Re>2100) the flow is characterised as turbulent flow, whereas below this it is laminar.

The discharge coefficient can be considered as a measurement of the flow losses and it is defined as the ratio of the actual discharge to the theoretical discharge (Equation 2.12). An increase in C_d corresponds to decreased flow losses.

$$C_d = \frac{\overset{\square}{m}}{\rho V} = \frac{\overset{\square}{m}}{\rho A u} = \frac{\overset{\square}{m}}{\rho A \sqrt{\dfrac{2\Delta P}{\rho}}}$$

Equation 2.12

Where: m: Mass flow rate of fluid through constriction (unit mass of fluid per unit time), ρ: Density of fluid (unit mass per unit volume), V: Volumetric flow rate of fluid through constriction (unit volume of fluid per unit time), A: Cross-sectional area of flow constriction (unit length squared), u: Velocity of fluid through constriction (unit length per unit time), ΔP: Pressure drop across constriction (unit force per unit area).

Another important parameter involved in the study of cavitation phenomena is K-factor. K-factor refers to the nozzle hole geometry with regards to its conicity It is defined as the ratio of the difference in

diameter between the inlet (D_{inlet}) and the outlet (D_{outlet}) of the nozzle passage over the nozzle passage length (l) [59].

$$K = \frac{D_{inlet} - D_{outlet}}{l} \times 100 \qquad\qquad \text{Equation 2.13}$$

A negative K-factor indicates a diverging hole ($D_{inlet} < D_{outlet}$), while a positive K-factor a converging ($D_{inlet} > D_{outlet}$). It has been argued that a converging nozzle supresses cavitation phenomena.

2.2.4   Cavitation patterns

It was previously mentioned that cavitation phenomena occur when the local pressure drops below the saturated vapour pressure of the working liquid. However, several theoretical and experimental studies investigating the pressure-temperature level required for a liquid to undergo the transition from the liquid to gas state, have shown that liquids often tolerate tension; this implies that the pressure threshold for cavitation onset is not the vapour pressure of the liquid, as it is conventionally assumed, but it depends on the nuclei distribution in the liquid [60]. In general, the generation of the bubbles can be achieved by two distinct nucleation mechanisms. The first one refers to the generation of microscopic voids, due to thermal motion, which are capable of rupturing the liquid continuum and of forming microscopic bubbles. This mechanism is known as homogeneous nucleation. The second mechanism is called heterogeneous nucleation and involves the presence of a wall boundary. The irregular surface of the wall often acts like cavitation nuclei[45,48]. The population and size distribution of these nuclei is unknown and rather difficult to be estimated. They depend on the flow conditions and chemical composition of the working fuel. Additionally, the dependence of the population and size distribution of these nuclei on the amount of the dissolved gas in the liquid fuel, adds another level of complexity to the cavitation phenomena. It is known that wall surface roughness and temperature significantly affect the internal flow phenomena occurring in FIE, hence it can be argued that heterogeneous nucleation has a more pronounced effect relative to homogeneous[61]. Under favourable conditions, the interaction of the formed bubbles in the vicinity of the wall with the fuel leads to their growth and eventually to their collapse. Summarising, it can be argued that homogeneous nucleation seems to be

the dominant nucleation process in case of enlarged diesel nozzle injectors, while heterogeneous is pronounced in real-sized models, due to their very small dimensions.

Independent of the position where these bubbles appear in the nozzle geometry, distinct flow regimes have been identified[53,56,62]. Initially, a bubbly flow (incipient cavitation) is formed and it mostly consists of small bubbles of uniform size, easily distinguishable. This pattern is commonly evident within the CN range between 0.65 and 1. Figure 2.6 shows an example of incipient cavitation flow regime.
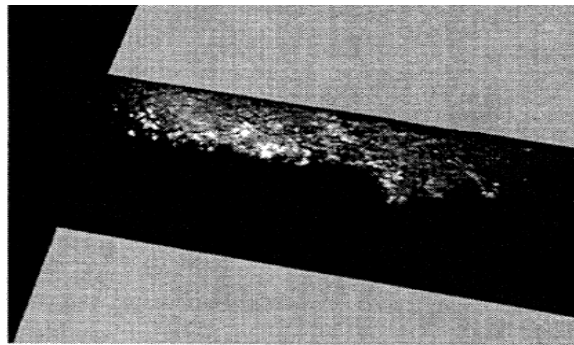
Figure 2.6: Caption of the incipient cavitation flow regime[53].

An increase in CN results in a denser bubble cloud, which does not allow the observation of individual bubbles. Above a certain level (CN~1.2) the flow changes significantly, creating low pressure regions and wider re-circulation zone at the top corner of the nozzle passages (Figure 2.7). The cavitation bubbles often collide with each other giving rise to the formation of a local cavitation film. This flow regime is known as pre-film cavitation.[56,62].
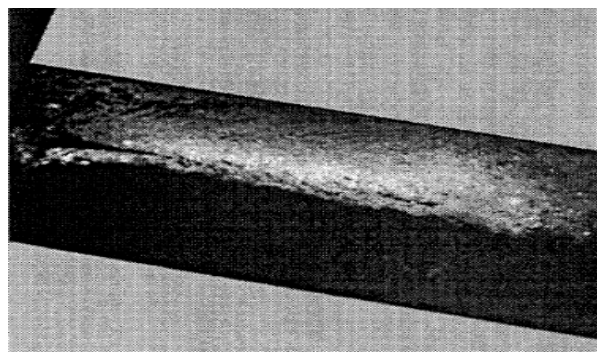
Figure 2.7: Example of pre-film cavitation flow regime[53].

A further increase in CN results in the full separation of the flow and the formation of a vapour film at the top corner of the nozzle hole inlet. This spatial continuous film often reached the exit of the nozzle hole. This regime is known as film cavitation. The optical observation of the phenomena taking place inside the injector nozzle revealed the presence of two separate clouds of bubbles originating either from the vapour film or the low-pressure regions in the vicinity of the nozzle hole entrance. The vapour film often mixed with the bubble stream and eventually reached the nozzle exit. The cavitation structures observed at the nozzle entrance are the dominant structures and frequently cover a substantial fraction of the total nozzle hole cross section (Figure 2.8). Lastly, it was observed that high CN seem not to have a further impact on the flow, since it kept its original appearance[53,54].
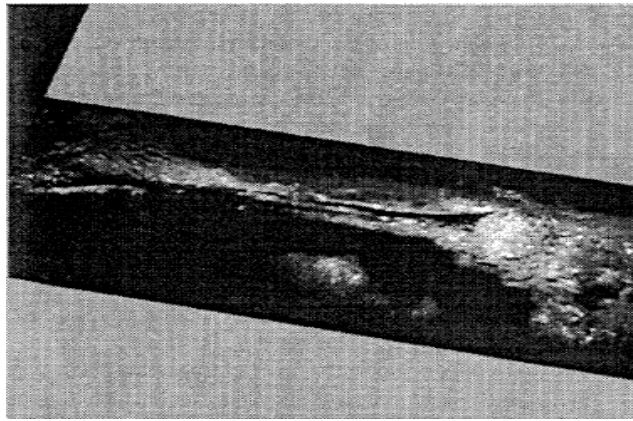
Figure 2.8: Example of film cavitation regime[53].

The three above mentioned cavitation patterns are geometrically induced phenomena and it is believed to be strongly dependent on the CN, needle lift and needle eccentricity. In more detail, the description of these phenomena above revealed that CN is a useful tool in determining the microscopic transition from one cavitation pattern to another.

An increase in CN indicated more intense cavitation phenomena up to a specific value, where its impact became insignificant. Needle lift has been demonstrated to significantly affect the resulting internal flow phenomena. The length of the vapour film at the nozzle entrance appeared to shorten with decreasing needle lift. At high needle lift, the extent of the film formed remained unchanged exhibiting quite stable behaviour. At intermediate needle lift, turbulence was more pronounced relative to high needle lift; hence, the film length shortened and the vortex phenomena developed inside the nozzle

passage. Finally, in the case of very low needle lift, turbulence became significant giving rise to the formation of a large population of individual bubbles, which often occupied the whole length of the passage[53,56,62,63].

Needle eccentricity was found to have a significant impact on the evolution of the cavitation phenomena inside diesel injector nozzles. Arcoumanis et al.[53] suggested that the region of the minimum pressure inside the nozzle passages tended to move from the upper side of the hole to the lower, when the needle was eccentric towards this particular passage. This trend was attributed to the stronger upcoming flow from the sac, which caused the separation of the flow at the lower part of the passage. This led to intensive, chaotic cavitation structures, especially in the holes closer to the needle. It was also reported that at low needle lifts, the impact of needle eccentricity was pronounced, due to the intensive turbulent phenomena, the selective restriction of the holes by the position of the needle and the less available sac volume as a consequence of the needle presence[64].

One profound effect of hole cavitation was the change of the discharge coefficient, due to the increased nozzle hole volume occupied by the cavitation structures. The investigation of this effect was essential, since it provided information with regards to the optimal design of diesel injector nozzles and the accurate prediction of the injected mass and injection rate. Soteriou et al.[65] and Arcoumanis et al.[53,62] showed that within the range of operating conditions of practical application, the discharge coefficient was dependent on CN rather than Re. After the first flow regime (CN~1.2), the discharge coefficient dropped asymptotically till it reached a minimum value, while CN increased.

In addition to geometrically induced cavitation, string cavitation was also observed to form in both the nozzle passages and the nozzle sac geometry; a phenomenon which possibly explained the needle erosion observed. This cavitation pattern appeared like a cross-flow linking two opposite sides of the nozzle sac, laying either between the needle and the needle seat or between two adjacent nozzle holes (Figure 2.9)[62,66,67]. Their formation was based on the sudden elongation of existing cavitation structures usually located at the upper corner of the nozzle holes close to the axis of symmetry. This elongation could result in the formation of the observed strings within a very short period of time[68].
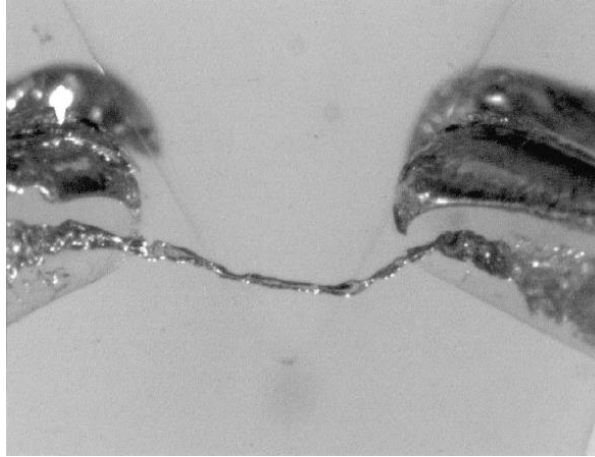
Figure 2.9: Example of string cavitation inside an enlarged diesel injector nozzle[62].

Additionally, the interaction between the high upstream annulus flow and the in-sac cross flow created high velocity gradients at the vortex core, which in turn led to the creation of low-pressure regions and consequently cavitation structures. Several studies [53,63,68] have shown that at the areas of string formation, the pressure was well-above the critical pressure for cavitation inception; therefore, the formation of such structures was unlikely to be a result of low local pressure, but rather a consequence of a vapour transfer mechanism. The presence of the in-sac cross-flow was not continuous; they frequently appeared in the vicinity of the nozzle hole entrance, while their appearance further downstream of the nozzle hole was less often. It has been also suggested that the formation of such structures was a consequence of the abrupt turning of the upstream flow at the nozzle hole entrance[68].

Apart from the strings appearing inside the nozzle sac volume between adjacent holes, stings have been observed to be formed inside the nozzle passages, at the regions where the flow vortices developed[55,67]. Gavaises et al.[68] showed that the in-hole flow exhibited a swirling pattern with a central vortical structure. This could be attributed to the non-symmetric design of the feed pipe which could introduce a non-uniform flow at the nozzle entrance. Additionally, a small degree of needle eccentricity along with the highly transient nature of the flow itself could also contribute to the development of such structures. Figure 2.10 shows string cavitation structures between adjacent holes as well as entering nozzle passages.
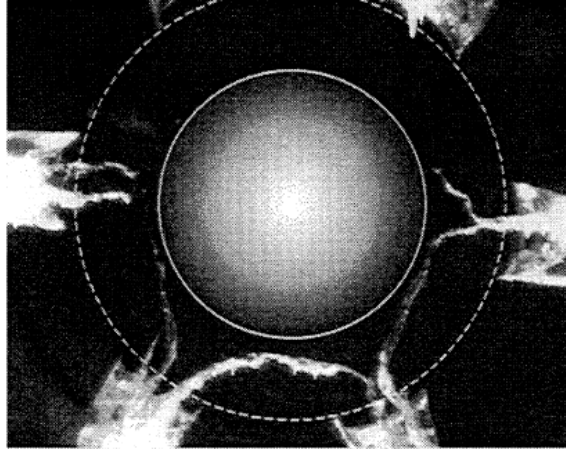
Figure 2.10: String cavitation structures linking two neighbouring holes and entering nozzle passages[53].

Another form of string cavitation, mostly seen in VCO type orifices, is known as needle string cavitation. This type seems to form on the needle surface facing a nozzle passage and eventually extending along the whole length of the passage (Figure 2.11). The root cause of this type of strings is the strong vortex flow developing at the hole axis which is capable of creating low pressure regions at its core. The frequency of this type of cavitation increases at low needle lift[56]. The CN, Re and needle lift are believed to be factors which greatly affect the evolution of the string cavitation and geometric cavitation inside diesel injector nozzles.
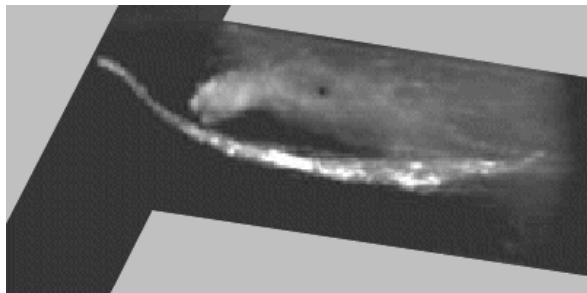
Figure 2.11: Example of needle string cavitation entering the nozzle passage and extending over the whole length of the nozzle passage[56].

The effect of cavitation number is strongly related to the needle lift and the liquid flow rate. In more detail, an increase of CN by keeping the flow rate constant and the needle at its lowest lift leads to the formation of thicker strings which maintain their original shape. On the other hand, in the case of

constant Re number and increasing CN, the appearance of strings becomes more frequent and usually extend over the total hole length[68] (Figure 2.12).
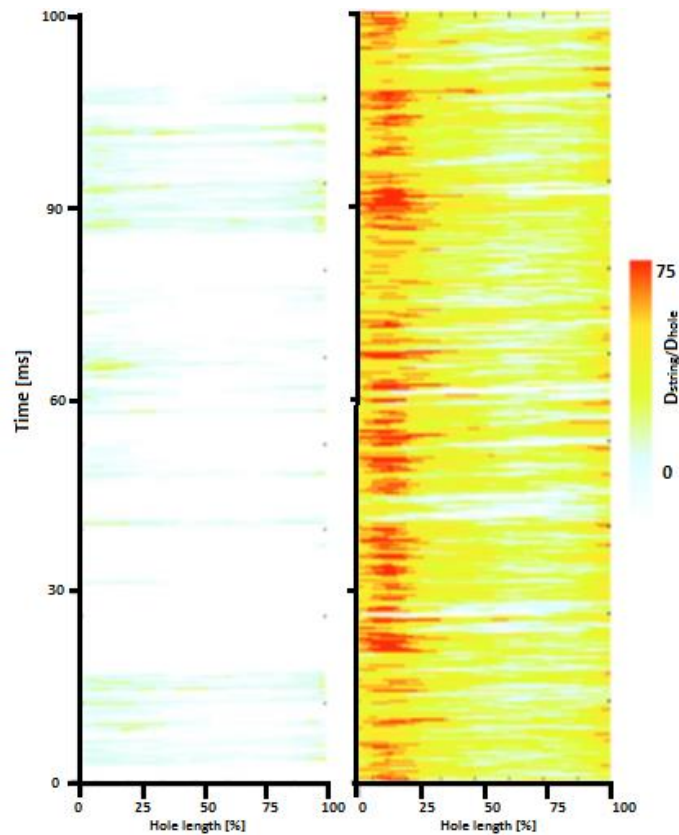
Figure 2.12: Effect of needle lift on spatial and temporal evolution of string cavitation. (a) low needle lift and (b) higher needle lift [68].

Afzal et al.[64] and Arcoumanis et al. [53] have reported that the strings appearing inside the nozzle sac volume were strongly dependent on Re number, needle lift and needle eccentricity. Reynolds number appeared to affect the structure of the string formed; an increase in Re resulted in more stable strings, indicating that their development. The needle eccentricity has been identified to be the main parameter responsible for the in-sac cross flow. This type of flow increased the likelihood of vortex formation on the one side of the sac and its suppression on the opposite side. As a result, the holes facing the eccentric needle often exhibited altered cavitation structures in comparison to those at the opposite side. For low needle lift, the effect of needle eccentricity was enhanced leading to more intensive cavitation phenomena, due to the increased turbulence. In summary, two distinct types of cavitation have been identified occurring in diesel injector nozzles, geometric cavitation and string cavitation. String

cavitation was more difficult to control, due to its more complex structure and its dependence on a number of parameters

Several studies [5,68–70] have suggested a number of ways to control or even supress cavitation. The employment of a convergent nozzle reduced the cavitation tendency compared to the cylindrical nozzles. Another, geometrical feature that has been shown to be a key to the suppression of cavitation was the rounding radii of the hole inlets. It was believed that hydro-grinded orifice inlet facilitated the development of a uniform flow in the orifice, which in turn led to less intensive cavitation phenomena and higher discharge coefficient[69]. However, these geometrical alterations were capable of reducing or even eliminating geometric cavitation structures, but not cavitation strings, which appeared less frequently but were not eliminated completely.

2.2.5   Internal flow phenomena inside enlarged and real-sized diesel injector nozzles.

The investigation of the internal flow in diesel injector nozzles required the optical access to the nozzle geometry in order to visualise the phenomena occurring. The associated cavitating flow was highly turbulent and was characterised by large pressure gradients developing during a very short period of time, typically of the order of a few milliseconds. Additionally, the flow velocities achieved reached quite large values (a few hundred meters per second). Considering the above flow characteristics and the very small dimensions of the nozzles employed in modern FIE, the optical observation of the internal flow was quite challenging. In order to overcome these limitations, early groups of researchers who studied these phenomena developed enlarged models made from transparent material (commonly Perspex) and attempted to achieve geometric and dynamic similarity between the enlarged and real-sized nozzles.

Amongst the first studies regarding the investigation of the flow pattern in diesel nozzle holes obtained in an enlarged model was the work done by Bergwerk[71]. He utilised a Perspex model with a 10mm diameter 'sac' and a 2.5mm hole. The working fluid was Shell fusus oil which exhibited a similar refractive index to the Perspex material. The optical observation led to the identification of cavitation structures and hydraulic flip. The author highlighted that the likelihood of the presence of hydraulic flip

decreases as the scale of the nozzle model decreases. He also suggested that the flow in small scale models was highly sensitive to geometrical imperfections, which can potentially result in cavitation.

Later on, Hiroyasu et al.[72] investigated the correlation between the internal flow and the emerging sprays. Water was continuously injected through two single-hole enlarged nozzles which had hydro-grinded and sharp hole inlet respectively. In the case of the sharp inlet, the authors found that a fixed cavitation structure was formed at the entrance of the hole, when the velocity exceeded a threshold value. A further increase in velocity led to the extension of this structure over the whole length of the hole and progressively to its separation from the walls. On the other hand, in the case of the smooth nozzle inlet, the flow exhibited the tendency to cavitate less due to a smoother upstream flow entering the hole.

A year later, Arcoumanis et al.[73] performed Laser Doppler Velocimetry (LDV) measurements at critical locations in an enlarged acrylic model. The diesel circulation was achieved through the employment of a steady flow rig. Their working fluid was a mixture of hydrocarbon fuel which matched the refractive index of the acrylic material of the model. The goal of the matching refractive index between the working fluid and the nozzle material was the acquisition of images with limited optical distortion, since the light was able to pass through the solid-liquid interface without refractive distortion. This experiment facilitated the quantitative characterisation of the internal flow as a function of the nozzle geometry, needle lift and pressure, providing spatially resolved, three-dimensional mean velocity and turbulent component measurements. The results obtained revealed that the recirculation zones were located (1) between the needle and the emerging jet, (2) between the nozzle body and the jet, and (3) at the sharp inlet of the nozzle passage.

A few years later, Soteriou et al.[65] carried out an investigation with regards to the structures developing in four different enlarged and real-sized nozzle models. The tests with the real-sized equipment involved pressures up to 60MPa, Re numbers between 5,000 and 30,000 and CN numbers between 0.4 and 50. The corresponding tests with the enlarged models consisted of same CN and Re range and scaled pressure to match the pressures developing in the real-sized nozzle models. The authors claimed that the transition between the different flow regimes occurred at the same CN for both models and the flow

characteristics observed exhibited great similarities under the under steady flow conditions. They also highlighted the effects of hydraulic flip, explaining that its presence suppressed turbulence and consequently reduces the quality of atomisation. Hydraulic flip has never been observed in real-sized models, however the authors claimed that there was a possibility for partial hydraulic flip to be formed inside real-sized nozzles. Lastly, they demonstrated that the discharge coefficient was independent of the scale of the model under investigation.

In the same year, Chaves et al.[74] reported findings that conflicted with that reported by Soteriou et al.[65]. They reported the formation of foamy cloud bubbles instead of cavitation films at the nozzle entrance and claimed that the cavitation bubbles had their own scale which did not scale up in enlarged models. They also claimed that the interaction between the liquid flow and the cavitation structures significantly differed in enlarged models in relation to real-size models, due to the different bubble lifetime and residence time. However, both research groups found that the discharge coefficient was not affected by the scale of the model, but by the CN.

A few years later, Arcoumanis et al.[53,62] provided an insight on the internal flow phenomena occurring inside enlarged and real-sized diesel injector nozzles. Their experimental equipment involved fast, high resolution CCD cameras along with high magnification lenses. Their optical observation revealed the presence of geometrically induced cavitation initiated at the upper side of the nozzle hole and string cavitation in both nozzle passages and sac volume. The investigation of these phenomena included the dependence of cavitation on several parameters, such as CN, Re, needle lift and needle eccentricity. The cavitation number was identified to be the most critical parameter, since the nature of the flow was strongly dependent on it. The results obtained confirmed the findings of Chaves et al.[74] regarding the formation of a vapour film instead of an opaque cloud of bubbles, when CN exceeded a certain threshold value. In particular, the present authors reported that the vapour film was a consequence of the bubble collapse at the separation zone which often extended up to the hole exit. Further downstream, a stream of bubbles was seen to detach from the film and mixed with another stream of bubbles originating from the nozzle hole entrance. The merged bubble streams eventually recombined with the original film, producing a thicker vapour film. However, the film thickness at the nozzle entrance was much greater

relative to the one observed further downstream, implying that cavitation structures at the nozzle entrance occupied a greater fractional area of the cross section relative to the exit. They also performed a comparison between the results obtained from the investigation of the enlarged and real-sized nozzles. They concluded that similar flow regimes formed in both cases, but that the transient evolution of cavitation was believed to be different, due to the different residence and life time of the cavitation bubbles. It was argued that the bubble dynamics did not scale according to the size of the nozzle model under investigation.

Other experimental and experimental studies[55,56,58,75] have investigated cavitation phenomena occurring in both enlarged and real-sized models of mini-sac or VCO diesel injector nozzles, providing quantitative information on the formation mechanisms of geometric and string cavitation. They suggested potential locations where string cavitation originated and the described potential formation mechanisms. A vortex structure was suggested to be a pre-requisite for strings to be formed, due to the low-pressure conditions at the core of these vortical structures. The strings created exhibited a helical motion, especially in the case of VCO injectors. Additionally, in this type of injector needle string cavitation was frequently observed, especially at low needle lifts. The low needle lift seemed to enhance turbulence and hence cavitation phenomena, whereas the flow at high needle lift exhibited much more stable behaviour and less intense cavitation phenomena.

In 2013, Lockett et al.[57] carried out an experimental investigation of the internal flow phenomena occurring inside two identical, conventional, six-hole, VCO diesel injector nozzles. One of them was anodised at the inner surface of the base, whereas the other was silvered. The transparent real-sized models were illuminated with white light and the resultant elastic scattering was captured on a high-speed camera. The main objective of this work was the determination of the dependence of the cavitation flow on the physical properties of diesel samples and the pressure conditions. The authors identified the presence of both geometric and string cavitation structures which contributed approximately 10% to 15% and 85% to 95% to the total area covered by cavitation structures. Furthermore, they suggested that an increase in pressure gave rise to the volume of the vapour present inside the nozzle holes. The area occupied by cavitation was found to be strongly related to the viscosity

of the fuel. In particular, fuels with high viscosity exhibited the tendency to cavitate less; hence the amount of the injected mass together with the discharge coefficient were greater relative to fuels with lower viscosity.

The recent work of Mitroglou et al.[76] utilised time-averaged X-ray micro-computed tomography and high speed shadowgraphy in an enlarged diesel nozzle, aiming to obtain quantitative fuel vapour measurements and to visualise the internal flow phenomena. Their study was based on Re and CN numbers similar to the those of a real-size nozzle model. The results obtained revealed that a vapour cloud extended over a great fraction of the bottom side of the hole, whereas the one appearing at the upper side collapsed at shorter lengths, possibly due to the flow asymmetry. They also reported that at low needle lift, the cavitation and turbulent phenomena became more intense and consequently the liquid volume fraction dropped dramatically. The utilised method was capable of capturing geometric cavitation structures, but not string cavitation, due to its highly transient nature. However, the results indicated the existence of increased vorticity at various locations which often was a requirement for string formation.

Taking into consideration the findings obtained by the investigation of enlarged and real-sized diesel injector nozzles, it can be argued that there was a great similarity between the flow regimes developed in a scaled-up and real-sized model, but also fundamental differences concerning the evolution of bubble dynamics. It was suggested that the dominant nucleation processes in the case of enlarged and real-sized nozzles were the homogeneous and the heterogeneous respectively. This observation implied that the onset and the development of cavitation were expected to differ. The growth rate of the cavitation bubbles seemed to be dependent on the pressure surrounding the cavitation bubbles rather than on the cavitation number; this added another level of difficulty to the extrapolation of the results obtained from the enlarged model to the real-sized nozzles. Overall, it could be argued that the bubble dynamics did not scale according to the size of the geometry under investigation, possibly due to the significant differences in the residence and the life time of the cavitating bubbles.

2.3 Diesel injector deposits

The existence of deposits inside the Fuel Injection Equipment (FIE) is not a new phenomenon. Material deposition is believed to be a consequence of the usage of lubricant oils, mis- or over- treatment of fuels with additives and bio-fouling effects[77]. However, recent studies have reported an increase in the frequency of occurrences where deposits are found inside FIE. Modern common rail injection systems operate at high temperature and pressure conditions, employ multiple injection schemes and high efficiency nozzles offering great flexibility in terms of precision and repeatability of an injection event. The high fuel pressure achieved in the common rail leads to elevated temperatures. The extreme operating conditions increase the likelihood of chemical reactions and deposit formation. Additionally, the protracted fuel recirculation occurring in such systems extends the residence time of the fuel in the system resulting in fuel ageing and degradation. Any material deposition on the internal surfaces is of particular importance, since they are highly susceptible to blockage, sticking or even failure. Furthermore, the stricter national/international regulations regarding the exhaust gas emissions levels have led the fuel industry to improve and/or develop fuels which incorporate bio-derived components. The new fuel blends produce lower emissions, but at the same time they exhibit an increased propensity to form deposits[78,79]. Considering the consequences arising from the improvements to CR injection system and new fuel blends, it is reasonable to suggest four main candidates contributing to the increased propensity for deposit formation in FIE[77]; (1) high injection pressure, (2) increased shear and/or temperature, (3) excessive hydro-treatmen[67]t of fuels and, (4) employment of biofuels. However, the above candidates are clearly not the only causes. A number of other possible contributors are shown in Figure 2.13.
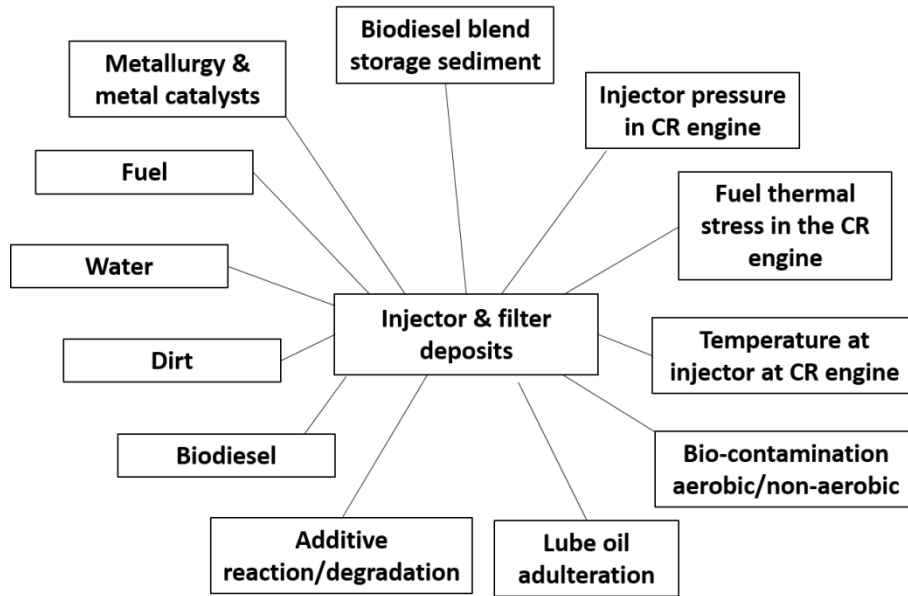
Figure 2.13: Possible causes of FIE deposits[79].

2.3.1 Types of deposits in diesel fuel injection systems

The first reports of deposit formation in FIE refer to the nozzle-hole deposits which have been managed satisfactorily through the development and use of Deposit Control Additives (DCA) together with careful design of injector nozzles[80]. Nozzle hole deposits have been the first type of deposits reported, due to issues relating to the fuel flow and injection quality. It is believed that during the combustion process, the remaining liquid fuel inside the nozzle is subjected to high temperatures resulting in expansion during the power stroke. The subsequent fuel evaporation of the lighter fuel components and degradation can possibly result in the formation of deposits. The formation process of such deposits has been shown to be affected by metal contamination, operating temperature and nozzle geometry. Zinc has been identified to significantly affect the deposit formation in diesel injection equipment. The presence of a considerable amount of zinc in the fuel and/or lubricant oil increases the propensity to form deposits[79]. Tang et al. [12] have confirmed this finding and claimed that there is a critical concentration threshold of zinc above which the rate of deposit formation increases significantly.
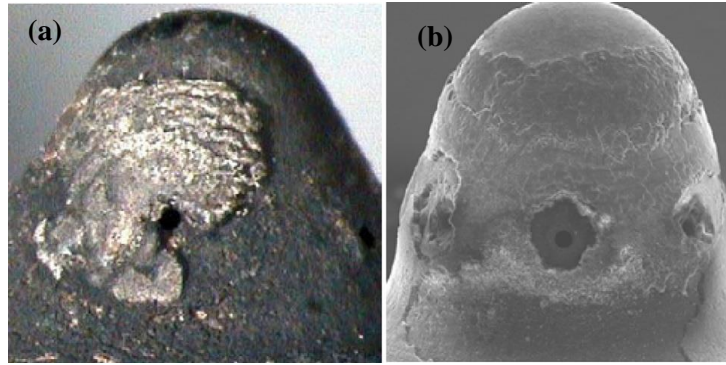
Figure 2.14: Nozzle coking. a) optical observation, b) Microscopic observation[81].
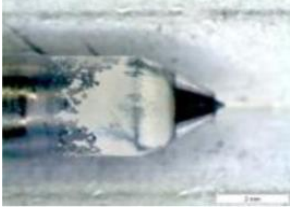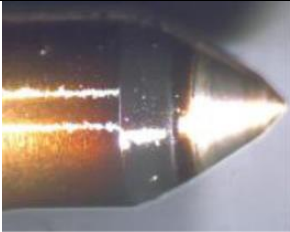
Zinc-derived deposits are believed to be at least partially reversible under zinc-free conditions or high temperature conditions, which themselves are capable of initiating decomposition process. In general, an increase in temperature leads to the acceleration of material deposition; however, when the temperature reaches a critical value, deposit decomposition is likely to occur[79,82]. Finally, several authors have reported the influence of cavitation in the process of material deposition. It is known that cavitation phenomena are strongly linked to the geometry of the injector nozzles, and seem to have beneficial effects in terms of deposit prevention on the surfaces of the injector, as a consequence of its erosion property. Tang et al.[12] investigated the impact of cavitation on deposit formation utilizing two cylindrical nozzles with and without hydro-grinded hole inlets. As expected, the nozzle without hydro-grinded inlet exhibited more intensive cavitation and therefore, the amount of the deposits observed was lower than that produced by the hydro-grinded nozzle.

Recent reports refer to deposits formed inside the injector body, widely known as Internal Injector Deposits (IID). Several methods have been used to analyse deposits in terms of composition, morphology, chemical structure and molecular weight. Some of the most applicable techniques include Scanning Electron Microscopy/ Energy Dispersive X-ray Spectroscopy (SEM/EDS), Fourier Transform Infrared Spectroscopy (FTIR), Mass Spectroscopy (MS), Liquid Chromatography/Mass Spectroscopy (LC/MS) and Mass Spectroscopy/Mass Spectroscopy (MS/MS). The investigation of the IDDs utilising the methods above have revealed that there are three distinctive types of deposits[81,83–85] (a) Metal carboxylate salts, (b) Amide lacquer and (c) Carbonaceous deposits. Table 2.2 summarises

the most frequent observed internal injector deposits including the descripiton of their root cause, typical appearance and identification based on the results obtained by EDX and FTIR analyses[80].

Table 2.2: Summary of internal injector deposits including their root cause, typical appearance and identification[80].

Deposit type	Root cause	Typical appearance	Identification
Metal carboxylate salts	Metal contamination: mostly Na, Acidic material (alkenyl succinic acids)		Soapy deposit, Soluble, EDX: C, O, Na, FTIR: 1438, 1415, 1560 cm^{-1}
Amide lacquer	Additives: DCA or residual components from PIBSI manufacture		Very hard, Insoluble, EDX: C, O, N, FTIR: 1658&1555 cm^{-1}
Carbonaceous deposits	Hydrocarbon base: Poor H/C stability. High temperature and cavitation		Fine black particulate. Coating, filter plugging EDX: C, FTIR: N/A as black

Carboxylate salts

The vast majority of carboxylate internal deposits has been observed in US heavy duty vehicles as well as in European vehicles. The investigation of this type of deposits reveals that they consist of mostly sodium or calcium ion and a carboxylate functional group[80,85,86]. Based on their physical appearance and consistency, these carboxylate deposits are known as waxes or soaps (Figure 2.15). The formation of such deposits is a consequence of the reaction between metal (sodium or calcium) contaminant and an appropriate acid source; the resulting product is an easily soluble carboxylate salt.

Figure 2.15: Appearance of a typical carboxylate salt[85].

The most common acidic and metal contaminant sources include refinery salt dryers, caustic washes, motor oil, anti-corrosion agents and most importantly Fatty Acid Methyl Esters (FAME). A number of reports in European markets suggests that the presence of Dodecenyl Succinic Acid (DDSA) or/and Hexadecenyl Succinic Acid (HDSA) anti-corrosion agents is of particular importance, as they seem to be the dominant species present in the observed deposits. It has been suggested that such agents react with the existing ions of sodium, forming an insoluble salt. The insoluble products are very fine in size and they are capable of passing via the filters and consequently depositing on the internal surfaces of the FIE[9]. The most common metal elements found in IIDs are sodium, calcium, zinc, and chlorine, with sodium being the most dominant species. On the other hand, nozzle-hole coking deposit is composed of measurable mount of zinc and small proportions of the rest of the previously mentioned elements (Figure 2.16).
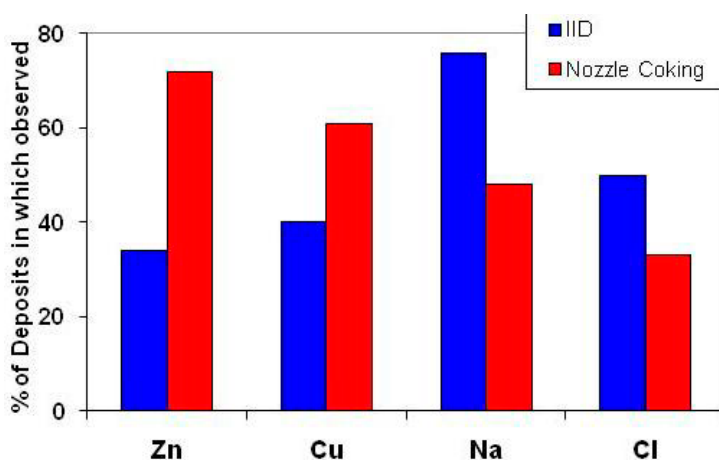
Figure 2.16: Comparison of elements found in IIDs and nozzle-hole deposits[83].

Such observations suggest that the mechanisms responsible for the formation of these two types of deposits have different origins therefore, the composition of the resulting deposits exhibits such differences.

Lacey et al.[80] attempted to reproduce the reactions taking place in FIE in laboratory scale. Their experiment involved a B5 diesel sample, a solution of sodium hydroxide (NaOH) and DDSA in high concentration to indicate the potential reaction under accelerated conditions. It was observed that the salt formation reaction is accelerated with increasing temperature, but it did not require elevated temperatures to occur. They also suggested that the precipitation process took place only in the vicinity of regions where pressure release occurred, even though the fuel was recirculated into the low-pressure circuit of the injection system. The suggested mechanisms for deposit build-up referred firstly to the natural adhesion of the formed salt without the presence of a reactive layer on the internal surfaces and secondly, to the disruption of the inverse micelles, when a temperature threshold was exceeded. Figure 2.17 shows a schematic diagram of the potential formation mechanism of the carboxylate salts.
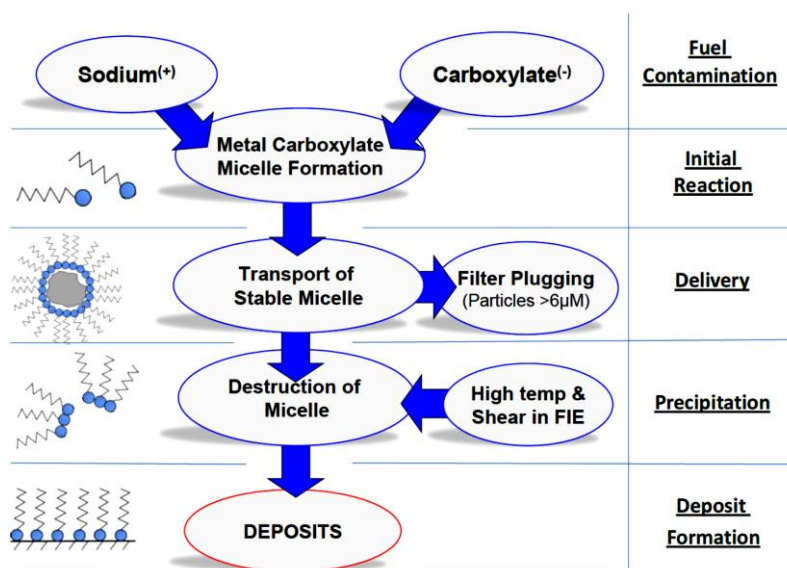
Figure 2.17: Potential formation mechanism of carboxylate salts[80].

Several authors have highlighted the effects of FAME presence in terms of deposit formation. In particular, the quality of FAME in terms of sodium content seems to greatly affect the deposit formation rate. Lacey et al.[83] compared the deposits produced by three diesel samples; an additive-free diesel

sample and two samples of high quality low sodium FAME, B10 and B30. The results indicated very low deposits with both high quality samples, similar to these obtained by the additive-free diesel. They also examined a range of poor quality FAME samples, varying the concentration of the sodium dissolved in the fuel. They concluded that poor quality FAME had a significant impact on IID formation, possibly due to the presence of several compounds containing sodium, e.g. sodium hydroxide, originating from the production process or the ageing process of biodiesel.

Organic amide lacquer

Another type of internal injector deposits is the organic amide lacquer; lacquer for its physical appearance and amide for its functional marker (Figure 2.18). This type of deposits has been associated with polyisobutylene succinimide species (PIBSI). They include any species resulting from the interaction of a polyisobutylene anhydride (PIBSA) with an amide. Such an interaction leads to the formation of a succiminide[87]. The presence of PIBSI residues on the internal surfaces of the injectors, is presumed to be the source of the observed lacquer deposits.

Figure 2.18: Typical appearance of organic amide lacquer deposits[85].

It is assumed that the formation of such deposits is a consequence of the chemical reactions taking place between the PIBSI species and the fatty acid based compounds, such as mono-acidic and di-fatty acidic materials[86]. The chemical structure of the succinimide ring in PIBSI species is believed to be unstable between the temperature range of 130℃ and 150℃. Therefore under such conditions, the ring opens

offering free carboxylate functional groups to react with other molecules[88]. Some potential reactants could be fuel additives or some fuel derived components.

A study of Ullmann et al.[84] suggested that certain types of PIBSI detergents interact with mono-acidic lubricants forming amide lacquer deposit. However, several researchers[9,86,89] attempted to re-produce the reported observations. Their findings do not provide any indication of high molecular polymeric material, which would be expected to be found in case of organic amide lacquer deposits.

Lacey et al.[80] performed some tests attempting to reproduce the material found in diesel injectors. They utilised commercial diesel fuel mixed with an ethanolic solution of sodium hydroxide (NaOH). The final solution was heated at 180ºC for 20 hours. After the cooling and the filtration process, the solution was applied onto a metal surface. The appearance of the resulting deposit was similar to the organic amide lacquer observed in FIE. Additionally, the obtained FTIR spectra showed a very good agreement with the spectra obtained by the actual IIDs.

The most important parameters affecting the formation of amide lacquer deposits are the molecular weight, the quality and the processing method of the PIBSI species. Many researchers have reported that PIBSI species with low molecular weight are susceptible to deposit formation. In particular, Ullmann et al.[84] performed a laboratory study testing two PIBSI samples, exhibiting difference in their molecular weight. The injector bench and the engine tests revealed that the PIBSI containing high levels of species with low molecular weight produced significant IDD. Similar findings were reported by Galante-Fox, Lacey et al.[80,89] who also stated that the low solubility of the low molecular weight chains along with their high reactivity at elevated temperatures are the main parameters affecting the deposit formation mechanisms. Lastly, the processing conditions of the PIBSI seem to greatly affect the deposition rate. In particular, Reid and Barker [87] prepared a range of PIBSI using different processing conditions but always utilising the same amide and low molecular species. They found that the processing conditions alter the tendency of the PIBSI to form deposits and also stated that in some cases PIBSI samples containing low molecular species did not produce significant deposits.

Literature review

<u>Carbonaceous deposits</u>

Carbonaceous deposits refer to a black material (Figure 2.19), frequently observed on nozzle springs and internal surfaces of injectors[80]. The root cause of such deposits has proved somehow difficult to identify; however, it is hypothesized to be a consequence of degradation of fuel (diesel, biodiesel) or existing deposits.

Barker et al.[10] analysed the deposits formed on an injector tip using the novel technique of hydropyrolysis. They identified a strong C_{18} peak which was associated with carboxylic acids. They also performed a GC-MS analysis for alkylbenzenes, alkylnapthalynes and alkylphenanthrenes to identify the dominant species.
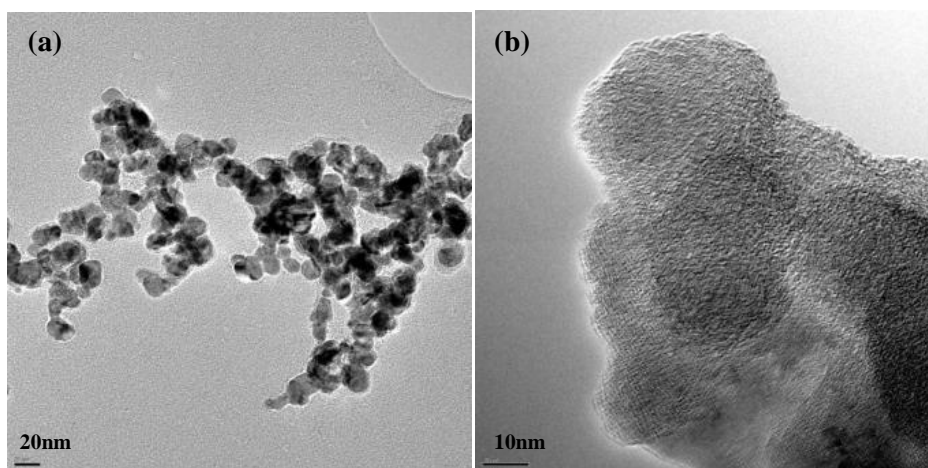
Figure 2.19: TEM images (a and b) of carbonaceous particles[90].

Despite the high complexity of the Single Ion Chromatographs (SIC) obtained, they concluded that the released hydrocarbons after hydro-pyrolysis consist of relatively small ring size and heavily alkyl substituted with no unsaturated PAHs. Such an observation suggested the occurrence of rapid fuel degradation in the cases of extreme temperature and pressure conditions. Lacey et al.[80] attempted to create black carbonaceous particles on a test stand under 240Mpa and in the temperature range between 90°C and 170°C. After a 20hours long fuel re-circulation, black carbonaceous precipitates were identified in the diesel sample. It should be noted that the fuel sample prior testing was clear without any visible contamination. The fine precipitates formed appeared to resemble the appearance of soot. It was believed that their formation occurred during the extended re-circulation process, possibly due to

the elevated temperatures developed by the cavitation bubbles collapse or the presence of hot combustion gases admitted through the nozzle holes.

2.3.2   Deposit formation mechanisms

The formation mechanism of deposits has been described by Lepperhoff and Houben[8] implementing means of basic mechanisms. This work is important from a historical point of view since later work was based on these basic mechanisms. Their model describes the interaction of a wall with gas and/or liquid flow moving down the wall. The governing effect responsible for the transport of particles is thermophoresis, which refers to the high collision frequency of gas molecules and particles as a consequence of the pressure difference developed. In practice, the outcome of this process was an increased concentration of disposable components in the vicinity of the wall. Gaseous components have the tendency to condense or adsorb at the wall, due to the lower temperature of the wall. On the other hand, liquid species were deposited by sticking, incorporation and impaction effects. Two main stages have been suggested to take place during the deposit build-up process.
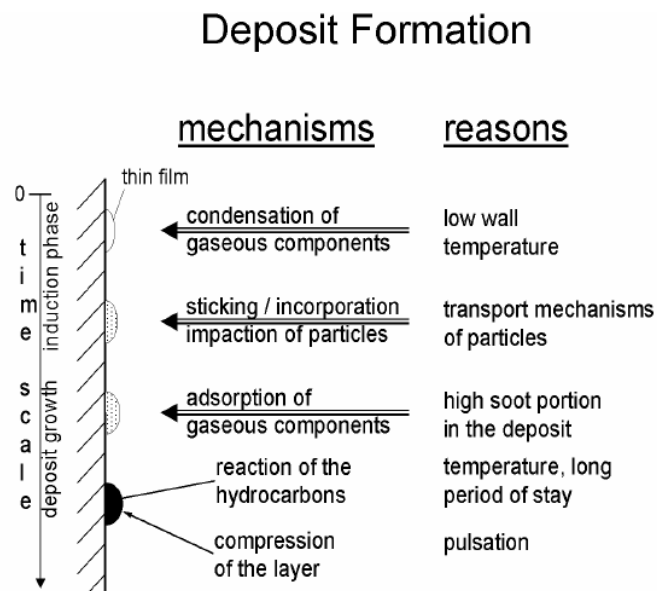
Figure 2.20: Potential deposit formation mechanism[8].

The first stage referred to the induction phase, which involved the creation of a very thin layer of high boiling point hydrocarbons through condensation process. The sticky layer formed continued to grow by additional sticking and incorporation of particles to it (growth phase). In the case of a thick deposit,

insulation effects were inevitable; consequently, the local temperature increased and gave rise to additional chemical reactions such as pyrolysis, polymerisation etc. The deposit formation mechanism described is summarised in Figure 2.20.

Another fairly similar mechanism was suggested by Caprotti et al.[91]. They claimed that the fuel present inside the nozzle volume between successive injection events was subjected to high temperatures and expansion during the combustion process and expansion stroke respectively. These processes resulted in the formation of a thin layer covering the surfaces of the nozzle. The synergy between the thin layer of deposits formed and the high temperature environment facilitated the evaporation and degradation of the fuel, which in turn resulted in deposit formation. The growth of such deposits could be attributed to the accumulation of particles present in the fuel and the adsorption of fuel components during the next combustion cycle. Table 2.3 summarises the principles of the described mechanism.

Table 2.3: Mechanism of nozzle fouling[91].

	Phenomenon	**Reason**
T I M E	• Expansion of the fuel in the nozzle (after needle sealing) • Liquid fuel at the external surfaces of the injector tip	• Expansion stroke: - Combustion pressure decreases - Injector tip temperature increases
	• Fuel degradation (sticky deposit)	• Time for degradation • Hot nozzle tip surface
	• Soot and HC adsorption	• Transport of particles • Unburned hydrocarbons
	• Deposit build up into injector holes and onto tip surface	

More recently, the group of Ikemoto et al.[82] proposed another nozzle coking mechanism. Their findings suggested that the material deposition inside the nozzle passage was not the same along its length in terms of composition and quantity. They performed an engine test utilising a |Denso common rail

injection system capable of achieving pressures up to 200MPa. A diesel sample mixed with 3ppm of zinc was injected via a mini-sac type nozzle. The authors employed the well-stablished effect of zinc in deposit formation in order to identify the specific components, locations and amounts of deposits inside the nozzle geometry. Their final aim was the understanding of the formation mechanism. The results obtained revealed that larger amounts of deposits were formed at the nozzle hole entrance relative to the exit, indicating a sign of deposit removal, possibly due to thermal decomposition or cavitation effects. The composition of the deposits at these two locations was found to be different; the composition of the species found at the nozzle exit implied that the fuel reacted with acidic components originating either from the fuel itself or the combustion gases. On the contrary, the analysis of the deposits located at the nozzle hole entrance suggested that the quantities of CO_2 and carboxylic acid observed were unlikely to be supplied by the fuel; thus, they proposed that the presence of these quantities was a result of the admission of hot combustion gases through the nozzle holes[92]. Lastly, it was evident that the hot combustion gases often reached the nozzle sac through the nozzle holes. Consequently, the admitted hot gases containing oxygen and nitrogen could easily initiate chemical reactions with the existing liquid and gaseous fuel components and eventually form deposits.
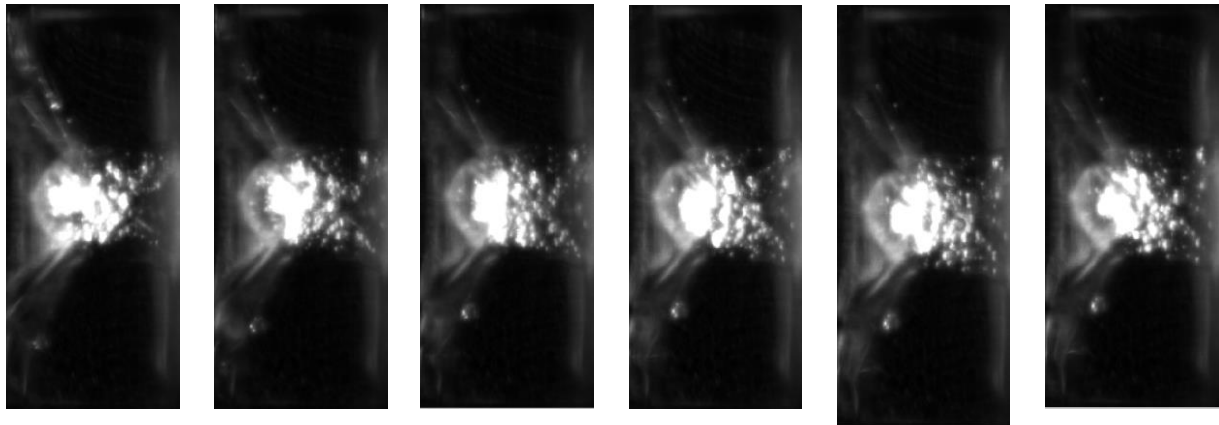
Figure 2.21: Images taken 1ms after the needle sealing. Vapour structures are moving towards the sac inside the lower passage with 1ms time steps[16].

2.4 Spray break-up mechanisms

Sprays are widely used for various applications such as agricultural, industrial and biomedical. Of particular importance is the study of the sprays involved in combustion engineering applications such as diesel injection systems. Such systems require optimum atomisation of the liquid fuel, such that suitable droplet size, spray velocity, cone angle are achieved, when the spray is injected into the combustion chamber. The optimisation of atomisation process results in improved fuel and energy efficiency and reduced exhaust gas emissions.

Sprays are tortuous fluid structures resulting from the fragmentation of liquid sheets or jets in a gaseous medium. The jet break-up can be classified into four main regimes depending on the properties of the injected fuel, the surrounding gas (inertia, surface tension) and the acting forces, (aerodynamic forces)[93]. Table 2.4 shows the four break up regimes along with the relevant drop formation criteria. The first regime is known as the Rayleigh jet break-up and refers to the jet break-up occurring many jet diameters downstream of the nozzle exit. Such a process yields structures (drops and ligaments) with greater diameters relative to the diameter of the liquid jet. It is believed to be a consequence of the generated axisymmetric oscillations acting on the surface of the liquid jet, due to surface tension effects.

When surface tension effects are enhanced by the relative motion of the surrounding medium and the jet, the break-up process becomes faster. This regime is known as first wind-induced break-up regime. This relative motion of the surrounding medium and the jet gradually increases and leads to the formation of unstable short wavelength surface waves on the liquid jet surface. Despite the opposition of the surface tension, the diameter of the subsequently formed drops is of the order of the diameter of the jet. This break-up regime is called second wind-induced break-up. Lastly, the fourth regime, known as atomisation, refers to the jet break-up occurring in the vicinity of the nozzle exit and results in an immediate disruption of the liquid jet. Such a process yields drops with an average diameter of less than the diameter of the liquid jet.

Table 2.4: Illustration of the four main break up regimes along with the associated dominant droplet formation mechanisms[94]

Break- up regime	Picture	Dominant mechanism for droplet formation
Rayleigh break-up		- Surface tension force
First wind induced break-up		- Surface tension force - Interaction with surrounding medium
Second wind induced break-up		- Surface tension force - Liquid flow turbulence - Aerodynamic forces
Atomisation		- Flow turbulence - Aerodynamic and shear forces - Surface tension force - Flow expansion

Lin and Reitz[95] reviewed the attempts of delimiting the regimes on the basis of non-dimensional numbers. Table 2.5 summarises the criteria associated with the four breakup regimes. The first two regimes are characterised by typical values of liquid Weber number (We_L), gas Weber number (We_g)

and Ohnesorge number (Oh), whereas the second wind-induced and atomisation regimes are associated to Taylor parameter (T), We_g and liquid to gas density ratio (ρ_L/ρ_G). The definitions of these dimensionless parameters are given in Equation 1.10:

$$We_L = \frac{\rho_L U_L^2 d}{\sigma} \,^a \quad , \quad We_G = \frac{\rho_G U_G^2 d}{\sigma} \,^b \quad , \quad Re_L = \frac{\rho_L U_L d}{\mu_L} \,^c ,$$

$$Oh = \frac{\mu_L}{\sqrt{\rho_L d \sigma}} \,^d \quad , \quad T = \frac{\rho_L}{\rho_G} \left(\frac{Re_L}{We_L} \right)^2 \,^e$$

Equation 2.14

where ρ_L, ρ_G are the liquid and gas density, σ is the surface tension, d is the diameter of the nozzle, μ_L is the dynamic viscosity and U_L, U_G is the liquid and gas flow velocity.

In principle, atomisation is the process associated with the disintegration of bulk liquid into a jet or a sheet and evolves into a gaseous medium with the growth of disturbances which eventually lead to the formation of ligaments and smaller droplets. The disintegration or break-up of the jet occurs when the disruptive forces exceed the effect of the consolidating forces. The stabilizing effects of liquid surface tension tend to shape the liquid into a geometry that exhibits the least surface energy, while the liquid viscosity effects oppose any change in the geometry of the liquid.

Table 2.5: Criteria of liquid jet disintegration regimes[95].

Break-up regime	Criteria
Rayleigh break-up	$We_L > 8, We_G < 0.4 \;\; or \;\; 1.2 + 3.41 Oh^{0.9}$
First wind induced break-up	$1.2 + 3.41 Oh^{0.9} < We_G < 13$
Second wind induced break-up	$13 < We_G < 40.3$
Atomisation	$40.3 < We_G , \dfrac{\rho_G}{\rho_L} > K \dfrac{\sqrt{3}}{6} [1 - \exp(-10T)]$

On the other hand, the enhancement of the external forces (centrifugal, aerodynamic forces etc.) give rise to the distortion of the liquid surface and promote the disruption of the jet[25]. Under favourable

conditions, the generated oscillations and perturbations in the liquid can be amplified to such an extent that the bulk liquid breaks up into ligaments and droplets. The foremost spray break-up into large droplets and ligaments is known as primary atomisation. The liquid structures formed reach a critical size, they become unstable; therefore, such droplets may undergo further disintegration which leads to the formation of smaller droplets. This ensuing break-up is known as secondary atomisation. It is believed that the spray characteristics result from the synergy of both primary and secondary break-up mechanisms[96]. The contribution of each process depends on the initial energy of the liquid flow. More specifically, in the case of low energy levels, primary atomisation is believed to be the dominant process, resulting in the formation of relatively stable droplets as well as large liquid ligaments, which may undergo secondary break-up. On the other hand, for liquid flows with high initial energy, secondary atomisation seems to play be the most important process leading to the formation of small droplets. Some other influential factors reported to affect the relative importance of each break-up mechanism are the transient nature of injection process/profile, the turbulence level of the liquid flow and the conditions (velocity, pressure) of the medium surrounding the spray[97]. In general, atomising sprays consist of a sequence of four fluid zones; (1) the liquid core, (2) the dense region, (3) the dilute region and (4) the evaporation zone (Figure 2.22).
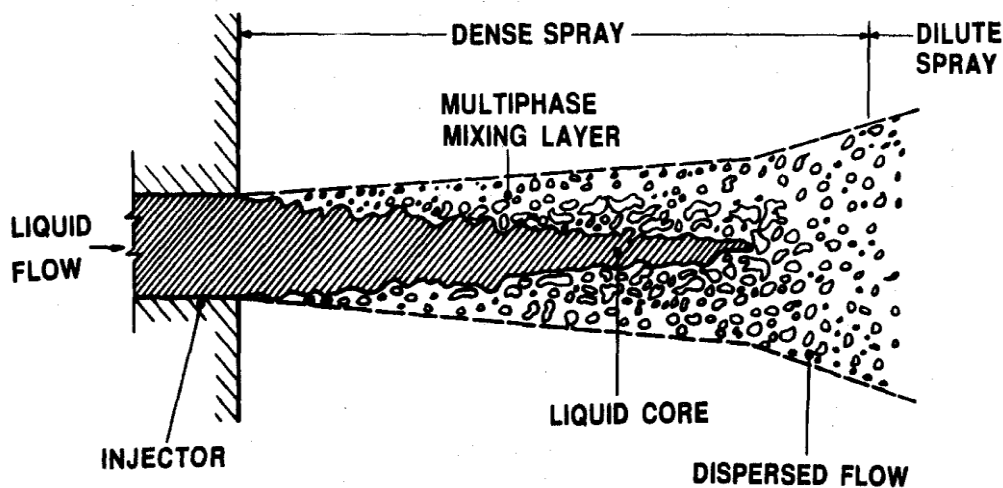
Figure 2.22: Illustration of the near injector region of an atomising spray[98].

Literature review

The four regimes are briefly described below:

- The liquid intact core is the extension of the liquid injected.

- The dense region involves multi-phase mixing layers, which consist of irregular-shaped ligaments and large droplets.

- The dilute region is associated with well-formed round droplets.

- The evaporation zone is the region where the fine droplets undergo evaporation.

Several studies[25,98] on combusting and non-combusting sprays have investigated the spray behaviour and spray characteristics in the dilute region and many nozzle diameters downstream of the nozzle exit. However, during the past decades the scientific community has been more interested in the spray dynamics developed in the vicinity of the nozzle exit, where the sprays are dense and turbid. The dilute region consists of a well-defined dispersed phase such as spherical droplets. In such a spray regime, droplet collisions are relatively infrequent and the heat, mass transfer with the drag coefficients of individual droplets are independent of the liquid volume fraction or the drop spacing. On the other hand, the dense spray region is composed of ligaments of irregular shape, large droplets and the liquid core. Such structures exhibit large liquid volume fractions which in turn affect the interphase transfer rates and the break-up of the liquid elements[99]. The importance of the atomisation process relies upon the fact that it not only determines the structure, shape and the penetration of the emerging spray, but also its macroscopic features such as drop size, velocity etc. It is believed that spray characteristics are strongly dependent on the nozzle geometry, the physical properties of the liquid, the properties of the surrounding medium and the nature of the liquid and gas flow.

Liquid viscosity seems to play the most significant role in the atomisation process, as it greatly affects the droplet size, the liquid flow rate and the shape of the emerging spray. An increase in liquid viscosity usually hinders the disintegration of the liquid jet resulting in the formation of narrow sprays with large drops[25].

Surface tension is the second most important parameter in the atomisation process, due to its resistance to an increase in the liquid jet surface area. In principle, the external forces (aerodynamic, centrifugal forces) acting on a liquid with large surface tension seems to affect the disintegration process less, as surface tension opposes an increase in liquid surface area. The effects of large liquid density in the atomisation process involve the formation of large ligaments and droplets, due to the pronounced resistance of the liquid to the disintegration process[100] (liquid inertia). On the other hand, high gas density seems to have the opposite outcome on the atomisation process. A high density gas environment is often used to improve the atomization effect of liquid sprays[101] (larger aerodynamic drag → larger We).

The most influential parameters of the liquid flow are the liquid velocity, turbulence, cavitation and injection pressure. Ghuri et al.[102]and Jankowski et al.[103] investigated the effect of the injection pressure on various spray characteristics such as drop size, spray cone angle etc. They concluded that high injection pressures result in smaller droplets due to the increased turbulent flow drag applied to the large droplets by the surrounding gas medium. According to Faeth et al.[98] flow turbulence affects the primary breakup mechanism. The sudden change in boundary conditions and pressure distribution enhances the shear, radial flow acceleration and the development of surface instabilities. The generated drag forces applied onto the moving turbulent liquid by the surrounding gas (which may itself be subjected to turbulence) contribute to the surface instabilities which eventually lead to jet break up.

It has also been observed that the contribution of cavitation to the atomisation process is important. It is believed that cavitation flows cause a rupture of the liquid jet as a result of the excessive stress being present as soon as the local pressure drops below the saturated vapour pressure[95,104]. The growth of the cavitation bubbles has been suggested to be the primary mechanism of atomisation process. Turbulence is believed to play a significant role in the determination of the location of the cavitation bubbles at the nozzle exit. The implosion of cavitation bubbles is thought to be responsible for the creation of disturbances on the liquid jet surface and for the subsequent liquid jet breakup[105,106]. Additionally, cavitation phenomena have an important impact on the spray characteristics and the structure of the emerging sprays. Several authors[54,107] have reported that intensive cavitation phenomena lead to smaller

drop sizes and large penetration lengths as a result of the enhanced turbulent effects. It has been also observed that cavitation occurring inside the nozzle volume inhibits the existence of a long spray liquid core[108,109] and may cause a significant spray asymmetry[14]. Such observations suggest noteworthy deviations from the existing theories regarding the spray structure and the phenomenological features of the sprays. Cheroudi et al.[110] developed a phenomenological model, which was further implemented by Faeth et al.[98]. This model enables the calculation of the downstream distance (x_i) from the nozzle exit where primary atomisation occurs, the length of the liquid core (l_c) and the Sauter Mean Diameter (SMD) of the spray droplets as a result of primary and secondary atomisation. The corresponding expressions are presented in Equation 2.15-Equation 2.19 .Distance x_i from the nozzle exit where turbulent primary breakup begins:

$$x_i/\Lambda = C_{xt}\left(\overline{u_o}/v'_{rms}\right)^{9/5} We_{L\Lambda}^{-0.4} \xrightarrow{\text{exp.data}} x_i/\Lambda = 3890 We_{L\Lambda}^{-0.67}$$

Equation 2.15

Nozzle diameter (d) normalized distance the liquid core survives primary atomization (l_c):

$$l_c/d = C_c\left(\rho_L/\rho_G\right)^{1/2}$$

Equation 2.16

SMD produced by primary break-up

$$d_{32} = 0.65\Lambda\left(\frac{x}{\Lambda We_{L\Lambda}^{1/2}}\right)^{2/3}$$

Equation 2.17

SMD produced by secondary break-up:

$$d_{32} = \frac{6.2\sigma}{\rho_G u_o^2}\left(\rho_L/\rho_G\right)^{1/4} We\, Re_{Ld}^{-1/2}$$

Equation 2.18

SMD for droplets formed as a result of primary and secondary breakup:

$$d_{32} = \frac{12.9\sigma}{\rho_G u_o^2}\left(\frac{x}{\Lambda}\right)^{1/3}\left(\rho_L/\rho_G\right)^{3/2} We_{L\Lambda}^{5/6} Re_{L\Lambda}^{-1/2}$$

Equation 2.19

Where C_{xt}, C_c: empirical constants, ρ_L: density of liquid phase, ρ_G: density of gas phase, σ: surface tension of the liquid phase, Λ: radial spatial integral scale of turbulence, $\overline{u}_o$: injection velocity, v_{rms}:

Cross-stream rms velocity, $We_{L\Lambda}$: Weber number, Re_{Ld}: liquid jet Reynolds number, d_{32}: Sauter mean Diameter.

2.4.1   Sprays emerging from diesel injector nozzles

A complete characterisation of diesel sprays involves the determination of their macroscopic and microscopic characteristics. The macroscopic characteristics express the interaction of the diesel spray with the surrounding medium. The physical parameters used for the macroscopic description of a diesel spray are (a) the spray tip penetration, (b) the spray cone angle and (c) the break-up length. On the other hand, the microscopic description mostly involves the characterisation of the resulting drop sizes[111].

The spray tip penetration refers to the total distance covered by the spray in the surrounding medium. It is believed to be a consequence of the synergy between the momentum of the liquid fuel and the consequent resistance exhibited by the surrounding medium. Spray tip penetration has been found to be dependent on the injection pressure, density ratio and temperature. In particular, an increase in pressure facilitates the development of spray tip penetration, while increasing temperature seems to hinder its evolution, due to the subsequent fuel density decrease. Lastly, density ratio was found to be strongly linked to aerodynamic interaction, which in turn defines the spray tip penetration[112].

A typical diesel spray angle is typically between 5 and 30 degrees and strongly affects the fuel distribution in the combustion chamber. An increase in spray cone angle leads to shorter penetration length and possibly to spray interference in the case of multi-hole injectors. It depends on the geometry of the orifice, the density ratio, the injection pressure and the Reynolds number. An increase in injection pressure and density ratio results in increased spray cone angle, while an increase in temperature to a decrease[111].

The liquid length or liquid intact core is believed to be an important parameter in terms of combustion behaviour. It is defined as the distance between the nozzle exit and the point where the separation of the first droplets occurs. Within the years several expressions (Equation 2.15, Equation 2.16) have been proposed to calculate this length, which consists of a part of the phenomenological analysis of the sprays. The liquid intact core length depends on the geometrical features of the orifice, the operating

temperature, the physical properties of the fuel and the density ratio. In particular, the length of the intact core was found to be linearly dependent on the nozzle hole diameter; hence, an increase in diameter leads to a proportional increase of the intact core length. An increase in temperature of the fuel results in decreased length due to temperature effects on density. The same impact has been observed in the cases where the density ratio increases[111].

The available literature is mostly devoted to then description of the external and peripheral characteristics of the diesel sprays. The characterisation of the internal structure of the sprays is quite challenging, due to the high optical density, especially in the vicinity of the nozzle exit. The leading controversy referring to the internal spray structure involves the length of the liquid intact core. Early experimental studies [110,113,113] attempted to determine the break-up length of the sprays emerging from diesel nozzles. The method initially developed to serve this purpose involved the measurement of the electric resistance between the nozzle and a fire wire detector located at various locations along the spray. The sprays were injected into a medium which was pressurised at two different levels, in order to identify the effect of back pressure on the break-up length. It was found that with increasing back pressure the break-up length decreased. The results obtained showed that the intact core length survived up to a few hundred nozzle diameters downstream of the nozzle exit. Similar findings were obtained by Reitz and Bracco[104] who performed a computational analysis.

However, the afore-mentioned studies involved continuously injected sprays; hence, the relevance of the measurements to the intermittent and the highly transient diesel sprays is questionable. Gülder et al.[114] investigated the structure of diesel sprays using laser diffraction and laser sheet illumination techniques. The results obtained were inconsistent with the existence of liquid intact core extending up to a few hundred nozzle diameters. The authors suggested that a complete atomisation occurred within 20 nozzle diameters. Similar findings were obtained by more recent studies[108,109,115] which also supported the argument that the liquid core did not survive up to a few hundred nozzle diameters. In more detail, Yue et al.[115] attempted to determine the mass distribution of diesel fuel sprays close to the nozzle using X-ray absorption. Their experimental setup involved the employment of a high-pressure common rail injection system, operating at pressures between 20-80MPa and a central single orifice

nozzle (⌀~187μm). The discharge of the working fluid (Diesel + Cerium) was in ambient inert gas. The quantitative, time-resolved results revealed that the core region close to the nozzle exit was a mixture of liquid and gas, with the liquid volume fraction not exceeding 77.5% in the leading edge of the spray, even in the case of low pressure. This implies that the liquid intact core broke up soon after its discharge into the surrounding medium.

A few years later, Leick et al.[109] performed X-ray measurements on diesel sprays injected from a real-sized nozzle at pressures up to 180MPa and back pressures up to 1.9MPa, in order to determine the fuel mass distribution in the dense primary break-up region. The authors argued that the fuel mass was mostly concentrated in a narrow-region around the nozzle axis. The sprays at this region was found to be a mixture of liquid and gas, implying that the existence of a long liquid intact core was unlikely.

The structure of the diesel sprays has been shown to be a result of the four main break-up mechanisms:

- Cavitation

- Turbulent instability

- Bulking

- Aerodynamic shear

The contribution of each mechanism to the final spray structure is a result of many factors, including the transient nature of the injection pressure profile, the ambient density, the geometry features of the nozzles[105]. The most dominant view of the break-up mechanism responsible for the atomisation of diesel sprays involves the initial poorly atomised fuel followed by complete atomisation, due to the highly disruptive effects of cavitation. It is known that cavitation is present throughout the injection duration, resulting in the formation of small droplets. Studies[14,116] on drop-size measurement revealed that there was no significant size variation over time and the fuel was completely atomised at a distance very close to the nozzle exit.

Considering the above, it is evident that the drop size distribution in diesel sprays is strongly dependent on the break-up mechanisms. Recent studies [14,15] have identified the significant impact of injection pressure and fuel's physical properties on the determination of the spray droplet sizes. In particular,

they found that an increase in rail pressure led to finer spray droplets possibly due to more intense cavitation and turbulent phenomena. It was also found that fuels with lower viscosity relative to conventional diesel produced smaller droplets. Jeshani[16] performed LSD measurements in sprays produced by a range of diesel fuel samples with different physical properties. The distributions of relative size indicated an axial spray asymmetry; on average larger droplets were obtained on the same side of the nozzle hole as where geometric sheet cavitation appeared in the nozzle passages[14].

With regards to the drop size variation across the spray body several experimental and computational studies [105,114,117–119] argued that the mean drop sizes show a statistically important decrease as the measurement location moved from the spray periphery to the centre-axis. However, other studies [14,16,120] and the findings of the present work indicated that the opposite to be true. This is believed to be a consequence of the different experimental techniques utilised for the execution of the experiments, the nozzle geometry and the region at which the measurements were performed.

2.5 Optical diagnostics for spray characterisation

The importance of the optical characterization of the sprays relies upon the necessity to obtain an insight into a) the physics behind the spray formation mechanisms, b) the effects of the spray properties and the geometrical features (i.e. nozzle type) on the atomisation efficiency and c) the parameters controlling and governing the structure of the emerging sprays. Due to the high complexity of atomisation process, break-up mechanisms are not fully understood, especially at the regions in the vicinity of the nozzle exit. However, during the past decades, the research community has witnessed an exponential growth in understanding of the physics and mechanisms related to spray formation and consequently to the behaviour of multiphase flows. This growth can be attributed to the rapid improvement of the laser diagnostics, due to the significant technological evolution which, made fast computers, software, lasers, fast-responding detectors and high-speed cameras available to a wider audience. Initially, the photographic, electric and mechanical methods were utilised, but were quickly replaced by laser diagnostics, due to their non-intrusive and highly accurate nature. In the following review, a description of well-established, recently developed laser techniques is reported, with regards to their main principles, applications, advantages and limitations.

2.5.1   Point Interferometry techniques

The first successful interferometry technique, developed by Yeh and Cummins[119], was employed for the determination of flow velocity, using seeding particles. Durst and Whitelaw[121] proposed a variety of optical arrangements which facilitated the optimisation of measurements regarding the local mean and fluctuating velocity components together with shear stress distributions in turbulent flows. This method involved the intersection of two coherent laser beams at a given angle θ (Figure 2.23). The recombination of the two beams led to the formation of an interference pattern in the probe volume, as a result of the superposition of the two electric fields.
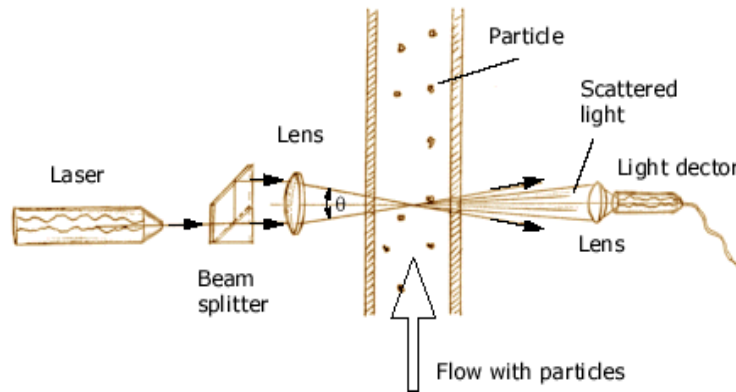
Figure 2.23: Basic experimental setup for PDA measurements[121].

In particular, the intensity-modulated light was scattered by droplets crossing the interference fringes and eventually was collected by a photo-detector, which converted the light intensity fluctuations into voltage fluctuations. Therefore, it was possible to measure the time required for a droplet to cover the distance between two subsequent fringes $\left(d = \dfrac{\lambda}{2\sin\theta} \right)$ by estimating the rate of intensity variation, known as Doppler frequency. The determination of the flow velocity using interference fringes is called Laser Doppler Velocimetry (LDV) or Laser Doppler Anemometry (LDA) method.

An extension to LDA method is Phase Doppler Anemometry (PDA) technique, which enables the measurement of droplet velocity and diameter. When light from two incident coherent laser beams is reflected, or refracted by a particle, the resultant interference fringes move in space and exist only in the direction of the reflected or refracted beams. As the particles travel within the volume under

investigation, the location of the fringe system changes; hence, the fringes crossing the mask in front of the detector cause intensity variations[122]. The frequency of the signal detected is suggested to be sensitive to the flow velocity. Furthermore, this method is capable of determining the size of the particles. The two photo-detectors record the Doppler frequency at slightly different scattering angles. This angle difference is responsible for the changes observed in the phase ($\Delta\Phi$) of the modulated light. It has been also reported[123] that in case of spherical, homogeneous particles, the detected signal is dominated by one scattering mode and the corresponding phase shift ($\Delta\Phi$) is linearly dependent on the droplet diameter. Depending on the nature of spray droplets, the scattering mode varies and subsequently the phase shift. For example, the dominant scattering mode in the case of opaque particles is reflection, whereas for transparent particles is the 1st order reflection. This is achieved by positioning the detectors at the Brewster's angle θ_s $\left(\theta_s = 2\tan^{-1}\left(\dfrac{1}{n_r} \right), \ 30^{\circ} < \theta_s < 80^{\circ} \right)$. The phase shift between two detectors is[123]:

- for reflection

$$\Phi = \frac{2\pi d_p}{\lambda} \frac{\sin\theta \sin\psi}{\sqrt{2(1-\cos\theta\cos\psi\cos\varphi)}}$$

Equation 2.20

- for 1st order refraction

$$\Phi = \frac{2\pi d_p}{\lambda} \frac{m\sin\theta\sin\psi}{\sqrt{2(1-\cos\theta\cos\psi\cos\varphi)(1+m^2 - m\sqrt{2(1+\cos\theta\cos\psi\cos\varphi)})}}$$

Equation 2.21

Where θ is the scattering angle, ψ is the elevation angle and D is the particle diameter.
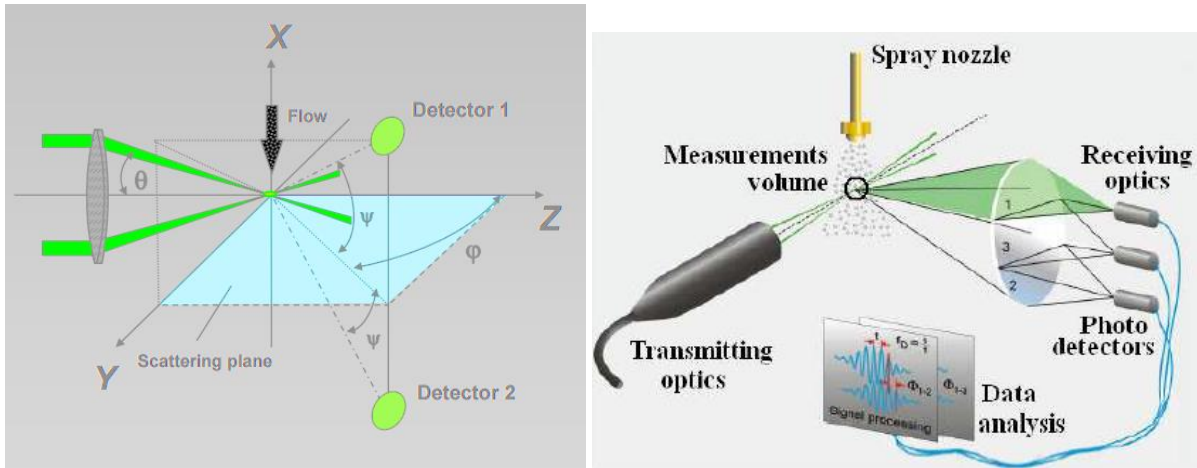
Figure 2.24: Optical configurations of Phase Doppler Anemometry. a) annotation of characteristic angles, b) Standard optical configuration[124].

The PDA technique has been shown to be useful and widely applicable, but the existence of several error sources set some limits to its application. Most of the error sources have been eliminated, but in the cases of complex phenomena such as multiple scattering effects, the solution remains unknown.

Firstly, the Gaussian beam defect stems from the Gaussian intensity distribution of the laser beam and appears for particles larger than the diameter of the focused laser beam. The resultant non-uniform droplet illumination results in the detection of both refracted and reflected rays on the detector. The non-domination of one single scattering mode leads to erroneous droplet size measurements, due to the deviation of the linearity between the phase shift and the droplet size[125,126]

Another source of error, known as slit effect, is a consequence of a droplet traversing the edge of the detection volume. In some cases, the desired scattering mode is completely suppressed. Xu and Tropea[127] investigated experimentally the influence of the slit aperture in front of the detector and suggested that the flow alignment with Y-axis avoids inaccuracies with regards to flux and concentration measurements.

The third source of errors is related to phase shifts greater than 360°. Such phase shifts usually appear in the cases of poly-disperse sprays, where the droplet sizes are unknown a priori. In order to overcome such problems, the addition of another detector is recommended[128].

Droplet shape effects should be also encountered as error sources for PDA measurements. One fundamental assumption for reliable PDA measurements refers to the spherical shape of the droplets;

however, in extreme pressure conditions the shape of the droplets becomes irregular. In such occasions, the droplet size is overestimated, mostly due to distortion effects[129]. Modern PDA optical arrangements employ multiple detectors in order to validate the spherical shape of the droplets. Any significant fraction of droplets of irregular shape are rejected.

In the cases of high density of droplets in the probe volume (phenomenon known as multiple occupancy), the detected signals overlap each other leading to reduced measurement quality. One possible solution would be the reduction of the probe volume. However, by reducing the volume, the number of the interference fringes will be reduced resulting in weak signal. Hence, the determination of the Doppler frequency becomes challenging and doubtful. Furthermore, it has been suggested[130] that the signal processing based on DFT transformation shows great potential for accurately and reliably inferring the velocity and size of multiple particles, however it does not totally resolve the multiple occupancy effects. Another side effect of multiple occupancy refers to count errors which affect the flux and the concentration measurements. Roismann and Tropea[131] proposed a statistical model to correct the errors induced by multiple drop signals.

Lastly, multiple scattering presents the most important source of errors limiting PDA application to the dilute region of the spray. Due to the complexity of multiple scattering, no corrective methods have been suggested yet. Berrocal[132] suggested that the simulation of the propagation of laser light within the spray body would provide information which will improve the understanding of the error propagation. Several researchers[127,133,134] have proposed ways to overcome the above mentioned limitations opposing reliable PDA measurements. They suggested the employment of two additional detectors (dual-mode PDA) which facilitate the comparison between the droplet sizes obtained by the standard PDA arrangement and by the added ones. They also attempted to improve the performance of the method by reducing the probe volume and increasing the laser power.

Overall, PDA has been suggested to be a highly accurate, absolute (no calibration required) technique which, enables concentration, velocity, mass flux and droplet size measurements with high spatial resolution. However, the application of the method is doubtful when the density of droplets in the probe volume is high and multiple scattering occurs.

2.5.2   Shadowgraphy - Ballistic imaging technique

Shadowgraphy is a density (pressure, temperature) sensitive technique that allows the observation of cavitation development together with the determination of droplet sizes and spray structures. It is based on back illumination and appropriate defocusing; therefore, it is capable of revealing the presence of density gradients such as pressure[135].

The principle of shadowgraphy relies upon the shadow effect that is produced onto the recording plane, due to the position of a deflected ray. The position of the deflected ray becomes brighter in comparison to the position of an undeflected ray which remains dark. Subsequently, a visible pattern of illumination variations is produced on the recording plane (Figure 2.25).
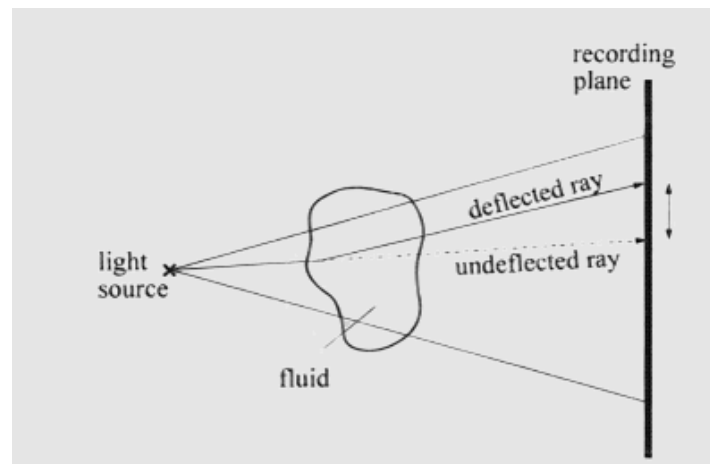
Figure 2.25: Schematic representation of shadowgraphy principles

In particular, the chosen medium is illuminated by a point light source which is incident on a collimating lens focused onto a plane. The images are recorded on a CCD sensor as a consequence of the curved trajectory of the light caused by the refractive index gradients of the medium which in turn result in the displacement and the angle deviation of the deflected ray with respect to the un-deflected ray (Figure 2.26).

According to Marzkitch[136], the signal intensity is dependent on the second derivative of the refractive index, thus the technique is sensitive to the changes of the 2nd derivative of the fluid density. As a result, he concluded that shadowgraphy is most suitable for quantitative fluid density measurements, but it can be employed for a quick survey of the flow pattern.
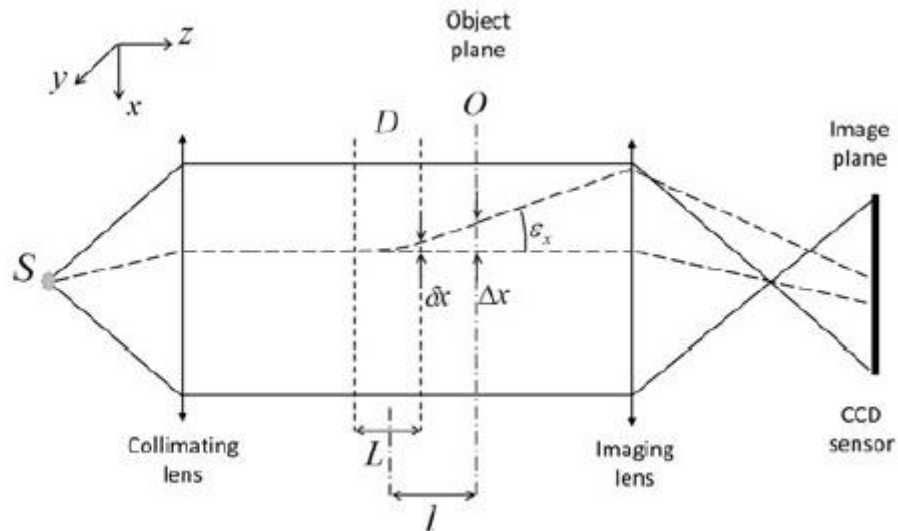
Figure 2.26: Typical shadowgraph optical arrangement[135].

Ultimately, taking into account the full potential of the method and its limitations, it can be pointed out that shadowgraphy is highly sensitive to any noise sources, due to the required double integration for obtaining the density field and to the difficulty involved in the calibration of the method as a consequence of the lack of samples with well-known second derivatives of the refractive index.

Ballistic imaging technique can be considered as an extension of shadowgraphy method, designed to mitigate obscuration caused by multiply-scattered, spatially disorganized light ("spatial noise") in the measurement volume. It is a two-dimensional, time gated method which facilitates the investigation of dense regions of sprays. Its main principle relies upon the fact that a fraction of photons traversing a turbid medium does not experience scattering; hence, the photons exit the medium with the same solid angle[137]. Such photons are called ballistic photons, because they exit the medium first after travelling the shortest possible path. There is also another group of photons, termed as snake photons, which are scattered more than once, within the forward direction and travel for a longer distance; therefore, they exit the medium at a larger solid angle and later relative to the ballistic photons. The snake photons scattered less than 4 times are called early snake photons and contain useful information with regards to the spray features. The combination of the ballistic and early photons constructs a quasi-undistorted image of the spray structure. Lastly, in the cases where the photons are scattered multiple times and exit the medium last, there is no information retained about the spray and are termed diffuse photons[138].
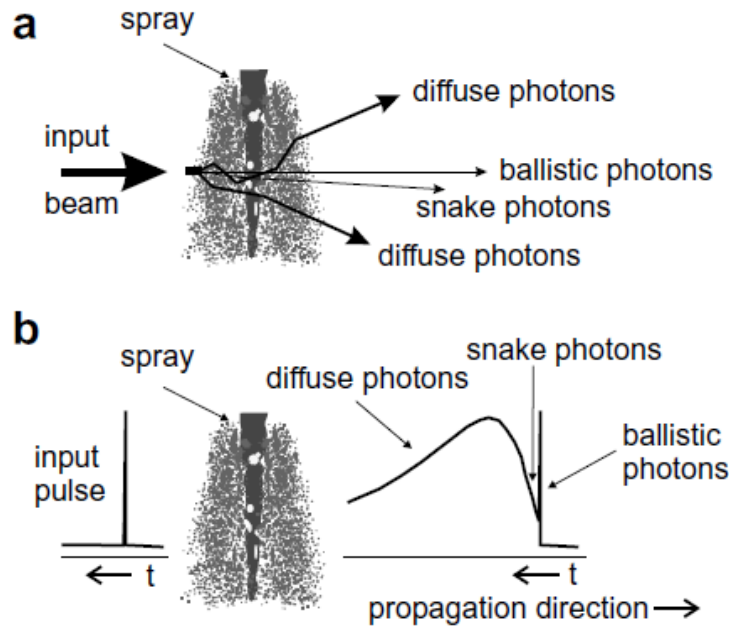
Figure 2.27: Representation of ballistic, snake and diffuse photos with a) geometric dependence and b) time dependence[138].

The key for a successful application of ballistic imaging technique relies upon the coherence of the light components, while exiting the medium, and the elimination of the diffuse photons from the collected light. This separation process can be achieved using discrimination methods that are based on the properties of the ballistic and snake photons including a) early exit time, b) coherence with the input beam, c) directionality and d) preservation of the input polarisation[138]. The separation methods refer to the employment of spatial, polarisation filters together with ultra-fast detection systems and femtosecond incident laser pulses, which enable the discrimination of the desired photons (ballistic and early snake photons). Additionally, the time gating method has been suggested to be a highly efficient separation method[137]. This method utilises a system that implements a very fast time gate (~2ps) by using the optical Kerr-effect along with a CCD camera with an on-chip multiplication gain. Such arrangements facilitate the acquisition of high resolution, two-dimensional, single shot ballistic images through dense, scattering media (Figure 2.28).
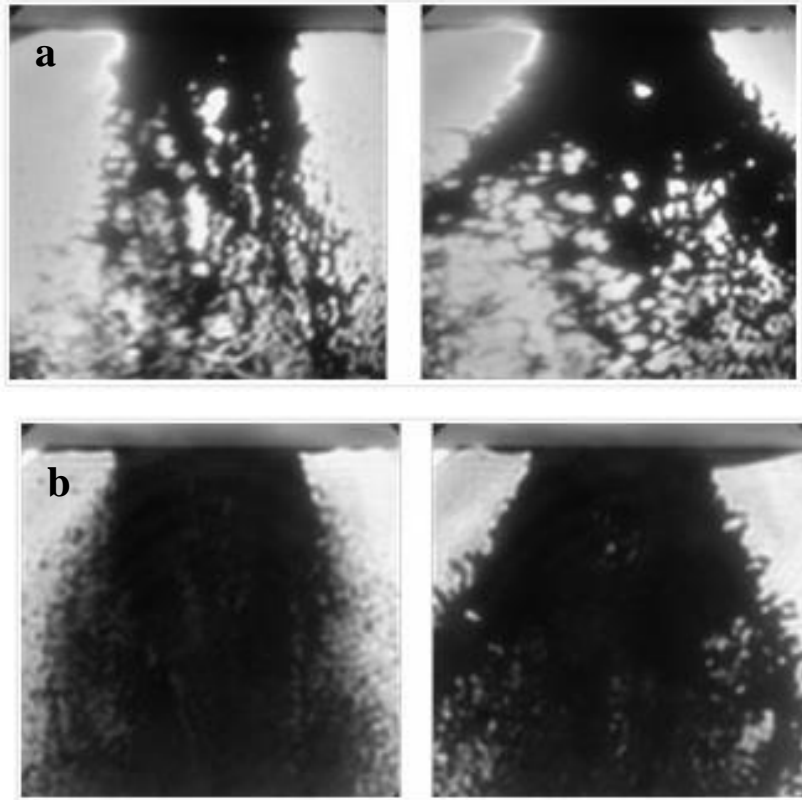
Figure 2.28: Shadowgraph images in a dense spray a) with no time gating, b) time gating to supress diffuse light.

The main advantage of ballistic imaging technique is based on the spatial resolution obtained and on the clear discrimination between the two phases appearing in the sprays. Such features provide the capability to acquire instantaneous images in dense sprays, even in the spray core. It also offers great visualisation of primary and secondary atomisation, even in the cases of dense regions where other techniques are not reliable[139]. Additionally, the ballistic imaging technique has been utilised for the determination of the statistics of various spray characteristics such as mean droplet size, number density etc. and the information extraction with regards to the spray velocity field[140].

On the other hand, the ballistic imaging method suffers from the effects stemming from the lack of contrast within the spray body, mostly due to the shadowgraph nature of the images. Furthermore, it necessitates a very fine adjustment of the time gate which basically requires the calculation of the photons traveling time within a spray by utilising sophisticated models such as Monte Carlo[132].

Ultimately, the optical arrangement is more complex and expensive relative to other techniques and demands a very fine alignment of the optics.

2.5.3   X-ray absorption technique

X-ray absorption is a non-intrusive, quantitative, time resolved technique utilised for the characterization of sprays in terms of their structural features (i.e. divergent angle, mass distribution, liquid core length). X-ray measurements have revealed that the method is capable of locating the phase transitions in 2D images and also that the high-pressure diesel sprays travel at supersonic speeds when they are subjected to high pressure. The first measurements made in diesel sprays involved polychromatic X-ray sources[141], but such high-energy dispersive X-ray beam is not suitable for quantitative spray analysis, due to the difficulties involved in the quantification of the absorption. Therefore, modern X-ray absorption technique employs monochromatic X-ray sources which, are capable of achieving time resolution of at least 1μs[142]. Figure 2.29 shows a schematic of X-ray absorption experimental setup for studying diesel sprays. The X-ray beam passes through the injection chamber in which the spray under investigation is located. The purpose of the ionization chambers placed prior and after the injection chamber is the achievement of the required alignment of the collimated beam relative to the injector. The X-ray transmission signal is then measured by a photodiode which normally offers a high temporal resolution. It is found that the transmitted signal is directly proportional to the mass and it attenuates according to Beer-Lambert Law. This relationship is expressed by Equation 2.22   .

$$I/I_0 = \exp(-\mu_M M)$$ Equation 2.22

where I and I_0 are the incident, μ_M is the mass coefficient and M is the total mass in the beam.

The photodiodes used in such arrangements are point detectors; hence, the mapping of the signal attenuation over the spray geometry is achieved by the collection of multiple measurements at various points. The averaged measurement value at each point decreases the statistical uncertainties and maximises the Signal to Noise Ratio (SNR). Since the mass absorption coefficient can be determined

accurately for a medium at a single wavelength, the time evolution of the amount of fuel traversing the beam path can be deducted by the transmission.
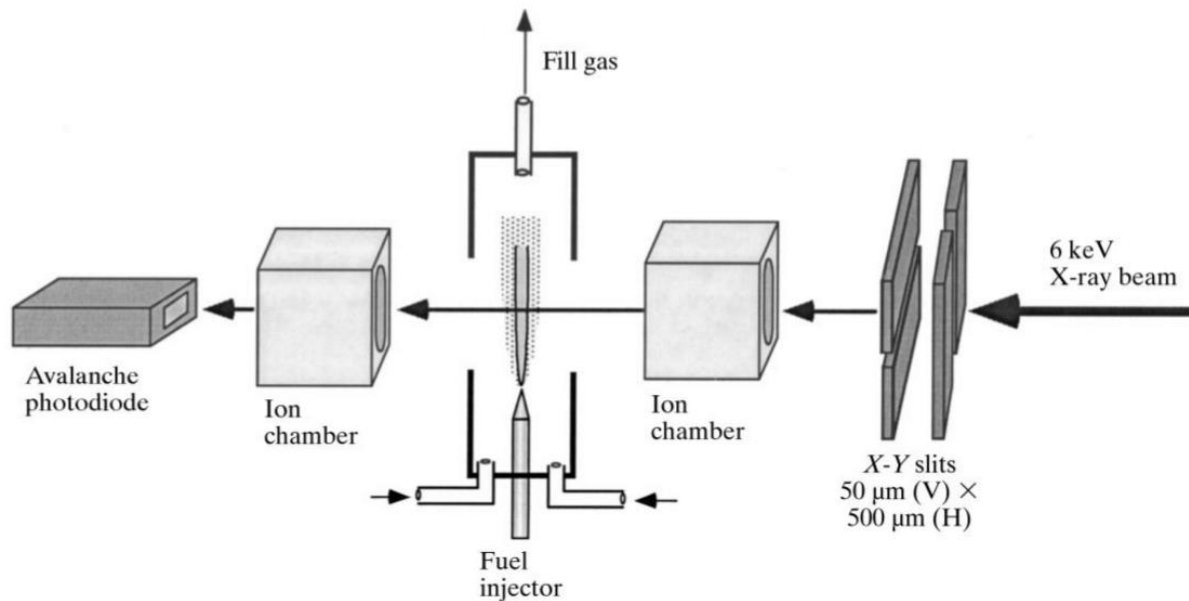
Figure 2.29: Schematic of X-ray absorption experimental setup[142].

The main advantage of X-ray absorption technique relies upon the fact that the extinction of the beam is solely a consequence of absorption without any scattering effects involved. This is a very important feature of the method, as the majority of the optical diagnostics suffer from the effects of multiple scattering. Additionally, X-rays are highly penetrative in material with low atomic number and in regions where number density is quite high. This enables the investigation of the dense spray regions in terms of the fuel mass, liquid jet break-up etc. (Figure 2.30 and Figure 2.31) where, other methods are not applicable. However, no conclusion with regards to the state (liquid, gas) of the fuel can be drawn directly from the mass measurements; further post processing of the data with appropriate models gives qualitative information about the void fraction distribution in the vicinity of the nozzle exit [142,143]. Furthermore, the fuels usually demonstrate insufficient absorption; thus, additives are required which often alter the properties of the fuel. It also cannot provide reliable results with a single shot image due to low SNR, hence image averaging over a number of injections is essential. Ultimately, the equipment required is fairly expensive and sensitive making the method less attractive to the research community.
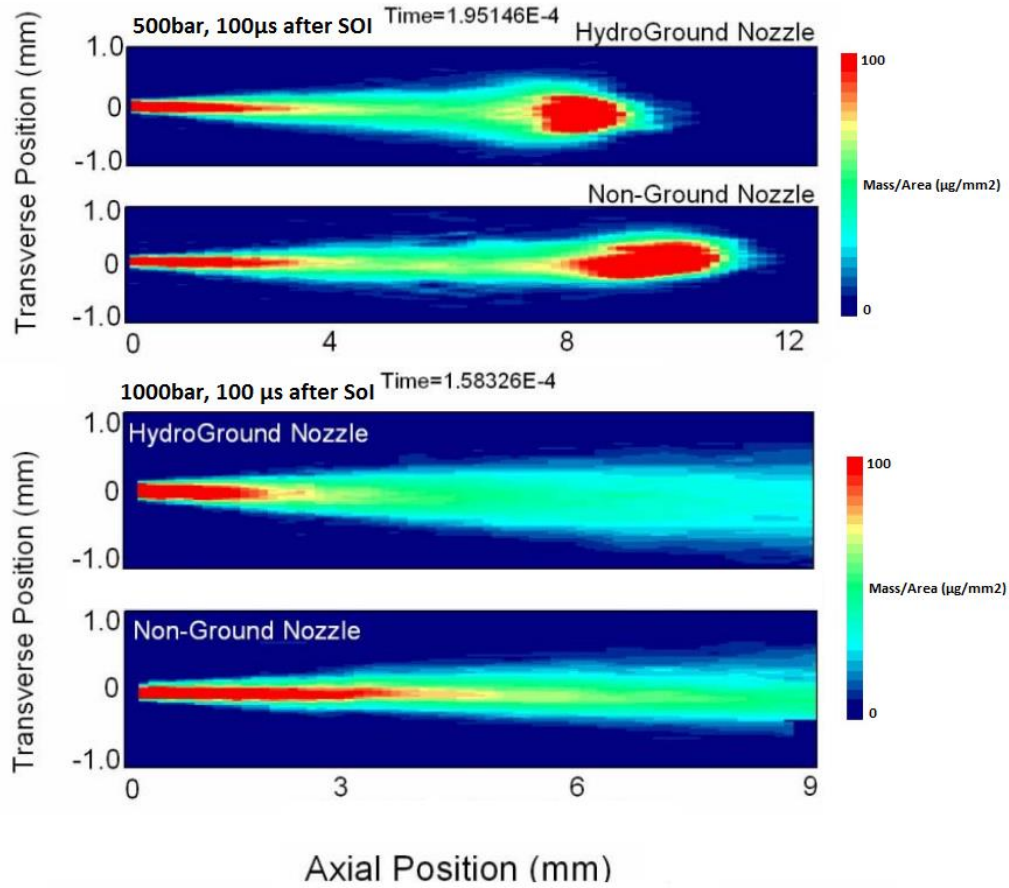
Figure 2.30: X-ray images from two different nozzles showing the mass distribution along the spray[142,143].
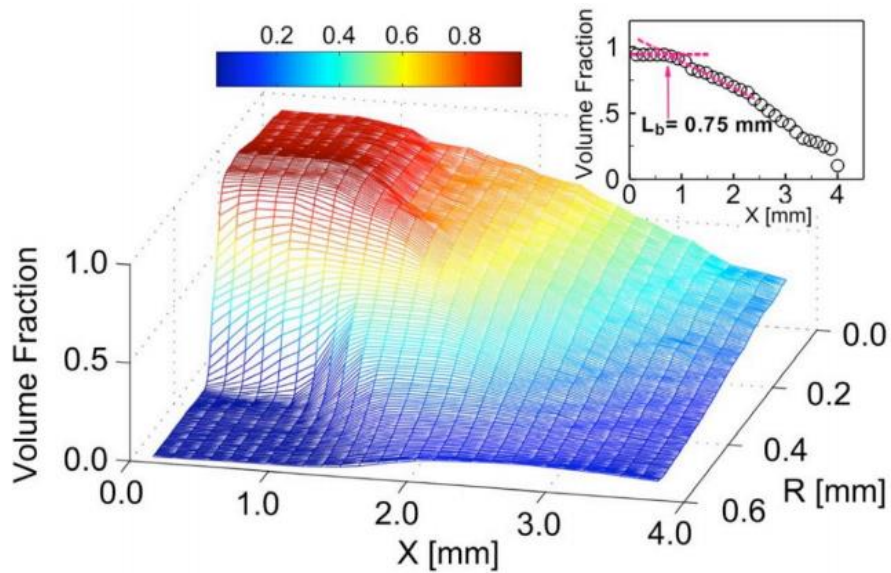
Figure 2.31: 3-D volume fraction distributions along both radial and axial direction of the spray[144].

2.5.4 Planar Laser Imaging techniques

The main principle of planar laser imaging relies upon the transverse illumination of the diesel spray with a thin laser sheet. The formation of the laser sheet is achieved by the employment of a lens assembly (positive or negative lenses), which converts the laser beam into a sheet (converging or diverging). The laser sheet traverses the spray; hence the spray droplets scatter the incident light. The scattered photons are collected by a CCD camera, usually at a 90-degree scattering angle. Such a geometry facilitates spatially resolved measurements which are capable of providing information on the spray structure (spray cone angle, length of the liquid core etc.), microscopic characteristics (SMD, number density, liquid volume fraction etc.) and spray dynamics (gas velocity vectors, vortices etc.).

2.5.4.1 Planar Mie imaging technique

Matter is composed of discrete electric charges such as electrons and protons. Particle interaction with incident radiation (light) sets the charges in oscillation, which in turn leads to emission of secondary radiation, widely known as scattering. This oscillatory motion results in a periodic separation of charge within the molecules and is called induced dipole moment (Figure 2.32). The oscillating dipole moments at a uniform frequency are considered as a source of electromagnetic (EM) radiation, resulting in elastic scattered wavelets emitted in all directions. The interference between the scattered wavelets leads to preferential scattering directions, amongst which back and front scattering are the most dominant. The determination of the final scattered directions depends on both the size and shape of the scatterer as well as on the polarization of the incident light [145] .

The penetration of light into a medium containing a number of scatterers, such as droplets, leads to its intensity attenuation. This can be attributed to the energy loss caused by the interference between the particles and the incident light. There are two types of interactions a) scattering and b) absorption. The sum of the absorption and scattering processes is known as extinction process. Lambert-Beer law (Equation 2.23) describes the intensity attenuation, assuming the light travels across a homogeneous medium with constant extinction coefficient μ_e.

$$I_f = I_i e^{-\mu_e l} \qquad\qquad \text{Equation 2.23}$$

Where I_f is the attenuated intensity, I_i is the intensity of the incident beam and l is the length of the line of sight.
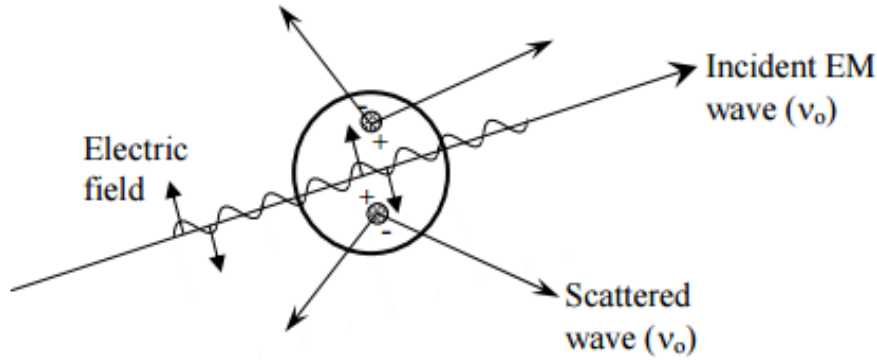
Figure 2.32: Light scattering by an induced dipole moment due to incident EM wave[145]

The sum of the absorption and scattering coefficients is equal to the extinction coefficient and they are all proportional to the density number N (number of scatterers per volume unit) and to the extinction (σ_e), absorption (σ_a), and scattering(σ_s) cross sections.

$$\mu_e = N\sigma_e \quad , \quad \mu_a = N\sigma_a \quad , \quad \mu_s = N\sigma_s \qquad\qquad \text{Equation 2.24}$$

The scattering cross section refers to a surface area where the falling energy of the incident wave is equal to the total energy scattered in all directions. Similarly, the amount of energy absorbed may be set equal to the energy of the wave incident on the area σ_a. Lastly, the energy removed from the incident wave is equal to the sum of the scattering and absorbed energies. According to the derivation of each cross section provided by Van Hulst and Huffman[146,147], it is found that in case of spherical particles the scattering cross section (σ_s) is linearly dependent on the surface area (D^2) of the scatterer. The dependence of the scattered light upon the droplet surface was also confirmed recently by several researchers [148,149]. Depending on the properties of the medium, the incident light and the scatterers, one interaction process (absorption or scattering) dominates the other. A parameter that quantifies the importance of scattering over extinction is called albedo (A) and it is described by Equation 2.25.

$$A = \frac{\mu_s}{\mu_s + \mu_a} = \frac{\sigma_s}{\sigma_s + \sigma_a}$$

Equation 2.25

The scattering of light occurring in a medium is dependent on the scattering cross section of the scaterrer. The intensity of the scattered light (I_s) is described by Equation 4.7.

$$I_s = CI_i\sigma_s$$

Equation

2.26

Where I_i is the intensity of the incident beam and C is a proportionality constant.

The deduction of the extinction efficiency Q_e is achieved by dividing the extinction cross section by the geometrical cross-sectional area projected onto a plane perpendicular to the incident beam. Similarly, the scattering and absorption efficiencies Q_s and Q_a are deduced:

$$Q_e = \frac{\sigma_e}{G}, \ Q_s = \frac{\sigma_s}{G}, Q_a = \frac{\sigma_a}{G}$$

Equation 2.27

The results of Conwell et al. [150] which were more recently confirmed by Le Gal et al.[148] show that i) the scattering efficiency dramatically increases with increasing droplet diameter from the Rayleigh limit, ii) Q_s approaches the geometrical optics limit as the diameter increases and iii) the overall spectrum consist of rapid oscillations superimposed on a slowly varying background.

In principle, light scattering theory is classified into two frameworks. Firstly, Rayleigh scattering is pertinent to small, non-absorbing (dielectric), spherical particles, whereas Mie scattering encounters a generic spherical scattering solution, without any limitations on the scatterer's size. In order for Rayleigh scattering to be applicable, χ should much less than 1, where χ is a dimensionless size parameter described by Equation 2.28.

$$\chi = \frac{\pi dm}{\lambda}$$

Equation 2.28

This criterion physically corresponds to the assumptions that the scatterer encounters a uniform electric field at any moment, due to its sufficiently small size. Therefore, the period of the oscillating EM wave is much greater than the time required for the penetration of the electric field.

On the other hand, in cases where $\chi \gg 1$, the scattering process is described by Lorentz-Mie theory [145,146]. It is based on the EM wave concept and on the application of Maxwell's equations on an isotropic, homogeneous sphere to derive the incident, scattered and internal fields. Mie scattering theory can be applied to spheres of all sizes and refractive indices as well as to radiation propagated at all wavelengths. Because of the sphere symmetry, Maxwell equations are solved using spherical coordinates; Legendre polynomials are also employed for the expansion of the incident plane wave, such that the solutions inside and outside the scatterer match at the boundary. The solution sought corresponds to a distance much greater than the wavelength, in the so called far-field zone. This solution can be expressed into two functions (Equation 4.10, Equation 4.11) [146,151] .These functions are called amplitude equations and describe an outgoing spherical wave with direction dependent amplitude and state of polarization.

$$S_1(\theta) = \sum_{n=1}^{\infty} \frac{2n+1}{n(n+1)} \{ \alpha_n \pi_n \left(\cos(\theta) + b_n \tau_n \cos(\theta) \right) \} \qquad \text{Equation 2.29}$$

$$S_2(\theta) = \sum_{n=1}^{\infty} \frac{2n+1}{n(n+1)} \{ b_n \pi_n \left(\cos(\theta) + \alpha_n \tau_n \cos(\theta) \right) \} \qquad \text{Equation 2.30}$$

where θ represents the scattering angle and the angular dependent functions τ_n and π_n are expressed in terms of Legendre polynomials by Equation 2.31 and Equation 2.32,

$$\pi_n(\cos\theta) = \frac{P_n^1(\cos\theta)}{\sin\theta} \qquad \text{Equation 2.31}$$

$$\tau_n(\cos\theta) = \frac{dP_n^1(\cos\theta)}{d\theta} \qquad \text{Equation 2.32}$$

while the scattering coefficients α_n and b_n are described by Ricatti - Bassel (Equation 2.33, Equation 2.34)

$$\alpha_n = \frac{\psi'(y)\psi_n(x) - m\psi_n(y)\psi'_n(x)}{\psi'_n(y)\zeta_n(x) - m\psi_n(y)\zeta'_n(x)} \qquad \text{Equation 2.33}$$

$$b_n = \frac{m\psi'(y)\psi_n(x) - \psi_n(y)\psi_n'(x)}{m\psi_n'(y)\zeta_n(x) - \psi_n(y)\zeta_n'(x)}$$

Equation 2.34

A more generic concept of scattering amplitudes includes the effects of the polarization of light. Any scattering problem in any direction can be described by four amplitude functions S_1, S_2, S_3, S_4, which conveniently form the Scattering Matrix $S(\theta, \varphi) = \begin{bmatrix} S_2 & S_3 \\ S_4 & S_1 \end{bmatrix}$. Therefore, the far-field electric field can be represented by

$$\begin{pmatrix} E_{\parallel S} \\ E_{\perp S} \end{pmatrix} = \frac{\exp^{(-ikR+ikz)}}{ikR} \begin{bmatrix} S_2 & S_3 \\ S_4 & S_1 \end{bmatrix} \begin{bmatrix} E_{\parallel S} \\ E_{\perp S} \end{bmatrix}$$

Equation 2.35

This equation describes a combination of effects which include the: a) different phase velocities of the plane-polarized light vibrating in different planes (double refraction), b) different phase velocities of the circularly polarized light of different sense of rotation (rotation of the plane polarization), c) different extinction of the plane polarized light vibrating in different planes, d) different extinction of the plane-polarized light of difference sense of rotation. The Scattering matrix $S(\theta,\varphi)$ relates the initial state and the final state of a physical system undergoing a scattering process. The term $\frac{\exp(-ikR)}{ikR}$ describes the outgoing scattering wave, $\exp(ikz)$ represents the incident plane wave, whereas the term $\frac{\exp(-ikR+ikz)}{ikR}$ is a transport factor that depends on the distance between the scatterer and the observer. If the scattered light is measured at a constant distance R from the scatterer, for example as a function of angle or orientation of polarization, then the transport factor becomes a constant. The total electric field (E_{tot}) depends on the incident field (E_i), the scattered field (E_S) and the interaction between the two (E_{int}). In the case of spherical particles, the scattering elements S_3, S_4 are equal to zero and the amplitude functions S_1, S_2 depend only on the scattering angle θ. Therefore, in practice all scattering measurements could be described by:

$$\begin{pmatrix} I_{\square S} \\ I_{\perp S} \end{pmatrix} = \text{const an t} \begin{bmatrix} |S_2|^2 & 0 \\ 0 & |S_1|^2 \end{bmatrix} \begin{bmatrix} I_{\square S} \\ I_{\perp S} \end{bmatrix} \qquad \text{Equation 2.36}$$

In the case of unpolarised light passing through a scatterer, the scattered light will be consisted of polarised light in the planes of observation (plane formed by the incident light source), perpendicular polarisation and parallel polarisation. Additionally, the orientation of the polarisation of the incident light significantly affects the intensity of the scattered light. Figure 2.33 shows that the light scattered from different scattering modes is altered at different scattering angles.
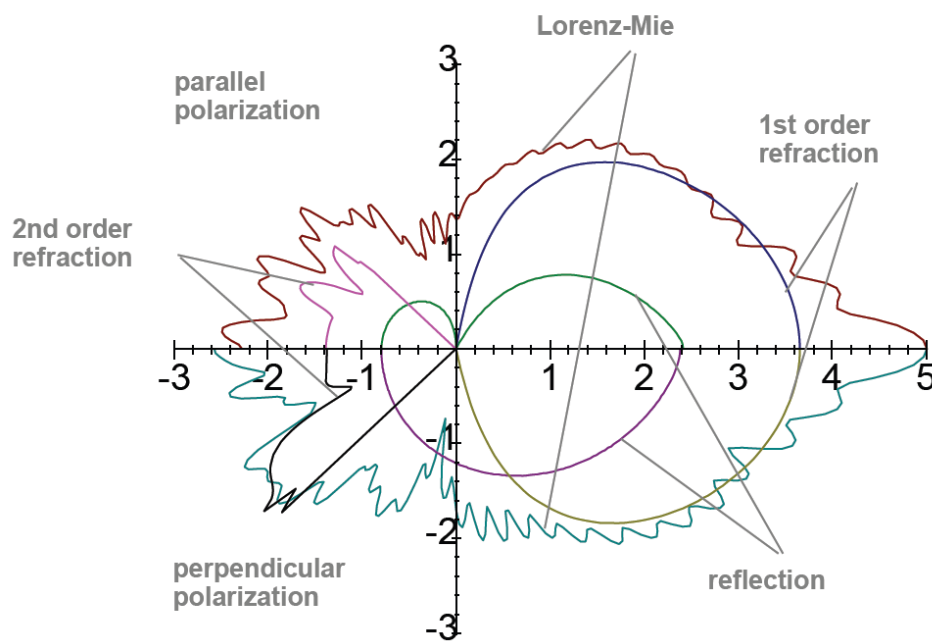
Figure 2.33: Diagram showing the intensity of scattered light from different scattering modes[152].

Parameters such as optical depth, scattering regimes and scattering orders are of a great relevance to the media containing a number of scatterers, i.e. droplets in sprays. The number of times that a photon interferes with the scatterer defines the scattering order. When no interaction occurs, the scattering order is equal to zero. The photons pass across the medium (spray) and keep their original direction. Such photons are called ballistic photons. The photons experiencing one interaction while crossing the collection of scatterers, (1st scattering order) contain most of the information about the crossed medium as their characteristics are directly related to its characteristics, i.e. spray droplets size, concentration. The range of scattering order between 2 and 9, corresponds to photons, known as snake photons, which travel a longer path along the medium relative to the ballistic photons and exit the medium along

approximately the same axis as the incident light at a greater angle[153]. In case of scattering order greater than 10, the photons are called diffused photons and exit the medium with a large solid angle after covering a long path. Additionally, the phenomenon where the radiation is scattered by particles more than one times, is called multiple scattering and induces a number of secondary effects such as light extinction and signal attenuation. Optical depth (OD) is a parameter which measures the probability of photons experiencing multiple scattering effects[132]. It is the ratio between the sample thickness and the mean free path length (Equation 2.37)

$$OD = \frac{l}{\overline{\overline{l_f}}}$$
<div align="right">Equation 2.37</div>

Depending on the value of OD or of the average scattering order, the light scattering within the medium can be categorised into 3 regimes, which are summarised in Table 2.6.

Table 2.6: Classification of the scattering regimes as a function of optical depth and scattering order.

Single scattering regime	Intermediate scattering regime	Multiple scattering regime
OD≤1, scattering order<2	2≤OD≤9, Mean scattering order	OD≤10 No dominant order

Planar Mie imaging technique is based on the principles of Mie theory and corresponds to the detection of elastic light scattered by spray scatterers, i.e. droplets and liquid ligaments. It is widely employed to obtain information with regards to the geometrical features of the spray structures. It is also possible to get information about the surface area of the droplets, as a result of the linear dependence of the scattering cross section on the square of the droplet diameter. However, Domman and Hardalupas[154] and Reveille[155] showed that there is a deviation from the D^2 dependence in the case of very small particles (less than 10μm) and a given collection of angles ($\theta_s=90°$ or $\theta_s=60°$); therefore, the application of this method needs to be carefully done or the data obtained require to be subjected to correction processes.

2.5.4.2 Planar Laser Induced Fluorescence (LIF)

Laser Induced Fluorescence (LIF) is an optical, non-intrusive technique widely used for quantitative pressure, temperature and concentration measurements. It is also capable of capturing small and large-scale flow structures as well as of providing information with regards to the mixing performance or industrially relevant devices. The use of LIF for determining the relative populations of individual quantum states was first realized by the research group of R.N.Zare[156]. They demonstrate that the utility of such measurements for investigation of a single collision chemical reactions and for molecular beam diagnostics. It has become a common detector of atoms and molecules allowing to determine their internal state distributions.

The main principles of this method are fairly simple. Laser light is impinged onto the sample to be investigated. Prior to this, the liquid flow is seeded with suitable for the application tracer particles. The molecules within the irradiated sample are excited from a lower energy level to a higher one by the absorption of a light photon. The excited state is at non-equilibrium; therefore, the molecules tend to return to equilibrium by transitioning to a lower energy level. The return to the lower state occurs by the emission of photons (fluorescence) at a longer wavelength compared to the absorption wavelength to eliminate illegitimate signal due to light scattering[157] (Figure 2.34).
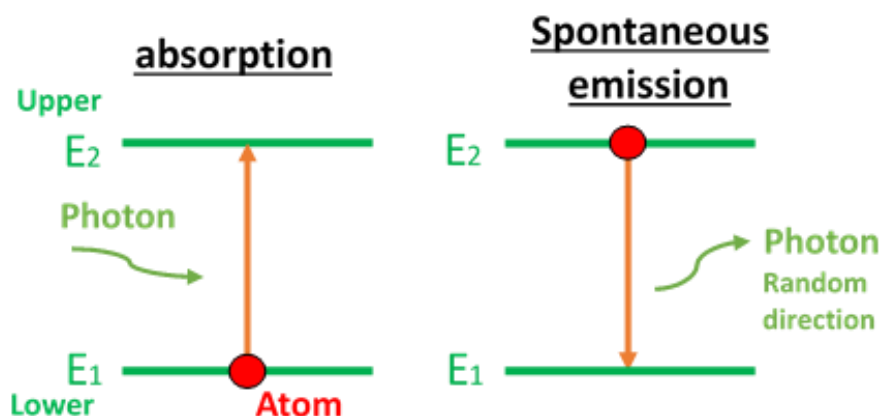
Figure 2.34 : Electronic state diagram illustrating the excitation of an atom to a higher energy level by photon absorption, followed by the emission of fluorescence.

However, there are a number of other pathways that can be followed during the de-excitation process (Figure 2.35), such as stimulated emission, internal conversion (direct return to the ground state, no photon emission occurs), intersystem crossing (most likely emission of phosphorescence) or intramolecular charge transfer[158].
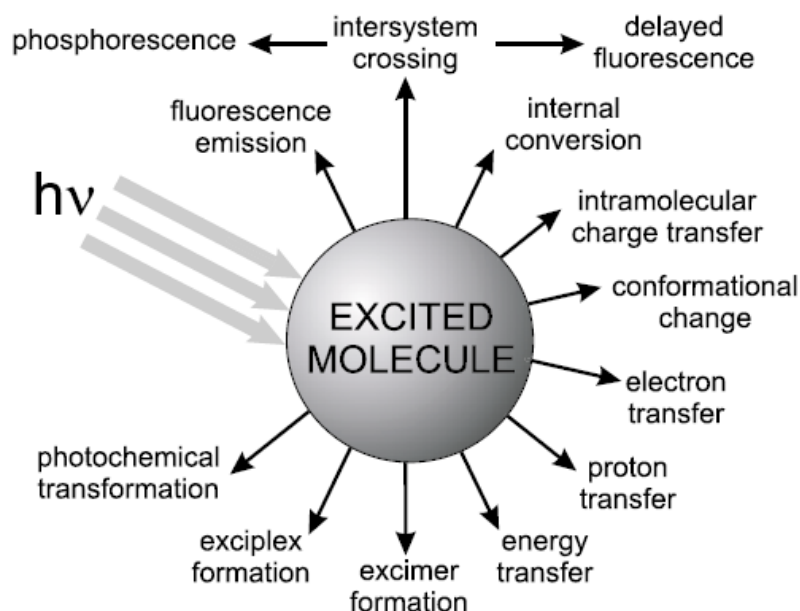
Figure 2.35: Possible de-excitation pathways of excited molecules[158].

Additionally, the interaction of molecules in the excited state with other molecules (quenching) is believed to compete with the de-excitation process: excimer or exciplex formation, proton transfer, electron transfer, energy transfer.

This energy transition from a lower energy state to a higher one is achieved by the promotion of an electron from an orbital of a molecule in the ground state to an unoccupied orbital is achieved by absorption of a photon. The most common orbitals are the σ and the π orbitals. The formation of σ orbital, which eventually leads to the construction of an σ bond, can be attributed to either the combination of two s atomic orbitals or one s and one p or two p orbitals in a collinear axis symmetry. On the other hand, the formation of a π bond is a result of the overlap of two atomic orbitals. The promotion of π electrons to an anti-bonding orbital by photon absorption is denoted by π^*.
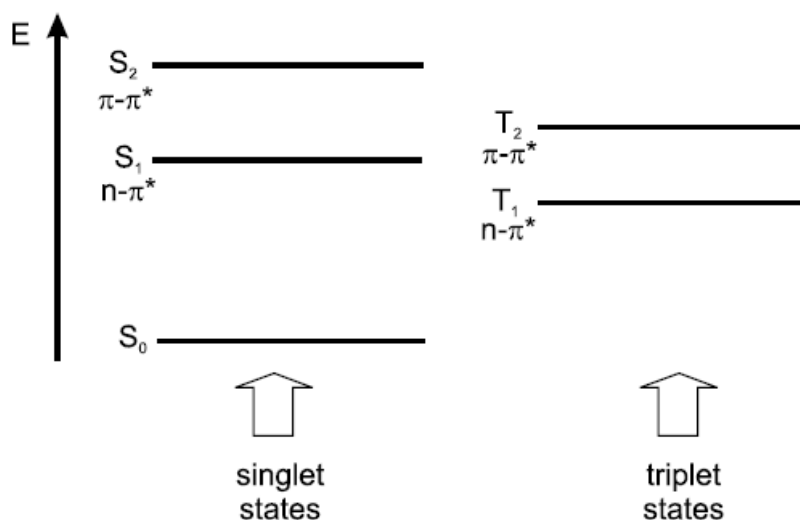
Figure 2.36: Example of singlet and triplet vibrational states[158].

Lastly, there are molecules (i.e. oxygen, nitrogen) commonly located on heteroatoms, which possess non-bonding electrons. Such orbitals are called n orbitals. In absorption and fluorescence spectrometry two orbitals are taken into account: Highest Occupied Molecule Orbitals (HOMO) and Lowest Unoccupied Molecule Orbitals (LUMO), which both refer to the ground state of the molecule. The HOMO is the n orbital and the LUMO is the π^* orbital. The shift between different electronic states is associated with the transition between the vibrational states of each electronic state. Depending on the orientation of the spin of the electrons occupying an orbital, while in transition, there are singlet and triplet electronic states, denoted by S_o, S_1, S_2 … and T_1, T_2 … respectively. The absorption of a photon can bring a molecule to one of the vibrational levels S_1, S_2 … from level S_o (ground state). The emission of photons accompanying the $S_1 \rightarrow S_0$ relaxation is called fluorescence. The fluorescence emission occurs from S_1 and therefore its characteristics do not depend on the excitation wavelength. The fluorescence spectrum is located at higher wavelengths than the absorption spectrum because of the energy loss in the excited state due to vibrational relaxation. In most cases, absorption spectrum overlaps the fluorescence spectrum e.g. a fraction of light is emitted at shorter wavelengths than the absorbed light. It should be noted that the emission of a photon is as fast as the absorption of a photon. Excited molecules stay in S_1 state for a certain time before emitting a photon or undergoing other de-excitation processes. Thus, after excitation of a population of molecules by a very short pulse of light, the

fluorescence intensity decreases exponentially with a characteristic time, reflecting the average lifetime of the molecule in the S_1 excited state.

$$I_\lambda = I_o \exp(-t/\tau_s)$$

<div align="right">Equation 2.38</div>

Where I_λ: leaving light intensity and I_λ^o: entering light intensity.

The fluorescence decay time τ_s is one of the most important characteristics of a fluorescent molecule because it defines the time window of observation of dynamic phenomena. No accurate information occurring on the rate of $\tau_s/100$ or longer than about 10τ can be obtained, whereas at intermediate times the time evolution of phenomena can be followed. The energy of the emitted photon ($h\nu_{EM}$) is the difference between the energy levels of the two states and that energy difference determines the wavelength of the emitted light (λ_{EM}).

$$\lambda_{EM} = \frac{hc}{E_{EM}}$$

<div align="right">Equation 2.39</div>

where E: energy difference between the energy levels of the two states during emission (EM) of light, h is Planck's constant, c is the speed of light.

The governing equations for the molecular ground state (N_g) and excited state populations (N_e) (Equation 4.21, Equation 4.22) are a result of the employment of a two-level fluorescence model, considering collision quenching.

$$\frac{dN_g}{dt} = (A_{eg} + Q_{eg} + u_\omega B_{eg})N_e - u_\omega B_{ge}N_g$$

<div align="right">Equation 2.40</div>

$$\frac{dN_e}{dt} = -(A_{eg} + Q_{eg} + u_\omega B_{eg})N_e + u_\omega B_{ge}N_g$$

<div align="right">Equation 2.41</div>

Where A_{eg}, B_{ge} and B_{eg} are the local spectral energy density of the laser radiation.

Considering the total number of molecules $N = N_g + N_e u_\omega$, Equation 2.42 and Equation 2.43 become:

$$\frac{dNg}{dt} = (A_{eg} + Q_{eg} + u_\omega B_{eg})N_e - u_\omega B_{ge}(N - N_g)$$

<div align="right">Equation 2.42</div>

$$\frac{dN_e}{dt} = -(A_{eg} + Q_{eg} + u_\omega B_{eg})N_e + u_\omega B_{ge}(N - N_e)$$

<div align="right">Equation 2.43</div>

In the case of saturation condition where $\dfrac{dN_e}{dt} = 0$, the steady-state ratio of excited fluorescent molecules over the number of ground state fluorescent molecules is

$$\frac{N_e}{N_g} = \frac{u_\omega B_{ge}}{u_\omega B_{eg} + A_{eg} + Q_{eg}}$$

Equation 2.44

Ultimately, the fluorescence energy transmitted into an element of solid angle $\Delta\Omega$ in a time period T is described by Equation 2.45.

$$\Delta E_{LIF} = \int_0^T \frac{N_e(t)A_{eg}\hbar\omega\Delta\Omega}{4\pi} dt \approx \frac{\overline{u_0}B_{ge}\Gamma\Delta V\hbar\omega\Delta\Omega\tau}{4\pi(\overline{u_0}(B_{eg} + B_{ge}) + A_{eg} + Q_{eg})}$$

Equation 2.45

Where $\overline{u_0}, \Gamma, \hbar, C, \Delta V$ and τ are the local laser energy density, a linewidth integral defining the overlap of the laser band-width with the absorption band line-width, Planck's angular momentum constant, the concentration of fluorescent agent in the scattering spheres, the volume that the laser traverses, and the duration of the laser respectively. Equation 2.46 describes the proportionality among the number of the fluorescent molecules, the local fluorescent yield and the volumetric dependence ($\propto D^3$) of the latter. However, not every absorbed photon is re-emitted as fluorescence light. There are several processes that lead to non-radiative dissipation of the absorbed energy. The fluorescence quantum yield (Φ_F) is the ratio of the absorbed energy over the energy emitted by fluorescence. It also quantifies the fluorescence efficiency and is dependent on the structure and the environment of the tracer particles

$$\Phi_F = \frac{\text{number of emitted photons}}{\text{number of absorbed photons}} = \frac{N_F}{N_A}$$

Equation 2.46

The volumetric dependence of the fluorescence signal is true in the case of small spherical droplets containing the suitable doping agent at correct concentration and being radiated by a constant beam. In such conditions, the fluorescence signal can be also considered isotropic and proportional to the light intensity. An increase in size or concentration of the droplet leads to increased light attenuation within the droplets; consequently, the emitted light becomes anisotropic and the back scattering dominates the scattering process.

Several authors[148,159–161] have reported that high tracer concentration leads to saturation effects which in turn result in violation of the linearity between the emitted signal and the incident intensity and of D^3 dependence of the fluorescence signal. Duwel et al.[162] stated that the concentration variation of the tracer is a consequence of the different vapour pressures of the fuel and the tracer. In particular, in the case that the boiling point of the tracer is below the boiling point of the fuel, the evaporation rate of the tracer will be faster resulting in decreased tracer concentration within the droplet volume and in under predicted fluorescence signal. They also reported that the synergy between poor mixing of the doped fuel and the surface-active molecules may lead to either molecule accumulation in the droplet or to molecule depletion from the droplet surface. Therefore, ideally a LIF tracer should have the same properties as the fuel with respect to evaporation process and the mixing process should be carried out thoroughly. Secondly, the tracers must show efficient absorption at the chosen laser wavelength as well as a high fluorescence quantum yield. In order to reduce any de-activation effects, the tracers should also meet the following requirements[163]:

- Rigid structure without rotating functional groups to reduce internal conversion, unless a strong temperature dependence of the fluorescence is desired for temperature measurement.

- Slow intersystem crossing rate. That means the spin-orbit coupling should be weak, which can be achieved by avoiding heavy atoms in the tracer molecule.

- Short fluorescence lifetime. That enables multiple excitation within one single laser pulse and reduces quenching effects.

Ultimately, it has been suggested that the quantification of fluorescence intensities emitted by naturally fluorescent compounds present in the fuels is difficult, due to their different photo physical and photochemical behaviours[164] which usually lead to simultaneous fluorescence emission. Additionally, it has been reported[165] that natural fluorescence signal produced by isothermal diesel sprays showed significant dissymmetry in the radial distance profiles, due to high signal distortion and low quantum yield of the natural signal, resulting in doubtful measurements. However, the addition of RhB in the flow showed an excellent performance and provided interesting results with regards to the bubble

diameter at various locations within the spray structure. Hence, the flow seeding with florescent particles/dyes is critical.

Since, most of the fluorescent dyes are applicable after being diluted in solvents, it is essential to take into account any possible effects may have on the broadening spectral lines and on relaxation process. The variety of atoms present in an organic dye molecule results in a distinctive vibrational line-emission spectrum. However, the interaction between the tracer molecules and the solvent cannot be considered as uniform, due to the slight differences in the molecule structure. Therefore, the emission spectra contain a whole ensemble of fluorescing molecules, which takes into account the contributions of each molecule and results in strong broadening of vibrational lines. Furthermore, the solvent relaxation process is responsible for the lowered energy of the excited state during the emission compared to absorption. The relaxation process takes place within 10^{-10}s and is terminated during the fluorescence emission. In general, the spatial expansion of the electron shell due to electronic excitation leads to increased polarizability, decreased excitation energy and to changed molecule orientation. According to Frank-Condon law, the transition from the S_1 vibrational state to a ground state S_0 is possible employing equal nuclear coordinates and same solvent molecule orientation. Hence, the emission maximum is always dependent on the solvent properties, e.g. polarity, viscosity.

In a summary, LIF technique has been proven to be applicable for the visualisation of the liquid phase in non-evaporating sprays[108] as well as for the determination of both states in evaporating sprays due to its large range of sensitivity (its high signals enable measuring even minor species of gas-phase flows)[155,162]. High selectivity can be achieved by tunable, narrowband laser-light sources. Short laser pulse durations provide for high temporal resolution, high enough to study turbulent objects. It is also possible to get two or three-dimensional images, since fluorescence takes place in all directions.

2.5.4.3 Structured Laser Illumination Planar Imaging (SLIPI)

The most important problems that most of the laser diagnostics for spray characterisation suffer from, are the effects of multiple scattering and the strategies to supress them. Structured Laser Illumination Planar Imaging is suggested to offer a robust solution to overcome such problems[166,167] and also to provide information regarding the droplet size[168], the spray temperature[169] and the extinction

coefficient[170]. The main principle of this method relies upon the addition of a recognizable pattern (usually a sinusoidal pattern) to the intensity of the beam used for the illumination of the probe volume. It is suggested that the single scattered photons preserve this predetermined structural information while traveling via the medium (spray), whereas the multiply scattered photons retain no memory of it. This implies that the amplitude of the modulated light (ac) is directly linked to single light scattering, while the remaining non-modulated light (dc) is a consequence of multiple scattering[171] Therefore, a SLIPI process involves the collection of the modulated laser sheet along the direction of the light propagation. The intensity of the modulated light is reduced, while crossing a homogeneous scattering medium, as shown in Figure 2.37. The separation of the modulated light from the non-modulated light can be achieved using three phase (3P), two phase (2P) or single phase SLIPI approaches.
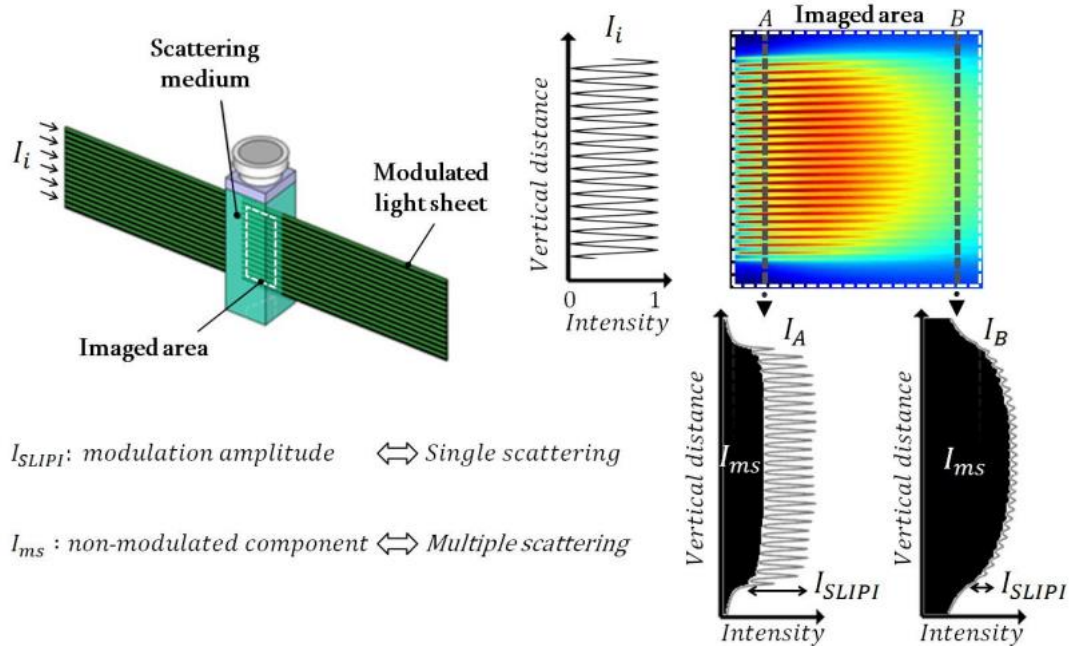
Figure 2.37: Representation of a spatially modulated light traversing a scattering medium[172].

The 3P SLIPI approach is the first implemented approach and involves the extraction of a spatial sinusoidal modulation by using three signals which are separated by a shift phase of one third of the period. The first measurements were performed in a hollow-cone water sprays and they involved the acquisition of 3 images (signals) separated by a phase shift equal to $120°$ (I_0, I_{120}, I_{240})[166]. The root mean square of the three distinctive signals is equal to the final SLIPI image

$$I_{3P-SLIPI} = \frac{\sqrt{2}}{3}\sqrt{[(I_0 - I_{120})^2 + (I_0 - I_{240})^2 + (I_{120} - I_{240})^2]}$$ Equation 2.47

In Figure 2.38, the resultant SLIPI image clearly demonstrates visible spray hollowness, higher image contrast and reliable light signals with respect to the results obtained from the laser sheet drop-sizing method. Although the 3P-SLIPI method does not have any significant losses in image resolution, it is limited by its requirement in recording 3 sub-images. This need reduces greatly the opportunity of obtaining single shot spray images.
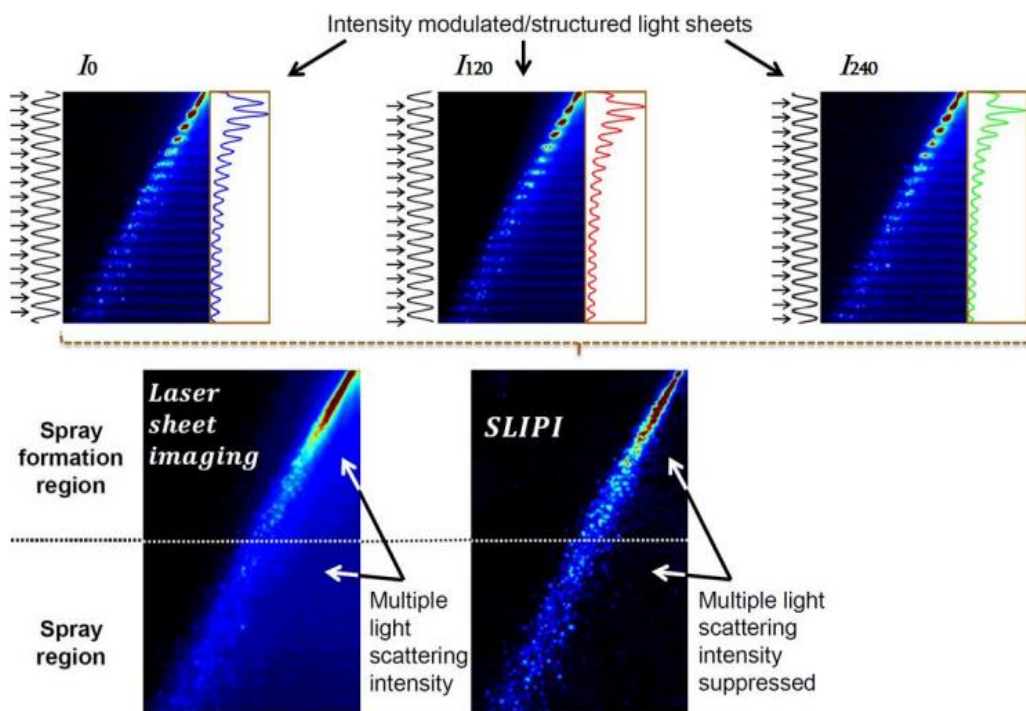
Figure 2.38: An example of 3P-SLIPI application on a cone spray[172].

However, recently Kristensson et al.[173] tested a hollow-cone water spray by using a nanosecond SLIPI system capable of freezing flow motions up to ~600m/s. They managed to obtain high resolution, single-shot images of the complex flow dynamics occurring in the dense regions of the emerging sprays, in which the multiple scattering effects are effectively suppressed. However, the cost of the required equipment along with the demanding and sophisticated optical set-up make this method widely inaccessible.

Therefore, another approach, termed as 2P-SLIPI approach is suggested to mitigate the above mentioned limitations[174]. This method involves the illumination of the probe volume with a 2-phase

modulated laser light and eventually the extraction of the absolute value of the intensity difference in the two obtained sub-images. It can effectively remove the identical image components, but it will also lead to repeated zero values at the cases where the frequency of the incident modulation is halved as a consequence of the modulated light crossing at every half of a period. Such an effect leads to poor image quality, visually observed as black lines (residuals) in the final SLIPI image, and consequently to incomplete demodulation process (Figure 2.39).
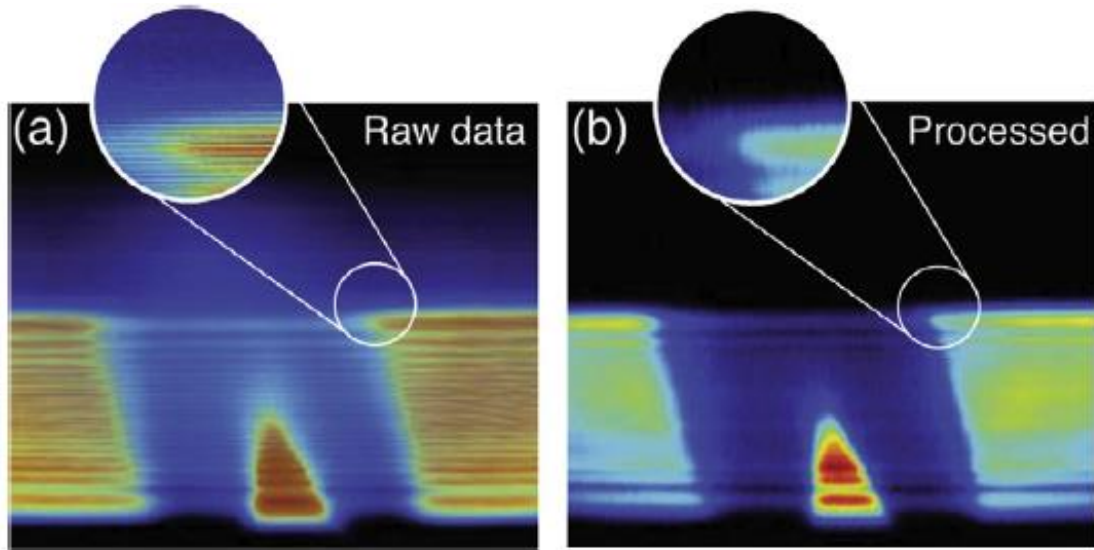
Figure 2.39: An example of 2P-SLIPI measurement of a premixed Bunsen Flame. a) raw image prior to any correction methods applied, b) processed 2P-SLIPI image[174].

However, it is suggested that the removal of the residuals can be accomplished by creating a high frequency incident modulation and by applying suitable Fourier filters. As a result, the majority of the residuals is removed from the final SLIPI image and the structural features are shown in detail.

Ultimately, the use of an individual modulated image, known as 1P-SLIPI approach, has been proven to be applicable to smooth flows where there is no high frequency information[174]. In this case, the extraction of the amplitude of modulation from the single modulated signal is achieved by applying a peak detection algorithm, which basically refers to the deduction of the signal minima and maxima from each pixel column of the modulated image. Finally, the expected intensity reduction occurring across the medium is in a good agreement with the predicted by the Beer-Lambert law (Figure 2.40).
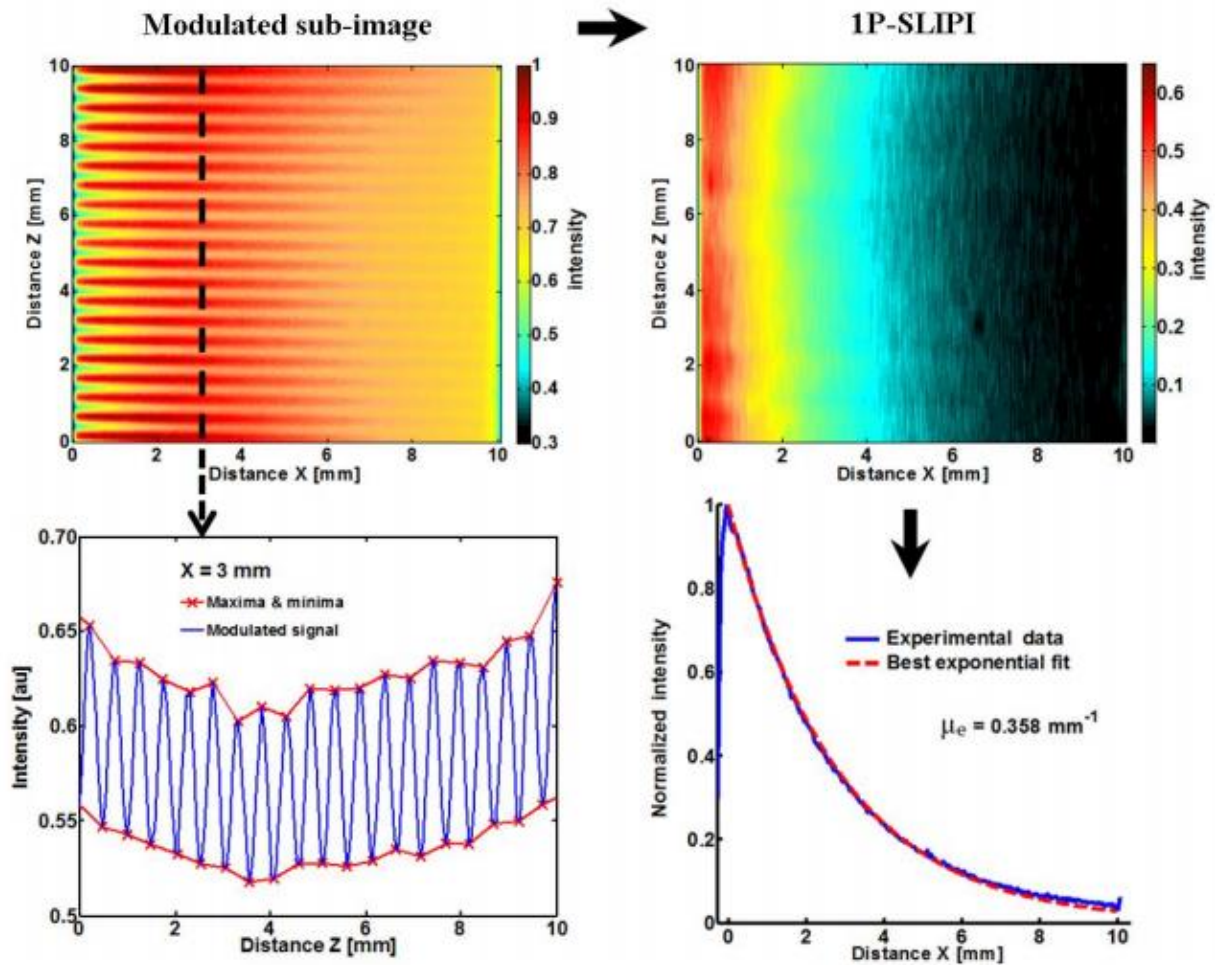
Figure 2.40: Example of averaged 1P-SLIPI technique[172].

Overall, SLIPI technique has been proven to provide quantitative two-dimensional data, corrected for laser extinction, signal attenuation and multiple scattering effects. It is also applicable to inhomogeneous turbid scattering and absorbing media without any calibration required prior to its direct application to the centre of the probe volume. Its main limitations rely upon its quite sophisticated optical setup, the expensive equipment and lastly upon its limited depth resolution[175].

2.5.4.4 Laser Sheet Drop-sizing method (LSD)

Laser Sheet drop-sizing technique is a method for spray characterization which, was originated by Yeh et al.[119] and was further developed and implemented by several researchers at the late 90s , early 2000[148,176,177]. It combines the laser sheet imaging of elastic Mie scattering and inelastic Laser Induced Fluorescence, producing a 2D map of the droplet size distribution in the spray region irradiated by a laser sheet. In more detail, when a droplet is illuminated by a laser sheet, a fraction of the incident light

is absorbed by the molecules that is then emitted as fluorescence, while the remaining light energy is elastically scattered by the droplets. The information contained in both elastic and inelastic signals is then used for the determination of the size of the droplets present on a single plane of the spray. The scattered signal S from a droplet of diameter D is expressed by Equation 2.48 and neglects any Morphology Dependent Resonance (MDR) effects[148].

$$S = CD^n$$

Equation 2.48

Where C is a calibration constant dependent on the laser fluence, the signal collection angle and n is an index of dependence.

The determination of the elastically scattered light behaviour is achieved using the principles of Lorentz-Mie theory. In cases of small, homogeneous spherical particles, Mie signal is proportional to the squared droplet diameter (Equation 2.49). This proportionality is not valid when the droplet size is very small and the collection angle obtain certain values.

$$S_{Mie} = C_{Mie}D^2$$

Equation 2.49

On the other hand, the fluorescence signal is a result of the de-excitation of the fluorescent molecules. It is red-shifted with respect to the laser wavelength and its discrimination from the elastic scattered light is achieved by the employment of spectral filters. It is suggested that the inelastic LIF signal is proportional to the droplet volume.

$$S_{LIF} = C_{LIF}D^3$$

Equation 2.50

However, this cubic dependence has theoretically and experimentally been investigated[148,159,160] and the results reveal that it is quite sensitive to the tracer concentration, the droplet diameter and the collection angle. Figure 2.41 shows the dependence of the diameter exponent (n) in the intensity to volume relation on concentration.
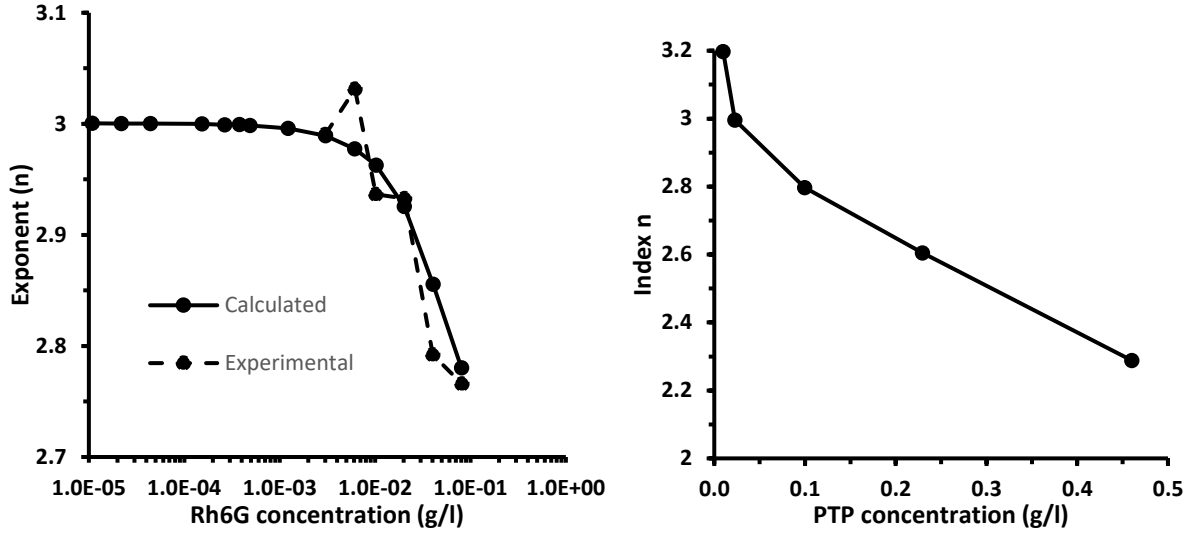
Figure 2.41: Index of dependence relation on dye concentration[159,148].

In particular, in cases of low concentrations the volume proportionality is valid, whereas at high dye concentrations the intensity to droplet relation gradually transits from exponent value 3 to 2. This can be attributed to the strong light extinction effects on the refracted rays and the dominant absorption[159].

The obtained signals contain drop-size information for the whole population (even in case of dense sprays) of droplets (denoted by i) present in the probe volume; particularly LIF signal provides the liquid volume fraction distribution. The ratio of the inelastic fluorescence signal over the elastic Mie scattering signal is proportional to the Sauter Mean Diameter distributions and it is expressed by (Equation 2.51).

$$\frac{S_{LIF}}{S_{Mie}} \propto \frac{C_{LIF}\sum\limits_{i} D_i^3}{C_{Mie}\sum\limits_{i} D_i^2} \propto C \cdot SMD \qquad \text{Equation 2.51}$$

Hardalupas and Domman[154] applied the LSD method to measure the droplet size in a spray generated by a pressure swirl atomiser in a liquid-fuelled burner operated with water at isothermal conditions. They reported that the calibration constant C between the intensity ratio and the SMD is dependent on the droplet size. In particular, they found that for droplet less than 60μm, the induced error can reach up to 30%. The suggested processing method facilitated the reduction of the error (~10%) resulting in data which showed a satisfying agreement with PDA measurements.

An accurate and reliable LSD measurement requires a) LIF and MIE signal to be proportional to the cubed and squared diameter of the droplet, respectively, b) the maintenance of the same optical paths at all times and c) spherical droplets of relatively small size. When all requirements are met, LSD technique offers a droplet size distribution with high spatial resolution, even in cases of dense sprays, where conventional methods are not reliable, due to signal attenuation effects. The better performance of the LSD method relative to PDA relies upon its higher spatial resolution and on the employment of high energy pulsed lasers. The obtained data need to be calibrated against PDA data. Jemry and Greenhalgh[149] quantified the random uncertainty present in LSD measurements performed in water jets of fine droplets (SMD~15-20μm). They concluded that such uncertainties are a consequence of the calibration factor used. Despite the induced uncertainties, the comparison between LSD and PDA measurements show a good agreement[148,149] (Figure 2.42, Figure 2.43).
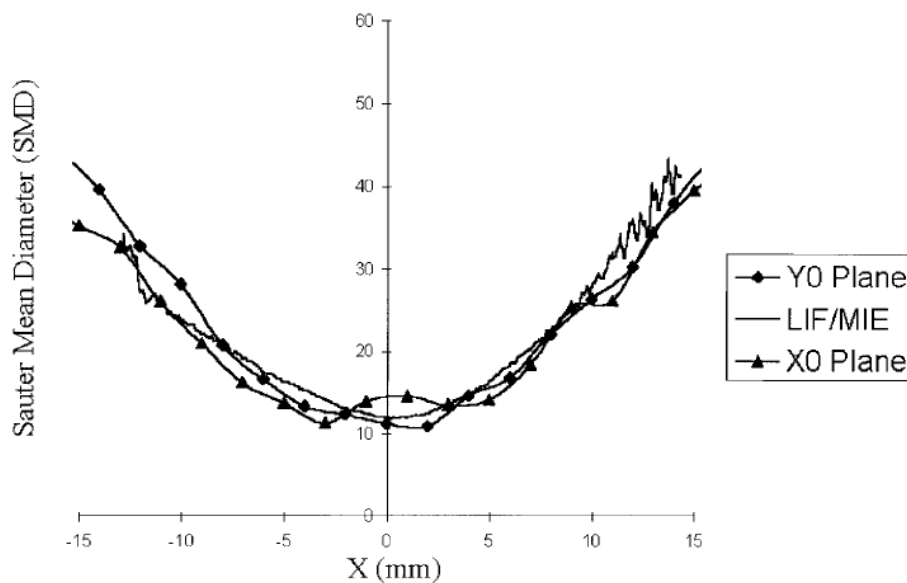
Figure 2.42: Comparison between LSD and PDA measurements[148].

Despite the satisfying performance of the LSD method in the characterization of sprays, there are several sources of uncertainty involved in the measurements. As it mentioned earlier, the SMD of the spray droplet is proportional to the ratio of the LIF and Mie signals. However, apart from the inelastic and elastic light signals, additional contributions are encountered into the collected signal due to background light, laser profile variations and imperfect image reconstruction.
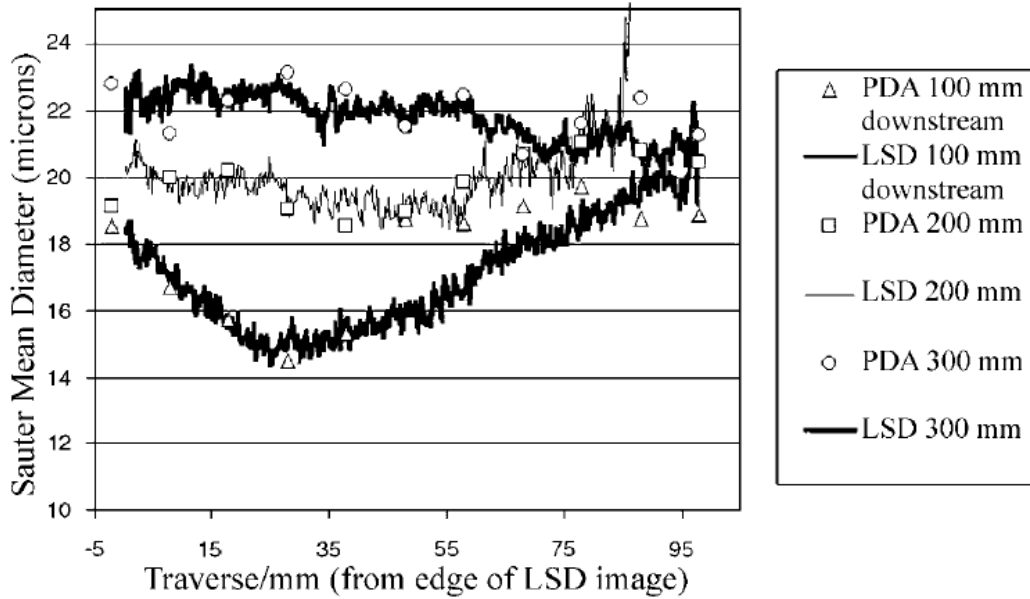
Figure 2.43: Comparison of SMD measurements from PDA and LSD methods[149].

These effects are expected to cancel out, since they are common in the rationed signals. The most significant source of uncertainties in LSD measurements is the multiple scattering effects. In this case, the suppression of such effects by the rationing of the signals is not satisfying, as the multiple scattering generated by the two signals is different[132].

In the case of optically dense sprays, laser attenuation becomes significant, hence the LSD measurement could be doubtful. Abu-Gharbieh[178] suggested a way to compensate this attenuation based on Lambet-Beer's law. The scheme suggested was used to sum up the loss of light along the laser path in the image and progressively compensate this loss pixel by pixel. However, in the case of relatively low density sprays the LSD technique is considered to be precise and reliable as long as the transmission coefficient T is greater than 1/e at all times (negligible secondary scattering) [167] .

The successful application of the LSD technique relies on the assumptions about the evaporation or accumulation of the fluorescent tracers during the evaporation process in combusting sprays.[162] investigated the variations of LIF signal intensities with different tracers in evaporating poly-dispersed sprays and the influence on LSD measurements. They highlighted the importance of understanding the way in which the tracer concentration changes in the spray droplets and how the intensity of the fluorescence signal changes over the evaporation process. They stated that the changes in the tracer

concentration mainly was mainly dependent on the differences between the vapour pressure of the fuel and the tracer, the incomplete mixing and/or the depletion/accumulation of surface active molecules of surface active molecules. In the case that the boiling point range was lower than fuel's, the tracer evaporated faster compared to the fuel, resulting in increased tracer concentration inside the spray droplets and subsequently the SMD of the spray droplets was underpredicted. On the other hand, when the vapour pressure of the tracer was larger in relation to the fuel, the tracer molecules were accumulated in the droplets and the SMD measurements overpredicted the actual droplet size. Additionally, they stated that such effects were further influenced by the evaporation rate.

Some other factors which influence the reliability of the LSD measurements are the self- absorption of the LIF signal and the uncertainties induced by the image registration (alignment of LIF and Mie images). According to Guilbault[179], the fluorescence intensity emitted due to absorption over a specific path length b within a liquid dye concentration c could be calculated using Equation 2.52. This term takes into account the intensity i_0 at the beginning of the absorption, the quantum field φ and the molar extinction cross section ε.

$$i_f = \varphi \cdot i_0 \left(1 - e^{sbc}\right)$$
Equation 2.52

Finally, since the reliability of this method is based on the ration of LIF and Mie signals, it is essential to guarantee that the registration of the images obtained is highly accurate. It is crucial for both LIF and Mie images to perfectly overlap each other such that all the spray feature locate exactly at the same location in both images. The incorrect image registration leads to doubtful measurements, which do not reflect the actual size of the spray droplets.

Overall, the LSD technique offers certain advantages over other drop-sizing techniques. It seems to cope better in sprays at realistic flow rates and hence it can be widely used for automotive fuel injections. It can be applied for a rapid analysis of spray systems and for experiments with short and expensive duration.

Chapter 3

Experimental arrangements and methods

The following chapter was devoted to the detailed description of the experimental arrangements and method used for the purpose of this work. As it was mentioned in earlier chapters, the experimental investigation of fuels A to E was executed by Jeshani[16], while fuels 1 to 4 by the author of this dissertation. Both experimental arrangements used common equipment (i.e. fuel injection system) and had a few distinctive differences. In the case of Jeshani's work, the characterisation of the internal nozzle flow was achieved using white light scattering method, while the present author's work Laser Induced Fluorescence (LIF). On the other hand, in both experiments, the spray characterisation in terms of droplet size and phenomenology was achieved using Laser Sheet Drop-sizing (LSD) and Laser Induced Fluorescence (LIF) techniques. The optical access to the nozzle sac and nozzle holes was achieved by manufacturing an optically accessible, real-sized, mini-sac type, 6-hole nozzle from acrylic material. The design of this tip was initially done by Liverani[180] and was further developed by Jeshani. A detailed description of the experimental equipment and procedures were presented in the present chapter.

3.1 Experimental apparatus

3.1.1 Diesel fuel injection system

The fuel injection system employed for the purpose of this experiment was custom manufactured at City, University of London and could pressurise the fuel up to 600 bar. It was capable of accurately feeding a fuel quantity into the injector at a specific rate and pump angle position, to guarantee repeatability between successive injection events. A simple schematic of the fuel injection system is shown in Figure 3.1. The fuel stored in the fuel tank was led to a low-pressure pump, which delivered the fuel to the high-pressure pump after passing through a 5μm polypropylene filter. The high-pressure pump was driven by an electric motor operating at 1490rpm.
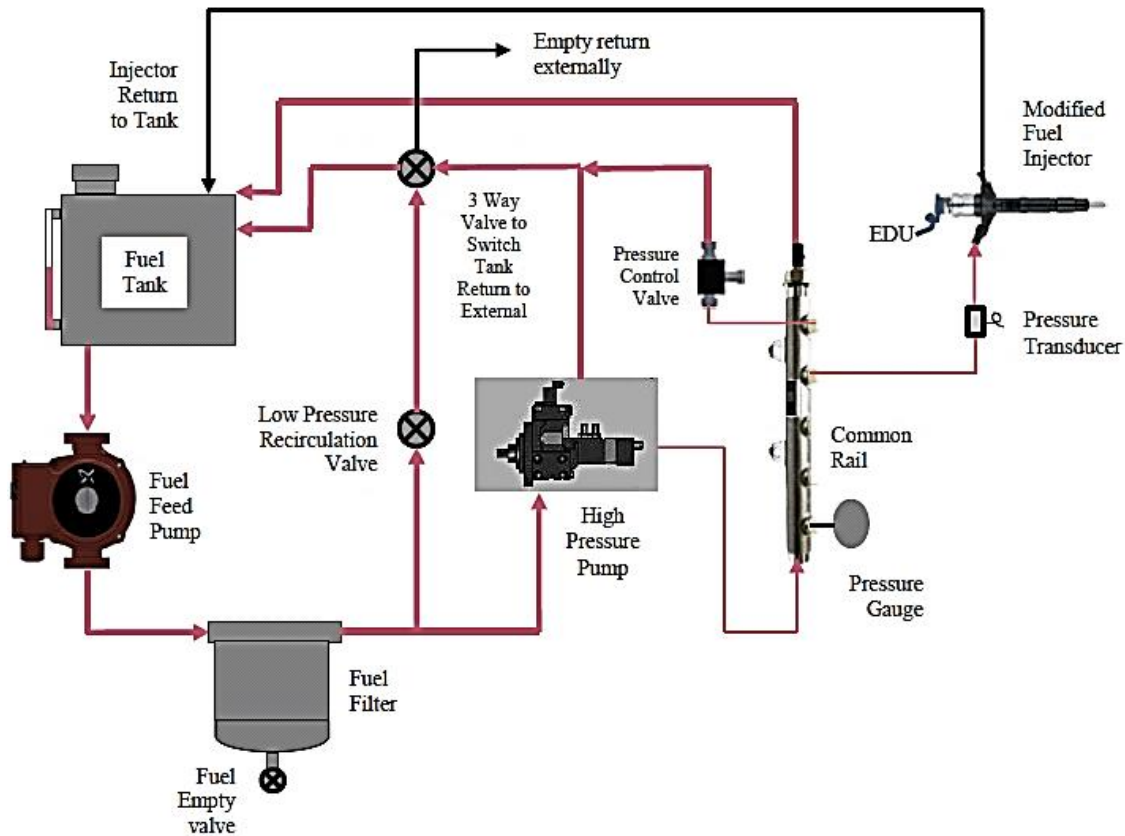
Figure 3.1: Schematic of the custom manufactured fuel injection system[16].

Then the fuel was compressed and eventually discharged into the common rail. The high-pressure fuel was finally delivered to the injector, which injected the fuel into ambient air. A custom-made control box was utilised to control the injection parameters, such as injection duration, number of skip cycles, number of injections etc. The injector utilised for the purposes of this experiment was a modified Denso injector.

A key parameter for the successful execution of the experiments was the capability to produce the same operating conditions in a set of successive injections. The injection pressure was one of the most important parameters that had to be maintained throughout a complete set of measurements. A Kulite ETMER-1-375M-3500BAR pressure transducer installed prior to the injector measured the pressure over the injection events. The pressure transducer was capable of measuring up to 3500bar SG (Seal Gauge) and its sensitivity was 1.189mV/bar. There was a zero offset of 500mV ± 50mV, which was

measured prior to each experiment. The zero offset was required to accurately calculate the injection pressure and also quantify the zero-balance error.

A valve installed past the filter was utilised to direct the flow either back to the fuel tank or into the high-pressure pump. The fuel return line leading to the tank acted as a vent during the filling/draining procedures of the system. Apart from this return line, there were three additional return lines coming from the high-pressure pump, the common rail and the injector. The return lines on the high-pressure pump and the common rail relieved the pressure developed and led the fuel excess back to the fuel tank. The fuel which was not injected, returned to the fuel tank via the injector return line.

The measurement and control of temperature and pressure of the system were achieved using an K-type thermocouple and an adjustable pressure control valve respectively. In more detail, the K-type thermocouple was installed on the high-pressure pump to check the temperature of the fuel circulating in the system. The temperature was shown on a display mounted on the rig. The maintenance of temperature within the desired range was achieved utilising a cooling system installed in the fuel tank. Cold mains water was passing through a spiral coil which was cooling the fuel as required. The heated water was led to the sewer system. The desired temperature range was set between 40 and 70 degrees. On the other hand, the pressure adjustment inside the common rail was achieved by an adjustable pressure control valve which was installed on the common rail. A pressure gauge fitted on the common rail facilitated the pressure measurement.

The injector was activated by an electronic injector driver, which sent a high voltage square wave to the magnetic solenoid of the injector. When the solenoid was charged, the injector needle lifted allowing the fuel to flow inside the injector body. Figure 3.2 shows the needle lift profiles obtained from a modified VCO diesel injector[180] (solid black line), a mini-sac diesel injector used by Jeshani[16] (solid grey line, nozzle 1) and lastly a mini-sac diesel injector used for the purpose of the present work (dashed black line, nozzle 2). In the cases of the VCO and mini-sac nozzle 1, the lift rate during the opening phase of the needle appeared to be slower relative to mini-sac nozzle2 nozzle.
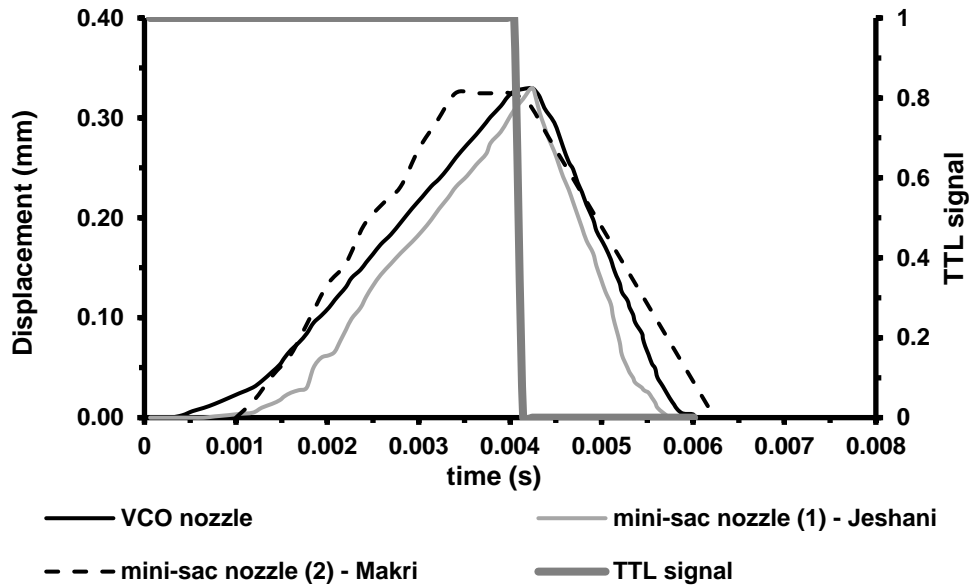
Figure 3.2: Needle lift profiles for a modified Denso injector, Jeshani's mini-sac nozzle and Makri's mini-sac nozzle.

On the contrary, the rate of the needle return of the mini-sac nozzle 2 appeared to be faster relative to the other profiles. It was also observed that the needle of mini-sac nozzle 2 remained longer at the maximum lift. Lastly, it was noted that the injection duration and lift rate varied from nozzle to nozzle. In particular, the injection durations of the VCO, the mini-sac nozzle 1 and the mini-sac nozzle 2 were approximately 5.6ms, 4.4ms and 5.4ms respectively. These differences could be attributed to the condition of the injector in terms of lubrication. For example, in the case of Makri's experimental work, the injector was stripped out and was lubricated in an oil bath. This could potentially explain the faster response of the needle compared to Jehani's profile. All needle profiles corresponded to operating pressures between 200bar and 400bar and were typical for engines operating at idle or low loads.

3.1.2 Injection control unit

The successful execution of the experiment required the prevention of large fluctuations in pressure. In this regard, an encoder fitted in the pump facilitated a pulse generation every 5-degree rotation; therefore, all injections occurred at a selected pump angle. This signal was sent to the control unit to trigger the injector. The control box allowed the manual adjustment of the number of skip cycles of the rotating pump, the injection duration and the number of the injection cycles. In the case of Jeshani's

experiments, the pulse generated was a 10kHz signal, which triggered the synchronised initiation of the injection process, laser firing and image acquisition. The injection rate, duration and delay could be manually set on the control unit. For the purpose of these experiments, the injection rate was set at 3Hz and the injection duration at 4ms. The injection delay referred to the time period between the start pulse produced by the control unit and the pulse sent to the injector driver and could be set between 100-500μs. A more detailed description of the settings of the injection control system was presented in Jeshani's PhD dissertation [16].

In the case of Makri's experiments, the skip rate, the injection duration and the number of injection cycles were set at 7, 4.0ms and 50injections respectively. A skip rate of 7 revolutions per injection provided an injection rate of 3.5Hz. The control box was also capable of introducing a dialled delay between the start pulse and the pulse sent to the injector; In this experiment the delay was set at 900μs. Therefore, the injection would start 900μs after receiving the start pulse. Normally, this signal would be used to trigger the injection, the image acquisition system and to synchronise the cameras with the laser fire pulse. However, the employment of a shutter to block the unnecessary laser illumination of the injector introduced another delay. In order to ensure that the shutter was fully opened when the injection and image acquisition started, a delay of 15ms was introduced to the signal triggering the cameras and the injector. According to the manufacturer of the shutter, a 14.0ms period is required for the shutter to be fully opened. The minimum shutter opening time was 17.2ms, while the period for the shutter to be fully closed was approximately 1.2ms. Considering all the above, a delay of 15ms was inserted to the signal coming from the control unit and then the delayed signal was fed to the shutter. The overall duration of the pulse driving the shutter was 25ms. The timing settings are presented in detail later in this chapter.

3.1.3 Optically accessible diesel injector nozzle

The nozzle geometry has been shown to play a decisive role in combustion and atomisation processes, due to its influence on the spray characteristics, cavitation and internal flow[70,181]. For the purpose of the present experiment, an optically accessible mini-sac type, 6-hole, real-sized injector nozzle was employed. A conventional nozzle was modified such that its holes were replicated in clear acrylic to

enable a good view of the nozzle interior (Figure 3.3). The acrylic material was chosen because it did

not react with the diesel fuels and could be machined easily, providing an acceptable view. However,

acrylic was a fairly soft material; therefore, the experiment could not be carried out at elevated pressures

similar to real diesel engines.
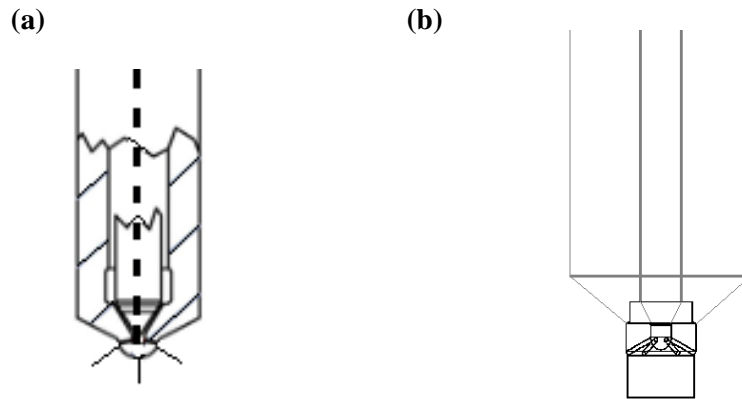
Figure 3.3: Simple designs of: (a) a conventional diesel injector nozzle, (b) modified nozzle with acrylic

tip.

The acrylic nozzle tips were custom manufactured at City, University of London. The internal nozzle

hole diameter was ~136μm, while the diameter of the sac was approximately 0.8mm. The nozzle cross

section shown in Figure 3.4 displays the dimensions of the nozzle interior.
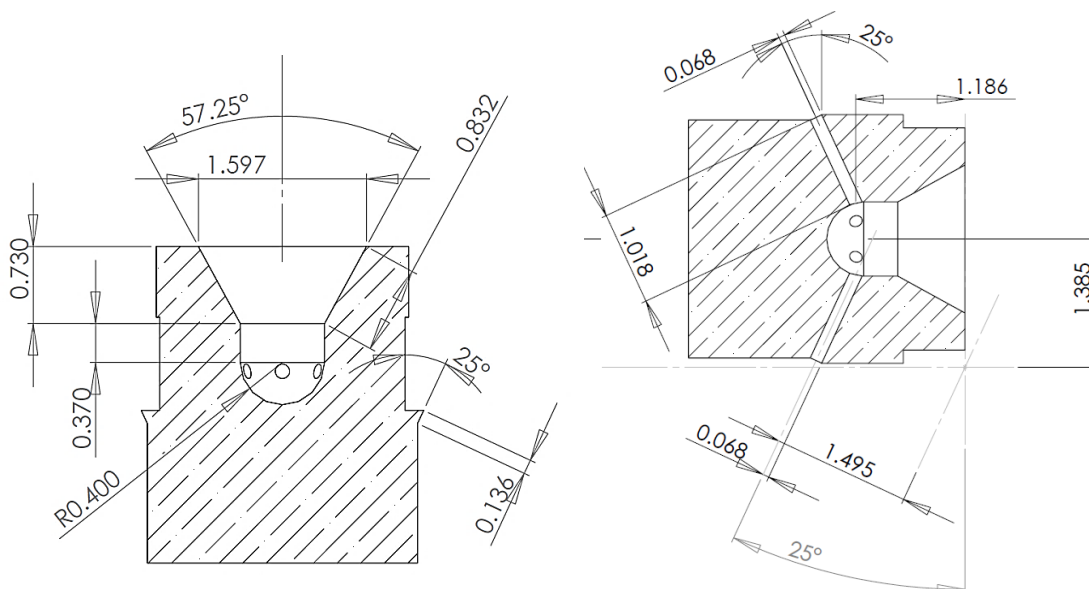
Figure 3.4: Acrylic nozzle cross sections showing the internal dimensions[16].

Experimental arrangements and methods

The nozzle exterior was designed in a way that became a 4-profile nozzle. The main difference between the conventional and modified nozzle was the angle of the holes; which was modified to 25 degrees, facilitating a better view of the nozzle passages.

The design of the acrylic nozzle provided a good view of two out of the six passages. These holes are shown in Figure 3.5 . The 25-degree hole angle facilitated good optical access at the entrance of the nozzle passage and replicated the cylindrical holes of a conventional nozzle. The acrylic nozzle included sections of different shape, each of which served a different purpose (Figure 3.6). It should be noted that the initial designs of this nozzle were produced by Liverani[180] and were further improved by Jeshani[16]. The nozzle tips used in this experiment were manufactured according to the designs made by Jeshani[16].
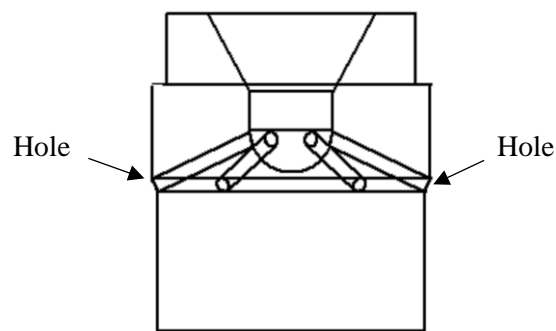
Figure 3.5: Modified diesel injector nozzle tip showing the view of the holes of interest[16].
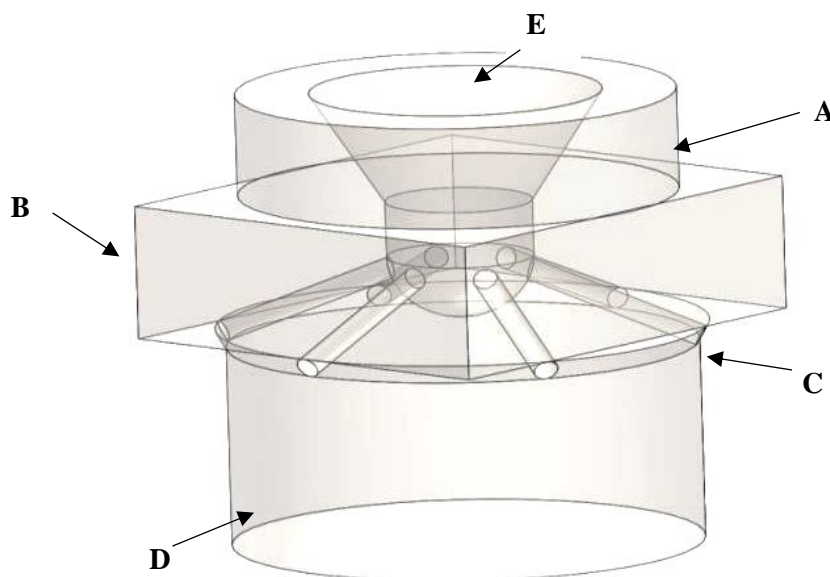
Figure 3.6: Injector tip projective transparent view.

Experimental arrangements and methods

Section A was designed to mount on the modified injector body, providing an adequate seal. Section B was a rectangular part which facilitated the view of the angled holes. Figure 3.6 shows that the longer sides reached the end of the passages of interest. On the other hand, the shorter sides were chosen to prevent any interference of this edge with the spray emerging from the holes of interest. This interference could potentially affect the internal flow occurring in the holes of interest and consequently the fuel atomisation. It could be also argued that the angled passages ended at an angle to the horizontal, achieving almost perfect cylindrical passages. This angled end was represented by section C. The nozzle tip extension (section D) was manufactured to prevent spray interference with the assembly utilised to seal the tip onto the injector. Lastly, section E was the chamber in which the injector needle moved.

Prior to experiments, a set of 30 acrylic nozzle tips were investigated under a Keyence VHX-700F microscope coupled with a Keyence VH-Z20R lens (magnification range x20-x200) in order to identify any significant geometry imperfections. Initially, the nozzle tips were polished at all rectangular sections and bottom surfaces.
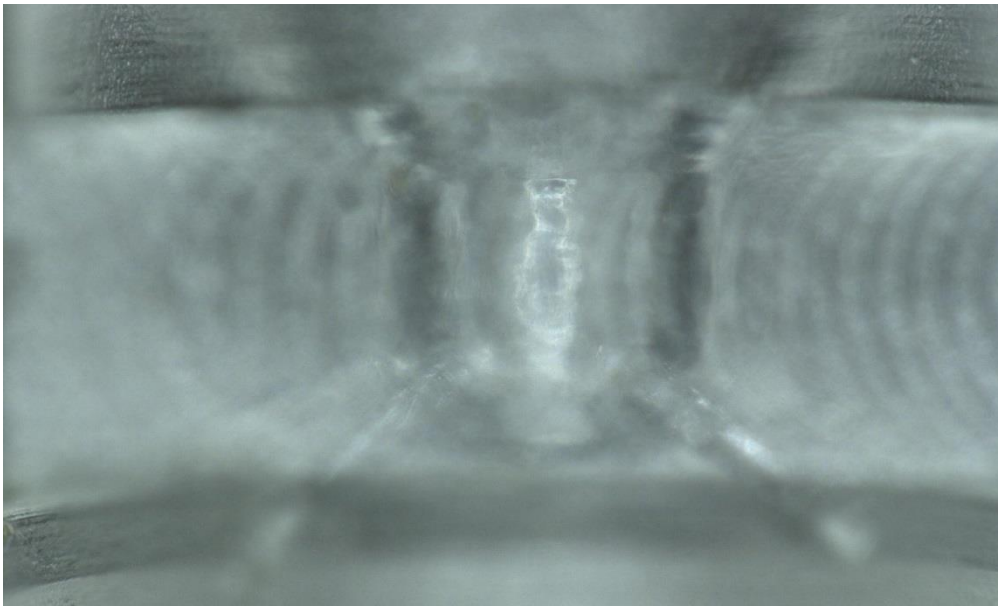
Figure 3.7: Limited optical access through an unpolished surface of the acrylic nozzle.

The aim of polishing the surfaces was the achievement of better optical access to the nozzle interior, by minimising light scattering. The smoother surfaces allowed the laser light to pass through the tip. The polishing was done on a rotating polisher utilising both 6μm and 1μm pastes for better polishing quality.

Experimental arrangements and methods

Then the nozzles were investigated under the high magnification microscope at x100 magnification to identify manufacturing imperfections. The criteria chosen for nozzle selection were:

- the nozzle passages must enter the sac at the same height

- the nozzle passages must be symmetric and parallel from the bottom view.

- the diameter of the nozzle passages must be 136μm, ± 4μm.

The majority of the manufactured nozzle tips was suitable to be used for the experiments. The rest of them were discarded, due to badly scratched surfaces or eccentric nozzle sac. The purpose of the thorough investigation of the nozzles relied upon the fact that the nozzle geometry has a significant impact on the internal flow and subsequently on atomisation.
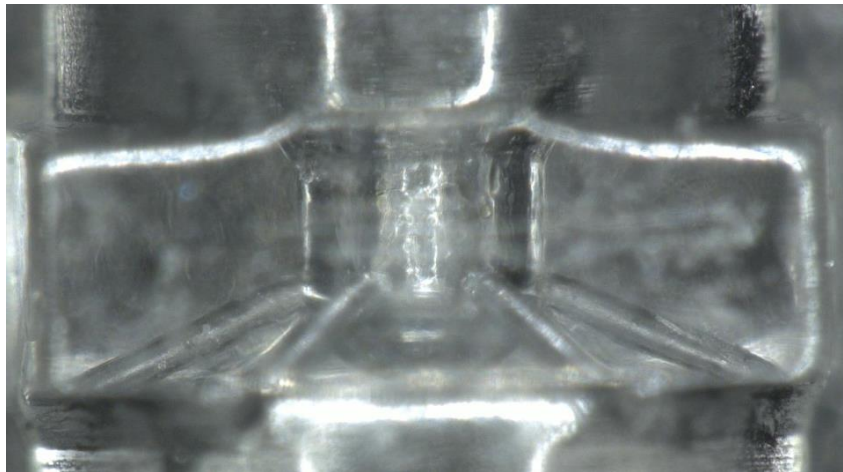
Figure 3.8: Polished nozzle surface, providing good optical access to the nozzle passages. The sac is located at the centre of the geometry and the passages entering in the sac are at the same height.

A key factor for the successful execution of the experiment was the adequate seal of the acrylic nozzle on the injector body. The suitable sealing was achieved using a compression system, which provided the force required to keep the nozzle tip in place throughout the duration of the experiment. Initially, it was essential to determine the magnitude of the forces acting on section E of the nozzle. Considering that the operating pressure was up to 350bar and the dimensions of the section E, the force developed was calculated to be 99N. Therefore, the compression force applied onto the bottom surface of the nozzle tip should balance the one developed at section E.

Experimental arrangements and methods

In this regard, a double acting hydraulic cylinder was employed to provide the compression force required to seal the nozzle tip on the injector body. In more detail, this compression system used a controllable air pressure via a pressure regulator to control a piston attached to a metal rod (Figure 3.9). The operating principle of such a system is fairly simple and is described in Figure 3.10.
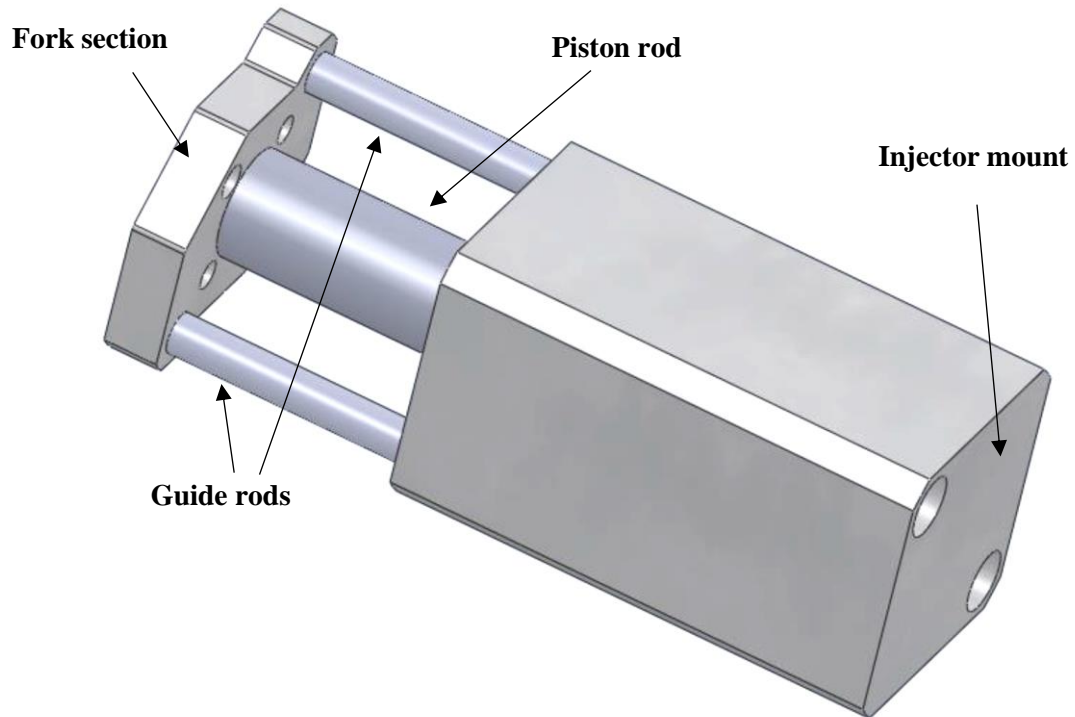
Figure 3.9: Double acting hydraulic ram[16].
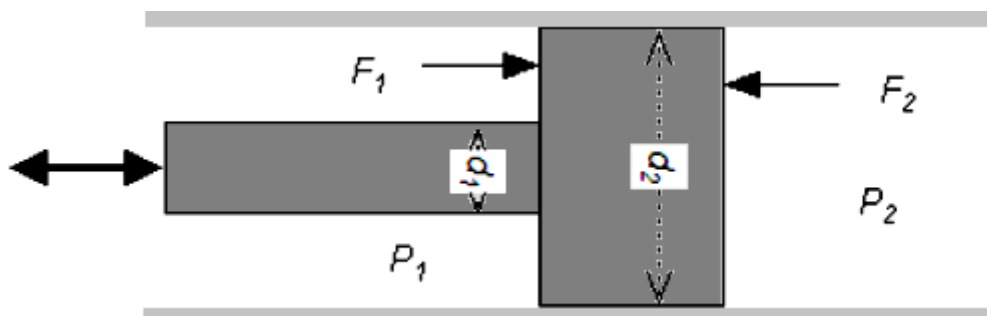
Figure 3.10: Operating principle behind a double acting hydraulic cylinder[16].

The force denoted as F_1 can be described mathematically as shown in Equation 3.1. It represented the relationship between the force and pressure developing on the side of the rod of the double acting cylinder.

$$F_1 = \frac{P_1 \pi (d_2^2 - d_1^2)}{4}$$

<div align="right">Equation 3.1</div>

Where F: rod pull force, P: pressure in the cylinder, d_1: rod diameter (16mm), d_2: piston diameter (40mm), piston stroke (50mm).

Additionally, the compression system assembly included a balancing screw which was installed parallel to the injector. The screw undertook half of the force produced by the hydraulic ram; hence, the applied compression force had to double. Consequently, the required compression force to properly seal the acrylic tip onto the injector was ~200N (2x99N), which corresponded to an equivalent pressure of ~2bar. Figure 3.9 shows that the ram consisted of a fork section, which was used to hold a fused silica cuboid and an injector mount which held the injector body in place. The cuboid was designed to fit firmly into the fork section and flush with the conical injector tip stand.

3.1.4   Injector holder mount and spray extraction assembly

3.1.4.1 Assembly of fuel injection components

A successful execution of the experiments required a rigid assembly, which would firmly hold the injector horizontally at all times. The design and orientation of the components, i.e. injector nozzle tip, injector mount, hydraulic ram, prevented any interference with the emerging diesel sprays.

Figure 3.11 show the design of the injector holder mount. It can be seen that it stood at an angle of 60 degrees from the horizontal level. In the case that the injector holder mount was vertical, the spray coming from the bottom hole of the nozzle would be incident on the hydraulic ram attached on the injector holder mount. At the top of this assembly, there was a mount where the injector was placed and held it firmly. Lastly, the whole assembly was installed on an optical table. The double acting hydraulic ram was attached to the injector holder mount. Figure 3.12 shows the whole assembly of fuel injection components.
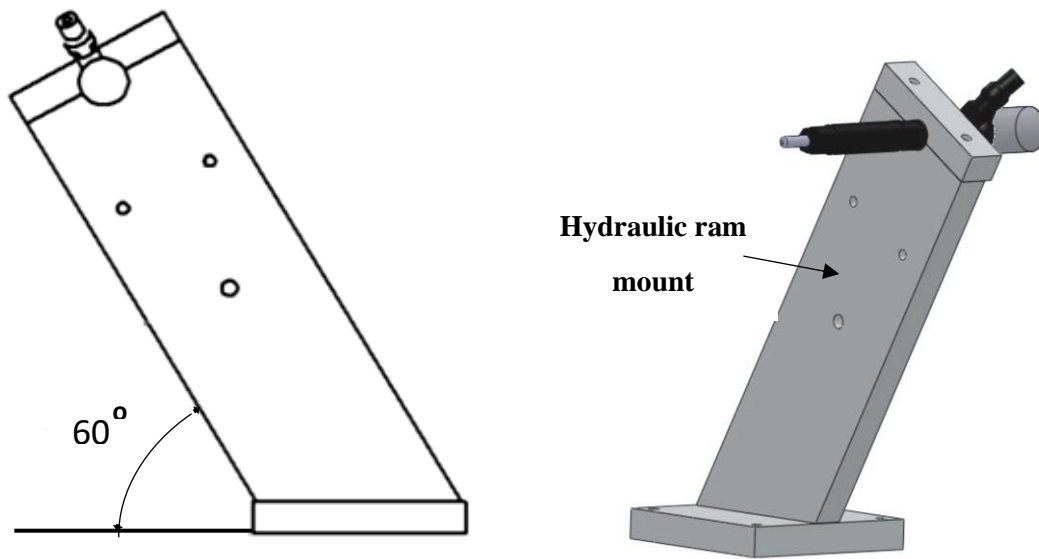
Figure 3.11: Injector holder angled at 60 degrees to prevent any interference with the emerging spray[16].
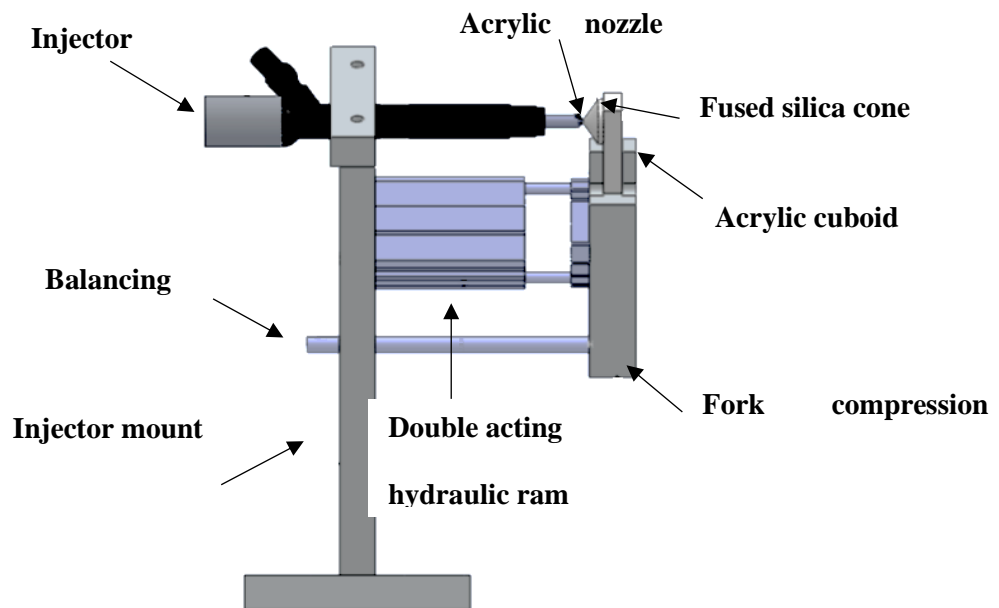
Figure 3.12: Assembly of fuel injection components[16].

As mentioned previously, the angled injector holder mount allowed the injection of the diesel fuel from the six holes without any interference with the components of the fuel injection assembly (Figure 3.13); hence, the contamination of the surrounding optics with fuel droplets was unlikely. It should be also noted that the present design facilitated the investigation of the spray between approximately 2mm and 18mm downstream of the nozzle exit.
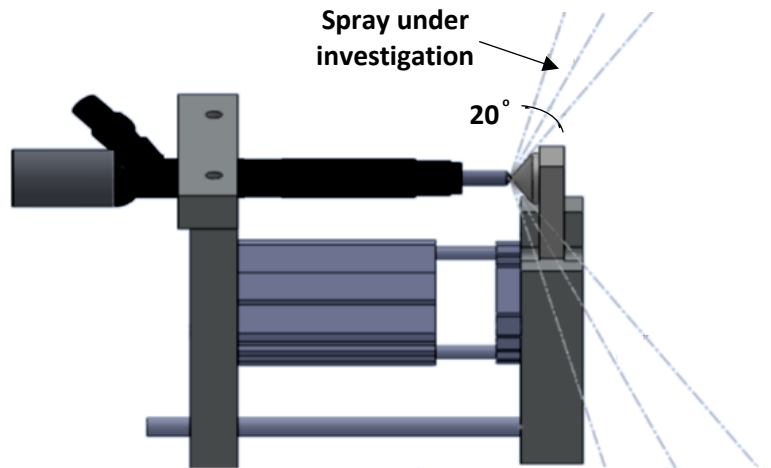
Figure 3.13: Image showing the emerging fuel sprays without interfering with the fuel injection assembly[16].

The compression force required to seal the acrylic nozzle tip onto the injector body was applied through a fused silica cone, as shown in Figure 3.12. These two components were made from transparent materials to allow optical access to the injector tip. The cone was made in fused silica to undertake the elevated temperatures developed by the laser.

3.1.4.2 Spray extraction assembly

For the purpose of this experiment, the fuels were seeded with Rhodamine B (RhB). RhB is chemical compound and a dye which can potentially cause breathing problems, if inhaled, and skin irritation. The fuel atomisation leads to the formation of fine aerosol, which is spread in the air and can be breathed in easily. Therefore, the employment of a spray extraction assembly was essential. In this regard, a fuel spray exhaust design was utilised along with an exhaust tunnel to draw the fuel aerosol after passing through an air filter. The assembly had six holes aligned against the six sprays emerging from the acrylic

nozzle (Figure 3.14). It was installed at a distance from the acrylic nozzle such that the spray cone angle was not too wide. Wider sprays would require thicker side flaps, which in turn would limit the optical access to the spray. The placement of the catch at the optimal distance (~30mm from the acrylic tip) facilitated optical access to the spray for approximately 2 cm of the spray length.
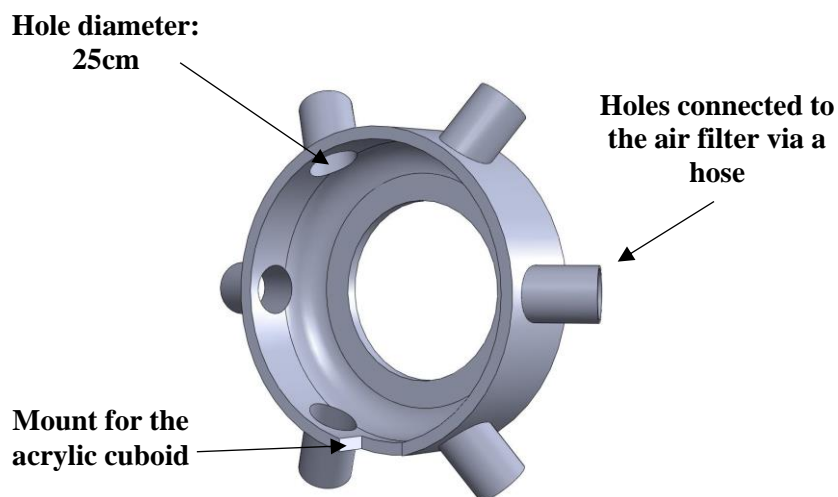
Figure 3.14: Spray extraction design[16].
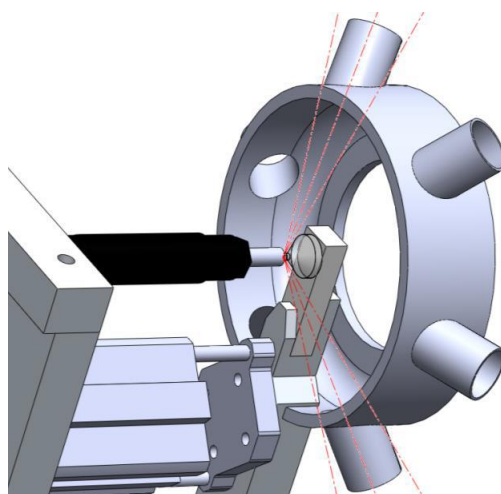
Figure 3.15: Complete assembly of fuel injection components and fuel exhaust extract[16].

Each of the six holes was connected to an air filter via a hose. Suction generated by a compressor drew the air/fuel aerosol to an exhaust tunnel. The air filter filtered out the RhB particles; as a result, the air drawn in the exhaust tunnel was clean. Figure 3.15 shows the complete assembly of both the fuel injection components and the fuels spray exhaust extract.

3.2 Optical arrangements

3.2.1   Laser optics

The 10kHz laser pulse used for the execution of Jeshani's experiment was initially elevated to the height it would be angled into the fuel jet by a periscope like arrangement with two mirrors. The elevated laser light was then passed through a series of sheet forming optics; 1m focal length planar convex lens and 2 cylindrical lenses. The convex lens converged the laser beam and led it to a -25mm planar concave cylindrical lens which formed a diverging vertical sheet. The last optic of the sheet forming assembly was a +150mm cylindrical lens which expanded the laser sheet from approximately 2mm high to 12mm. The laser sheet formed travelled an approximately 50cm distance to reach the spray position at a height of approximately 20mm. Finally, the vertical sheet (0.2mm wide at focus) was directed to the spray after being reflected on to a mirror. A more detailed description can be found in Jeshani's dissertation[16].

The optical arrangement used for the present author's experiments was similar to Jeshani's, but it also had distinctive differences. A 5kHz laser signal initially passed through an inverted Galilean telescope to achieve a laser expansion from ~1.5mm to ~6mm. This telescope consisted of a -25mm diverging lens and a +200mm converging lens. The ratio of the focal lengths of the two lenses determined the expansion factor of the beam. The expanded beam was then reflected on a $\varnothing$ 25mm mirror and led to a 50:50 beam splitter, which equally separated the laser signal into two paths, the LSD path and INF path.

The laser light of the LSD path was initially elevated from the level of the beam splitter by 30cm. The laser beam converted into a laser sheet approximately 0.2mm wide (at focus) and 20mm high, after passing an inverted telescope assembly consisted of a 1m spherical lens, a -25mm cylindrical lens and a +150mm cylindrical lens. The spherical lens converged the incident laser light from approximately 2mm down to 0.2mm, while the -25mm planar concave cylindrical lens expanded the beam only in y-axis from approximately 2mm to 12mm. The final optical component of the telescope assembly determined the final width and height of the forming laser sheet at approximately 0.2mm and 20mm respectively. The laser sheet exiting the telescope assembly was then incident on a 50mm mirror which reflected it onto the spray path after traveling a distance of approximately 30cm. Fine adjustments of

the last two optics of the telescope assembly determined the final position of the laser sheet such that it passed through the 25-degree angled fuel jet.

Figure 3.16 shows the cylindrical telescope arrangement and the mirror reflecting the laser sheet onto the spray path. The final orientation of the laser sheet at the spray position was perpendicular to the horizontal level. In order to ensure the laser sheet verticality, a plumb line was placed at the spray position. The plumb line was then illuminated with the laser operating at lower power. Fine adjustments of the optics led to a perfectly vertical laser sheet. Lastly, it was essential to preserve the Gaussian laser profile at all times. This required proper positioning of the mirrors and the sheet forming optics. Once the position of the optics was finalised, the mounts of the optics were tightened to ensure that no optic movement would occur during the execution of the experiments.

Figure 3.16: Picture showing the cylindrical telescope arrangement and the $\varnothing$ 50mm mirror.

On the other hand, the INF laser path passed through three $\varnothing$ 25mm mirrors mounted on lockable high precision mirror mounts. The reflected beam was elevated from the optical table level to approximately 40cm upwards, where three $\varnothing$ 50mm mirrors were installed. The elevated laser beam was reflected onto the mirrors and eventually passed through a +200mm focusing lens which focused the circular beam just above the nozzle passage of interest.

Figure 3.17 shows the assembly of the three mirrors and the focusing lens installed above the acrylic nozzle tip. The last two mirrors of the assembly determined the axial and transverse position of the laser

beam against the nozzle tip. After a series of test injections, the final position of these optics was determined. The mounts utilised for these optics were not lockable; hence the location of the beam was checked regularly and fine adjustments were made if it was necessary.
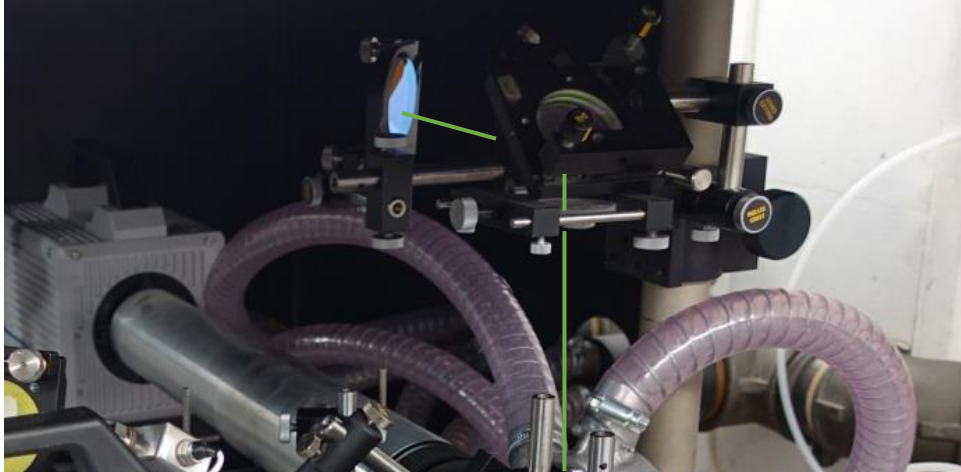
Figure 3.17: Picture showing the mirror and lens assembly above the acrylic nozzle tip. The green line shows the laser path.

3.2.2 Internal flow imaging using white light scattering and Laser Induced Fluorescence (LIF)

The imaging of the nozzle geometry using white light scattering was part of Jeshani's work, while the employment of LIF was part of the present author's work. The illumination of the nozzle geometry involved continuous white light obtained from a collimated Arri 400W POCKETT PAR lamp, after passing through a hot mirror to eliminate the 'hot' UV light.

The light was then converged after passing through a $\varnothing$150mm planar convex lens with 50cm focal length. The converged light was then reflected by a 45-degree mirror onto a $\varnothing$50mm biconvex lens with 150mm focal length. Therefore, the light was eventually focused on the acrylic nozzle. A simple schematic of the optical configuration is shown in Figure 3.18.

Experimental arrangements and methods
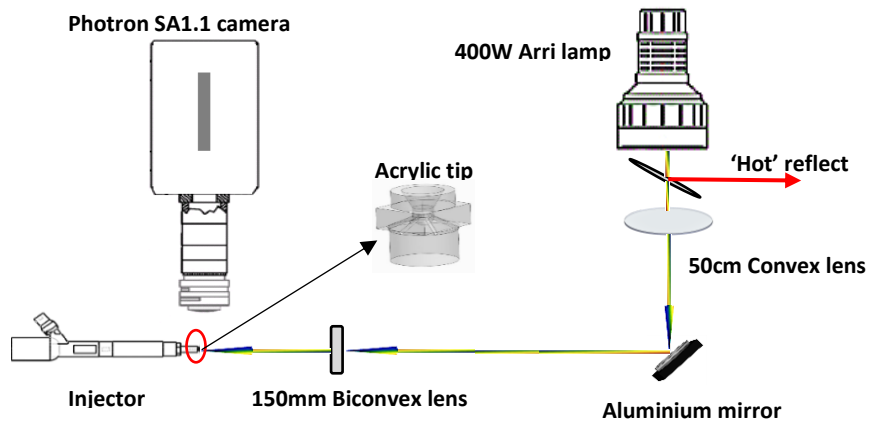
Figure 3.18: Schematic of the optical configuration.

In the case of the second set of experiments (carried out by Makri), the imaging of the internal flow phenomena involved the capture of the fluorescence emitted (LIF signal) from the structures formed inside the acrylic nozzle geometry. Figure 3.19 shows a schematic of the internal flow imaging optical configuration.
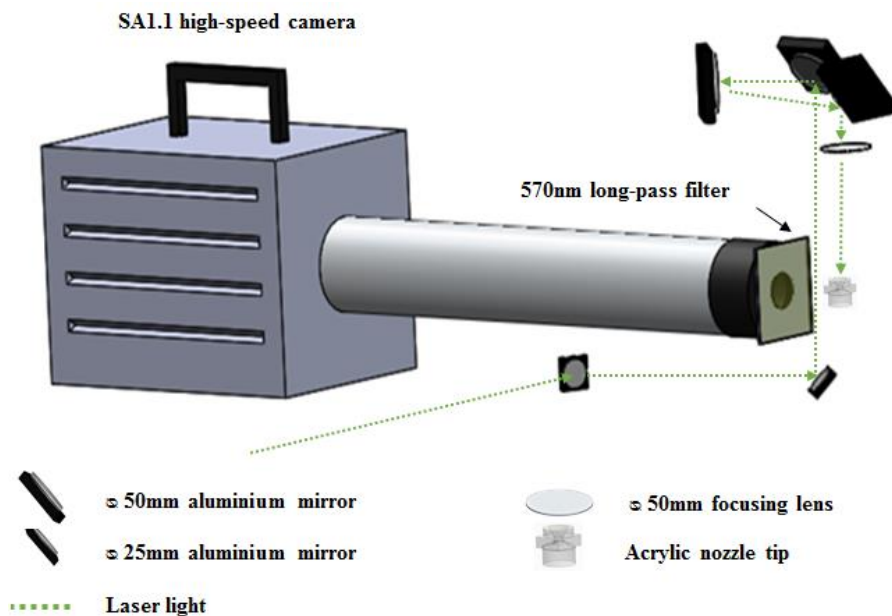
Figure 3.19: Schematic of the internal flow imaging configuration.

The internal flow imaging configuration consisted of the laser focusing lens, a series of mirrors and a 570nm long-pass filter to eliminate any wavelengths below 570nm, ensuring that the signal captured on the INF camera was only the fluorescence emitted. In more detail, the laser path (INF path) created past

the beam splitter was led to a $\varnothing$25mm aluminium mirror mounted on lockable mounts. The reflected light was then incident on another $\varnothing$25mm aluminium mirror, which elevated the beam 46cm from the level of the optical table. The elevated laser beam was then reflected on a series of three $\varnothing$50mm aluminium mirrors, which finally led the beam to a focusing lens which focused the laser bean just above the nozzle passage of interest.

The fluorescence obtained from the cavitating diesel inside the acrylic nozzle geometry was captured by a high-speed Photron SA1.1 camera (INF camera). A Nikon 85mm f/1.4 camera lens reversed coupled to 60cm extension tube (including the mounted lens). This optical arrangement facilitated a high image resolution of approximately 3.55μm/pixel which corresponded to an image magnification of ~5.6. The configuration of the INF camera allowed the acquisition of 1024 x1024 pixel images with a 1μs shutter speed. The camera lens aperture was set at f/11.0 and operated at a frame rate of 5kHz.The image acquisition began synchronously with the leading edge of the injection trigger pulse which was delayed by 900μs plus the 15ms delay required for the laser shutter to be fully opened. On the receipt of the delayed trigger pulse, the camera captured 75 frames at 5kHz for 15ms duration. This provided 6 frames prior to the injection, 26 frames during the injection and 43 frames post injection, depending on the operating rail pressure.

3.2.3   External spray image acquisition using Laser Sheet Drop-sizing (LSD)

Jeshani's experiment involved the simultaneous capture of LIF and Mie scattering signals on the two halves of a single image through a two-channel imaging setup. The configuration consisted of a 50:50 beam splitter, a 527nm band pass filter coupled with neutral density filter to attenuate the transmitted signal, an aluminium mirror, a high OD neutral density filter utilised as a mirror and a 550nm long pass filter coupled with a neutral density filter.

The light scattered from the spray structure was initially incident on the beam splitter, which reflected 50% of the scattered light and allowed the rest 50% to pass through it, resulting in the creation of two paths. The reflected light was then led to the 550nm long pass filter and neutral density filter OD 0.3 in order to eliminate the wavelengths below 550nm and also to attenuate the intensity of the incident light.

Experimental arrangements and methods

The attenuated scattered light was then reflected by an aluminium mirror onto the OD 2.0 neutral density filter and lastly onto the left half of the camera. Figure 3.20 shows a schematic of the LIF/Mie two-channel imaging setup.
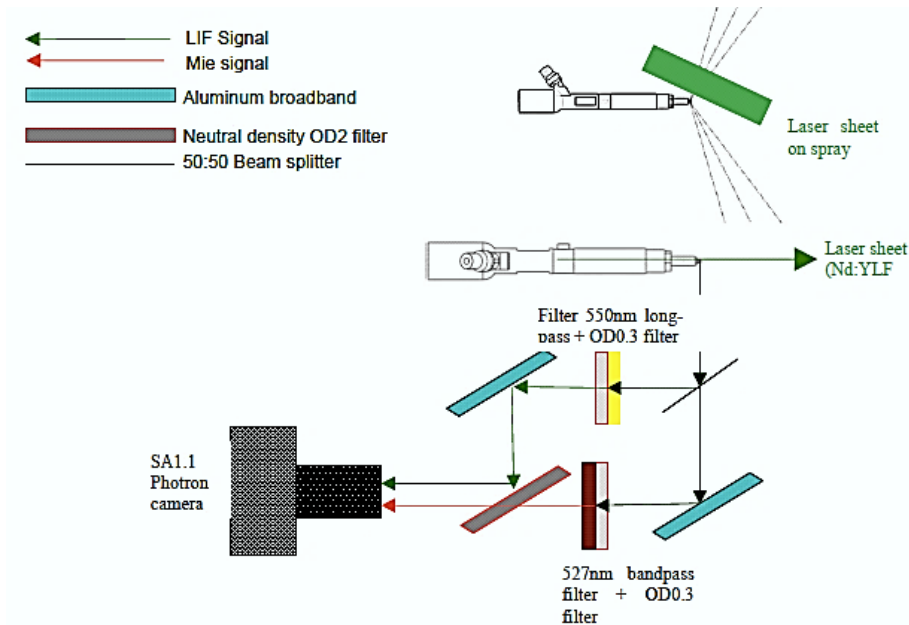
Figure 3.20: Schematic of the LIF/Mie two-channel imaging setup[14].

The light transmitted through the beam splitter was incident on an aluminium mirror which reflected the light onto a OD 0.3 neutral density filter and a 527nm band pass filter, in order to eliminate any wavelengths above 527nm and to attenuate the light intensity such that its intensity matched the intensity of the light travelling on the other path. Lastly, the attenuated light was incident on a OD 2.0 neutral density filter which reflected the light on the right half of the camera.

Similar to Jeshani's work, the optical configuration for the spray image acquisition in the case of Makri's experiments involved the concurrent imaging of LIF and Mie scattering obtained from the emerging sprays on the same high-speed camera (LSD camera). The two-channel imaging configuration consisted of a beam splitter, a 527nm band-pass filter, a 550nm long-pass filter, two aluminium mirrors and a neutral density 0D2.0 filter utilised as a mirror. Initially, the light scattered from the spray passed through a 50:50 beam splitter which allowed 50% of the light to be transmitted while the rest 50% was reflected, resulting in two light paths. The transmitted light was then reflected onto an aluminium mirror, which led the light to a 527nm band-pass filter which blocked any wavelengths above 527nm.

The filtered light finally reached a neutral density OD2.0 filter, which reflected it onto the right half of the LSD camera. On the other hand, the light reflected from the beam splitter was led to a 570nm long-pass filter, which transmitted light with wavelengths greater than 570nm. The filtered light was then incident on an aluminium mirror, which directed the light on the neutral density OD2.0 filter. Lastly, the reflected light was led to the left half of the LSD camera. Figure 3.21shows a simple schematic of the LSD optical arrangement showing all the optics involved.
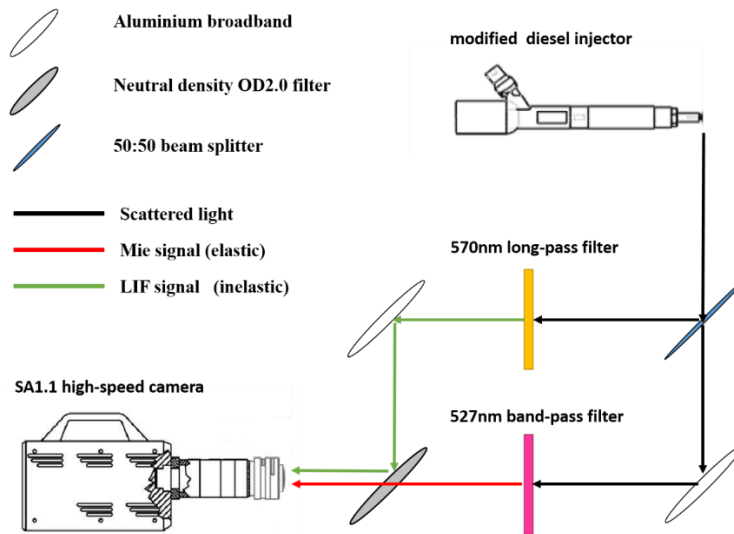
Figure 3.21: LSD optical arrangement.

A Nikon 85mm f/1.4 camera lens was reversed coupled to a 65mm extension tube and was mounted on the LSD camera. This facilitated an image magnification of ~0.6 corresponding to an image resolution of approximately 33μm/pixel. The camera settings were set to image 1024 x 1024 pixels at 5kHz with an exposure of 370ns and a dynamic range of 12 bits (0-4095 counts). Each experimental set involved the acquisition of 75 frames (15ms) per acquisition pulse. These settings facilitated the acquisition of approximately 6 frames prior to the injection, 26 frames during the injection and 43 frames post injection, depending on the operating rail pressure.

3.3 Control setup for high-speed data acquisition

This sub-section described the control setup for the image acquisition and the data in the case of the experiments executed by the author of this dissertation. A detailed description for Jeshani's experiments can be found in his PhD thesis[16].

Experimental arrangements and methods

The high-speed data acquisition required complex and precise timing settings. The control unit initially produced a 10kHz signal synchronised with the encoder signal of the pump which was fed to an even-odd separating box to generate a stable 5kHz signal. The purpose of the signal frequency change was the laser power instability when it exceeded 7.5kHz. The 5kHz signal produced corresponded to a pulse period of 200μs.

An optical shutter was installed in the INF path to ensure that the acrylic nozzle tip was illuminated by the laser only when it was necessary. Test injections suggested that a prolonged exposure of the acrylic nozzle tip to the high-energy laser led to the permanent deformation and eventually failure of the tip. According to the shutter manufacturer, a 14.2ms period is required for the shutter aperture to be fully opened. The minimum exposure was 17.2ms and the closing time was14.0ms. Hence, the duration of the shutter trigger pulse was determined to be 25ms. The leading edge of the shutter trigger pulse was synchronous against the 5kHz reference signal.

The control unit facilitated the adjustment of the cycle skip rate, the injection cycles and duration, the laser trigger activation and the delay between the injection trigger pulse and the reference signal. For the purpose of this experiment, the cycle skip rate and injection duration were set at 7 cycles (corresponding to an injection rate of 3.5Hz) and 4.0ms respectively, for 50 injections per experimental set. A 900μs delay was also induced to the signal governing the injector driver. In order to ensure that the shutter opened on the inception of the injection, an additional delay of 14.2ms was necessary. The delayed signal was then fed to the injector driver to trigger the fuel injection process.

Figure 3.22 shows a schematic of the synchronisation setup. The SA1.1 cameras required a sync-in pulse and then a trigger pulse to start the image acquisition. For the successful execution of the experiment, a delay was necessary to synchronise the cameras with the laser firing. Initially, a 192μs delay was inserted to the camera sync-in signal. This signal was then fed to a pulse generator which induced another delay of 4.84μs. The delayed signal of 196.84 μs period was then received from the laser control unit. The measurement of the laser Q-switch pulse on an oscilloscope showed that there was a delay of 180ns embedded in the laser unit response (Q-switch pulse period=197.02 μs).

Experimental arrangements and methods
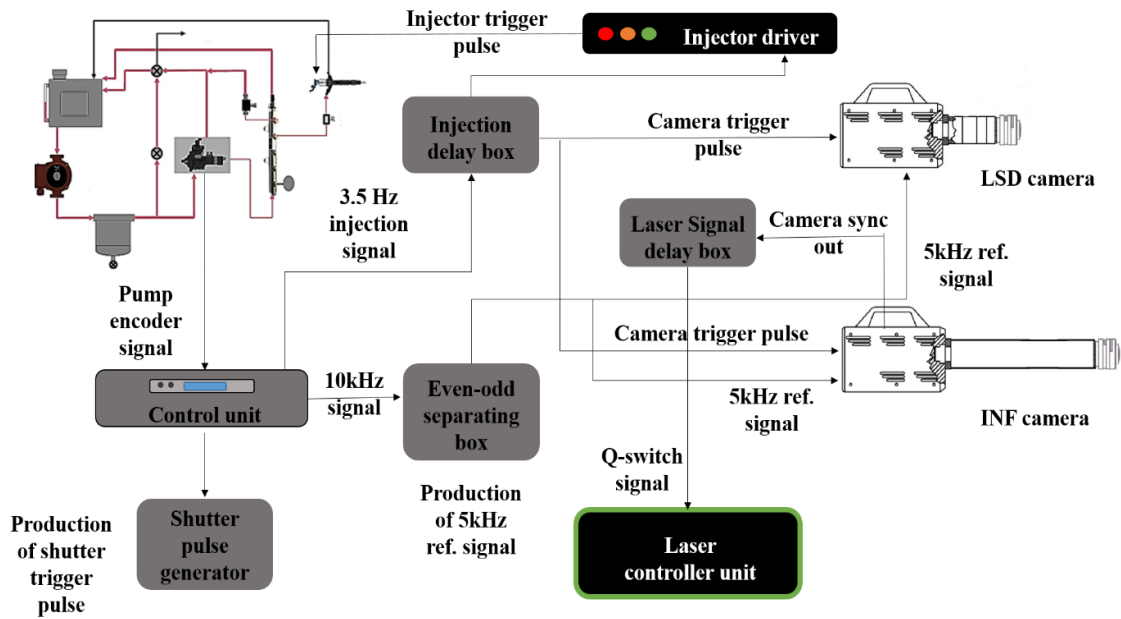
Figure 3.22: Schematic of synchronisation setup.

The read-out time of the cameras occurred at the end of each cycle and it was measured to be 670ns. Therefore, considering the camera exposure of 1 μs and the read-out time, the image acquisition occurred between 198.33μs and 199.33μs after the leading edge of the reference signal. It was essential to ensure that the laser would fire within the camera exposure duration. In this regard, the laser was tuned to fire 1.15 μs after the leading edge of the camera exposure pulse. The latter signal together with the camera exposure pulses were checked prior to the execution of the experiment.

In order to obtain reliable experimental data, it was essential to ensure that each injection event was repeated under the same conditions. In this regard, the injection duration pulses, the laser fire pulses, the INF camera exposure pulses and the injection pressure signals were recorded on a PC using a National Instrument (NI) data acquisition card. The sampling rate was set at 200kHz corresponding to 1200 samples over a 6.0ms period after the SoI. The NI acquisition card was capable of receiving both analogue and digital signals. The camera exposure pulse, the injection trigger pulse and the laser pulse were digital signals, whereas the pressure transducer produced an analogue voltage signal, which had to be calibrated to convert it into pressure. All digital and analogue signals were recorded in an excel separated comma file via a Lab View algorithm produced to record data on the receipt of the injection pulse. Considering the camera exposure duration of 1μs and a sampling rate of 200 kHz, the recording

of this signal was not possible. To overcome this problem, a 30μs pulse synchronised to the camera exposure signal substituted the original exposure pulse allowing the NI card to record it at 200 kHz.
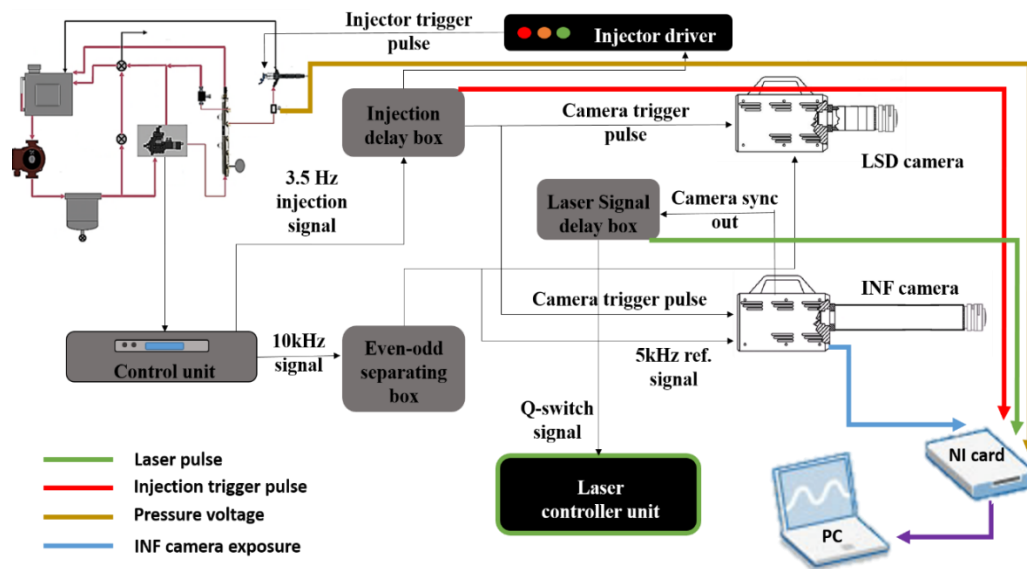
Figure 3.23: Schematic of data acquisition setup.

A consistent methodology during experimentation was essential to obtain reliable and comparable data. This section describes the diesel fuel samples used, the methodology followed for the fuel seeding with RhB and the calibration work required to be able to compare the different fuel data. The latter involved the investigation of the injected mass variation per nozzle and the effect of the physical properties of the utilised fuel and solvent on their fluorescence yield.

3.4 Experimental methodology

A consistent methodology during experimentation was essential to obtain reliable and comparable data. For completion, the first sub-section was a brief description of Jeshani's experimental methodology; a detailed description can be found in his PhD dissertation[16].This section was mostly devoted the diesel fuel samples used in the experimental work, the methodology followed for the fuel seeding with RhB and the calibration work required to be able to compare the different fuel data. The latter involved the investigation of the injected mass variation per nozzle and the effect of the physical properties of the utilised fuel and solvent on their fluorescence yield.

3.4.1 Diesel fuels and fuel seeding with fluorescent dye

For the purpose of both Jeshani's and Makri's experiments, five and four diesel fuel samples, provided by Shell Global Solutions, were employed. For convenience, the fuels were denoted as fuel A, B, C, D, E and fuel 1, fuel 2, fuel 3 and fuel 4 respectively.

Fuel A was an un-additised crude oil derived middle distillate diesel, which has a wide boiling point range between 172˚C-342˚C. Its density and kinematic viscosity were 825 kg/m^3 and 2.078mm^2/s respectively. Fuel B is a gap fuel; there were no intermediate products in the middle of the boiling point range and its density and viscosity were quite similar to the ones of Fuel A, 826.1 kg/m^3 and 2.102 mm^2/s respectively. On the contrary, Fuel C and D were lighter than the two previous fuels; their distillation profiles were between 201˚C-259˚C and 200˚C-300˚C respectively. Fuel C was kerosene combined with a lubricity additive, while Fuel D was a light kerosene based fuel. Ultimately, fuel E was the heaviest of the fuels under examination and was a blend of diesel and 20% FAME. Its viscosity and density were higher than the rest of the fuels.

Fuel 1 was an un-additised diesel with a distillation profile between 173 and 358 degrees. Its density and viscosity were 833.7 kg/m^3 and 2.803 mm^2/s respectively. Fuel 2 was a B20 diesel blend which had the largest viscosity (3.031mm^2/s) and density (843.1 kg/m^3). The corresponding boiling point range was fairly similar to fuel 1. The third fuel under consideration, fuel 3, was a gap diesel sample. This fuel type consisted of only light and heavy fractions. The fractions corresponding to approximately 40% to 60% recovered volume did not exist; this explained the sharp slope between this range, as shown in Figure 3.24. The viscosity and density of this sample were 2.084 mm^2/s and 823.0 kg/m^3 respectively. Lastly, fuel 4 was a jet fuel and was the lightest amongst the fuels under investigation. As shown in Figure 3.24, its distillation profile was narrower relative to the rest of the fuels, since it ranged between 160 and 260 degrees. The corresponding viscosity (1.222 mm^2/s) and density (820.4 kg/m^3) values were lower than the other diesel samples. All the physical properties and the distillation profiles of the fuels under inspection are summarised in Table 3.1 and Figure 3.24.

.

Table 3.1: Physical properties of the fuels under investigation. (*R655 additive was believed to introduce viscoelastic properties in the fuels (non-Newtonian fluids))

Fuel type	Physical properties		
	Viscosity@40 ºC (mm²/s)	Density (kg/m³)	Boiling point range (ºC)
fuel A - diesel	2.078	825.0	172-342
fuel B – gap diesel	2.102	826.1	158-351
fuel C* – kerosene + R655 (250ppm)	1.691	801.9	201-259
fuel D – light kerosene	1.664	800.3	154-208
fuel E – B20 diesel	2.389	836.2	200-300
fuel 1 - diesel	2.803	833.7	173-358
fuel 2 – B20	3.031	843.1	178-353
fuel 3* – gap diesel + R655	2.084	823.0	156-350
fuel 4* – jet fuel + R655	1.222	820.4	161-260
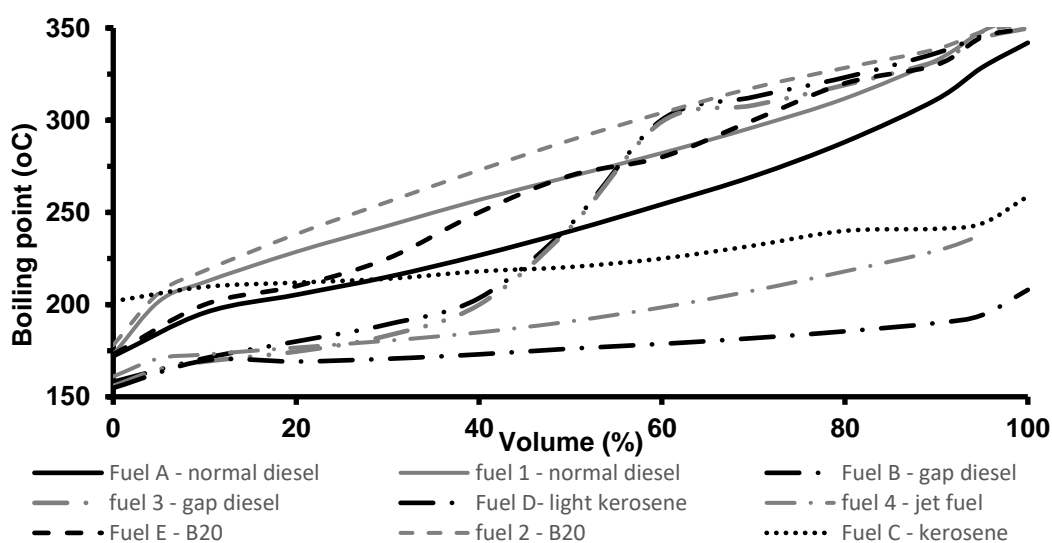
Figure 3.24: Distillation profiles of the fuels under investigation.

Experimental arrangements and methods

The techniques chosen for the execution of the experiments involved the capture of the fluorescence produced by the de-excitation of the dye particles in the fuel bulk. Theoretically, a reliable and quantitative measurement of fluorescence is obtained when is produced by a single compound. When fluorescence is produced by a number of different species, the integrated intensity signal obtained exhibits a complex dependence on various factors, such as species concentration, operating conditions etc. It can also vary in terms of thermo-physical and physical properties, such as diffusion coefficient, boiling point range etc. Hence, it can be argued that a quantitative LIF analysis requires systems which usually produce fluorescence from single components.

The fluorescence emission is a consequence of initially the excitation of the fluorescent particles by a laser light to a higher energy level and their return to the original energy level by fluorescence emission. It is essential for the excitation wavelength to be within the absorbance spectrum of the dye. In the ideal case where the excitation wavelength matches the peak absorption wavelength, the excitation efficiency maximises. Additionally, another important parameter to obtain optimal detection efficiency is the employment of suitable optical filters, which refine the emitted fluorescence such that only the desired wavelengths are captured by the high-speed cameras.

In the present experiment, the fuels were seeded with Rhodamine B (RhB), whose excitation wavelength was at 527nm and emission wavelength at 568nm. The molecular structure of RhB is shown in Figure 3.25.
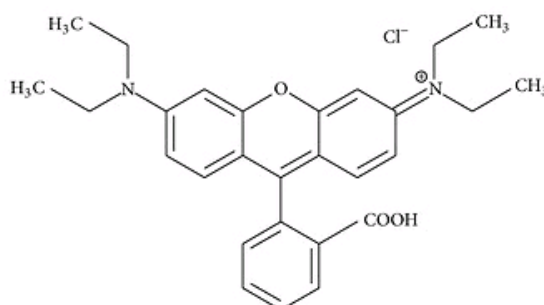
Figure 3.25: Molecular structure of Rhodamine B[16]

Experimental arrangements and methods

As mentioned previously, the selection of a suitable optical filter improves the measurement sensitivity; the chosen filters on the LSD path and INF paths were two 570nm long pass filters, which transmitted wavelengths greater than 570nm and blocked all shorter wavelengths. The selection of these filters was not only because of their close value to the emission peak of the dye, but also because of the need to separate Mie scattering (532nm) from the obtained signal.

It should be noted that RhB was not directly mixed with the fuel, but it was initially pre-mixed with a suitable solvent which matched the boiling point of the fuel. Hence, the chosen solvent for all the fuels apart from fuels C and 4 was HLPC 1-Decanol, whereas in the case of fuels C and 4 was 1-Octanol. Preliminary tests involved the illumination of samples of RhB directly dissolved in fuels with laser at 527nm. It was shown that the fluorescence path length was not adequate for the successful execution of the experiments. Therefore, the fluorescent dye was initially dissolved in a solvent and then was mixed with the corresponding fuel. A key element in this procedure was the determination of the optimal dye concentration; the final solution should provide a non-saturated signal, meaning that the linear relationship between the fluorophore concentration and intensity were not violated.

The optimum concentration of RhB in the solvent was 600mg/L. This stock solution was then mixed with the corresponding fuel in a 4(fuel):1(stock solution) ratio, resulting in a final solution of 120mgRhB/L. The measurement of the mass of the RhB powder was made on a high precision (±0.0001g) scale. The fuel and solvent volumes were measured utilising 500ml (±2.5ml) and 250ml (±1ml) Pyrex measuring cylinders. The 600mg of RhB were dissolved in 1 litre of solvent using an ultrasonic bath for approximately 30 minutes. The solution was investigated regularly to check the mixing progress. This stock solution was then mixed with 4 litres of fresh diesel fuel to create a final concentration of 120mgRhB/L. The final mixture was stored in glass 2.5L bottles. This procedure was repeated one more time to produce 10L of 120mgRhB/L. Approximately 9 out of 10 litres of the final mixture were used for flushing purposes and the actual experiments. The remaining fuel was kept tobe used for the fluorescence yield measurements.

3.4.2   Experimental procedure

Due to the increased complexity of the experiment, it was essential to develop a methodology that would be followed during each experimental session. This methodology involved the filling, emptying, flushing procedures of the rig and the necessary steps undertaken during the experiments.

For the successful execution of the experiment, it was crucial to avoid any significant fuel contamination every time a new fuel was tested. This was achieved by flushing the rig twice prior to use of the new fuel. In between the successive flushing procedures, the rig was emptied completely; the fuel from both low and high-pressure lines of the fuel injection system was removed. After the second flushing, it was necessary to empty the line connecting the fuel delivery system with the injector. This line contained approximately 200cc of fuel. The emptying procedure of this line was achieved setting an injection rate of ~20Hz (50% duty cycle) for a duration of approximately 30seconds. After emptying the rig, a new 5μm polypropylene filter was installed on the rig. A detailed description of the steps followed during the filling, emptying and flushing procedures is presented in Appendix B.

3.4.2.1 Laser imaging experimental procedure

After the completion of the above-mentioned procedures, the fuel injection system was ready for use. Prior to the fuel testing, a new acrylic tip was used. Each acrylic tip would be used for 4 sets of 50 injections; two sets at 250bar and 350bar with one fuel and then one set at 350bar with the next fuel. The final set of 50 injections involved the injected fuel mass measurements. The injected mass measurements were performed to investigate the effect of the synergy between the nozzle geometry and the physical properties of the fuels.

Additionally, it was essential to ensure that the nozzle passages were aligned against the holes of the fuel spray exhaust extract and the spray under investigation was in line with the vertical laser sheet. The alignment was achieved by carefully inserting a 136μm blank drill bit into the hole of interest, which would model the injected spray. The acrylic tip with the drill bit inside the nozzle hole was then mounted on the modified injector body and was held in place by applying a weak force via the compression system. At this point, the INF path was blocked using a laser damper. The laser started firing at low

power producing a low intensity vertical laser sheet. Then, the nozzle tip was rotated by means of a small spanner designed to fit the rectangular section of the acrylic tip such that the drill bit would be equally illuminated along its geometry. A small piece of cardboard was placed in the path past the drill bit to note the position of the drill bit relative to the laser sheet. When the bit was equally illuminated along its body, its projection on the cardboard piece would be a small bright green section surrounding a dark section (drill bit shadow). Once the alignment was achieved, the laser damper was removed so both laser paths were visible. The vertically focused beam coming from the top was checked against the laser sheet. The correct position of the optics forming the laser spot was determined by checking that the vertical sheet was intersecting the spot in a way that two equally spaced segments were formed. After the completion of the alignment procedures, the air pressure was increased to approximately 3.5 bar to ensure that the tip would be held in place and finally the blank drill bit was removed from the hole. The air pressure remained the same throughout the experimental session; any change in air pressure could potentially misalign the assembly. The next step of the laser imaging experimental procedure involved the adjustment of the control unit parameters, which controlled the injection process. The camera and control unit settings in the case of Jeshani's experiments are summarised in

Table 3.2 and

Table 3.3.

Table 3.2: Summary of camera settings[16] (Jeshani's experiments).

Software settings	**Camera settings**
Exposure	1/2700000
Frame size	1024 pixels x 512 pixels
Camera lens setting	85mm, f1.4
Sync in	Synchronised against the other camera

Exposure out	To National Instruments data acquisition card

Table 3.3: Summary of the control unit settings[16] (Jeshani's experiments).

Injection pressure (bar)	Injection duration (ms)	Injection skip rate (count)_	Injector trigger delay (μs)	No. of injection cycles (count)
250 or 350	4.0	8 (3Hz)	500	100

For the purposes of the second set of experiments conducted by the present author, each experimental session consisted of 50 injection cycles of 4.0ms duration each at an injection rate of 3.5Hz. The injection trigger delay was set at 900μs and the laser trigger was switched on. Both cameras were synced with the 5kHz sync pulse coming from the even-odd separator box. Both cameras were triggered simultaneously. Their settings are summarised in Table 3.4.

Table 3.4: Camera inputs and settings.

Camera settings	INF camera	LSD camera
Exposure (μs)	1	1
Image resolution (pixels)	1024 x 1024	1024 x 1024
Camera lens aperture	f11	f4
Sync in	Sync pulse from the even-odd separator box	E-sync pulse from INF camera
Sync out delay (μs)	192	-
Trigger out	To LSD camera	-
Exposure out	To NI acquisition card	To NI acquisition card

Experimental arrangements and methods

Prior to image acquisition, both cameras were calibrated for zero light. The calibration was done when the black aluminium panels were covering the optical table. A key parameter for the successful execution of the experiments was the correct synchronisation of the laser firing and the cameras' exposures. It was essential for the laser to fire soon after the start of the camera exposure period. Additionally, the laser firing should occur within the exposure duration, but also not towards the end of the exposure period since fluorescence was emitted approximately 400ns after the excitation of the fluorescent molecules. This additional delay to the laser sync in signal was tuned on a pulse generator; the laser fired 1.15μs after the leading edge of the camera exposure signal.

Each time a new acrylic tip was employed, a set of 75 background images was taken from both cameras at full laser power. It was important to ensure that there was no fuel present in the nozzle geometry because the laser would excite the tracer molecules and consequently the cameras would capture fluorescence signal instead of the background. It should be also mentioned that no more than one laser shots could be undertaken, since the laser could easily damage the acrylic tip.

The last check made before starting the experiment was measurement of the pressure voltage offset. A zero-pressure voltage reading was obtained from the pressure transducer via the NI acquisition system. This was in the range of 500 mv ± 50mv. The pressure setting for 350 bar injection pressure was calculated taking into account the sensitivity of the transducer, which was 1.189 mV/BAR. The injection pressure was adjusted to this value.

After the completion of the preliminary tests, the experimental setup was ready for image acquisition. During the experiments, the spray exhaust suction was switched on. Each experimental set involved the acquisition of 75 frames over a set of 50 injections at both 250bar and 350bar. During the fuel testing, data with regards to the injection pressure, camera exposure and laser trigger signal were acquired with the NI acquisition card. An additional set of 50 injection at 350bar was also done in order to determine the injected fuel mass corresponding to each nozzle tip.

The collection of the injected fuel mass was done by placing three latex condoms around the injector body. The three pre-weighted condoms were held in place using a plastic-coated wire tie. The condoms

were sitting loosely around the injector tip to be able to sustain the force applied by the emerging fuel jets. After the completion of the 50 injections, the condoms were carefully removed from the injector. The injected fuel mass was measured on a high precision scale three times and the mean fuel mass was calculated. After subtracting the mass of the three condoms from the measured mass, the net fuel mass was obtained. Lastly, the acrylic tip was investigated under the high magnification microscope to identify the level of the erosion/damage of the hole inner surface due to cavitation. The dimensions of the cross sections together with their corresponding pictures were taken.

Each experimental fuel was tested with two different acrylic tips to check the consistency of the mass flow measurements and the impact of the physical properties on the fuel mass flow rate. One of the acrylic tips was brand new, while the other was used to test another experimental fuel. The experiments conducted with the new acrylic tip were two sets of 50 injections at 250 and 350bar and an additional set of 50 injection for the injected fuel mass measurements. On the other hand, the experiments with the used nozzle tip involved a set of 50 injections at 350bar and another set of 50 injections for the fuel mass measurements. Table 3.5 shows the acrylic tips utilised for the investigation of the fuels. It should be noted that the table shows only the commercial fuels and not the whole range of fuels tested. This is the reason for which nozzles 8 and 9 are not shown twice in the table.

Table 3.5: Summary of the nozzle tip used for the fuel testing.

	Fuel 1	**Fuel 2**	**Fuel 3**	**Fuel 4**
New nozzle tip	Nozzle 26	Nozzle 8	Nozzle 3	Nozzle 1
Used nozzle tip	Nozzle 6	Nozzle 17	Nozzle 9	Nozzle 3

3.5 Calibration procedures

The main purpose of this work was the determination of the impact of the fuels' physical properties on the external sprays and the internal flow. It was essential for the results obtained to be corrected in a way such that the results were comparable. In this regard, calibration procedures were necessary to eliminate the effects of the different solvents and fuels under examination.

3.5.1 Gaussian laser profile measurements

Samples of the four fuel mixtures under investigation and a sample of GTL fuel were utilised for the purposes of these measurements. The GTL sample was used to take a set of background images since its refractive index was similar to the fuel mixtures' refractive indices and it was transparent to the passage of the 527nm laser. Each experimental set involved the acquisition of 75 frames while the laser was running at full power at 5kHz and the lens aperture was set at f4. An average of the acquired images provided the corresponding laser sheet intensity profile. Each fuel sample was filled in a 2cm x 2 cm x 4.5cm acrylic cuvette with a wall thickness of ~2mm.
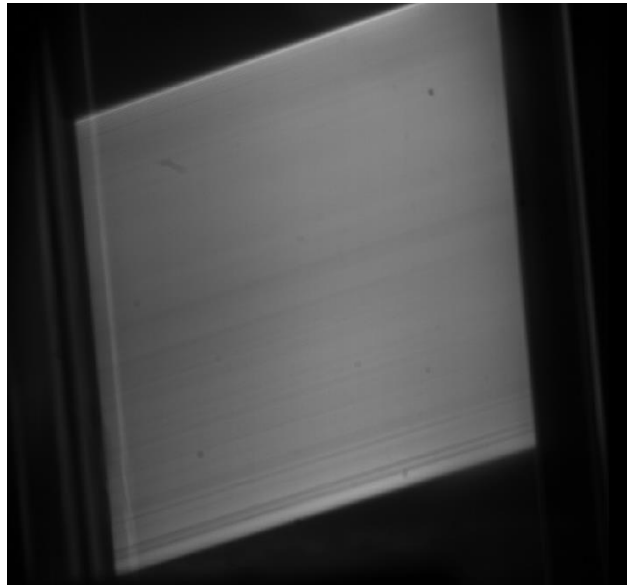
Figure 3.26: An example of a laser sheet intensity profile produced by fuel 1 diesel sample.

The cuvette was then placed at the same position as the position of the diesel spray. The laser sheet was entering the cuvette from the right-hand side, as shown in Figure 3.26. The laser was triggered once since the laser could potentially permanently damage the cuvette.

It should be noted that there was no need to correct both LIF and Mie data against the corresponding laser profiles in the case of LSD analysis, since both sets were produced by the same laser profile and the ratio obtained from the two signals would cancel out any effects. On the other hand, the correction of LIF data against the laser profile was necessary in order to be able to compare the results obtained by the different fuel samples. It should be mentioned that all averaged laser profile images were

translated against the spray origin, prior any further image correction. Additionally, the laser profiles were utilised to determine the calibration ratios, since the fluorescent yield produced by the RhB particles was strongly dependent not only on the solvent used, but also on the nature of the fuel. Fuel 1 was considered as the reference fuel; hence all fuels were compared to fuel 1. Even though the laser intensity appeared to remain fairly uniform across the cuvette, there was a region close the right-hand side of the image that the local intensity was slightly higher. This higher intensity region was chosen to calculate the calibration ratios. It should be noted that the region of interest remained the same in all four diesel samples. The calibration ratio of fuel 2 obtained the lowest value, while the ratio of fuel 4 the highest. In the former case, it was believed that the RhB particles interacted (quenching effect) with the oxygenated function group present in B20 diesel blend. This could possibly lead to the formation of a complex in the ground state which usually exhibits different properties than the RhB molecules (static quenching). The calibration ratio of fuel 4 obtained the highest value, since the utilised solvent is 1-Octanol and not 1-Decanol as the rest of fuel samples. Jeshani followed a similar procedure for the determination of the fluorescence yield calibration ratio corresponding only to fuel D. The calculated calibration ratios for both experiments are summarised in Table 3.6.

Table 3.6: Fluorescent yield calibration ratios for RhB fluorescent yield in different fuel mixtures.

Fuel samples	Fluorescent yield calibration ratio
Fuel D / Fuel A	1.04
Fuel 2 / Fuel 1	0.85
Fuel 3 / Fuel 1	0.98
Fuel 4 / Fuel 1	1.09

3.5.2   Injected fuel mass

As it was mentioned previously, a set of 50 injections at 350bar was performed with every acrylic tip tested. Some acrylic tips were used for two fuels to investigate the impact of physical properties and nozzle geometry on the injected fuel mass. The aim of this investigation was the determination of the

discharge coefficient, as a function of the physical properties of the fuels. The methodology followed for the collection of the injected fuel is described in 3.4.2.1.

For the purposes of this analysis, it was necessary to determine the minimum cross section of each of the six holes of the acrylic tip, since the mass flow rate of the fuel is mostly affected by the minimum cross section. In this regard, all acrylic tips were thoroughly investigated under a high magnification microscope and the minimum cross section was determined. The next step involved the calculation of the speed developed by the fuel inside the nozzle holes using Bernoulli's equation (Equation 3.2).

$$u_{Bernoulli} = \sqrt{\frac{2\left(P_{upstream} - P_{back}\right)}{\rho_{fuel}}}$$ Equation 3.2

The back pressure was atmospheric pressure (10^5 Pa), while the upstream pressure was considered to be $3 \cdot 10^7$ Pa instead of the injection pressure at $3.5 \cdot 10^7$ Pa, due to the pressure drop occurred as soon as the fuel entered the injector. Another important parameter in the determination of the Bernoulli velocity was the density of the fuel. It is known that density changes with changing temperature and pressure. Considering the temperature difference between the cooled fuel in the tank and the injected fuel to be 45 degrees and the thermal expansion coefficient of diesel and kerosene to be $\beta = 8.3 \cdot 10^{-4}$ K^{-1} and $\beta = 9.9 \cdot 10^{-4}$ K^{-1} respectively, the given density (measured at 15°C and 1atm) was corrected accordingly employing Equation 3.3.

$$\Delta\rho = -\beta\Delta T\rho$$ Equation 3.3

where β: thermal expansion coefficient [K^{-1}], ΔT: temperature difference [K], ρ: fuel density [kg/m^3] (15°C, 1atm)

Based on the Bernoulli's velocity, the cross sections of each hole, the corrected density and the injection duration of 4.0ms the calculation of the theoretical fuel mass flow rate was achieved. The ratio of the measured injected fuel mass flow rate over the theoretical mass flow rate defined the discharge coefficient. It should be noted that the actual injection duration was approximately 5.4ms, but for the purpose of this analysis, the typical value of 4.0ms injection duration was used. The results obtained are summarised in Table 3.7.

Table 3.7: Calculated discharge coefficient for all four diesel samples with different nozzle tips.

	Discharge coefficient (%)						
	Nozzle 26	Nozzle 6	Nozzle 17	Nozzle 3	Nozzle 8	Nozzle 9	Nozzle 1
Fuel 1	58.8	74.2					
Fuel 2			71.0		71.1		
Fuel 3				81.3		60.7	
Fuel 4				81.7			62.3

The data shown in Table 3.7 referred only to the commercial fuels and not to the whole range of fuels tested. This explained why some fuels were not tested with a common nozzle tip. However, it could be argued that the dependence of the discharge coefficient on the physical properties is not as significant as on the nozzle geometry (i.e. nozzles 16 and 6, nozzle 3). Comparing these values to a typical discharge coefficient values ($C_d \sim 75\%$ - 80%) of a conventional diesel nozzle, it could be argued that the acrylic nozzle tips exhibited lower discharge coefficient. This could be attributed to the roughness of the internal surfaces of the acrylic nozzle passages, which promoted cavitation and consequently reduced the fuel mass flow rate. The nozzles used in this analysis were nozzles 26 (fuel 1), nozzle17 (fuel 2) and nozzle 3 (fuels 3 and 4).

However, in the case of Jeshani's experiments the injected fuel mass consistency was tested in a slightly different and was not as detailed as described above. The calculation of the theoretical mass flow rate of each nozzle was performed using Bernouli's velocity; facilitating the calculation of the corresponding discharged coefficient. A comparison of the coefficients obtained provided a fairly accurate assessment on the consistency of the injected mass per nozzle. The discharge coefficient of the conventional nozzle was also calculated. These calculations were made for fuel A, which was considered as the reference fuel for the purpose of this analysis. The minimum and maximum injected

masses obtained from the acrylic nozzle were 2.781g and 2.802g respectively for a set of 50 injections. Hence, the averaged fuel injected mass was 55.82mg. This corresponded to a discharge coefficient of ~66% for a 4.0ms injection duration. The corresponding discharge coefficient of the conventional nozzle was larger by 20.4% (~83%), implying that the surface roughness of the acrylic nozzle hole interior enhanced the in-hole cavitation.

Chapter 4

Internal flow characterisation using optical diagnostics

This chapter was devoted to the characterisation of the internal flow inside the acrylic tip, based on the results obtained from the white light scattering and LIF experiments. The white light scattering experimental data was part of Jeshani's PhD project and referred to fuels A-E. However, the processing methodology and the interpretation of the results were performed by the author of this work. On the other hand, the LIF measurements and the subsequent processing were also performed by the present author.

The optical observation of the white light scattering experimental data nozzles revealed the presence of vapour capsules/bubbles both in the sac and the nozzle passages as soon as the needle sealed. The bubbles formed appeared to form a vortex flow inside the sac which was believed to be responsible for the generation of pressure gradients, capable of pushing/pulling the vapour capsules/bubbles present in the passages. The admission of vapour structures through the nozzle passages has been also observed by other researchers[67,92].

Based on these observations, the following work attempted to correlate the in-hole bubble movement observed with the post-injection in-sac vortex flow as a function of the physical properties of a range of diesel fuel samples. Under real diesel engine conditions, the admitted vapour structures can be hot combustion gases which could easily react with the remaining liquid fuel in the nozzle passage, resulting in the formation of deposits. The following sections consisted of the description of the experimental arrangement and the image processing methodology, followed by the discussion of the results. To the best of the author's knowledge, there is no available literature with regards to the root cause and the implications of such phenomena on diesel injector deposit formation.

Internal flow characterisation using optical diagnostics

The last part of this chapter was focused on the analysis of the data obtained from the nozzle passage using LIF, aiming to obtain quantitative information with regards to the LVF of the internal flow as a function of the physical properties, rail pressure and transient movement of the needle. Laser Induced Fluorescence (LIF) is widely utilised for the identification of the liquid phase in a multi-phase flow. Due to the optimal concentration of RhB in the diesel samples, the liquid phase was characterised by high quantum efficiency; hence the identification of liquid structures is possible. However, it was observed that there were strong beam steering effects, due to the scattering of fluorescence from the flow discontinuities and the curved surfaces of the tip geometry; therefore, the results obtained did not refer to the conventional liquid volume fraction. Additionally, it was observed that the post injection signal obtained was lower compared to the signal during the injection. This could be attributed to the increased flux density of the laser during the injection process. The optical arrangement (INF path) facilitated the illumination of the bottom of the emerging spray, which focused the laser beam on the hole. Hence, for the purpose of this analysis, a new term, called Scattered Fluorescence Liquid Volume Fraction (SFLVF) was introduced and described the fluorescence produced inside the nozzle passages. It basically describes the fluorescence intensity captured in the ROI. This cannot be directly related to the LVF of the flow due to the experimental limitations mentioned above and later in this chapter.

To keep this dissertation to a reasonable length, the injection pressure dependence was investigated only in the case of fuel 1, while the dependence on the physical properties of the fuels was shown by the comparison between fuel 1 and fuel 3, which had an approximately 25% difference in viscosity. Another parameter of this analysis was the lift of the injector needle; the analysis was performed at three different needle positions, 1.8ms, 3.8ms and 5.6ms after SoI. In this regard, the distributions of the corresponding mean images were produced and compared. The mean images and the corresponding STD images were also produced in false colour to provide a comprehensive visualisation of the outcomes obtained. To the best of the author's knowledge the measurements and results were original and novel and there was no literature available for comparison.

4.1 In-nozzle and sac flow data analysis

The following sections attempted to highlight the relationship between deposit formation and internal nozzle flow phenomena occurring towards the end and post injection, as a function of the fuel's physical properties. They described the methodology developed to extract information from the raw data, with regards to the size of the in-sac vapour structures, the decaying rate of the in-sac vortical flow, the vapour structures' motion in the nozzle passages and the possible implications of buoyant effects on the bubble/fluid motion observed.

4.1.1 Sac bubble formation

When the needle reached its final seal position, bubble formation was observed in the sac, possibly due to needle sheet cavitation occurring during the late stages of the needle return phase. The calculation of the size of the bubbles generated, together with the corresponding pressure differential created in the sac was achieved employing a Matlab code developed at City, University of London. The structures under investigation appeared like bright, white regions due to elastic scattering (Figure 4.1).
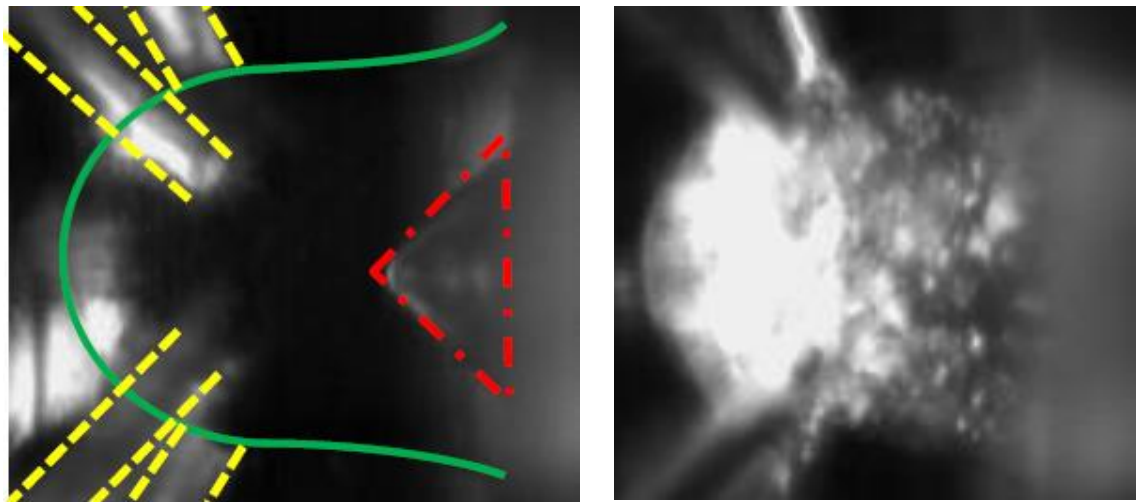
Figure 4.1: Frame obtained at 6.0ms after SoI (fuel D) showing the in-sac structures represented by the bright white regions due to white light elastic scattering from the structure interface. (green line: sac volume, red dotted dash profile needle tip, the yellow dashed line: nozzle holes).

Internal flow characterisation using optical diagnostics

Initially, the raw data was subjected to a sequence of morphological operations in order to remove the image background and the existing noise. In particular, the first operation performed was a bottom-hat filtering (dilation followed by erosion) process applied on the raw image using a disk-shaped structuring element of 6 pixels in size. The resulting image corresponded to the image background which was then subtracted from the raw image. A Gaussian filter was then applied onto the resulting image utilising a smoothening kernel with standard deviation of 0.5, followed by a top-hat filtering (erosion followed by dilation) process using a disk-shaped structuring element of 2 pixels in size. Such processes excluded the large bright regions which could either be a cloud of small bubbles or a large vapour capsule. Hence, it could be argued that this analysis was biased towards smaller structures. The noise removal was achieved using a Weiner low-pass filter, which filtered the image using neighbourhoods of size 8 by 8 pixels to estimate the local mean and standard deviation. In order to obtain sharp, well-defined bubble boundaries, the code eliminated pixels whose intensity was greater than their surroundings and connected to the structure boundary. Any structures less than 2 pixels in diameter were eliminated since these structures were most likely artefacts.

The code then detected the co-ordinates of the pixels with the local maximum intensity in all the structures present in the filtered image. For the purpose of this analysis, it was assumed that each structure included only one local maximum and the structures detected were spherical. The determination of the structure boundaries was achieved by scanning the 18-by-18-pixel neighbourhood around the pixel of local maximum intensity. Three criteria were employed to determine whether a pixel was part of the structure or not. In particular, the intensity of the surrounding pixels must be less than or equal to the intensity of the adjacent pixels in all directions and the intensity of the centre pixel and greater than the threshold defined. The code utilised three threshold values, depending on the intensity of the centre pixel, whose values were determined after a careful optical observation of the raw data. In more detail, for local maximum intensities greater than 3600 counts or less than 1300 counts the threshold values were 0.65 and 0.5 times the maximum intensity respectively, while for the ones between 1300 counts and 3600 counts the threshold value was 0.55 times the maximum intensity. The final image contained all the structures whose pixels satisfied the criteria described above;

consequently, the bubble boundaries were clearly defined and the calculation of the bubble diameter was quite accurate. Lastly, the calculation of their size was made using Equation 4.1. Considering the image resolution to be 7.54μm/pixel, the calculated diameters converted into microns (μm).

$$A = pi * r^2 \Rightarrow r = \sqrt{\frac{A}{pi}} \Rightarrow d = 2 * \sqrt{\frac{A}{pi}}$$
Equation 4.1

Where: A: surface area, r: bubble radius, d: bubble diameter

The next step involved the calculation of the developed in-sac pressure difference utilizing the simplified version of the Young-Laplace equation (Equation 4.2).

$$\Delta P = \frac{2\gamma}{r}$$
Equation 4.2

Where, ΔP: pressure difference (kPa), γ: surface tension of the fuel (N/m), r: radius of the bubble (μm).

Lastly, the code produced time-resolved intensity frequency distributions of bubble diameter and pressure difference over a set of 50 injections. All results were exported in excel worksheets for later use.

The detection of the bubble boundaries was based on intensity thresholding. The values of the chosen thresholds were determined after a thorough investigation of the raw images. The curved surfaces of the objects (bubbles/capsules) under inspection caused an optical distortion. This distortion appeared like a fading bright ring around the main body of the object. It was believed that the intensity of the actual bubble boundaries was approximately 50%-60% of the local maximum intensity. A significant proportion of the results obtained were subjected to an optical comparison against the raw data. There was a very good agreement between the sizes detected by the code with the bubble sizes obtained by the visual inspection. Lastly, there is no optical deformation since the refractive indices of the acrylic and the working fluid were matched.

4.1.2 Vorticity in the sac

The key part of the present analysis was the in-sac flow and structures forming as soon as the needle returned to its seal position (5.9ms after SoI). The structures formed were believed to form a

circumferential vortex flow, which initially exhibited a high radial velocity which quickly subsided with time, since its angular momentum decayed. The following section was dedicated to the description of the methodology followed to capture the vorticity decay observed. For the purpose of this analysis, the time at which the needle returned (5.9ms after SoI) was set to 0ms.

During the first 1.2ms after the needle return, the in-sac flow was quite intense and turbulent, hence the observation of individual structures was not possible. Hence, the phenomena occurring during this time period were excluded from this analysis. The identification of the vorticity decay rate was achieved by tracking a number of individual bubbles between 1.2ms and 5.5ms (43 successive frames) after the needle sealing. In particular, the X and Y co-ordinates of the structures were manually obtained using Matlab and were saved in an excel file for later use. It was essential to record the co-ordinates of the same structure over time; when a structure merged with another structure or disappeared in the background, its tracking stopped and a new structure was chosen to be recorded. Prior to any further calculations, the location of the central axis of each nozzle was determined. The intersection point between the nozzle symmetry axis and the needle tip defined the reference point, which was used for the rest of the analysis. The distance between the reference point and a bubble laying on AB line defined the constant distance R_o. Figure 4.2 shows the movement of an individual structure in three successive images. It was crucial to initiate or terminate the tracking of a structure at these two points, since the value of angle theta (θ) is known and equal to $-\frac{\Pi}{2}$ and $\frac{\Pi}{2}$ respectively. The values for the intermediate angles were calculated using   Equation 4.3. Due to the assumption of a circumferential in-sac vortex flow, distance R_o was kept constant throughout the analysis.

(a)

(b)
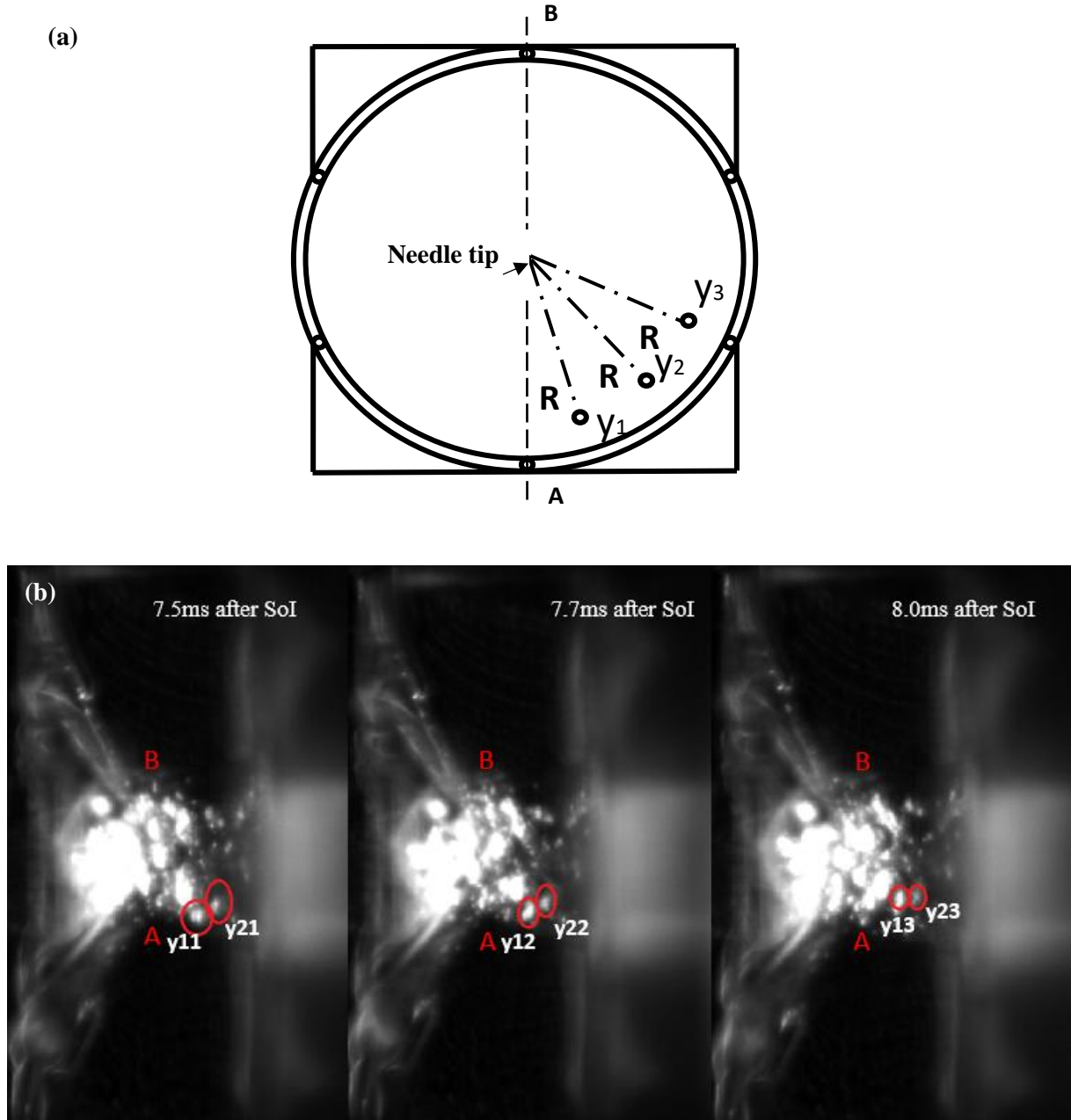
Figure 4.2: (a) Representation of tracking process of an individual structure. y_1 to y_3 are the y-co-ordinates in three successive frames (nozzle view from the bottom), (b) an example of bubble tracking in a series of raw images (the red circles indicate the bubbles of interest).

$$\text{Angle theta } (\theta)=\sin^{-1}\frac{y_{i,j}}{R_o} \qquad \text{Equation 4.3}$$

Where: y_i: y-coordinate of the structure, i: structure number in a sequence of images, j: frame number.

The next step of this analysis involved the calculation of the instant angular velocity of each structure. This was expressed mathematically by Equation 4.4. The time interval between the successive frames was $\Delta t = 10^{-4}$s. The averaged angular velocity was then calculated at each time step/frame (Equation 4.5) and injection. Lastly, the overall averaged angular velocity was calculated over a set of 20 injections (Equation 4.6). The overall mean angular velocity was plotted against time to identify the rate of the decay.

$$\Omega_{i,j} = \frac{\theta_{i,j+1} - \theta_{i,j}}{\Delta t}$$

Equation 4.4

$$\overline{\Omega}_{i,1} = \mathrm{average}(\Omega_{1,1}, \Omega_{2,1}, \cdots, \Omega_{i,1})$$

Equation 4.5

$$\overline{\Omega}_{j,m} = \mathrm{average}(\Omega_{1,1}, \Omega_{1,2}, \cdots, \Omega_{1,m})$$

Equation 4.6

Where: m is the number of the injection.

4.1.3 Sac vorticity induced nozzle flow

When the needle sealed, bubbles appeared not only inside the sac volume but also inside the nozzle passages. The bubble movement observed inside the passages has been also notified by other researchers[52,67,92], however they did not provide further details about it. The following methodology described the calculation of the size, velocity and displacement of the bubbles/vapour capsules detected in both upper and lower nozzle passages.

A Matlab code developed at City, University of London was employed to investigate the phenomena occurring post injection only, namely between 0ms and 5.4ms after the needle return, inside the upper and lower nozzle hole. Initially, the code applied a mask onto the raw image, such that the resulting image contained only the region of interest (upper or lower hole). Prior to image masking, the image background and existing noise were removed by subtracting the background image from the raw imaged and applying a carefully chosen intensity threshold. At this point, the code allowed the user to manually zoom in the structures of interest and selected the X and Y co-ordinates of the front and back interfaces

of the structure. It should be noted that the code allowed the analysis of maximum 2 structures or alternatively 4 interfaces.
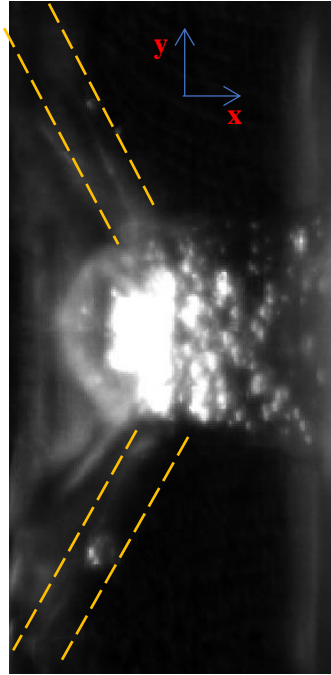
Figure 4.3: Picture of the imaging nozzle side. The yellow dashed lines define the boundaries of the nozzle passages under investigation[16].

Additionally, the entrance of the nozzle passages was considered as the reference point for the analysis of the same passage and same nozzle/fuel. The manually obtained x and y coordinates of the four interfaces (denoted as x_1 and y_1) and the reference point (denoted as x_o and y_o) were utilised to calculate the displacement of each interface over time, employing Equation 4.7. Taking into consideration the image resolution of 7.54μm/ pixel, the displacement was converted into millimetres and was finally plotted against time. The hole entrance was represented by 0mm, whereas the nozzle hole exit by approximately 1.1mm.

$$\text{Displacement} = \sqrt{\left(x_1 - x_o\right)^2 + \left(y_1 - y_o\right)^2} \qquad \text{Equation 4.7}$$

The calculation of the corresponding speed of the structures was achieved by taking the ratio of the change in displacement of each interface in two successive images over the corresponding time ($\Delta t = 10^{-4}$s). This is expressed mathematically by Equation 4.8.

$$v = \frac{\Delta r_{(i+1)} - \Delta r_{(i)}}{\Delta t} \qquad \text{Equation 4.8}$$

Where v: the speed of the interface (mm/s), Δr: displacement (mm), i: the frame number and Δt: the time interval (s).

Consequently, two sets of data were produced per object, one per interface. The average of the two sets provided the mean speed of the vapour structure over time (Equation 4.9).

$$\bar{v} = \text{average}(v_{i,\text{front inter.}}, v_{i,\text{back inter.}}) \qquad \text{Equation 4.9}$$

Where $\bar{v}$: the mean structure speed (mm/s), $v_{i,\text{front inter.}}$: the speed of the front interface in frame I, and

$v_{i,\text{back inter.}}$: the speed of the back interface in frame i.

Lastly, the code calculated the diameter of the detected structures utilising the co-ordinates of the front and back interfaces of each structure in Equation 4.10. All the results were exported and saved into an Excel file for later use.

$$\text{diameter} = \sqrt{\left(x_{\text{front inter.}} - x_{\text{back inter.}}\right)^2 + \left(y_{\text{front inter.}} - y_{\text{back inter.}}\right)^2} \qquad \text{Equation 4.10}$$

4.1.4 Analysis on the buoyant effect on the in-nozzle flow

The diesel/bubble flow in the nozzle passages could be argued to be a consequence of buoyant effects. Buoyancy could be responsible for the bubble floating to the liquid interface present in the nozzle passages. Therefore, the following analysis involved the calculation of the speed that the structures would develop if buoyant forces were responsible for their movement. In later sections, the theoretical speed values were compared to the experimental ones to determine whether the bubble movement observed occurred due to buoyancy or the pump-like phenomenon described in earlier subsections of this chapter.

The determination of the theoretical speed values was based on the work by Plesset and Epstein[182]. The formulas (Equation 4.11, Equation 4.12 (Rybczynski's formula)) used took into account the buoyant,

the drag effects and the properties of the liquid and gas fluids (e.g. surface tension, viscosity). The diffusion effects were ignored, since the gas density was considered to be much higher than the concentration of the dissolved gasses in the surrounding medium. The radius range used was between $7\mu m$ and $300\mu m$ to match with the sizes of the structures present in the nozzle passages. The gas enclosed inside the vapour structures was considered to be a mixture of 95% air and 5% fuel. This mixture composition represented an extreme case. It should be noted that the nozzle passage was angled at an angle $\theta=25$degrees from the vertical plane, therefore Equation 4.11 and Equation 4.12 took this angle into consideration.

$$F_R = \frac{4\pi}{3} g \left(\rho_L - \rho_G \right) R^3 \cos(\theta)$$

Equation 4.11

$$F_R = 6\pi\mu_L Ru \frac{2\mu_L + 2\mu_G}{3\mu_L + 3\mu_G} \Rightarrow u = \frac{F_R}{6\pi\mu_L R} \frac{3\left(\mu_L + \mu_G\right)}{2\left(\mu_L + \mu_G\right)}$$

Equation 4.12

The calculation of the experimental speed was based on the results obtained from the analysis described in section 3.2.3. The ratio of the structure displacement over the corresponding time interval gave the corresponding speed of the structure (Equation 4.13).

$$v_{exp.} = \frac{\Delta y}{\Delta t}$$

Equation 4.13

Where: $v_{exp.}$: experimental speed (mm/s), Δy: calculated displacement (mm) and Δt: time interval (s).

4.2 Discussion on the in-nozzle and sac results

The following sections were devoted to the discussion of the results obtained with regards to post injection phenomena. The results included in the main body of this work refer to fuel A at 250bar and 350bar, but the discussion referred to all five fuels (fuel A-E, at 350bar) under consideration. The results (graphs, tables) corresponding to fuels B to E are presented in 0.

The main objective of this piece of work was the investigation of the relation between internal flow phenomena and deposit formation as a function of fuel's physical properties. The following analysis was carried out between 5.9ms and 11.3ms after the SoI or 0ms and 5.4ms after the needle sealing over a set of either 20 injections (in-sac vorticity analysis) or 50 injections. The results obtained were a good

estimate of most of the parameters under investigation (i.e. mean angular velocity, bubble sizes). The in-sac flow together with the back flow observed inside the nozzle passages were 3D phenomena which have been approached utilising 2D images; therefore, a number of assumptions have been made to be able to quantify certain parameters.

4.2.1 Mini-sac diesel vorticity

An optical observation of the phenomena occurring towards the end and post injection revealed the presence of vapour structures/bubbles inside the sac volume, which were not present during the injection event. Figure 4.4 shows the bubble generation as soon as the needle returned. The bubbles appeared in the sac as bright, white structures due to elastic scattering of the white light on the bubble surfaces.
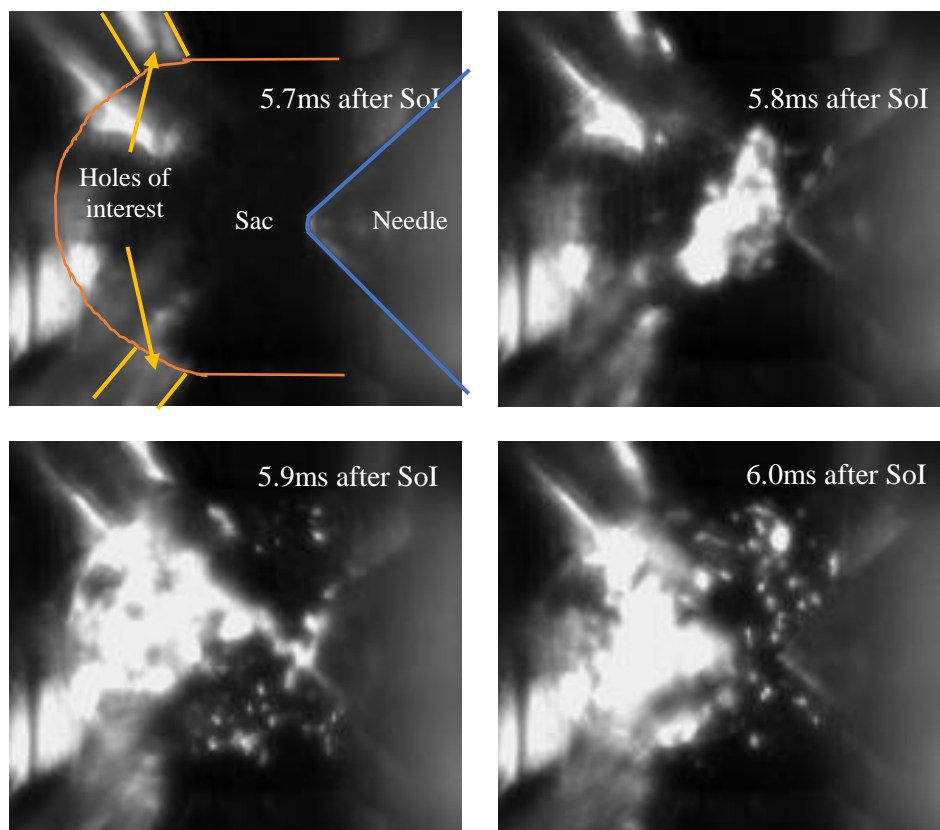
Figure 4.4: Images captured between 5.7ms and 6.0ms after the SoI showing the bubble formation in the sac due to needle sheet cavitation (fuel A, 350bar)[16].

Internal flow characterisation using optical diagnostics

This bubble generation was believed to be a consequence of needle sheet cavitation taking place during the end stages of needle return. Needle cavitation formed as a result of the small gaps between the needle and the injector body when the needle was close to its sealing position. The bubbles were suggested to follow a circumferential vortex flow, which at the early stages of post injection had high radial velocities, which quickly slowed down with time due to the decreasing flow momentum. The post injection vortex flow could be attributed to the retained angular momentum originating from the flow vorticity during injection.

An optical inspection of Figure 4.4 revealed that the bubble formation initiated when the needle was close to its sealing position (5.8ms after SoI), due to needle sheet cavitation. As soon as the needle sealed (5.9ms after SoI), the in-sac diesel flow was assumed to be circumferential and had a high angular velocity, which progressively slowed down. Figure 4.5 and Figure 4.6 show the mean vorticity decay rate as a function of the physical properties of the fuels at 250bar and 350bar respectively over a set of 20 injections.
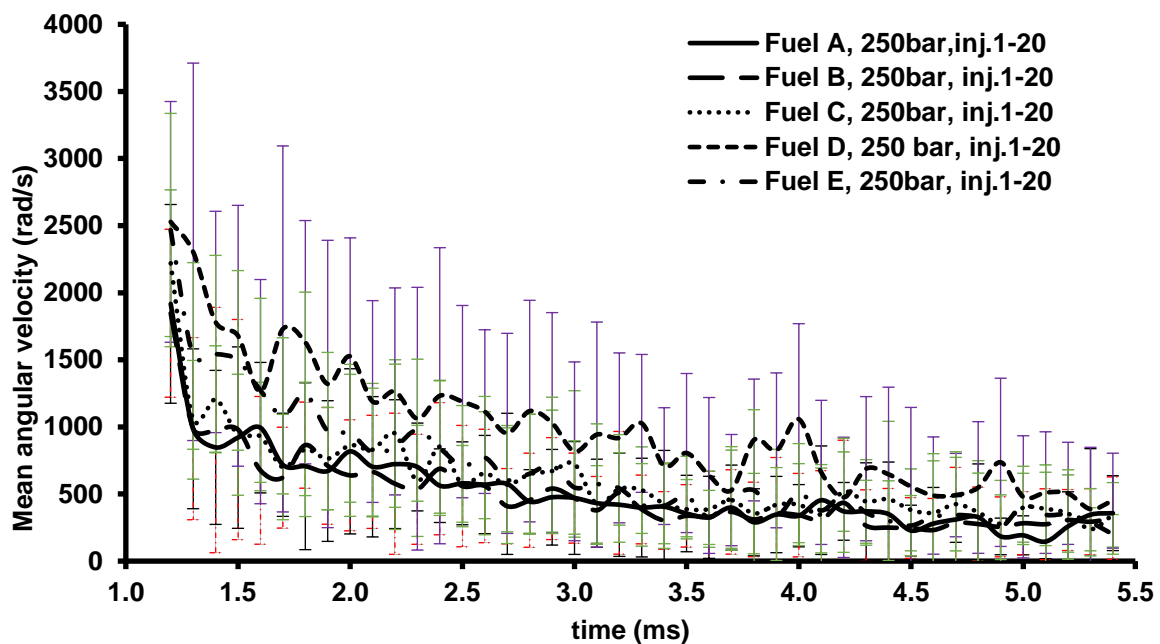
Figure 4.5: Vorticity decay rates as a function of fuel physical properties at 250bar over a set of 20 injections.

The decay of the vorticity in the sac was consistent with the viscosity of the fuel type, i.e. the decay rate of the lighter fuel samples occurred with a larger scale than the corresponding decay of heavier fuel

samples. The decay rate of fuel D, which was the lightest amongst the fuel samples under consideration, was much slower than the decay rates obtained from the rest diesel samples. It was believed that this was a result of the lower viscosity of fuel D relative to the rest diesel fuel samples. Fuels samples A (diesel) and B (gap diesel) exhibited similar decaying rates, due to their similar physical properties. The decay rate of fuel sample C was slower in comparison to fuel samples A and B and agreed with the expected trend. However, it could be seen that the decaying profile was closer to fuel A rather than fuel D, whose physical properties were closer to fuel C. This was believed to be a consequence of the addition of the lubricity additive R655, which altered the viscosity of the fuel. This additive was widely used not only in the fuel industry, but also in the food industry. It mainly consisted of glyceryl mono-oleate which exhibited viscoelastic behavior. In principle, viscoelastic fluids create non-Newtonian behavior[183]; therefore, it could be argued that the addition of R655 additive in fuel C was capable of altering the viscosity of the fuel which in turn had an impact on the faster rate than expected. On the other hand, the vorticity decay rate in case of fuel E (B20) initially was slower relative to fuel samples A and B, but when the flow settled down their decay rates were fairly similar. However, this was not the expected behavior since fuel E was the heaviest amongst the fuels under consideration. According to the expected trend, the decay rate should have been the fastest due to the high viscosity of fuel E. This anomaly was believed to be a consequence of the Fatty Acid Methyl Esters (FAME) being in a 20% proportion in the fuel. During the early stages of post injection, the vortex circumferential flow was quite intense; therefore, it was suggested that the fuel possibly underwent a separation process which separated the esters from the main fuel bulk and created an inhomogeneous flow. This separation could possibly cause this unexpected behavior.

Figure 4.6 shows the vorticity decay rates of the five fuels at 350bar. It could be seen that the initial angular velocity in all five samples was higher relative to 250bar. This could be attributed to the higher angular momentum of the flow, due to the increased rail pressure. Even though the initial angular velocity was higher, a comparison between the results shown in Figure 4.5 and Figure 4.6 indicated that the corresponding decay rates remained more or less the same as in case of 250 bar, suggesting that the rail pressure did not have a significant impact on the vorticity decay rate, with an exception in case of

fuel C. It was believed that an increase in rail pressure affected the phenomena occurring during the early stages of post injection (5.9ms–7.1ms after SoI), when the in-sac flow was still intense and had a high radial velocity. When the flow settled down, the dynamics of the flow seemed to be independent of the rail pressure.
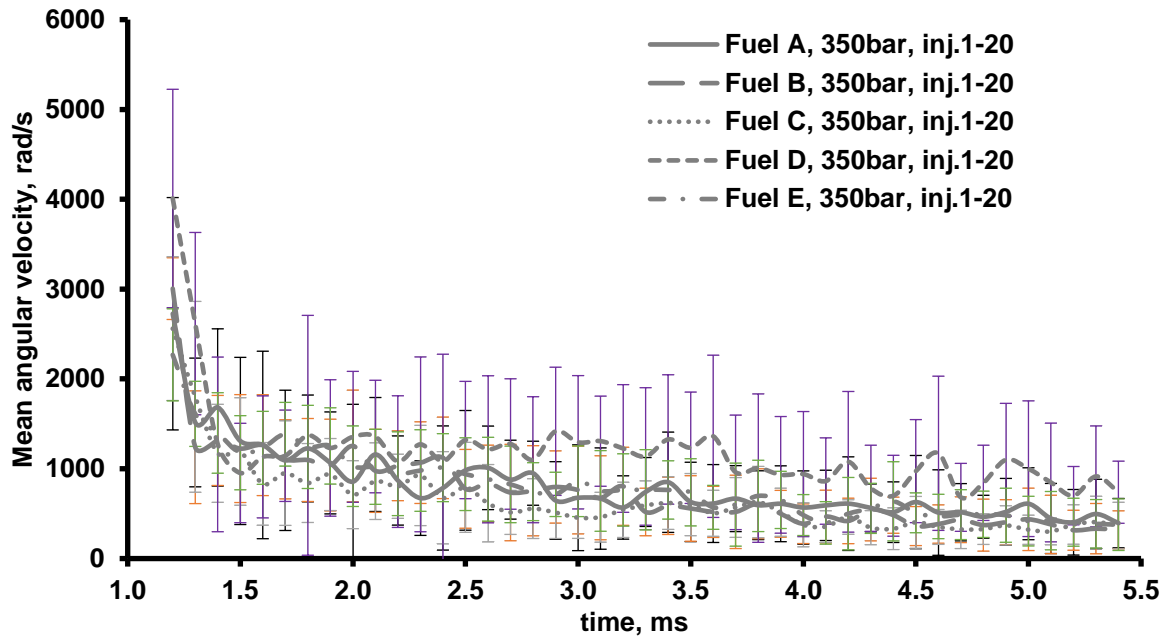
Figure 4.6: Vorticity decay rates as a function of fuel physical properties at 350bar over a set of 20 injections.

In the case of 350 bar, fuel D showed the slowest decay rate relative to the rest of the fuels. Fuels A, B exhibited very similar behaviour due to their fairly similar viscosities. The decay rate of fuel sample E exhibited a slightly different trend, as a result of the separation process explained previously. The most unexpected trend was obtained by fuel C which seemed to have the fastest decay rate. It was suggested that fuel C exhibited non-Newtonian properties, due to the addition of the lubricity additive; therefore, it could be argued that the viscosity change was expected to be profound, as a consequence of the rail pressure increase from 250bar to 350bar. In most non-Newtonian fluids, viscosity increases with increasing pressure as a consequence of the decrease of the amount of free volume in the internal structure, due to compression effects[184]. Considering the above, the viscosity of fuel C at 350bar was

expected to be greater relative to 250bar. An increased viscosity could possibly explain the faster decay rate.

The large scattering intensity coming from the structures in the sac volume created large saturation regions (Figure 4.4); thus, the bubbles were not well-defined and could not be tracked for the whole post injection duration. Their replacement with new bubbles led to fluctuations in the values of angular velocity as it could be seen in Figure 4.5 and Figure 4.6.Figure 4.5 and Figure 4.6 show the error bars corresponding to the standard deviation of each measurement at each time event. It was evident that there were large fluctuations in the angular velocity. This was a consequence of human error during the manual bubble tracking and the bubble replacement when disappeared in the background. It should be noted that this analysis was rather quantitative and aimed to point out the crude differences between the fuels as a function of the fuels' physical properties and the pressure conditions. The next part of this analysis involved the identification of the correlation between the in-sac flow direction and the physical properties of the fuels. After an optical observation of the internal flow phenomena, a statistical analysis was performed for all five fuels over a set of 50 injections.

Table 4.1 summarises the findings of this analysis and Figure 4.7 shows examples clockwise and anti-clockwise in-sac flow.
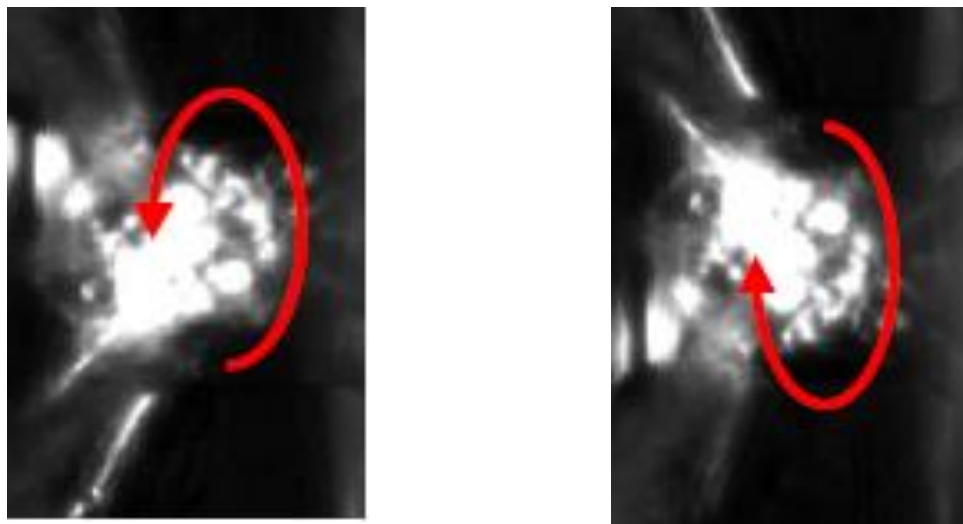
Figure 4.7: Examples of a. anti-clockwise and b. clockwise flow direction inside the sac volume[16].

Internal flow characterisation using optical diagnostics

Table 4.1: Statistics of the in-sac flow direction for fuels A-E at 250bar and 350bar.

Fuel Type	Clockwise (%)	Anti-clockwise (%)	Irregular (%)
Fuel A			
250bar	4	80	16
350bar	0	92	8
Fuel B			
250bar	12	56	32
350bar	2	90	8
Fuel C			
250bar	76	8	16
350 ar	54	12	34
Fuel D			
250bar	98	0	2
350bar	96	0	4
Fuel E			
250bar	6	80	14
350bar	8	84	8

In the cases of the fuels A, B and E the majority of the injections involved an anti-clockwise in-sac flow at both rail pressures. The second most common in-sac flow direction at 250bar was irregular, with fuel B at 250bar obtaining the value of 32%, while the percentages of fuels A and E were 16% and 14 % respectively. The percentage of an irregular flow in case of 350bar was 8% for all three fuels. The clockwise in-sac flow appeared to be less frequent in all three fuels and at both rail pressures. On the other hand, in the case of the lighter fuels (fuels C, D) at both rail pressures, the most dominant in-sac flow direction was clockwise. In the case of fuel C, 16% and 34% of the injections exhibited an irregular sac flow at 250bar and 350bar respectively, whereas fuel D had 4%. The anti-clockwise flow direction

was the least frequent for both fuels and rail pressures. The above results suggested that the heavier fuels formed a clockwise in-sac vortex flow more frequently than the lighter fuels which formed a clockwise in-sac vorticity.

4.2.2 Bubble and fluid motion inside the nozzle passages

In the previous section, it was suggested that needle sheet cavitation was responsible for the bubble formation inside the sac volume as soon as the needle sealed. However, an optical observation of the post injection phenomena (5.9ms-11.4ms after SoI) revealed the existence of vapour capsules/bubbles inside the nozzle passages. It was believed that the bubbles entered the passages either from the sac or from the surroundings, due to a pressure rise or drop caused by the flow velocity decay during needle sealing. The bubbles present inside the nozzle passages were observed to move in an unpredictable manner due to sudden momentum changes. However, their movement has been identified to be synchronous with the in-sac vortex flow; the motion dampening in the passages appeared to occur concurrently with the dampening of the flow in the sac. The latter observation led to the hypothesis that the circumferential vortex flow in the sac created regions of high and low pressures in the sac, which were capable of governing the fuel motion in the nozzle passages. The vapour structures were observed to move outwards or inwards in both holes or in opposite directions to each other; there were also cases where they initially moved outwards and then inwards or the opposite, depending on the pressures acting on them.

The present analysis referred to the displacement of vapour structures in both nozzle passages under consideration as function of the fuels' physical properties during the time period between 0.1ms and 5.4ms after the needle return over a set of 20 injections. This period matched with the period investigated in the case of the in-sac vorticity decay, in order to identify whether the dampening process in the passages was synchronous with the dampening in the sac.
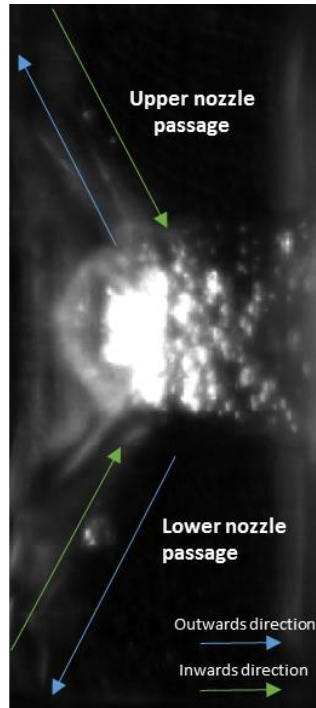
Figure 4.8: Description of flow direction inside the nozzle passages.

This analysis also attempted to investigate the correlation between the in-sac flow direction and the direction of the bubble movement in the passages. The results produced by fuel A were presented in the main body of this work, while the results produced by the rest of the fuels were presented in Appendix A1. A thorough discussion of the results obtained for all five fuels was held in this section. Figure 4.9 - Figure 4.16 show the displacement of the vapour structures inside the lower (Figure 4.9-Figure 4.13) and upper (Figure 4.14-Figure 4.16) hole as a function of time. Each graph corresponded to a group of five injections and the whole analysis per passage involved the investigation of 20 injections or 4 groups of 5 injections. The methodology followed for the determination of the bubble displacement allowed the detection of maximum two vapour structures, namely four interfaces in total. Every injection was denoted by a different marker; the filled markers corresponded to the front and back interfaces of object 1, while the hollow markers corresponded to object 2 interfaces. However, there were several cases, especially in the case of fuel sample B (Figure A1.5 - Figure A1.8), upper hole, where one of the two interfaces could not be seen, therefore the data recorded referred to one of the two interfaces, while the second was missing. In such cases the vapour structure most likely occupied the whole length of the nozzle hole. The graph origin represented the hole entrance (0mm) and the nozzle exit was located

approximately 1.1mm downstream of the hole entrance. However, the raw images did not provide a clear view of the hole between approximately 0.9mm and 1.1 mm downstream of the nozzle entrance. Therefore, the present analysis included the bubble displacement up to approximately the first 0.9mm of the hole length. The displacement history of a vapour structure over an injection event was represented by adjacent scatter points. In the case that the slope of the resultant curve was negative, the bubble movement in the hole was inward (i.e. fuel A, inj.11, obj.1, lower hole (Figure 4.12), fuel D, inj.2, obj.2, lower hole , fuel D, inj.1, obj.1, lower hole (Figure A1.17), whereas the corresponding motion of a positive slope was outward (i.e. fuel A, inj8, obj.2 (Figure 4.14). However, there were numerous cases where the slope of the curve changed as the vorticity dampened down. The pressure gradients generated changed the bubble momentum resulting to a flow direction change. In particular, a negative slope followed by a positive one indicated an inward followed by an outward motion (i.e. fuel B, inj.12, obj.2, lower hole (Figure A1.3)). The opposite bubble motion (outward to inward) was a combination of a positive slope followed by a negative one (i.e. fuel A, inj.17, obj,1, lower hole (Figure 4.12), fuel E, inj.12,14 (Figure A1.31)). Ultimately, there were also cases where there was no bubble motion inside the nozzle passages (i.e. fuel A, inj.6, lower hole (Figure 4.10)), especially in case of fuel E, lower hole (Figure A1.25 - Figure A1.28). In such cases, there was no data included in the graphs and this explained why some injection events were missing from the analysis. Generally, the motion of the bubble inside the upper hole was mostly outward in all five fuels, whereas the bubble motion inside the lower passage was inward, outward or a combination of the two.

 In some cases, such as fuel C, inj.16, upper hole (Figure A1.16), fuel D, inj.3, lower hole (Figure A1.17) and fuel E, inj4, upper hole (Figure A1.29), during the early stages of post injection there was only one interface tracked, which was then replaced by three interfaces. This meant that during the first stages of post injection, the nozzle passage was occupied by one big vapour structure which eventually broke down into two smaller structures. This bubble break-down was observed mostly in the cases of the lighter fuels (fuel C and fuel D), while was less frequent in the case of fuel E. Fuels A and B did not exhibit such a behavior. It ass believed that the bubble break-up was a consequence of the lower surface tension and viscosity of fuels C and D. On the other hand, based on the physical properties of fuel E, it

was expected to obtain a behavior similar to fuels A and B. It has been suggested that fuel E could possibly undergo a separation process, which separated FAME from the liquid fuel bulk. This suggested that the separation of the lighter and heavier compounds in fuel sample E could be responsible for the bubble break-up inside the nozzle passages.

An optical observation of Figure 4.9 - Figure 4.16 revealed that in most of the cases the slope of the obtained curves during the first half of the post injection duration (0ms-1.2ms after the needle sealing) was much steeper relative to later stages. It was mentioned that the in-sac vortex started to settle down at approximately 1.2ms after the needle return and progressively slowed down with time; therefore, it could be argued that the bubble motion inside the nozzle passages was governed by the circumferential motion of the sac bubbles, since the timing of their motion dampening coincided.
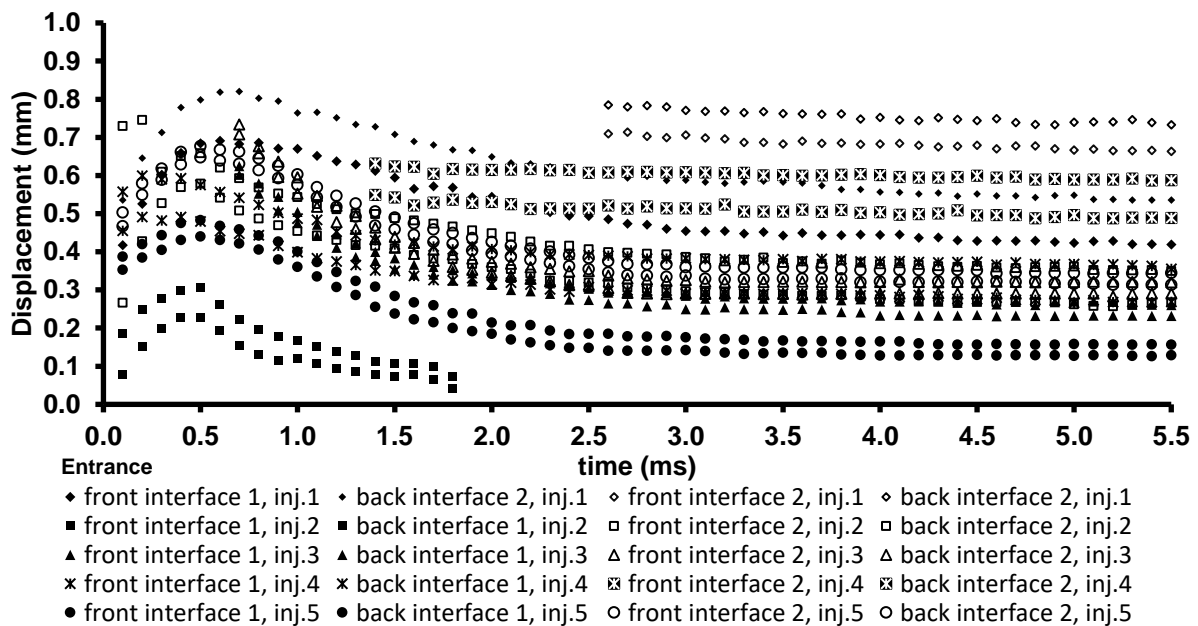
Figure 4.9: Displacement vs time graph, fuel A at 350bar, lower hole, inj.1-5.
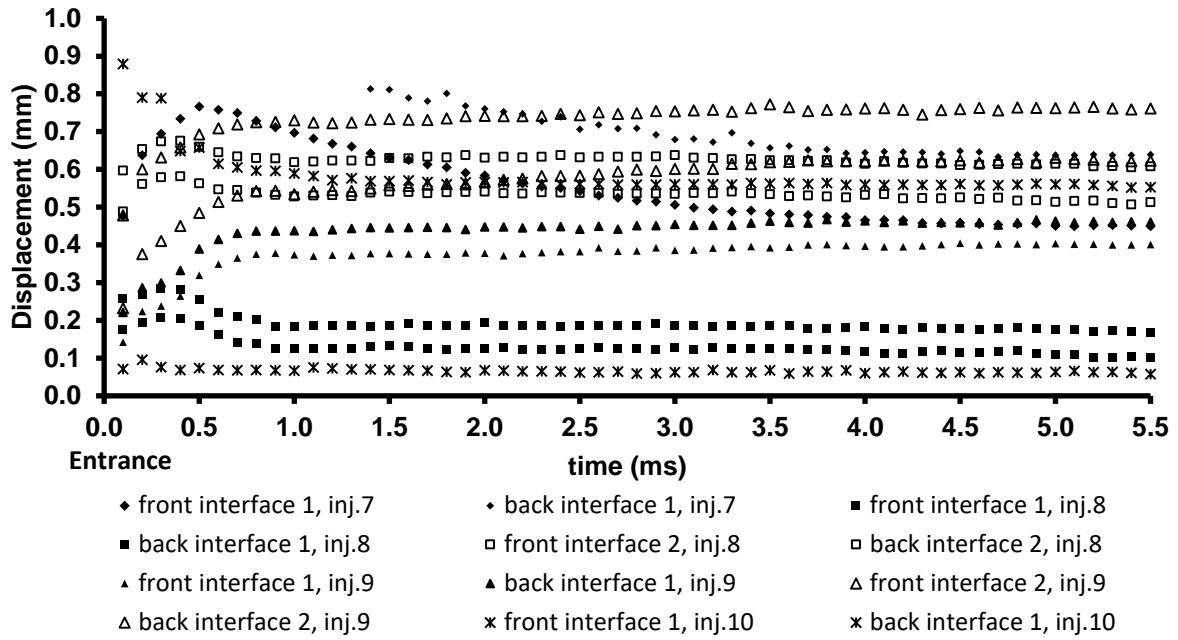
Figure 4.10: Displacement vs time graph, fuel A at 350bar, lower hole, inj.6-10.
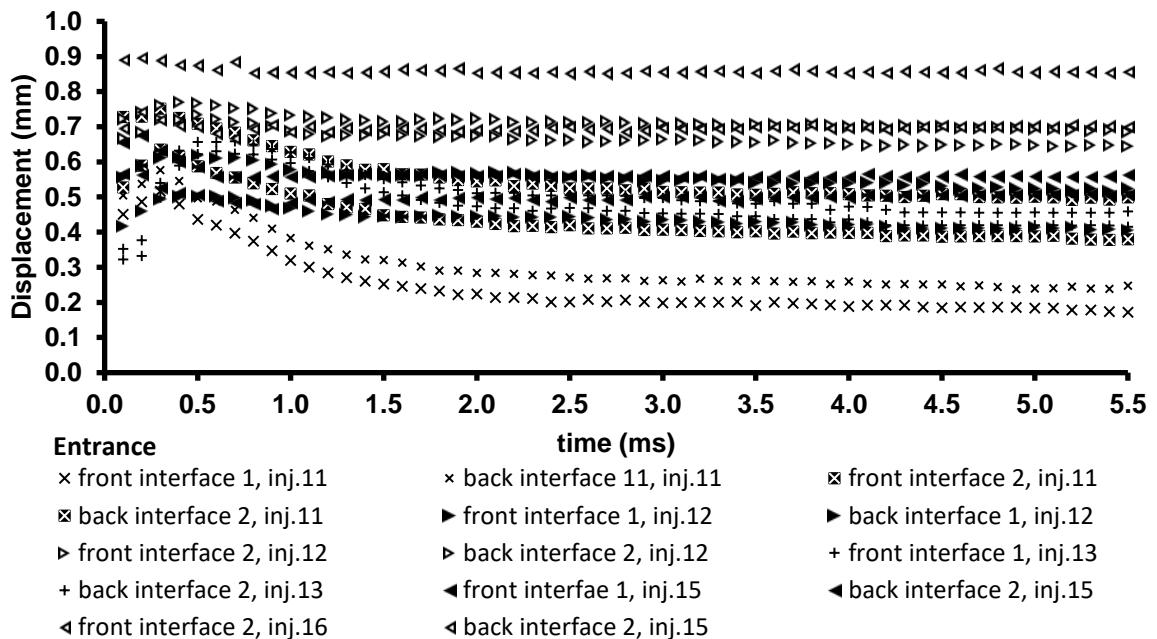
Figure 4.11: Displacement vs time graph, fuel A at 350bar, lower hole, inj.11-15.
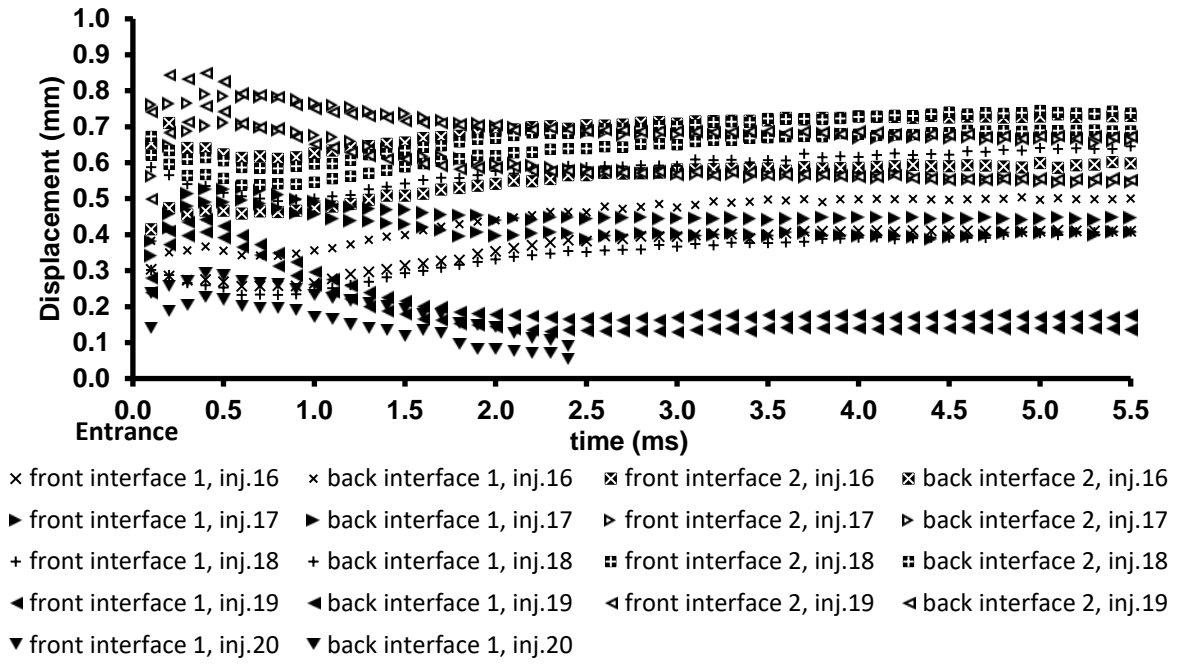
Figure 4.12: Displacement vs time graph, fuel A at 350bar, lower hole, inj.16-20.
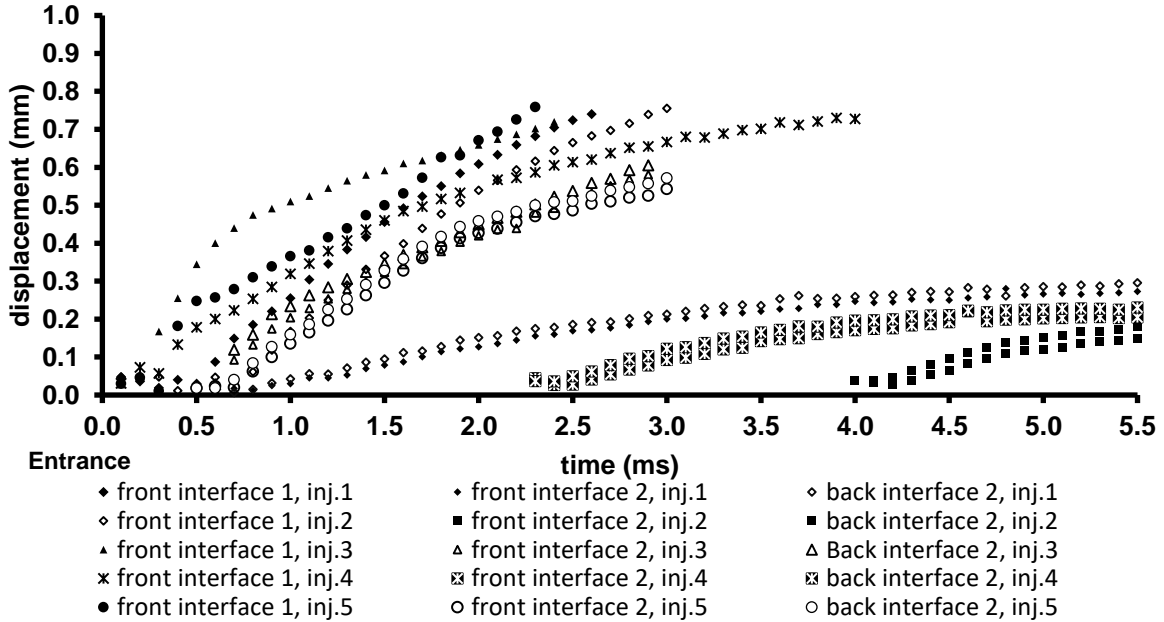
Figure 4.13: Displacement vs time graph, fuel A at 350bar, upper hole, inj.1-5.
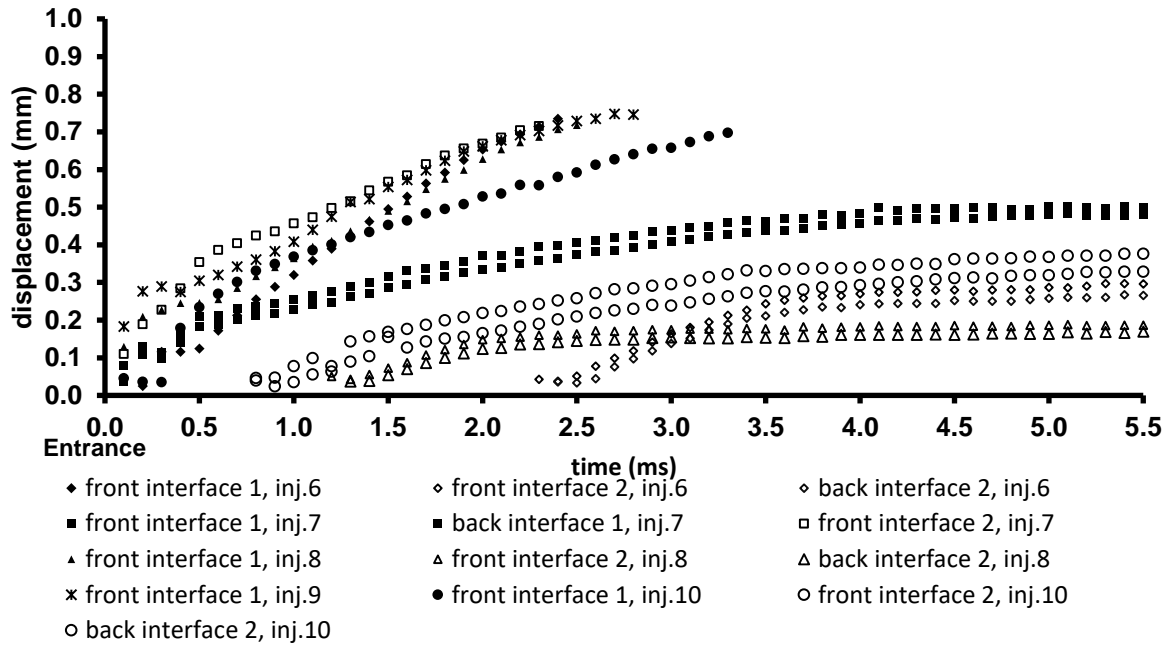
Figure 4.14: Displacement vs time graph, fuel A at 350bar, upper hole, inj.6-10.
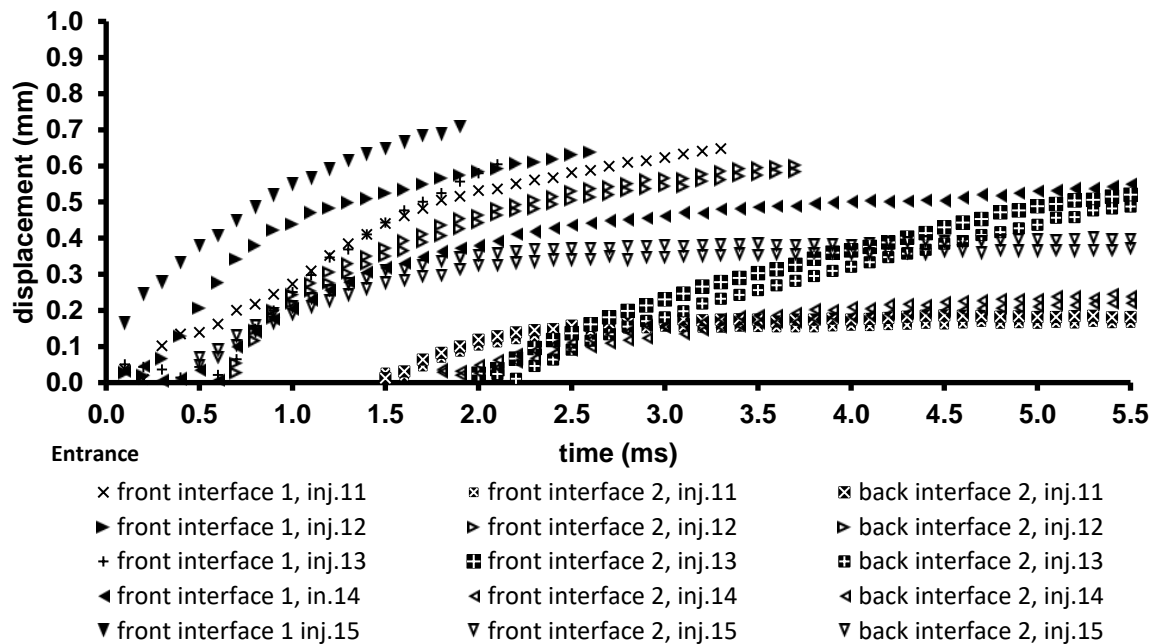
Figure 4.15: Displacement vs time graph, fuel A at 350bar, upper hole, inj.11-15.
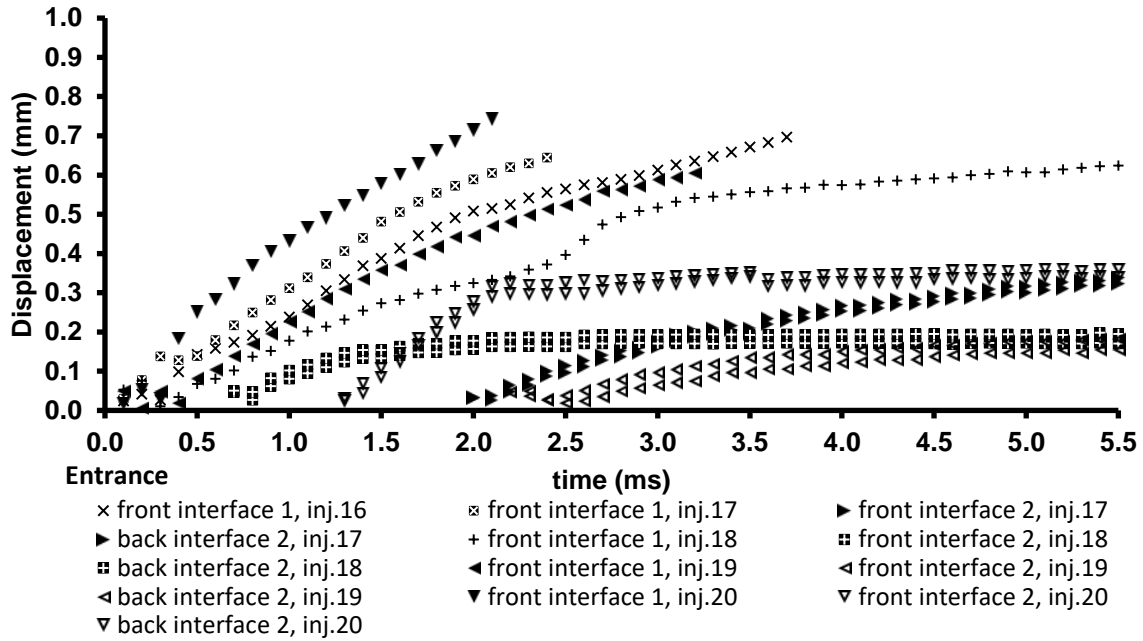
Figure 4.16: Displacement vs time graph, fuel A at 350bar, upper hole, inj.16-20.

Another supportive evidence of the hypothesis that the in-nozzle bubble motion was synchronous to the circumferential vortex flow in the sac is the correlation between the mean radial velocity of the in-sac bubbles and the mean speed of the in-nozzle bubbles. Figure 4.17- Figure 3.32 show the relationship between the mean speed of the vapour structures moving in the upper and lower passages and the mean angular speed in the sac volume. Each graph represents a group of five injections (inj.1-5, inj.6-10, inj.11-15, inj.16-20) and the notation retains the meaning explained above. The vast majority of the results suggest that the mean decay rate of the radial velocity in the sac is synchronous with the mean speed in the passages. The large mean speed values of the in-nozzle bubbles coincide with the large mean angular speed values. In general, it can be argued that the decay rate of the in-nozzle speed is slightly faster than the in-sac rate. This can be attributed to the weak pressure gradients generated by the circumferential fuel motion in the sac which is believed to be the dominant mechanism for the observed fuel motion in the passages. A clearer view of the suggested correlation was given by the plotted fitting curves and the corresponding R^2values. The R^2 values appearing on the graphs correspond to the data series in the same order as shown in the legend of each graph. Considering the sample size taken from 50injections, a satisfactory R^2 values for the regression lines was between 0.5 and 1.0 (i.e.

fuel A,obj2,inj.3). Such cases implied that the large mean speed values of the capsules/fuel in the passages matched the large mean angular velocity values obtained in the sac. However, there were cases where the R^2 ranged either between 0.2 and 0.49 (i.e. fuel A, obj1, inj.4) or close to zero (i.e. fuel A, obj.2, inj.1). These findings could be attributed to either weak in-sac vorticity or the application of other forces (e.g. buoyancy). However, these observations were not as frequently observed as the first case, therefore the main hypothesis remained valid.
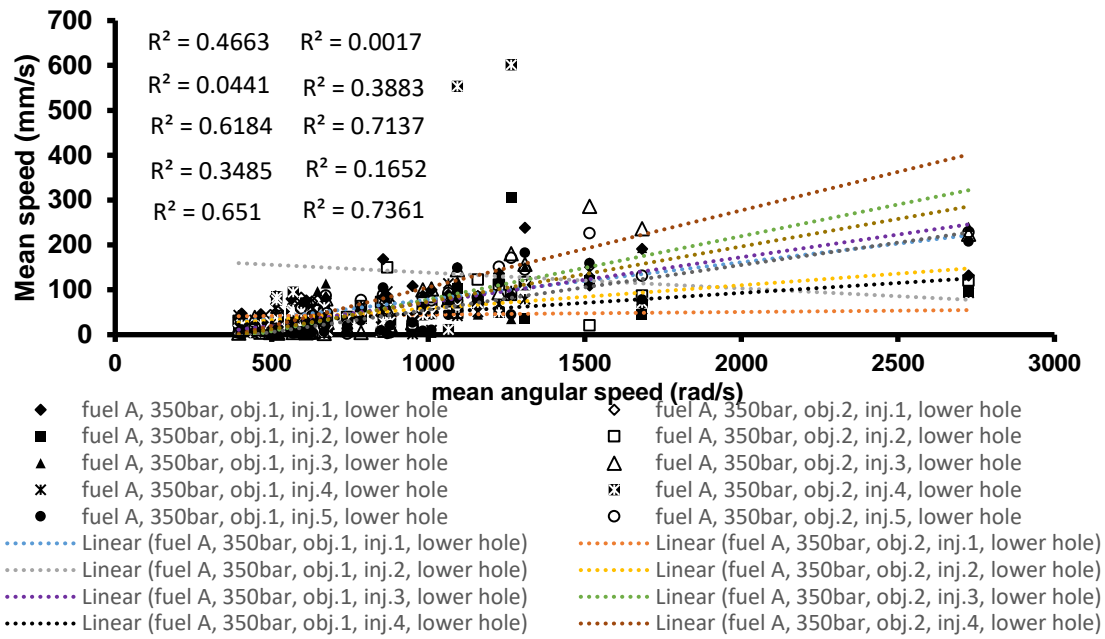
Figure 4.17: Mean speed vs. mean angular speed graph, fuel A, 350bar, inj.1-5, lower hole.
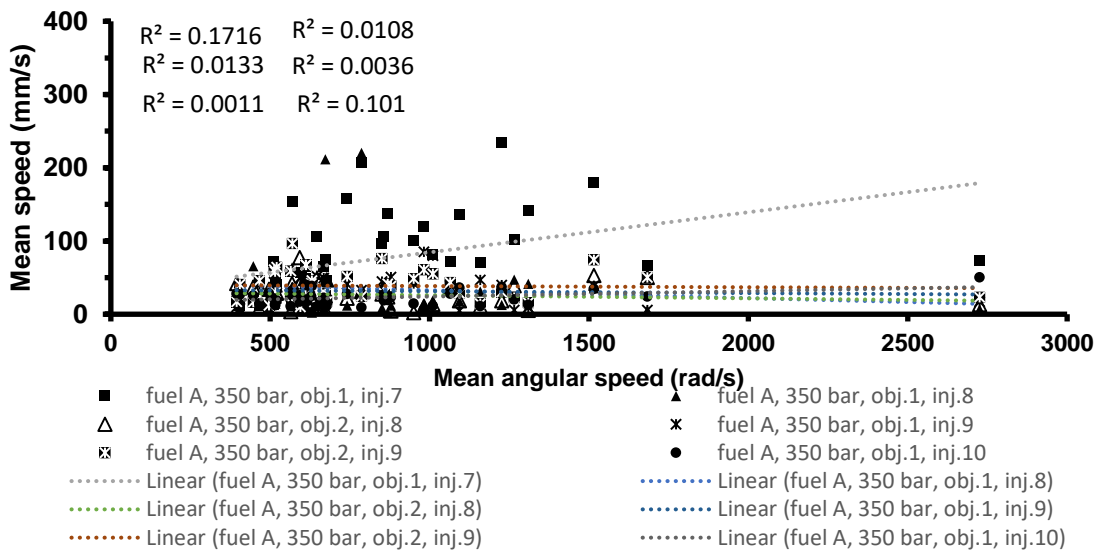
Figure 4.18: Mean speed vs. mean angular speed graph, fuel A, 350bar, inj.6-10, lower hole.
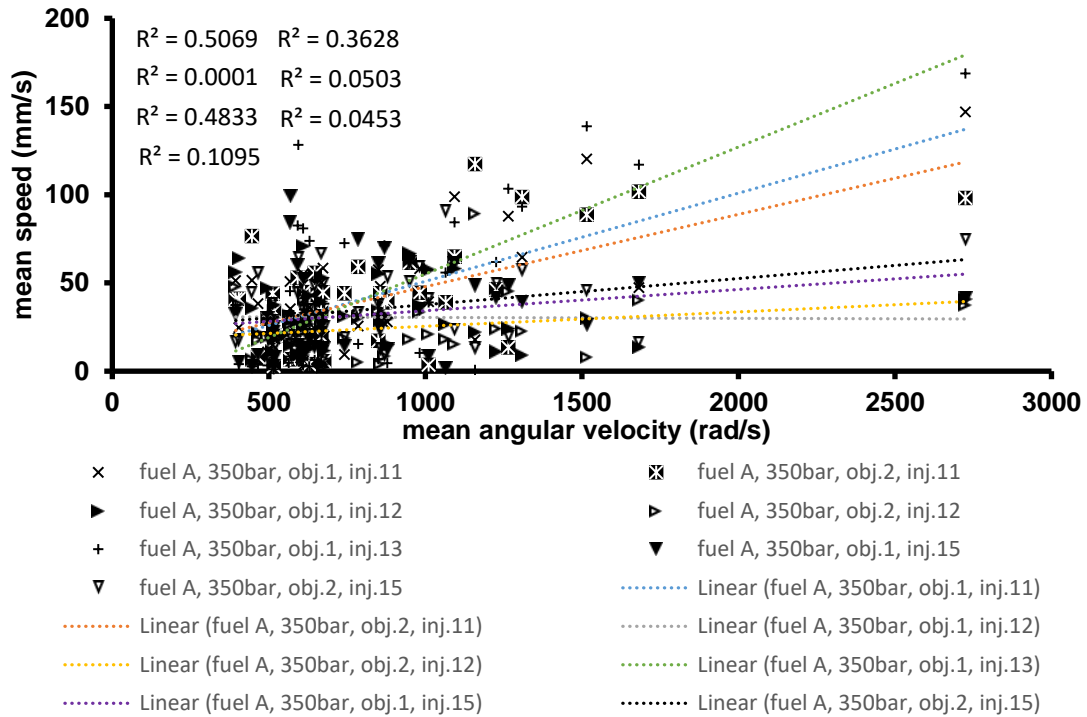
Figure 4.19: Mean speed vs. mean angular speed graph, fuel A, 350bar, inj.11-15, lower hole.
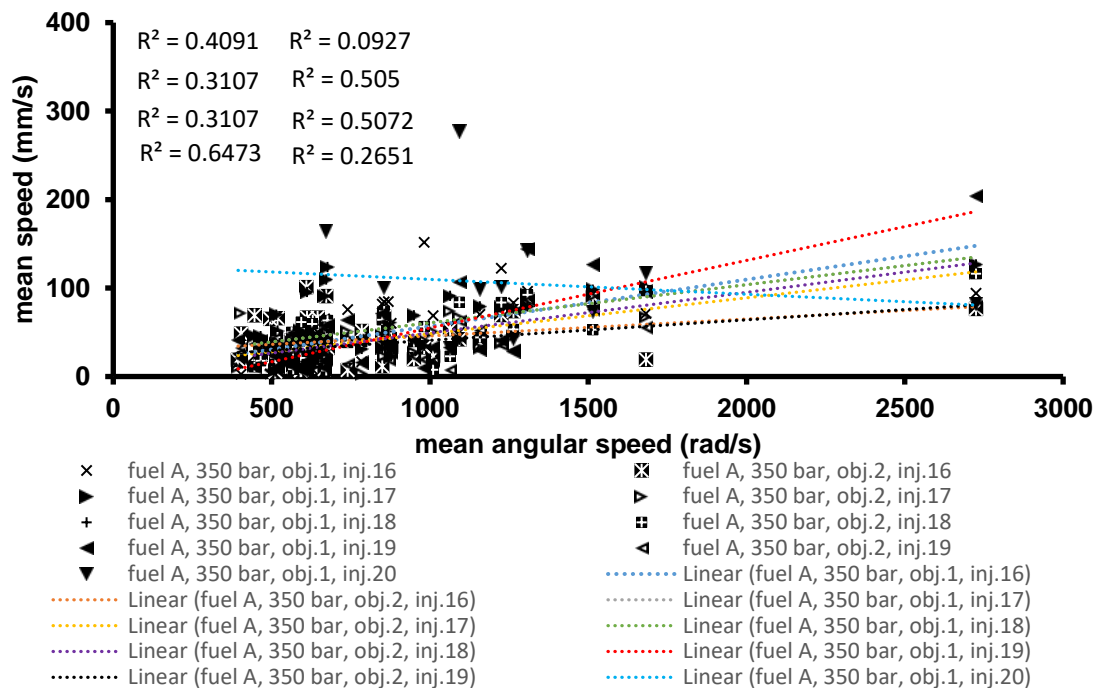
Figure 4.20: Mean speed vs. mean angular speed graph, fuel A, 350bar, inj.16-20, lower hole.
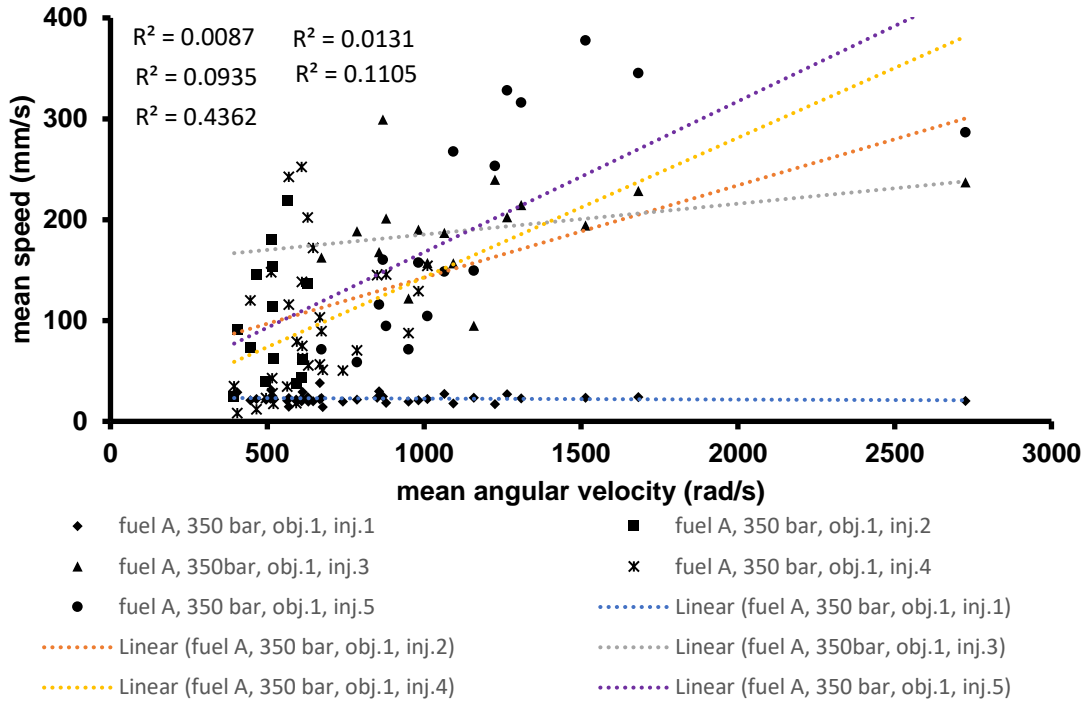
Figure 4.21: Mean speed vs. mean angular speed graph, fuel A, 350bar, inj.1-5, upper hole.
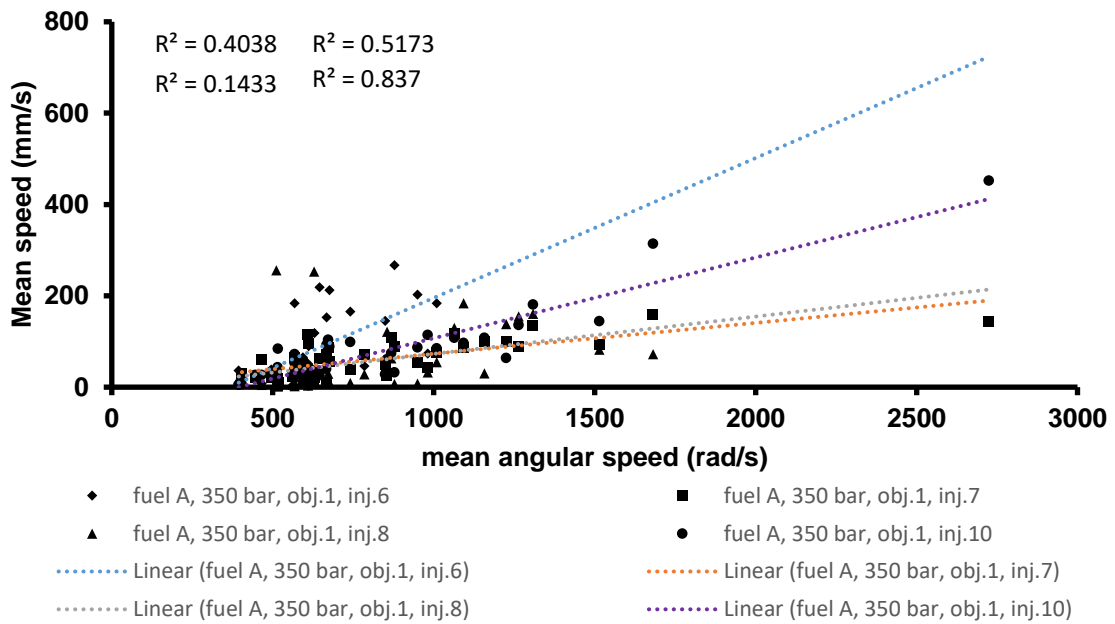
Figure 4.22: Mean speed vs. mean angular speed graph, fuel A, 350bar, inj.6-10, upper hole.
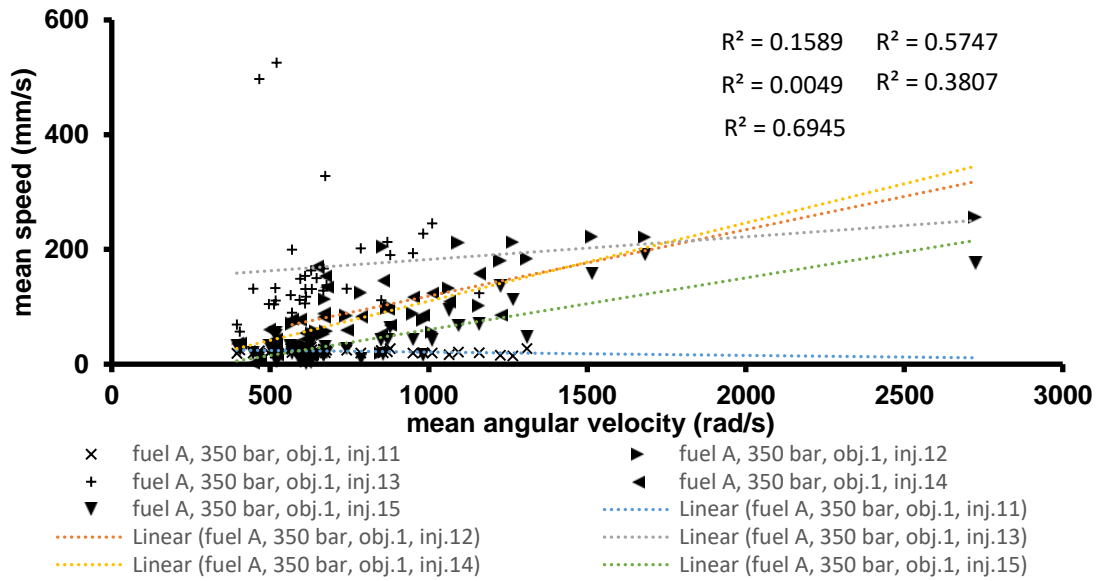
Figure 4.23: Mean speed vs. mean angular speed graph, fuel A, 350bar, inj.11-15, upper hole.
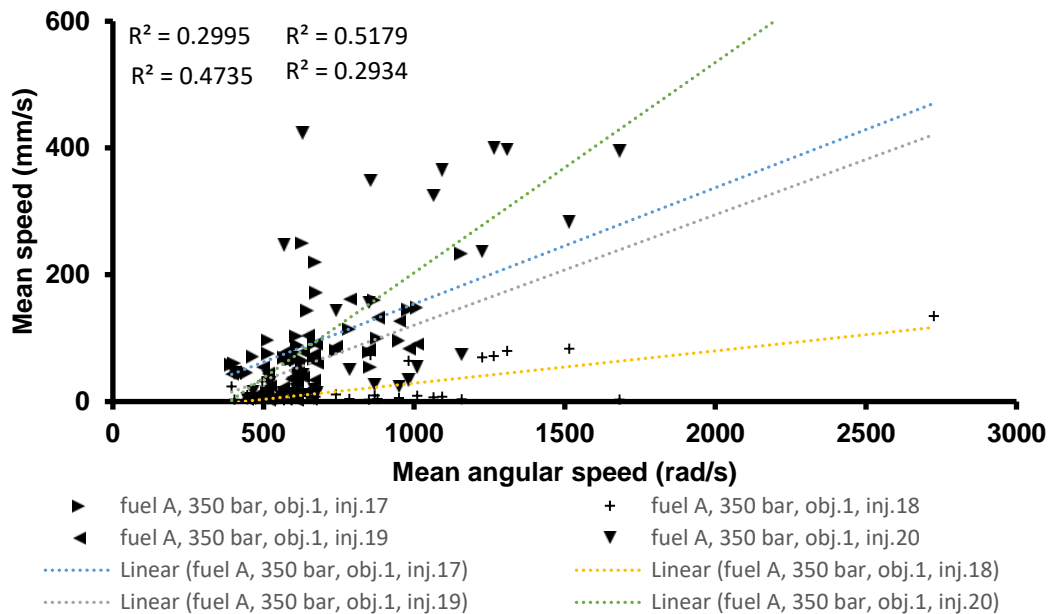
Figure 4.24: Mean speed vs. mean angular speed graph, fuel A, 350bar, inj.16-20, upper hole.

The graphs generated from the rest of the fuels (fuels B to E) are presented in Appendix A2. The results obtained from fuel B showed that the majority of the R^2 values corresponding to the regression lines was greater than 0.5, suggesting a synchronous decay of the in-sac angular velocity and capsule speed in the passages. There were also very few cases where the R^2 values ranged either between 0.2 and 0.5 or were very close to zero. The former case implied the generation of weak pressure gradients, which

partially drive the fluid inside the passages. Finally, the negligible correlation between some data series and the corresponding regression lines suggested the existance of other external forces, such as buoyancy.

Similarly, the resutls obtained from fuel C suggested a strong correlation between the in-passage capsule motion and sac vorticity. The R^2 values corresponding to the regression lines mostly ranged between 0.5 and 1.0, which were considered satisfactory taking into account the relatively small sample size (2 objects/injection over 50 injections). The occasions of weaker in-sac vorticity and/or the appearence of other external forces (i.e. buoyancy) were more frequent, due to the lower viscosity and surface tension compared to fuels A and B. However, these occassions were not observed as frequently as the first case, hence the main hypothesis remained valid.

In the case of fuel D , the R^2 values corresponding to the regression lines mostly ranged between 0.5 and 1.0, but the cases where R^2 was either small or very close to zero became more frequent. The large R^2 values implied a strong correlation between the in-sac vorticity and the fluid/bubble motion inside the nozzle passages. On the other hand, the relatively low and very small values suggested that the correlation between the in-passage and in-sac velocities was weaker and /or some other external forces were also present (i.e buoyancy). Then latter argument was believed to be a consequence of the fairly low viscosity and surface tension of fuel D compared to the rest of the fuels.

Finally, the results obtained from fuel E showed that the majority of the R^2 values of the was between 0.3 and 1.0, suggesting the pressure gradients, generated by the in-sac vortical flow, to be the dominate mechanism for the fuel motion in the passages. The increase of the occurancies of weaker correlation between the in-sac and the in-passage velocities could be attributed to the capsule break-up over the duration of the post injection. There were plenty of cases where a large vapour capsule was formed in the nozzle passages and eventually broke into two smaller ones. By the time the capsule break-up was completed , the sac vorticity reduced significantly, resulting in insignificant bubble/fuel movement in the passages.

It was previously mentioned that in the cases where the correlation between the in-nozzle and in-sac bubble flow was not achieved, the governing forces responsible for the in-nozzle bubble flow could be the synergy between the pressure gradients and buoyancy forces. The following analysis attempted to investigate the significance of buoyancy in the bubble/fuel motion observed. In general, buoyancy could be responsible for the bubble floating in the liquid present in the nozzle passages. If buoyancy forces were the only forces acting on the vapour structures, then the bubbles would move outwards and inwards inside the upper and lower hole respectively. However, the experimental results showed that there were numerous cases which contradicted this statement. For example, in the case of fuel A inj.8-9 (Figure 4.10) the direction of the flow changed within a single injection event, suggesting a sudden change in momentum due to changing pressure in the sac. Additionally, buoyancy forces were not capable of causing the suggested momentum change. It has been also noticed that there were cases where the bubbles were observed to travel in the opposite directions to the ones suggested by buoyancy effects. In support to these statements, the following analysis compared the experimental bubble speed to the theoretically calculated speed value corresponding to bubbles subjected to buoyancy forces. The determination of the theoretical values was based on the work by Plesset and Epstein[182]. **Error! R eference source not found.**Figure 4.25 shows the comparison between the experimental and theoretical bubble speed in case of fuel A.
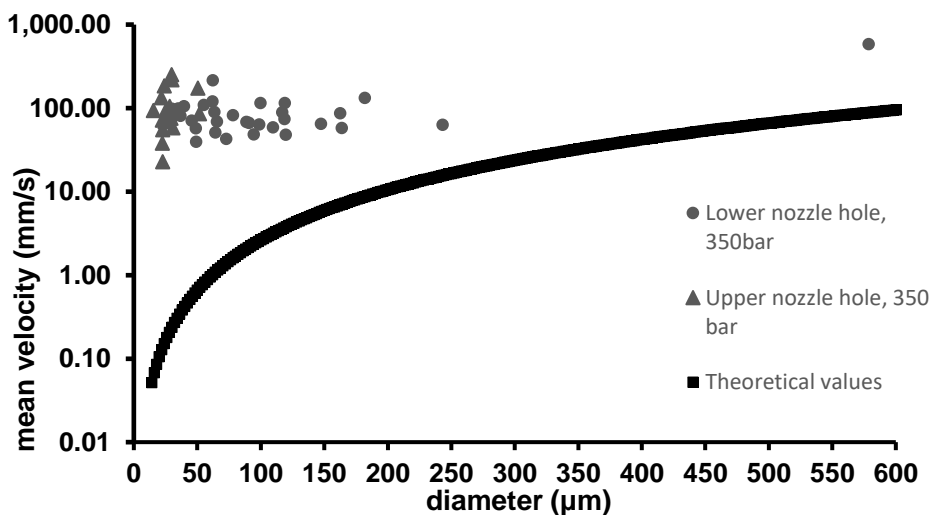
Figure 4.25: Experimental bubble speed vs theoretical bubble speed based on buoyancy effects (fuel A, upper and lower passages)

The results corresponding to the rest of the fuels are presented in Appendix A3. The circular and triangular markers correspond to the experimental values obtained from the vapour structures flowing inside the lower and upper passage respectively, while the square markers to the theoretical values. It should be noted that in Y-axis the utilized scale was logarithmic.

Figure 4.25 demonstrated that the experimental speed of the flowing bubbles was at least two orders of magnitude greater than the theoretical, implying that the in-nozzle bubble motion was not governed by buoyant forces. This trend was generally followed by the bubbles produced from the rest of the fuels (Figure A3.1 – A3.4). However, there were a few cases where the experimental speed almost matched with the theoretical values. This finding was more frequent in the case of the large bubbles produced by fuel D (Figure A3.3), which is the lightest amongst the fuels under consideration. In general, the lightest fuels (fuel C and fuel D) exhibited higher in-nozzle speed due to their lower viscosity and surface tension relative to the rest of the fuels; in principle, the fluids with high liquid viscosity resist the liquid flow and consequently the bubble speed decreases.

According to Yang et al.[185] the dominant forces acting on a bubble were the upward forces including buoyant forces, gas momentum and the downward resistance which included liquid drag and viscous forces along with bubble inertia and surface tension effects. In the case of small bubbles, viscosity and surface tension seemed to play the most dominant role, whereas in the case of bubbles of intermediate and large size their impact could be considered negligible. The bubble speed developed was suggested to be strongly dependent on the bubble size. In particular, the speed developed by small bubbles was affected by the liquid physical properties, such as surface tension and viscosity. On the contrary, in the case of large bubbles, the velocity seemed to be insensitive to the liquid properties. Consequently, the downward resistance produced by lighter fuels was weaker than the upward forces, due to lower surface tension and viscosity. As a result, the dominant forces acting on the bubble were the upward forces and mostly buoyancy. This could possibly explain the overlap between the experimental and theoretical speed values in the case of large bubble produced by fuel D.

In summary, the findings of the present analysis confirmed the main hypothesis made regarding the synchronous in-nozzle and in-sac bubble flow. This analysis attempted to correlate the flow direction

of the bubbles inside the passages and the in-sac flow direction as a function of the fuels' physical properties. In this direction, the findings provided an overview of the travelling bubbles inside the upper and lower holes as a function of the radial flow direction in the sac. Table 4.2 and Table 4.3 show the results obtained from bubbles produced by fuel A and travelling inside the lower and upper nozzle passages. The results corresponding to the rest of the fuels are presented in Appendix A4. The discussion over the results obtained is presented below. For convenience, an inward followed by outward bubble movement was called inwards/outwards while an outward followed by an inward motion was called outwards/inwards. The tables presented included the percentages of each in-nozzle flow type as a function of the in-sac flow direction. The present analysis referred to a complete set of 50 injections per fuel. The percentage values below each in-sac flow type were obtained from §4.2.1 and corresponded to the frequency of each flow type in the sac over a complete set of 50 injections.

Fuel sample A (normal diesel)

The dominant circumferential flow formed in the sac volume by fuel A seemed to be clockwise followed by irregular flow (Table 4.2, Table 4.3) The bubbles present inside the lower hole appeared to mostly travel outwards/inwards while the least frequent flow types were inwards/outwards and inwards with percentages 6.52% and 4.35% respectively. On the contrary, the bubbles travelling inside the upper hole (Table 4.3) followed the opposite trend; the most frequent in nozzle-flow was inwards/outwards (78.26%) followed by outwards (21.74%). The same observation was made in case of the irregular in-sac flow where the bubbles seemed to travel in opposite directions.

Fuel sample B (gap diesel)

In the majority of the injection events, the radial in-sac motion developed in a clockwise manner (90%,Table A4.1 and Table A4.2). The second most often in-sac flow was irregular which was followed by the clockwise motion. In all three cases, the majority of the travelling bubbles inside the lower hole moved outwards/inwards, while the rest of the bubbles travelled either outwards or inwards/outwards. On the other hand, the bubbles inside the upper hole move in the opposite directions; the dominant bubble flow direction was outwards/inwards while the rest of the bubbles move outwards.

Fuel sample C (kerosene)

Fuel sample C had a relatively high percentage of irregular radial flow (34%) (Table A4.3, Table A4.4), while the most frequent flow direction was clockwise (54%). The bubble flow in these two cases followed a fairly similar trend. In particular, the majority of the bubbles appearing inside the lower nozzle passage travelled outwards/inwards, while the second most frequent bubble motion was outwards. On the contrary, in the case of the anti-clockwise radial flow, it was observed that the inwards and outwards/inwards movements were equally frequent and were followed by the also equally frequent outwards and inwards/outwards bubble movements. On the other hand, the majority of the bubbles appearing inside the upper nozzle passage seemed to travel outwards regardless of the radial flow direction. The percentages obtained for the inwards/outwards motion were fairly similar in all three cases, suggesting that the in-sac flow direction did not play a decisive role in the determination of the in-hole bubble movement.

Table 4.2: Correlation between the in-hole bubble motion and the radial in-sac motion (fuel A, lower hole).

Fuel A, lower hole			
Flow direction	**In-sac flow direction**		
	Clockwise (0%)	Anti-clockwise (92%)	Irregular (8%)
Inwards (%)	0.00	4.35	0.00
Outwards %)	0.00	13.05	0.00
In/out (%)	0.00	6.52	25.00
Out/in (%)	0.00	76.08	75.00
No movement (%)	0.00	0.00	0.00

Table 4.3: Correlation between the in-hole bubble motion as a function of the radial in-sac motion (fuel A, upper hole).

Fuel A, upper hole			
Flow direction	**In-sac flow direction**		
	Clockwise (0%)	Anti-clockwise (92%)	Irregular (8%)
Inwards (%)	0.00	0.00	0.00
Outwards (%)	0.00	21.74	75.00
In/out (%)	0.00	78.26	25.00
Out/in (%)	0.00	0.00	0.00
No movement (%)	0.00	0.00	0.00

Fuel sample D (light kerosene)

The in-sac circumferential motion produced by fuel sample D seemed to develop almost in a clockwise manner (96%, Table A4.5, Table A4.6). The most common bubble movement in both holes was outwards/inwards, followed by inward motion. However, the second most often bubble movement differs from hole to hole. The bubbles appearing inside the lower nozzle passage travel inwards (16.68%), whereas in the upper hole they moved inwards/outwards (39.60%). The percentages corresponding to outwards movement in the lower and upper holes were 6.25% and 12.5% respectively. Lastly, there was a 4% fraction of irregular in-sac motion, which led to no bubble movement in both holes.

Fuel sample E (B20 diesel)

The most common radial flow direction was anti-clockwise (84%,

Table A4.7 and Table A4.8) followed by equally frequent clockwise and irregular in-sac flow directions. When the circumferential flow was either anti-clockwise or irregular, the dominant bubble motion in both holes was outwards/inwards followed by either outwards or no bubble movement. The least frequent bubble motion in both holes appeared to be inwards with percentages of 4.8%, 2.38% and

0.0% in the cases of anti-clockwise and irregular in-sac flow directions. On the contrary, the clockwise radial flow created conditions which had opposite effects on the bubbles travelling in the lower and upper holes. In particular, in the lower hole the most frequent bubble direction was outwards/inwards, whereas in the upper hole the bubbles moved inwards/outwards.

General discussion

A comparison of the results obtained from the five fuels revealed that the circumferential flow formed by the heavier fuels, fuel A, fuel B and fuel E was mostly anti-clockwise, whereas in case of the lighter fuels was clockwise. This observation suggested a correlation between the physical properties of the fuels and the in-sac flow direction. Another interesting finding referred to the in-nozzle flow direction as a function of the in-sac direction. It was observed that for the vast majority of the injections examined, an anti-clockwise in-sac flow most likely generated pressure gradient which most frequently drove the bubbles inside the lower and upper passage to move outwards/inwards and inwards/outwards respectively. On the other hand, a clockwise in-sac flow created such conditions that the bubbles inside the lower hole most likely travelled outwards/inwards, while the bubbles inside the upper hole travelled either outwards/inwards or outwards. Such observations suggested that each in-sac flow direction created particular pressure gradients, which governed the movement of the in-nozzle vapour structures in a particular manner.

4.2.3 In-nozzle bubble size as a function of time and fuel properties

In the previous section, evidence was provided to confirm the hypothesis that the in-nozzle flow was synchronous to the in-sac flow and dependant on the fuel properties. The following analysis provided information with regards to the size of the in-nozzle bubbles as a function of fuel properties and time. Figure 4.26 and Figure 4.27 show the mean size distribution produced by the vapour structures travelling inside the lower and upper nozzle passage respectively. Each data series had a different pattern and indicated a different fuel sample. The patterns used were large checker board, dotted fill, diagonal stripes, solid fill and horizontal stripes corresponding to fuels A, B, C, D and E respectively. The notation described above retained its meaning in the case of Figure 4.27, but the data series were

in black colour. Bubbles of size up to approximately 140μm were considered spherical, whereas sizes larger than 140μm (passage diameter) described elliptical vapour capsules.
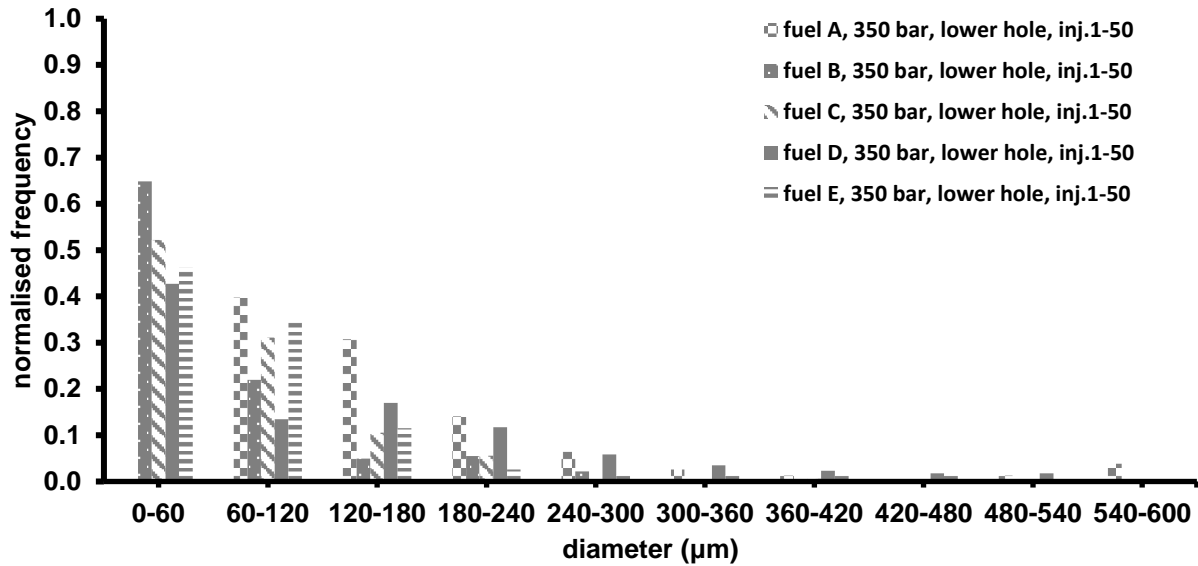
Figure 4.26: Size distributions of the bubbles and vapour capsules present inside the lower nozzle passage over 50 injections. Each series corresponds to a different fuel.
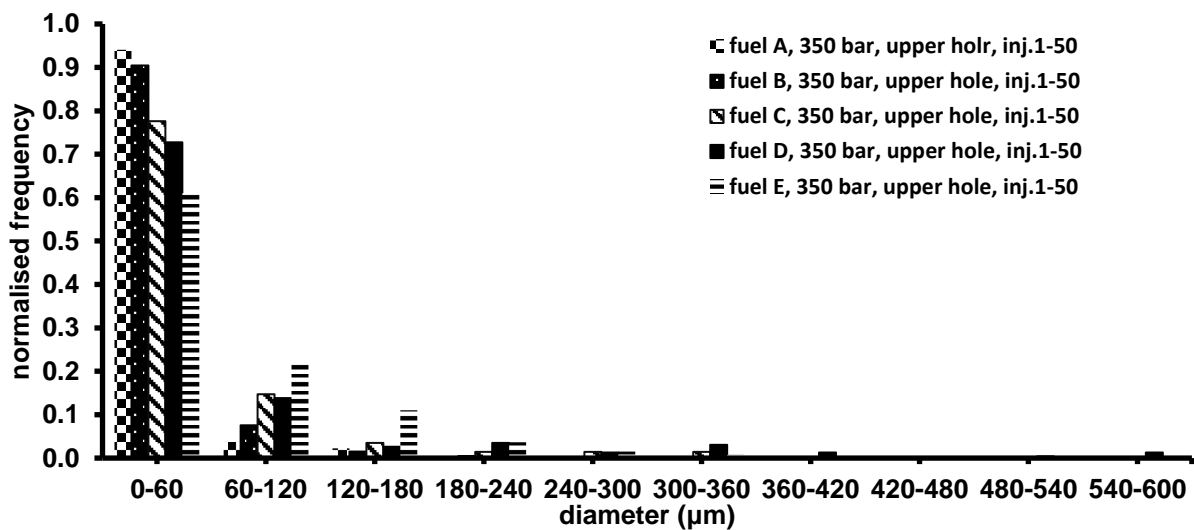
Figure 4.27: Size distribution of the bubbles and vapour capsules present inside the upper nozzle passage over 50 injections. Each series corresponds to a different fuel.

Internal flow characterisation using optical diagnostics

Fuel sample A (normal diesel)

An optical observation of Figure 4.26 revealed that fuel sample A did not produce bubbles within the range of 0-60μm, whereas bubbles of size between 60μm and 120μm exhibited the highest normalised frequency (~0.4). The normalised frequency of the vapour capsules and bubbles gradually decreased with increasing diameter. It was also observed that fuel A produced the largest capsules (up to 600μm) amongst the rest of the fuels, but their appearance in the lower nozzle passage was not frequent (norm. freq~0.04). The greater population of the smaller bubbles relative to large capsules could be attributed to the relatively high viscosity and surface tension of fuel A. In principal, fluids with high surface tension exhibited an increased tendency to retain the least surface possible; as a result, the capsules produced by such fuels did not break up into smaller ones and retained their original relatively small size. Therefore, fuel A was expected to produce a large number of small bubbles, but in the case of a large capsule, it would most likely survive break-up, due to its relatively high surface tension and viscosity. Figure 4.27 indicated that vapour capsules travelling inside the upper nozzle passage were smaller relative to the lower passage. In particular, the normalised frequency corresponding to bubbles of size up to 60μm was the highest (norm.freq.~0.95), followed by bubbles of sizes up to 120μm whose normalised frequency sharply dropped to approximately 0.04. The largest capsules found in the upper passage were up to 180μm; although such large capsules were not seen frequently (norm.freq.~0.02).

Fuel sample B (gap diesel)

According to the results shown in Figure 4.26, fuel sample B produced the largest population of small bubbles (up to 60μm) corresponding to normalised frequency of approximately 0.65. The normalised frequency of the bubbles and capsules decreased with increasing diameter. The largest capsule size observed in the lower passage laid within the range of 300μm and 360μm; however, the presence of such structures was not frequent (norm. frequency ~0.01). The bubbles or capsules laying within the range of 120μm -180μm and 180μm-240μm respectively were equally frequent exhibiting normalised frequency of approximately 0.05. Lastly, the second most frequent bubble size observed in the lower passage was from 60μm up to 120μm. The relatively high viscosity and surface tension of fuel sample B justified the increased population of small bubbles, since viscous fluids exhibited an increased

propensity to form small bubbles and to retain the least surface area possible. As a result, the formation of large capsules was not expected to occur frequently. In the unlikely case of large capsule formation, the relatively high surface tension and viscosity of fuel sample B opposed bubble breakup.

An inspection of Figure 4.27 demonstrated that the structures observed in the upper nozzle passage were smaller in comparison to those formed in the lower passage. The largest capsules found were between 180μm and 240μm, but they hardly appeared in the upper passage (norm. freq.~0.005). The majority of the bubbles produced by fuel sample B appeared to be up to 60μm with normalised frequency of approximately 0.9. The normalised frequency of bubbles or capsules seemed to decrease with increasing diameter. In particular, the quite low normalised frequency corresponding to structures within the range of 180 μm -240μm and 240 μm -300μm suggested that the likelihood of capsule being present in the upper passage was low.

Fuel sample C (kerosene)

The results presented in Figure 4.26 and Figure 4.27 showed that the normalised frequency of the vapour structures inside the lower and upper nozzle passage respectively gradually decreased with increasing diameter. The largest capsules observed in the lower and upper passages were up to 420μm and 360μm respectively; however, the corresponding normalised frequency was very low at approximately 0.001, suggesting that the presence of such structures was not common. The size of the majority of the bubbles travelling in the passages was up to 60μm, implying that they were small spherical bubbles approximately half of the passage diameter in size. The second most frequently observed bubble size range was between 60μm and 120μm for both passages corresponding to normalised frequency of 0.31 and 0.14 respectively. The lower viscosity and surface tension of fuel sample C compared to fuel sample A and B explained the observation of large capsules (up to 420μm). In general, lighter fuels were expected to form relatively large capsules, since the viscous and surface tension forces are relatively weak, unable to retain the least surface area possible. Additionally, the large capsules produced by lighter fuels (e.g. fuel sample C) opposed bubble break-up less, due to low surface tension and viscosity. Specifically, a large capsule kept elongating along the passage during the early stages of post injection

and when the in-sac vorticity settled down (~1.0ms after NR) it broke into two smaller bubbles (Figure 4.28).
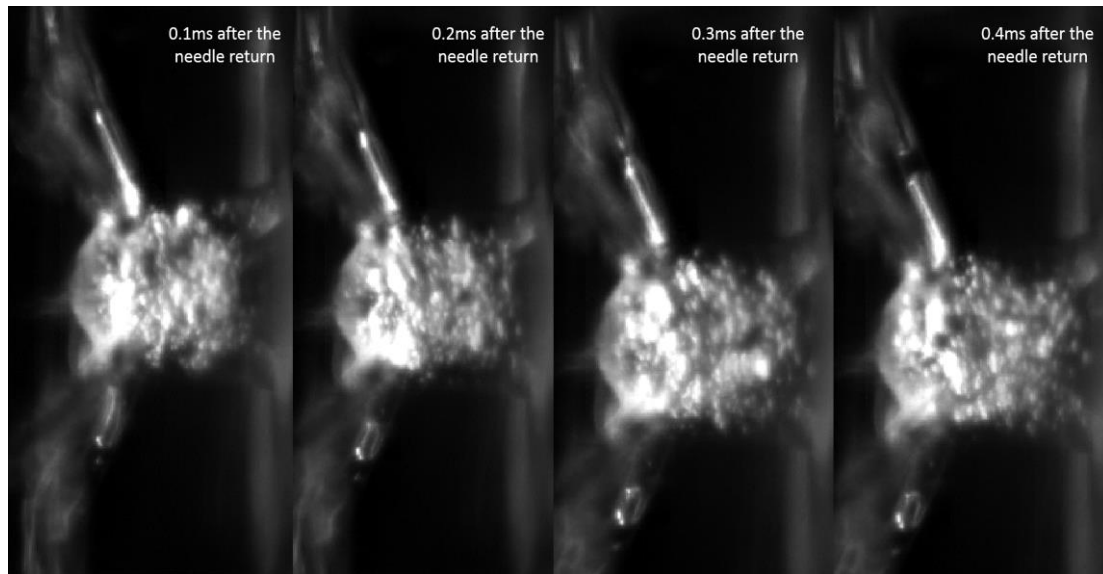
Figure 4.28: A sequence of images produced by fuel sample C showing the progressive break-up of a capsule in the upper nozzle passage during the early stages of post injection[16].

Fuel sample D (light kerosene)

Fuel sample D was the lightest amongst the fuels under consideration, exhibiting the lower viscosity and surface tension relative to the rest of the fuels; thus, it was expected to form larger bubbles or capsules. Figure 4.26 showed the normalised frequency corresponding to diameters greater than 240μm to be larger relative to the rest of the fuels. The greatest proportion of the vapour structures observed in the lower nozzle passage was up to 60μm in size (norm. freq~0.42), followed by bubbles in the range of 120μm-180μm (norm.freq.~0.17). The normalised frequency dropped in the second bin and then increased in the third (~25% increase), whereas a further increase in diameter seemed to lead to a gradual decrease in the normalised frequency, from approximately 0.16 to 0.02. It was mentioned above that the proportion of larger capsules formed by fuel sample D was greater than the rest of the fuels. In general, less viscous fuels exhibited an increased propensity to form large capsules and were more susceptible to break-up phenomena. Theoretically, the surface tension exerts a force towards the centre of the vapour structure while at the same time this force is resisted by an opposing pressure developed

inside the capsule volume. In the cases where the surface tension was low, the developed 'inward' force was weaker that the developed pressure resulting in the formation of large capsules and possibly to break-up phenomena when it exceeded a certain threshold value. In particular, a large capsule kept elongating along the passage during the early stages of post injection and when the in-sac vorticity settled down (~1.0ms after the needle sealing) it broke into two smaller bubbles (Figure 4.29).

Similar findings were obtained by the results presented in Figure 4.27. The proportion of the large capsules was greater than the rest of the fuels, as a consequence of its lower viscosity and surface tension. However, the vast majority of the bubbles travelling inside the upper nozzle passage were up to 60μm (norm. freq.~0.72) in size, followed by bubbles in the range of 60μm-120μm (norm. freq.~0.15). The normalised frequency corresponding to the rest size ranges fluctuated between 0.025 and 0.001, suggesting that the likelihood of large capsule formation to be low.
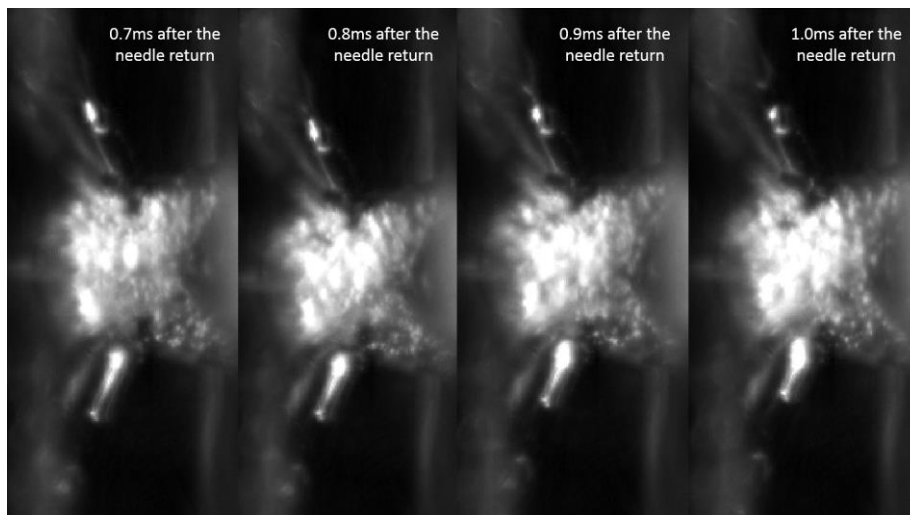
Figure 4.29: A sequence of images produced by fuel sample D showing the progressive break-up of a capsule in the upper nozzle passage during the early stages of post injection[16].

Fuel sample E (B20 diesel blend)

Fuel sample E was the heaviest amongst the fuels under consideration, having the highest viscosity and surface tension. Considering this, it was expected to obtain large populations of small bubbles and very few large capsules. The results presented in Figure 4.26 and Figure 4.27 indicated that the normalised frequency of the bubbles up to 60μm was either the lowest or the second lowest obtained. Fuel sample

E formed a noticeable amount of bubbles between 60μm-120μm; thus, it can be argued that the greatest proportion of the bubbles appearing in both nozzle passages was up to 120μm, confirming the expected trend. Overall, the normalised frequency decreased with increasing diameter. The normalised frequency of the larger capsules (>120μm) for both passages was approximately 0.001, suggesting that the formation of large capsules was rather unlikely. Overall, it can be argued that the population of smaller bubbles observed in the lower hole was lower than the upper hole. It should be also noted that fuel sample E produced the least bubbles or capsules than the rest of the fuel samples. In other words, both passages were occupied by quiescent fuel in most of the injections undertaken. An optical observation of the data revealed that there were numerous cases where there were no bubbles present in the passages, especially in the lower hole. Furthermore, there were very few cases where bubble break-up phenomena occurred. In more detail, a large capsule kept elongating along the passage during the early stages of post injection and when the in-sac vorticity settled down (~0.5ms after the needle sealing) it broke into two smaller bubbles (Figure 4.30).
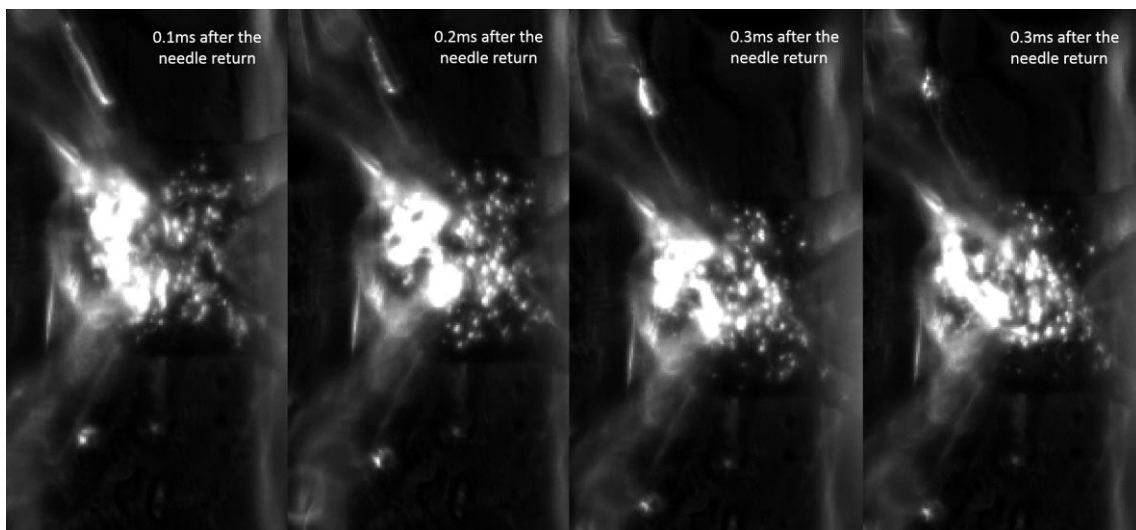
Figure 4.30: A sequence of images produced by fuel sample E showing the progressive break-up of a capsule in the upper nozzle passage during the early stages of post injection[16].

This observation was more common in lighter fuels which were more susceptible to break-up phenomena, due to their lower surface tension and viscosity. The break-up observed in the case of fuel E could be attributed to the presence of Fatty Acid Methyl Esters (FAME) in the fuel bulk. It was

suggested that the circumferential fuel flow in the sac separated the lighter from the heavier fuel components; therefore, the lighter components behaved similarly to the lighter fuels.

<u>General discussions</u>

A comparison of the results obtained by the examination of all five fuel samples revealed that the size of the vapour structures observed inside the lower and upper nozzle passage was dependent on the physical properties of the fuel. The proportion of the larger capsules increased with decreasing viscosity and surface tension. In principal, fuels with greater surface tension and viscosity exerted a strong force towards the centre of the vapour structure, while the developed pressure inside the structure volume was relatively weaker; hence, the structures retained their original size which ideally occupied the least surface area possible and they were also less susceptible to break-up phenomena. The opposite trend applied to less viscous fluids, resulting in the formation of larger capsules which could easier undergo break-up. Fuel samples C and D produced larger capsules in both holes whereas, fuel samples A, B and E produced lower population of large capsules. However, even though the proportion of larger capsules was increased in the cases of the lighter fuels, the corresponding normalised frequency was very low suggesting that in general, the likelihood of large capsule formation was relatively low. Another interesting finding was the correlation between the bubble break-up and the physical properties of the fuels. As explained above, lighter fuels were more susceptible to break-up phenomena in comparison to heavier fuels. In the cases of fuel samples C and D, there were numerous examples of bubble break-up during the early stages of post injection (Figure 4.28 and Figure 4.29). It was observed that during the first ~0.5ms after the needle return, a large vapour structure elongated along the passage (particularly inside the upper nozzle passage) and eventually occupied almost three quarters of the nozzle length. As soon as the sac vorticity settled down, the large capsule broke into two smaller ones. Even though such an observation was common in lighter fuels, an optical observation of fuel sample E raw data revealed that such break-up phenomena also occurred approximately at 0.5ms after the needle sealing. This could be attributed to the presence of Fatty Acid Methyl Esters (FAME) in the fuel bulk. It was suggested that the circumferential fuel flow in the sac separated the lighter from the heavier fuel components; therefore, the lighter components behaved similarly to the lighter fuels.

4.2.4 Bubble formation in the sac – Bubble size and pressure difference analysis

As it was mentioned in previous subsections, the formation of the bubbles in the sac volume was believed to be a consequence of needle sheet cavitation occurring during the late stages of needle return phase. The following analysis attempted to provide quantitative results with regards to the size of the bubbles or capsules formed and the pressure differential developed in the sac as a function of time and physical properties of the fuels. Figure 4.31 - Figure 4.40 show the size and pressure difference distributions at 5 different times after the needle return, in order to identify the dependence of the bubble formation process on the flow dynamics and the correlation between the physical properties of the fuels and the bubble size or the pressure difference (ΔP). The calculation of ΔP was based on the simplified version of Young-Laplace equation (Equation 4.2); hence an increase in bubble size led to a decrease in pressure difference as they are inversely proportional. The dominant physical property in the present analysis was the corresponding surface tension of the fuels under consideration. Figure 4.31 - Figure 4.35 show the bubble size distribution at 5 different times after the needle return (0.2ms, 2.2ms, 4.2ms, 6.2ms, 8.2ms). Each fuel was denoted with a different marker; dot, dash dot, solid, dash and long dash dot dot marker corresponded to fuel A to E respectively. Figure 4.36-Figure 4.40 show the corresponding pressure difference distributions at the same times after the needle return. The notation was retained the same, but the markers were in grey colour. All the distributions were normalized against the total number of bubbles observed in the sac at each time event. It should be noted that these distributions were biased towards smaller bubbles, since the large, bright areas observed in the sac were excluded from this analysis, due to the uncertainty on whether they were a cloud of bubbles or a single, large capsule. For the purpose of this analysis, the vapour pressure values of the fuels were required. According to the available literature, the vapor pressure corresponding to conventional diesel fuels was approximately 1.4kPa, while the corresponding value for kerosene was approximately 0.7kPa at ambient temperature conditions. The temperature inside the sac was estimated to be approximately 62 degrees Celsius; therefore, the vapour pressure of the fuels under consideration was considered to be slightly higher than the values mentioned above. The temperature estimate was based on the assumption that there were negligible losses and the operating temperature of the rig was approximately 40 degrees

Celsius. The temperature increase was believed to be a consequence of the fuel stagnation in the sac at 320bar (rail pressure was 350bar but the data obtained from the pressure transducer at the injector entrance suggested a pressure drop of 30bar), which can be calculated using $v\Delta P/c$. The specific volume v is equal to $1/\rho$ (where ρ=835kg/m^3), while the specific heat of diesel fuel is 1750J/kg K. Based on the above the temperature rise was ΔT= 21.9°C. Therefore, the temperature estimate in the sac is T=40+21.9=61.9 °C.
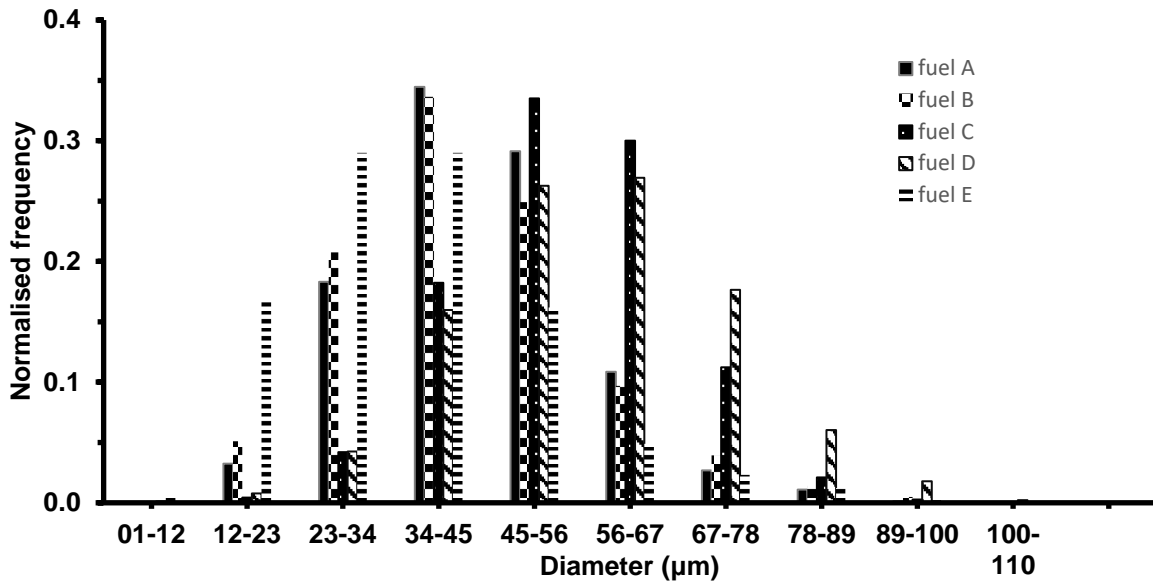
Figure 4.31: Normalised bubble size distribution for fuels A-E at 0.2ms after the needle return.
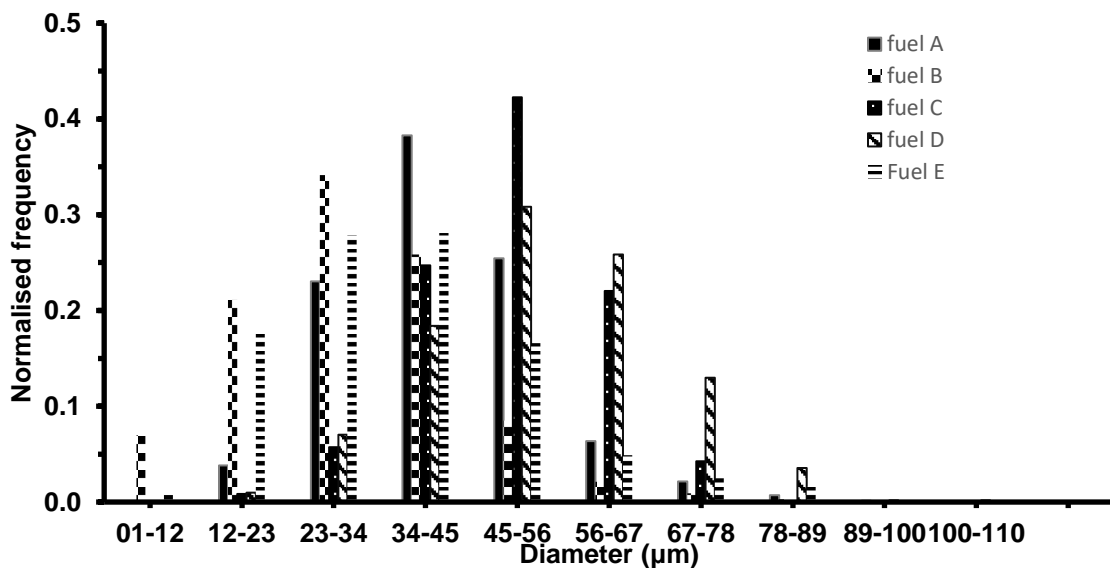
Figure 4.32: Normalised bubble size distribution for fuels A-E at 2.2ms after the needle return.
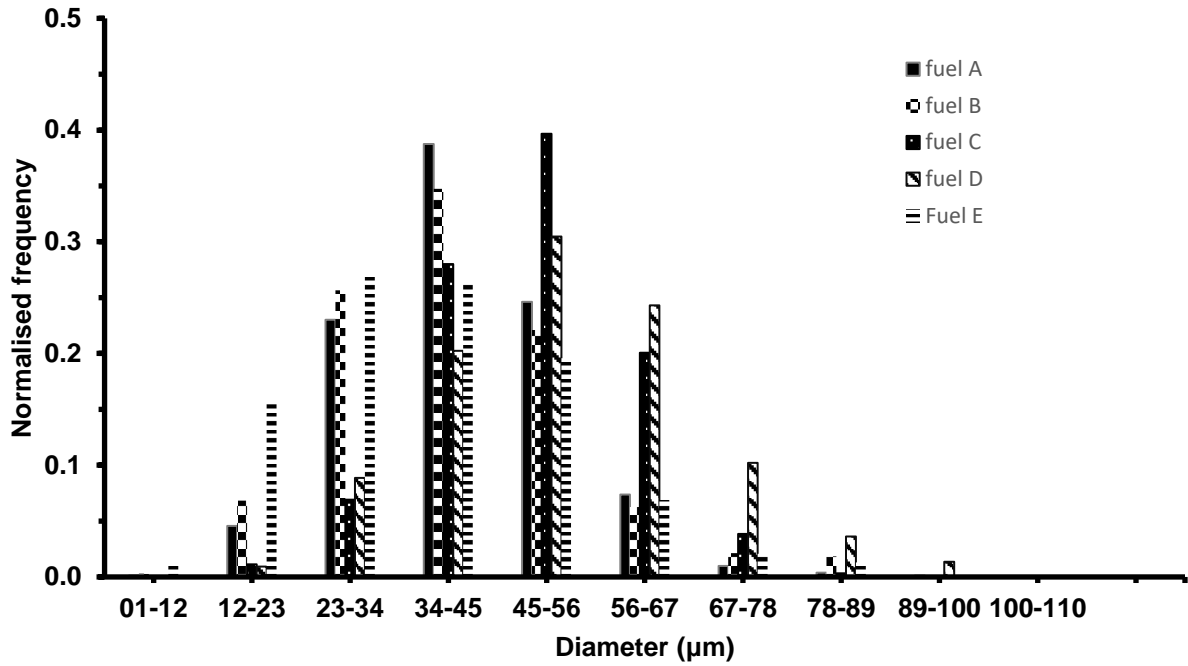
Figure 4.33: Normalised bubble size distribution for fuels A-E at 4.2ms after the needle return.
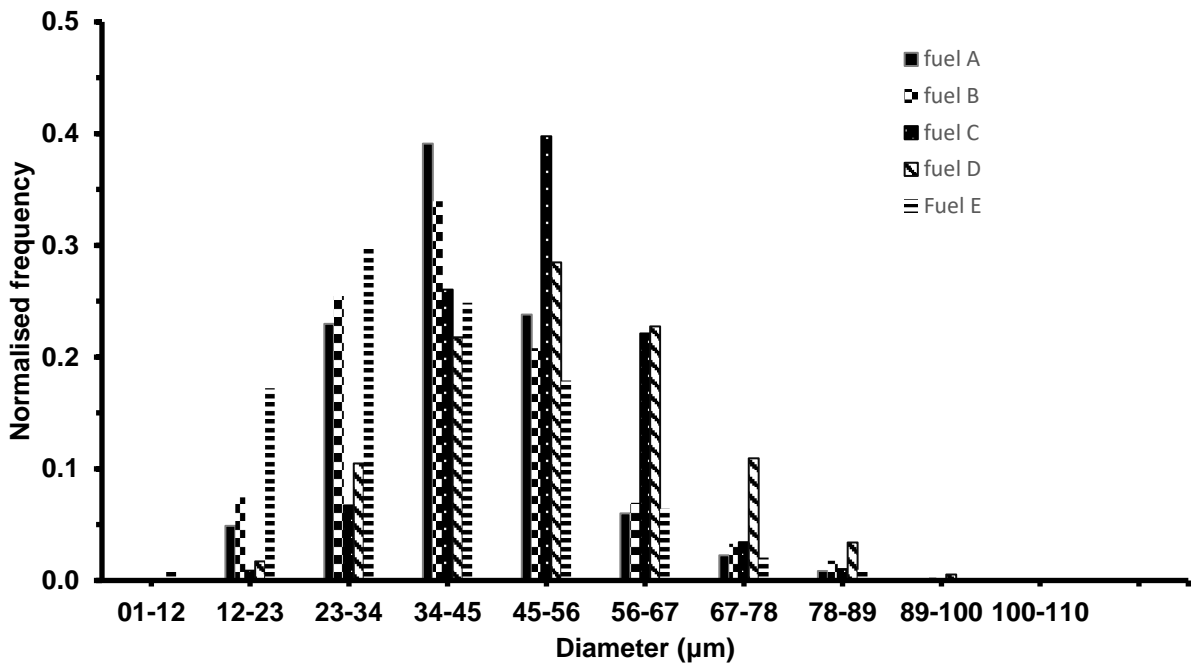
Figure 4.34: Normalised bubble size distribution for fuels A-E at 6.2ms after the needle return.
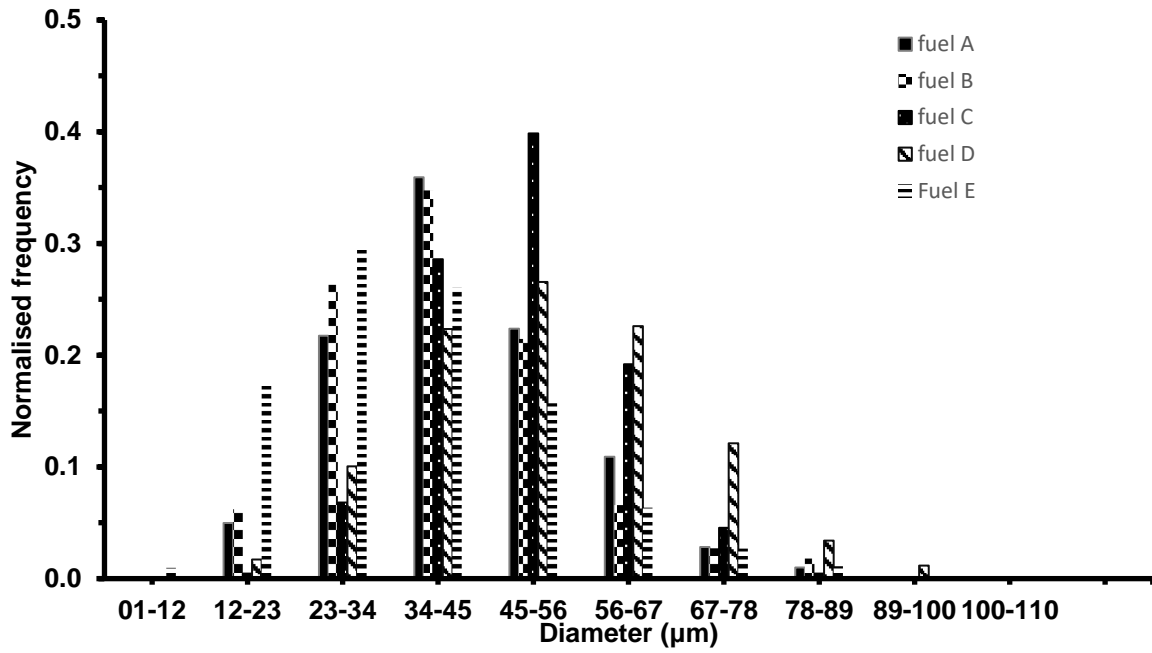
Figure 4.35: Normalised bubble size distribution for fuels A-E at 8.2ms after the needle return.
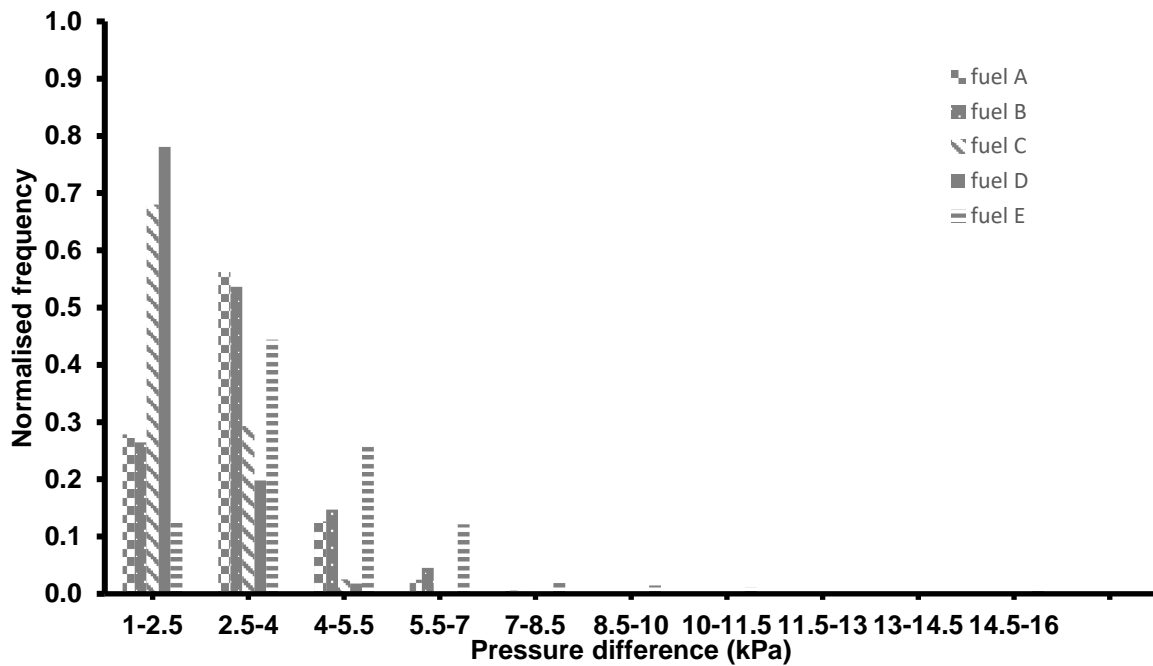
Figure 4.36: Normalised pressure difference distribution for fuels A-E at 0.2ms after the needle return.
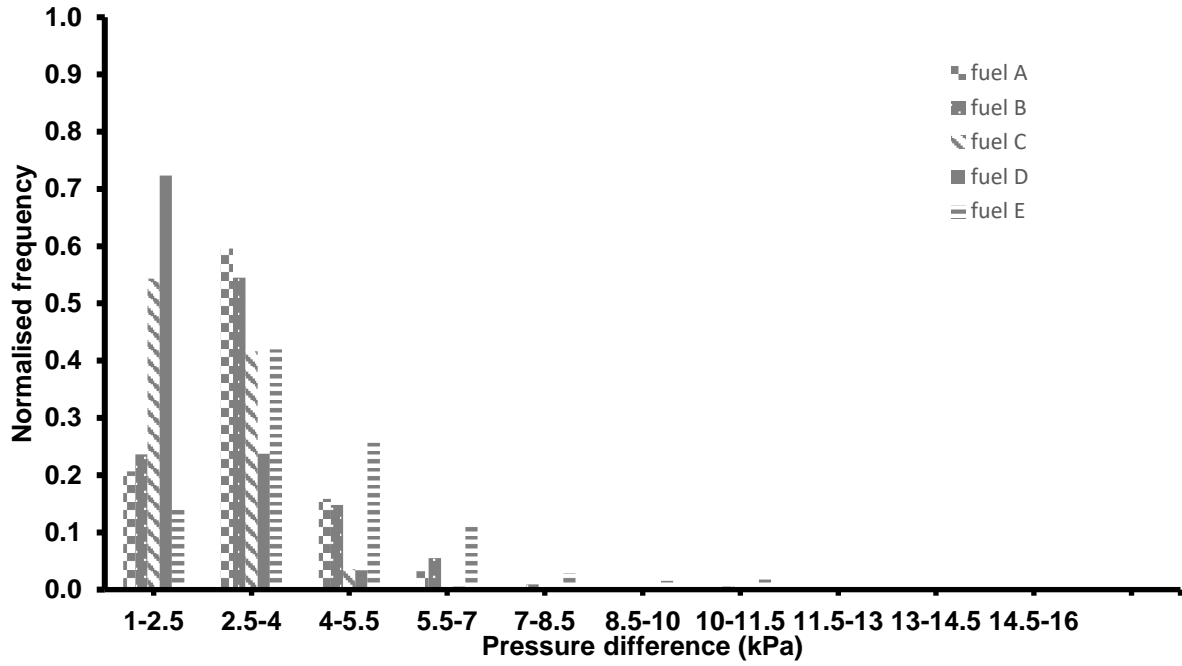
Figure 4.37: Normalised pressure difference distribution for fuels A-E at 2.2ms after the needle return.
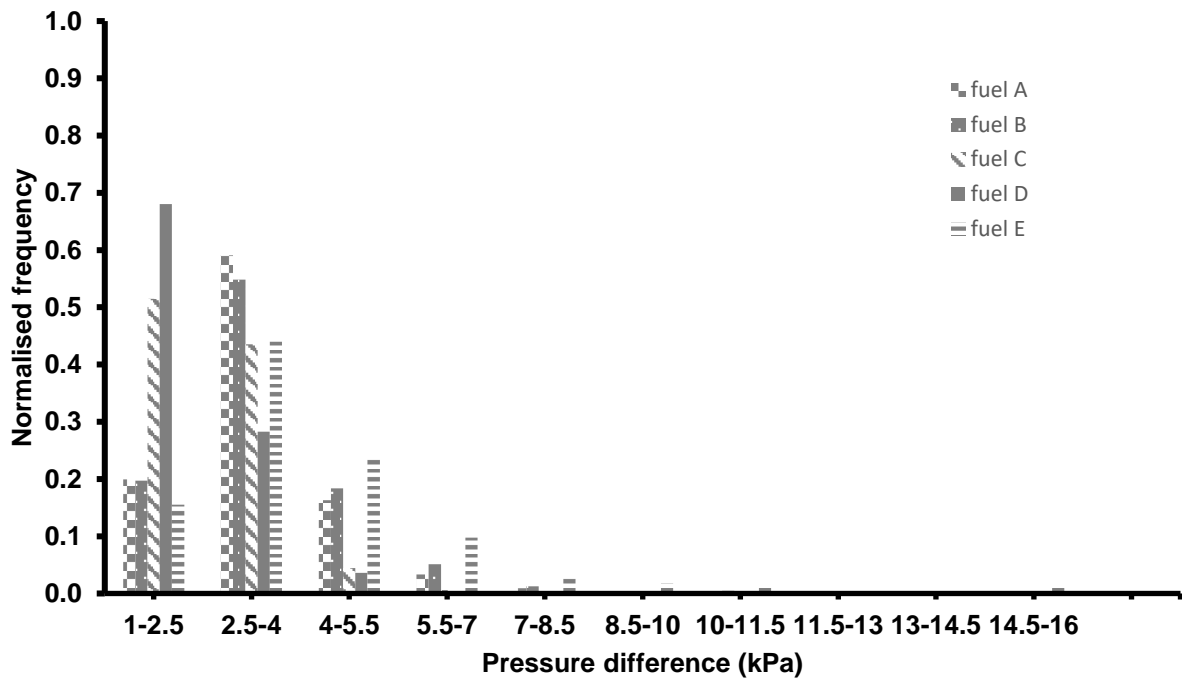
Figure 4.38: Normalised pressure difference distribution for fuels A-E at 4.2ms after the needle return.
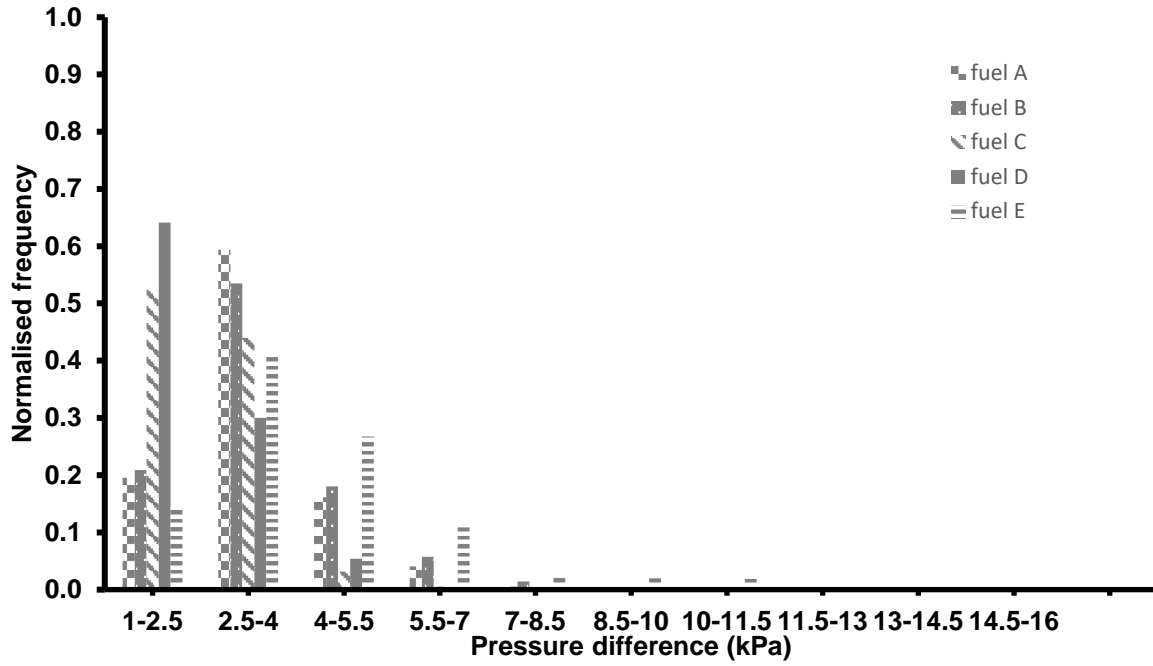
Figure 4.39: Normalised pressure difference distribution for fuels A-E at 6.2ms after the needle return.
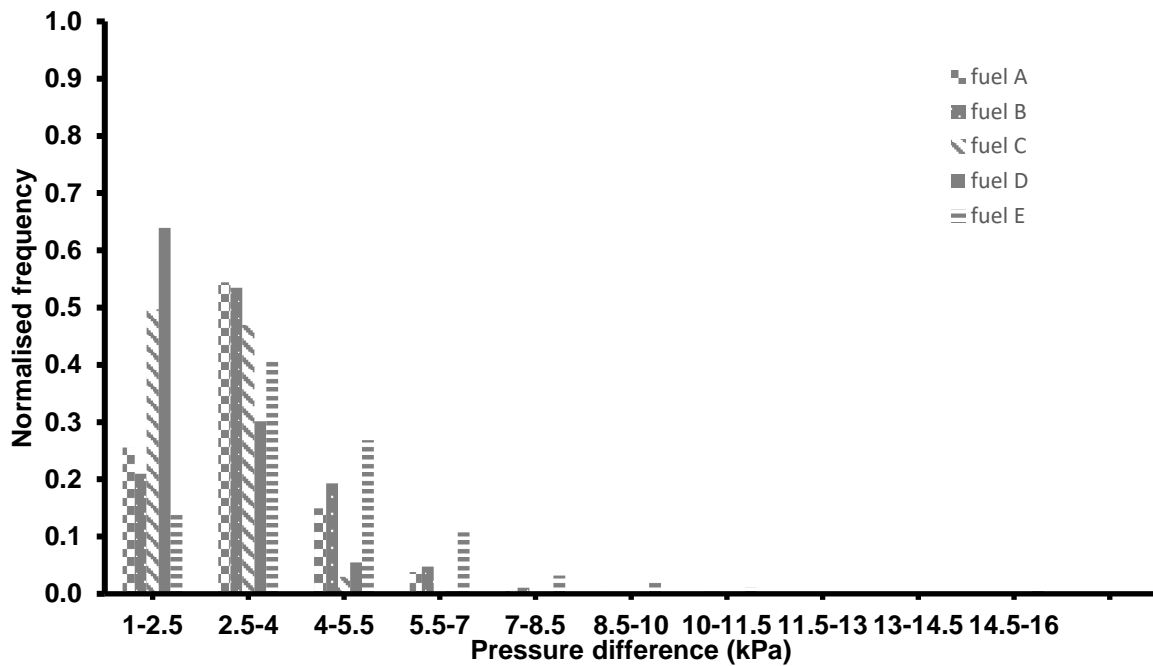
Figure 4.40: Normalised pressure difference distribution for fuels A-E at 8.2ms after the needle return.

Fuel sample A (additive-free diesel)

An optical observation of Figure 4.31 - Figure 4.40 revealed that fuel sample A produced bubbles of

intermediate size and consequently intermediate pressure difference values. It can be also observed that

the bubble size remained practically unchanged (~35μm) throughout post injection duration, suggesting that the flow dynamics did not significantly affect the bubble formation process. Additionally, the unchanged size of the bubbles could be attributed to the relatively high viscosity and surface tension of the fuel. In principal, viscous fluids with large surface tension form relatively small bubbles, since the surface tension forces tend to maintain the least surface area possible. The average value for the pressure difference calculated was approximately 2.0kPa, but overall it ranged between 0.1kPa and 8.0kPa. Considering the vapour pressure of diesel to be around 1.4kPa, it can be argued that the bubbles formed were not composed of fuel vapor, but also of small amounts of other components such as nitrogen, oxygen.

Fuel sample B (gap diesel)

The physical properties of fuel sample B were fairly similar to fuel sample A; hence it was expected to exhibit a behaviour comparable to fuel A. Indeed, the results presented in Figure 4.31 - Figure 4.40 confirmed the expected behaviour. In particular, the size of the bubbles forms seemed to remain almost unchanged (~34μm) over the duration of post injection phenomenon. The slightly smaller mean bubble size of fuel B relative to fuel A could be attributed to the slightly larger viscosity and surface tension. Similar findings were obtained from the pressure difference results, which on average was approximately 2.1kPa. Overall the pressure difference distribution ranged between 0.1kPa and 8.0kPa. The inverse proportionality between the bubble size and pressure difference explained the slightly higher mean value of fuel B relative to fuel A. The uncharged size of the bubbles could be attributed to the relative large viscosity and surface tension which opposed any change in size. Lastly, it can be stated that the bubbles produced by fuel B consisted of not only fuel vapor but also other components (O_2, N_2) since the pressure developed in the bubbles was greater than the corresponding vapour pressure of the fuel.

Fuel sample C (kerosene)

Fuel sample C was the second lightest fuel under consideration, whose viscosity and surface tension were lower than fuel A and fuel B. Fluids with relatively low viscosity and surface tension were

expected to form bubbles, which were more susceptible to break-up phenomena. The surface tension exerted a force towards the centre of the bubble which was resisted by the pressure developed in the bubble volume. The surface tension force became eventually weaker than the pressure developed resulting in bubble growth and often in bubble break-up. The expected behaviour was confirmed by the results in Figure 4.31 - Figure 4.35 which showed that the bubble size decreased during the early stages of post injection (d=48μm at 0.2ms, d=45μm at 8.2ms). This implied that the surface tension forces could not resist the external and internal forces applied resulting in bubble break-up. However, as soon as the in-sac vorticity settled down, the bubbles retained their size. The pressure difference distributions seemed to be narrower than the rest laying between 0.1kPa and 6.0kPa, while their modes appeared at approximately 1.8kPa. According to literature, the vapour pressure of kerosene was approximately 0.7kPa; therefore, it could be argued that the bubbles formed by fuel C consisted of fuel vapour and small amounts of other components, such as oxygen and nitrogen.

Fuel sample D (light kerosene)

Fuel sample D was the lightest amongst the fuels under consideration. It had the lowest viscosity and surface tension; hence, it was expected to form the largest bubbles and to develop the lowest pressure difference, since surface tension forces opposed internal bubble forces less. Additionally, the bubbles formed from such fuel were susceptible to break-up phenomena; surface tension forces could not resist the external and internal forces applied resulting in bubble break-up. An optical observation of Figure 4.31 - Figure 4.40 confirmed the expected behaviour. The modes of the size and pressure difference distributions were fluctuating from 53μm to 44μm and 2.0kPa to 1.7kPa respectively. It can be argued that the bubble size decreased progressively with time, suggesting that the occurrence of break-up phenomena. These phenomena were more pronounced during the early stages of post injection where the in-sac vorticity was still intense. As soon as the vorticity settled down, the decrease in size became less significant. The pressure difference distributions shown in Figure 4.36 - Figure 4.40 were relatively narrow and ranged between 0.1kPa and 6.0kPa. Considering this range and the vapour pressure of fuel D which was slightly lower than kerosene (~0.7kPa), it could be argued that the bubbles formed were a mixture of fuel vapour and small amounts of other components such as nitrogen and oxygen.

Internal flow characterisation using optical diagnostics

<u>Fuel sample E (B20 diesel blend)</u>

Fuel E the was the heaviest amongst the fuels under consideration. It had the largest viscosity and surface tension. Viscous fluids were expected to form relatively small bubbles which had the tendency to retain their original volume, with the least surface area possible. The surface tension forces developed strongly opposed the internal forces, resulting in fairly stable bubbles. An optical observation of Figure 4.31 - Figure 4.35 showed that fuel sample E produced the smaller bubbles relative to the rest of the fuels. However, it was shown that the mode of the size distributions was slightly shifted to the left with increasing time, suggesting that the bubbles were present in the sac during the later stages of post injection. It was believed that the fuel underwent a separation process, as a result of the circumferential in-sac flow; the lighter components possibly separated from the heavier ones. The lighter components were more susceptible to break-up phenomena than the heavier. This could possibly explain the decrease in the size of the bubbles formed. The modes of the pressure difference distributions were between 2.4kPa and 2.2kPa while the overall distributions were wider (0.1kPa – 11.0kPa) relative to the rest of the fuels. According to the literature[187], the vapor pressure of biodiesel within the temperature range of 323.15K – 343.15K was between 0.145kPa and 1.11kPa. Comparing these values to the results presented in Figure 4.36 - Figure 4.40 it could be argued that the bubbles formed by fuel sample E consisted of fuel vapour and small amounts of other components such as nitrogen and oxygen.

<u>General conclusions</u>

A comparison of the results presented in in Figure 4.31-Figure 4.40 revealed that the bubble size and the corresponding pressure difference developing in the sac were strongly dependent on the physical properties of the fuels and in some cases on the flow dynamics. In more detail, it was observed that the size of the bubbles formed increased with decreasing viscosity and surface tension. The surface tension forces developed by lighter fuels were weaker than the forces developed inside the bubble volume. As a result, the bubbles grew and often broke up into smaller ones. Fuels A and B exhibited fairly similar behaviour, since their physical properties were fairly similar. It was observed that the bubbles retained their original size throughout post injection duration, due to their relatively large viscosity and surface tension. On the contrary, fuels C and D, which had lower surface tension and viscosity, seemed to be

more susceptible to bubble break-up phenomena. As soon as the needle sealed, the produced bubbles were relatively large and progressively broke up into smaller ones. It should be noted that the bubble break-up was pronounced during the earlier stages of post injection, whereas the bubbles formed as soon as the in-sac vorticity settled down seemed to be more stable. Lastly, fuel sample E, which was the heaviest amongst the fuels under consideration, formed the smallest bubbles. Considering its high viscosity and surface tension, the bubbles formed were expected to retain their original size throughout post injection duration. However, the results presented in Figure 4.31 - Figure 4.35 showed that the bubble size progressively decreased with time. This was believed to be a consequence of the presence of FAME in the fuel bulk. The circumferential fuel flow in the sac was suggested to lead to the separation of the lighter components from the heavier ones; hence, the lighter components were expected to behave similarly to the lighter fuels which were susceptible to break-up phenomena. This could possibly explain the progressive decrease of the bubble size over time. Table 4.4 summarises the modes obtained from the size and pressure difference distributions presented in Figure 4.36-Figure 4.40.

Table 4.4: Bubble mean size and pressure difference statistics at 0.2ms, 2.2ms, 4.2ms, 6.2ms and 8.2ms after the needle return (NR).

	Distribution modes									
	0.2ms after NR		**2.2ms afterNR**		**4.2ms after NR**		**6.2ms after NR**		**8.2ms after NR**	
Fuel type	Size (μm)	DP (kPa)	Size (μm)	DP (kPa)	Size (μm)	DP (kPa)	Size (μm)	DP (kPa)	Size (μm)	DP (kPa)
Fuel A	36	2	35	2.1	35	2.1	35	2	35	2
Fuel B	34	2.1	36	2	34	2.1	34	2.1	34	2.1
Fuel C	48	1.8	46	1.9	45	1.8	45	1.8	45	1.8
Fuel D	53	2	48	1.8	47	1.9	46	1.95	44	1.7
Fuel E	29	2.4	29	2.4	28	2.2	25	2.45	26	2.3

In this case, the pressure difference decreased with decreasing viscosity and surface tension, due to the inverse proportionality between the bubble size and pressure difference. The lighter fuels seemed to

produce narrower distributions relative to the heavier fuels, within the range of 0.1kPa – 6.0kPa and 0.1kPa – 11.0kPa respectively. In some cases, the pressure difference calculated for all five fuels was found to be greater than the corresponding vapor pressure. This observation implied that the bubbles formed were a mixture of not only fuel vapour, but also of some other components such as nitrogen and oxygen. Under engine conditions, the synergy between the hot metal surfaces, the hot and volatile gas-liquid bubbles create ideal conditions for reactions to occur. Pyrolysis reaction takes place in fuels at high temperatures leading to particulate formation. On the other hand, the chemical conversion of the existing precursors to species of high molecular weight eventually leads to carbonaceous deposit formation. These precursors are often consisted of nitrogen and sulfur containing compounds, reactive olefins and organic acids. Several authors[12,90] have reported the existence of IIDs which often are capable of nozzle fouling or even equipment failure.

4.2.5 Implications of the internal flow on the deposit formation inside the diesel injectors

The optical observation of the internal flow towards the late stages of the injection process and during post injection revealed the formation of bubbles inside the sac volume, as soon as the needle sealed. It was suggested that the bubble formation was a consequence of needle sheet cavitation forming at the late stages of an injection event. The bubbles formed and diesel fuel in the sac were believed to form a circumferential flow which was capable of generating regions of low and high pressure. Under these pressure conditions, the in-sac flow created a pump-like phenomenon which was responsible for the bubble/capsule/fuel motion observed inside the nozzle passages. Depending on the pressure developed, the structures present in the passages could either travel towards or away from the sac. There were also cases where the in-hole structures exhibited a combined inward and outward displacement, due to sudden momentum change. Under engine conditions, the inward movement described was suggested to be enhanced by the piston movement during the exhaust stroke. Thus, it could be argued that the admission of hot combustion gases from the cylinder to at least the nozzle passages or even as far as the injector body was highly possible. The circumferential in-sac flow consisted of highly reactive bubbles which were a mixture of fuel vapour and small amounts of other compounds, such as oxygen and nitrogen. This finding implied that there was an amount of air dissolved in the fuel, the fraction of

which was dependent on the temperature, pressure conditions and the physical properties of the fuel itself. The air solubility in various fluids and specifically in hydrocarbons was discussed in detail in the work by Batino et al[188]. It has been also suggested that the air release into the sac volume occurs during needle sheet cavitation phenomenon, as a result of a sudden pressure drop, temperature rise or fuel saturation. The analyses presented in the previous sub-sections indicated that fuels with lower viscosity and surface tension (fuels C and D) initially formed relatively large bubbles which progressively broke-up into smaller ones. On the contrary, fuels A and B which had relatively large viscosity and surface tension retained their original bubble size. These findings implied that the overall population of the bubbles produced by lighter fuels was greater than the heavier fuels. Consequently, lighter fuels were suggested to form numerous highly reactive bubbles, which could be considered as potential reaction sites. Considering the above, it can be argued that under engine conditions, where the temperature and pressure are quite high, the synergy between the potentially admitted hot combustion gases through the nozzle passages, the hot metal surfaces and the highly reactive bubbles present both in the passages and the sac could create ideal conditions for chemical reactions (e.g. pyrolysis, oxidation) to take place. Such reactions usually lead to deposit formation on various locations of the FIE. Pyrolysis reaction takes place in fuels at high temperatures leading to particulate formation. The chemical conversion of the existing precursors to species of high molecular weight eventually leads to carbonaceous deposit formation. Additionally, depending on the physical properties and chemical composition of the fuels as defined by the addition of various additives or the type of diesel distillate used, some fuels showed an increased propensity to form deposits due to their unexpected behavior (e.g. non-Newtonian flow, separation process, reactions with fuel components etc.) during post injection.

4.3 Scattered Fluorescence data analysis

The purpose of the following analysis was the characterisation of the diesel flow inside the nozzle passage as a function of the injection pressure, the needle lift and the physical properties of the fuels. The LSD and INF camera were triggered simultaneously and acquired a set of seventy-five (75) 1024 x 1024 pixels images for a complete set of 50 injections. The internal flow images were mathematically described by R_{ij}^{klm} where k was the frame number, $k \in \{1, 2, ..., 75\}$, l was the injection number ,

$1 \in \{1, 2, ..., 50\}$, m was the fuel type, $m \in \{1, 2, ..., 6\}$ and i, j were the row and column indices of the image matrix, $i, j \in \{1, 2, ..., 1024\}$. The first step of the image processing methodology involved the determination of the mean of the post injection images containing only quiescent fluid. The region of interest was approximately the first third of the nozzle passage, where the optical access was good and the laser beam steering effects, due to the incident laser light on the curved surfaces of the acrylic nozzle tip, did not cause significant optical contamination. A sequence of post injection images of each experimental fuel was carefully chosen to include only quiescent fluid without any bubbles or vapour capsules being present in the region of interest. Any post injection frames with vapour capsules or/and bubbles were discarded. The chosen quiescent fluid images from each injection were then utilised to construct the mean image with quiescent fluid. This procedure led to the construction of one mean quiescent fluid image per injection event ($\overline{M_{ij}^{lm}}$). A careful optical observation of the raw data revealed that the nozzle passage of interest was translated on both X and Y axes. Initially, it was believed that the translation observed was a consequence of the compression of the acrylic tip, but it was observed that the size of tip remained unchanged for the whole duration of the experiment. Hence, it was concluded that the translation of the hole was an optical effect, which could be possibly attributed to the wetted surfaces of the acrylic tip with the experimental fuel. Both raw data and mean images (R_{ij}^{klm} and $\overline{M_{ij}^{lm}}$) were corrected in terms of X and Y translation. In this regard, a Matlab code was developed enabling the track of either the left or right hole boundaries and the upper boundary of the sac. The former facilitated the correction of the translation along the X-axis, while the latter along the Y-axis. This correction ensured that the Region Of Interest (ROI) had the same size and corresponded to the same hole segment at all times. The code would then crop this region of interest and save the images for later use. Such a procedure would produce a set of mean images equal to the number of the injection, which satisfied the above-mentioned criteria. At this point, another Matlab code was employed to produce images, which did not contain any data corresponding to quiescent fluid. This was achieved by subtracting each mean image from the corresponding set of raw images (corrected against X, Y axes, $P_{ij}^{klm} = R_{ij}^{klm} - \overline{M_{ij}^{lm}}$). The following step involved the construction of an artificial background of the

region of interest using a Matlab code. A carefully defined mask was initially applied onto the mean quiescent fluid images to exclude the data in the region of interest. The code then detected the intensity of the pixels surrounding the binary mask. It was found that the intensity of the background surrounding the region of interest was almost linearly decreasing from the right-hand to the left-hand side of the mask; therefore, the intensity of the optical contamination within the mask boundaries was estimated by performing a linear interpolation between the values found on the right-hand and left-hand side of the spray geometry; the interpolated values were lastly substituted to the masked region. The resultant image (B_{ij}^{lm}) was a good estimate of the surrounding optical contamination. The correction of the mean images with quiescent fluid for each injection event was achieved by subtracting the corresponding mean constructed image background. The corrected mean images with quiescent fluid (Q_{ij}^{lm}) were then added to the corresponding injection corrected images (P_{ij}^{klm}) resulting in the original image without significant background contamination. Lastly, the images obtained were normalised against the corresponding corrected mean images with quiescent fluid. The results provided information with regards to the transient variation of the LVF of the flow inside the hole. Ideally, LIF is a volumetric technique that is capable of providing quantitative LVF within the range 0 to 1. However, the distributions obtained from the processed data ranged between the range of 0 to 5. This could be attributed to the limitations of LIF technique. The flow discontinuities produced strong signal which did not reflect the actual intensity of the liquid fluid. It was observed that the intensity of the quiescent fluid was lower than the intensity of the flow during the injection by approximately 400 to 700 counts on average. This could be attributed to the saturation of the RhB particles, due to the incident laser light over post injection duration. However, the main objective of this analysis was the identification of differences between fuels, which were tested at different operating pressures and needle lifts. It should be mentioned that fuel 3 data were corrected against the corresponding fluorescence yield calibration ratio in order for the results of fuels 1 and 3 to be comparable to each other. Lastly, the comparison of the different fuels was made by comparing the distributions obtained from the time-resolved mean images. In more detail, the time resolved images were produced by calculating the mean of the images

$1, 76, 151, 226, ..., 3676$, frames $2, 77, 152, 227, ..., 3677$ and so on up to frames $75, 150, 225, ..., 3750$ for all the fuels under inspection. To the best of the author's knowledge this is the first attempt to apply LIF technique on the internal nozzle flow and the quantity used to describe the percentage of liquid inside the passage was called Scattered Fluorescence Liquid Volume Fraction (SFLVF).

4.4 Discussion on the SFLVF results

The following results were obtained from the internal flow data of fuel 1 at 250bar and 350bar to investigate the effect of rail pressure. The analysis was performed during the opening, maximum lift and closing phases of the needle or alternatively at 1.8ms, 3.8ms and 5.6ms after SoI. An optical inspection of the raw data revealed that only the first third of the nozzle passage of interest could be clearly seen; therefore, the investigation was performed at the 200μm downstream of the nozzle hole entrance. Figure 4.41 shows an example of a raw internal flow image, highlighting the nozzle passage and the Region Of Interest (ROI). For results consistency, the size and position of the ROI was kept the same at all times.
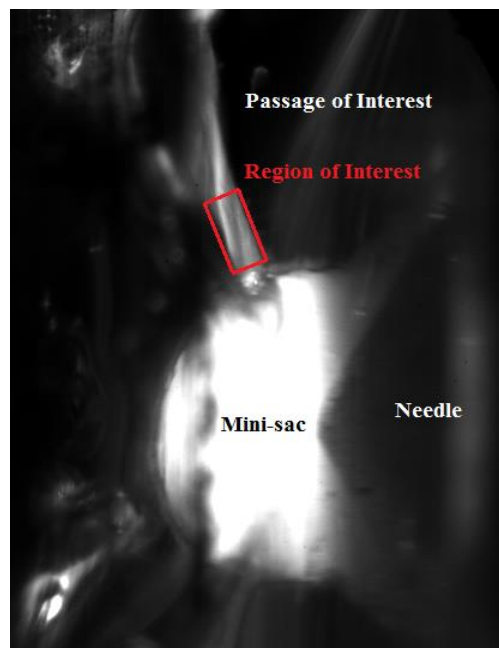
Figure 4.41: An example of a raw image showing the passage and Region Of Interest (ROI).

4.4.1 Dependence of Scattered Fluorescence Liquid Volume Fraction (SFLVF) on rail pressure and needle lift

The distributions obtained were the projections of either the cumulative histograms or the histograms obtained from the mean images. The results corresponding to 250bar were presented in black colour, while 350bar in light grey. The opening, maximum lift and closing phases of the needle were represented by solid, dotted and dashed lines respectively. All distributions were self-normalised against the total number of pixels contained in the ROI; hence, the region below the plotted curve was always equal to 1. The normalisation facilitated the comparison between the data of different rail pressure and physical properties. Lastly, the mean SFLVF and STD images were converted into false-colour to provide a comprehensive visualisation of the flow.

Figure 4.42 shows the mean SFLVF distribution of fuel 1 at 250bar. It was shown that the SLVF gradually decreased as the injection progressed. This observation suggested an interesting correlation between the SLVF of the flow and the needle lift. The largest SFLVF values were obtained in case the of 1.8ms after SoI followed by 3.8ms and 5.6ms after SoI. However, the difference between the last two cases was not significant, suggesting similar flow patterns inside the nozzle hole.
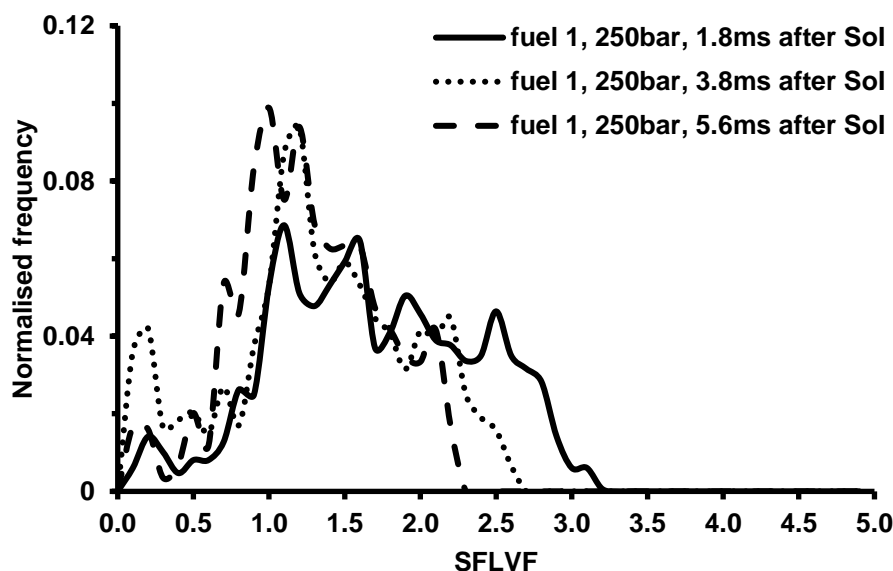
Figure 4.42: SFLVF distributions produced by the mean images obtained from fuel 1 at 250bar (1.8ms, 3.8ms and 5.6ms after SoI)
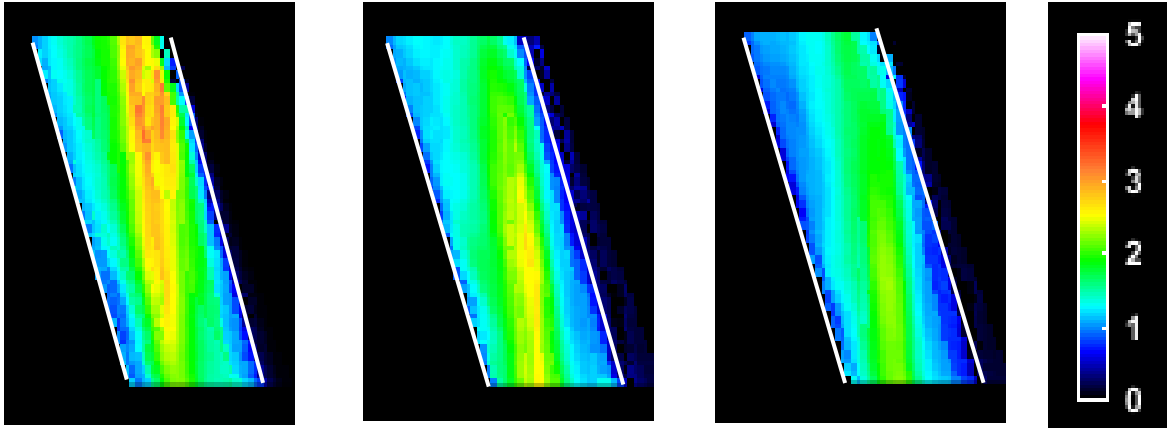
Figure 4.43: Mean false coloured images produced by fuel 1 at 1.8ms, 3.8ms and 5.6ms (left to right) after SoI and 250bar.

The false-coloured SFLVF images shown in Figure 4.43 demonstrated that the largest SFLVF values located close to the central axis and the upper right corner of the ROI. In the vicinity of the lower right corner of ROI, the SLVF obtained fairly low values, suggesting the possible existence of geometric cavitation. It should be also mentioned that the raw data were contaminated by beam steering effects, which were mostly removed after image processing. However, the corrected images contained a small amount of contamination, which could not be removed without losing useful data.
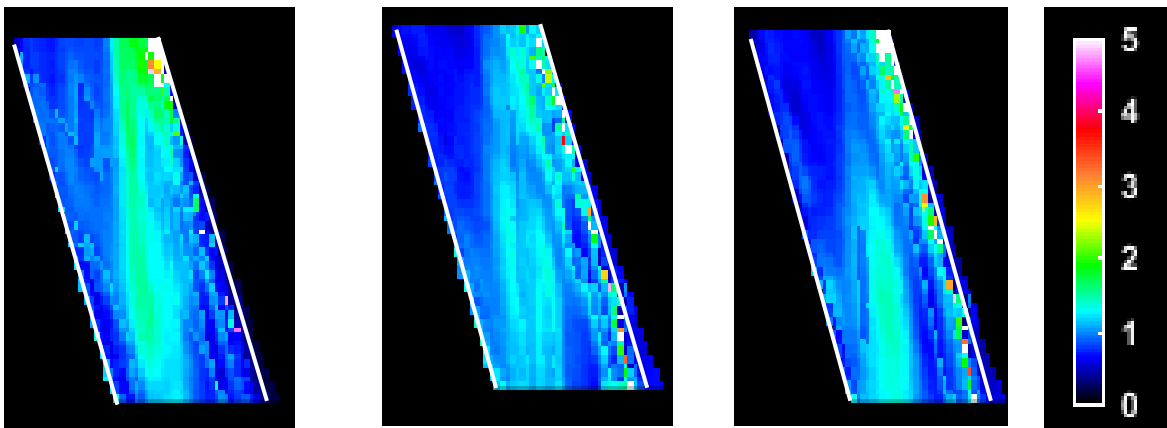
Figure 4.44: False coloured STD images produced by fuel 1 at 1.8ms, 3.8ms and 5.6ms (left to right) after SoI and 250bar.

Figure 4.44 shows the STD false coloured images at 1.8ms, 3.8 and 5.6ms after SoI to identify the SFLVF variation in each data set. It was observed that the largest variation occurred at the same region,

as where the largest SFLVF locate. Such an observation suggested that the internal flow patterns occurring over a complete set of 50 injections were not the same. However, the STD values obtained from the rest of the passage exhibited low STD. Additionally, in all three images there was a pixelated region close to the right boundary of the passage. This was an artefact caused by the significant X and Y translation of the passage during the experiment (see §4.3). The achieved image alignment deviated by ±1 pixel. A comparison of the three images showed that the largest STD values were obtained at 1.8ms followed by 5.6ms and 3.8ms after SoI. The increased variation during the opening and closing phases of the needle was believed to be a result of the developing complex and intensive cavitation.

Figure 4.45 show the distributions of the mean SFLVF images obtained from fuel 1 at 350bar. The results demonstrated that the SFLVF distribution produced at 3.8ms after SoI is shifted towards smaller SFLVF values relative to 1.8ms and 5.6ms after SoI, suggesting a correlation between the SLVF and needle lift.
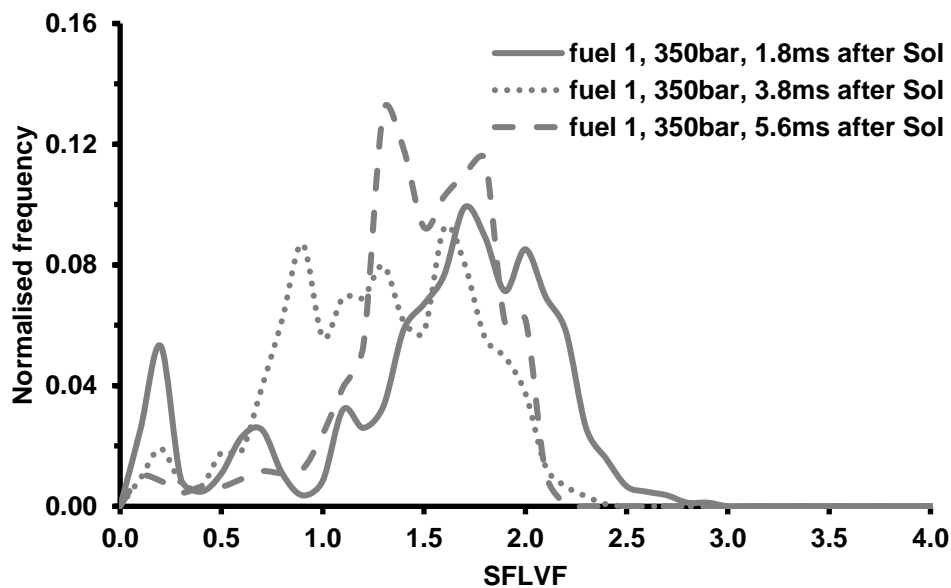
Figure 4.45: SFLVF distributions produced by the mean images obtained from fuel 1 at 350bar (1.8ms, 3.8ms and 5.6ms after SoI)

A comparison between the results at 250bar and 350bar revealed that the SFLVF decreased with increasing rail pressure, with an exception in the case of 5.6ms after SoI. Such an observation suggested intensive cavitation phenomena in the case of 350bar, since the amount of liquid in the passage of

interest decreased. The largest SFLVF values were obtained during the opening phase of the needle, followed by the closing and maximum lift phases.

The mean false coloured images presented in Figure 4.46 showed that the vast majority of the large SFLVF values located close to the central axis of the region of interest. In the case of 3.8ms after SoI, it was observed that the SFLVF gradually decreased with increasing axial distance from the central axis. The mean image at the maximum needle lift demonstrated that the central axis was surrounded by lower SLVF values. This observation came to an agreement with the observations made in Chapters 5,6, where the vast majority of the larger droplets with high LVF were located in the vicinity of the spray central axis. Moreover, the mean images produced at 3.8ms and 5.6ms after SoI provided a hint for the existence of geometric cavitation structure close to the lower right corner. This argument further supported the argument with regards to the correlation between the spray asymmetry and the location of geometric cavitation. In more detail, it was shown that the sprays developed at 3.8ms and 5.6ms were asymmetric; the larger droplets were mostly located on the right-hand side of the spray.
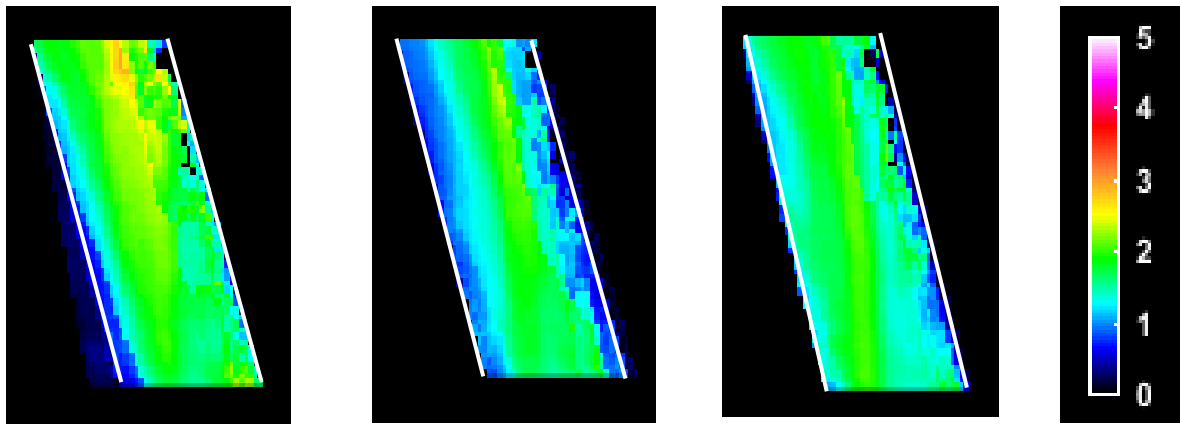
Figure 4.46: Mean false coloured images produced by fuel 1 at 1.8ms, 3.8ms and 5.6ms (left to right) after SoI and 350bar.

Figure 4.47 shows the standard deviation false coloured images at 350bar to identify the SFLVF variation of each data set. It was observed that the largest STD values were obtained close the right boundary of the nozzle passage. Such an observation implied that the flow patterns varied over a complete set of 50 injection. Additionally, in all three images there was a pixelated region close to the

right boundary of the passage. This was an artefact caused by the significant X and Y translation of the passage (see §4.3).
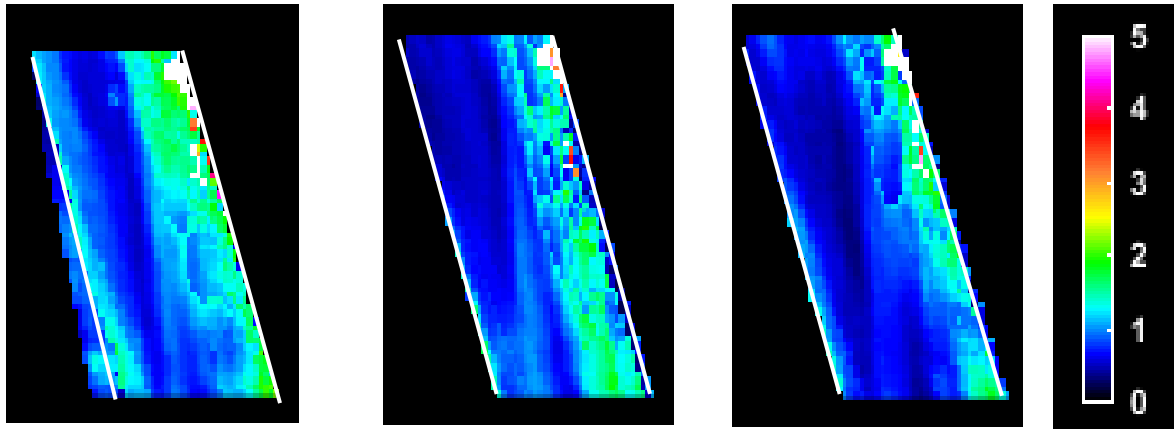
Figure 4.47: False coloured STD images produced by fuel 1 at 1.8ms, 3.8ms and 5.6ms (left to right) after SoI and 350bar.

It should be also noted that the signal exceeding the wall boundaries, which were identified in the images as white lines, corresponded to the remaining background signal, due to the significant translation of the images during a complete set of 50injections. Additionally, there were a few images where the hole appeared magnified. This could be attributed to the wetted surfaces of the tip after a number of injections. Such an effect led to the imperfect image overlap; the deviation from the perfectly overlapped images was between 1pixel and 3pixels.

4.4.2 Dependence of Scattered Fluorescence Liquid Volume Fraction (SFLVF) on the physical properties of the fuels and needle lift

The dependence of the physical properties of the fuels on the SFLVF inside the nozzle passage was investigated by the comparison between fuels 1 and 3 at 350bar. The density and viscosity of fuel 3 were lower relative to fuel 1 by approximately 2% and 25% respectively. Hence, it was expected to obtain smaller SFLVF values, since lighter fuels exhibited an increased propensity to cavitate.

Figure 4.48 represent the mean SFLVF distributions of fuel 3 at 350bar. The obtain results suggested that the needle lift did not have a significant effect on SFLVF, suggesting similar flow patterns during an injection event.
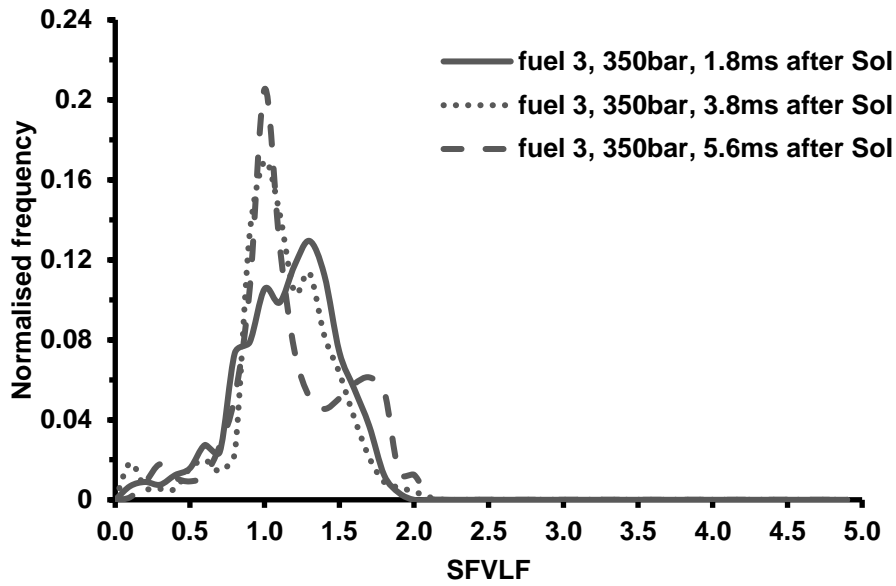
Figure 4.48: SFLVF distributions produced by the mean images obtained from fuel 3 at 350bar (1.8ms, 3.8ms and 5.6ms after SoI)

A comparison between the results obtained from fuels 1 and 3 reveals that fuel 3 produced smaller SFLVF values as expected. This could be attributed to the increased tendency of less viscous fuels to cavitate more. The false-coloured images shown in Figure 4.49 demonstrated that the majority of the large SFLVF values located on either the right-hand side or on both sides of the region of interest.
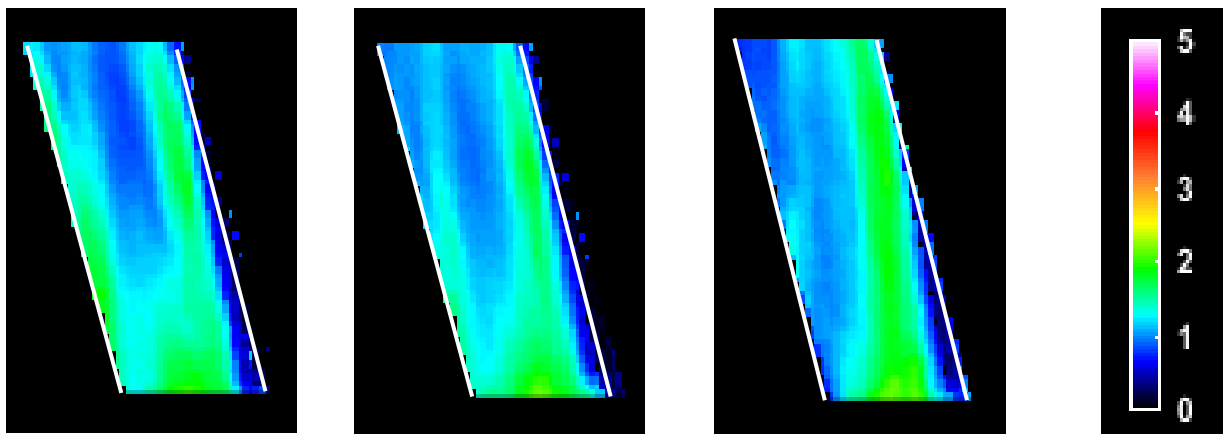
Figure 4.49: Mean false coloured images produced by fuel 3 at 1.8ms, 3.8ms and 5.6ms (left to right) after SoI and 350bar.

Lastly, the mean SFLVF images suggested the existence of geometric cavitation in the vicinity of the lower right corner. Such an observation came to an agreement with the argument made in Chapter 5 regarding the correlation between the spray asymmetry observed and the location of geometric cavitation inside the passage.
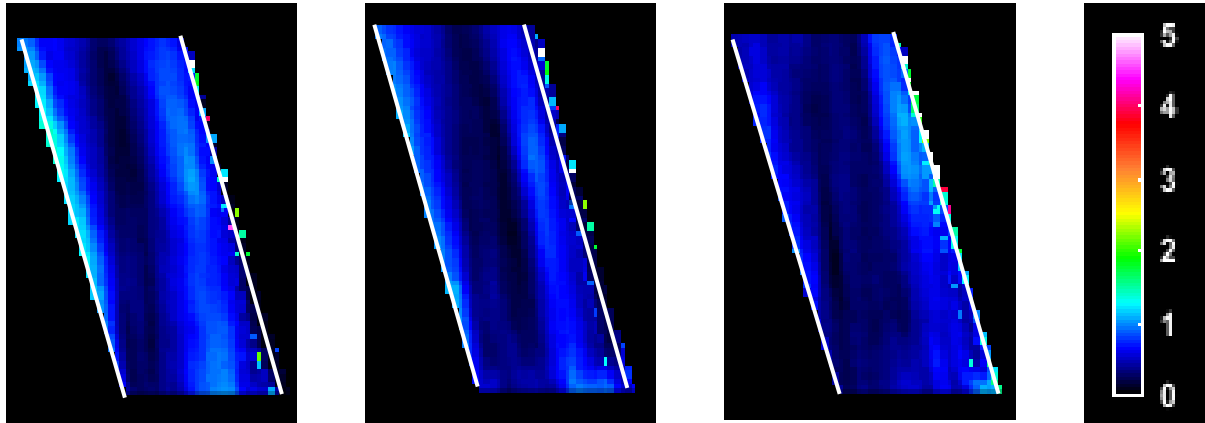
Figure 4.50: False coloured STD images produced by fuel 3 at 1.8ms, 3.8ms and 5.6ms (left to right) after SoI and 350bar.

The false coloured STD images produced by fuel 3 are presented in Figure 4.50. It was observed that the STD values were low for all three cases, suggesting similar flow patterns over a set of 50 injections. The largest STD values in all three cases located close to the nozzle passage walls, but did not significantly differ from values around the central axis of the passage. Such an observation suggested the development of similar flow patterns during an injection event. It should be noted that the location of the largest STD values in the passage coincided with the largest STD values in the sprays. This observation suggested an interesting correlation between the internal flow and the external sprays. In the case of fuel 3, it could be argued that the vast majority of the signal was found between the wall boundaries. Such an observation implied that there was no significant translation of the nozzle hole and most of the images overlapped perfectly.

4.4.3 Summary

The discussion presented above suggested that an increase in rail pressure led to smaller SFLVF values, due to enhanced cavitation phenomena. In the case of fuel 1 at 250bar and 350bar, it was shown that

the needle lift had an impact on the produced SFLVF distributions, while in the case of fuel 3 at 350bar this effect was not as significant. The results obtained from fuel 1 at 250bar showed that SFLVF gradually decreased within an injection event, whereas the results at 350bar demonstrated that the flow at the maximum needle lift produced the lowest SFLVF followed by the closing and opening phases of the needle. Moreover, in the case of fuel 1, a comparison amongst the false-coloured images revealed that the largest SFVLF values were in the vicinity of the central axis, while fuel 3 on either sides or the right-hand side of the region of interest. Additionally, the images also provided a hint for the existence of a geometric cavitation structure close to the lower right corner of the passage. Such an observation came to an agreement with the argument made in earlier chapters regarding the spray asymmetry being a result of geometric cavitation developing at the entrance of the passage. Lastly, it should be highlighted that fuel 3 produced more capsules/bubbles relative to fuel 1 during post injection period, possibly due to its lower viscosity.

Chapter 5

External spray drop-sizing analysis using Laser

Sheet Drop-sizing technique

The characteristics of diesel sprays forming in modern direct injection common rail diesel engines are believed to have a significant impact on combustion efficiency, thermal efficiency and emissions. Therefore, a thorough investigation of atomisation process of a diesel engine is crucial in order to improve pre-combustion fuel air mixing and engine performance and to reduce the engine-out emissions.

The primary objective of the work presented in this chapter was the determination of the dependence of droplet size distribution and spray structure on diesel physical properties, i.e. viscosity, surface tension, distillation profile, density etc. The sprays under consideration were non- evaporating sprays obtained from a custom manufactured system operating at moderate pressures (250bar and 350bar). There are numerous diagnostics suitable for an experimental investigation into diesel sprays, but for the purpose of this work Laser Sheet Drop-sizing technique was selected as the most appropriate diagnostic in terms of capability and experimental complexity. The results presented were obtained from fuels A-E (Jeshani's data) and fuels 1-4. To keep this dissertation to a reasonable length, the dependence of SMD distributions on pressure and needle lift was shown only in the case of fuel A and fuel 1, which were inspected at both 250bar and 350bar at three different needle lift positions. The rest of the fuels referred to data obtained at 350bar when the needle was fully opened (3.7ms, 3.8ms after SoI).

5.1 Image processing methodology

5.1.1 External spray drop-sizing distribution

The methodology followed to process the images obtained from the LSD camera was similar to the one followed in the case of Jeshani's processing methodology. A detailed description can be found in his PhD thesis[16]. The main difference between the two experiments was the employment of LIF instead of

white light Mie scattering induced additional optical contamination to the LIF signal; hence, the images were subjected to preliminary correction before proceeding to the final processing.

A set of 75 background 1024x1024pixel images was obtained prior to the experiment, when there was no fuel inside the nozzle geometry. The averaged background intensity corresponded to the natural background of the image. The indexed intensity variable $\overline{B_{ij}^{mq}}$ represented the intensity of the pixel located on the mean image background at the position defined by the row index $i \in \{0,1,2,...,1024\}$ and the column index $j \in \{0,1,2,...,1024\}$. The index numbers m and q referred to the diesel fuel sample tested (fuel 1- fuel 4) and the background frame number (frame1-frame75), respectively.

During the experiment, the LSD camera acquired 1024x1024pixel images containing both LIF (left spray) and Mie (right spray) signals as shown in Figure 5.1. The mean image background was subtracted from the experimental raw images eliminating the background features. The mathematical representation of the subtracted raw image was described as I_{ij}^{klm}. The index numbers i, j and m retained their meanings from above, while the index numbers k, l referred to the frame number within a single injection event (frame 1 – frame 75) and the injection event (inj.1 -inj.50).
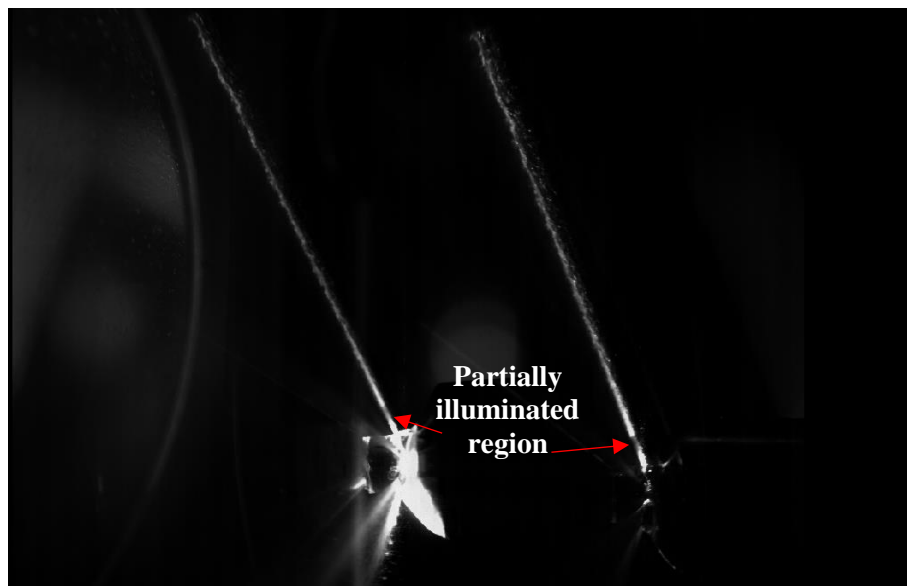
Figure 5.1: An example of a raw combined LIF (left)-Mie (right) image.

External spray drop-sizing analysis using Laser Sheet Drop-sizing technique

An optical observation of the raw image revealed that the signal in both LIF and Mie cases gradually attenuated between the nozzle exit and 2mm downstream of the nozzle exit. The acrylic nozzle tip geometry obstructs the vertical laser sheet to reach the first 2mm of the emerging spray. However, the vertical laser spot utilised for the LIF measurements inside the passage was partially illuminating the spray region in the vicinity of the nozzle exit. This explained the lower intensity signal and its sudden increase at 2mm downstream of the nozzle exit. Considering the above, the signal in the first 2mm of the spray was not reliable to perform further calculations. Hence, the trusted field of view was determined between 2mm and 18 mm downstream of the nozzle exit; the rest of the data were excluded from the analysis. At this point the raw image was split into two images, each of which contained the LIF and Mie signal respectively. The raw image could not split into two images of the same size, thus the obtained LIF and Mie images were resized to obtain images of 512x1024pixel. The mathematical representation of LIF and Mie images is described as LIF_{ij}^{klm}, Mie_{ij}^{klm} respectively.

An optical inspection of the LIF data revealed an optical contamination of the image, due to the fluorescence emitted. On the left-hand side of the image (Figure 5.2), it was shown that an optical element of the experimental arrangement was also captured into the image and interfered with the LIF spray signal. Therefore, it was necessary to eliminate this optical contamination prior to any further processing. In this regard, a Matlab code developed at City was employed. The first step included the calculation of the mean LIF images over a set of 50 injections, i.e. the mean of frames 1,76, 151, … ,3676, frames 2, 77, 152, …, 3677 and so on up to frames 75, 150, 225, …,3750. A carefully defined mask was applied onto the mean LIF images to eliminate the useful spray data. Then, the code facilitated the detection of the intensity of the pixels surrounding the spray mask. It was found that the intensity of the optical contamination was almost linearly decreasing from the left-hand side to the right-hand side of the spray. Therefore, the intensity of the optical contamination within the spray boundaries was estimated performing a linear interpolation between the values found on the right-hand and left-hand side of the spray geometry. The interpolated values were substituted to the masked spray region. The resultant image was a good estimate of the mean optical contamination. As a result, this algorithm produced a set of 30 time-resolved, mean LIF contamination images. Lastly, each mean image was

subtracted from the corresponding time-resolved LIF image resulting in the corrected LIF image. An example of the above described subtraction in was expressed mathematically in Equation 5.1. The example showed that the 32nd corrected fuel 2 LIF image of an injection l was equal to the 32nd LIF image of the same injection l minus the 32nd mean LIF contamination image.

$$\text{LIF}^{32,l,fuel2}_{corr\ i,j} = \text{LIF}^{32,l,fuel2}_{ij} - \overline{\text{LIF}}^{\ 32,fuel2}_{opt.cont_{ij}} \qquad \text{Equation 5.1}$$
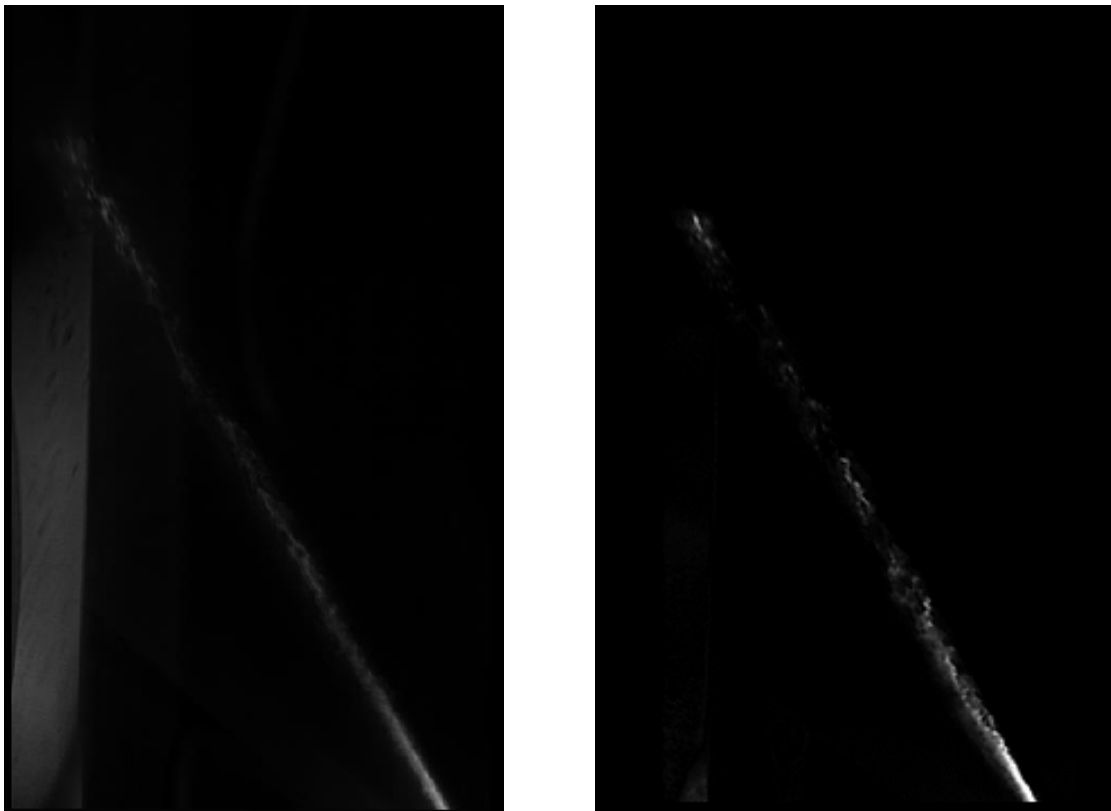
Figure 5.2: a) An example of a contaminated LIF image, b) an example of a corrected LIF image

After the correction of the LIF images, both LIF and MIE data sets were utilised to produce the LSD ratio. An observation of Figure 5.3 revealed that the ratio could not be taken directly, since the position of Mie spray image was translated with respect to the LIF spray image. Reliable SMD results required a precise overlap of LIF and Mie data. However, the translation of Mie image in reference to LIF image was not sufficient, due to projective transformations induced by the optical elements (i.e. mirrors) utilised to lead both signals on the CCD sensor. The transformations induced had eight degrees of freedom; translation, rotation, shear and scaling across both x and y axes of the image. Therefore, in

order to obtain a truthful and reliable SMD distribution, the corrections performed on Mie image should take into account all affected parameters.

In this regard, the images were subjected into a homographic transformation (homography). Homography is an invertible mapping of points and lines on the projective plane P^2. A homogeneous representation of a 2-D point (x; y) in an image can be represented by a 3-D vector $(x_1; x_2; x_3)$ which lies on P^2. According to Hartley and Zisserman[189], homography is an invertible mapping from a projective plane P^2 to itself if and only the mapped points of three collinear points are also collinear. They also claimed that homography is feasible only when a non-singular 3x3matrix H exists and the relationship between the points in P^2 (x') and their mapped ones is always $x' = Hx$ where

$$x' = \begin{pmatrix} x'_1 \\ x'_2 \\ x'_3 \end{pmatrix}, \quad H = \begin{bmatrix} h_{11} & h_{12} & h_{13} \\ h_{21} & h_{22} & h_{23} \\ h_{31} & h_{32} & 1 \end{bmatrix}, \quad x = \begin{pmatrix} x_1 \\ x_2 \\ x_3 \end{pmatrix}$$

Consequently, the determination of matrix H is sufficient to perform a homographic transformation and to finally map two images. The homogeneous matrix H has 8 degrees of freedom, even though it contains 9 elements, eight of which need to be solved. The most common algorithm utilised for the definition of the above parameters includes point feature correspondences.

The algorithm described above was embedded in a script developed by Jeshani[16]. The reference image and the image to be corrected were the inputs to the matlab script. The homographic transformation was then performed utilising the ECC algorithm. The only modification made to the original algorithm was the addition of an extra iteration check that if achieved would terminate the iterations and would continue to the next image. The purpose of this alteration was to minimise the execution time. The LIF image dataset LIF_{ij}^{klm} was used as the reference image. The transformation of the corresponding time step Mie_{ij}^{klm} resulted in the homographically corrected image $MieHOM_{ij}^{klm}$. Then the script allowed the calculation of the ratio of LIF image LIF_{ij}^{klm} over the corresponding time resolved corrected Mie image $MieHOM_{ij}^{klm}$ (Equation 5.2) to determine the Sauter Mean Diameter. The homographically

corrected Mie images, the LSD images and the critical parameters of this analysis were saved for later use. Prior to any further processing, the homographically corrected image was compared to the reference image to ensure that the code performed a highly accurate image registration. In all the cases they had a geometric similarity above 97%; the vast majority of the spray features were found at exactly same location in the images under comparison.

$$\text{LSD}_{ij}^{klm} = \frac{\text{LIF}_{corr\ ij}^{klm}}{\text{MieHOMO}_{ij}^{klm}}$$

Equation 5.2
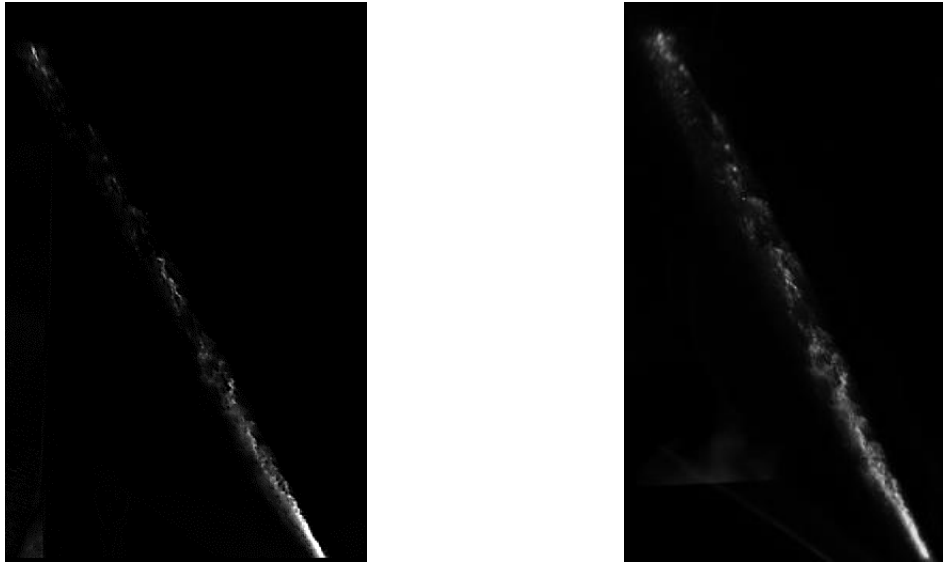
Figure 5.3: Examples of corrected LIF (left hand side) image and Mie image (right-hand side)

Additionally, the author also tested the sensitivity of the SMD distributions when the parameters determining the homography matrix were modified. In particular, the image data used for this test was Mie image dataset, since LIF images were chosen as reference. This analysis was performed for the fuel A sprays produced at 250bar and at maximum needle lift (3.7ms after SoI). Each parameter obtained from the original homography matrix (original referred to the matrix used to produce the results presented in this work) was reduced by 0.1%. One parameter was modified at a time, while the rest were kept unchanged. In all 8 cases (8 DoF), the reduction in mean SMD ranged between 6% and 9% when compared to the original mean ($\overline{SMD} = 0.64$). Figure 5.4 shows the residuals after subtracting one from the ratio of the mean SMD values. The values reveal the sensitivity of the mean SMD due to the 0.1% change of each parameter when compared to the original mean SMD. The results suggested

that the SMD was mostly sensitive to the change of the 5th element of the homographic matrix and least sensitive to the change of the 1st element. The rest of the results appeared to have the same impact on the mean SMD.
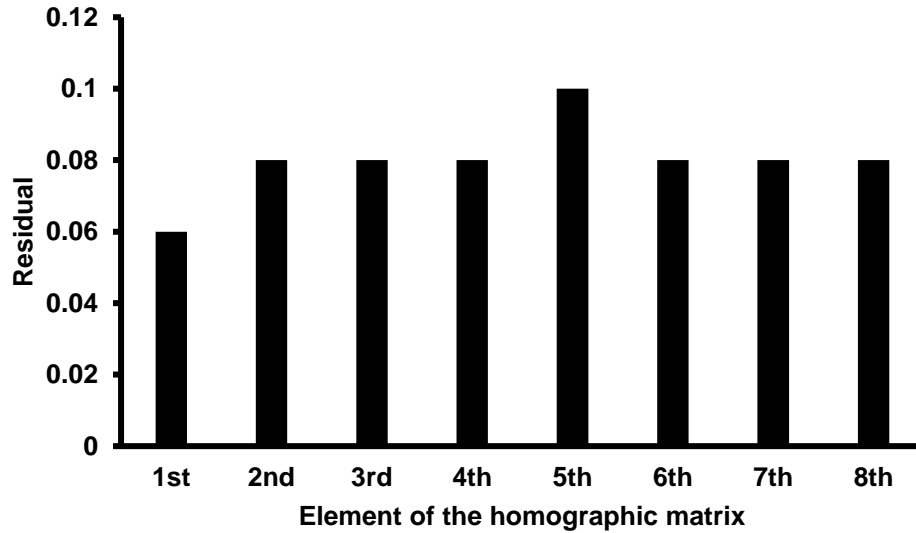
Figure 5.4: Residuals of the ratio of the original mean over the means produced after the sensitivity test

The LSD data were then utilised to produce the mean images associated with frames 1,76, 151, …,3676, frames 2, 77, 152, 3677 and so on up to frames 75, 150, 225, …,3750 for all four fuels under investigation. This was expressed mathematically in Equation 5.3. It should be noted that a global threshold of 1.5 was applied to all fuel data. The spray images were processed using a Gaussian edge filter to determine the spray boundaries. This eliminated the majority of the low intensity secondary reflections along the spray boundaries.

$$\overline{\mathrm{LSD}_{ij}^{klm}} = \frac{1}{\mathrm{no.inj}} \sum_{l=1}^{75} \mathrm{LSD}_{ij}^{klm}$$

Equation 5.3

Prior to the calculation of the mean images, it was essential to calibrate the LIF images with the corresponding fluorescent yield factor. The calibration of all fuel data led to comparable results regardless of the fuel and solvent type. Hence, the LSD dataset corresponding to each fuel was divided by its corresponding calibration ratio.

$$\text{LSD}_{\text{calibrated } ij}^{\text{klm}} = \frac{\text{LSD}_{ij}^{\text{klm}}}{\text{calibration ratio}}$$

Equation 5.4

The next step involved the normalisation of the LSD data obtained from all fuels. The mean of the top 0.1% of pixel intensities has been normalised to provide an SMD ratio value of 1.0. The largest normalisation value amongst the fuels under investigation was utilised to normalise the data produced by all four fuels. The largest mean SMD signal found in the case of fuel 1 at 250bar, while in the case of Jeshani's fuels the largest mean SMD signal was obtained by fuel E at 250bar.

The normalised mean SMD images were converted into false colour within the relative SMD range of 0-1.0pixel intensity. An example of the false colour map for the spray and the corresponding user defined colour bar is shown in Figure 5.5. The final step of the present analysis involved the production of normalised intensity frequency histograms of the time-resolved mean SMD images. The resulting histograms provided information with regards to the relative SMD distribution of the spray droplets at different needle lifts and highlighted the effect of the physical properties of the fuels on the relative SMD.
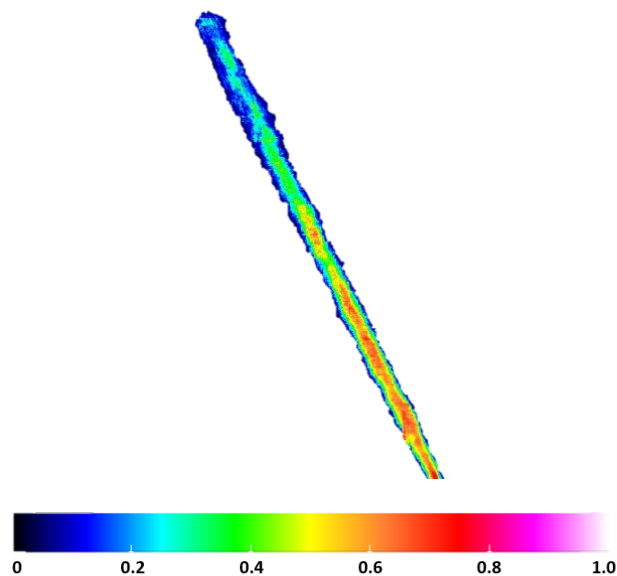
Figure 5.5: An example of a false colour relative SMD image of the spray (2mm to 18mm) in the range of 0 - 1.0pixel intensity.

5.1.2 Diesel spray asymmetry

An optical observation of the false coloured SMD images obtained indicated a spray asymmetry. In order to investigate this observation in more detail, a Matlab code developed at City was employed to accurately determine the relative SMD distributions at six different spray regions. The code facilitated the accurate determination of the spray central axis, which was at first utilised to split the spray into two equal vertically oriented segments and then to split these into three equally spaced horizontal segments. Initially, the sprays were rotated by ~25degrees to be vertically oriented. Any artefacts or scattering effects were eliminated by masking the SMD image with a binary mask. The key parameter of the present analysis was the accurate determination of the spray central axis. The first step involved the scanning of the image to detect the pixels whose intensity was greater or equal to the 10% of the maximum intensity in the image. Lastly, the code split the spray body into three horizontal equal divisions, the upper, middle and lower segments. Each division was then divided into two equally spaced segments. Consequently, the spray was divided into six equal segments and the distribution of the relative SMD was produced for each segment. All the distributions were self-normalised against the total number of pixels of the region of interest. Adopting this approach, the area under the graph was properly normalized to one. The normalized frequency represented the probability of finding droplets in the spray with the specified range of relative Sauter Mean Diameter. The histograms were produced in a way such that the graphical projections of the normalized histogram frequencies were representative of the number of pixels in the mean spray image frame. All the data were exported into an excel worksheet for further processing.

5.2 Results and discussion

5.2.1 Spray drop-sizing distribution as a function of rail pressure and needle lift

For the purpose of this analysis, the spray data produced by fuels A and 1 at 250bar and 350bar during the opening (1.8ms after SoI), closing phases (5.6ms after SoI) of the needle and at the maximum needle lift (3.7ms, 3.8ms after SoI) were used. The false coloured images together with the corresponding relative SMD distributions were produced by the corresponding normalised, time-resolved, mean images obtained from 100 injections and 50 injections respectively. The normalised mean images did

not show any information with regards to the spray structure, but they provided a good overview on the SMD distributions between the different needle lifts and rail pressures. The standard deviation (STD) of the normalised images was also produced in false colour to identify the degree of droplet size variation of the emerging sprays.

1.8ms after SoI

During the initial stages of needle lift, cavitation phenomena had a pronounced effect. At low needle lifts, the fuel flow was expected to be choking, since most of the nozzle sac entrance cross section was occupied by the needle. Thus, strong cavitation was expected to be present during this period. He et al.[92] reported recently the formation of needle sheet cavitation in early stages of needle lift, supporting the above mentioned argument. Several research reports have stated that cavitation enhances atomisation process[3,181], which in turn leads to the formation of smaller droplets. Additionally, it has been also suggested that an increase in rail pressure enhances atomisation process. Figure 5.7 shows the false coloured images of the sprays produced by fuel A at 250bar and 350bar, while Figure 5.6 shows the corresponding SMD distributions.
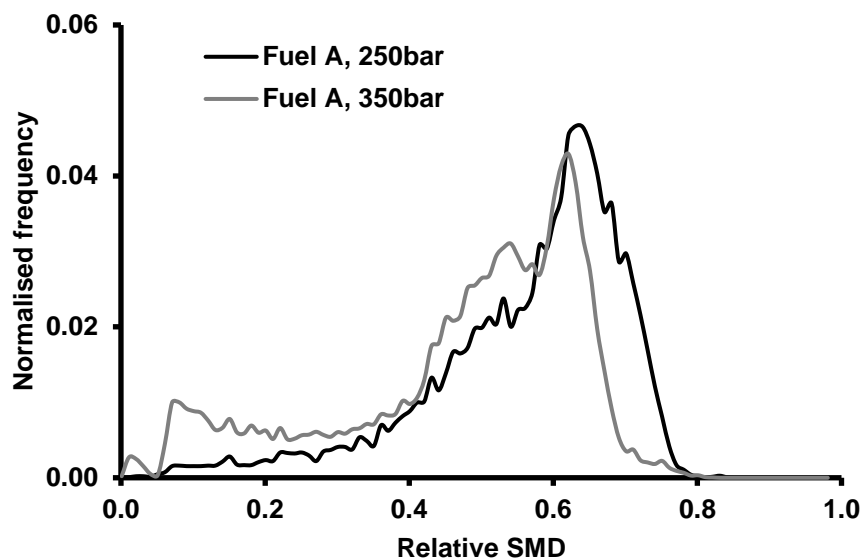
Figure 5.6: Relative SMD distributions corresponding to sprays produced by fuel A at 250bar and 350bar (1.8ms after SoI).

Figure 5.7: False coloured mean image produced at 1.8ms after SoI in case of 250bar (left hand side) and 350bar (right hand side), showing the relative SMD distribution.

An optical observation of the figures revealed that the spray at 250bar produced larger SMD values than the spray at 350bar. The mean relative SMD values calculated from the distributions at 250bar and 350bar were 0.56 and 0.47 respectively. The increased rail pressure and low needle lift generated favourable conditions (stronger cavitation phenomena, turbulence) for better atomisation, resulting in the formation of smaller droplets.

Figure 5.8 shows the false coloured standard deviation images obtained from fuel A at 250bar during the opening phase (1.8ms after SoI) of the needle. It was shown that in the case of 250bar, the larger STD values were observed at the top spray segment and particularly at the top left-hand side of the spray. Such an observation suggested greater SMD variation at the upper segment of the spray where secondary atomisation became more significant. It was also shown that the standard deviation of the spray boundaries was larger relative to the main spray body. This was more evident in the case of 350bar, where the majority of the spray exhibited low STD values, while the periphery larger; this is believed to occur as a result of dominant secondary atomisation, whose mechanism is more complicated relative to primary atomisation. A comparison between the two sprays, shown in Figure 5.8, suggested greater instability at 250bar, since the SMD variation was overall larger compared to 350bar. The

instability suggested is believed to be a consequence of the spray flapping effects which were minimised with an increase in rail pressure and subsequently an increase in flow momentum.

Figure 5.8: False coloured STD image produced at 1.8ms after SoI in case of 250bar (left hand side) and 350bar (right hand side), showing the variation of the relative SMD distribution from the calculated mean image.

Figure 5.9 and Figure 5.10 show the relative SMD distribution and the corresponding false coloured image produced by fuel 1 at 250bar and 350bar during the opening phase of the needle (1.8ms after SoI).
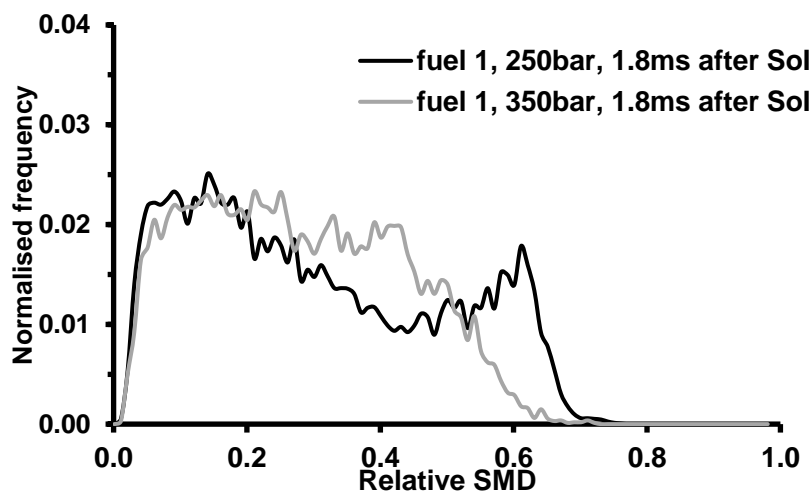
Figure 5.9: Relative SMD distributions corresponding to sprays produced by fuel 1 at 250bar and 350 bar (1.8ms after SoI).

External spray drop-sizing analysis using Laser Sheet Drop-sizing technique

A visual comparison of the distributions obtained revealed that 250bar distribution is shifted towards larger SMD values relative to 350bar. Such an observation implied that an increase in rail pressure led to the formation of smaller droplets. This effect has been reported by many researchers[3,14,70] ,who have suggested that an increase in rail pressure enhances cavitation and turbulence, which in turn promote the formation of smaller droplets. The mean SMD values obtained from the distributions (Figure 5.9) were 0.31 and 0.28 in case of 250bar and 350bar respectively. Therefore, an increase of 100bar from 250bar to 350bar led to a size reduction of approximately 10%.

Figure 5.10 suggested that the relative SMD of the spray droplets gradually decreased with increasing axial distance. This was believed to be a consequence of the pronounced effects of secondary atomisation with increasing axial distance. This became more evident in the case of 350bar, due to enhanced atomisation. Additionally, it was observed that the majority of the large droplets were distributed in the vicinity of the central spray axis, while the smaller droplets were found in the spray periphery. However, in both sprays, most of the droplets with larger SMD appeared to locate on the right-hand side of the spray, suggesting a slight spray asymmetry. The asymmetry observed was investigated in more detail and is discussed in the following subsection.
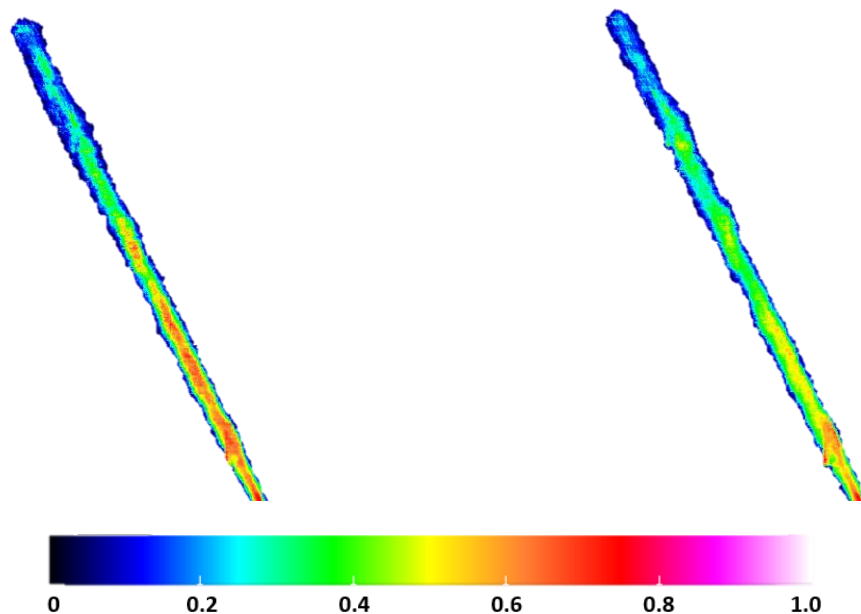
Figure 5.10: Normalised false coloured mean image produced at 1.8ms after SoI in case of fuel 1 at 250bar (left hand) and 350bar (right hand) showing the relative SMD along the spray.

External spray drop-sizing analysis using Laser Sheet Drop-sizing technique

Figure 5.11 shows the STD false coloured images obtained from fuel 1 sprays at 250 and 350bar. It was observed that the largest STD values were obtained at the upper half of the spray. This was believed to be a consequence of dominant secondary atomisation.

Figure 5.11: False coloured STD image produced at 1.8ms after SoI in case of fuel 1 at 250bar (left hand) and 350bar (right hand) showing the variation of the relative SMD along the spray.

In the regions where, primary atomisation drove the spray break-up (the region in the vicinity of the nozzle exit, central spray axis in the first half of the spray) it was shown that STD of the spray droplets was small. A comparison of the STD image obtained at 250bar and 350bar revealed that an increase in rail pressure led to the formation of more stable sprays, possibly due to increased flow momentum and decreased flow instabilities.

3.7ms- 3.8ms after SoI

When the needle reached its maximum lift, cavitation effects became less significant, since the fuel freely flowed inside the nozzle passages. The analysis presented in the next chapter with regards to the LVF distributions of the sprays, revealed that the LVF obtained higher values compared to lower needle lifts, suggesting that the reduction of the amount of vapour fuel (cavitation structures). As a result, the relative SMD distributions at maximum needle lift were expected to be shifted to the right, reflecting the obtained larger droplets. An increase in rail pressure was expected to produce smaller droplets.

Figure 5.13 and Figure 5.12 show the relative SMD distributions and the corresponding false coloured images produced by fuel A at 250bar and 350bar.
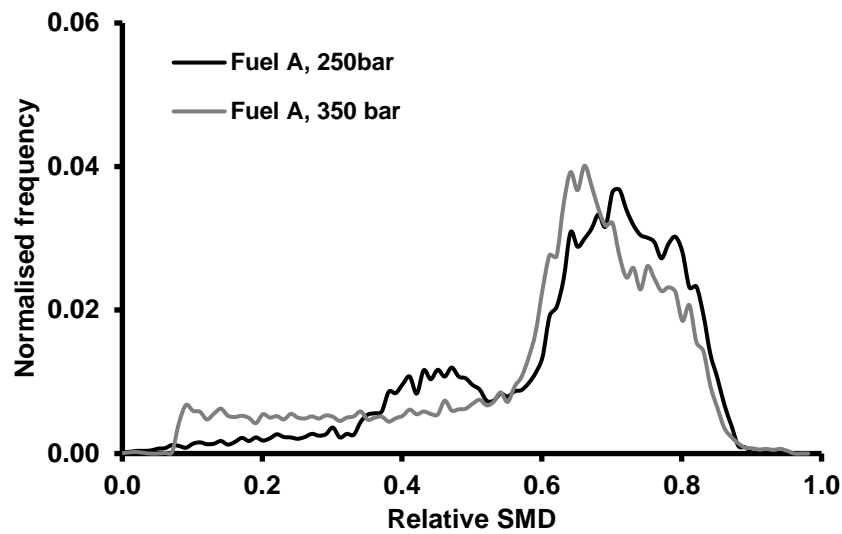
Figure 5.12: Relative SMD distributions corresponding to sprays produced by fuel A at 250bar and 350bar (3.7ms after SoI)

Figure 5.13: False coloured mean image produced at 3.7ms after SoI in case of 250bar (left hand side) and 350bar (right hand side) showing the relative SMD distribution.

An optical observation of the figures revealed that the relative SMD values obtained were larger than the ones obtained at 1.8ms after SoI. The mean SMD values corresponding to the distributions shown

in Figure 5.12 were 0.64 and 0.6 in case of 250bar and 350bar respectively, suggesting that the rail pressure effect was not as significant as at the opening phase of the needle.

Figure 5.14: False coloured STD image produced at 3.7ms after SoI in case of 250bar (left hand side) and 350bar (right hand side) showing the variation of the relative SMD of the spray droplets.

The false coloured STD spray images shown in Figure 5.14 demonstrate that the droplet size variation at spray periphery was greater relative to the main body of the spray, possibly due to pronounced secondary atomisation effects. The upper right segment of the spray produced at 250bar included the largest STD, while in case of 350bar such an observation was not true. In both cases, the spray segments in the vicinity of the nozzle exit exhibited relatively low STD, suggesting similar flow patterns throughout a set of 100 injections. Overall, it can be argued that an increase in rail pressure led to more stable sprays which did not exhibit significant SMD variation. However, when the needle reached its maximum lift, it was shown that the variation of the SMD in both sprays increased. This could be attributed to flow dynamics (turbulence, aerodynamic instabilities etc.) developing at the maximum lift.

Figure 5.15 and Figure 5.16 show the relative SMD distribution and the corresponding false coloured SMD images produced by fuel 1 at 250bar and 350bar during the maximum needle lift (3.8ms after SoI). A comparison of the distributions suggested that an increase in rail pressure led to the formation of smaller droplets, due to enhance cavitation and turbulence phenomena. The corresponding mean

SMD values were 0.53 and 0.43 in the case of 250bar and 350bar. An increase of 100bar, from 250bar to 350bar, led to a decrease of approximately 20% in mean size.
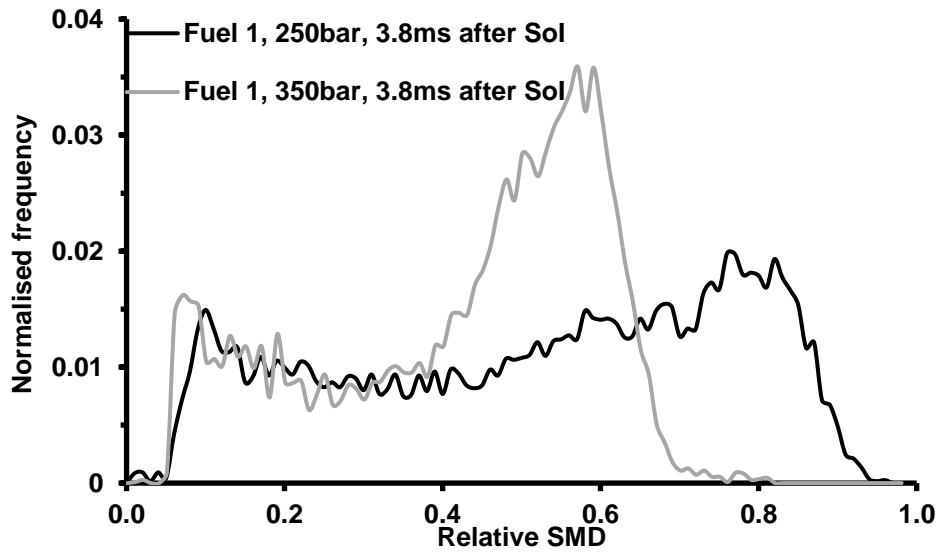
Figure 5.15: Relative SMD distributions corresponding to sprays produced by fuel 1 at 250bar and 350bar (3.8ms after SoI).

The false coloured SMD images shown in Figure 5.16 demonstrated a gradual decrease in SMD with increasing axial distance, due to pronounced secondary atomisation.
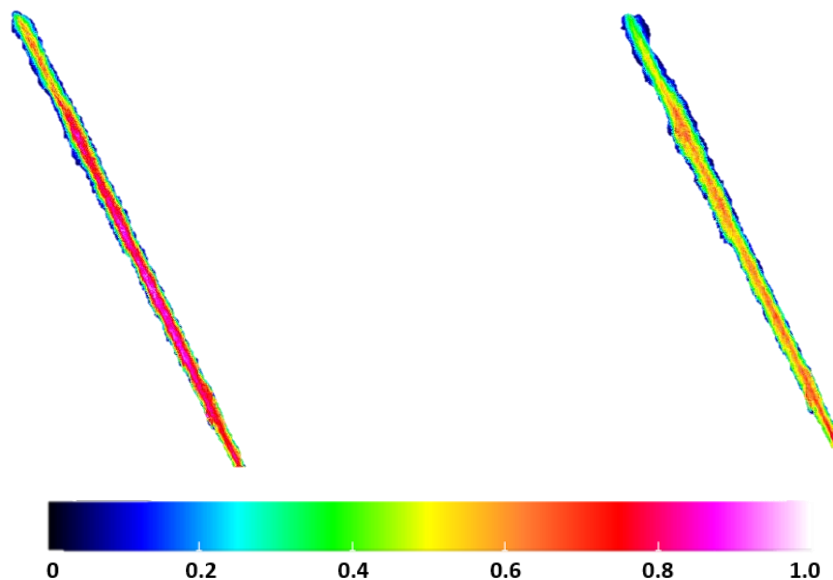
Figure 5.16: Normalised false coloured mean image produced at 3.8ms after SoI in case of fuel 1 at 250bar (left hand) and 350bar (right hand) showing the relative SMD along the spray.

An increase in radial distance from the central axis of the spray also showed a decrease in the SMD. The false coloured images also suggested a spray asymmetry, since the larger droplets appeared to locate on the right-hand side of the spray. The asymmetry observed is discussed in more detail in the following subsections.
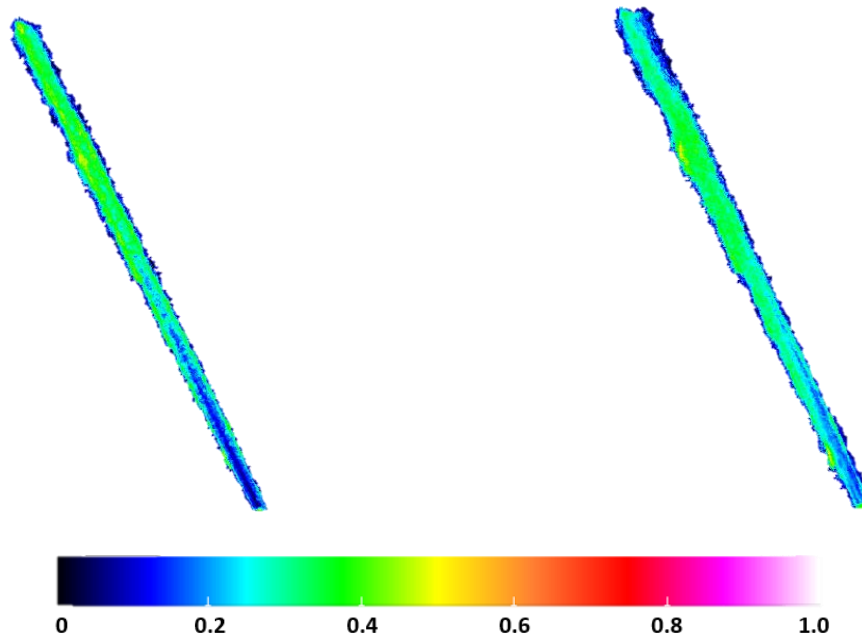
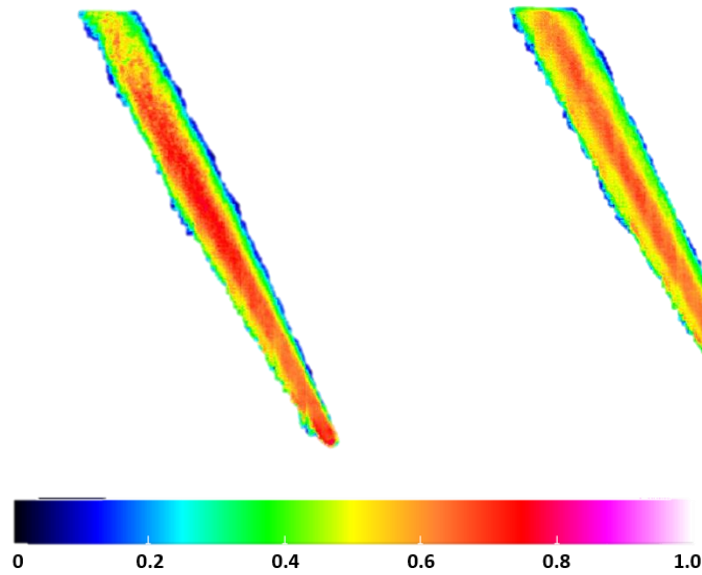Figure 5.17: False coloured STD image produced at 3.8ms after SoI in case of fuel 1 at 250bar (left hand) and 350bar (right hand) showing the variation of the relative SMD along the spray.

A comparison of the results obtained at 1.8ms and 3.8ms after SoI indicated an increase in the SMD of the droplets formed, regardless of the rail pressure. Such an observation implied that the flow dynamics developed in the case of low and maximum needle lift were responsible for the observed increase in the SMD. It was believed that cavitation was more intensive during the early stages of needle lift; hence, it was expected to observe stronger break-up phenomena (mostly primary atomisation) during this period. Additionally, it was observed that the decrease in SMD with increasing axial distance became less significant when the needle reached its maximum lift. This could possibly be a consequence of the dominant secondary atomisation effects as soon as the spray exited the nozzle passage.

The STD images produced by fuel 1 at 250bar and 350bar are shown in Figure 5.17. It was demonstrated that the largest SMD variation occurred at the upper half of the spray, where secondary atomisation was the dominant mechanism. In the vicinity of the nozzle exit, the STD obtained ranged between 0.15 and

0.4 for both 250bar and 350bar. It was also observed that the SMD variation at 3.8ms after SoI was greater than 1.8ms after SoI, suggesting pronounced instabilities when the needle reached its maximum lift. It was also shown that the largest STD values were uniformly distributed across the upper part of spray. This increased variation was believed to be a consequence of the spray flapping during the injection process.

5.6ms after SoI

During the closing phase of the needle, cavitation phenomena were expected to play an important role in atomisation, due to the flow choking occurring in the vicinity of the mini-sac entrance as a result of the needle return. The LVF results discussed in detail in the following chapter, showed a small decrease in LVF values, suggesting an increase in the proportion of vapour fuel in the flow. As a result, the relative SMD values obtained were expected to be smaller relative to the maximum needle lift. An increase in rail pressure was expected to enhance cavitation and atomisation.

Figure 5.18 and Figure 5.19 show the relative SMD distribution and the corresponding false coloured image of the spray produced during the closing phase of the needle at 250bar and 350bar. The mean SMD values obtained from the distributions are 0.56 and 0.54 in the cases of 250 bar and 350bar respectively. It can be seen that an increase in rail pressure led to the formation of slightly smaller droplets. Comparing the mean SMD values to the results obtained at 1.8ms and 3.7ms, it can be argued that the relative SMD obtained during the opening and closing phase of the needle was smaller relative to the maximum needle lift. This could be attributed to the pronounced effects of cavitation during the initial and final stages of the needle lift. Considering the displacement of needle at 1.8ms and 5.6ms after the SoI to be approximately the same, it was expected to obtain similar distributions in both cases.
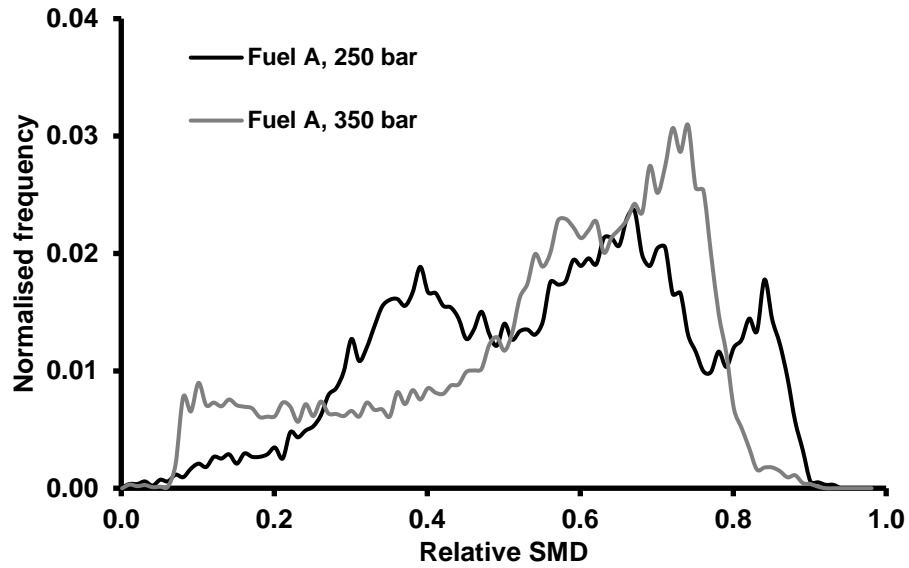
Figure 5.18: Relative SMD distributions corresponding to sprays produced by fuel A at 250bar and 350bar (5.6ms after SoI).
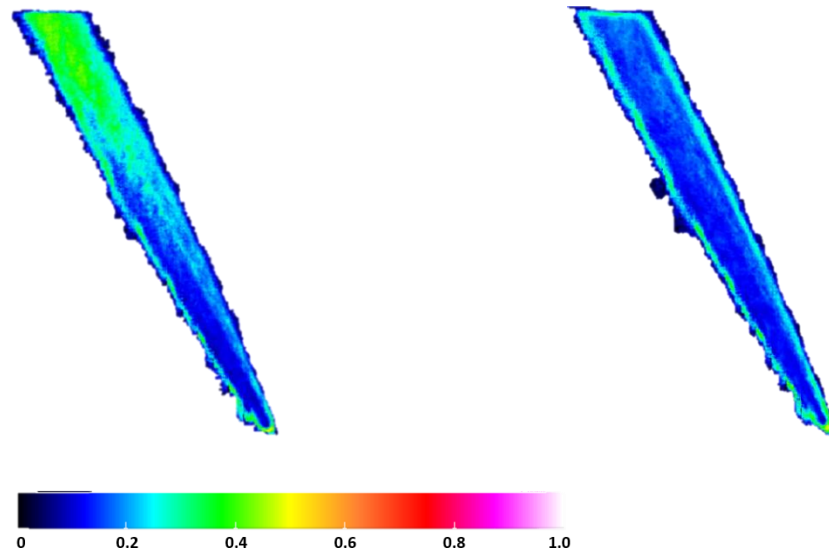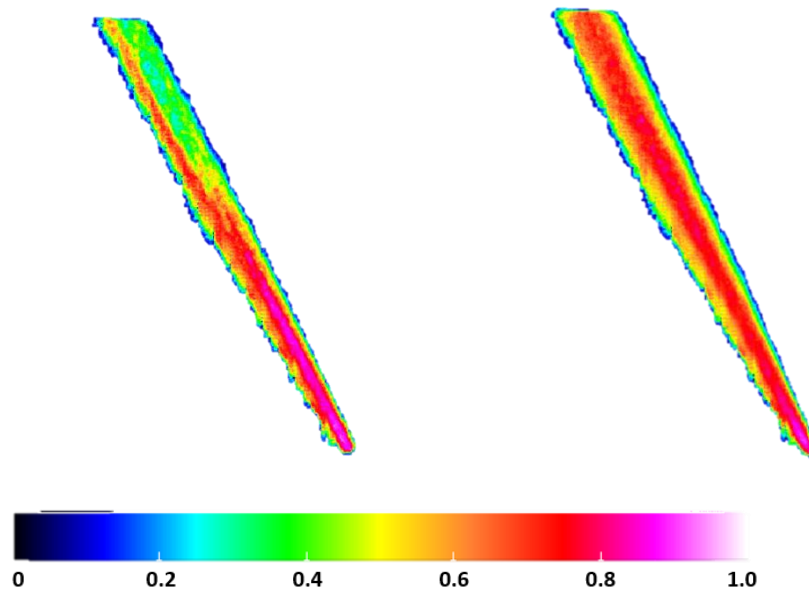

Figure 5.19: False coloured mean image produced at 5.6ms after SoI in case of 250bar (left hand side) and 350bar (right hand side) showing the relative SMD distribution

A comparison of the results obtained at 1.8ms after SoI and 5.6ms after SoI at 250bar revealed that the distributions were similar. The SMD distributions produced by the sprays at 350bar at 1.8ms after SoI and 5.6ms after SoI showed that the mean SMD value obtained during the closing phase of the needle

was slightly larger than the opening phase. These observations suggested that the flow patterns developed at 1.8ms and 5.6ms after SoI were fairly similar, explaining the similarities in the distributions obtained.

Figure 5.20 reveals that an increase in rail pressure led to more stable sprays, since the STD values obtained from fuel A at 350bar were lower relative to 250bar, possibly due to increased flow momentum. In both cases, the largest STD values were obtained at the upper spray segments. It has been suggested earlier that this could be a consequence of pronounced secondary atomisation. Additionally, it was observed that the area surrounding the spray axis in the first half of the spray exhibited approximately 20% lower STD compared to the top spray segment; the flow patterns developed in this region appeared to be similar throughout the injections events, resulting in fairly low SMD variation.
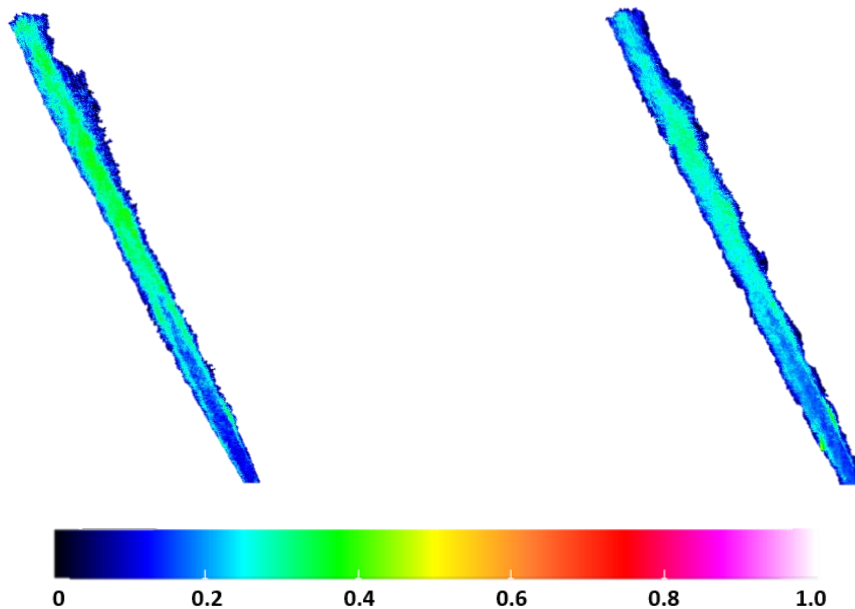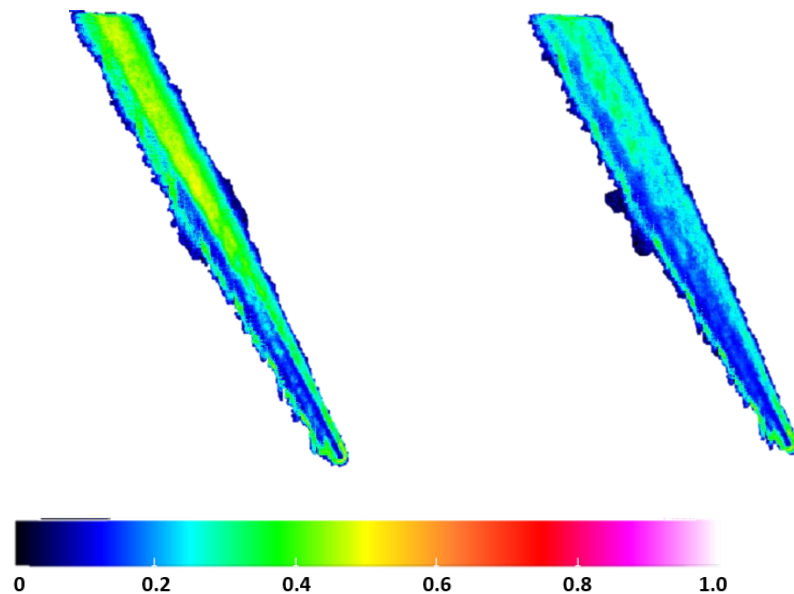

Figure 5.20: False coloured STD image produced at 5.6ms after SoI in case of 250bar (left side) and 350bar (right side) showing the variation of the relative SMD distribution from the calculated mean.

The comparison of the results obtained at 1.8ms, 3.7ms and 5.6ms suggested increased spray instability towards the late stages of the needle return; the phenomena (needle cavitation, string and geometric cavitation) occurring during this phase created a complex environment, which induced greater instability to the spray (larger STD). Overall, it can be argued that an increase in rail pressure led to the

formation of more stable sprays. It has been also observed that the spray segment containing the largest STD values located on the opposite side as where the largest droplets were found. Lastly, the largest STD values were obtained in the case of 3.7ms after SoI, suggesting the development of complex and changing flow patterns throughout a set of 100 injections.

Figure 5.21 and Figure 5.22 show the relative SMD distribution and the corresponding false coloured image produced by fuel 1 at 250bar and 350bar during closing phase of the needle (5.6ms after SoI). A comparison of the distributions shown in Figure 5.21 suggested that an increase in rail pressure shifted the SMD distribution towards smaller SMD values. Such a shift was expected, since an increase in rail pressure has been shown to lead to the formation of smaller droplets. The corresponding mean SMD values were 0.42 and 0.33 respectively. The distributions suggested an approximately 20% decrease in the SMD for a 100bar pressure increase, from 250bar to 350bar. The wider distribution at 250bar suggested the synergy of primary and secondary atomisation, while the much narrower distribution at 350bar spray implied that secondary atomisation was the dominant break-up mechanism.
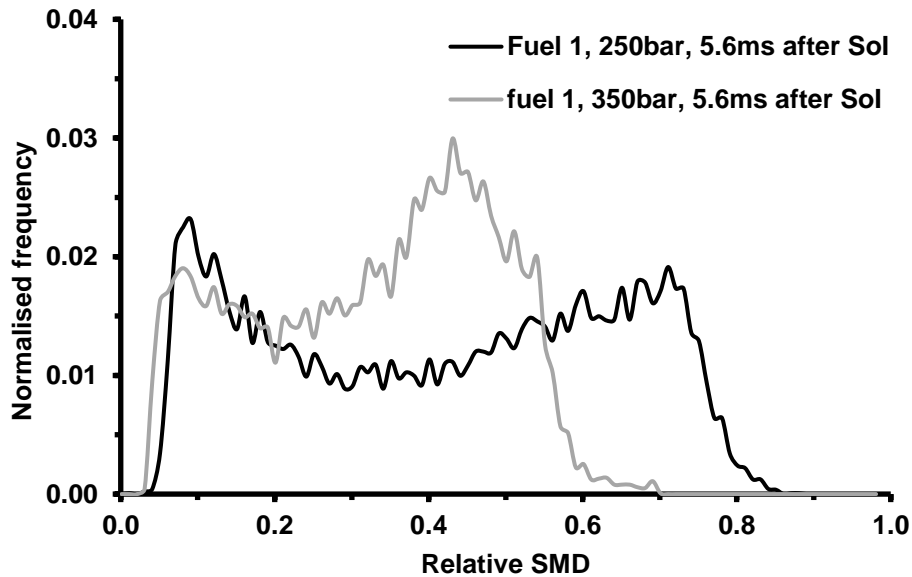
Figure 5.21: Relative SMD distributions corresponding to sprays produced by fuel 1 at 250bar and 350bar (5.6ms after SoI).
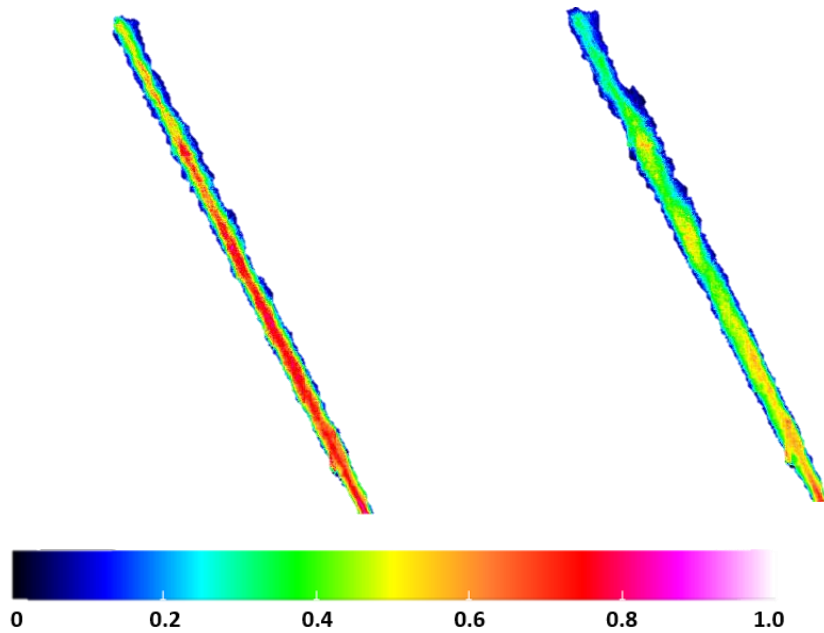
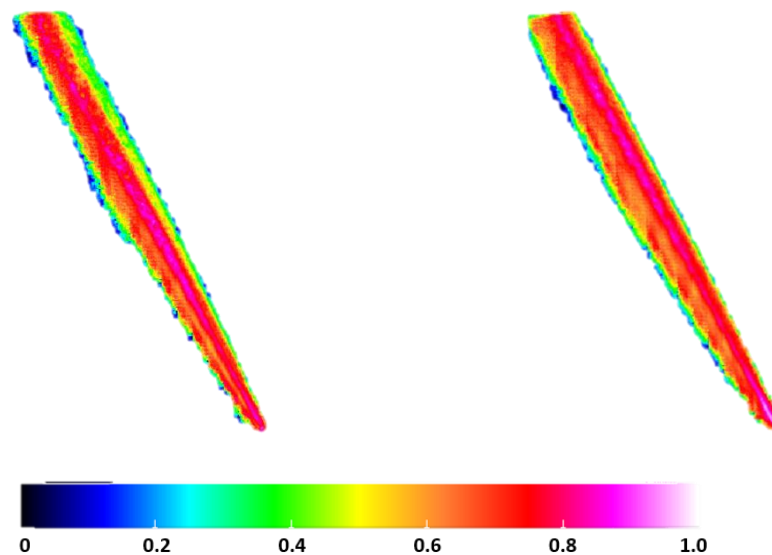Figure 5.22: Normalised false coloured mean image produced at 5.6ms after SoI in case of fuel 1 at 250bar (left hand) and 350bar (right hand) showing the relative SMD distribution along the spray.

The false coloured images shown in Figure 5.22 suggested a gradual decrease of the spray droplet SMD with increasing axial distance, due to enhanced secondary atomisation downstream of the nozzle exit. It was also observed that the SMD of the droplets gradually decreased with increasing radial distance from the central axis of the spray. In the case of 250bar spray, it was shown that the majority of larger droplets located on the left-hand side of the spray, suggesting the existence of a spray asymmetry. On the other hand, 350bar spray appeared to be more symmetric relative to 250bar. The asymmetry observed is discussed separately in the following subsection of this chapter.

Figure 5.23 shows the STD images produced by fuel 1 at 5.6ms after SoI, at 250bar and 350bar respectively. It was shown that largest STD values were mostly obtained at the upper half of the spray, where secondary atomisation was the dominant break-up mechanism. It was also observed that on average the STD of the droplets formed at 350bar were greater relative to 250bar, suggesting larger spray instabilities. This was a finding that was not seen in the case of Jeshani's fuel jets. Additionally, it was shown that the larger STD values were uniformly distributed across the spray. Such an observation confirmed the spray flapping observed after the optical examination of the raw data. Lastly, the images shown in Figure 5.11, Figure 5.17 and Figure 5.23 suggested that the greatest SMD variation

was found during the maximum and closing phase of the needle. However, the differences between all images were not significant, suggesting that the spray flapping was present throughout the injection events.
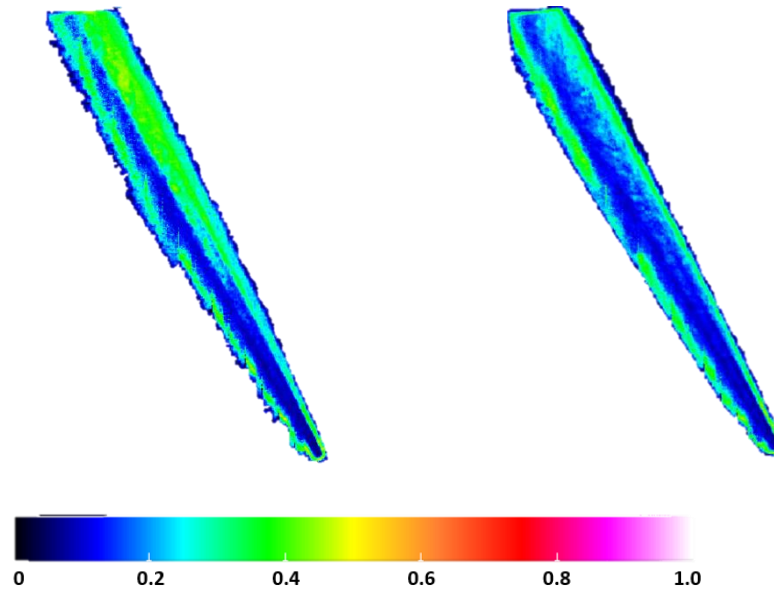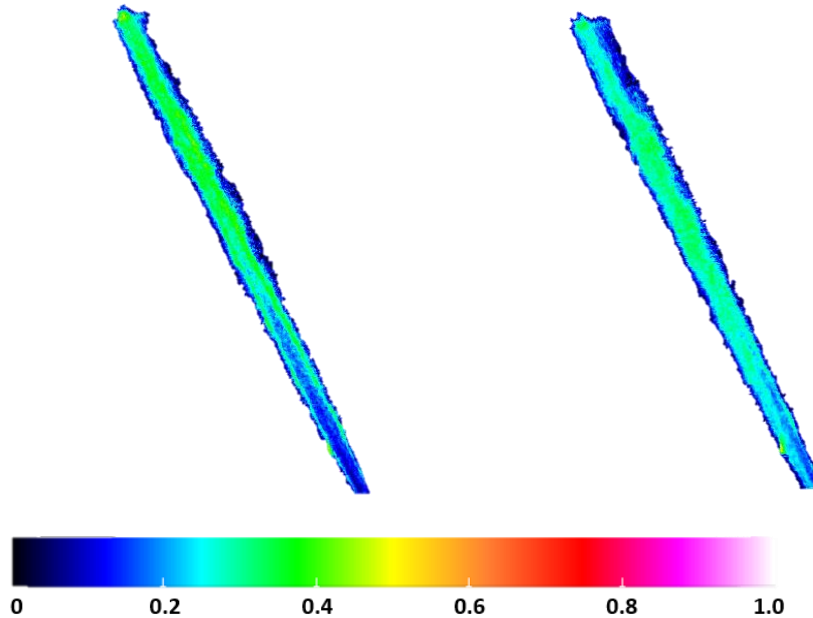

Figure 5.23: False coloured STD image produced at 5.6ms after SoI in case of fuel 1 at 250bar (left hand) and 350bar (right hand) showing the variation of the relative SMD along the spray.

A comparison of the results obtained at 1.8ms and 3.8ms after SoI revealed that on average the droplets formed at 5.6ms were larger than 1.8ms and smaller than 3.8ms after SoI. Such an observation suggested that the needle lift played a decisive role in the flow dynamics developed inside the nozzle passage and consequently affected the atomisation process. It was believed that during the opening and closing phases of the needle, cavitation was more intensive, leading to stronger break-up phenomena.

5.2.1.1 Diesel spray asymmetry

An optical observation of the false coloured images presented in the previous subsection revealed that in some cases the fuel A sprays exhibited significant asymmetry, especially during the intermediate and late stages of the needle lift. In order to investigate this observation in more detail, relative SMD distributions of different segments of the spray are produced at 1.8ms, 3.7ms and 5.6ms after SoI. These segments are the right and left-hand side of the upper, middle and lower segments.

1.8ms after SoI (opening phase of the needle)

Figure 5.24 and Figure 5.25 show the projections of the normalised histograms (100bins) obtained at the upper (solid line), middle (dotted line), lower (dashed line) spray segments and provide information about the relative SMD distribution at the left-hand side (black colour) and right-hand side (grey colour) of each spray segment at 250bar and 350bar respectively. In Figure 5.24 and Figure 5.25, it was observed that the left-hand side distributions were shifted towards larger SMD values while the right-hand side to smaller. This observation indicated a spray asymmetry to left hand side of the spray, regardless of rail pressure. It was believed that the observed spray asymmetry was a consequence of the geometric cavitation appeared in the same side of the nozzle passage. It can be also argued that the SMD values of the sprays at both rail pressures remained practically the same with increasing axial distance from the nozzle exit, suggesting secondary atomisation to be the dominant break-up mechanism. The mean SMD values from the distributions shown in both figures are summarised in Table 5.1. The mean SMD values obtained suggested that an increase in rail pressure led to smaller spray droplets, especially in the vicinity of the nozzle exit.
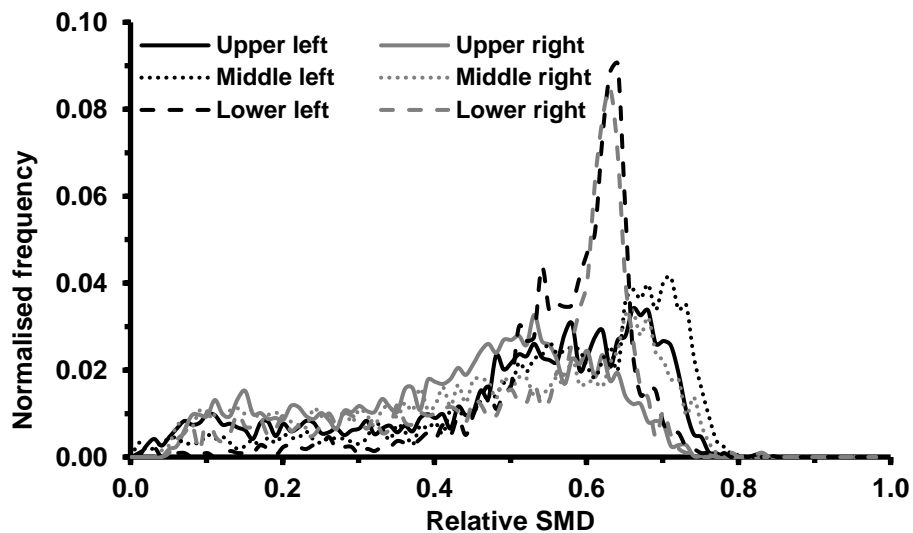
Figure 5.24: Relative SMD distributions of the six segments of fuel A spray captured at 1.8ms after SoI, 250bar.
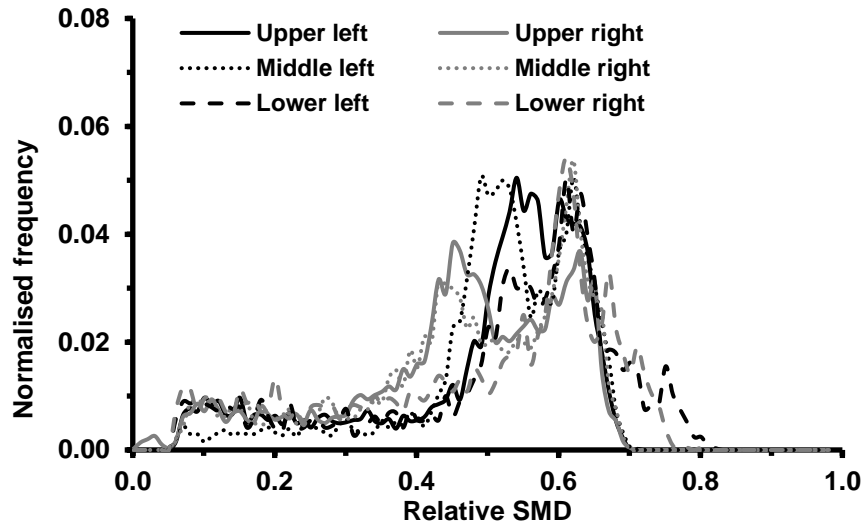
Figure 5.25: Relative SMD distributions of the six segments of fuel A spray captured at 1.8ms after SoI, 350bar.

Table 5.1: Mean relative SMD values obtained from fuel A sprays at 250bar, 350bar (1.8ms after SoI).

	Mean SMD values (1.8ms after SoI)					
	Upper segment		Middle segment		Lower segment	
	left	right	left	right	left	right
250bar	0.50	0.44	0.55	0.47	0.57	0.51
350bar	0.50	0.46	0.52	0.47	0.52	0.49

Figure 5.26 and Figure 5.27 show the projections of the normalised histograms (100bins) obtained at the upper (solid line), middle (dotted line), lower (dashed line) spray segments and provide information about the relative SMD distribution at the left-hand side (black colour) and right-hand side (grey colour) of each spray segment at 250bar and 350bar respectively. An observation of the distributions shown in Figure 5.26 and Figure 5.27 suggested that the SMD of the droplets increased with decreasing axial distance. This could be attributed to the pronounced effect of primary atomisation in the vicinity of the nozzle exit and the dominance of secondary atomisation with increasing axial distance. However, it could be argued that in the case of 350bar, this decrease in SMD became less significant, due to stronger secondary atomisation as a consequence of the increased rail pressure. Table 5.2 summarises the mean

SMD values of the distributions obtained. Based on these results, it could be argued that overall the right-hand side of the spray contained a larger proportion of larger droplets, resulting in a spray asymmetry.

Figure 5.26: Relative SMD distributions of the six fuel 1 spray segments captured at 1.8ms after SoI, 250bar.
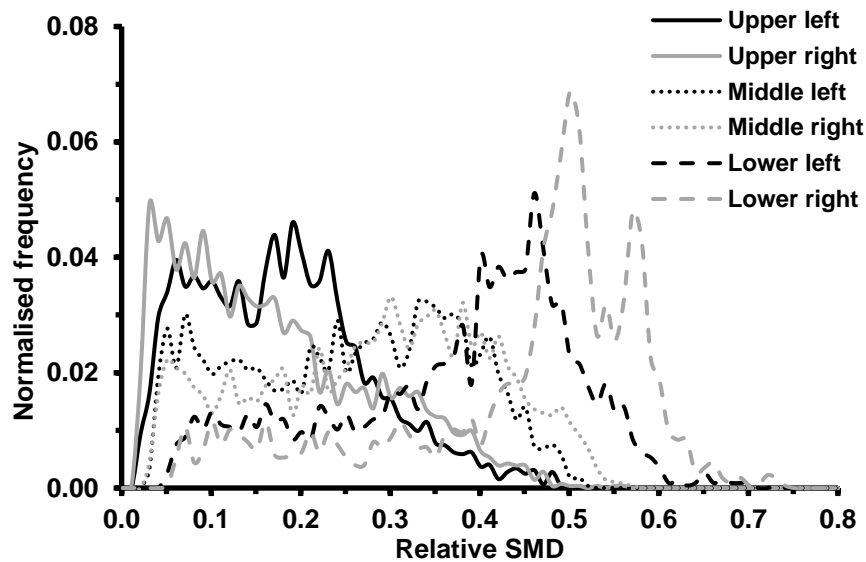
Figure 5.27: Relative SMD distributions of the six fuel 1 spray segments captured at 1.8ms after SoI, 350bar.

External spray drop-sizing analysis using Laser Sheet Drop-sizing technique

The mean SMD values obtained from the upper segments at both 250bar and 350bar implied that the larger proportion of larger droplets located on the left-hand side of the spray. However, the difference between the mean SMD of the left and right-hand side distributions at the lower segment was not significant, suggesting that the top of the spray was fairly symmetric. Overall, it could be argued that the spray asymmetry was a consequence of the flow asymmetry introduced into the nozzle holes as a result of the geometric cavitation developing at the entrance of the nozzle holes. The geometry of the acrylic mini-sac nozzle tip promoted the development of geometric sheet cavitation to occur at the upper side of the hole entrance, due to the local flow acceleration as soon as the fuel flow entered the nozzle passage. It has been observed, that on average, the larger droplets were obtained on the same side of the nozzle hole as where the geometric sheet cavitation was located.

Table 5.2: Mean relative SMD values obtained from fuel 1 diesel sprays at 250bar, 350bar (1.8ms after SoI).

	Mean SMD values (1.8ms after SoI)					
	Upper segment		Middle segment		Lower segment	
	left	right	left	right	left	right
250bar	0.182	0.165	0.278	0.370	0.425	0.478
350bar	0.184	0.176	0.259	0.287	0.376	0.448

<u>3.7ms-3.8ms after SoI</u>

Figure 5.28 and Figure 5.29 show the SMD distributions of upper, middle and lower spray segments produced by fuel A at 250bar and 350bar, when the needle reached its maximum lift (3.7ms after SoI). The various line styles and colours in both figures retained their meaning as defined above. In particular, the sprays produced at 250bar showed a strong asymmetry to the left-hand side of the spray, since the left-hand side distributions in all segments exhibited a larger mean SMD value relative to the right-hand side. The larger mean SMD values were obtained in the vicinity of the nozzle exit, suggesting that primary break-up was the dominant atomisation mechanism. With increasing axial distance from the

nozzle exit, the mean SMD values dropped indicating the introduction of secondary atomisation. On the contrary, the spray produced at 350bar showed a strong asymmetry on the opposite side (right hand side of the spray). All distributions corresponding to the right-hand side segments exhibited larger mean SMD values relative to the left-hand side.
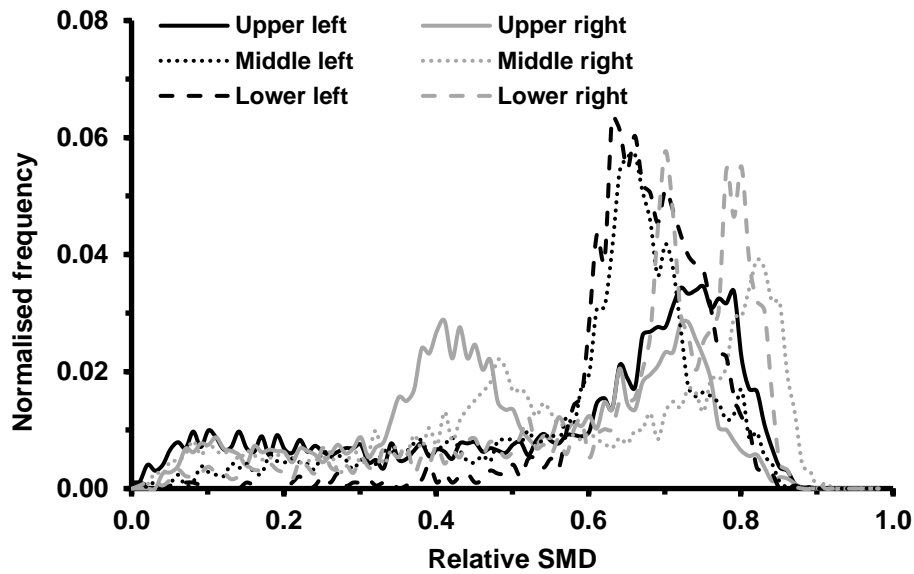
Figure 5.28: Relative SMD distributions of the six fuel A spray segments captured at 3.7ms after SoI, 250bar.
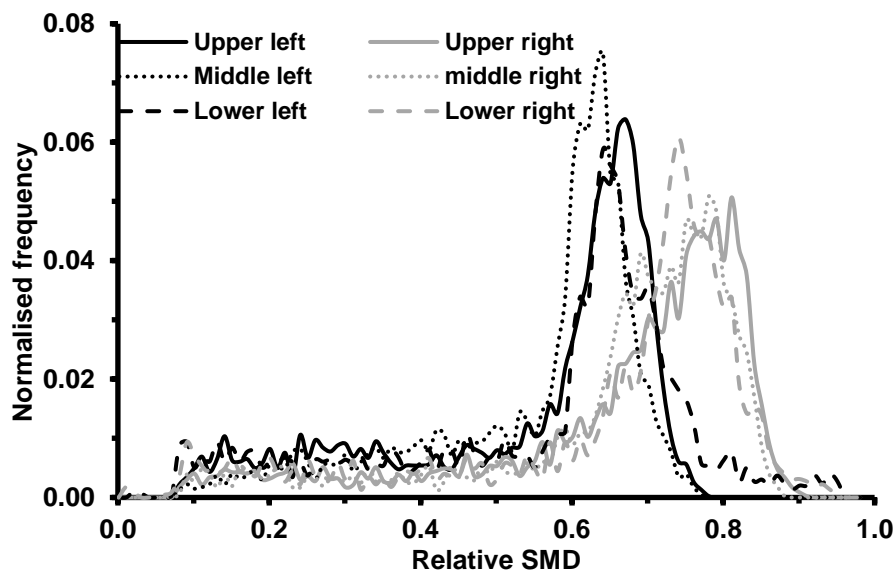
Figure 5.29: Relative SMD distributions of the six fuel A spray segments captured at 3.7ms after SoI, 350bar.

External spray drop-sizing analysis using Laser Sheet Drop-sizing technique

The lower segment distributions exhibited the larger mean SMD values, which could be attributed to less pronounced effects of secondary atomisation. Additionally, the mean SMD value remained approximately the same with increasing axial distance from the nozzle exit, implying the dominance of secondary atomisation. Table 5.3 summarises the mean relative SMD values of all distributions shown in Figure 5.28, Figure 5.29.

Table 5.3: Mean relative SMD values obtained from fuel A sprays at 250bar, 350bar (3.7ms after SoI).

	Mean SMD values (3.7ms after SoI)					
	Upper segment		Middle segment		Lower segment	
	left	right	left	right	left	right
250bar	0.60	0.52	0.66	0.62	0.67	0.65
350bar	0.56	0.67	0.56	0.67	0.57	0.67

Figure 5.30 and Figure 5.31 show the normalised SMD distributions of upper, middle and lower spray segments produced by fuel 1 at 250bar and 350bar when the needle reached its maximum lift (3.8ms after SoI). The various line styles and colours in both figures retained their meaning as defined above. In more detail, the mean relative SMD values (Table 5.4) obtained from the distributions produced by the sprays at both pressures indicated that the larger proportion of larger droplets appeared on the right-hand side of the spray, suggesting a spray asymmetry. It has been suggested that the observed spray asymmetry was a result of the flow asymmetry inside the nozzle passage, due to geometric cavitation structures at the hole entrance. The results also suggested that the SMD of the spray droplets decreased with increasing axial distance from the nozzle exit, as a consequence of secondary atomisation. The larger droplets found in the lower spray segments could be attributed to the dominant primary breakup phenomena. A visual comparison of Figure 5.30 and Figure 5.31 revealed that in the case of 250 bar the obtained distributions were wider relative to 350bar, suggesting the presence of larger droplets. The smaller mean SMD of the droplets obtained from the sprays at 350bar were a result of the increased rail pressure, which enhanced atomisation process.
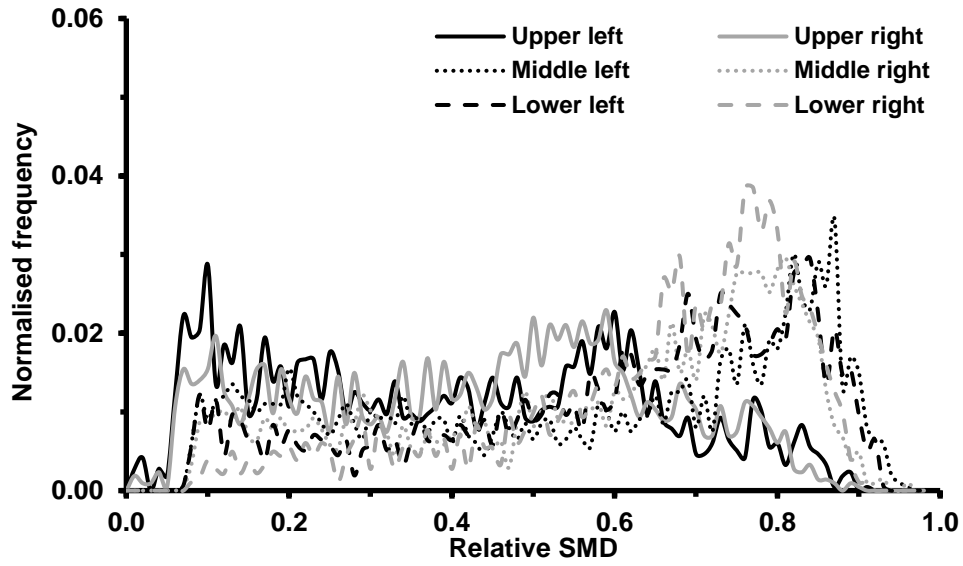
Figure 5.30: Relative SMD distributions of the six fuel 1 spray segments captured at 3.8ms after SoI, 250bar.
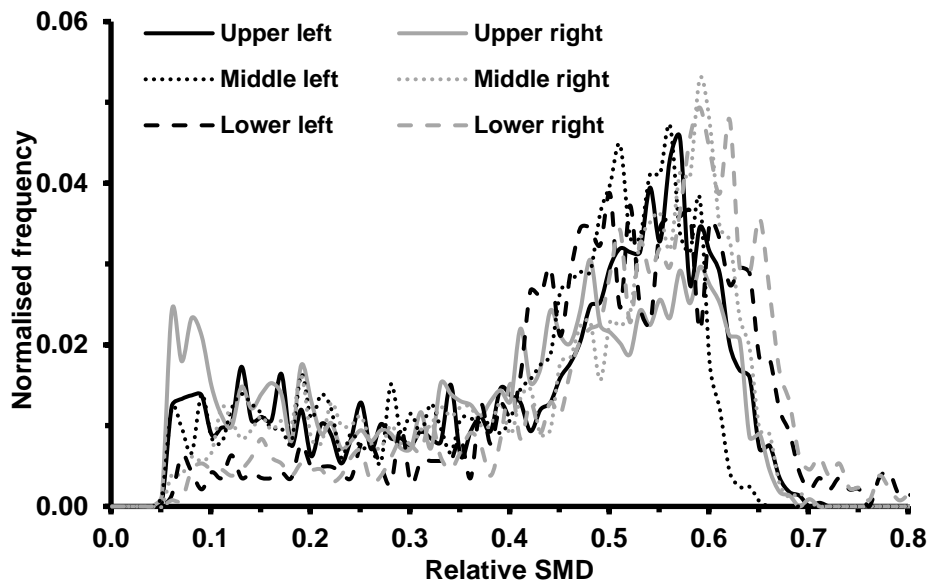
Figure 5.31: Relative SMD distributions of the six segments of fuel 1 spray captured at 3.8ms after SoI, 350bar.

Table 5.4: Mean relative SMD values obtained from fuel 1 diesel sprays at 250bar, 350bar (3.8ms after SoI).

	Mean SMD values (3.8ms after SoI)					
	Upper segment		Middle segment		Lower segment	
	left	right	left	right	left	right
250bar	0.405	0.434	0.567	0.582	0.602	0.642
350bar	0.431	0.396	0.419	0.453	0.497	0.516

The comparison between the results produced at 1.8ms and 3.8ms after SoI suggested that in the latter case the mean SMD of the spray droplets was larger. It was believed that this was a consequence of less intensive cavitation relative to the opening needle phase. Additionally, the distributions obtained at 1.8ms after SoI exhibited a significant shift towards smaller SMD values with increasing axial distance, due to the synergy between primary and secondary atomisation. On the other hand, the distributions produced at 3.8ms after SoI at both rail pressures indicated that this effect was less significant. It was suggested that when the needle reached its maximum lift, the dominant break-up mechanism was secondary atomisation. In the present case, the decrease in the SMD of the spray droplets as a function of axial distance was less evident compared the case where both primary and secondary atomisation occurred.

5.6ms after SoI

Figure 5.32 and Figure 5.33 show the projections of the normalised histograms obtained at the upper, middle, lower spray segments and provide information about the SMD distribution at the left-hand side and right-hand side of each fuel A spray segment. The various line styles and colours in both figures retained their meaning as defined previously. Figure 5.32 shows that the left-hand distribution of the upper and middle segments exhibited a larger mean SMD value relative to the right-hand side. Oddly enough, this trend was not followed in the case of the lower segment, in which the right-hand side had a larger mean SMD value relative to the left-hand distribution.
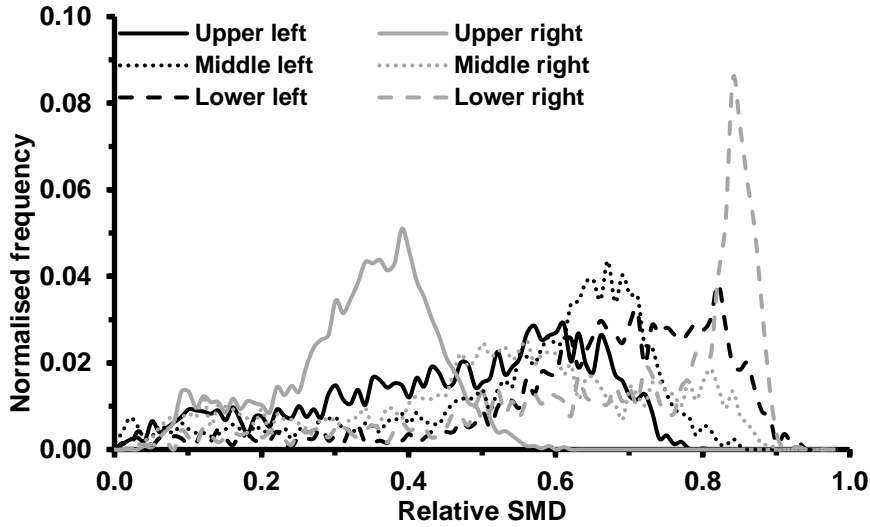
Figure 5.32: Relative SMD distributions of the six segments of fuel A spray captured at 5.6ms after SoI, 250bar.
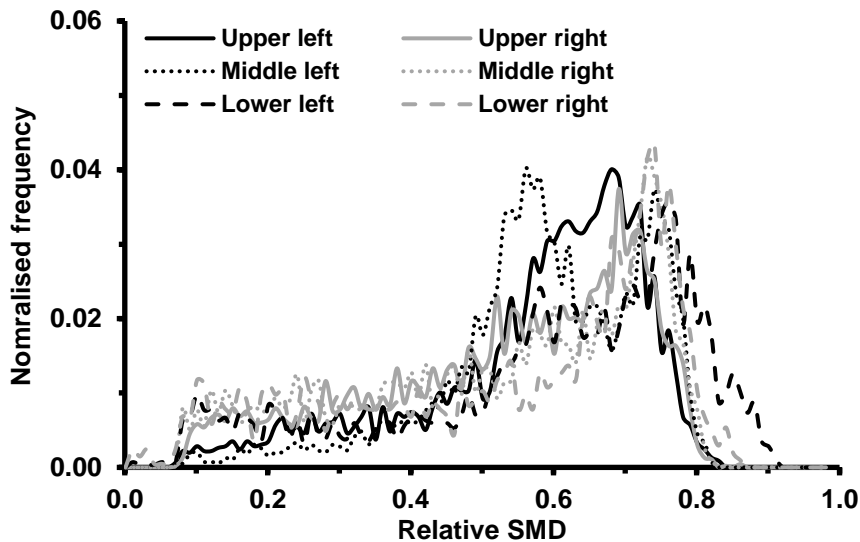
Figure 5.33: Relative SMD distributions of the six segments of fuel A spray captured at 5.6ms after SoI, 350bar.

However, it could be argued that overall the left-hand side of the spray obtained a larger mean SMD value, implying that there was a spray asymmetry to the left. The mean SMD values of all segments showed a gradual decrease with increasing axial distance from the nozzle exit. The SMD distributions obtained at 350bar showed that all left-hand side distributions exhibited a larger mean SMD value relative to the right-hand side, suggesting a spray asymmetry to the left half of the spray. The mean

SMD values appear to remain practically unchanged along the spray. This trend was also observed at 3.7ms after the SoI. Such a trend suggested that the dominant break-up mechanism was secondary atomisation, which had the same effect along the spray. Despite the unchanged SMD values along the spray geometry, in the case of 350bar, the overall SMD distribution was shifted towards smaller SMD values relative to 250bar sprays, suggesting that the droplet size decreased with increasing rail pressure. This effect was highlighted in the lower segment distributions where the mean SMD at 350bar was smaller than 250bar by approximately 12%. The mean SMD values obtained from the distributions shown in both figures are summarised in Table 5.5. A visual comparison of Table 5.1 and Table 5.5 showed that the mean SMD values obtained at 1.7ms and 5.6ms after SoI in the case of 350bar were fairly similar, suggesting similarity in the flow patterns developed. In the case of 250bar at 5.6ms after SoI, the results indicated slightly larger mean SMD values, possibly due to the flow instability generated as consequence of the lower rail pressure.

Table 5.5: Mean relative SMD values obtained from fuel A sprays at 250bar,350 bar (5.6ms after SoI).

	Mean SMD values (5.6ms after SoI)					
	Upper segment		Middle segment		Lower segment	
	left	right	left	right	left	right
250bar	0.46	0.33	0.55	0.52	0.66	0.69
350bar	0.58	0.54	0.59	0.53	0.59	0.54

Figure 5.34 and Figure 5.35 show the normalised SMD distributions of upper, middle and lower spray segments produced by fuel 1 at 250bar and 350bar during the closing phase of the needle (5.6ms after SoI). The various line styles and colours in both figures retained their meaning as defined above.
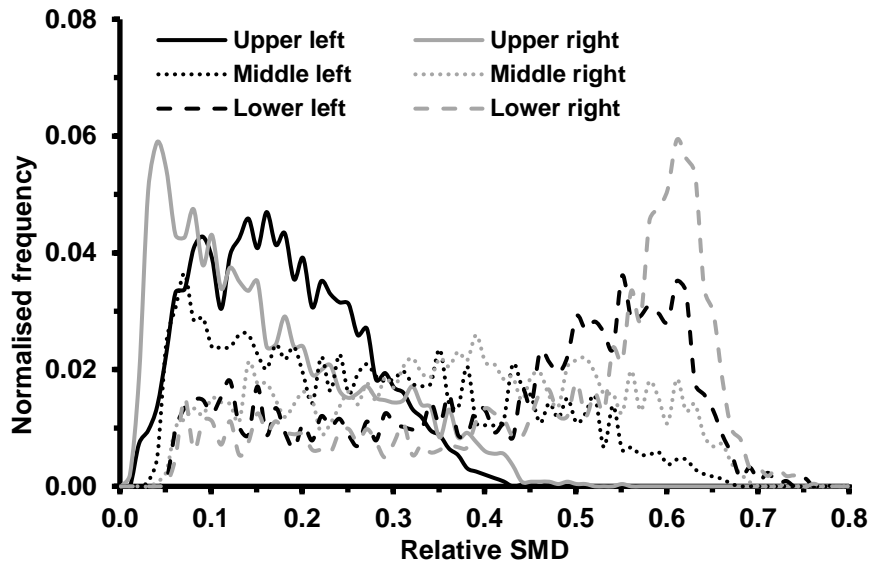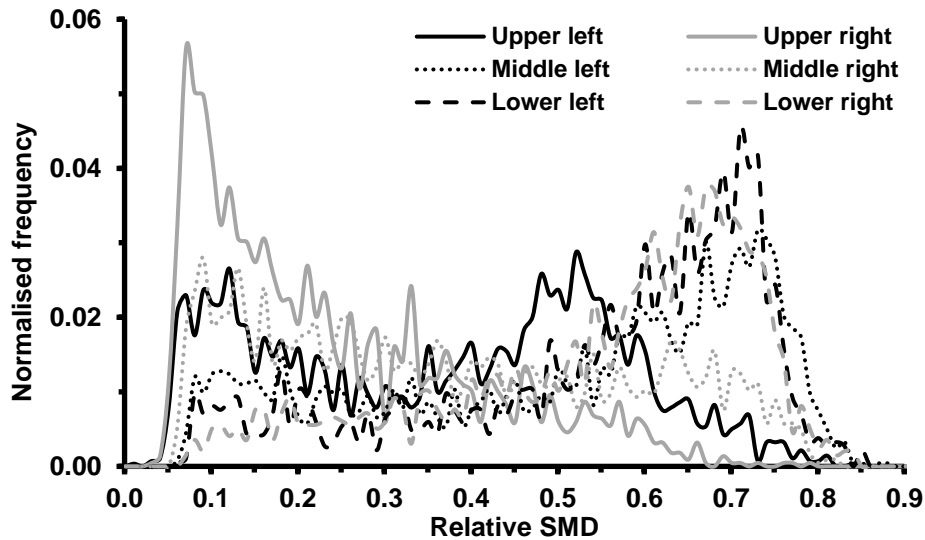
Figure 5.34: Relative SMD distributions of the six fuel 1 spray segments captured at 5.6ms after SoI, 250bar.
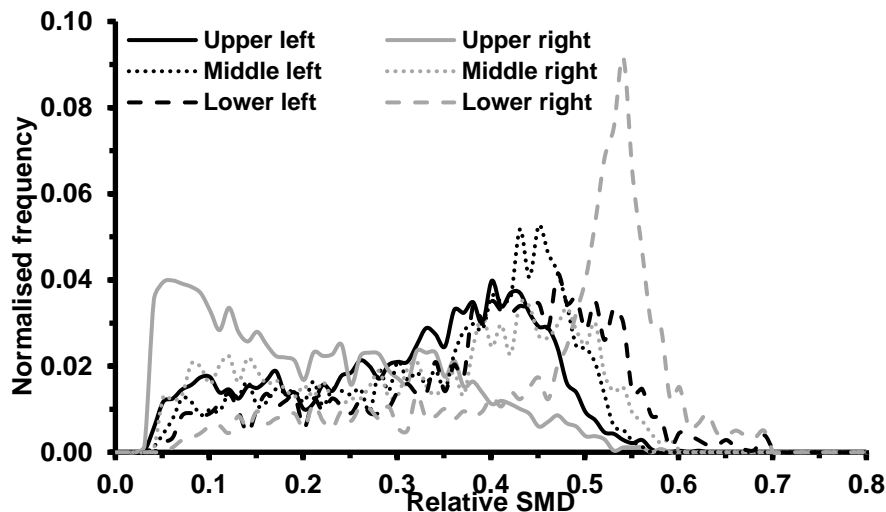
Figure 5.35: Relative SMD distributions of the six fuel 1 spray segments captured at 5.6ms after SoI, 350bar.

An optical observation of the distributions produced by the sprays at 250bar indicated that the spray developed in a less asymmetric manner. Nevertheless, the results shown in Table 5.6 suggested t that the majority of the larger droplets were found on the left-hand side of the spray, suggesting a spray asymmetry, especially at the middle spray segments. On the other hand, in the case of 350bar sprays, the larger droplets at the middle and upper segments located on the left-hand side of the spray, while at

the lower segments on the right. Overall, it could be argued that the left-hand side of the sprays contained the majority of the larger droplets. The spray asymmetry has been associated with the developing flow asymmetry inside the nozzle passage, as a consequence of geometric cavitation structures at the hole entrance. A visual comparison of Figure 5.34 and Figure 5.35 revealed that in the case of 250 bar, the distributions obtained were wider relative to 350bar, suggesting the presence of larger droplets. The smaller mean SMD values obtained from sprays at 350bar were a consequence of the increased rail pressure, which in turn enhanced atomisation process. The results also suggested that the SMD of the spray droplets decreased with increasing axial distance from the nozzle exit, as a result of secondary atomisation. The larger droplets found in the vicinity of the nozzle exit could be attributed to the dominant primary breakup.

Table 5.6: Mean relative SMD values obtained from fuel 1 sprays at 250bar, 350bar (5.6ms after SoI).

	Mean SMD values (5.6ms after SoI)					
	Upper segment		Middle segment		Lower segment	
	left	right	left	right	left	right
250bar	0.373	0.244	0.517	0.378	0.554	0.554
350bar	0.318	0.221	0.352	0.333	0.391	0.460

A comparison between the results produced during the opening, maximum lift and closing phases of the needle (1.8ms, 3.8ms and 5.6ms after SoI) revealed that in the former and latter cases the mean SMD values were smaller relative to maximum needle lift. It was believed that this was a consequence of intensive cavitation occurring during these periods. Additionally, the distributions obtained at 1.8ms and 5.6ms after SoI exhibited a significant shift towards smaller SMD values with increasing axial distance, due to the synergy between primary and secondary atomisation. On the other hand, the distributions produced at 3.8ms after SoI at both rail pressures indicated that this effect was less significant. It was suggested that when the needle reached its maximum position, the dominant break-up mechanism was secondary atomisation.

5.2.2   Spray drop-sizing distributions as a function of fuel physical properties

The following discussion was dedicated to the dependence of SMD of the spray droplets on the fuel properties of the fuels under consideration. For the purpose of this analysis, the spray data produced by fuel B to fuel E and fuel 2 to fuel 4 at 350bar and maximum needle lift (3.7ms, 3.8ms after SoI respectively). The false coloured images together with the corresponding relative SMD distributions were produced by the corresponding normalised, time-resolved mean images obtained from 100 and 50 injections respectively. The normalised mean images did not show any information with regards to the spray structure, but they provided a good overview on the SMD distributions obtained by the different fuels.

Fuel B (Gap diesel)

Fuel B was the second heaviest fuel under investigation, in terms of viscosity and surface tension. Viscosity and surface tension tended to stabilize the fuel, preventing its break-up into smaller droplets. Fuel B had relatively large viscosity and surface tension, hence the relative SMD distribution was expected to be shifted towards larger SMD values. Figure 5.36 and Figure 5.37 showed the normalised relative SMD distribution produced by fuel B spray at 350bar, when the needle reached its maximum needle lift and the corresponding false coloured SMD and STD images.
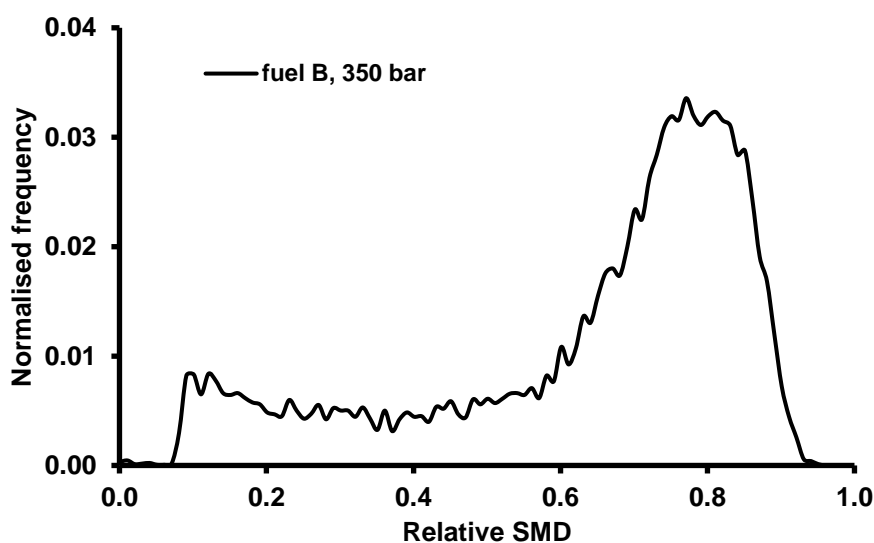
Figure 5.36: Relative SMD distribution produced by fuel B at 350bar (3.7ms after SoI).

Figure 5.37: False coloured mean image (left side) and STD image (right side) produced at 3.7ms after SoI in case of fuel B at 350bar showing the relative SMD distribution and variation along the spray.

It can be observed the distribution was shifted towards larger SMD values. Then mean SMD value was 0.64, which was approximately 7% larger than the mean SMD value obtained from fuel A at same pressure and needle lift. The formation of larger droplets was believed to be a consequence of the relatively large viscosity and surface tension of fuel B, which tended to oppose break-up phenomena. An optical observation of Figure 5.37 revealed that the larger droplets appeared around the spray axis of symmetry, while the smaller droplets in the spray periphery. It could be also observed that the spray showed an asymmetry to the right-hand side. This observation is discussed in more detail in the following subsection, where distributions of different spray segments are presented. Additionally, the drop size appeared to remain unchanged with increasing axial distance from the nozzle exit, suggesting that the dominant spray atomisation mechanism was secondary breakup from the moment the fuel exited the nozzle passage. The false coloured STD image shown in Figure 5.37 suggested greater SMD variation at the upper spray segment and especially on the right-hand side. It was also observed that the largest STD values located on the opposite side as where the largest SMD were found in the spray. However, it could be argued that in the vicinity of the spray axis the STD remained fairly low, while it increased close to the spray boundaries, where secondary atomisation was the dominant break-up mechanism. A comparison between fuels A and B revealed that the overall STD produced by fuel B

sprays was slightly larger relative to fuel A. However, this difference was not significant, since both fuels had similar physical properties.

Fuel C (Kerosene + lubricity additive)

Fuel C was the second lightest fuel under consideration after fuel D. Based on its relatively low viscosity and surface tension, the mean relative drop-sizing distribution was expected to be shifted towards smaller SMD values compared to fuels E, B and A. Figure 5.38 and Figure 5.39 show the normalised relative SMD distribution produced by fuel C spray at 350bar, when the needle reached its maximum needle lift and the corresponding false coloured SMD and STD images respectively. Oddly enough, the distribution shown in Figure 5.38 appeared to be similar to fuel A. The mean SMD value calculated was 0.59, similar to fuel A. It is believed that the additive utilised to improve fuel's lubricity altered the physical properties of the fuel, especially viscosity.
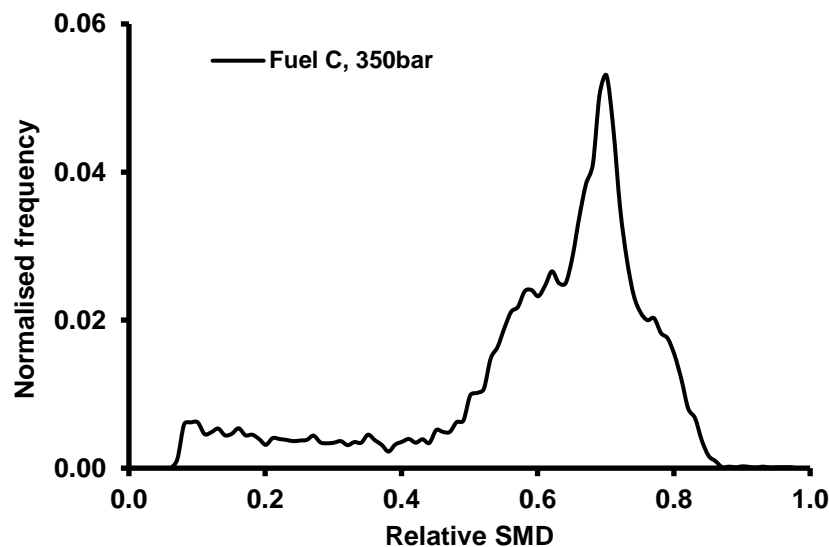
Figure 5.38: Relative SMD distribution produced by fuel C at 350bar (3.7ms after SoI)

In more detail, the additive added was an ester-based additive, which consisted of glycerol mono-oleate. This compound was responsible for the introduction of viscoelastic properties to the fuel, which created a non-Newtonian flow profile. Based on this, it was reasonable to argue that the fuel viscosity changed throughout the experiment, resulting in the formation of larger droplets than expected. It should be also noted that the data has not been corrected against the corresponding fluorescent yield calibration factor,

since it was assumed that the fluorescent yield was be similar to fuel A, as both fuel mixtures were mixed with a 600mgRhB/L 1-Decanol stock solution. Such a correction could possibly lead to the expected outcome of smaller SMD values. The fluorescent yield calibration ratio calculated for the experiments discussed in Chapter 7 cannot be used since there is no similar fuel to fuel C.

An optical inspection of Figure 5.39 (left spray) revealed that the majority of the larger droplets located around the spray axis of symmetry, while the smaller values in the spray periphery.

Figure 5.39: False coloured mean image (left) and STD (right) image produced at 3.7ms after SoI in case of fuel C at 350bar showing the relative SMD distribution and variation along the spray.

A spray asymmetry was also observed on the right-hand side of the spray; the spray asymmetry is discussed in more detail in the following subsection of this chapter. Lastly, it was shown that the relative SMD remained practically unchanged, suggesting that secondary atomisation was the dominant atomisation mechanism as soon as the spray exited the nozzle passage. The STD image of fuel C spray, shown in Figure 5.39 in false colour suggested no significant SMD variation across the spray, with an exception in the case of the left boundary. Such an observation suggested less instabilities induced throughout a complete of 100 injections. The region in the vicinity of the spray axis showed low STD suggesting similar flow patterns over the injections.

External spray drop-sizing analysis using Laser Sheet Drop-sizing technique

<u>Fuel D (light kerosene)</u>

Fuel D was the lightest fuel under investigation. Its low viscosity and surface tension suggested the formation of smaller droplets relative to the rest of the fuels, since the forces opposing break-up phenomena were weaker. Figure 5.40 and Figure 5.41 show the relative SMD distribution produced by fuel D spray at 350bar, maximum needle lift and the corresponding normalised, false coloured SMD and STD images. The mean SMD distribution shown in Figure 5.40 indicated that the mean SMD value (mean SMD=0.43) was shifted towards smaller SMD relative to the rest of the fuels, confirming the expected effect of the lower viscosity and surface tension on the droplet size. An optical inspection of Figure 5.41 suggested that Fuel D spray developed in a much more symmetric manner. The larger relative SMD were evenly distributed on both left and right-hand side of the spray. It can be also observed that the SMD values around the spray axis were larger than the periphery. Lastly, the SMD of the spray droplets gradually decreased with increasing axial distance from the nozzle exit, suggesting the synergy between both primary and secondary breakup mechanisms.
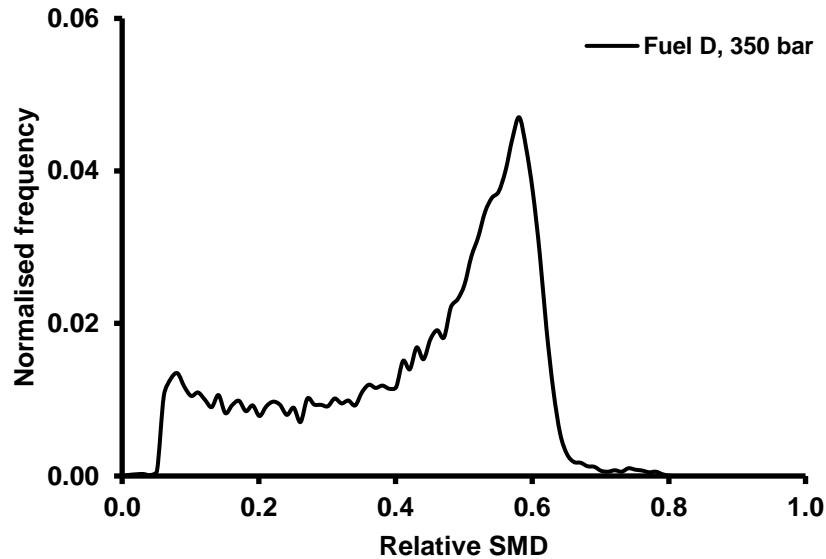
Figure 5.40: Relative SMD distribution produced by fuel D diesel at 350bar (3.7ms after SoI).

The STD image produced by fuel D is shown in false colour in Figure 5.41. It was observed that the STD was fairly low across the spray geometry. The STD obtained close to the spray boundaries was greater relative to the main spray body, as a result of dominant secondary atomisation. It can be argued

that fuel D produced lower STD relative to the rest of the fuels, implying less spray instabilities over the set of a hundred injections.
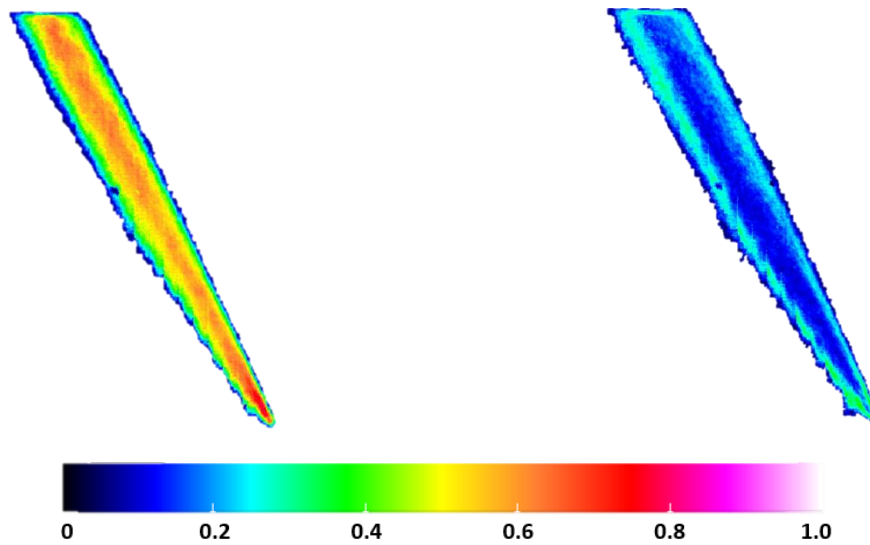
Figure 5.41: False coloured mean image (left) and STD image (right) produced at 3.7ms after SoI in case of fuel D at 350bar showing the relative SMD distribution and variation along the spray.

Fuel E (B20 diesel blend)

Fuel E was the heaviest amongst the fuels under investigation. Its higher viscosity and surface tension relative to the rest of the fuels suggested the formation of larger droplets. Figure 5.42 and Figure 5.43 show the normalised SMD distribution obtained from fuel E spray at 350bar and maximum needle lift and the corresponding false coloured mean image respectively. Oddly enough, the SMD distribution (black line) shown in Figure 5.42 was shifted towards smaller SMD values, which contradicted the expected trend. Three reasons could be responsible for this unexpected outcome:

- Different concentration of RhB in the final mixture.

- The presence of an additive which altered the viscosity/surface tension of the fuel sample

- Quenching effects, due to reactions between RhB and FAME (oxygenated compounds)

The preparation of the fuel mixtures was undertaken by following the same methodology and in a careful manner; therefore the concentration difference between the various fuel samples was low and could not justify the discrepancy shown in the results. Secondly, the formation of smaller droplets could

be a consequence of a fuel additive, which altered the surface tension or viscosity of the fuel mixture. However, according to the fuel E data sheet, there was no additive added in the B20 blend. Lastly, it is believed that the oxygenated compounds present in fuel E reacted with the solution of RhB-1-Decanol leading to quenching effects. The products of the reaction between RhB and FAME were believed to have different optical properties (absorption/emission wavelengths), hence the results obtained have to be corrected against the corresponding fluorescence yield calibration ratio. It should be noted that when these experiments were conducted by Jeshani[16], it was assumed that the fluorescent yield produced by fuel E was similar to fuel A, since both fuels were mixed with 600mgRhB/L 1-Decanol solution. The calibration ratio utilised for the correction of the data was calculated for the experiments (fuel 3 -B20) described in Chapter 7. The corrected results (grey line) are shown in Figure 5.42. Even though the corrected SMD distribution was shifted towards larger SMD values, the mean SMD value (mean SMD=0.41) was smaller than fuels A and B. This behaviour was not fully understood and requires further investigation.
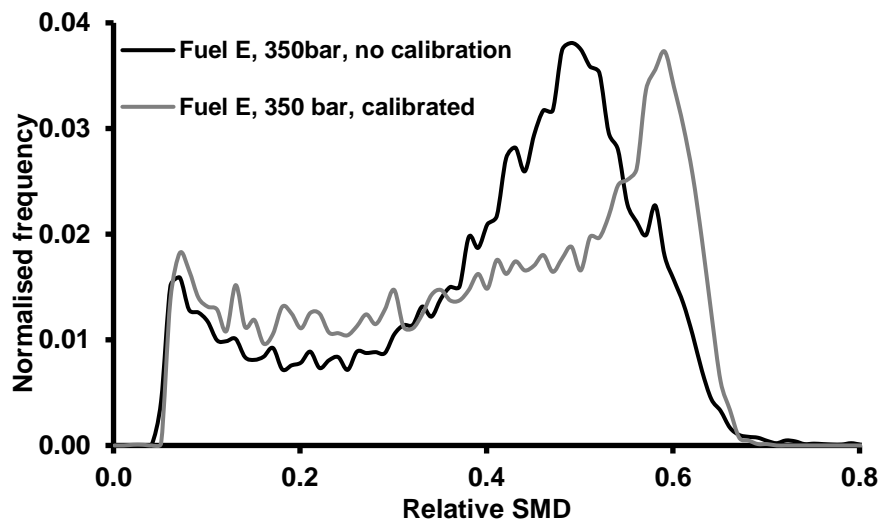
Figure 5.42: Relative SMD distributions produced by fuel E diesel at 350bar (3.7ms after SoI).

The false coloured mean SMD image shown in Figure 5.43 shows that the spray was developed in asymmetric manner. It was shown that majority of the larger droplets located on the left-hand side of the spray. It was also observed that SMD gradually decreased with increasing radial distance, due to pronounced secondary atomisation. On the other hand, the SMD of the spray droplets slightly dropped with increasing axial distance. This could be possibly attributed to less pronounced effects of primary

atomisation and the dominance of secondary atomisation, as soon as the spray exited the nozzle passage. The observed asymmetry is discussed in detail in the following subsection.
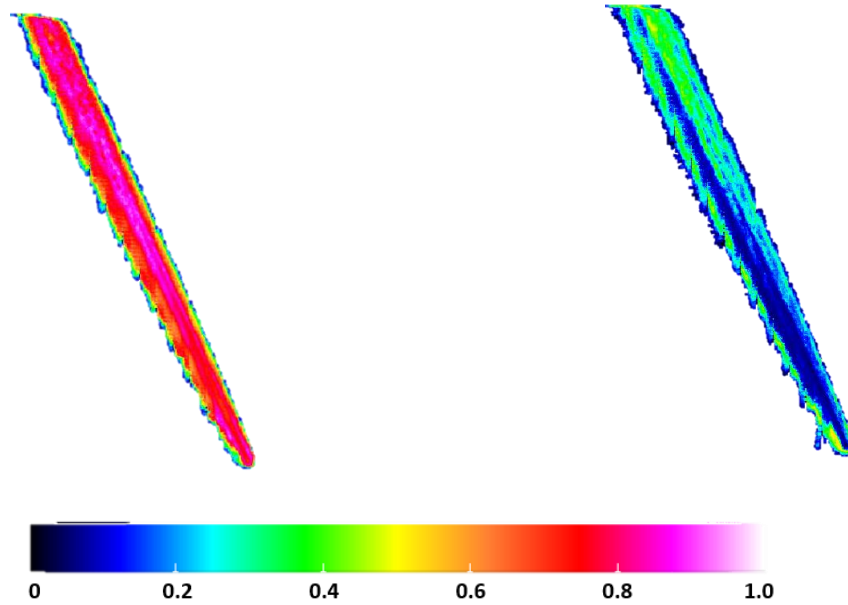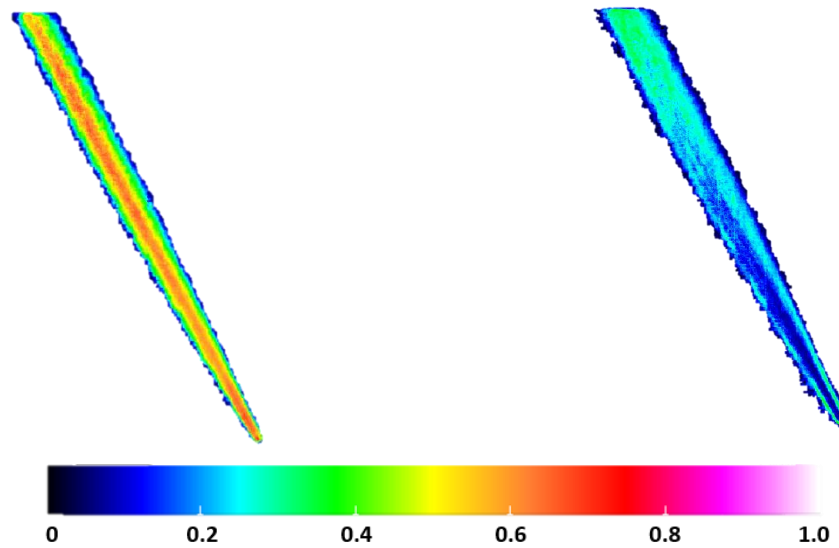

Figure 5.43: False coloured mean image (left side) and STD image (right side) produced at 3.7ms after SoI in case of fuel E at 350bar showing the relative SMD distribution and variation along the spray.

Lastly, the false coloured STD image shown in Figure 5.43 demonstrated that largest STD was obtained at the upper spray segment. Such an observation suggested greater induced instability at this region, possibly due to pronounced secondary atomisation. It was also observed that the STD of the droplets at the regions along and surrounding the first half of the spray axis was lower relative to the boundaries, suggesting that the flow patterns developed in the vicinity of the nozzle exit were similar over the set of 100 injections.

Fuel 2 (B20 diesel fuel)

Fuel 2 was the heaviest amongst the fuels under investigation. Considering its large viscosity, it was expected to obtain larger droplets relative to fuel 1. In principle, fuels with relatively high viscosity have been shown an increased propensity to cavitate less[57]. Less intensive cavitation leads to poorer atomisation and consequently to the formation of larger droplets.

External spray drop-sizing analysis using Laser Sheet Drop-sizing technique
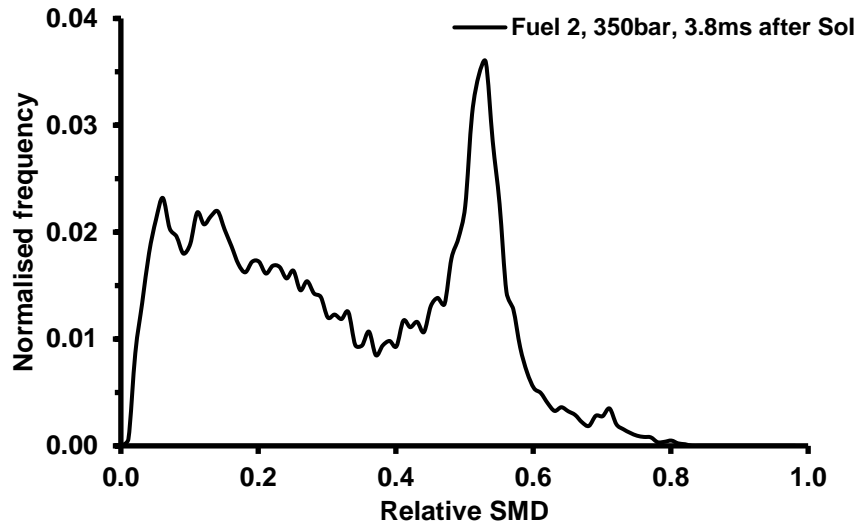
Figure 5.44: Relative SMD distribution produced by fuel 2 at 350bar (3.8ms after SoI).

The mean SMD value of the distribution shown in Figure 5.44 was 0.33, which was smaller than the corresponding value of fuel 1 by approximately 33%. Such a finding contradicted the expected trend discussed above. It should be noted that the spray data have been corrected with the corresponding fluorescence yield calibration factor, in order to eliminate any quenching effects caused by the interaction of RhB with the oxygenated component of FAME. The static quenching effects referred to the formation of a complex of RhB molecules, which had its own unique optical properties.

The false coloured image shown in Figure 5.45 suggested that the SMD of the spray droplets decreased with increasing axial and radial distance from the nozzle exit and the central spray axis respectively. Such an observation suggested that secondary atomisation progressively became the dominant breakup mechanism. The larger droplets found in the vicinity of the nozzle exit were produced mostly due to primary atomisation. It was also observed that the majority of the larger droplets located on the left-hand side of the spray, suggesting a spray asymmetry. The asymmetry observed is discussed in more detail in the following subsection. Lastly, it was shown that there were a few large droplets at the top of the spray body. This was believed to be an artefact; the large signal was believed to be a consequence of the remaining optical contamination in the LIF sprays (see §5.1.1).

The STD images produced by fuel 2 at 3.8ms are shown in false colour in Figure 5.45 on the right-hand side. It was shown that the majority of the largest STD values located at the top third of the spray, where

secondary atomisation occurred. Additionally, it was observed that the region in the vicinity of the nozzle exit exhibited low STD, suggesting similar flow patterns over the set of 50injections. Lastly, both mean SMD and STD images showed an abrupt reduce of the spray width at approximately the top third of the spray. This was not an artefact; fuel 2 exhibited significant instabilities at this region, which in the raw images appeared like swirling flow.
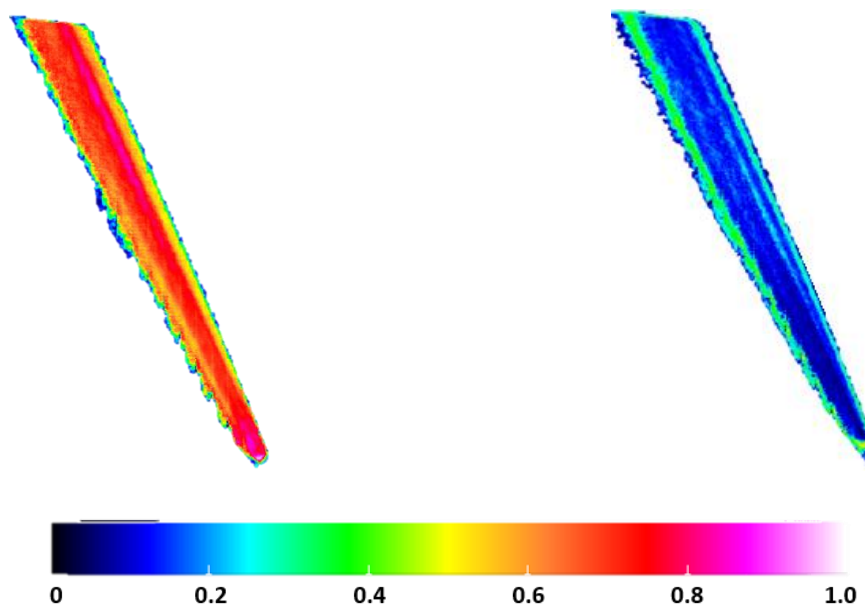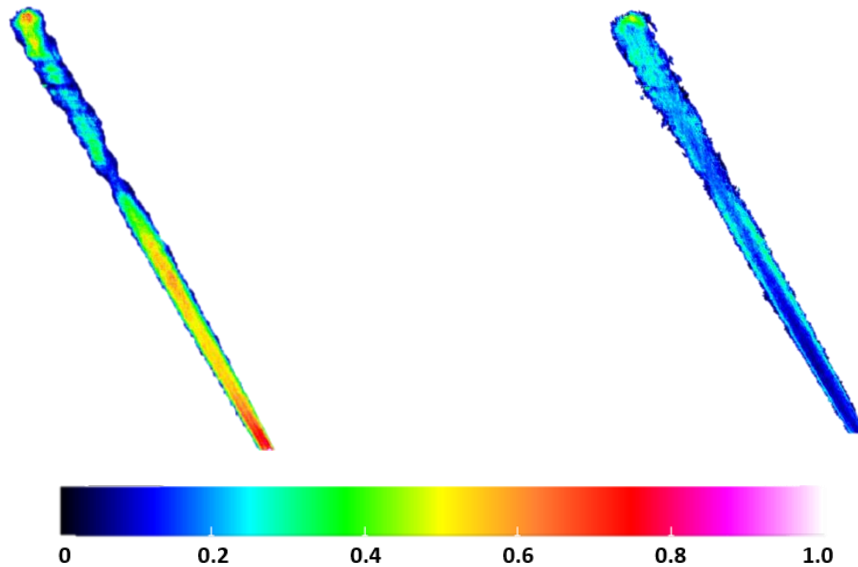

Figure 5.45: False coloured mean image (left) and STD image (right) produced at 3.8ms after SoI in case of fuel 2 at 350bar, showing the relative SMD distribution and variation along the spray.

Fuel 3 (Gap diesel + lubricity additive)

Fuel 3 was the second less viscous fuel under investigation. Considering its relatively low viscosity, it was expected to obtain droplets smaller than fuel 1, since the relatively low viscosity opposed break-up phenomena less. According to the distribution of fuel 3 shown in Figure 5.46, the mean SMD value of the spray droplets was 0.40, which was 7% smaller than the corresponding mean value of fuel 1. This decrease was believed to be a consequence of the lower viscosity of fuel 3 relative to fuel 1. In principle, less viscous fuels tend to cavitate more than viscous fuels. Cavitation has been shown to enhance atomisation and subsequently leads to the formation of smaller droplets. However, the viscosity difference of approximately 25% between fuels 1 and 3 suggested that the SMD of fuel 3 spray droplets should be smaller than the obtained. The formation of larger than expected droplets was believed to be a consequence of the lubricity additive added in fuel sample 3. Such an additive has been suggested to

introduce non-Newtonian flow properties. Hence, the fuel viscosity was expected to alter during the execution of the experiments. Such a change potentially explained the formation of the larger droplets shown in the distributions obtained. Gap diesel was a fuel consisted of light and heavy components with no components of intermediate boiling points. The heavier components were believed to be responsible for the formation of the larger droplets, while the lighter for the smaller ones.
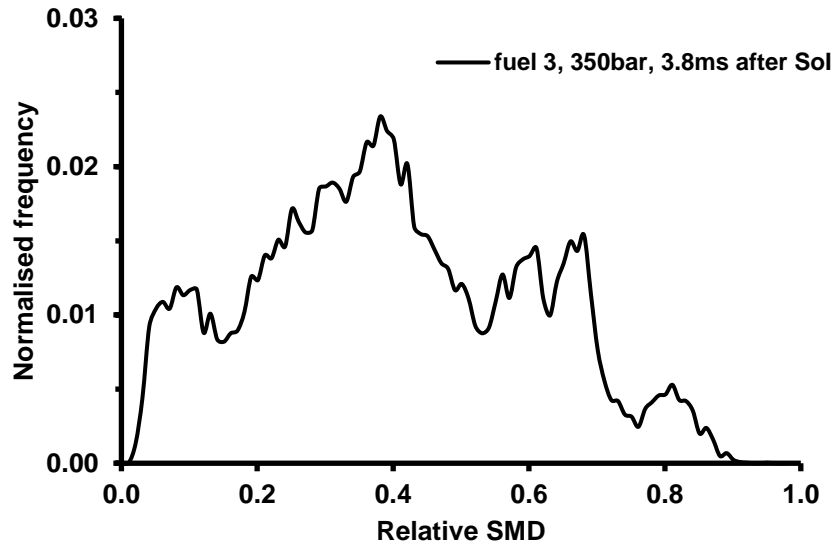
Figure 5.46: Relative SMD distribution produced by fuel 3 at 350bar (3.8ms after SoI).
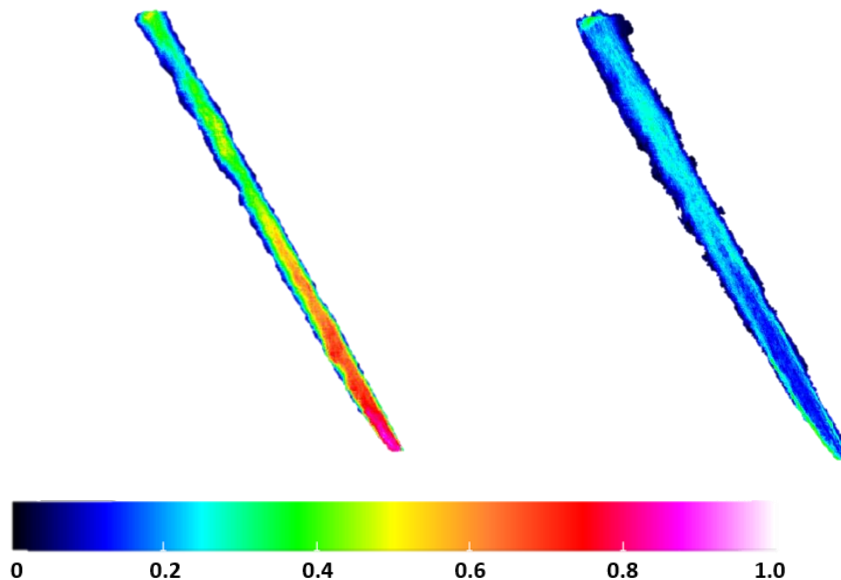
Figure 5.47: False coloured mean image (left) and STD image (right) produced by fuel 3 at 3.8ms after SoI and at 350bar.

External spray drop-sizing analysis using Laser Sheet Drop-sizing technique

The false coloured image shown in Figure 5.47 suggested the SMD of the spray droplets decreased with increasing axial and radial distance from the nozzle exit and the central spray axis respectively. Such an observation suggested that secondary atomisation progressively became the dominant breakup mechanism. The larger droplets found in the vicinity of the nozzle exit were mostly produced, due to primary atomisation. It was also observed that the majority of the larger droplets were located on the right-hand side of the spray, suggesting a spray asymmetry. The spray asymmetry is discussed in more detail in the following subsection.

The false coloured STD image shown in the right-hand side of Figure 5.47 showed that the majority of the large STD values located at the upper spray segment and close to the spray periphery. In both regions, the dominant break-up mechanism was secondary atomisation. It has been also observed that the spray was fairly unstable at the region, where the greatest SMD variation was found. This instability caused the spray flapping observed in the raw images. Lastly, in the vicinity of the nozzle exit, the STD was lower relative to the upper segment, suggesting that the dynamics responsible for atomisation are similar over the set of the injections.

<u>Fuel 4 (Jet fuel + lubricity additive)</u>

Fuel 4 was the lightest amongst the fuels under consideration. Considering its low viscosity, it was expected to obtain smaller droplets than fuels 1 and 3. Light fuels exhibited an increased propensity to cavitate more relative to heavier fuels; intensive cavitation improved atomisation process leading to the formation of smaller droplets. The mean SMD values obtained from the distribution shown in Figure 5.48 was 0.42, which was smaller than fuel 1 and larger than fuel 3 by approximately 2.5% and 5% respectively. Such findings contradicted the expected trend. The differences in viscosity amongst fuels 4 and 1 and fuels 4 and 3 were 56.5% and 41% respectively. Such differences suggested that the droplets formed by fuel 4 should be much smaller than the obtained. This anomaly was believed to be a consequence of the lubricity additive added in fuel sample 3. It was an ester-based additive which was capable of altering the properties of the fuel by introducing viscoelastic effects. Hence, it could be argued that the viscosity of the diesel sample was altered during the execution of the experiments, resulting in the above mentioned unexpected trend.
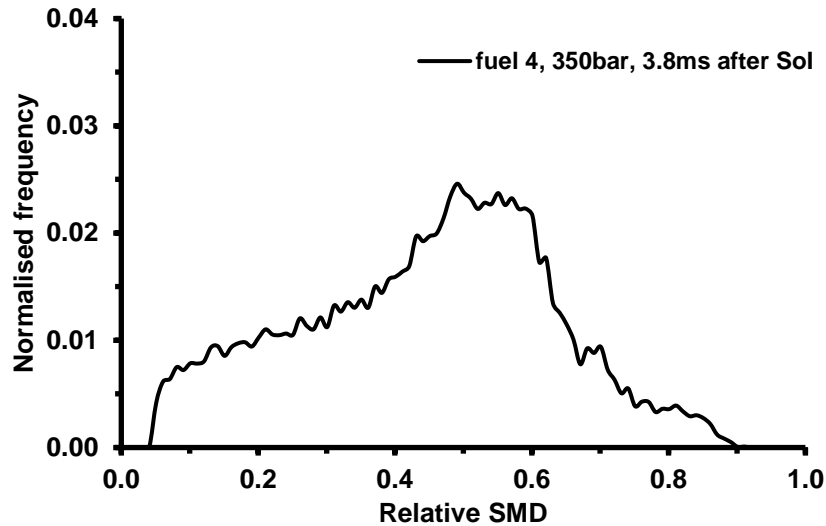
Figure 5.48: Relative SMD distribution produced by fuel 4 at 350bar (3.8ms after SoI).

An optical inspection of Figure 5.49 revealed that the majority of the larger droplets located around the spray axis of symmetry, while the smaller values in the spray periphery, as a result of secondary atomisation at the spray boundaries. A spray asymmetry was also observed on the left-hand side of the spray; the spray asymmetry is discussed in more detail in the following subsection of this chapter.
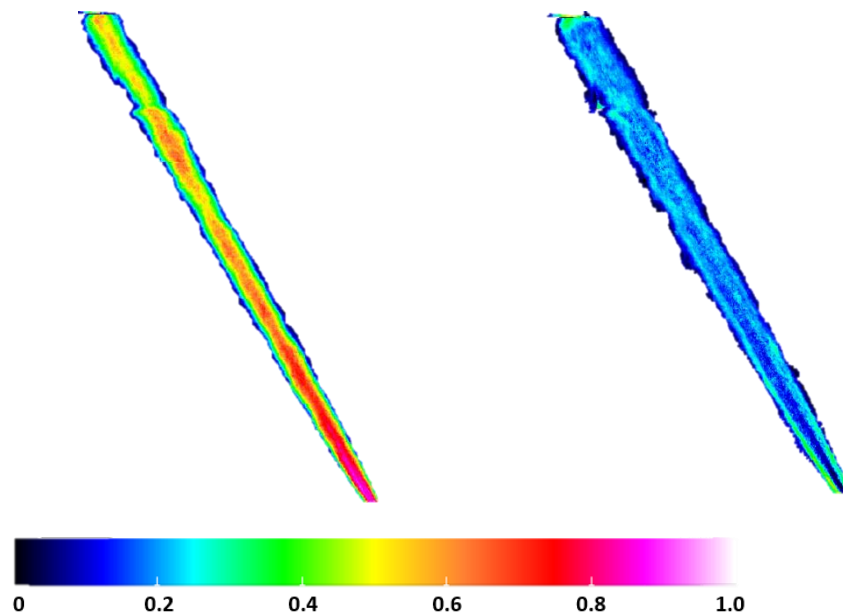
Figure 5.49: False coloured mean image (left) and STD image (right) produced at 3.8ms after SoI in case of fuel 4 at 350bar, showing the relative SMD distribution and variation along the spray.

Lastly, it seemed that the relative SMD of the spray droplets decreased with increasing axial and radial distance from the nozzle exit and the central spray axis respectively. In the vicinity of the nozzle exit the dominant breakup mechanism was primary atomisation, which led to the formation of large droplets, while secondary atomisation became more significant with increasing axial distance. The STD image presented in false colour in Figure 5.49 demonstrated a fairly uniform STD across the spray geometry, suggesting less spray instabilities compared to the rest of the fuels. This uniform profile implied similar flow dynamics over the injections. In this case, the effect of the aerodynamic instability induced at the upper spray segment was not as significant as in the previous fuels.

5.2.3   Diesel spray asymmetry as a function of fuels' physical properties

In the previous subsection, it was observed that the majority of diesel sprays developed in an asymmetric manner. The following discussion was dedicated to the detailed investigation of the asymmetry observed. The distributions of the six different spray segments were produced by fuels A to E and fuels 1 to 4 at 350bar and maximum needle lift to show the variation of the SMD of the spray droplets. The six segments were the right and left hand sides of the lower, middle and upper spray segments.

<u>Fuel B (gap diesel)</u>

Figure 5.50 shows the projections of the normalised histograms (100bins) obtained at the upper (solid line), middle (dotted line), lower (dashed line) spray segments and provide information about the relative SMD distribution at the left-hand side (black colour) and right hand side (grey colour) of each spray segment at 350bar. The right-hand distributions shown in Figure 5.50 shifted towards larger SMD values relative to the left-hand side. This observation implied that there was a spray asymmetry to the right-hand side of the spray. It was also observed that the spray asymmetry was more significant in the middle and upper segment of the spray.
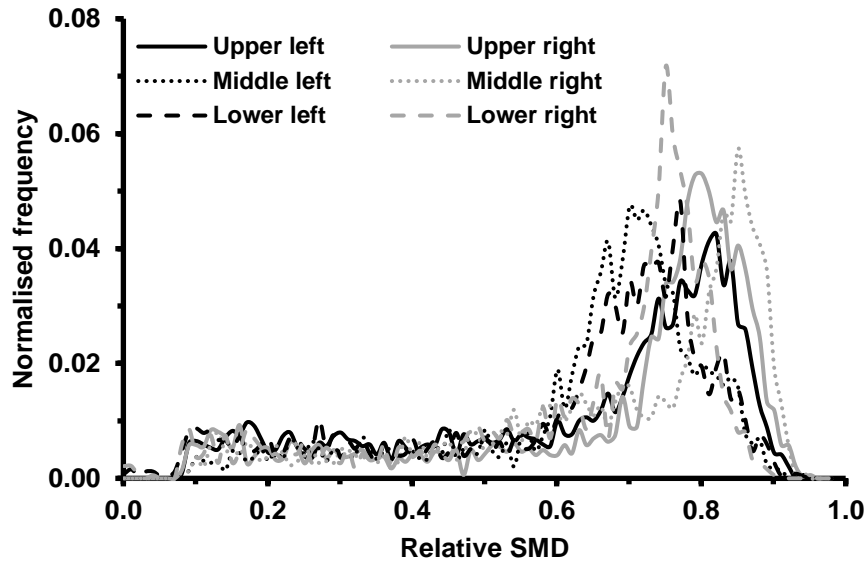
Figure 5.50: Relative SMD distributions of the six spray segments captured at 3.7ms after SoI, fuel B, 350bar.

The overlap of the lower right and left-hand sides of the distributions suggested spray symmetry at this region. Overall, the asymmetry observed was judged to be a consequence of the flow asymmetry introduced into the nozzle holes as a result of geometric cavitation developed at the entrances to the nozzle holes. On average, larger droplets were obtained on the same side of the nozzle hole as where the geometric sheet cavitation located (upper entrance to the nozzle holes). The mean SMD values of each distribution are summarised in Table 5.7. Based on the mean values, it could be argued that the obtained SMD values remained practically the same with increasing axial distance, suggesting that secondary atomisation was the dominant break-up mechanism, as soon as the spray exited the nozzle passage.

Table 5.7: Mean relative SMD values obtained from fuel B sprays at 350bar (3.7ms after SoI).

	Mean SMD values (3.7ms after SoI)					
	Upper segment		Middle segment		Lower segment	
	left	right	left	right	left	right
350bar	0.64	0.69	0.64	0.69	0.62	0.65

Fuel C (kerosene + lubricity additive)

Figure 5.51 shows the projections of the normalised histograms obtained from fuel C sprays at 350bar and maximum needle lift.
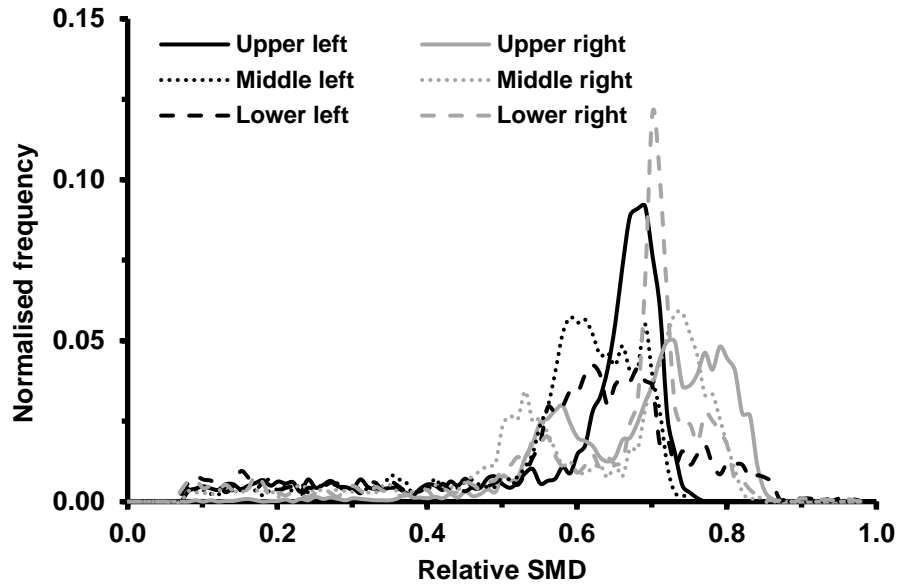
Figure 5.51: Relative SMD distributions of the six segments of fuel C spray captured at 3.7ms after SoI, fuel C, 350bar.

It could be observed that the distributions corresponding to the left-hand side of the spray were shifted towards smaller SMD values relative to the right-hand side. This observation implied that the spray developed in an asymmetric manner. The right-hand side of the spray was associated with the flow occurring adjacent to the upper surface of the injector nozzle, and the left-hand side of the spray was associated with the flow occurring close to the lower surface of the injector nozzle. The custom-made acrylic tips were believed to promote the development of geometric sheet cavitation at the upper entrance to the nozzle holes, due to the abrupt increase of the local flow speed, the generation of pressure gradients and shear flow when the flow entered the nozzle holes.

It was suggested that the asymmetry in the spray structure, as reflected in the SMD distribution, was a consequence of the flow asymmetry produced in the nozzle holes by the geometric sheet cavitation. Table 5.8 summarises the mean SMD values obtained from the distribution shown in Figure 5.51. It could be argued that the mean droplet size of both right and left hand segments remained practically

unchanged with increasing axial distance from the nozzle exit. This could be attributed to the dominant effect of secondary atomisation relative to primary.

Table 5.8: Mean relative SMD values obtained from fuel C sprays at 350bar (3.7ms after SoI).

	Mean SMD values (3.7ms after SoI)					
	Upper segment		Middle segment		Lower segment	
	left	right	left	right	left	right
350bar	0.59	0.69	0.57	0.69	0.59	0.63

Fuel D (light kerosene)

Figure 5.52 shows the normalised distributions of the upper, middle and lower right and left-hand side spray segments obtained from fuel D sprays at 350bar and maximum needle lift. Comparing the distributions obtained from fuel D to the rest of the fuels, it could be argued that Fuel D distributions were shifted towards smaller SMD values, implying the formation of smaller droplets.
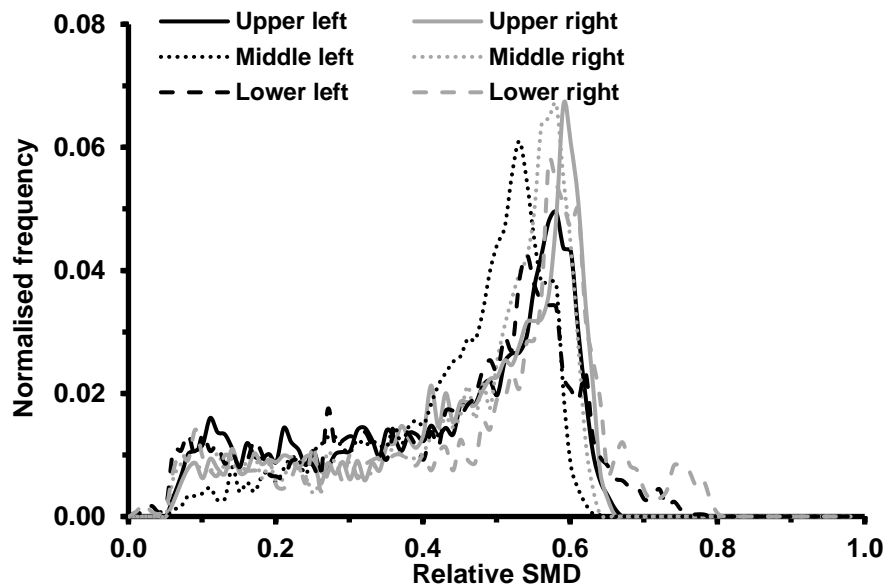
Figure 5.52: Relative SMD distributions of the six spray segments captured at 3.7ms after SoI, fuel D, 350bar.

This was a consequence of its lower viscosity and surface tension, resulting in earlier fuel atomisation. It could be observed that the distributions of both spray sides overlapped each other, implying that Fuel D sprays developed in a quite symmetric manner. The mean SMD values of the distribution obtained are shown in Table 5.9.

Table 5.9: Mean relative SMD values obtained from fuel D sprays at 350bar (3.7ms after SoI).

	Mean SMD values (3.7ms after SoI)					
	Upper segment		Middle segment		Lower segment	
	left	right	left	right	left	right
350bar	0.43	0.46	0.45	0.46	0.43	0.48

It could be argued that the right-hand side of the spray contained slightly larger SMD values than the left, suggesting a small spray asymmetry, especially in the case of the lower spray segments. It could be also argued that the mean SMD remains practically unchanged with increasing axial distance, suggesting secondary atomisation to be the dominant break-up mechanism, as soon as the spray exited the nozzle passage. The results shown in Figure 5.52 suggested that the dominant spray break-up mechanism was secondary atomisation, since there was no significant change with increasing axial distance in the mean SMD values of the spray droplets.

Fuel E (B20 diesel blend)

Figure 5.53 shows the projections of the normalised distributions obtained from the upper, middle, and lower segments of fuel E spray developed at 350bar and maximum needle lift. It was mentioned earlier in this chapter, that fuel E was expected to form the largest droplets in comparison to the rest of the fuels, but it seemed to obtain almost the smallest droplets. Such a behaviour was not fully understood and requires further investigation. In terms of spray symmetry, fuel E seemed to develop in a quite asymmetric manner. In more detail, the distribution shown in Figure 5.53 suggested that the left-hand side of the spray contained significantly larger droplets than the right-hand side, especially in the case of the middle and upper segments.
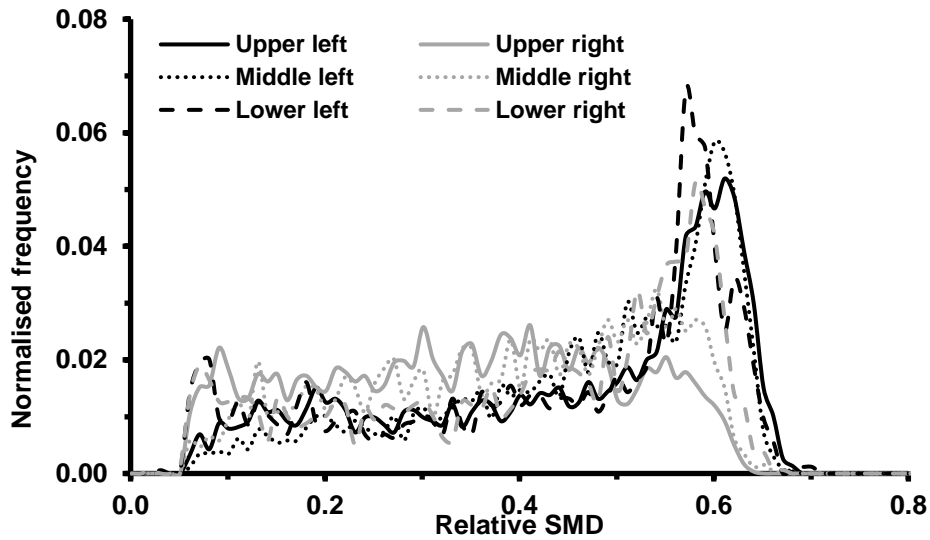
Figure 5.53: Relative SMD distributions of the six spray segments captured at 3.7ms after SoI, fuel E, 350bar.

In Chapter 4, it was suggested that the in-sac circumferential flow possibly promoted the separation of the heavier fuel components from the lighter ones. This suggestion could possible explain the strong spray asymmetry observed. As it was mentioned previously, the asymmetry developed has been associated with the geometric cavitation formed on the same side of the nozzle as where the larger droplets were located. Lastly, the mean SMD values of the distributions obtained are summarised in Table 5.10. It could be argued that the mean values remained practically unchanged with increasing axial distance, suggesting less pronounced effects of primary atomisation and the dominance of secondary atomisation.

Table 5.10: Mean relative SMD values obtained from fuel E sprays at 350bar (3.7ms after SoI).

	Mean SMD values (3.7ms after SoI)					
	Upper segment		Middle segment		Lower segment	
	left	right	left	right	left	right
350bar	0.46	0.35	0.47	0.39	0.44	0.42

External spray drop-sizing analysis using Laser Sheet Drop-sizing technique

Fuel 2 (B20 diesel)

Figure 5.54 shows the projections of the normalised histograms obtained at the upper (solid line), middle (dotted line), lower (dashed line) spray segments and provide information about the relative SMD distribution at the left-hand side (black colour) and right hand side (grey colour) of each spray segment at 350bar. The corresponding mean SMD values of the distributions obtained are summarised in Table 5.11.
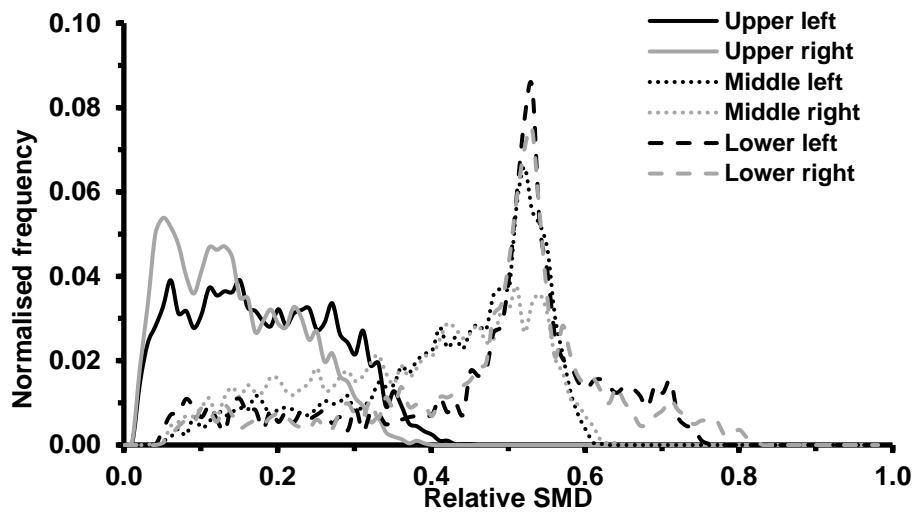
Figure 5.54: Relative SMD distributions of the six fuel 2 spray segments captured at 3.8ms after SoI, 350bar.

Table 5.11: Mean relative SMD values obtained from fuel 2 diesel sprays at 350bar (3.8ms after SoI).

	Mean SMD values (3.8ms after SoI)					
	Upper segment		Middle segment		Lower segment	
	left	right	left	right	left	right
350bar	0.185	0.150	0.426	0.385	0.473	0.483

The results suggested that the SMD of the spray droplets decreased with increasing axial distance from the nozzle exit. The larger droplets appearing in the lower segments could be attributed to the pronounced effects of primary atomisation. With increasing axial distance, secondary atomisation

became the dominant break-up mechanism, resulting in the formation of smaller droplets. The mean SMD values shown in Table 5.11 indicated that the larger droplets located on the left-hand side of the spray, suggesting a spray asymmetry. The asymmetry has been associated with the flow asymmetry inside the nozzle passage, as a consequence of geometric cavitation on the same side as where the larger droplets located.

Fuel 3 (Gap diesel + lubricity additive)

Figure 5.55 shows the relative SMD distributions of the lower, middle and upper segments of fuel 3 sprays produced at 350bar. The various line colours and styles retained their meaning as defined above. Table 5.12 summarises the mean relative SMD values obtained from the distributions shown in Figure 5.55. The results suggested that the majority of the larger droplets was located on the right-hand side of the spray, suggesting a spray asymmetry. On average, the larger spray droplets appear on the same side as where geometric cavitation appears inside the nozzle passage.
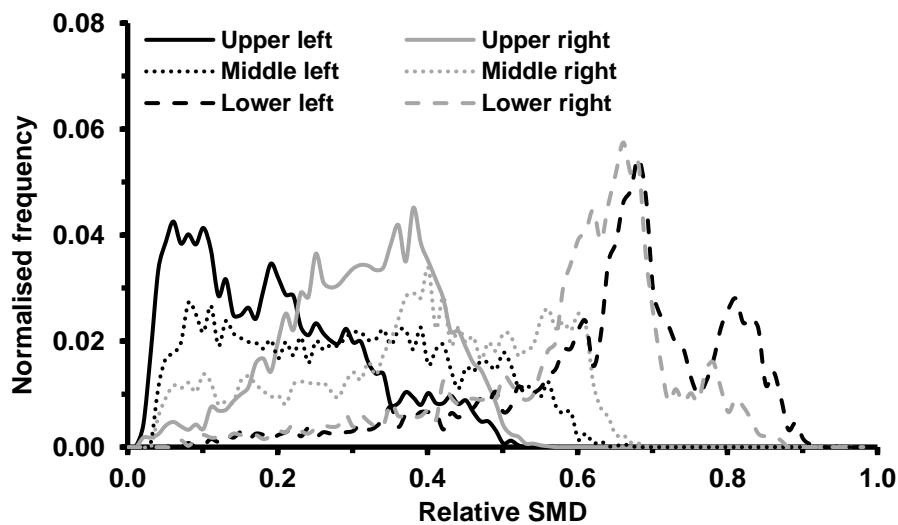
Figure 5.55: Relative SMD distributions of the six fuel 3 spray segments captured at 3.8ms after SoI, 350bar.

Additionally, the distributions indicated a gradual decrease in SMD with increasing axial distance, due to secondary atomisation. The largest droplets obtained in the vicinity of the nozzle exit were believed to be a consequence of primary atomisation, which disintegrated the jet into relatively large droplets and liquid ligaments. It should be noted that the mean SMD of right-hand side of the upper segment

was fairly large. This could be attributed to the remaining optical contamination, which was not possible to be removed from the spray data without excluding useful data.

Table 5.12: Mean relative SMD values obtained from fuel 3 diesel sprays at 350bar (3.8ms after SoI).

	Mean SMD values (3.8ms after SoI)					
	Upper segment		Middle segment		Lower segment	
	left	right	left	right	left	right
350bar	0.198	0.318	0.295	0.389	0.644	0.595

Fuel 4 (Jet fuel + lubricity additive)

The projections of the normalised frequency histograms shown in Figure 5.56 reflect the relative SMD distribution obtained from fuel 4 diesel sprays developed at 3.8ms after SoI and at 350bar. Table 5.13 summarises the corresponding relative mean SMD values.
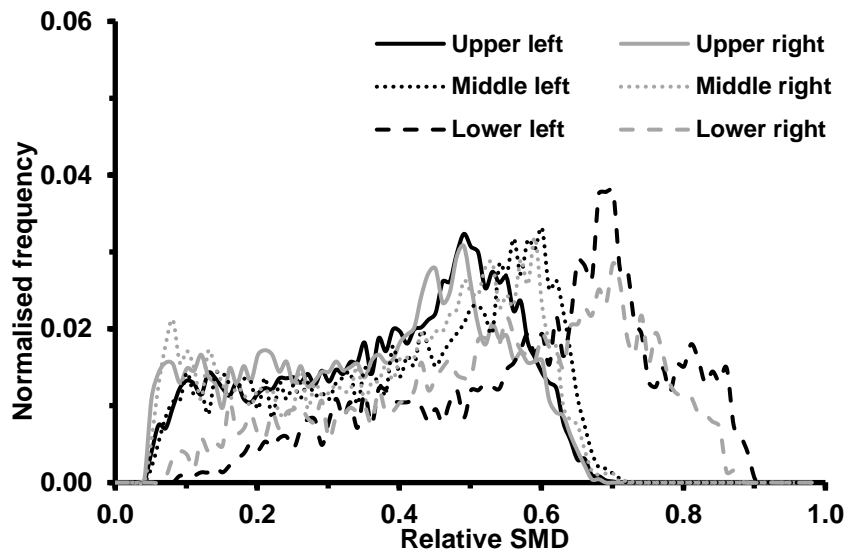
Figure 5.56: Relative SMD distributions of the six fuel 4 spray segments captured at 3.8ms after SoI, 350bar.

Table 5.13: Mean relative SMD values obtained from fuel 4 diesel sprays at 350bar (3.8ms after SoI).

	Mean SMD values (3.8ms after SoI)					
	Upper segment		Middle segment		Lower segment	
	left	right	left	right	left	right
350bar	0.392	0.367	0.418	0.392	0.597	0.542

The distributions obtained suggested a gradual decrease of the SMD of the spray droplets with increasing axial distance from the nozzle exit. This decrease became less apparent between the middle and upper segments, since secondary atomisation was the dominant break-up mechanism. On the other hand, the large droplets found in the lower segments were a consequence of primary atomisation. Additionally, the results suggested that the spray developed in a more symmetric manner relative to the rest of the fuels. The majority of the larger droplets appeared on the left-hand side of the spray. As it was mentioned earlier, the spray asymmetry has been associated with the flow asymmetry developed inside the nozzle hole, due to geometric cavitation at nozzle hole entrance.

5.3   Flapping spray angles

An optical inspection of the image data produced by fuel 1 to fuel 4 revealed that the emerging sprays developed a small, stochastic angular displacement during an injection event. This displacement was believed to be a result of the external aerodynamic instabilities or/and the flow distortion, due to the presence of cavitation in the nozzle passages and/or the competition between adhesion (responsible for hydraulic flip) and cohesion forces (mostly viscous and surface tension effects). In this regard, it was attempted to correlate the physical properties of the fuels and the different needle lift stages to the flapping spray angles. The pressure dependence was examined in the case of fuel 1 at 250bar and 350bar, while the rest of the fuels were examined at 350bar. It should be mentioned that the reference plane was the horizontal plane; all sprays were rotated such that the spray central axis became almost vertical.

External spray drop-sizing analysis using Laser Sheet Drop-sizing technique

<u>Fuel 1 (un-additised diesel) at 250bar and 350bar</u>

Figure 5.57 shows the projections of the spray angle normalised frequency histograms obtained from the time resolved fuel 1 sprays at 250bar and 350bar respectively.
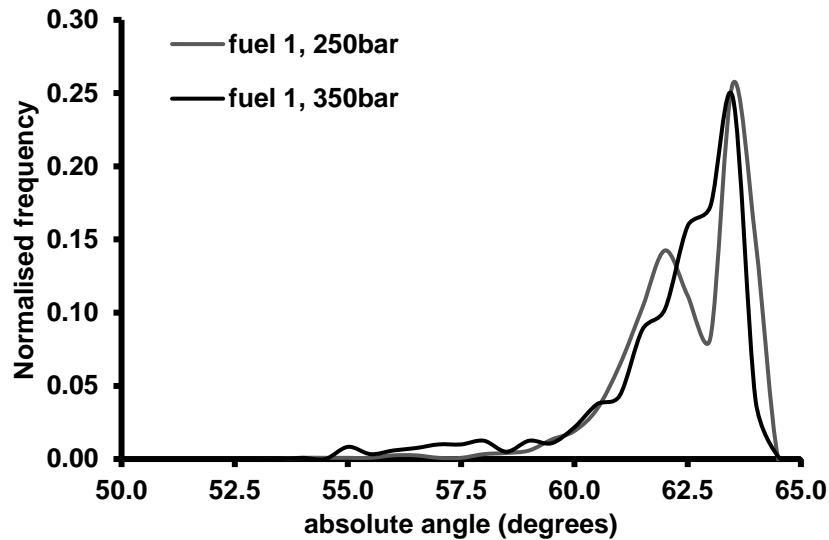
Figure 5.57: Flapping spray angle distributions obtained from fuel 1 at 250bar and 350bar.

The nozzle hole angle measured from the magnified images of the nozzles was 62.5 degrees, while the mean absolute angle obtained from the distributions were 62.5 degrees and 62.1 degrees in the cases of 250bar and 350bar respectively. The distributions also demonstrated that the majority of the flapping spray angles in the case of 350bar was in the range of approximately 58.0 degrees to 65.0 degrees. In particular, the most common angle variation in the case of 250bar was approximately 9 degrees, while the sprays at 350bar had an angle variation of approximately 7 degrees.

An optical inspection of Figure 5.57 revealed the spray angle distribution at 250bar was slightly wider in relation to the distribution at 350bar. Such an observation suggested that an increase in rail pressure led to the formation of more stable sprays. It was believed that the synergy between the presence of hydraulic flip and the surface tension adhesion occurring in the case of 250bar could be responsible for the bimodality observed in the corresponding distribution. On the other hand, the increased stability of the sprays with increasing rail pressure was believed to be a result of the relatively reduced effects of surface adhesion. A comparison between the measured hole angle and the mean absolute values

revealed that fuel 1 did not exhibit significant fluctuation. Lastly, it was observed that both distributions were left-skewed. Such an observation implied that the sprays exhibited an asymmetry towards the right-hand side of the spray, further supporting the arguments made in earlier subsections.

Fuel 2 (B20) at 350bar

Figure 5.58 shows the projection of the spray angle normalised frequency histograms obtained from fuels 1, 2, 3 and 4 at 350bar. The solid, dotted, dashed dotted and dashed lines represented fuel 1, fuels 1, 2, 3 and 4 respectively.
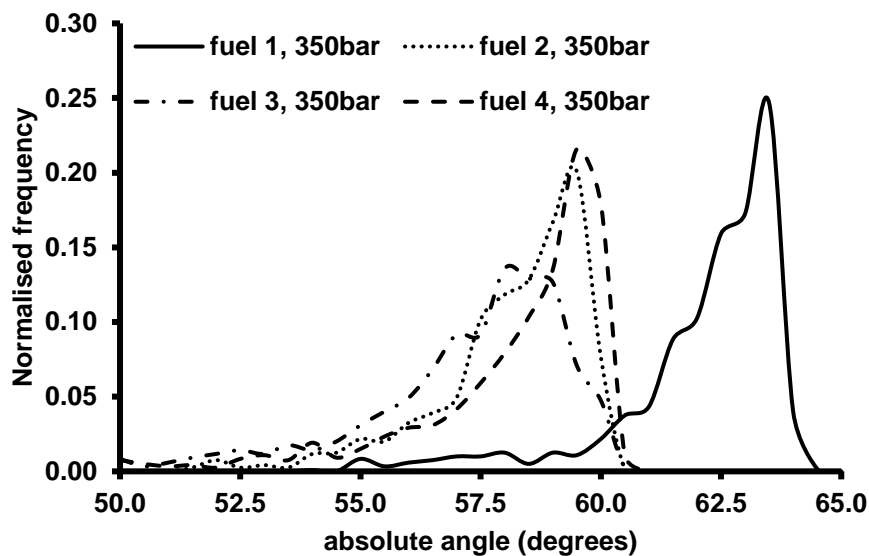
Figure 5.58: Flapping spray angle distributions obtained from fuel 1 to fuel 4 at 350bar.

The fuel sample 2 was the heaviest fuel amongst the fuels under consideration. In general, its higher viscosity suggested stronger stabilizing effects, which would oppose any instability, induced and would facilitate the formation of stable jets. It should be highlighted that fuel 2 had two simultaneous dynamics; the external aerodynamic instabilities and the instabilities induced by the flow distortion due to the cavitation inside the passage. The results shown in Figure 5.58 suggested that fuel 2 developed in a more unstable manner in relation to fuel 1, contradicting the expected behaviour. In particular, the mean absolute angle deviated from the nozzle hole angle measured from the magnified images by 6.5 degrees. This deviation suggested a strong instability induced in the developed sprays. Such an observation was also made in Chapter 5, where the mean SMD images of fuel 2 sprays exhibited a hint

of a swirling motion at the upper part of the spray, which was attributed to the retained vorticity of the flow.

Fuel 3 (gap diesel) at 350bar

The viscosity of fuel 3 was lower than fuel 1 by 25%, suggesting the formation of less stable sprays, due to the weaker stabilising effects of viscosity. The results presented in Figure 5.58 suggested that fuel 3 produced a wider distribution compared to fuel 1 and fuel 2. Such an observation implied that the fluctuation observed in the case of fuel 3 was greater, as a result of the increased turbulence levels. The mean absolute angle obtained from the distribution shown in Figure 5.58 was 57.8 degrees. The dominant flapping spray angle appeared to deviate from the hole angle measured from the magnified images by 3.2 degrees, suggesting a fairly strong spray fluctuation.

Fuel 4 (jet fuel) at 350bar

The results shown in Figure 5.58 suggested that fuel 4 had a similar behaviour to fuel 3, since they were the lightest fuels under investigation. The relatively low viscosity (weaker stabilising effects) of fuel 4 supported the increased spray fluctuation and the formation of unstable sprays. The distribution obtained from fuel 4 was wider in relation to fuels 1 and 2 and similar to fuel 3. The hole angle measured from the magnified images of the nozzles was 61 degrees, whereas the mean absolute spray angle was 58.1 degrees. This discrepancy suggested a strong spray fluctuation, greater than the one appeared in the case of fuel 1.

An optical observation of Figure 5.58 showed that the distributions obtained from fuel 1 at both rail pressures were shifted towards larger absolute angles compared to the rest of the fuels. This discrepancy could be attributed to the difference of the hole angles of the nozzles used. In particular, the hole angle difference between the nozzles used in the case of fuel 1 and fuel 2 was 4 degrees, while the difference between the nozzle used for fuels 3 and 4 was 3 degrees. An overview of the nozzle hole angles measured and the mean absolute spray angles is presented in Table 5.14.

External spray drop-sizing analysis using Laser Sheet Drop-sizing technique

Table 5.14: The actual nozzle passage angle measured from the magnified nozzle images and the mean absolute angle calculated based on the spray data.

Nozzle No.	Hole angle (measured)	Mean angle (calculated)
Noz.26 (fuel 1, 250bar/350bar)	62.5	62.5/62.1
Noz. 17 (fuel 2, 350bar)	65.0	58.5
Noz. 3 (fuels 3, 350bar)	61.0	57.8
Noz. 3 (fuels 4, 350bar)	61.0	58.1

Figure 5.59 shows the absolute spray angles after eliminating the effect of nozzle hole angles. In this case, the distributions highlighted the differences attributed to the physical properties of the fuels and the physics responsible for such trends.
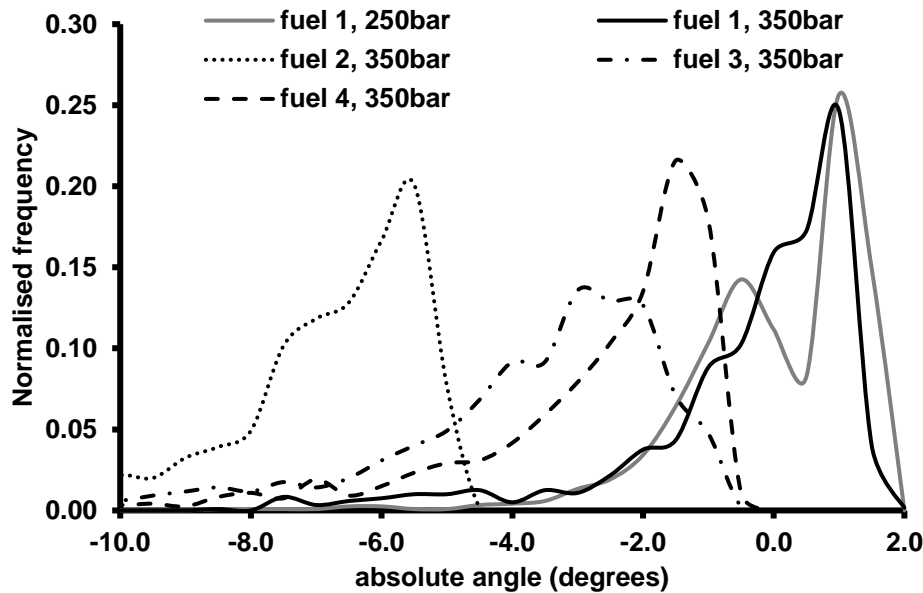
Figure 5.59: Flapping spray angle distributions obtained from fuel 1 at 250bar and fuel1 to fuel 4 at 350bar.

The negative values of the angles corresponded to an anti-clockwise displacement of the spray, while the positive values to a clockwise spray displacement. The mean values obtained from the distributions shown in Figure 5.59 represented the mean variation of the spray angle from the measured hole angle.

In particular, the mean values calculated for all cases were 0, -0.4, -6.5, -3.2 and -2.9 degrees. The results revealed that fuel 2 exhibited the largest deviation followed by fuels 3, 4 and 1. The large deviation (6.5 degrees) in the case of fuel 2 could be nozzle dependent (i.e. manufacturing imperfections) and related to the physical properties of the fuels. However, the results did not allow the identification of the root cause. On the contrary, the flapping angle deviation (between 0 and 3.2degrees) produced by the rest of the fuels showed an insignificant deviation.

Finally, the spray flapping observed was expected to affect the mean spray images. In particular, the distributions obtained from the mean images were shifted towards smaller SMD values. A way to overcome such an effect could be the separation of the frames in which the spray was located on the left and right hand side of the spray axis and the re-calculation of the mean images. This is part of the planned future work.

5.4 Comparison between the experimental mean drop-sizes and theoretical drop-sizes

The following analysis was devoted to the comparison of the experimental results obtained and the results obtained from an empirical relationship. Such a comparison aimed to correlate the present work to established relationships found in the literature. The empirical relationship used took into account the physical properties of the working fluid, the mass flow rate and the pressure differential in the nozzle orifice (Equation 5.5) and it could be applied only in the case of pressure atomisers. Equation 5.5 is the relationship reported by Lefebvre[32].

$$\overline{\text{SMD}} = 2.25 \sigma^{0.25} \mu_L^{0.25} \, \dot{m}_L^{0.25} \, \Delta P_L^{-0.5} \rho_{air}^{-0.25} \qquad \text{Equation 5.5}$$

where σ: surface tension (kg/s^2), μ_L: dynamic viscosity of the liquid phase (kg/ms), $\dot{m}_L$: mass flow rate (kg/s), ΔP_L: pressure differential in the orifice (Pa), ρ_{air}: density of air (kg/m^3)

The dynamic viscosity of the fuels was calculated at 45 degrees Celsius, since the temperature at the orifice was estimated around this value. The mass flow rate was measured as described in earlier chapters. The pressure differential was found from the pressure profiles acquired in each experimental test. It was observed that the pressure at the injector inlet was lower than the rail pressure by approximately 30bar. This pressure drop was a consequence of the needle movement, which allowed

the discharge of the fuel to the surrounding medium (ambient air). Lastly, due to lack of the surface tension data in the cases of fuel 1 to fuel 4, the surface tension values corresponding to fuel A to fuel E were utilised for both fuel sets. Table 5.15 shows the mean SMD droplets of the sprays produced by fuel A to fuel E and fuel 1 to fuel 4 at 350bar. The last column of Table 5.15 represented the mean relative SMD of the spray droplets based on the results presented in earlier chapters. For both sets of experimental fuels, the reference fuels were the un-additised diesel samples, fuels 1 and fuel A respectively.

Table 5.15: Mean SMD of the droplets produced by fuels A-E and fuels 1-4 at 350bar, based on the empirical relationship and the relative SMD values.

Fuel type	Mean SMD (equation 5.2), (μm)	Mean SMD based on relative SMD (μm)
Fuel A	12.07	12.07
Fuel B	11.79	12.88
Fuel C	11.37	11.87
Fuel D	11.08	8.65
Fuel E	12.61	8.25
Fuel 1	12.12	12.12
Fuel 2	11.90	9.30
Fuel 3	11.43	11.27
Fuel 4	9.73	11.83

An optical inspection of the results presented in Table 5.15 revealed that the empirical equation was unable to resolve the trends of the mean droplet sizes, since the difference between the mean drop sizes obtained from the different fuels appeared to be in the range of approximately 1-2μm. However, it was observed that in the case of Jeshani's experimental fuels (fuel A- fuel E) the results based on the relative SMD appeared to follow the same trend as the theoretical values, with an exception in the case of fuel E. On the other hand, the other fuel set appear to follow a different trend compared to the one suggested

by Lefebvre's formula. This could be attributed to the fuel additive added in the fuels 3 and 4, which has been suggested to alter the properties of the fuel during the execution of the experiments.

5.5 General discussion

The results obtained from the analysis discussed above suggested that the rail pressure, needle lift and fuel's physical properties played a significant role in the size of the spray droplets. It was shown that during the opening and closing phases of the needle the droplets were smaller relative to the maximum needle lift period. This could be attributed to the pronounced effect of cavitation and intensity of the turbulence developed during the early and late stages of the needle lift. Furthermore, an increase in rail pressure led to the formation of smaller droplets. It is known that a pressure increase enhances cavitation and turbulence. As a result, the jet disintegration into smaller droplets was promoted. In the case of Jeshani's results, the mean SMD value remained practically unchanged with increasing axial distance from the nozzle exit. This observation suggested that primary atomisation was less significant than secondary. It was believed that the secondary atomisation was the dominant break-up mechanism, as soon as the jet exited the nozzle passage. On the other hand, the results produced by the data of the author of the present thesis showed that the SMD of the spray droplets gradually decreased with increasing axial distance from the nozzle exit. This observation suggested that primary atomisation was more dominant in the vicinity of the nozzle exit, while secondary atomisation became more significant further downstream. A comparison between the two sets of fuels revealed that the mean SMD values were similar for fuels with similar physical properties, however their distributions were not quite similar. This could be attributed to several parameters, such as operating temperature, nozzle geometry etc. In particular, in the case of Jeshani's data the acrylic nozzles were handmade, hence it was expected to obtain surface irregularities and deviations from the design drawings. On the other hand, Makri's nozzle tips were manufactured using a CNC machine, therefore the resultant acrylic model was closer to the design specifications. Additionally, in the case of Makri's experiments the nozzle was illuminated by a laser beam which facilitated LIF measurements, while Jeshani used white light. The employment of laser increased the local temperature inside the nozzle which in turn possibly affected the fluid dynamics and properties (i.e. droplet size, viscosity, surface tension). Additionally, it should be noted

that the normalisation value used for the two sets of fuels was different. However, the mean SMD values obtained were fairly similar.

The physical properties of the fuels, i.e. viscosity and surface tension, appeared to play a critical role in the droplet size. It was shown that the SMD increased with increasing viscosity. Fuels with large viscosity tended to stabilize the fluid and opposed jet break-up mechanisms. The results based on Jeshani's data showed that the distributions of fuels C and E deviated from this trend. It was believed that this was a consequence of the additive added in fuel C and the dominance of surface tension during atomisation process in case of fuel E. Similar findings were obtained by Makri's results. The distributions obtained from fuels 2 and 4 deviated from this trend. It was believed that this was a consequence of the additive added in fuel 4 and the dominance of surface tension during atomisation process in case of fuel 2. Finally, all set of results revealed that the sprays developed in an asymmetric manner. The spray asymmetry observed was associated with the geometric cavitation formed inside the nozzle passages. On average, the larger spray droplets were found on the same side of the nozzle as where geometric cavitation structures appeared.

Finally, it should be mentioned that even though the timings of the needle lift (1.8ms, 3.7ms and 5.6ms after SoI) coincided in the analysis of Jeshani's and Makri's fuel sprays, the corresponding needle displacement was slightly different, due to the different lift rate. In Jeshani's sprays, the same needle lift was achieved 0.1-0.3ms earlier compared to Makri's sprays. A comparison between the sprays developed at the needle lift timings used for the purpose of this analysis and the timings where the same needle displacement was achieved showed negligible difference in terms of droplet size. Hence, the results obtained from both experiments were comparable to each other.

Chapter 6

Investigation of diesel jet structure using Laser Induced Fluorescence (LIF) technique

The following chapter was dedicated to the phenomenological analysis of the external diesel sprays as a function of the rail pressure, needle lift and physical properties of the fuels. The spray phenomenology referred to the investigation of the macroscopic features of the sprays, such as length of the liquid core, the LVF distributions along the spray axis and the processes related to them, i.e. primary atomisation. This work was compared to the results obtained by Faeth et al.[98]

For the purpose of this analysis, fuel A to fuel E (Jeshani's data) and fuel 1 to fuel 4 were tested at 250bar and 350bar. In order to keep the present work to a reasonable length, the dependence of the spray phenomenology on rail pressure and needle lift was performed for fuels A and 1 at three distinct phases of the needle lift (1.8ms, 3.8ms and 5.6ms after SoI) and both rail pressures. The results produced by the rest of the fuels corresponded to the spray developed at 3.8ms/3.7ms after SoI and 350bar. It should be noted that the experimental arrangement provided a field of view between 2.0mm and 18.0mm downstream of the nozzle exit.

6.1 Image processing methodology for the phenomenological analysis of the sprays

6.1.1 Phenomenological analysis of the external diesel sprays

The experiments involved the simultaneous capture of Mie and LIF signals on the same image, which were then split into two individual sets images, Mie and LIF images respectively. The present analysis was focused only on the LIF data. Initially, the data had to be corrected against the Gaussian profile of the laser, in order to eliminate any effects caused by the light sensitivity characteristics of every single pixel in the image. This image correction is known as image flat fielding. This is expressed mathematically in Equation 6.1.

Investigation of diesel jet structure using Laser Induced Fluorescence (LIF) technique

$$\text{LIF}_{ij,corr}^{klm} = \frac{\text{LIF}_{ij}^{klm} - \overline{\text{Bckg}_{ij}^{m}}}{\text{Gaussian laser profile} - \overline{\text{Bckg Gaussian laser profile}}} \qquad \text{Equation 6.1}$$

Indices i, j represented the row and column of the corresponding image under investigation. Index l referred to the injection event, while index k to the frame number within a set of 100 injections or 65 injections in case of fuels A, B, C, E and fuel D, respectively. Lastly, index m corresponded to the diesel fuel sample tested (A to E).

Additionally, the images obtained were also corrected against the fluorescent yield produced by the solutions of the reference fuels A and 1 with 1-Decanol, in the case of Jeshani's data and Makri's data respectively. Therefore, the data obtained from the rest of the fuels corresponding to the rest of the fuel solutions were divided by the corresponding calibration factor (see Table 3.6), such that the results become comparable to each other.

A set of instantaneous mean LIF images was obtained from $LIF_{ij,corr}^{klm}$ for a set of $l = 100$ injections in the case of fuels A, B, C and E and $l = 65$ injections in the case of fuel D. This involved the calculation of the mean images which were from obtained from image frames 1, 101, 201, … 9901; 2, 102, 202, …, 9902 and so on up to frame 100, 200, …, 10,000 for fuels A, B, C and E, and similarly frames 1, 101, 201, … 6401; 2, 102, 202, …, 6402 and so on up to frame 65, 165, 265, …, 6500 for fuel D.

Considering the main objective of this study regarding the determination of the Liquid Volume Fraction (LVF) of the diesel sprays, all spray data, regardless of fuel type or rail pressure, were normalised against the top 1% of the maximum pixel intensities found amongst all fuels at both rail pressures to obtain LVF values within the range of 0-1. The largest LVF signal was obtained by fuel B at 350bar; hence this value was utilised to normalise all spray data. The normalised value obtained provided direct information about the LVF across the length of the spray body. The experimental arrangement allowed a field of view of approximately 3mm to 17mm downstream from the nozzle exit.

6.1.2   Spray structure phenomenology

The phenomenological analysis performed is based on the work by Faeth et al[3] and refers to the determination of the length of the intact core and the location where primary atomisation occurs. They

Investigation of diesel jet structure using Laser Induced Fluorescence (LIF) technique

expressed mathematical expressions (Equation 6.2 and Equation 6.3) which attempted to quantify the parameters above, considering the physical properties of the injected fluid, the surrounding medium and the geometrical features of the nozzles.

$$\frac{x_i}{\Lambda} = C_{xt} \left(\frac{\overline{u_o}}{\overline{u_o'}} \right)^{9/5} We_{L\Lambda}^{-0.4} \xrightarrow{\text{emperical values}} \frac{x_i}{\Lambda} = 3890 We_{L\Lambda}^{-0.67}$$

$$\text{where } We_{L\Lambda} = \frac{\rho_L \Lambda \overline{u_o}^2}{\sigma}$$

Equation 6.2

where x_i: distance from the nozzle exit, Λ: radial spatial integral scale of turbulence, C_{xt}: constant of proportionality, $\frac{\overline{u_o}}{\overline{u_o'}}$: constant for fully developed turbulent pipe flow, $We_{f\Lambda}$: Weber number, ρ_L: density of the liquid, u_o: initial velocity, σ: surface tension

$$\frac{L_c}{d} = C_c \left(\frac{\rho_L}{\rho_G} \right)^{0.5}$$

Equation 6.3

where L_c: length of the intact core, d: nozzle hole diameter, C_c: constant related to the nozzle geometry, ρ_L, ρ_G: densities of liquid and gas.

The location where primary break-up occurred was estimated from the distance required for the critical size turbulent eddy to move from the jet exit and to form a droplet as a result of Rayleigh break-up applied to the protruding eddy-sized ligament; hence, the estimation of the radial spatial integral scale of turbulence (Λ) was essential and was found to be equal to one eighth of the diameter of the jet. The radial spatial integral scale of turbulence should be determined in the region before the onset of primary atomisation. In this experiment, primary atomisation was expected to occur in the vicinity of the nozzle exit (0-2mm downstream of the nozzle exit). However, the experimental arrangement facilitated a field of view between 2mm and 18mm downstream of the nozzle exit. Therefore, Λ was considered to be equal to the diameter of the nozzle passage (d~140μm).

6.1.3   Liquid Volume Fraction (LVF) distribution along the spray axis

The determination of the LVF distribution along the spray central axis was achieved utilising a Matlab code developed at City. The key parameter for an accurate LVF distribution was the precise definition of the spray central axis. Initially, a binary mask was applied onto the normalised mean LIF image to eliminate any scattering effects and/or artefacts from the surroundings of the spray. Then, the spray was rotated by 25 degrees such that it became vertical. The next step involved a row by row image scanning in order to initially detect and then remove pixels whose intensity was lower than 10% of the maximum pixel intensity in each row.

After the image thresholding, the code allowed the determination of the right and left extreme points of the top and bottom spray regions together with the middle points between the top left and right extreme points and the bottom left and right extreme points. The intermediate middle points between the top and bottom middle points were equal to the half of the radial distance between the right and left spray boundaries. The indices of the pixels corresponding to these middle points represented the local LVF. The top middle point corresponded to 18mm downstream of the nozzle exit, while the bottom middle point to 2mm. Then, the distance of the intermediate middle points was calculated taking into account the image resolution. Lastly, the local LVF values corresponding to the middle points were plotted against the increasing axial distance from the nozzle exit (2mm-18mm). The resultant graph represented the LVF distribution along the central axis of the emerging spray. All results and related graphs were exported into an excel worksheet.

6.1.4   Asymmetry of the diesel sprays

An optical observation of the raw images revealed a spray asymmetry. In order to investigate this observation into detail, eight LVF distributions were produced at 8 different regions of the diesel spray. These regions were: the right and left regions of the upper, middle and lower thirds of the sprays and the right and left hand side of the spray. This was achieved employing a Matlab code developed at City, which determined the spray central axis and split the spray into 6 equal segments. A binary mask was applied onto the images to eliminate any artefacts or scattering effects present around the main spray

structure. The obtained masked image was then scanned row by row to detect the pixels in which the intensity was equal to the 10% of the local maximum intensity found in each row; any value below the local low threshold was set to zero. Then, the code precisely calculated the middle points along the spray, determining the half of the radial distance between the right and left spray boundary in each row. Once the middle points were determined, the code fitted a linear curve (central line of the spray) to the mid-points, which had a R^2 value above 0.96. The code then split the spray body into three equal horizontal divisions, the upper, middle and lower segments. Each division was then divided into two equally spaced segments. Consequently, the spray was divided into six equal segments and the distribution of the spray droplet LVF was obtained for each segment. All data were exported into excel worksheets.

6.2   Results and Discussion

The following discussion was dedicated to the results obtained from the fuels tested by Jeshani and the new set of fuels tested by the present author. The results referred to the phenomenological analysis of the external spray as a function of the rail pressure, needle lift and the physical properties of the fuels. The dependence on rail pressure and needle lift was shown in the case of fuel A and fuel 1, which were investigated at both 250bar and 350bar during the opening/closing (1.8ms,5.6ms after SoI) needle phases and maximum needle lift (3.7ms, 3.8ms after SoI). The rest of the fuels referred to the sprays developed at 350bar and maximum needle lift. The two sets of fuels included equivalent fuels, whose results were comparable. However, the comparison was qualitative, since both data sets were normalised against different normalisation values. The actual values were not directly comparable, but the similarities in the trends obtained could be trusted.

6.2.1   Phenomenological analysis of fully developed diesel sprays

Table 6.1 summarises the results of the phenomenological study performed for fuels A to E and 1 to 4. The inspection of fuels A and 1 involved the examination of the sprays developed at 250bar and 350bar and different needle lift profiles. The rest of the fuels were investigated at 350bar and maximum needle lift. The analysis was focused on the spray developed between 0mm and 8mm downstream of the nozzle exit, since this region most likely contained the largest Liquid Volume Fraction (LVF); hence, primary

atomisation was expected to take place within this region. The results obtained showed that the onset of primary atomisation occurred at approximately 6 to 8 nozzle diameters downstream of the nozzle exit, depending on the operating conditions and fuel properties.

Table 6.1: Location of primary atomisation onset (mm) for fuels A to E and 1to 4.

Fuel type, rail pressure	Location of primary atomisation onset (mm)		
	1.8ms after SoI	3.7/3.8ms after SoI	5.6ms after SoI
Fuel A, 250bar	0.115	0.116	0.110
Fuel 1, 250bar	0.130	0.110	0.110
Fuel A, 350bar	0.090	0.091	0.089
Fuel 1, 350bar	0.110	0.09	0.110
Fuel B, 350bar	-	0.086	-
Fuel 3, 350bar	-	0.110	-
Fuel C, 350bar	-	0.089	-
Fuel D, 350bar	-	0.084	-
Fuel 4, 350bar	-	0.110	-
Fuel E, 350bar	-	0.081	-
Fuel 2, 350bar	-	0.120	-

The present analysis was compared with the results obtained from the work done by Faeth et al.[98]. The authors of this work did not take into account the effect of cavitation on atomisation process; they mostly focused on turbulence, flow instability and aerodynamic effects. Consequently, the results obtained over-estimated the length of the intact core and the location of the primary atomisation onset. It should be also noted that their experiments were performed on water sprays produced by an enlarged single hole nozzle, whereas the present work referred to diesel sprays produced by a real-sized, mini-sac type, 6-hole nozzle. More recent studies suggested that cavitation played a significant role in atomisation process[3,108]. Gulder and Smallwood[116] suggested that the liquid core did not exist more than

100 nozzle diameters downstream of the nozzle exit, due to intensive cavitation inside the nozzle geometry.

In the case of fuel A, diesel sprays produced at 250 bar, the onset of primary atomisation occurred at the furthest distance from the nozzle exit relative to fuels A, B, C, D and E at 350bar. This could be attributed to the difference in rail pressure. An increase in rail pressure was expected to enhance cavitation and turbulence, which in turn promoted the disintegration of the liquid spray body into smaller droplets. A comparison of the results obtained at different needle lift stages revealed that the axial distance of primary break-up onset at maximum lift was slightly larger relative the opening and closing phase of the needle. This was believed to be a consequence of the more pronounced effect of cavitation during the early and late stages of the needle lift. The results obtained from the rest of the fuels suggested that the distance of the primary breakup onset was almost independent of the fuel properties. It should be also noted that this was a qualitative analysis. The mean jet diameter, required for the calculations, was determined based on the mean images and interpolated values between 0mm and 3mm (the optical arrangement provided a field of view between 2mm and 17mm. The main objective of the present analysis was the comparison of the result obtained to earlier studies[98], which did not take into account the significance of cavitation in atomisation. In particular, Faeth et al.[98] suggested that primary atomisation occurred further downstream of the nozzle exit compared to the present results. It was believed that the main reason behind this result discrepancy was the presence of cavitation in the emerging diesel sprays. The highly cavitating flow accelerated the disintegration of the liquid spray body and ligaments into smaller droplets, not only when the fuel was injected into the surrounding gas, but also when it was still inside the nozzle passage. This statement was further supported by the short life time of the liquid spray core, as it is shown in the following subsections. In order for the results obtained to match with the results obtained from Equation 6.3, C constant should be a lot smaller relative to the values suggested by Faeth.[98]. The C constant suggested from the present calculations was approximately 0.15.

Similarly, the results corresponding to fuels 1, 2, 3 and 4 suggested that primary atomisation occurred within the first 0.13mm from the nozzle exit. Such an observation suggested intensive cavitation and/or

turbulence in the vicinity of the nozzle exit, which were responsible for the spray disintegration into large droplets and ligaments. Additionally, considering that the primary break-up occurred in a very short distance from the nozzle exit, it was believed that the dominant mechanism of jet disintegration from the first third of the spray up to its end was secondary atomisation. Hence, it was expected to observe a gradual decrease of LVF with increasing axial distance, which eventually became less evident after the first third of the spray. It was also shown showed that fuel 1 at 250bar exhibited a slightly later primary atomisation onset relative to 350bar, as a consequence of intensive cavitation. It was also observed the location of primary atomisation onset occurred approximately at the same distance from the nozzle exit regardless of the physical properties of the fuels.

6.2.2   Liquid Volume Fraction (LVF) distribution along the central axis of diesel sprays

The following analysis focused on the LVF distribution along a 3-pixel wide spray central axis. The experimental arrangement provided a field of view between 2mm and 17mm downstream of the nozzle exit. To keep this dissertation to a reasonable length, the pressure and needle lift dependence was shown only for fuels A and 1. The same analysis is planned to be carried out for the rest of the fuels and to be published in journal papers. The dependence of the LVF distribution obtained from the spray central axis as a function of the fuel's physical properties was presented for the rest of the fuel sprays produced at 350bar and at maximum needle lift.

6.2.2.1 **LVF distribution along the spray axis as a function of rail pressure and needle lift**

Figure 6.1 and Figure 6.2 show the LVF distributions along the spray central axis as a function of the axial distance from the nozzle exit captured at 1.8ms, 3.7ms and 5.6ms after SoI in the case of fuel A sprays at 250bar (black colour) and 350bar (grey colour) respectively. In both figures, the solid, dotted and dashed lines corresponded to the data captured at 1.8ms, 3.7ms and 5.6ms after SoI respectively.

Figure 6.1 demonstrated that the maximum LVF of the sprays developed at different needle lift approximately ranged between 0.65 and 0.85, suggesting that there were no purely liquid structures, even in the vicinity of the nozzle exit. The yellow, green and red error bars corresponded to the measurements taken at 1.8ms, 3.7ms and 5.6ms after the SoI respectively. The results obtained at 3.7ms

(green error bars) exhibited the largest variation, particularly in the vicinity of the nozzle exit, followed by 5.6ms and 1.8ms after the SoI results. It was believed both primary and secondary atomisation were taking place at this region, giving rise to the formation of smaller droplets and the disintegration of the larger droplets or fuel ligaments. Further downstream, the main breakup mechanism was secondary atomisation which led to the formation of droplets with fairly similar LVF. This possibly explained the smaller error bars with increasing axial distance.
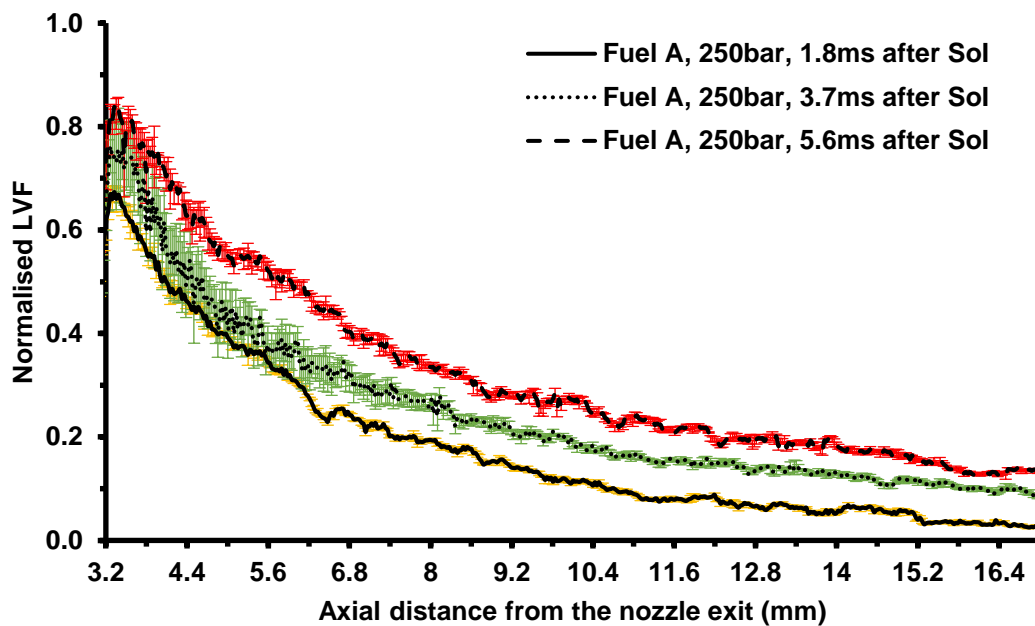
Figure 6.1: LVF distribution along the fuel A spray central axis produced at 250bar as a function of needle lift.

The maximum LVF along the spray axis was reached at approximately 3.6mm downstream of the nozzle exit, while the minimum at 17mm. In all three cases, the decay rate of the LVF was quite fast up to approximately 11mm and then it slowed down significantly. It was believed that in the vicinity of the nozzle exit, both primary and secondary atomisation mechanisms were responsible for the disintegration of the emerging jet into droplets, while further downstream secondary atomisation became the dominant mechanism, leading to smaller LVF values. The LVF values below 1.0 together with the fast decay of LVF observed close to the nozzle exit suggested that the liquid core did not survive up to 3mm; it was either destroyed between the distance (0mm-3mm), which was out from the

field of view or never exited the nozzle, due to intensive cavitation inside the nozzle passage. Lastly, a comparison of the LVF profiles obtained at different needle lift revealed that the maximum LVF values were obtained during the maximum needle lift and the closing phase of the needle. The lower LVF value in the case of 1.8ms after SoI could be attributed to the intense cavitation phenomena; needle sheet cavitation and string cavitation structures.

Figure 6.2 shows the LVF distributions produced at 350bar along the spray axis. The yellow, green and red error bars corresponded to the measurements taken at 1.8ms, 3.7ms and 5.6ms after the SoI respectively. The results obtained at 3.7ms (green error bars) exhibited the largest variation, particularly in the vicinity of the nozzle exit, followed by 5.6ms and 1.8ms after the SoI results.
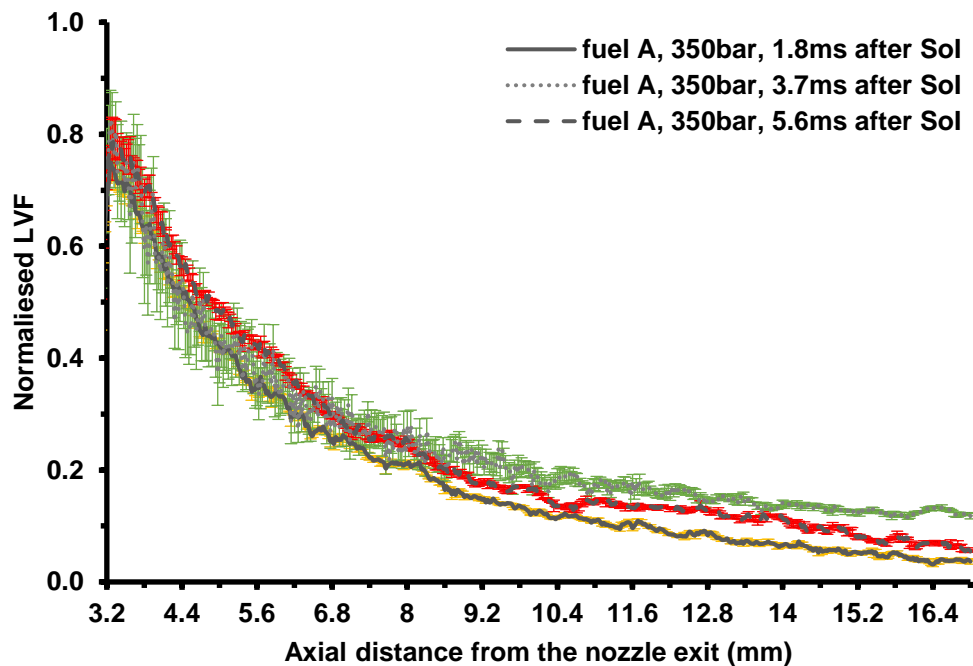
Figure 6.2: LVF distribution along the fuel A spray central axis produced at 350bar as a function of needle lift.

The maximum LVF values obtained in all three cases approximately ranged between 0.75 and 0.81, and rapidly decayed with increasing axial distance, with approximately the same rate. However, in the case of 3.7ms after SoI, the curve reached a plateau approximately between 3.2mm and 4.1 mm downstream of the nozzle exit, suggesting the existence of a liquid core. The fast decay of LVF values in all cases could be attributed to intensive cavitation and turbulence. Additionally, it was observed that there was

no significant difference between the LVF spray axis profiles obtained at 1.8ms, 3.7ms and 5.6ms after SoI. Such an observation suggested that the dominant mechanism throughout an injection event was secondary atomisation. Lastly, comparing the profiles of each time event obtained at 250bar and 350bar, it could be argued that an increase in rail pressure led to the development of more stable sprays throughout the injection, resulting in no significant differences between the different needle lifts. Overall, the LVF distributions at both rail pressures followed the same trend, with an exception in the case of 3.7ms after SoI at 350bar.

Figure 6.3 and Figure 6.4 showed the LVF profile of the central axis of fuel 1 sprays developed at 1.8ms (solid line), 3.8ms (dashed line) and 5.6ms (dotted line) after SoI and at 250bar (black colour) and 350bar (grey colour) respectively. The yellow, green and red error bars corresponded to the measurements taken at 1.8ms, 3.7ms and 5.6ms after the SoI respectively. The results obtained at 3.7ms (green error bars) exhibited the largest variation, particularly in the vicinity of the nozzle exit, followed by 5.6ms and 1.8ms after the SoI results. The jet break-up at this region was believed to be a result of both primary and secondary atomisation, which led to the formation of smaller droplets of lower LVF and the disintegration of the larger droplets or fuel ligaments with relatively high LVF. Further downstream, the main breakup mechanism was secondary atomisation which led to the formation of droplets with fairly similar LVF. This possibly explained the smaller error bars with increasing axial distance.

An optical observation of both figures revealed that the decay rate of LVF was faster in the case of 1.8ms after SoI relative, whereas at 3.8ms after SoI the slowest. The LVF profile corresponding to 5.6ms appeared to be closer to the profile of 1.8ms. Such observations implied that during the opening and closing phased of the needle, the flow dynamics developed differed from the dynamics at the maximum needle lift. It was suggested that cavitation effects were stronger when the needle was close to its sealing position. Therefore, greater and faster jet disintegration was expected to occur during the early and late stages of the needle lift.
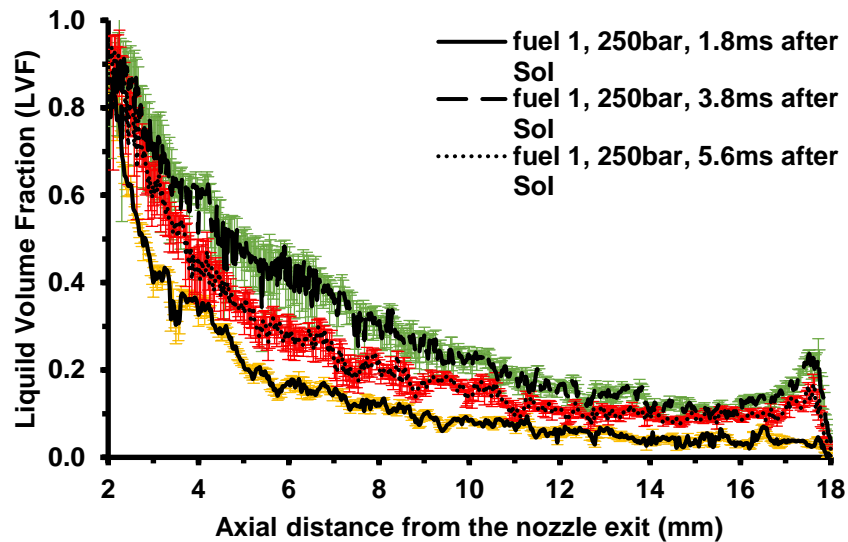
Figure 6.3: LVF distribution along the central axis of fuel1 spray at 1.8ms, 3.6ms and 5.6ms after SoI, 250bar.
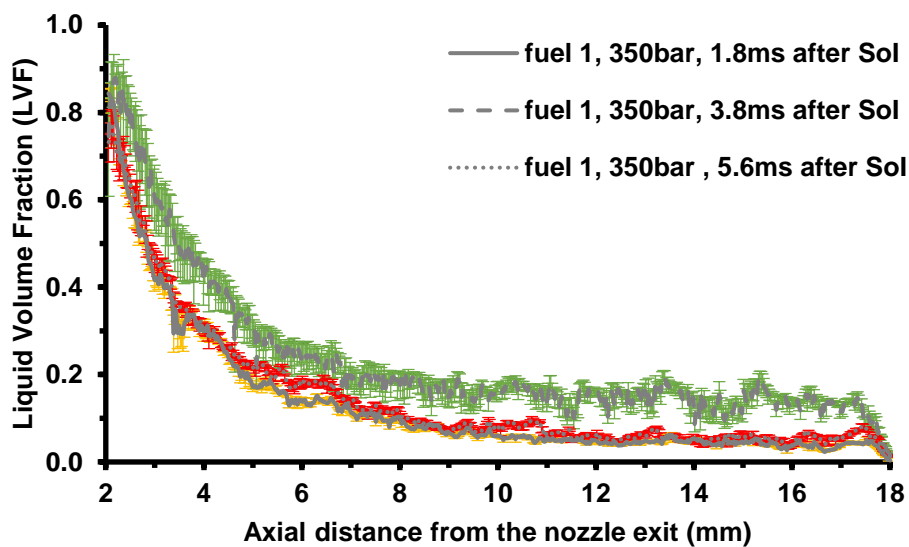
Figure 6.4: LVF distribution along the central axis of fuel 1 spray at 1.8ms, 3.6ms and 5.6ms after SoI after SoI, 350bar.

However, the rate difference described was less apparent in the case of 350bar, implying that cavitation and/or turbulence was stronger (faster decay rates) than 250bar and its intensity did not change significantly throughout an injection event. Additionally, it was observed that in case of 350bar, the LVF values at ~18mm downstream of the nozzle exit were smaller than 250bar. This was a consequence

of the rail pressure increase, which led to efficient atomisation process. Lastly, the results demonstrated that the existence of a liquid core was unlike, since the LVF continuously dropped with increasing axial distance. Such an observation suggested that the liquid core was destroyed either between the distance that is not captured by the images (0mm-2mm) or inside the nozzle passages, possibly due to intensive cavitation and turbulence. However, in the case of 1.8ms after SoI at 250bar (Figure 6.3) the LVF profile reached a plateau between approximately 2.7mm and 3.2mm suggesting the existence of a liquid core. This could be attributed to the relatively low rail pressure which in turn led to weaker cavitation and consequently poorer atomisation.

6.2.2.2 **LVF distributions along the spray axis as a function of fuel's physical properties**

Figure 6.5 shows the LVF distributions along the central axis of sprays produced by fuels B, C, D and E at 350bar and at maximum needle lift (3.7ms after SoI). The solid, dash followed by dot, dashed and dotted lines referred to fuel B, C, D and E respectively. The orange, yellow, green and red error bars correspond to the uncertainty of the LVF measurements obtained by fuels B, C, D and E respectively. It was shown that the error induced in the LVF measurements was fairly low in all the cases. In the vicinity of the nozzle exit the uncertainty induced appeared to be larger compared to further downstream. It was believed that in the region close to the nozzle exit the spray atomisation was the synergy between primary and secondary atomisation, which led to the formation of droplets of smaller and larger LVF. However, the uncertainty of the measurements with increasing axial distance appeared to gradually decrease. This can be attributed to the dominance of secondary atomisation which led to the formation of droplets of uniform LVF. The maximum LVF values appeared to approximately range between 0.51 and 0.98 depending on the fuel's physical properties. In all four cases, LVF appeared to decrease with increasing axial distance; their decay rate seemed to be dependent on the physical properties.

Investigation of diesel jet structure using Laser Induced Fluorescence (LIF) technique
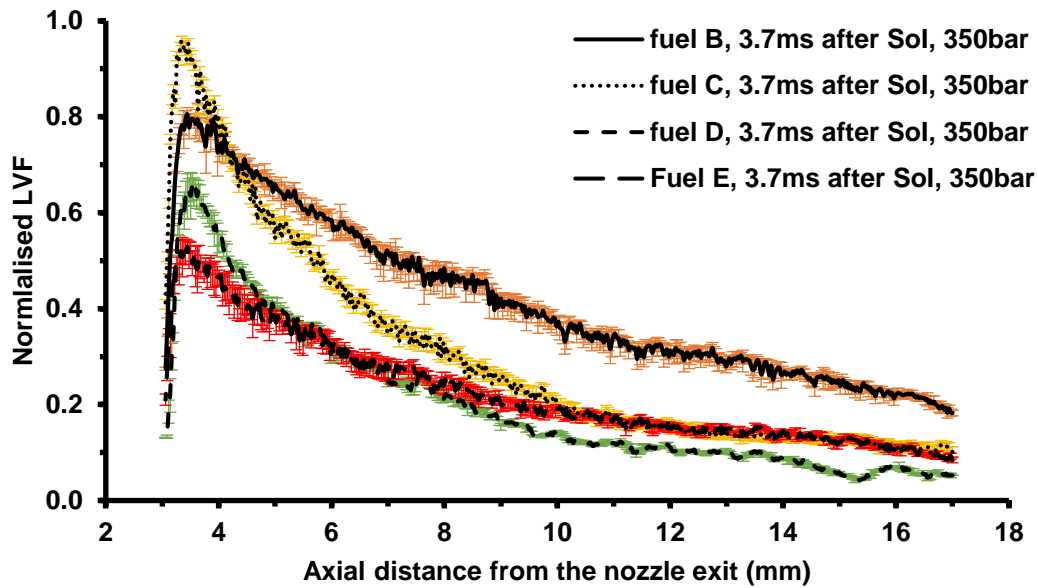
Figure 6.5: LVF distributions along the spray axis obtained from fuels B-E at 350bar (3.7ms after SoI).

In the case of fuel B (gap diesel), the higher LVF value obtained was approximately 0.79 at an axial distance of approximately 3.5mm. The central axis LVF profile suggested that between 3.5mm and 4.4mm downstream the nozzle exit the LVF remained the same, suggesting the existence of a liquid core. Between 4.4mm and 17.0mm the LVF appeared to gradually decrease with increasing axial distance, as a consequence of secondary atomisation. The overall decrease in LVF was about 75% from approximately 0.79 to 0.2. The decay rate appeared to be slower relative to fuels A, C, D and E. This could be attributed to its fairly large viscosity and surface tension which oppose break-up phenomena.

Fuel C was the second lightest fuel under inspection. Considering its relatively low viscosity and surface tension, it was expected to obtain a maximum LVF value lower than fuel A and B. However, the corresponding central axis LVF profile shown in Figure 6.5 indicated that in the vicinity of the nozzle exit fuel C had a maximum LVF value of approximately 0.98, suggesting the existence of liquid structures (~3.4mm downstream of the nozzle exit). However, fuel C exhibited a much faster decay rate relative to the rest of the fuels. This is believed to be a consequence of the fairly small viscosity and surface tension, which opposed breakup phenomena less. The LVF decrease observed was approximately 85%, implying pronounced secondary atomisation. Overall, fuel C exhibited an odd behaviour; the followed trend had some expected and unexpected features, such as fast decay rate and

highest maximum LVF value respectively. Fuel C was a blend of kerosene with a lubricity additive. In earlier chapters, it was suggested that the ester-based additive created a non-Newtonian flow with viscoelastic properties. As a result, the viscosity of the fuel was altered during the execution of the experiments, leading to this unexpected trend.

Fuel D is the lightest fuel under investigation; hence it was expected to obtain a faster LVF decay rate relative to the heavier fuels, i.e. fuel A and fuel B as well as a lower initial LVF value. The LVF profile shown in Figure 6.5 demonstrated that the maximum LVF of fuel D was approximately 0.66 at around 3.5mm downstream the nozzle exit, ~15% less than fuel A and fuel B. It was also observed that the LVF rapidly decayed with increasing axial distance, implying dominant secondary atomisation effects. The pronounced effects of secondary atomisation were believed to be a consequence of the intensive cavitation in comparison to the heavier fuels. The overall decrease in LVF along the spray body was approximately 88%, from ~0.66 to ~0.08. The differences between the profiles of fuel D and fuels A, B could be attributed to the much lower viscosity and surface tension of fuel D, which led to earlier primary and secondary atomisation relative to the heavier fuels.

The last fuel under investigation was fuel E, which was a B20 diesel blend. The oxygenated compounds of FAME possibly undergo reactions with RhB dissolved in 1-Decanol. The results obtained were corrected with the corresponding fluorescent yield calibration factor to minimise any quenching effects. However, it was shown that fuel E produced the smallest droplets amongst the fuels under investigation. The same observation was made for the LVF distribution along the central axis produced by fuel E. In Figure 6.5, it is shown that the initial LVF value of fuel E profile was approximately around 0.53, which oddly enough was the lowest amongst all fuels. Considering that fuel E had the highest viscosity and surface tension, it was expected to obtain a smaller decrease in LVF with increasing axial distance from the nozzle exit relative to the lighter fuels (i.e. fuel D). Indeed, the overall LVF decrease was approximately 76%, similar to fuels A and B. In earlier chapters, it was stated that the circumferential in-sac flow could possibly separate the heavier from the lighter components of fuel E; this could possibly explain the odd trend presented in the present work. The heavier components could potentially

be responsible for the expected slow decay rate of LVF with increasing axial distance, whereas the lighter could cause the fairly low LVF value in the vicinity of the nozzle exit.

Figure 6.6 showed the normalised projections of the normalised frequency LVF histograms obtained from fuel sprays 2 (solid line), 3 (dashed line) and 4 (dotted line) at 3.8ms after SoI, 350bar. The orange, red and green error bars corresponded to the uncertainty of the LVF measurements obtained by fuels 2, 3 and 4 respectively. It was shown that the error induced in the LVF measurements was fairly low in all the cases. The largest STD values were obtained in the region close the nozzle exit. This was believed to be a consequence of the synergy between primary and secondary atomisation for the formation of droplets with both low and relatively large LVF. Further downstream, the STD appeared to be fairly low and uniform, possibly due to the dominance of secondary atomisation (formation of droplets with uniform LVF).
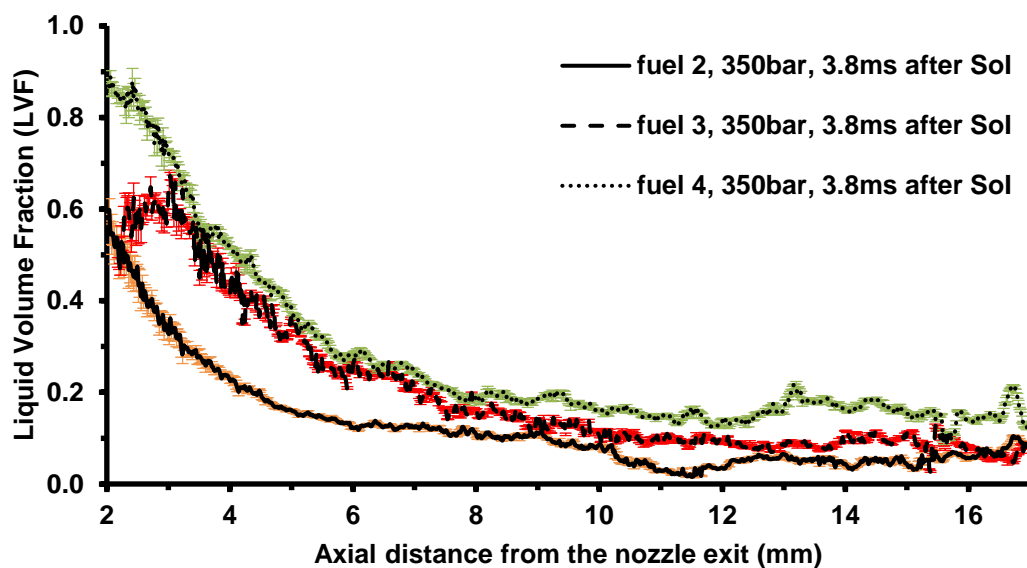
Figure 6.6: LVF distributions along the central axis of fuel sprays 2, 3 and 4 at 3.8ms after SoI, 350bar.

In general, heavier fuels have the tendency to cavitate less than lighter fuels. Consequently, the atomisation process was expected to be poorer resulting in larger LVF. Oddly enough, the LVF profile of fuel 2 (heaviest fuel under consideration) appeared to exhibit the lower LVF, even though the spray data have been corrected with the corresponding fluorescent yield calibration factor, which eliminated the quenching effects caused by the interaction of RhB molecules with the oxygenated compounds of

FAME. The reason behind this anomalous trend is unknown and requires further investigation. However, the trend obtained matched with the expected behaviour. In more detail, it could be seen that between 2.3mm and 3.8mm the LVF reached a plateau suggesting the existence of a liquid core, due to less intensive cavitation and consequently poorer atomisation.

Fuel 3 (gap diesel) produced an LVF profile, which indicated the absence of a liquid core since the LVF continuously dropped with increasing axial distance from the nozzle exit. The lower viscosity of fuel 3 relative to fuel 1 and 2 justified the faster decay rate of LVF observed. The initial LVF value of fuel 1 at 3.8ms after SoI, 350bar approximately reached 0.9 while fuel 3 was 0.8. This difference could be attributed to the lower viscosity of fuel 3, which opposed break-up phenomena less and promoted the disintegration of the jet.

Finally, fuel 4 (jet fuel + lubricity additive) was the lightest fuel under consideration. Considering its low viscosity, the spray was expected to develop intensive cavitation, which led to enhanced atomisation and consequently to lower LVF. The LVF profile of fuel 4 shown in Figure 6.6 appeared to deviate significantly from the expected trend. It seemed that fuel 4 produced a LVF profile similar to fuel 1, whose viscosity was larger by approximately 56%. In earlier chapters, it has been suggested that the lubricity additive present in fuel 4 introduced a non-Newtonian behaviour and viscoelastic properties. In such case, the viscosity of the fuel was expected to change in an unpredictable manner during the execution of the experiments. This behaviour potentially explained the odd behaviour of fuel 4. It should be also noted that fuel 4 exhibited a fast decay rate of LVF with increasing axial distance, suggesting the gradual dominance of secondary atomisation. It could be also observed that the LVF continuously dropped from approximately 0.88 to 0.2, suggesting that the existence of a liquid core was unlike, due to intensive cavitation, which destroyed the core either between 0.0mm and 2.0mm downstream of the nozzle exit or inside the nozzle passage.

6.2.3   LVF distribution across diesel sprays as a function of rail pressure and needle lift

The discussion presented in Chapter 5 suggested that all fuel sprays developed in an asymmetric manner. The following analysis investigated whether the observed asymmetry arose from the LIF spray signal. To keep this dissertation to a reasonable length, the dependence of LVF distribution on the rail pressure and needle lift was performed only for fuel 1 and fuel A at 1.8ms, 3.8ms and 5.6ms after SoI at 250bar and 350bar. The spray asymmetry was examined by producing the LVF distribution of six distinct spray segments; the right and left-hand side of the upper, middle and lower spray divisions.

<u>1.8ms after SoI</u>

Figure 6.7, Figure 6.8 show the projections of the normalised LVF histograms obtained from the right (black) and left (grey) hand sides of the upper (solid line), middle (dotted line) and lower (dashed line) segments of fuel spray A at 250bar and 350bar during the opening phase of the needle (1.8ms after SoI) respectively. The obtained LVF values ranged between 0.0 and 1.0 and were distributed in a hundred bins. The frequency normalisation was done against the total number of pixels of each segment; hence the area under each curve was equal to 1.

Figure 6.7: LVF distributions of the upper, middle and lower spray segments produced by fuel A at 250bar (1.8ms after SoI).

Figure 6.8: LVF distributions of the upper, middle and lower spray segments produced by fuel A at 350bar (1.8ms after SoI).

Both figures demonstrated that the LVF of the spray decreased with increasing axial distance from the nozzle exit. Such a trend was expected, since the spray was denser in the vicinity of nozzle exit, while further downstream it disintegrated into smaller droplets, due to pronounced effects of secondary atomisation. Furthermore, a visual comparison of the distributions obtained from the three segments revealed that the LVF distributuions of the lower segments were wider that the middle and lower ones. This was believed to be a consequence of the larger population of liquid ligaments close to the nozzle exit. On the other hand, at the middle and upper regions, the spray appeared to be better atomised, due to secondary atomisation. The comparison between the left and right hand side distributions shown in both figures suggested that the spray developed in a fairly asymmetric manner. This observation could be also made by comparing the mean LVF values of each distribution at both pressures. Table 6.2 summarises the mean LVF values obtained from all distributions at both rail pressures. The left hand side of the spray contained slightly larger LVF values that the right hand, suggesting a small asymmetry to the left hand side of the spray.

Table 6.2: Mean relative LVF values obtained from fuel A sprays at 250bar, 350bar (1.8ms after SoI).

	Mean LVF values (1.8ms after SoI)					
	Upper segment		Middle segment		Lower segment	
	left	right	left	right	left	right
250bar	0.035	0.033	0.090	0.072	0.240	0.220
350bar	0.045	0.046	0.090	0.084	0.240	0.220

Figure 6.9 and Figure 6.10 showed the normalised projection of the LVF distributions obtained from the right (grey colour) and left-hand (black colour) side of the upper (solid line), middle (dotted line) and lower (dashed lines) segments of fuel 1 at 1.8ms after SoI at 250bar and 350bar respectively.

Figure 6.9: LVF distributions obtained from the upper, middle and lower segments of fuel 1 at 1.8ms after SoI, 250bar.

Figure 6.10: LVF distributions obtained from the upper, middle and lower segments of fuel 1 at 1.8ms after SoI, 350bar.

Both figures demonstrated that the LVF of the spray decreased with increasing axial distance from the nozzle exit. This finding suggested that the spray was denser in the vicinity of the nozzle exit, while further downstream it became more dispersed, due to pronounced effects of secondary atomization. It is also shown that in the vicinity of the nozzle exit, the LVF distributions obtained were wider than the middle and upper segments. This was a consequence of the larger population of liquid ligaments (large LVF), due to dominant primary atomization. On the contrary, further downstream, the atomised spray was a result of the dominant secondary atomisation; the resultant smaller droplets had a lower LVF value. The comparison of the left-hand side and the right-hand side distributions appeared to be fairly similar to each other, suggesting that the spray developed in a quite symmetric manner.

However, the mean LVF of the distributions shown in Table 6.3 suggested that the right-hand side of the spray contained droplets of slightly higher LVF, suggesting a spray asymmetry. Lastly, it was also observed that the distributions produced by fuel 1 sprays at 350bar are marginally shifted towards smaller LVF values, as a consequence of stronger cavitation and turbulence, due to the pressure increase.

Table 6.3: Mean LVF obtained from the upper, middle and lower segments of fuel 1 at 1.8ms after SoI, 250bar.

Fuel type	Mean LVF at 1.8ms after SoI					
	Upper segment		Middle segment		Lower segment	
	Right	Left	Right	Left	Right	Left
Fuel 1, 250bar	0.022	0.034	0.043	0.059	0.160	0.180
Fuel 1, 350bar	0.026	0.029	0.036	0.043	0.136	0.157

3.7-3.8ms after SoI

Figure 6.11 and Figure 6.12 show the normalised frequency LVF distributions obtained at from the right and left hand sides of the upper, middle and lower segments of fuel spray A at 250bar and 350bar during the phase of the maximum needle lift (3.7ms after SoI) respectively. The various line styles and colours retained their meaning as defined above.
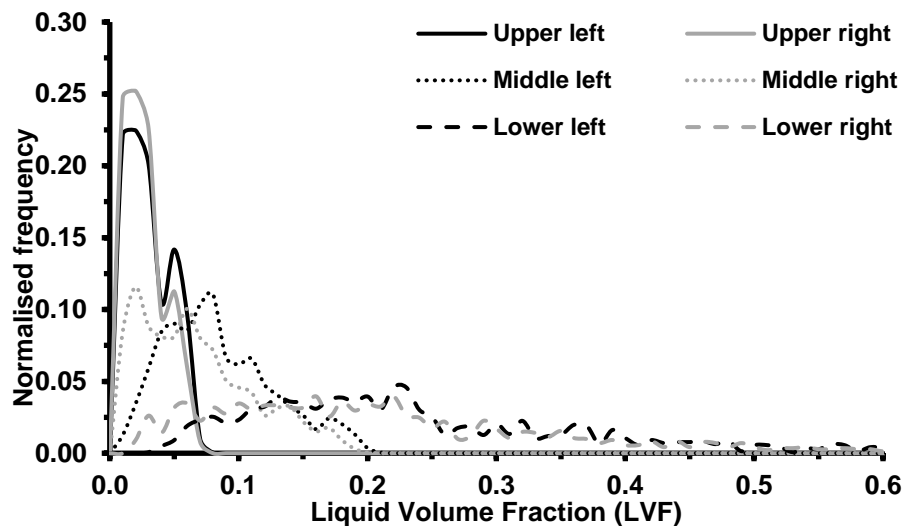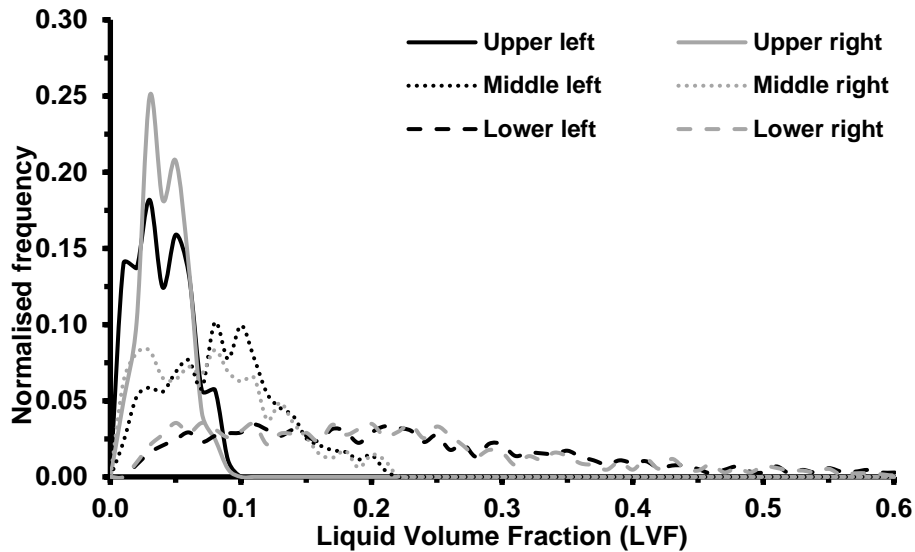

Figure 6.11: LVF distributions of the upper, middle and lower spray segments produced by fuel A at 250bar (3.7ms after SoI).

Figure 6.12: LVF distributions of the upper, middle and lower spray segments produced by fuel A at 350bar (3.7ms after SoI).

A comparison between the right and left hand distributions shown in both figures revealed that the right hand side of the sprays developed at both pressures were quite asymmetric, especially in the case of the middle and lower segments, where the right hand side distributions were significatly shifted towards larger values relative to the left hand side. The asymmetry observed was believed to be a consequence of the geometric cavitation appearing at the same side inside the nozzle hole entrance. Table 6.4 summarises the mean LVF values of all distributions shown in both graphs. Additionally, it could be argued that 250bar sprays produced larger LVF values than 350bar. An increase in pressure enhanced cavitation and turbulence resulting in better atomisation.

Table 6.4: Mean relative LVF values obtained from fuel A sprays at 250bar, 350bar (3.7ms after SoI).

	Mean LVF values (3.7ms after SoI)					
	Upper segment		Middle segment		Lower segment	
	left	right	left	right	left	right
250bar	0.090	0.081	0.132	0.145	0.246	0.320
350bar	0.086	0.110	0.119	0.169	0.206	0.353

Investigation of diesel jet structure using Laser Induced Fluorescence (LIF) technique

An optical observation of Figure 6.11 and Figure 6.12 suggested that the lower segments of the spray produced a wider distribution relative to the other spray segments, due to the increased population of liquid ligaments in the vicinity of the nozzle exit. It was also observed that the mean LVF values decrease with increasing axial distance, as a result of pronounced secondary atomisation. Overall, it could be argued that all distribution obtained at 3.7ms after SoI were shifted towards larger LVF values relative to 1.8ms, suggesting that lower needle lift led to smaller LVF, due to intensive cavitation phenomena.

Figure 6.13 and Figure 6.14 showed the normalised LVF distributions obtained from fuel 1 sprays at 350bar during the maximum needle lift phase (3.8ms after SoI). The various line styles and colours retained their meaning as defined above.
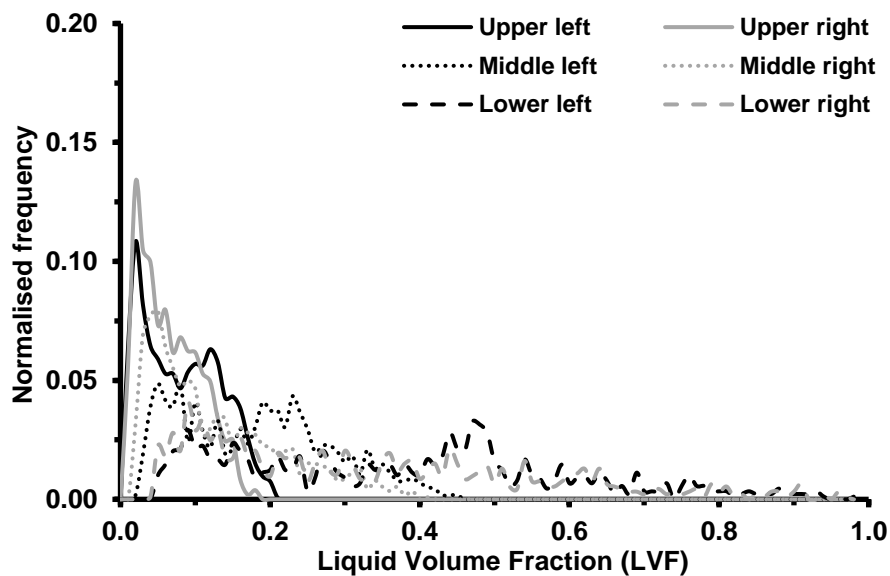
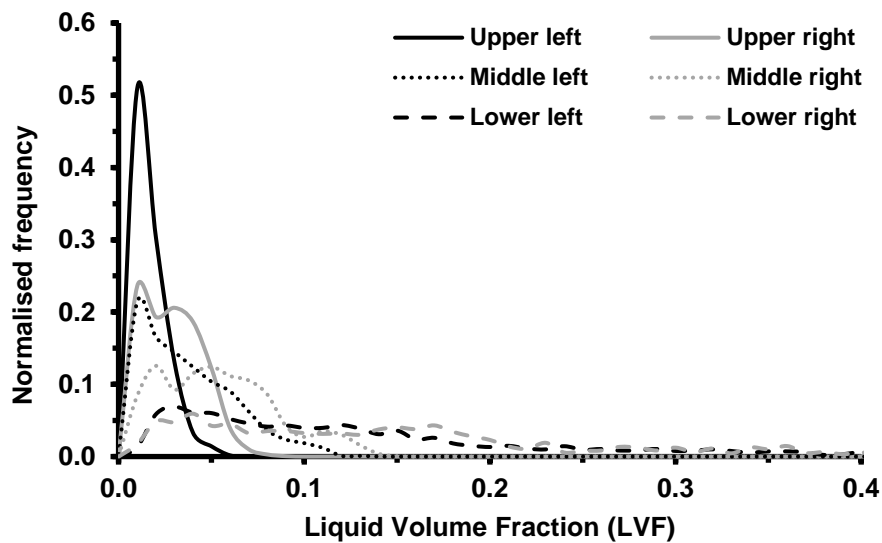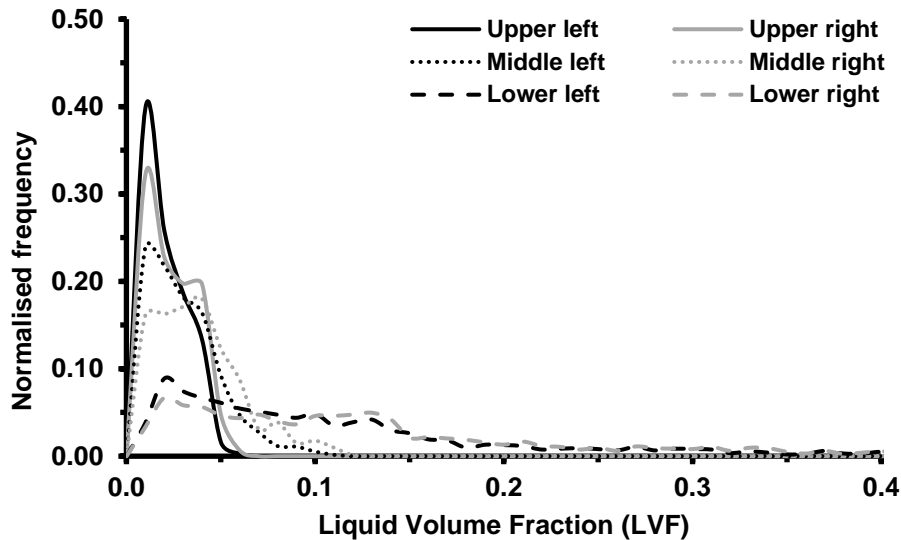Figure 6.13:LVF distributions obtained from the upper, middle and lower segments of fuel 1 at 3.8ms after SoI, 250bar.
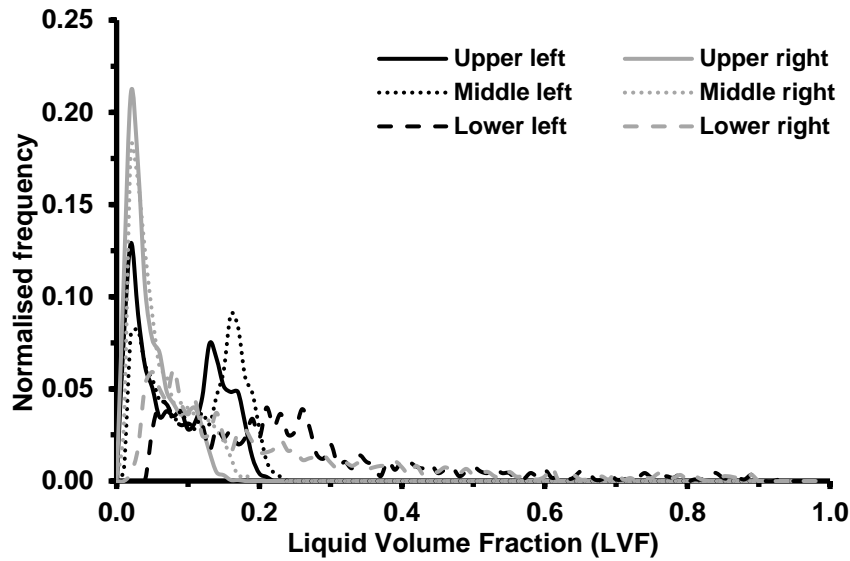
Figure 6.14: LVF distributions obtained from the upper, middle and lower segments of fuel 1 at 3.8ms after SoI, 350bar.

A visual comparison of the left-hand and the right-hand side of the spray in all three cases (lower, middle, upper segments) suggested that the sprays have developed in an asymmetric manner. In particular, the left-hand side distributions contained droplets of larger LVF values relative to the left-hand side of the spray at all segments at both rail pressures, implying a spray asymmetry. It has been suggested that the spray asymmetry observed was a consequence of the flow asymmetry developed by geometric cavitation. On average, the droplet of higher LVF appeared on the same side, as where geometric cavitation formed in the nozzle passage. The overall distributions shown in both figures suggested that the larger LVF values were present close to the nozzle exit, resulting to broader distributions than the middle and upper segments, indicating stronger primary atomisation effects. According to the results shown in Table 6.5, the spray droplets LVF appeared to gradually decrease with increasing rail pressure, due to pronounced secondary atomisation.

Finally, a visual comparison of Figure 6.13 and Figure 6.14 revealed that the distributions obtained at 350bar were shifted towards smaller LVF values. This could be attributed to the rail pressure increase that enhanced atomisation process and subsequently led to the formation of finer spray droplets of lower LVF.

Table 6.5: Mean LVF obtained from the upper, middle and lower segments of fuel 1 at 3.8ms after SoI, 350bar.

| Fuel type | Mean LVF at 3.8ms after SoI | | | | | |
| | Upper segment | | Middle segment | | Lower segment | |
	Right	Left	Right	Left	Right	Left
Fuel 1, 250bar	0.087	0.071	0.187	0.133	0.383	0.336
Fuel 1, 350bar	0.091	0.053	0.114	0.065	0.261	0.216

<u>5.6ms after SoI</u>

Figure 6.15 and Figure 6.16 show the the projections of the normalised LVF histograms obtained from the right and left hand sides of the upper, middle and lower segments of fuel spray A at 250bar and 350bar during the closing phase of the needle (5.6ms after SoI) respectively. The various line styles and colours retained their meaning as described above.
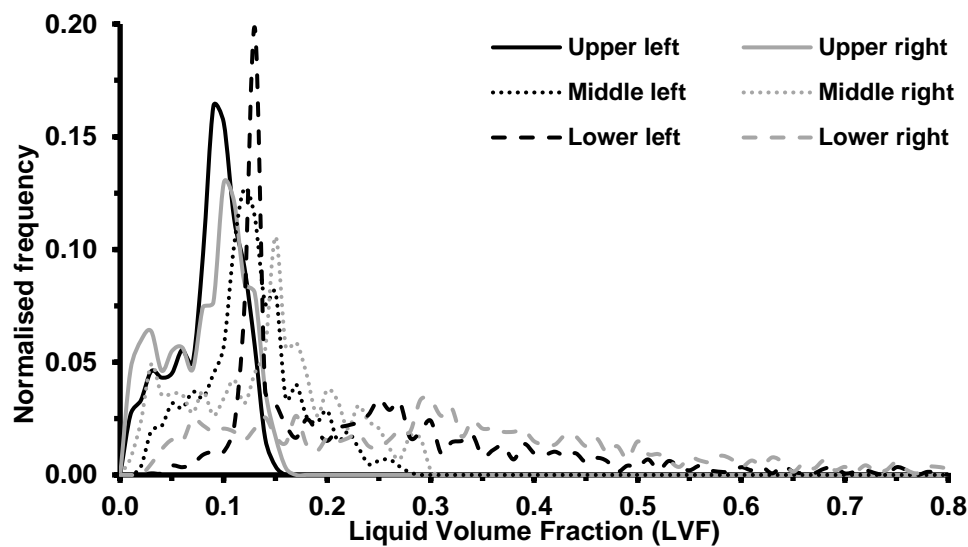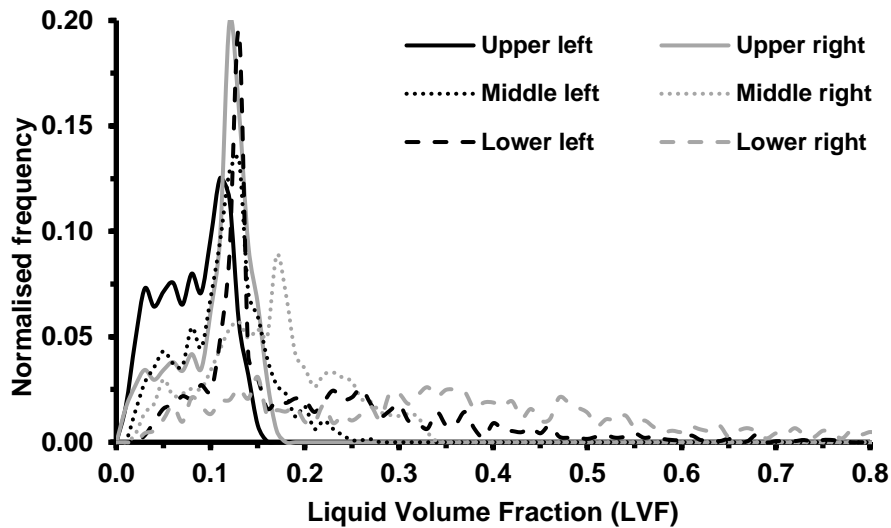

Figure 6.15: LVF distributions of the upper, middle and lower spray segments produced by fuel A at 250bar (5.6ms after SoI).

Figure 6.16: LVF distributions of the upper, middle and lower spray segments produced by fuel A at 350bar (5.6ms after SoI).

The distributions shown in both figures suggested that the sprays developed in a quite symmetric manner, since the distributions of the right and left hand side segments overlapped each other; the mean values of each segment obtained were similar to each other. Table 6.6 summarises the mean LVF values of all distributions shown in both figures.

Table 6.6: Mean relative LVF values obtained from fuel A sprays at 250bar, 350 bar (5.6ms after SoI).

	Mean LVF values (5.6ms after SoI)					
	Upper segment		Middle segment		Lower segment	
	left	right	left	right	left	right
250bar	0.107	0.100	0.149	0.169	0.316	0.329
350bar	0.063	0.072	0.111	0.102	0.265	0.253

Both figures demonstrated that the LVF of the spray decreased with increasing axial distance from the nozzle exit. Such a trend was expected, since the spray was denser in the vicinity of nozzle exit, while further downstream it disintegrated into smaller droplets, due to pronounced effects of secondary

atomisation. Furthermore a visual comparison of the distributions obtained from the three segments revealed that the LVF distributuions of the lower segments were wider that the middle and lower ones. This was a consequence of the larger population of liquid ligaments close to the orifice, due to primary atomisation. However, this decrease in LVF became less significant with increasing rail pressure. This was probably a consequence of the flow dynamics induced by the location of the needle at this particular moment.

Figure 6.17 and Figure 6.18 show the normalised LVF distributions obtained from fuel 1 at 250bar and 350bar during the closing phase of the needle (5.6ms after SoI), while Table 6.7 summarises the corresponding mean LVF values. The various line colours and styles retained their meaning as defined above.
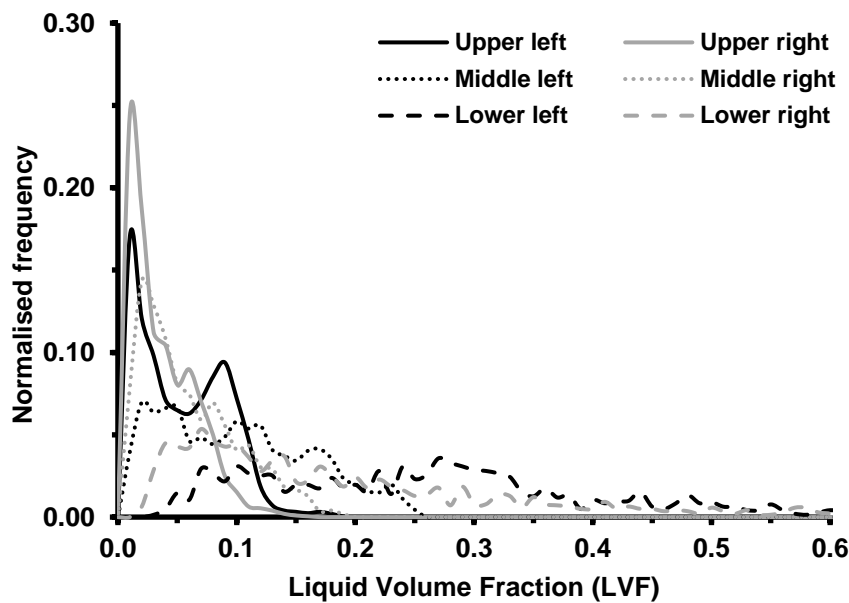
Figure 6.17: Mean LVF obtained from the upper, middle and lower segments of fuel 1 at 5.6ms after SoI, 250bar.
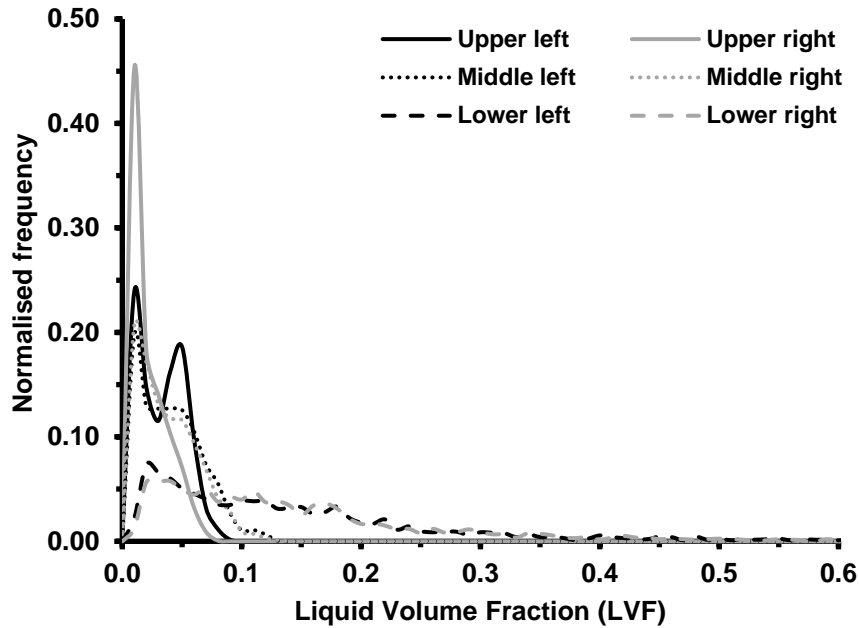
Figure 6.18: Mean LVF obtained from the upper, middle and lower segments of fuel 1 at 5.6ms after SoI, 350bar.

The comparison between the distributions obtained from the left-hand side of the spray segments and the right-hand side demonstrated that fuel 1 spray developed in a much more symmetric way relative to 1.8ms after SoI and 3.8ms after SoI. However, the asymmetry still remained, but was less distinctive. The left-hand side spray segments contained droplets with larger LVF values, suggesting a spray asymmetry. As it was mentioned previously, the flow asymmetry caused by the formation of geometric cavitation inside the nozzle passage was responsible for the asymmetry observed in the sprays. Moreover, in the vicinity of the nozzle exit, the LVF distributions were shown to be wider with respect to the ones produced by the middle and upper segments, possibly due to the less pronounced effect of secondary atomisation. Lastly, a visual comparison of Figure 6.17 and Figure 6.18 revealed that the distributions obtained at 350bar were shifted towards smaller LVF values. This could be attributed to the rail pressure increase that enhanced atomisation process which led to the formation of finer spray droplets of lower LVF.

Table 6.7: Mean LVF obtained from the upper, middle and lower segments of fuel 1 at 5.6ms after SoI, 350bar.

Fuel type	Mean LVF at 5.6ms after SoI					
	Upper segment		Middle segment		Lower segment	
	Right	Left	Right	Left	Right	Left
Fuel 1, 250bar	0.060	0.043	0.106	0.065	0.302	0.217
Fuel 1, 350bar	0.039	0.027	0.046	0.043	0.157	0.159

6.2.4   Spray LVF distributions as a function of the physical properties of the fuels

The LIF spray data produced by fuel B to fuel E referred to a rail pressure of 350bar and maximum needle lift (3.7, 3.8ms after SoI). The LVF distributions of the six different spray segments were produced by the corresponding time-resolved, normalised, mean images obtained from 100 injections in the case of Jeshani's fuels B, C, E and 65 in the case of fuel D. The mean images produced by fuels 1, 2, 3, and 4 were based on the data obtained from 50 injections. The six segments were the right and left-hand sides of the lower, middle and upper spray segments.

Fuel B (Gap diesel)

Fuel B was the second heaviest amongst the fuels under investigation. Considering its relatively high viscosity and surface tension, it was expected to obtain larger LVF relative to fuel A, due to later primary and secondary atomisation in fuel B. Figure 6.19 shows the normalised LVF distributions obtained from the right (black) and left (grey) hand sides of the upper (solid line), middle (dotted line) and lower (dashed line) of fuel spray B at 350bar and maximum needle lift (3.7ms after SoI).

Table 6.8 summarises the mean LVF obtained from the distributions shown in the figure below. Based on the results, it could be argued that all distributions were shifted towards larger LVF values relative to fuel A, confirming the expected trend.
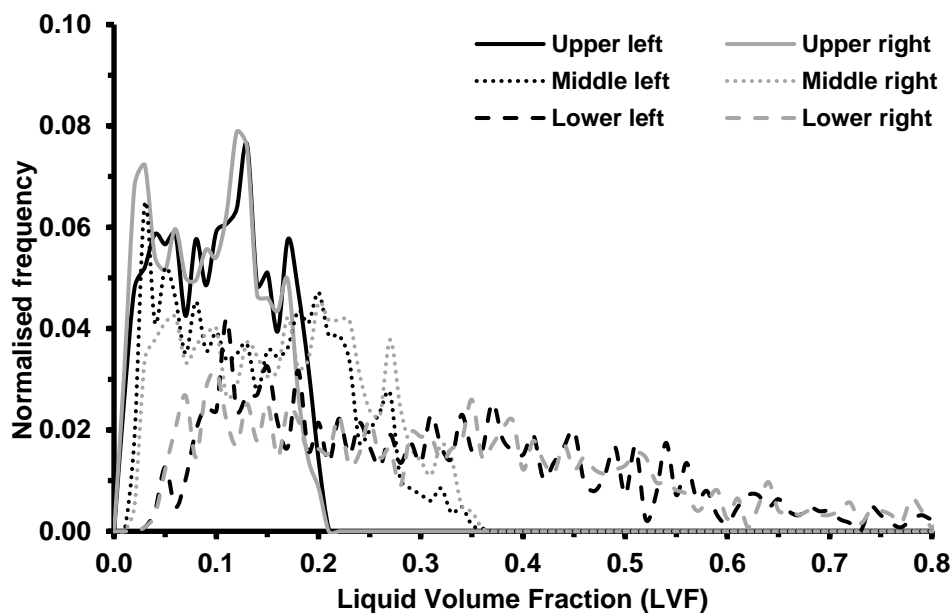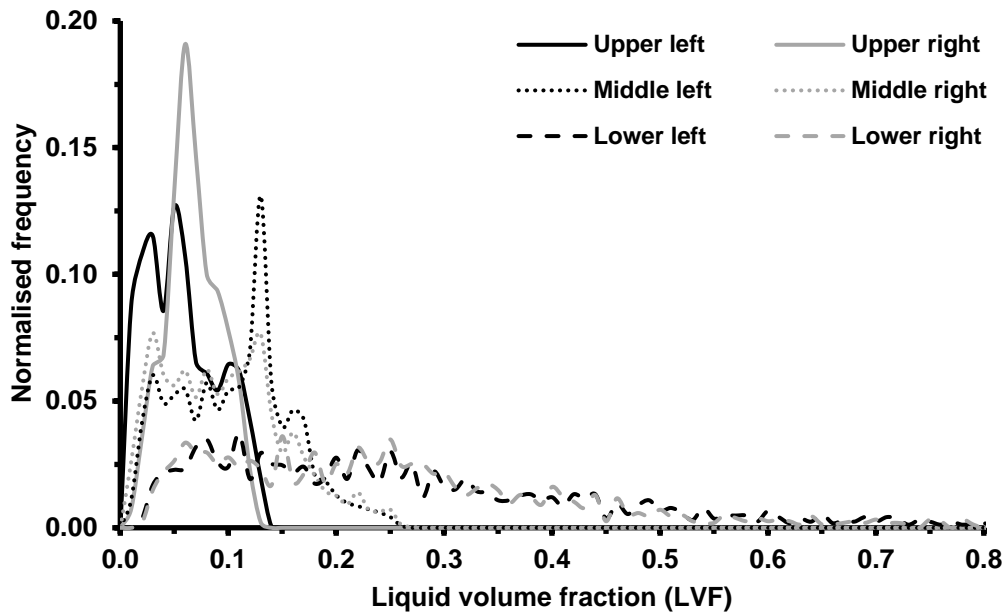
Figure 6.19: LVF distributions of the upper, middle and lower spray segments produced by fuel B at 350bar (3.7 ms after SoI).

It was also observed that the lower segment distributions were wider relative to the middle and lower segments. In the vicinity of the nozzle exit, the population of the liquid structures was expected to be higher, due to primary atomisation. With increasing axial distance, the LVF appeared to gradually decrease as consensequence of secondary atomisation.

Table 6.8: Mean relative LVF values obtained from fuel B spray at 350bar (3.7ms after SoI).

	Mean LVF values (3.7ms after SoI)					
	Upper segment		Middle segment		Lower segment	
	left	right	left	right	left	right
350bar	0.153	0.166	0.206	0.253	0.311	0.372

A comparison of the mean LVF values obtained from the left and right-hand side of the spray revealed that the right hand side of the spray had a larger mean LVF value than the left-hand side, suggesting a spray asymmetry especially at the lower and middle spray segments.

Investigation of diesel jet structure using Laser Induced Fluorescence (LIF) technique

Fuel C (kerosene + lubricity additive)

Fuel C was the second lightest fuel under investigation. Considering its relatively low surface tension and viscosity, it was expected to obtain distributions shifted towards smaller LVF values relative to fuels A and B. Figure 6.20 shows the projections of the normalised histograms obtained from fuel C sprays at 350bar and maximum needle lift. The various line styles and colours retained their meaning from above.

Figure 6.20: LVF distributions of the upper, middle and lower spray segments produced by fuel C at 350bar (3.7 ms after SoI).

Oddly enough, the results presented in Figure 6.20 and Table 6.9 contradicted the expected trend, showing a LVF distribution similar to fuel A. This unexpected behaviour could be attributed to the lubricity additive, which was believed to create a non-Newtonian flow with viscoelastic properties. In such cases, the fuel properties (i.e. viscosity) were altered during the execution of the experiments; subsequently, this alteration potentially led to the formation of droplets with larger LVF. The results also suggested a gradual decrease of LVF with increasing axial distance. In the vicinity of the nozzle exit, the spray was less dispersed than further downstream, due to less pronounced effects of secondary atomisation. Additionally, it could be argued that the spray developed in an asymmetric manner, since the right-hand side distributions contained droplets with larger LVF values relative to the left. However,

this asymmetry became less apparent with increasing axial distance. It has been suggested that on average, the spray asymmetry observed was associated with the geometric cavitation forming inside the nozzle passage; they both appeared on the same side.

Table 6.9: Mean relative LVF values obtained from fuel C sprays at 350 bar (3.7ms after SoI).

	Mean LVF values (3.7ms after SoI)					
	Upper segment		Middle segment		Lower segment	
	left	right	left	right	left	right
350bar	0.091	0.112	0.140	0.177	0.273	0.365

Fuel D (light kerosene)

Fuel D was the lightest amongst the fuels under investigation. Based on its low viscosity and surface tension, it was expected to obtain distributions shifted to smaller LVF values relative to fuels A, B and C. Figure 6.21 shows the normalised distributions obtained from the left and right hand sides of the upper, middle and lower segments of fuel D spray produced at 350bar and maximum needle lift (3.7ms after SoI).
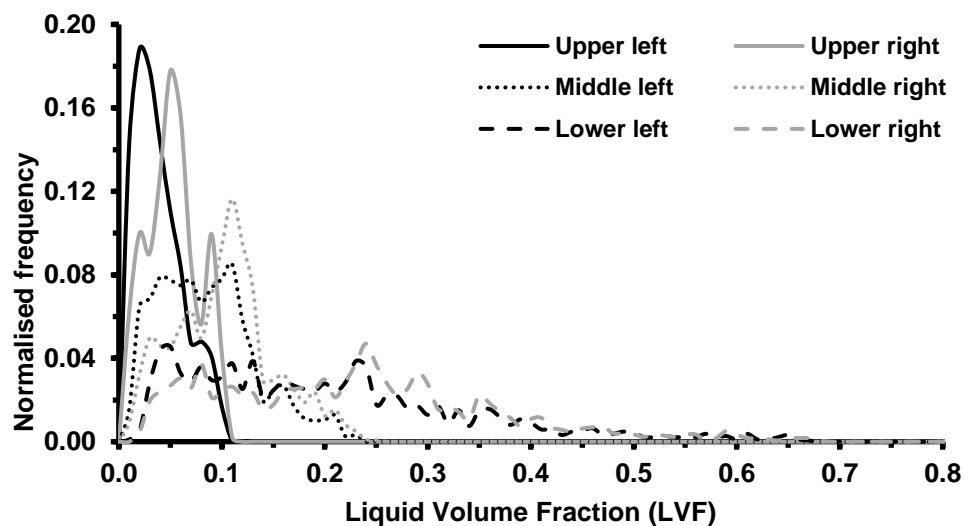
Figure 6.21: LVF distributions of the upper, middle and lower spray segments produced by fuel D at 350bar (3.7 ms after SoI).

Investigation of diesel jet structure using Laser Induced Fluorescence (LIF) technique

Comparing the distributions obtained from fuel D to the rest of the fuels, it could be argued that Fuel D distributions were shifted towards smaller LVF values, implying the formation of droplets with lower LVF. This was a consequence of its lower viscosity and surface tension which subsequently led to earlier jet disintegration.

In general, light fuels tend to cavitate more than heavier fuels. The intensive cavitation has been shown to enhance spray atomisation, resulting in the formation of smaller droplets. Furthermore, it could be observed that the distributions of both spray sides significantly overlapped each other, implying that Fuel D sprays developed in a symmetric manner. The mean LVF values of the obtained distributions are shown in Table 6.10. It could be argued that the right-hand side of the spray contained slightly larger LVF values than the left, suggesting a small spray asymmetry, especially in the case of the lower spray segments. The results obtained also suggested that the LVF decreased with increasing axial distance of the nozzle exit, due to secondary atomisation. In more detail, the distributions corresponding to the lower spray segments appeared to be much wider than the upper and middle segments, suggesting the presence of both large, intermediate and low LVF. Such an observation suggested that in the vicinity of the nozzle exit, the spray was less dispersed and consisted of more liquid structures relative to the regions further downstream.

Table 6.10: Mean relative LVF values obtained from fuel D spray at 350bar (3.7ms after SoI).

	Mean LVF values (3.7ms after SoI)					
	Upper segment		Middle segment		Lower segment	
	left	right	left	right	left	right
350bar	0.044	0.057	0.090	0.107	0.208	0.231

Fuel E (B20 diesel)

Fuel E was the heaviest fuel under investigation. Considering its high viscosity and surface tension, it was expected to obtain distributions shifted towards larger LVF values relative to the rest of the fuels. Figure 6.22 and Table 6.11 show the projections of the normalised distributions obtained from the

upper, middle, and lower segments of fuel E spray developed at 350bar and maximum needle lift and the corresponding mean LVF values respectively.
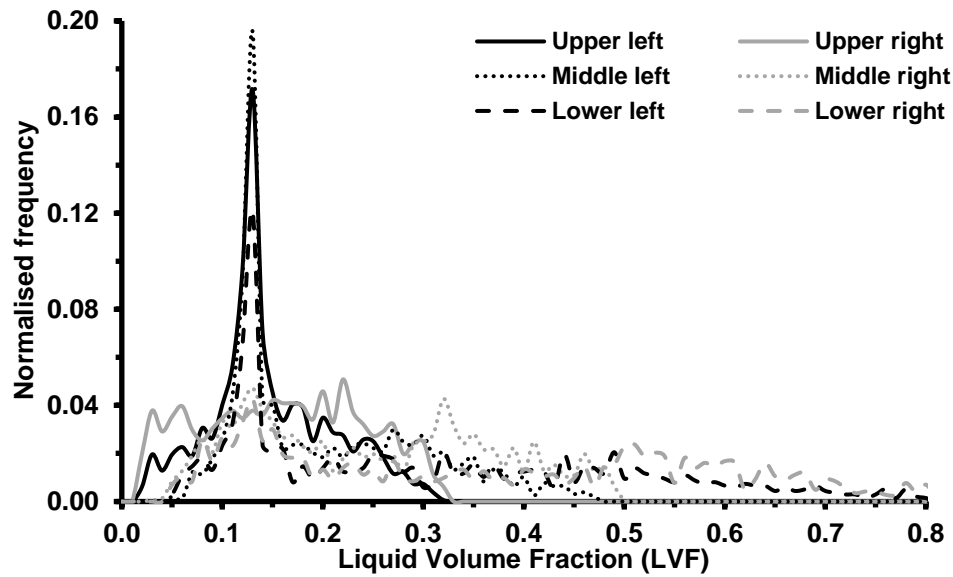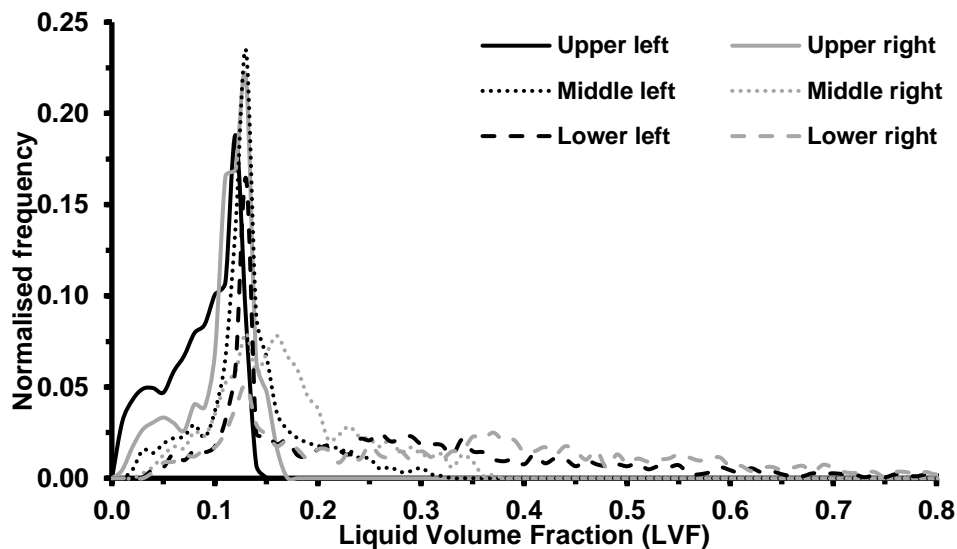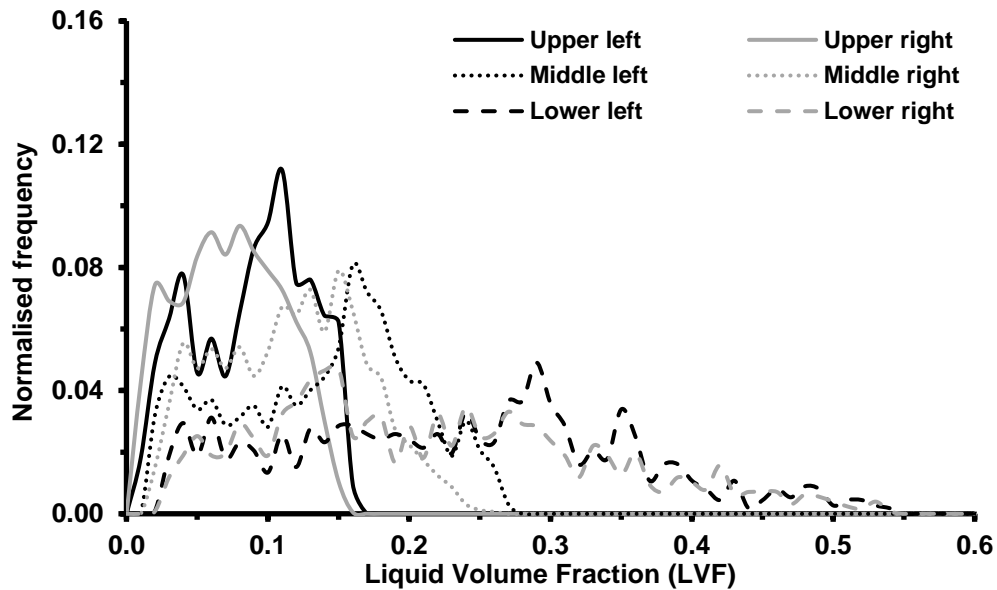

Figure 6.22: LVF distributions of the upper, middle and lower spray segments produced by fuel E at 350bar (3.7ms after SoI).

Table 6.11: Mean relative LVF values obtained from fuel E spray at 350bar (3.7ms after SoI).

	Mean LVF values (3.7ms after SoI)					
	Upper segment		Middle segment		Lower segment	
	left	right	left	right	left	right
350bar	0.094	0.078	0.143	0.122	0.238	0.223

Oddly enough, even though the data were corrected with the corresponding fluorescence yield calibration, the results contradicted the expected trend, suggesting the formation of droplets with low LVF. Such a behaviour was not fully understood and requires further investigation. However, in earlier chapters, it was stated that the circumferential in-sac flow could possibly separate the heavier from the lighter component of fuel E; this could possibly explain the odd trend presented in the present work. In terms of spray symmetry, fuel E seemed to develop in a quite asymmetric manner; the left-hand side of

the spray contained droplets with larger LVF values than the right-hand side, especially in the case of the middle and upper segments. Lastly, it has been suggested that the developed asymmetry has been associated with the geometric cavitation formed on the same side of the nozzle as where the droplets with large LVF locate. Finally, the results presented in Table 6.11 showed that the LVF of the spray droplets gradually decreased with increasing axial distance from the nozzle exit. This could be attributed to the pronounced effect of secondary atomisation with increasing axial distance.

The fuels investigated by Makri were fuel 2 (B20 diesel), 3 (Gap diesel + lubricity additive) and 4 (Jet fuel + lubricity additive) at 3.8ms after SoI (maximum needle lift), 350bar. The study of these fuels on the dependence of LVF distributions on needle lift and rail pressure is planned to be published in a journal paper. The present analysis involved the LVF distributions obtained from the right (grey colour) and left-hand side (black colour) of the upper (solid line), middle (dotted line) and lower (dashed line) segments of the sprays.

Fuel 2 (B20 diesel)

Figure 6.24 and Table 6.12 demonstrated the normalised LVF distribution obtained from the upper, middle and lower segment of fuel 2 sprays and the corresponding mean values respectively. The results suggested that the asymmetry of fuel 2 spray was less distinctive relative to fuel 1. The most significant asymmetry appeared at the lower segment, where the right-hand side of the spray contained more spray droplets of larger LVF. The right and left-hand side of the distributions of the middle and upper segments appeared to be very similar, suggesting that the spray asymmetry can be considered negligible. It was also observed that the lower segments produced broader distributions relative to the other segments. This could be attributed to the pronounced effects of primary atomisation, which was responsible for the formation of unstable large droplets and ligaments of large LVF. Further downstream of the nozzle exit, the LVF decreased as a consequence of secondary atomisation. Overall, the LVF of the droplets obtained from the spray of fuel 2 was lower than fuel 1.

Figure 6.23: LVF distributions obtained from the upper, middle and lower segments of fuel 2 at 3.8ms after SoI, 350bar.

Considering the higher viscosity of fuel 2, it was expected to obtain larger LVF values, since more viscous fuels had the tendency to cavitate less and oppose break-up phenomena less. However, the results contradicted the expected trend; the reason behind this behaviour is unknown and requires further investigation.

Table 6.12: Mean LVF obtained from the upper, middle and lower segments of fuel 2 at 3.8ms after SoI, 350bar.

Fuel type	Mean LVF at 3.8ms after SoI					
	Upper segment		Middle segment		Lower segment	
	Right	Left	Right	Left	Right	Left
Fuel 2, 350bar	0.036	0.039	0.047	0.046	0.138	0.170

Fuel 3 (Gap diesel + lubricity additive)

Figure 6.24 and Table 6.13 showed the normalised LVF distributions obtained from the upper, middle and lower segments of fuel 3 spray and the corresponding mean LVF values respectively. The distributions obtained from the right-hand side of the spray contained larger LVF values relative to the

left-hand side, suggesting a spray asymmetry. As it was mentioned previously, the flow asymmetry occurring inside the nozzle passage due to geometric cavitation was responsible for the asymmetry observed in the sprays. Additionally, the results indicated that the LVF gradually decreased with increasing axial distance, due to pronounced secondary atomisation. The broader distributions of the lower segments were believed to be a consequence of the dominant primary atomisation, which was responsible for the formation of large droplets and ligaments of larger LVF. Overall, the LVF of fuel 3 was lower than fuel 1, due to the lower viscosity of fuel 3. In principle, the less viscous fuels oppose break-up phenomena less, resulting in the formation of smaller droplets with lower LVF value. Even though fuel 3 produced sprays of lower LVF than fuel 1, it was expected to observe greater difference between the two fuels, since the viscosity of fuel 3 was approximately 25% lower than fuel 1. It was believed that the lubricity additive in fuel 3 altered the viscosity of the fluid during the execution of the experiments; this additive has been suggested to induce non-Newtonian flow properties. Therefore, the non-Newtonian flow was potentially responsible for the larger LVF.
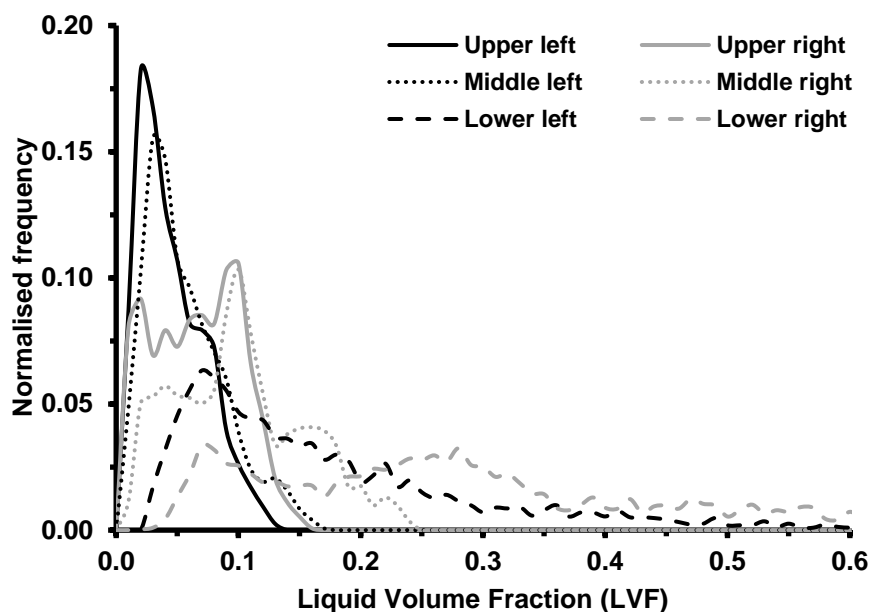
Figure 6.24: LVF distributions obtained from the upper, middle and lower segments of fuel 3 at 3.8ms after SoI, 350bar.

Table 6.13: Mean LVF obtained from the upper, middle and lower segments of fuel 3 at 3.8ms after SoI, 350bar.

Fuel type	Mean LVF at 3.8ms after SoI					
	Upper segment		Middle segment		Lower segment	
	Right	Left	Right	Left	Right	Left
Fuel 3, 350bar	0.050	0.071	0.061	0.107	0.175	0.298

Fuel 4 (Jet fuel + lubricity additive)

Figure 6.25 and Table 6.14 demonstrated the normalised LVF distributions obtained from the upper, middle and lower segments of fuel 4 spray and the corresponding mean LVF values respectively. The results suggested the sprays of fuel 4 developed in a much more symmetric manner relative to the rest of the fuels. Even though the asymmetry was less distinctive, it was observed that the right-hand side of the spray contained the majority of the larger LVF spray droplets. An optical inspection of Figure 6.25 revealed that the upper and middle spray segments produce narrower distributions compared to the lower. It was believed that in the vicinity of the nozzle exit the dominant break-up mechanism was primary atomisation, which led to the formation of unstable large droplets and ligaments of large LVF.

On the contrary, further downstream of the nozzle exit the dominant mechanism was secondary atomisation that was responsible for the formation of smaller droplet of lower LVF. Fuel 4 was the lightest fuel under consideration and had the lowest viscosity; hence, it was expected that the LVF of the spray would be smaller relative to the heavier fuels, i.e. fuels 1 and 3. However, a comparison of the results obtained from fuels 1, 3 and 4 revealed that fuel 4 produced results similar to fuel 1. Such an observation contradicted the expected trend described above.
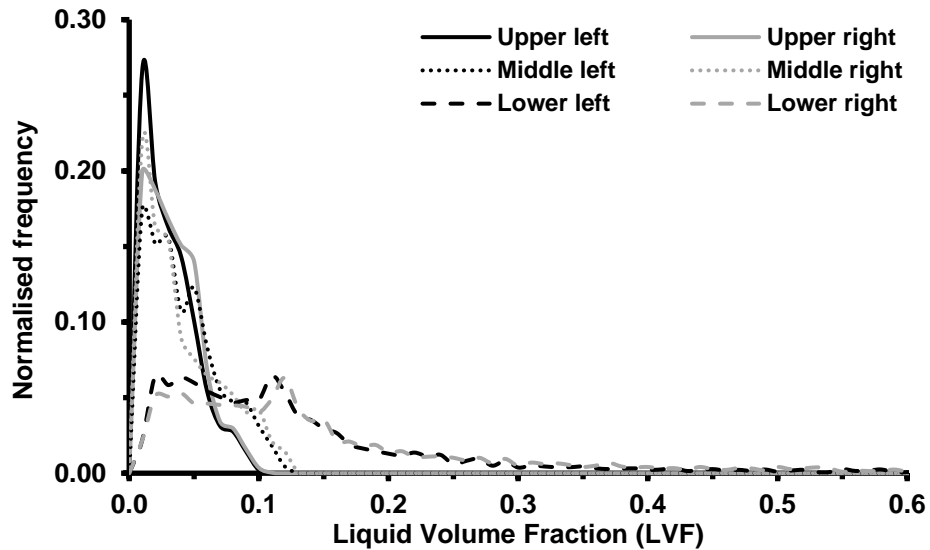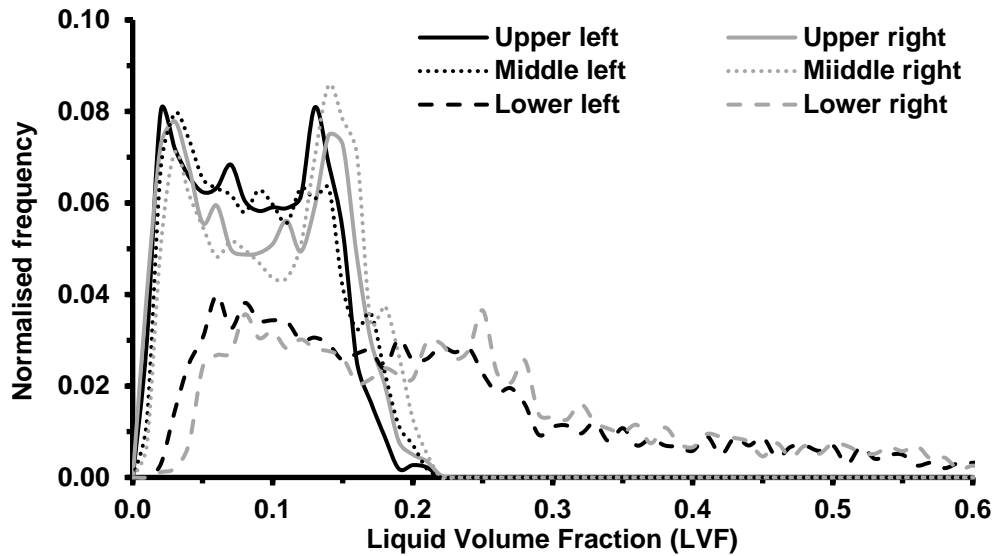
Figure 6.25: LVF distributions obtained from the upper, middle and lower segments of fuel 4 at 3.8ms after SoI, 350bar.

It has been suggested that the lubricity additive present in fuel 4 introduced non-Newtonian flow with viscoelastic properties; such a flow was capable of altering the viscosity of the fluid during the experiments. It could be argued that the odd behaviour of fuel 4 could be a result of the non-Newtonian flow properties induced.

Table 6.14: Mean LVF obtained from the upper, middle and lower segments of fuel 4 at 3.8ms after SoI, 350bar.

Fuel type	Mean LVF at 3.8ms after SoI					
	Upper segment		Middle segment		Lower segment	
	Right	Left	Right	Left	Right	Left
Fuel 4, 350bar	0.091	0.096	0.095	0.108	0.245	0.282

Chapter 7
Summary and Conclusions

The effects of rail pressure, needle lift and fuel's physical properties on the internal nozzle flow and external diesel sprays have been investigated by means of a complex experimental work, which involved the employment of optical diagnostics, such as Laser Sheet Drop-sizing, white light elastic scattering and Laser Induced Fluorescence. The analyses performed suggested potential deposit formation mechanisms inside the nozzle geometry, interesting correlations among the SMD and LVF distributions of the diesel sprays, the transient movement of the needle and the physical properties of the fuels. The main results and achievements of the present work are enumerated as follows:

- The circumferential in-sac fuel flow observed towards the late stages of an injection event and post injection period has been suggested to be a result of the flow obtained in the annulus surrounding the needle, emitted from the fuel gallery to the side of the needle, and formed during the closing phase of the needle. Such a movement created regions of low and high pressure, which were capable of pushing or/and pulling the vapour capsules/bubbles/fuel inside the nozzle passage. It was found that the circumferential in-sac flow dampened down synchronously to the motion of the vapour structures inside the holes. Under engine conditions, it was argued that the admission of hot combustion gases from the cylinder to at least the nozzle passages or even as far as the injector body was highly possible.

- The analysis presented in Chapter 4 suggested that the circumferential in-sac flow consisted of highly reactive bubbles, which were a mixture of fuel vapour and small amounts of other compounds, such as oxygen and nitrogen. Hence, it can be argued that under engine conditions, where the temperature and pressure are quite high, the synergy between the potentially admitted hot combustion gases through the nozzle passages, the hot metal surfaces and the highly reactive bubbles present both in the passages and the sac can create ideal conditions for chemical reactions (e.g. pyrolysis, oxidation) to take place. Such reactions usually lead to deposit formation on various locations of the FIE.

Summary and Conclusions

- The SMD distributions obtained from the diesel sprays showed a strong dependence on the rail pressure, the physical properties of the fuels and the transient movement of needle. An increase in rail pressure led to the formation of smaller droplets, due to enhanced cavitation and turbulence phenomena, while an increase in viscosity and surface tension led to smaller droplets, due to stronger viscous and surface tension effects. The results showed that the largest droplets were formed during the maximum lift of the needle. Similar findings were obtained from the analysis with regards to the LVF distributions.

- The results produced by fuels A-E (Jeshani's experimental fuels) suggested that the dominant break-up mechanism was secondary atomisation, while in case of fuels 1-4 was the synergy between primary and secondary break-up. In the former case, there was not any difference in SMD with increasing axial distance from the nozzle exit. This observation was confirmed by the phenomenological analysis which showed an earlier primary atomisation in case of Jeshani's diesel sprays. In both experimental fuel sets SMD decreased with increasing axial distance from the central spray axis. It should be mentioned that Jeshani's experiments were conducted with white light, while the experiments executed by the author of this dissertation with LIF. The employment of laser for the illumination of the acrylic tip increased the temperature of the fuel flowing through the tip.

- All sprays involved in the present work exhibited an asymmetry. This spray asymmetry was associated to the asymmetry introduced into the nozzle passage, as a result of geometric cavitation developing in the vicinity of the passage entrance. This observation was also implied by the results obtained from the internal flow analysis in Chapter 4.

- The phenomenological analysis showed that in most cases the liquid intact core of the sprays was destroyed either within the first 2mm downstream of the nozzle exit or inside the nozzle passage, regardless of the rail pressure and the physical properties of the fuels, mostly due to intensive cavitation phenomena.

- The addition of lubricity additive in several fuels (fuels C, 3 and 4) gave rise to unexpected behaviour. It was suggested that this ester-based additive altered the Newtonian to non-Newtonian flow, which in

turn was responsible for the changes in the physical properties of the fuel (i.e. viscosity) during the execution of the experiment.

- To the author's knowledge, no previous attempts have been made to perform LIF measurements inside the nozzle passage geometry. This attempt has been successfully completed in this project showing that the Scattered Fluorescence Liquid Volume Fraction (SFLVF) was dependent on rail pressure, needle position and fuel's physical properties. In more detail, an increase in rail pressure led to smaller SFLVF, due to enhanced cavitation and turbulence. Additionally, an increase in viscosity of the fuel led to larger SFLVF, since heavier fuels were less susceptible to cavitation.

Recommendations for future work:

- The results obtained from B20 diesel sprays (fuels E and 2) showed that both SMD and LVF were smaller relative to the rest of the fuels, even after the correction of the data against the corresponding fluorescent yield calibration factor. hence, further investigation is required on the matter.

- The addition of the lubricity additive in fuels C, 3 and 4 led to odd results. On average, the SMD and LVF values obtained were larger compared to the expected. It has been suggested that this ester-based additive created a non-Newtonian flow, whose properties changed throughout the execution of the experiment.

- A complete investigation of both spray and internal flow data is required to fully understand the impact of the physical properties of the fuels, operating conditions and transient movement of the needle on the SMD, LVF and SFLVF distributions. The completion of this investigation will provide interesting correlations between the internal flow and the external sprays.

- The employment of LIF for the characterisation of the flow inside the nozzle provided some useful information with regards to the proportion of vapour and liquid present in the hole. However, the results referred to the relative volume fraction. Therefore, it is needed to interpret the results in terms of LVF and overcome the problem of the fluorescence scattering from the flow discontinuities. A way to solve this issue could be an increase in the magnification from 5.6 to 6.0.

Summary and Conclusions

- In this experiment, the operating pressure could go up to 350bar due to the employment of an acrylic tip. The manufacture of a tip in a harder material (i.e. fused silica) would facilitate the execution of the experiment in much higher and realistic rail pressures.

- The SMD distributions produced referred to the relative SMD, therefore it is required to calibrate the results after performing PDA measurements on one of the fuels tested.

Appendix A

Appendix A1   Sac Vorticity Effects on Nozzle flow –

Complementary data and results

* front interface 1, inj.1, fuel B, 350 bar
* front interface 2, inj.1, fuel B, 350 bar
* back interface 1, inj.2, fuel B, 350bar
* back interface 2, inj.2, fuel B, 350bar
* back interface 1, inj.3, fuel B, 350bar
* back interface 2, inj.3, fuel B , 350bar
* back interface 1, inj.1, fuel B, 350 bar
* front interface 1, inj.2, fuel B, 350bar
* front interface 2, inj.2, fuel B, 350bar
* front interface 1, inj.3, fuel B, 350bar
* front interface 2, inj.3, fuel B, 350bar
* front interface 1, inj.5, fuel B, 350bar

Figure A1.1: Displacement vs. time graph, fuel B,350 bar, inj.1-5, lower hole.

* front interface 1, inj.6, fuel B, 350bar
* front interface 2, inj.6, fuel B, 350bar
* front interface 1, inj.7, fuel B, 350bar
* front interface 2, inj.7, fuel B, 350 bar
* front interface 1, inj.8, fuel B, 350 bar
* front interface 2, inj.8, fuel B, 350 bar
* front interface 1, inj.6, fuel B, 350bar
* front interface 2, inj.6, fuel B, 350bar
* back interface 1, inj.6, fuel B, 350bar
* back interface 2, inj.6, fuel B, 350bar
* back interface 1, inj.7, fuel B, 350 bar
* back interface 2, inj.7, fuel B, 350 bar
* back interface 1, inj.8, fuel B, 350 bar
* back interface 2, inj.8, fuel B, 350 bar
* back interface 1, inj.6, fuel B, 350bar
* back interface 2, inj.6, fuel B, 350bar

Figure A1.2: Displacement vs. time graph, fuel B,350 bar, inj.6-10, lower hole.

Figure A1.3: Displacement vs. time graph, fuel B,350 bar, inj.11-15, lower hole.
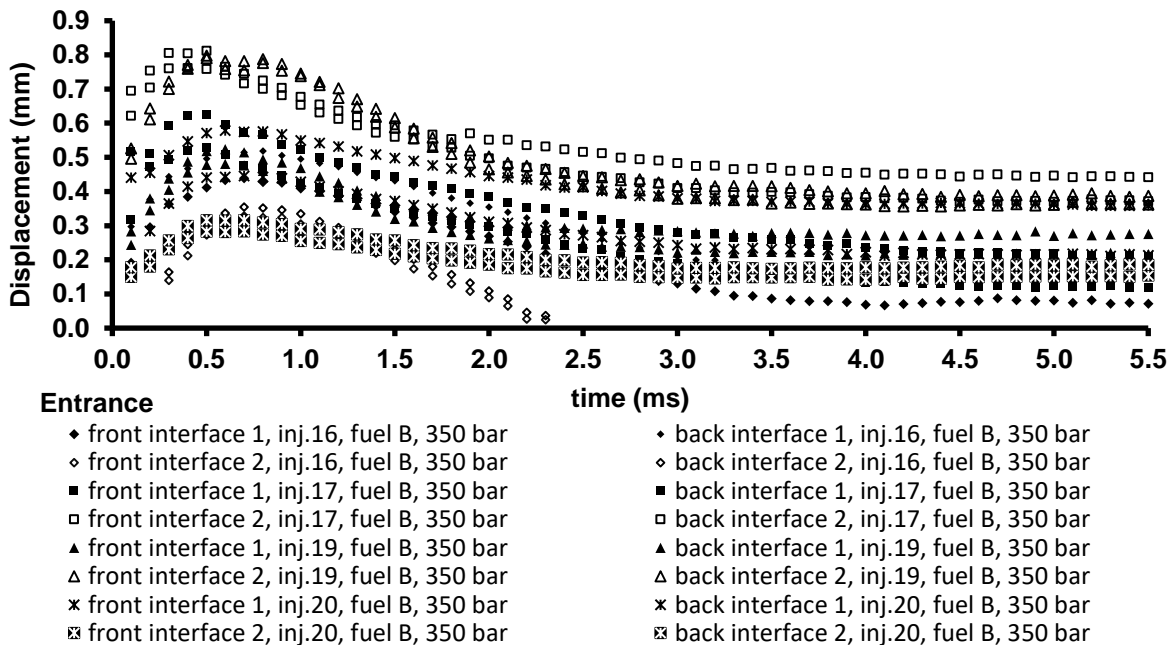
Figure A1.4: Displacement vs. time graph, fuel B,350 bar, inj.16-20, lower hole.

Figure A1.5: Displacement vs. time graph, fuel B,350 bar, inj.1-5, upper hole.
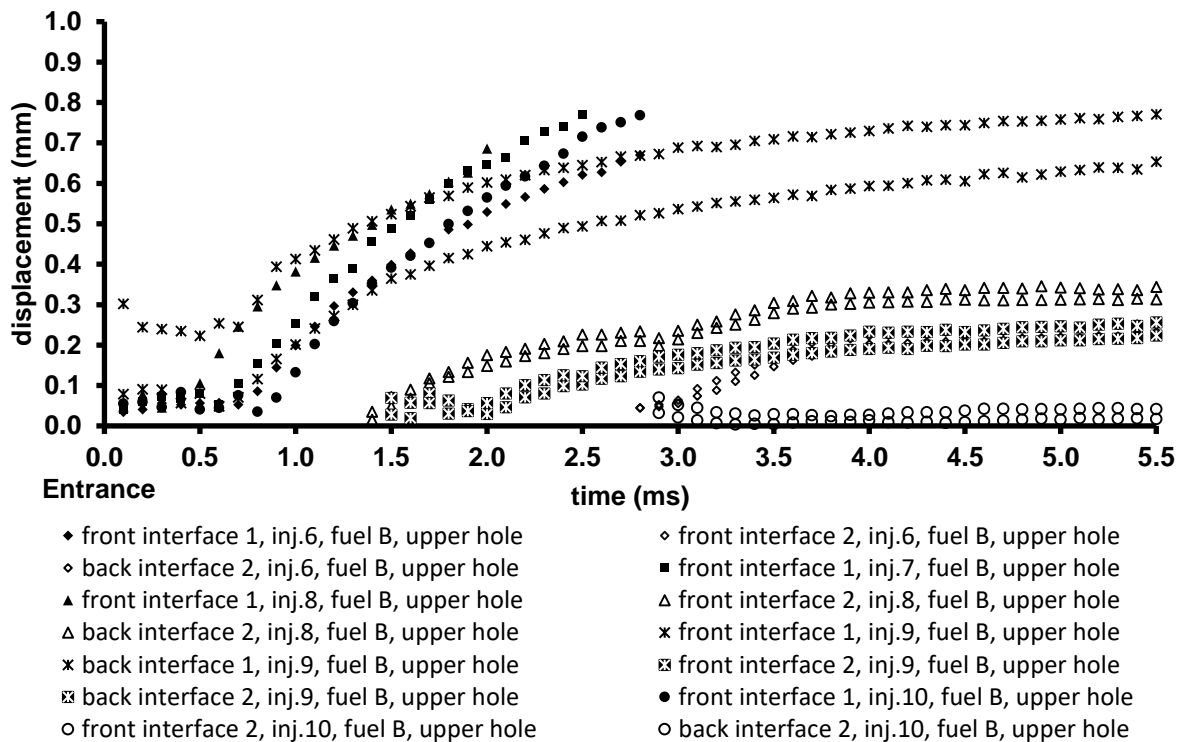
Figure A1.6: Displacement vs. time graph, fuel B,350 bar, inj.6-10, upper hole.

Figure A1.7: Displacement vs. time graph, fuel B,350 bar, inj.11-15, upper hole.
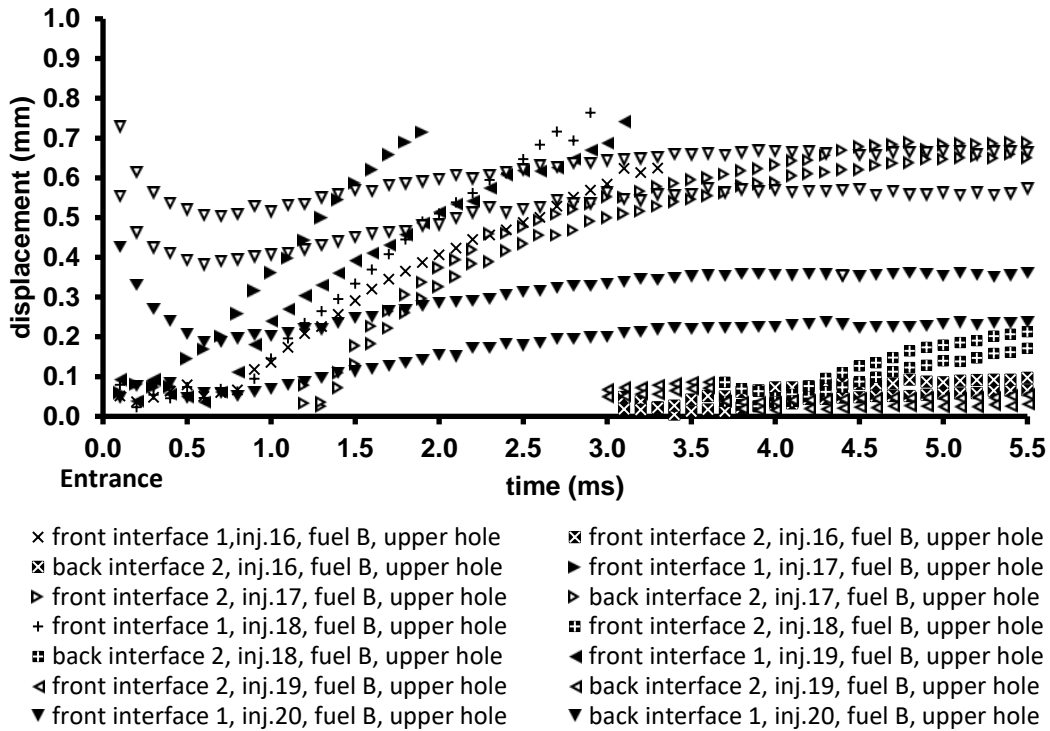
Figure A1.8: Displacement vs. time graph, fuel B,350 bar, inj.16-20, upper hole.

Figure A1.9: Displacement vs. time graph, fuel C,350 bar, inj.1-5, lower hole.

Figure A1.10: Displacement vs. time graph, fuel C,350 bar, inj.6-10, lower hole.

× front interface 1, inj.11, fuel C, lower hole
⊠ front interface 2, inj.11, fuel C, lower hole
► front interface 1, inj.12, fuel C, lower hole
▷ front interface 2, inj.12, fuel C, lower hole
+ front interface 1, inj.13, fuel C, lower hole
⊞ front interface 2, inj.13, fuel C, lower hole
◄ front interface 1, inj.14, fuel C, lower hole
▼ front interface 1, inj.15, fuel C, lower hole

× back interface 1, inj.11, fuel C, lower hole
⊠ back interface 2, inj.11, fuel C, lower hole
► back interface 1, inj.12, fuel C, lower hole
▷ back interface 2, inj.12, fuel C, lower hole
+ back interface 1, inj.13, fuel C, lower hole
⊞ back interface 2, inj.13, fuel C, lower hole
◄ back interface 1, inj.14, fuel C, lower hole
▼ back interface 1, inj.15, fuel C, lower hole

Figure A1.11: Displacement vs. time graph, fuel C,350 bar, inj.11-15, lower hole.

× front interface 1, inj.16, fuel C, lower hole
⊠ front interface 2, inj.16, fuel C, lower hole
► front interface 1, inj.17, fuel C, lower hole
▷ front interface 2, inj.17, fuel C, lower hole
+ front interface 1, inj.18, fuel C, lower hole
⊞ front interface 2, inj.18, fuel C, lower hole
◄ front interface 1, inj.19, fuel C, lower hole
◁ front interface 2, inj.19, fuel C, lower hole
▼ front interface 1, inj.20, fuel C, lower hole
▽ front interface 2, inj.20 , fuel C, lower hole

× back interface 1, inj,16, fuel C, lower hole
⊠ back interface 2, inj,16, fuel C, lower hole
► back interface 1, inj.17, fuel C, lower hole
▷ back interface 2, inj.17, fuel C, lower hole
+ back interface 1, inj.18, fuel C, lower hole
⊞ back interface 2, inj.18, fuel C, lower hole
◄ back interface 1, inj.19, fuel C, lower hole
◁ back interface 2, inj.19, fuel C, lower hole
▼ back interface 1, inj.20, fuel C, lower hole
▽ back interface 2, inj.20, fuel C, lower hole

Figure A1.12: Displacement vs. time graph, fuel C,350 bar, inj.16-20, lower hole.
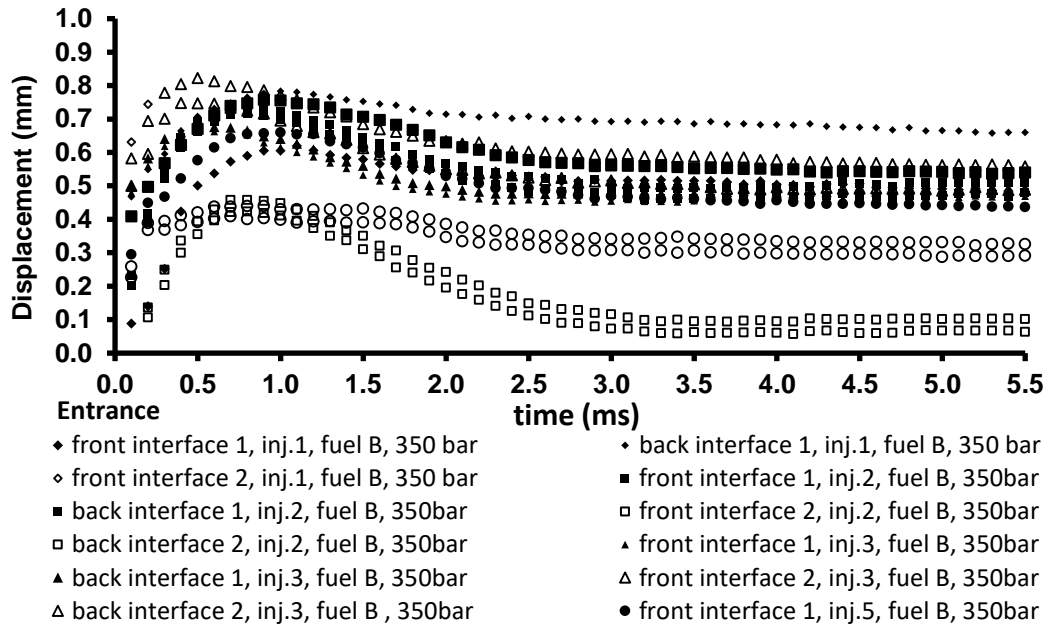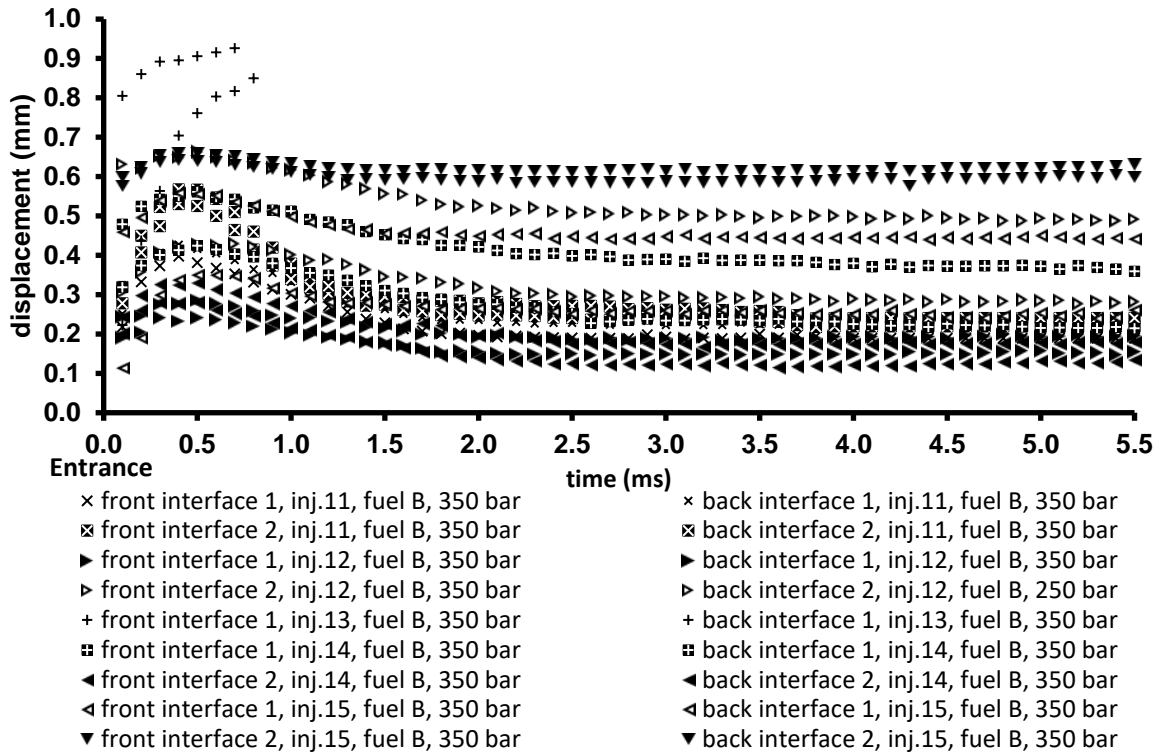
Figure A1.13: Displacement vs. time graph, fuel C,350 bar, inj.1-5, upper hole.

Figure A1.14: Displacement vs. time graph, fuel C,350 bar, inj. 6-10, upper hole.

Figure A1.15: Displacement vs. time graph, fuel C,350 bar, inj. 11-15, upper hole.

Figure A1.16: Displacement vs. time graph, fuel C,350 bar, inj. 16-20, upper hole.

Figure A1.17: Displacement vs. time graph, fuel D, 350bar, inj. 1-5, lower hole.

Figure A1.18: Displacement vs. time graph, fuel D, 350 bar, inj. 6-10, lower hole.

Figure A1.19: Displacement vs. time graph, fuel D, 350bar, inj. 11-15, lower hole.

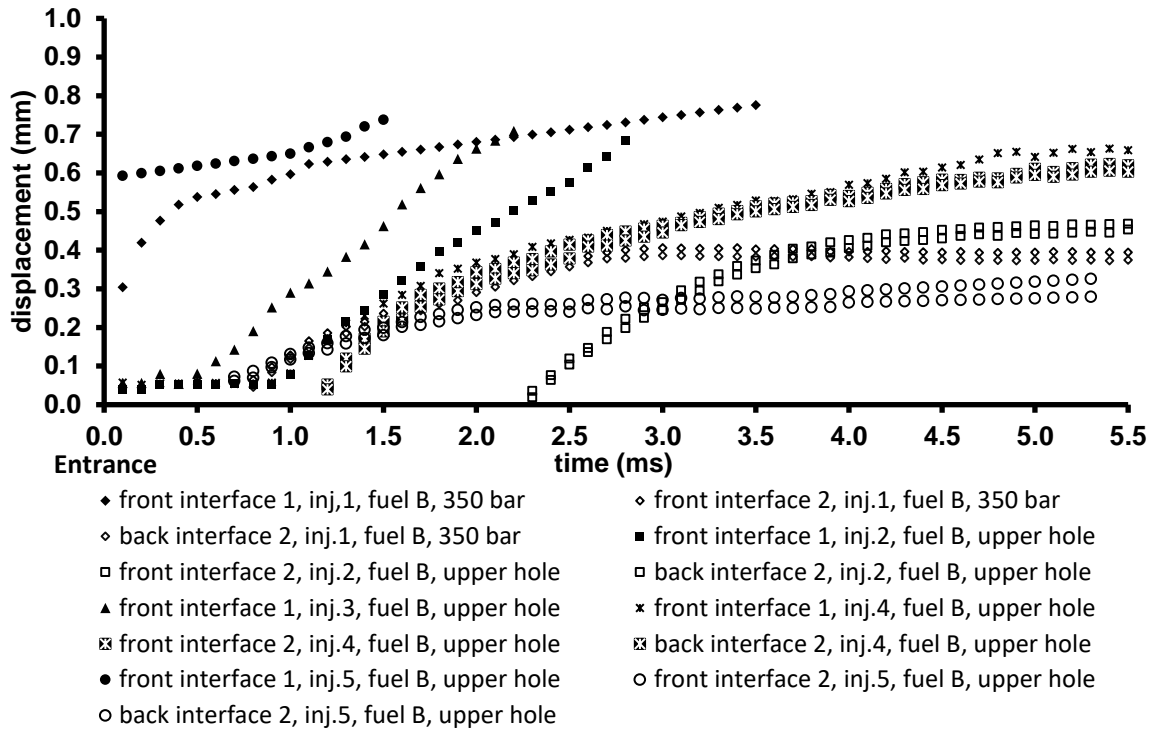Figure A1.20: Displacement vs. time graph, fuel D, 350bar, inj. 16-20, lower hole.

Figure A1.21: Displacement vs. time graph, fuel D, 350bar, inj. 1-5, upper hole.

Figure A1.22: Displacement vs. time graph, fuel D, 350bar, inj. 6-10, upper hole.

Figure A1.23: Displacement vs. time graph, fuel D, 350bar, inj. 11-15, upper hole.

Figure A1.24: Displacement vs. time graph, fuel D, 350bar, inj. 16-20, upper hole.

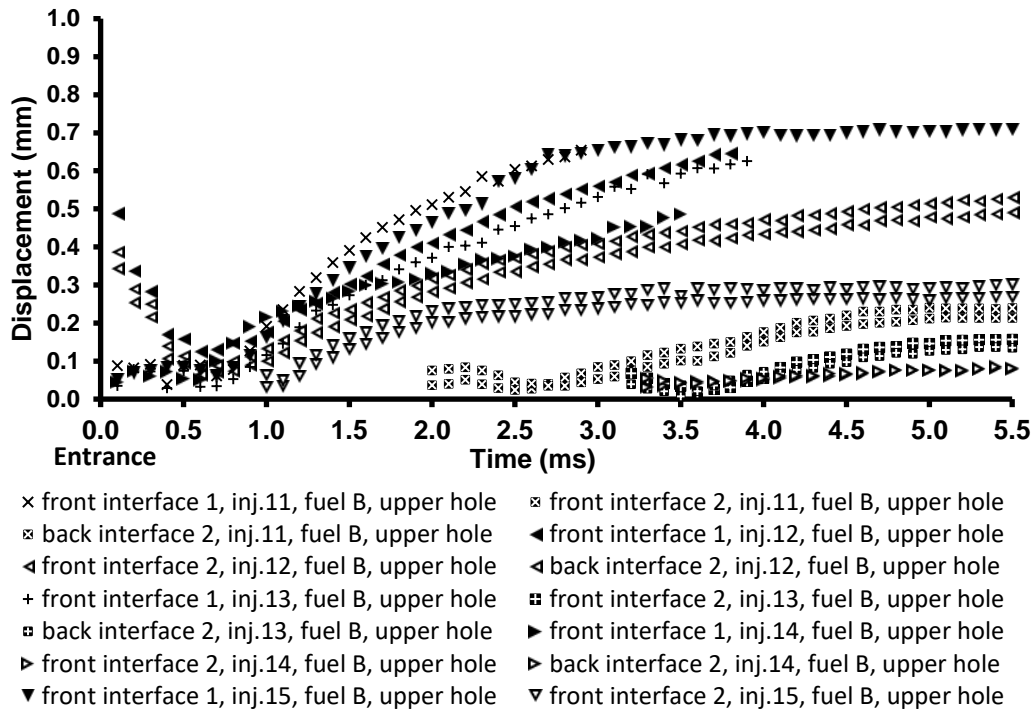Figure A1.25: Displacement vs. time graph, fuel E, 350bar, inj. 1-5, lower hole.

Figure A1.26: Displacement vs. time graph, fuel E, 350bar, inj. 6-10, lower hole.
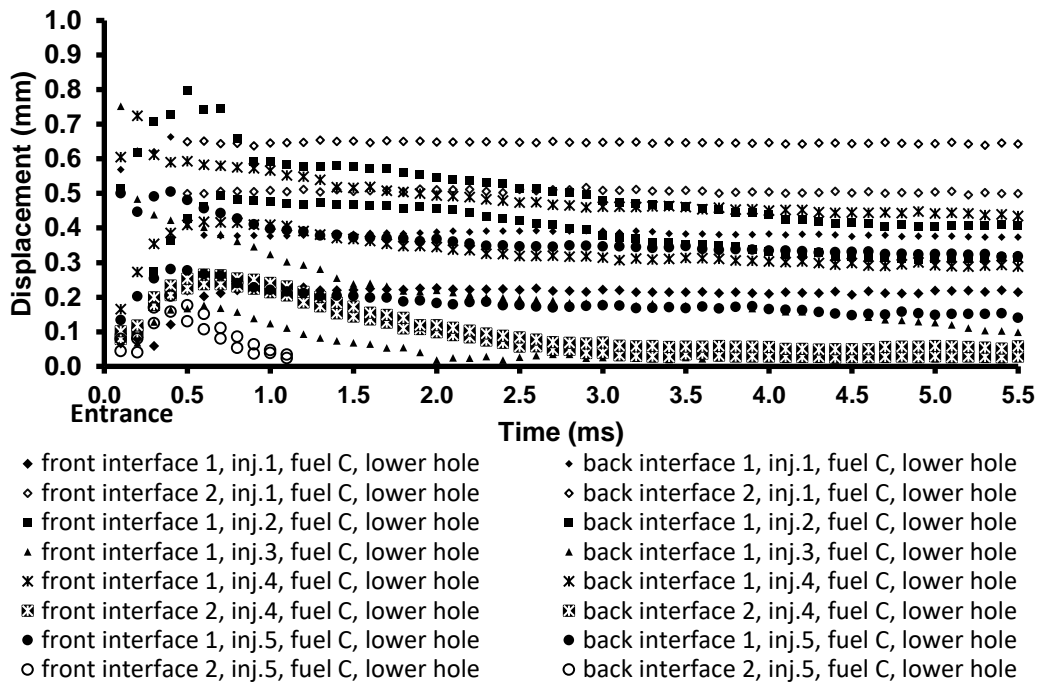
◄ front interface 1, inj.12, fuel E, lower hole   ◄ back interface 1, inj.12, fuel E, lower hole

◄ front interface 2, inj.12, fuel E, lower hole   ◄ back interface 2, inj.12, fuel E, lower hole

+ front interface 1, inj.13, fuel E, lower hole   + back interface 1, inj.13, fuel E, lower hole

▫ front interface 2, inj.13, fuel E, lower hole   ▫ back interface 2, inj.13, fuel E, lower hole

► front interface 1, inj.14, fuel E, lower hole   ► back interface 1, inj.14, fuel E, lower hole

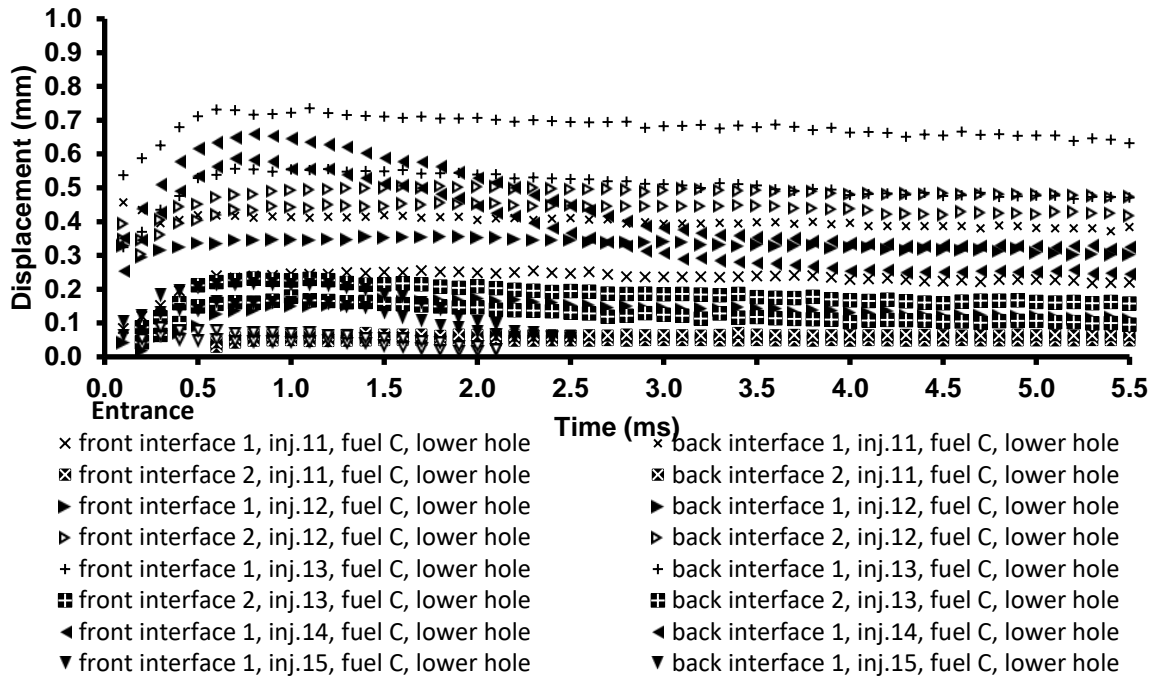Figure A1.27: Displacement vs. time graph, fuel E, 350bar, inj. 11-15, lower hole.

+ front interface 1, inj.18, fuel E, lower hole   + back interface 1, inj.18, fuel E, lower hole

▼ front interface 1, inj.20, fuel E, lower hole   ▼ back interface 1, inj.20, fuel E, lower hole

▽ front interface 2, inj.20, fuel E, lower hole   ▽ back interface 2, inj.20, fuel E, lower hole

Figure A1.28: Displacement vs. time graph, fuel E, 350bar, inj. 16-20, lower hole.

front interface 1, inj.1, fuel E, upper hole
front interface 2, inj.1, fuel E, upper hole
front interface 1, inj.2, fuel E, upper hole
front interface 2, inj.2, fuel E, upper hole
front interface 1, inj.3, fuel E, upper hole
front interface 2, inj.3, fuel E, upper hole
front interface 1, inj.4, fuel E, upper hole
front interface 2, inj.4, fuel E, upper hole
front interface 1, inj.5, fuel E, upper hole
front interface 2, inj.5, fuel E, upper hole

back interface 1, inj.1, fuel E, upper hole
back interface 2, inj.1, fuel E, upper hole
back interface 1, inj.2, fuel E, upper hole
back interface 2, inj.2, fuel E, upper hole
back interface 1, inj.3, fuel E, upper hole
back interface 2, inj.3, fuel E, upper hole
back interface 1, inj.4, fuel E, upper hole
back interface 2, inj.4, fuel E, upper hole
back interface 1, inj.5, fuel E, upper hole
back interface 2, inj.5, fuel E, upper hole

Figure A1.29: Displacement vs. time graph, fuel E, 350bar, inj. 1-5, upper hole.

front interface 1, inj.6, fuel E, upper hole
front interface 1, inj.7, fuel E, upper hole
front interface 2, inj.7, fuel E, upper hole
front interface 1, inj.8, fuel E, upper hole
front interface 2, inj.8, fuel E, upper hole
front interface 1, inj.9, fuel E, upper hole
front interface 2, inj.9, fuel E, upper hole
front interface 1, inj.10, fuel E, upper hole
front interface 2, inj.10, fuel E, upper hole

back interface 1, inj.6, fuel E, upper hole
back interface 1, inj.7, fuel E, upper hole
back interface 2, inj.7, fuel E, upper hole
back interface 1, inj.8, fuel E, upper hole
back interface 2, inj.8, fuel E, upper hole
back interface 1, inj.9, fuel E, upper hole
back interface 2, inj.9, fuel E, upper hole
back interface 1, inj.10, fuel E, upper hole
back interface 2, inj.10, fuel E, upper hole

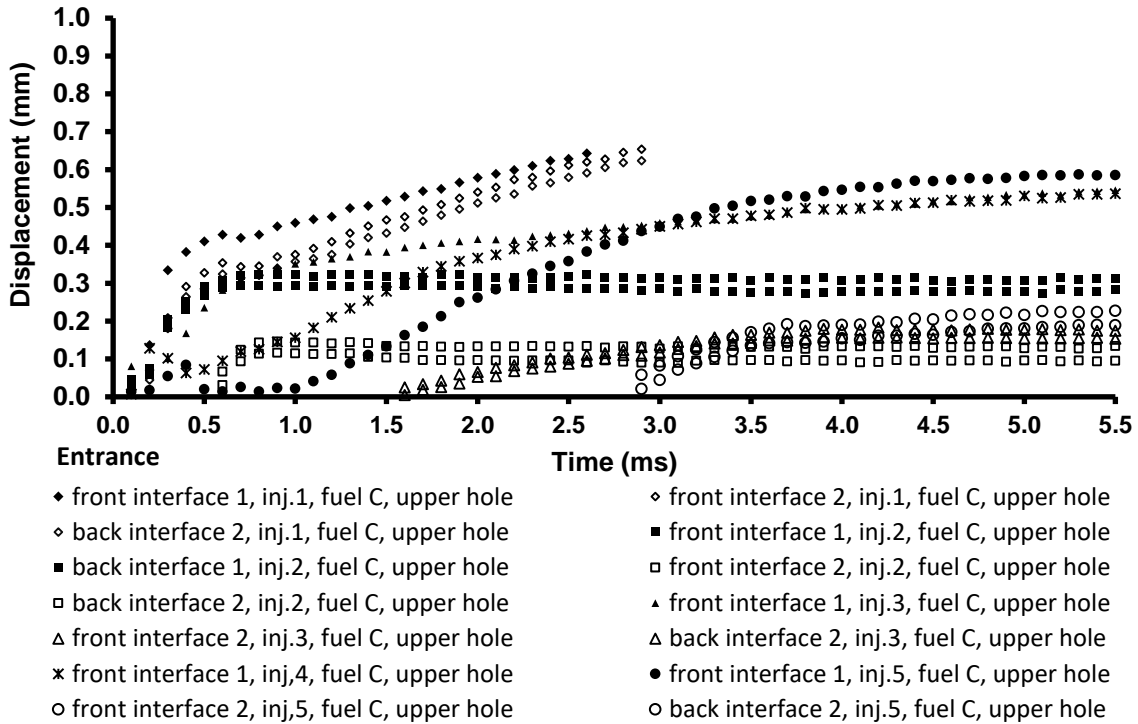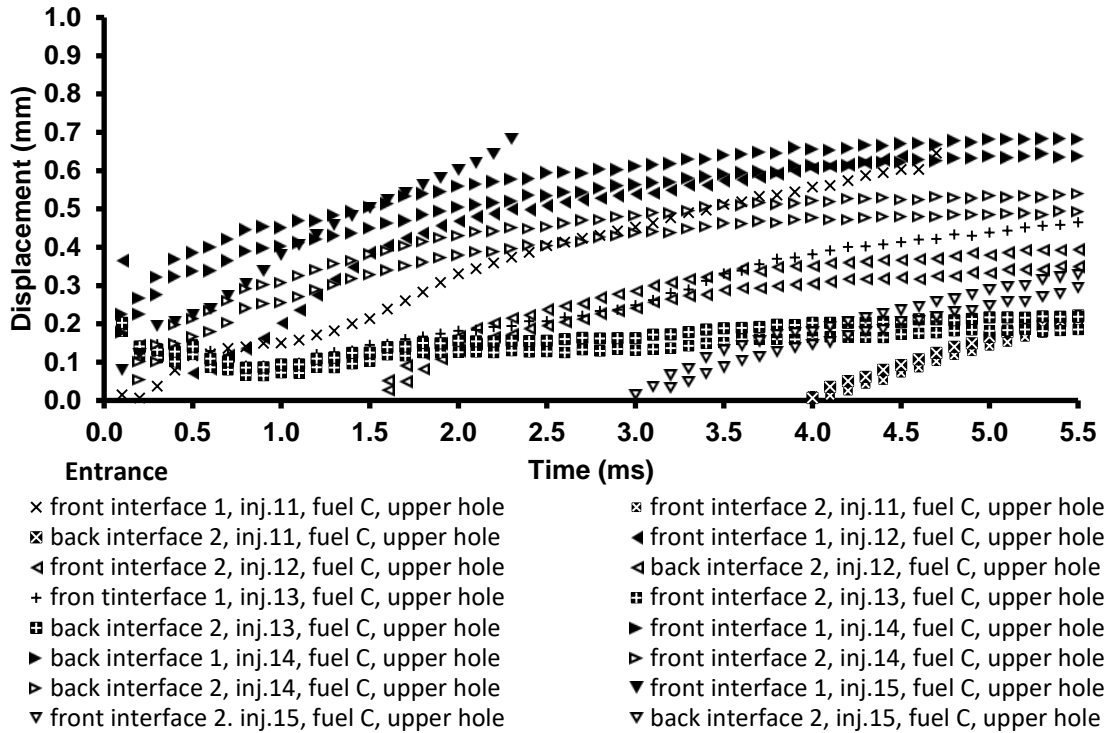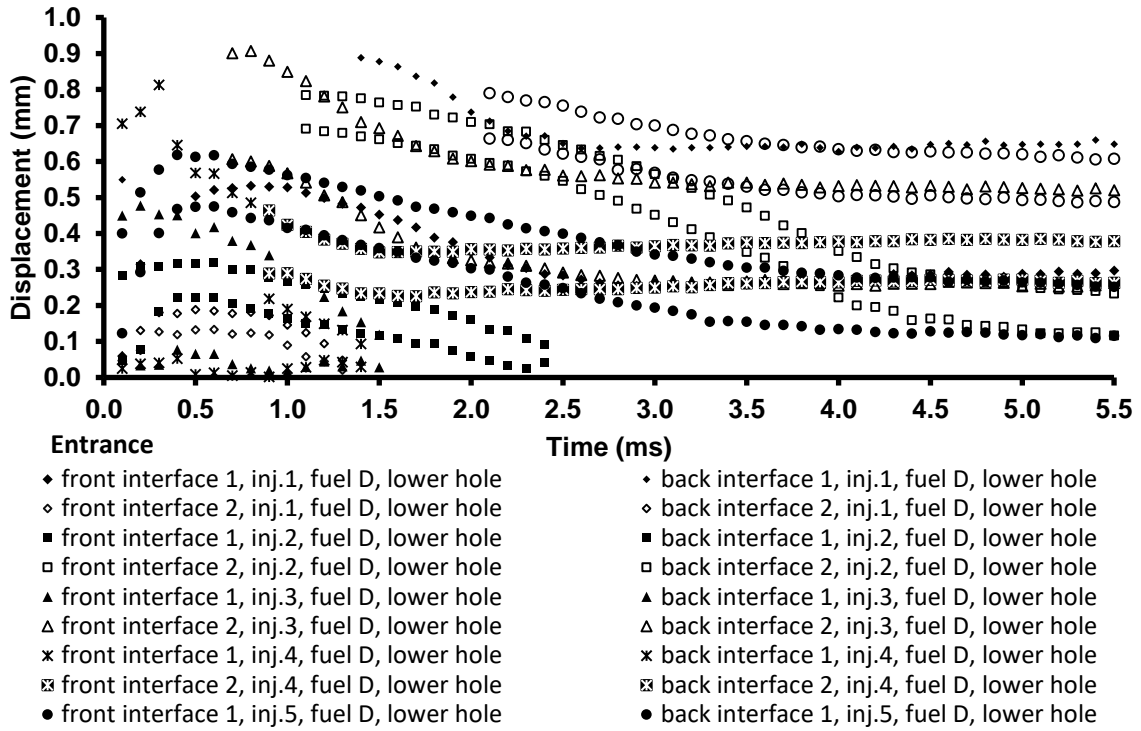Figure A1.30: Displacement vs. time graph, fuel E, 350bar, inj. 6-10, upper hole.

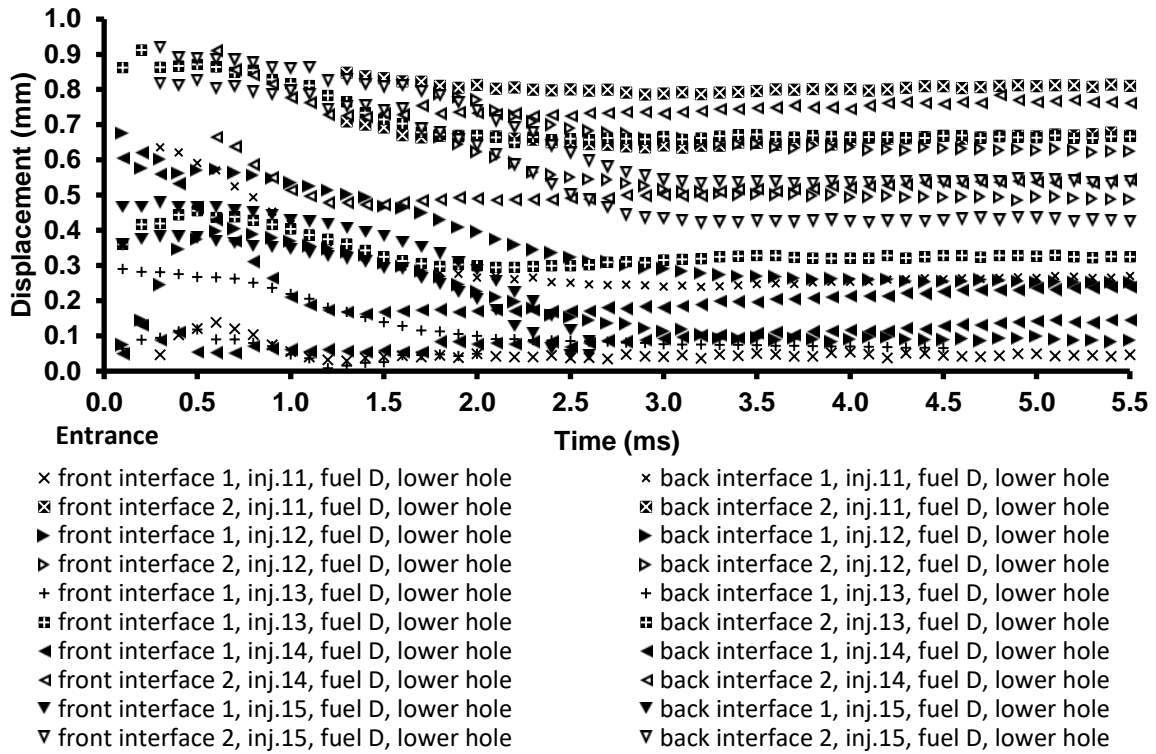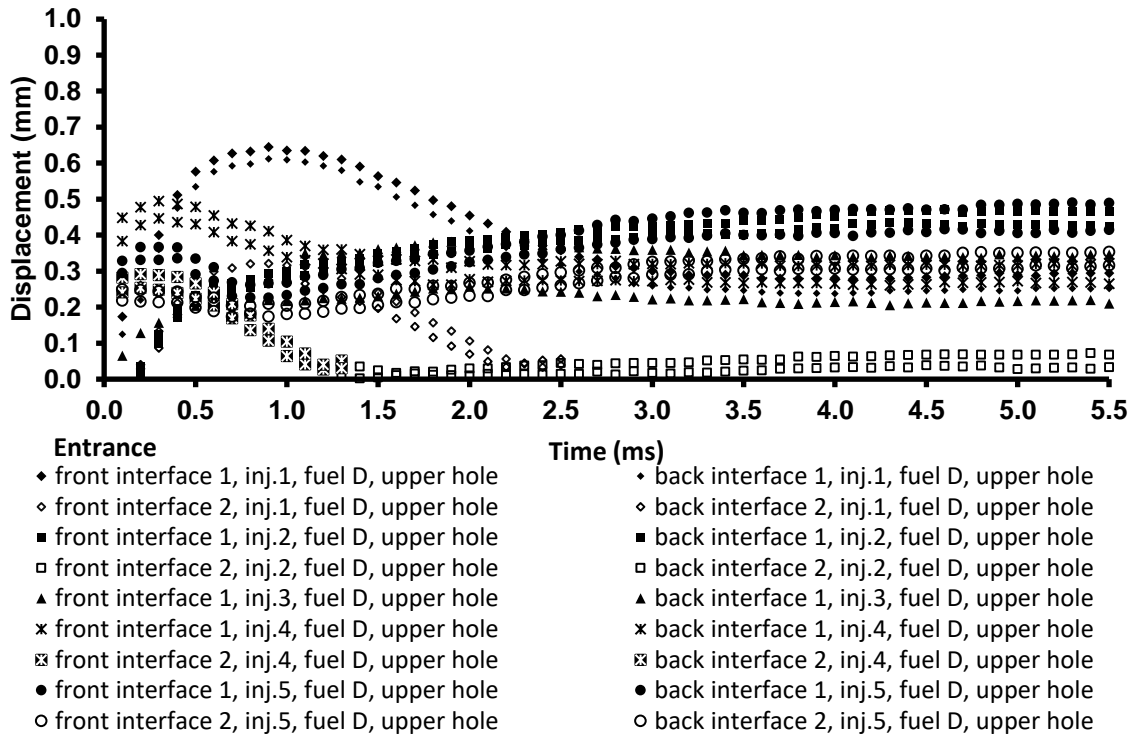Figure A1.31: Displacement vs. time graph, fuel E, 350bar, inj. 11-15, upper hole.

Figure A1.32: Displacement vs. time graph, fuel E, 350bar, inj. 16-20, upper hole.

Appendix A2   Correlation between mean in-hole speed and

mean in-sac radial flow

Figure A2.1: Mean speed vs. mean angular speed graph, fuel B, 350bar, inj.1-5, lower hole.

Figure A2.2: Mean speed vs. mean angular speed graph, fuel B, 350bar, inj.6-10, lower hole.

Correlation between mean in-hole speed and mean in-sac radial flow

Figure A2.3: Mean speed vs. mean angular speed graph, fuel B, 350bar, inj.11-15, lower hole.

Figure A2.4: Mean speed vs. mean angular speed graph, fuel B, 350bar, inj.16-20, lower hole.

Correlation between mean in-hole speed and mean in-sac radial flow

Figure A2.5: Mean speed vs. mean angular speed graph, fuel B, 350bar, inj.1-5, upper hole.

Figure A2.6: Mean speed vs. mean angular speed graph, fuel B, 350bar, inj.6-10, upper hole.

Correlation between mean in-hole speed and mean in-sac radial flow

Figure A2.7: Mean speed vs. mean angular speed graph, fuel B, 350bar, inj.11-15, upper hole.

Figure A2.8: Mean speed vs. mean angular speed graph, fuel B, 350bar, inj.16-20, upper hole.

Correlation between mean in-hole speed and mean in-sac radial flow

Figure A2.9: Mean speed vs. mean angular speed graph, fuel C, 350bar, inj.1-5, lower hole.

Figure A2.10: Mean speed vs. mean angular speed graph, fuel C, 350bar, inj.6-10, lower hole.

Correlation between mean in-hole speed and mean in-sac radial flow

Figure A2.11: Mean speed vs. mean angular speed graph, fuel C, 350bar, inj.11-15, lower hole.
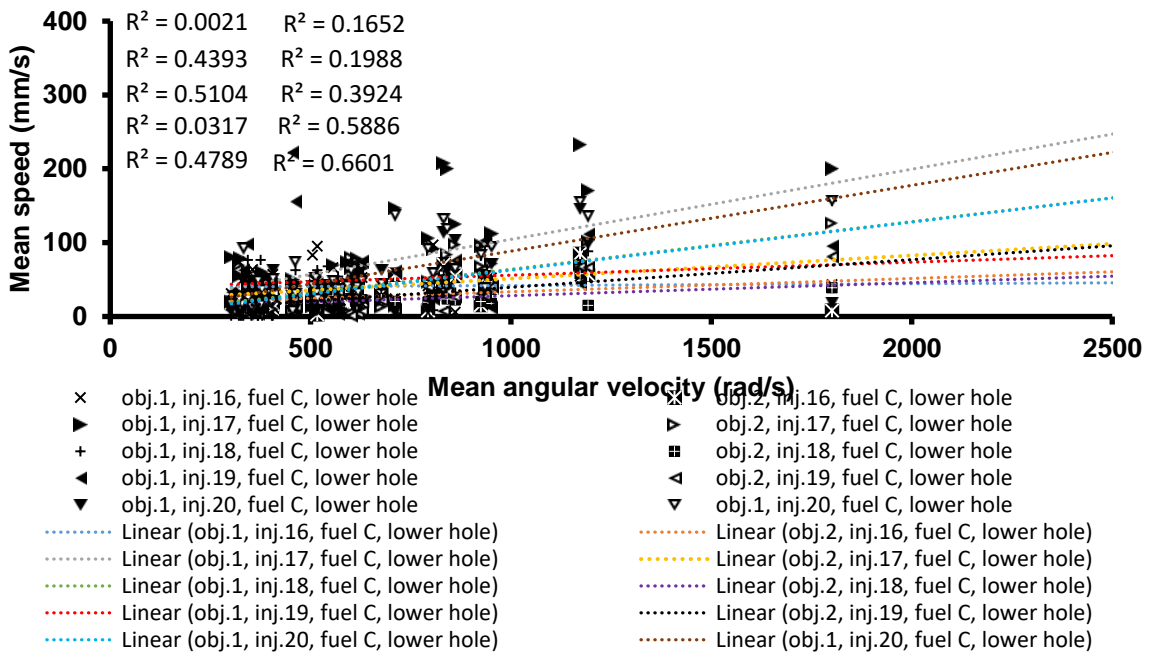
Figure A2.12: Mean speed vs. mean angular speed graph, fuel C, 350bar, inj.16-20, lower hole.

Correlation between mean in-hole speed and mean in-sac radial flow
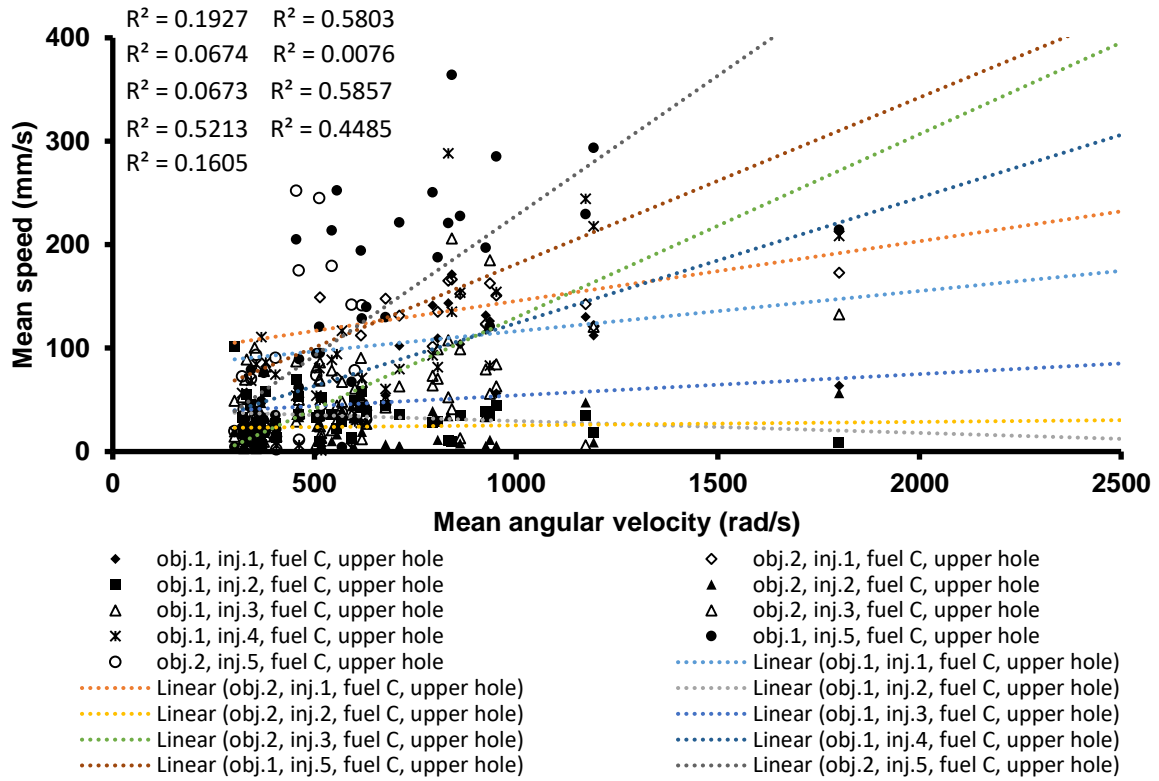
Figure A2.13: Mean speed vs. mean angular speed graph, fuel C, 350bar, inj.1-5, upper hole.
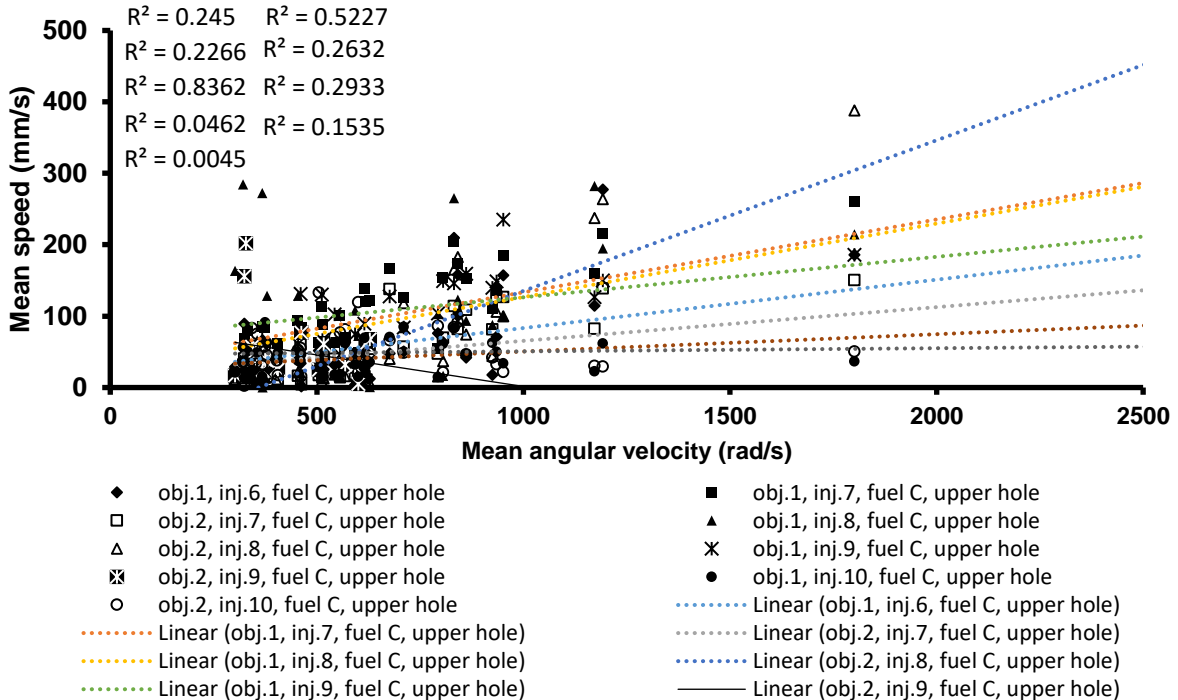
Figure A2.14: Mean speed vs. mean angular speed graph, fuel C, 350bar, inj.6-10, upper hole.

Correlation between mean in-hole speed and mean in-sac radial flow
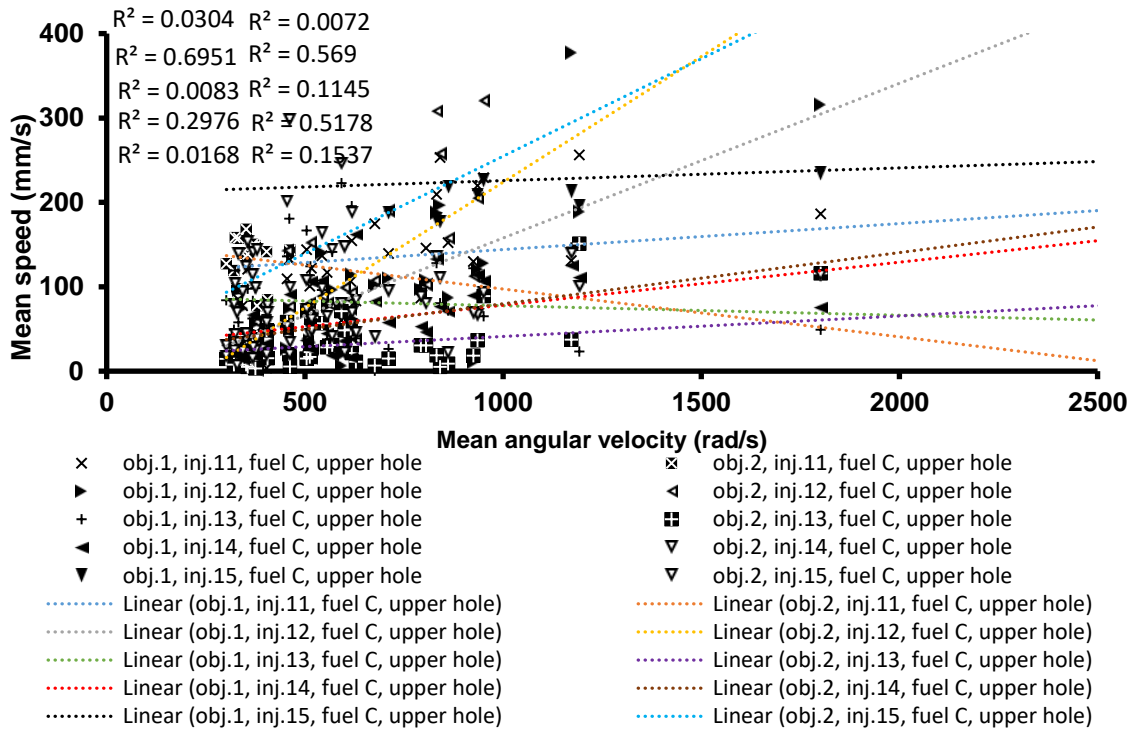
Figure A2.15: Mean speed vs. mean angular speed graph, fuel C, 350bar, inj.11-15, upper hole.
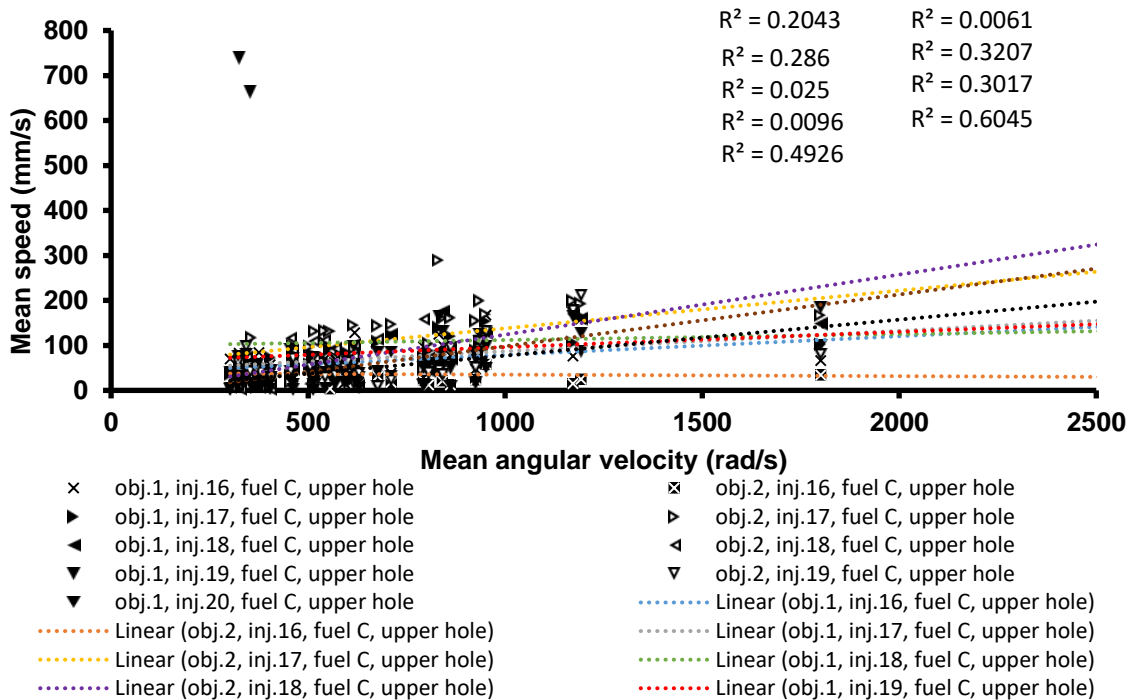
Figure A2.16: Mean speed vs. mean angular speed graph, fuel C, 350bar, inj.16-20, upper hole.

Correlation between mean in-hole speed and mean in-sac radial flow
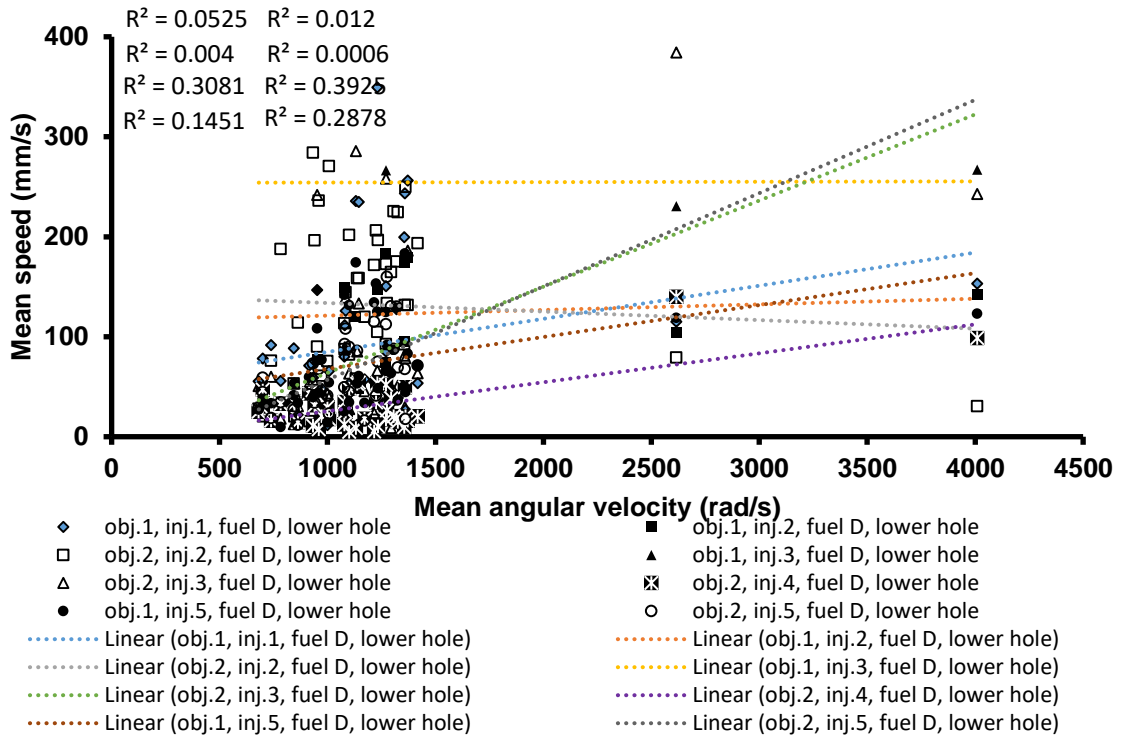
Figure A2.17: Mean speed vs. mean angular speed graph, fuel D, 350bar, inj.1-5, lower hole.
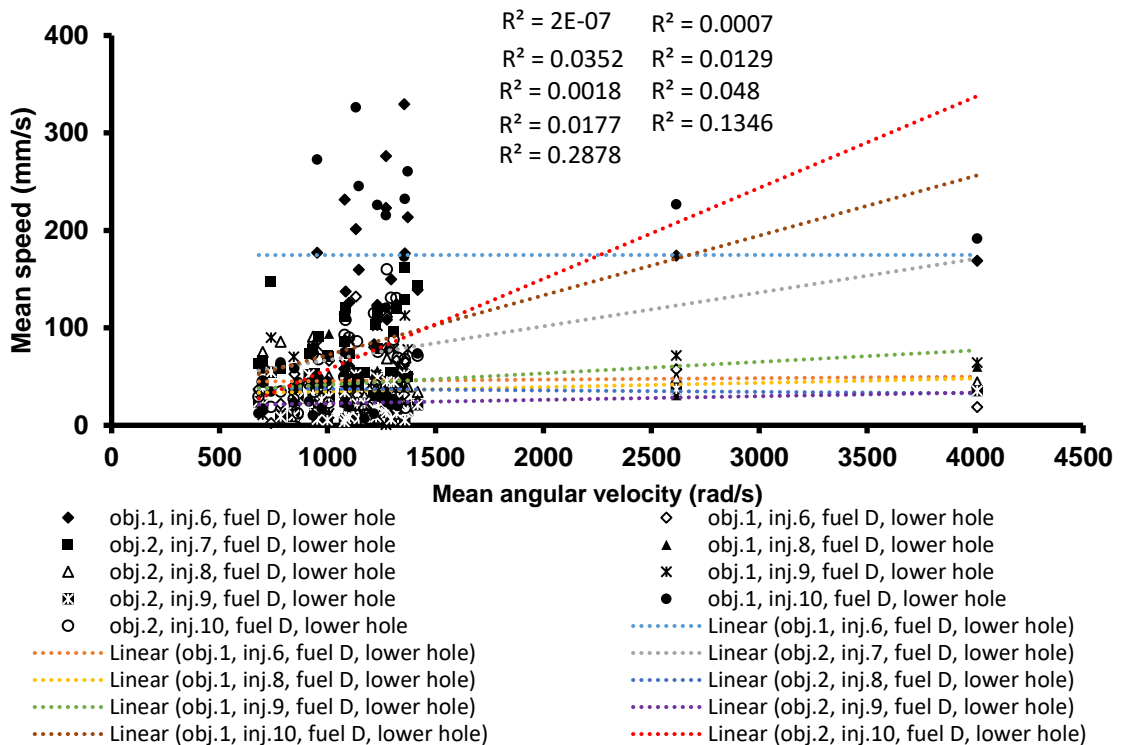
Figure A2.18: Mean speed vs. mean angular speed graph, fuel D, 350bar, inj.6-10, lower hole.

Correlation between mean in-hole speed and mean in-sac radial flow
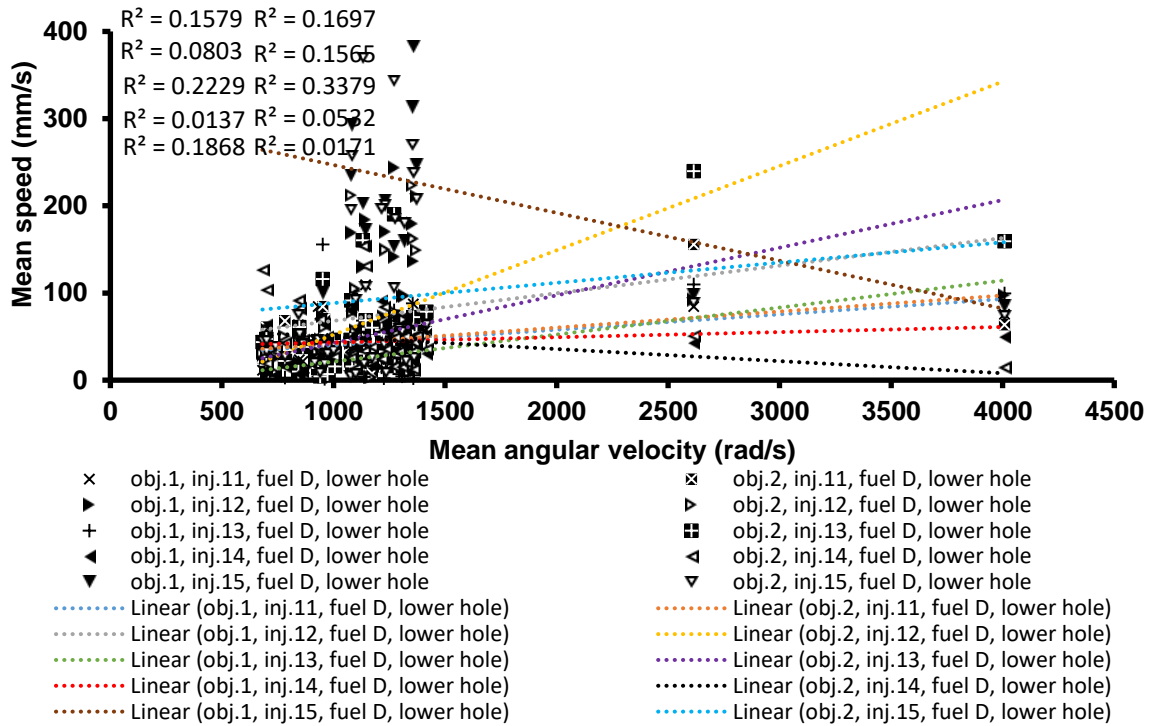
Figure A2.19: Mean speed vs. mean angular speed graph, fuel D, 350bar, inj.11-15, lower hole.
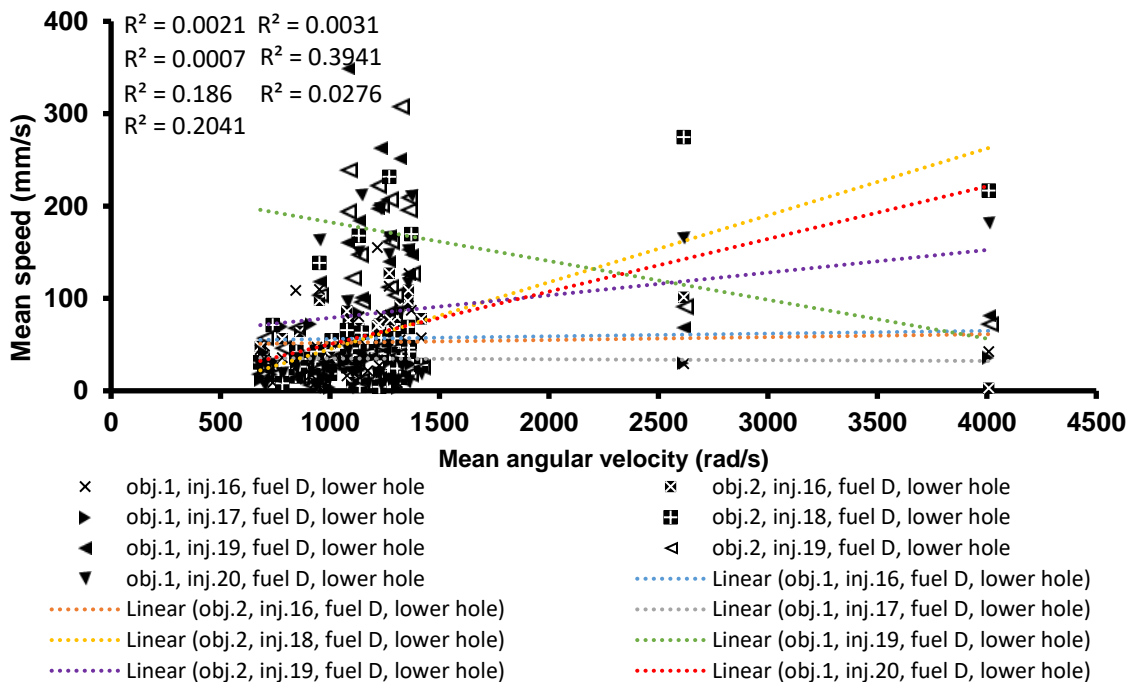
Figure A2.20: Mean speed vs. mean angular speed graph, fuel D, 350bar, inj.16-20, lower hole.

Correlation between mean in-hole speed and mean in-sac radial flow
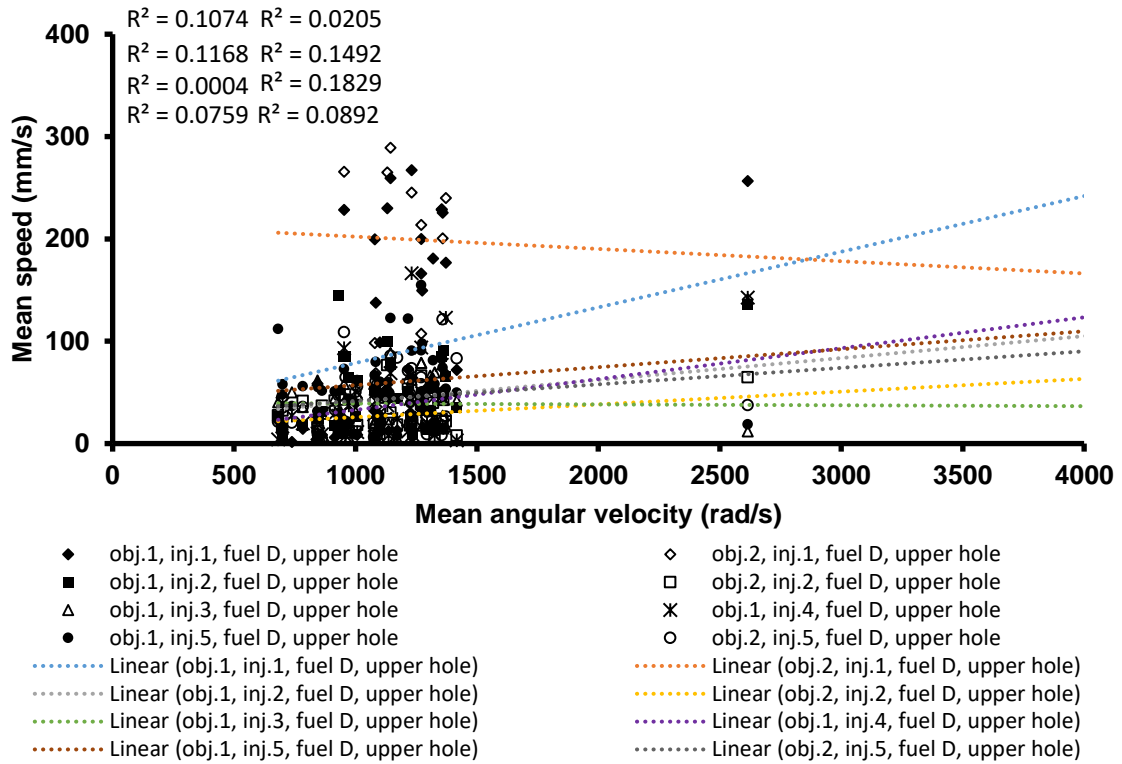
Figure A2.21: Mean speed vs. mean angular speed graph, fuel D, 350bar, inj.1-5, upper hole.
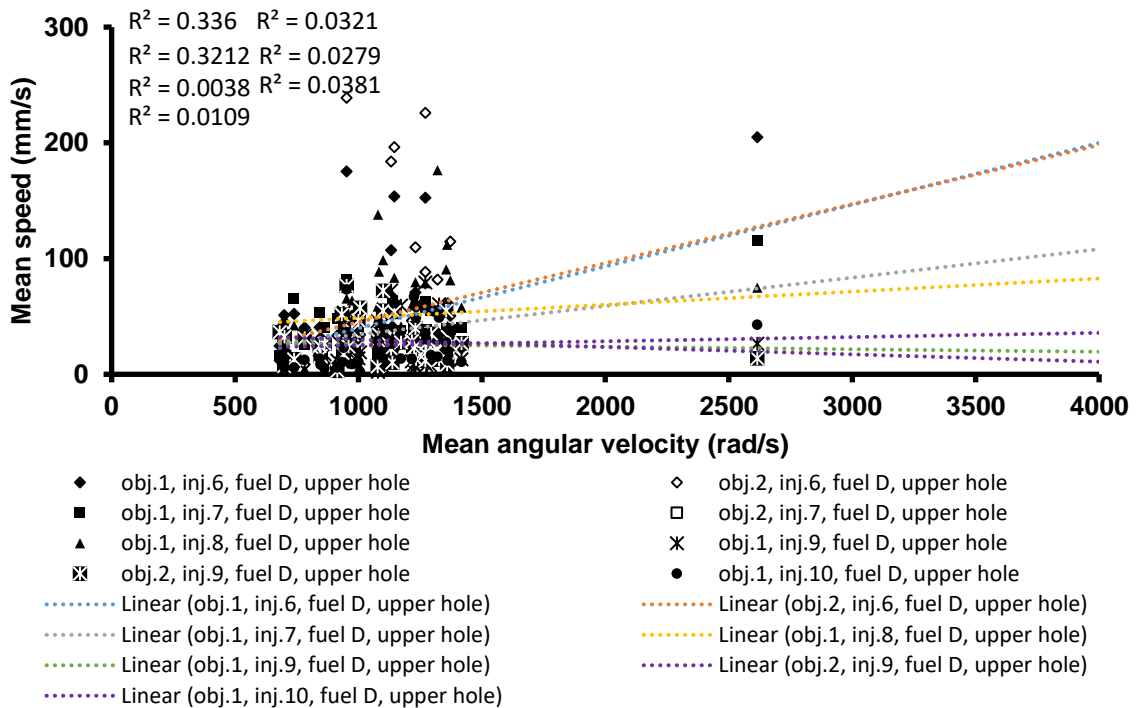
Figure A2.22: Mean speed vs. mean angular speed graph, fuel D, 350bar, inj.6-10, upper hole.

Correlation between mean in-hole speed and mean in-sac radial flow
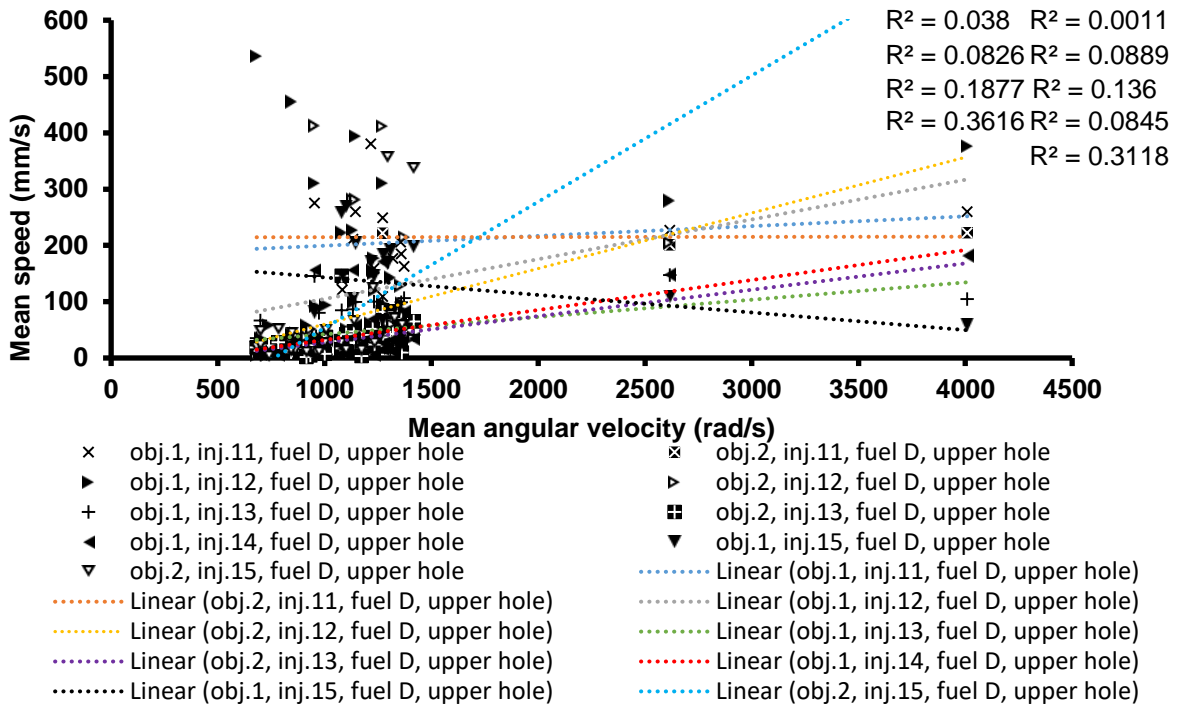
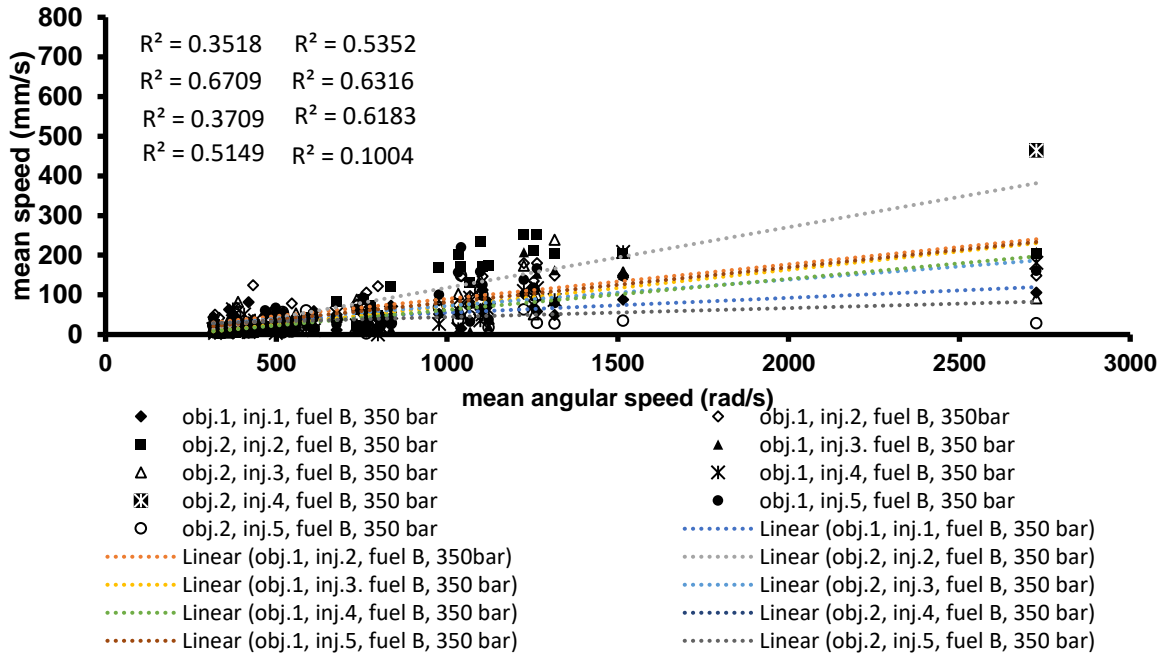Figure A2.23: Mean speed vs. mean angular speed graph, fuel D, 350bar, inj.11-15, upper hole.
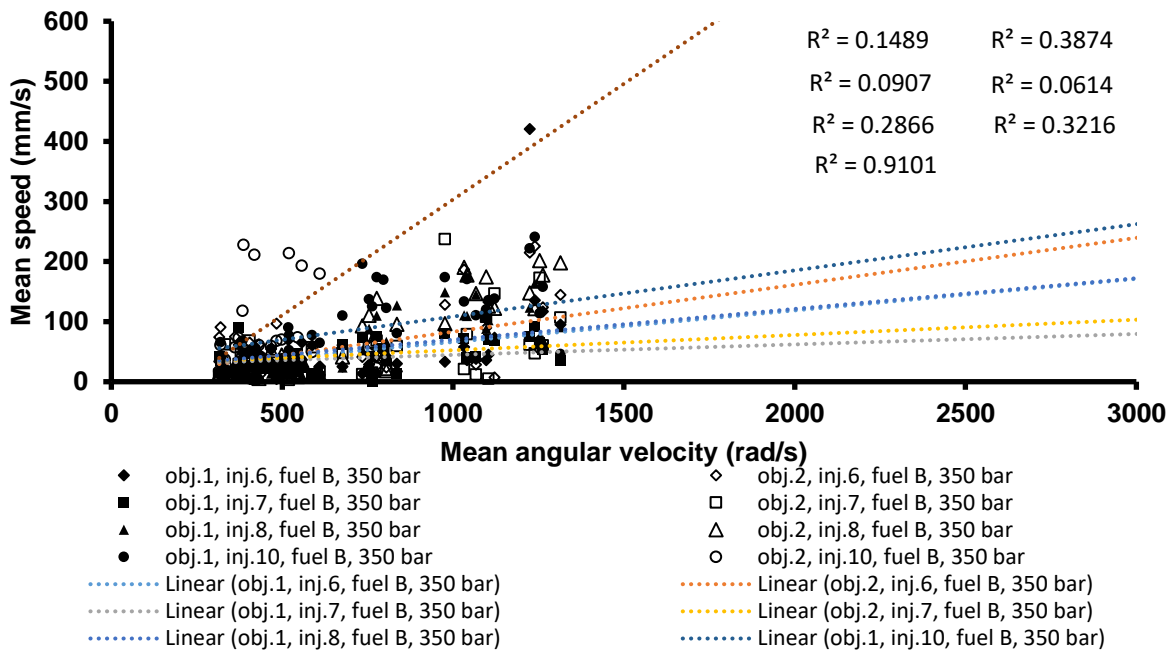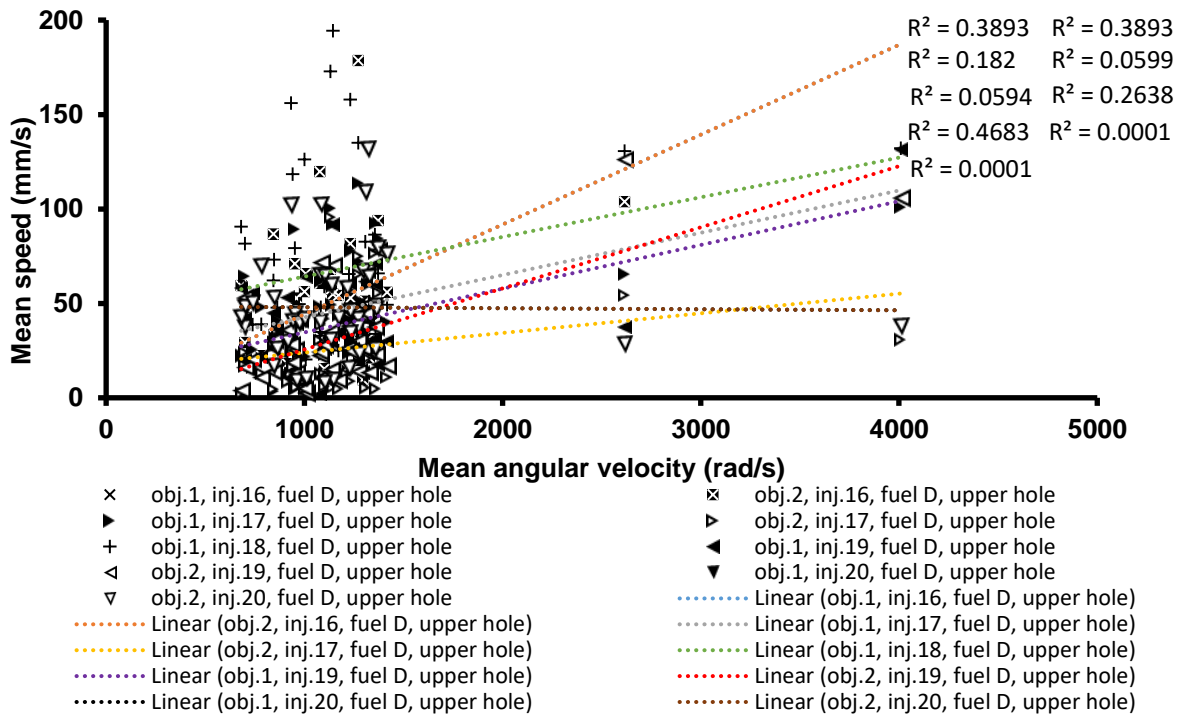

Figure A2.24: Mean speed vs. mean angular speed graph, fuel D, 350bar, inj.16-20, upper hole.

Correlation between mean in-hole speed and mean in-sac radial flow

R² = 0.1603   R² = 0.2576
R² = 0.5476   R² = 0.0001
R² = 0.3537   R² = 0.3957

Legend:
- ■ obj.1, inj.2, fuel E, lower hole
- □ obj.2, inj.2, fuel E, lower hole
- ▲ obj.1, inj.3, fuel E, lower hole
- ✳ obj.1, inj.4, fuel E, lower hole
- ⊠ obj.2, inj.4, fuel E, lower hole
- ● obj.1, inj.5, fuel E, lower hole
- ⋯ Linear (obj.1, inj.2, fuel E, lower hole)
- ⋯ Linear (obj.2, inj.2, fuel E, lower hole)
- ⋯ Linear (obj.1, inj.3, fuel E, lower hole)
- ⋯ Linear (obj.1, inj.4, fuel E, lower hole)
- ⋯ Linear (obj.2, inj.4, fuel E, lower hole)
- ⋯ Linear (obj.1, inj.5, fuel E, lower hole)
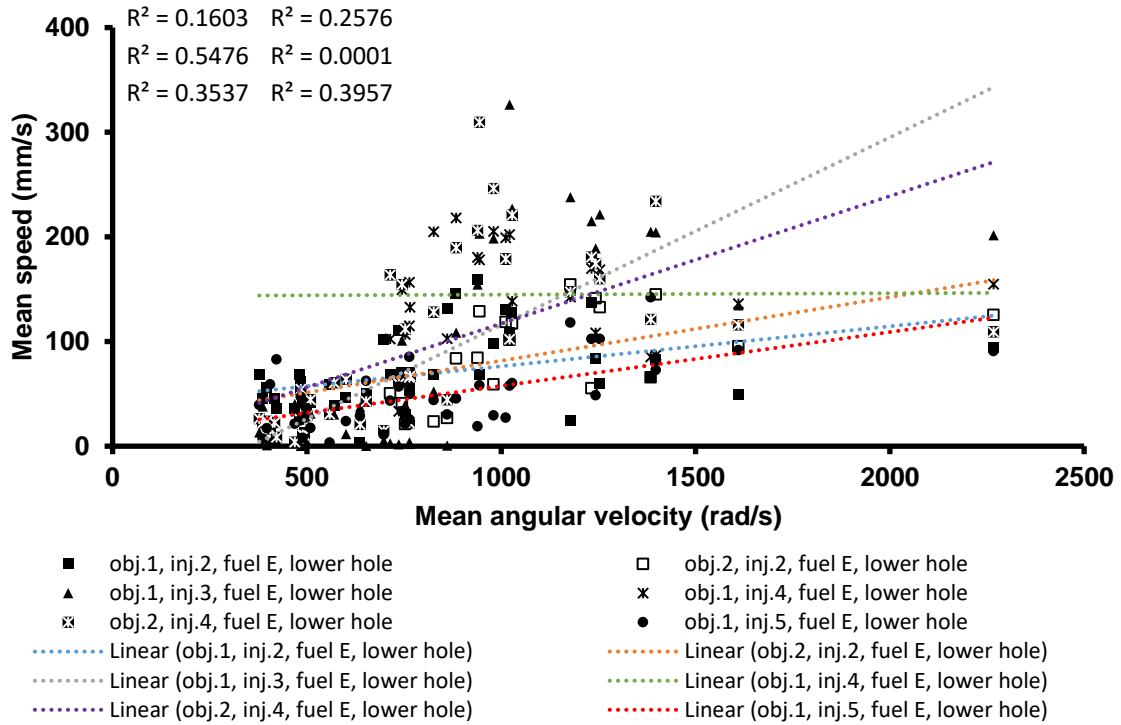
Figure A2.25: Mean speed vs. mean angular speed graph, fuel E, 350bar, inj.1-5, lower hole.

R² = 0.0053   R² = 0.2009
R² = 0.5363   R² = 0.0696
R² = 0.0087   R² = 0.0294
R² = 0.0294

Legend:
- ■ obj.1, inj.7, fuel E, lower hole
- ■ obj.1, inj.8, fuel E, lower hole
- ▲ obj.2, inj.8, fuel E, lower hole
- ✳ obj.1, inj.9, fuel E, lower hole
- ⊠ obj.2, inj.9, fuel E, lower hole
- ● obj.1, inj.10, fuel E, lower hole
- ○ obj.2, inj.10, fuel E, lower hole
- ⋯ Linear (obj.1, inj.7, fuel E, lower hole)
- ⋯ Linear (obj.1, inj.8, fuel E, lower hole)
- ⋯ Linear (obj.2, inj.8, fuel E, lower hole)
- ⋯ Linear (obj.1, inj.9, fuel E, lower hole)
- ⋯ Linear (obj.2, inj.9, fuel E, lower hole)
- ⋯ Linear (obj.1, inj.10, fuel E, lower hole)
- ⋯ Linear (obj.2, inj.10, fuel E, lower hole)

Figure A2.26: Mean speed vs. mean angular speed graph, fuel E, 350bar, inj.6-10, lower hole.

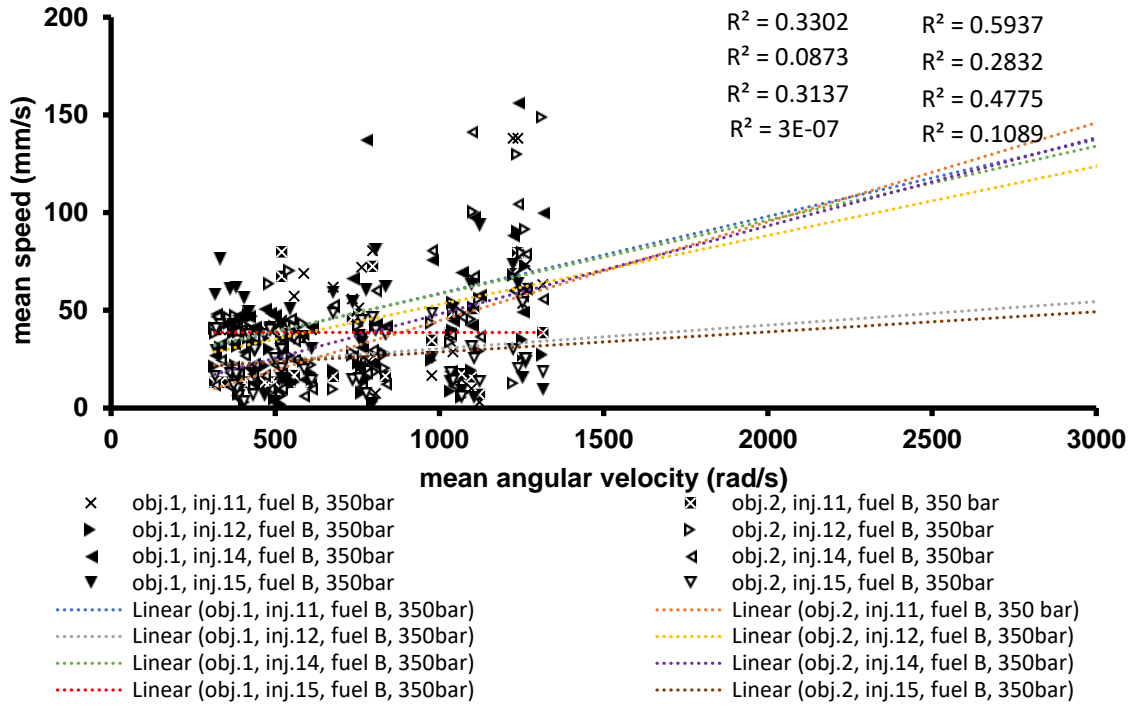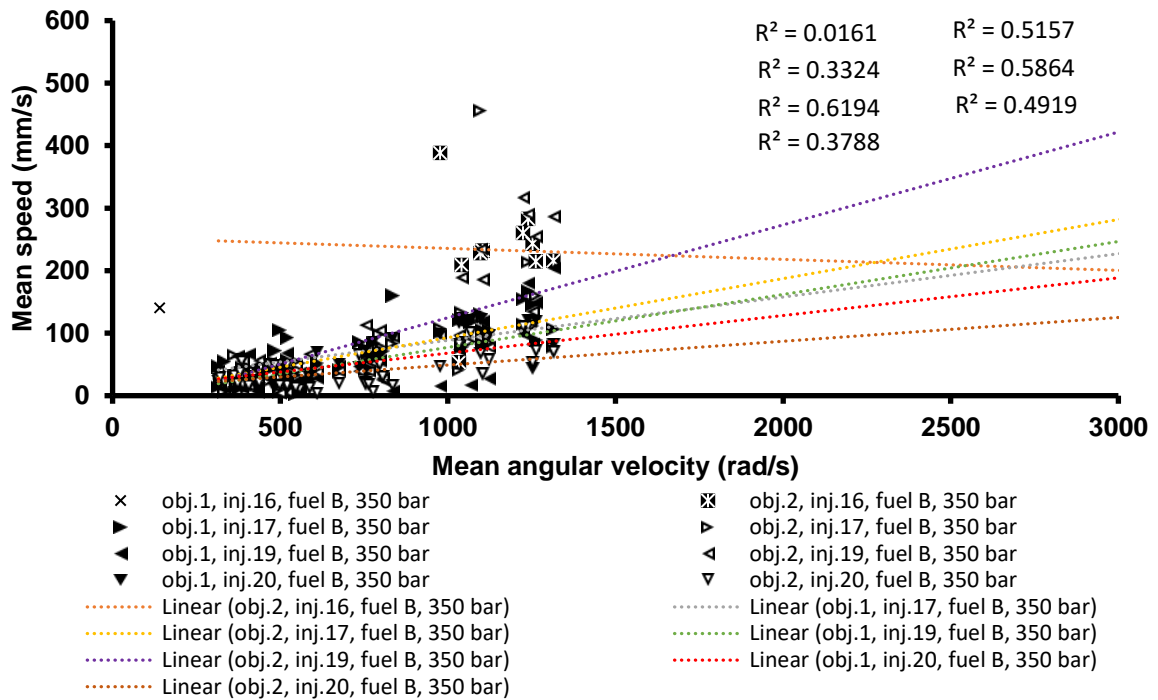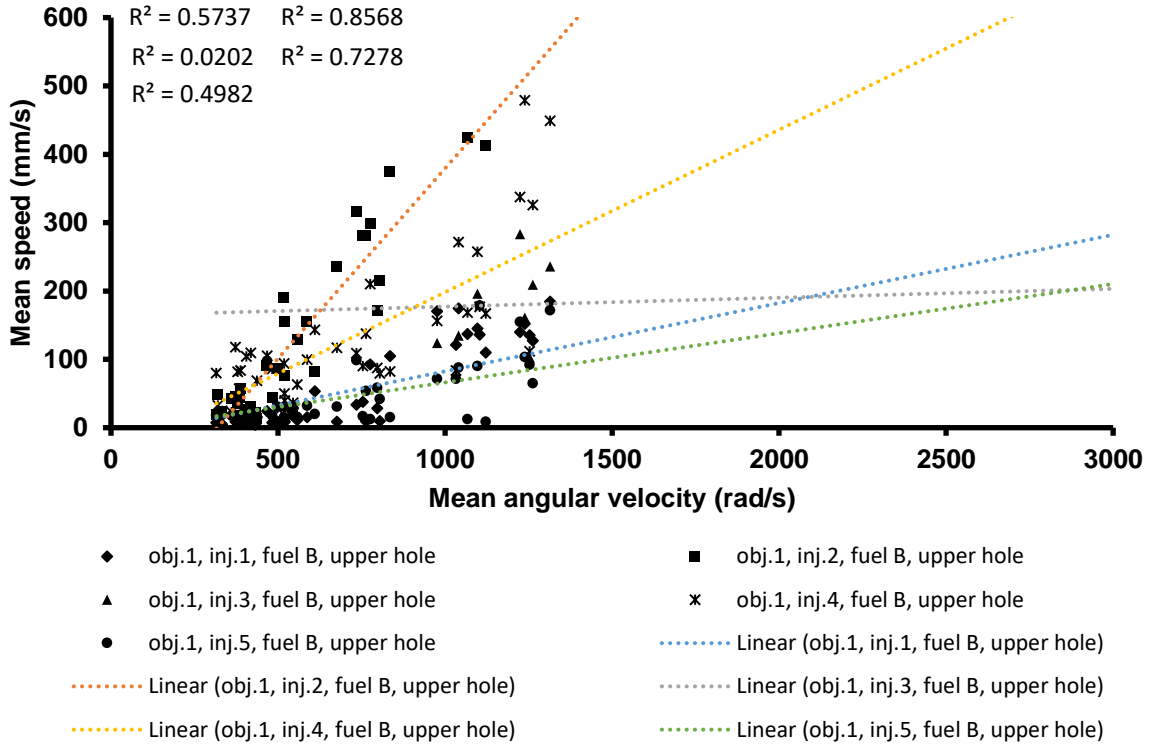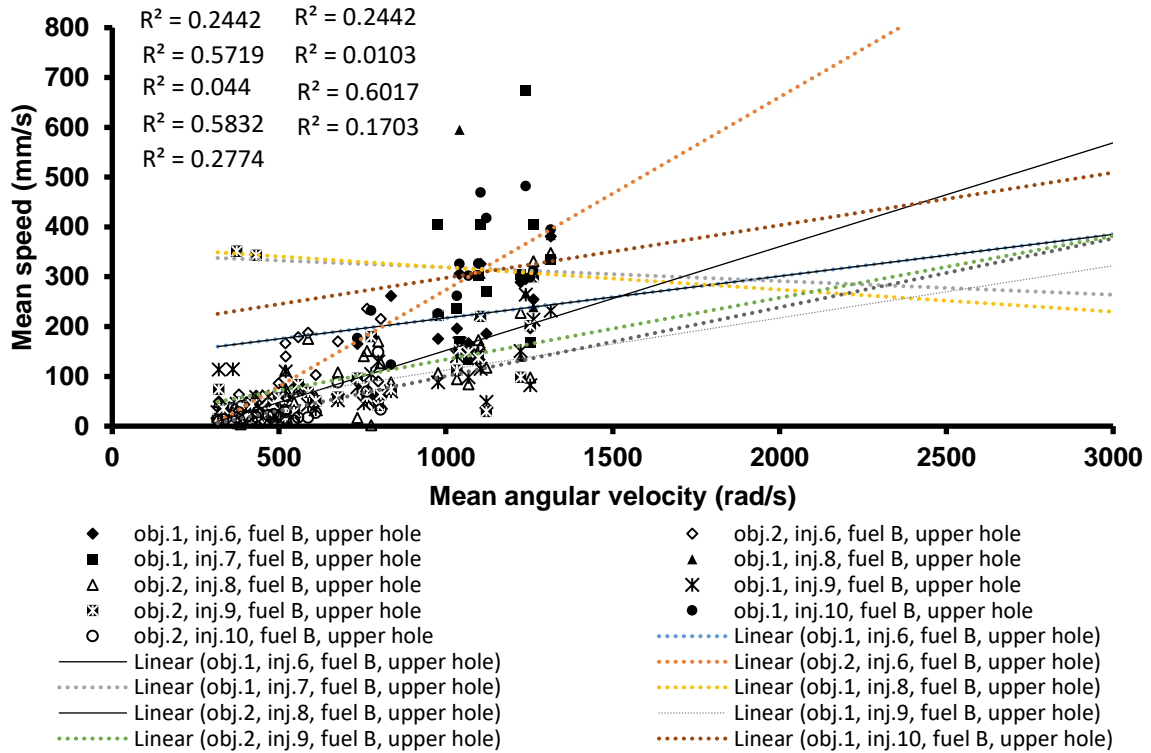**Correlation between mean in-hole speed and mean in-sac radial flow**

R² = 0.0059   R² = 0.0359
R² = 0.0017   R² = 0.045
R² = 0.1297   R² = 0.1297
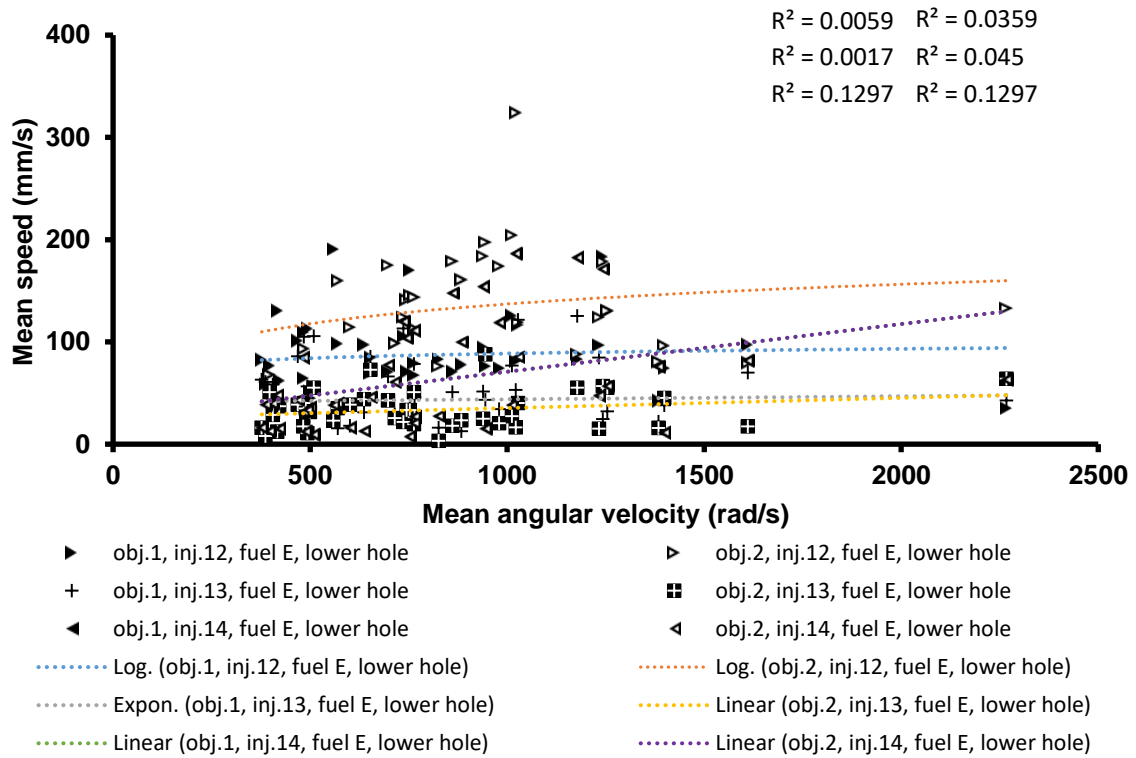
Figure A2.27: Mean speed vs. mean angular speed graph, fuel E, 350bar, inj.11-15, lower hole.

R² = 0.0012   R² = 0.2637
R² = 0.2476
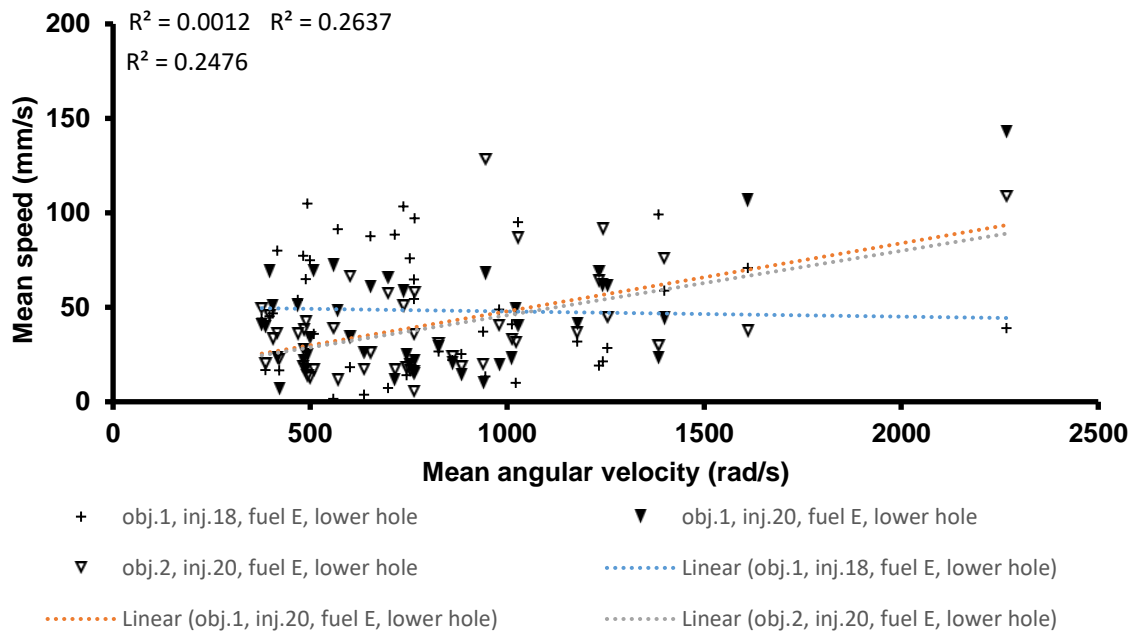
Figure A2.28: Mean speed vs. mean angular speed graph, fuel E, 350bar, inj.16-20, lower hole.

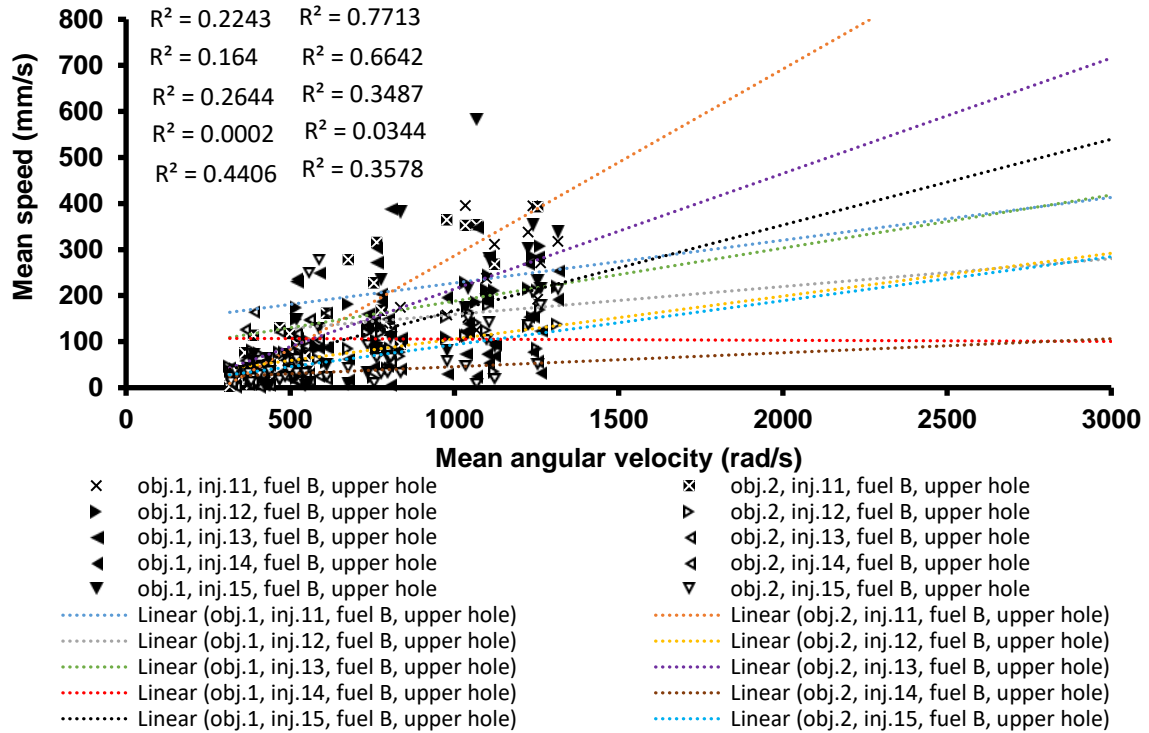**Correlation between mean in-hole speed and mean in-sac radial flow**
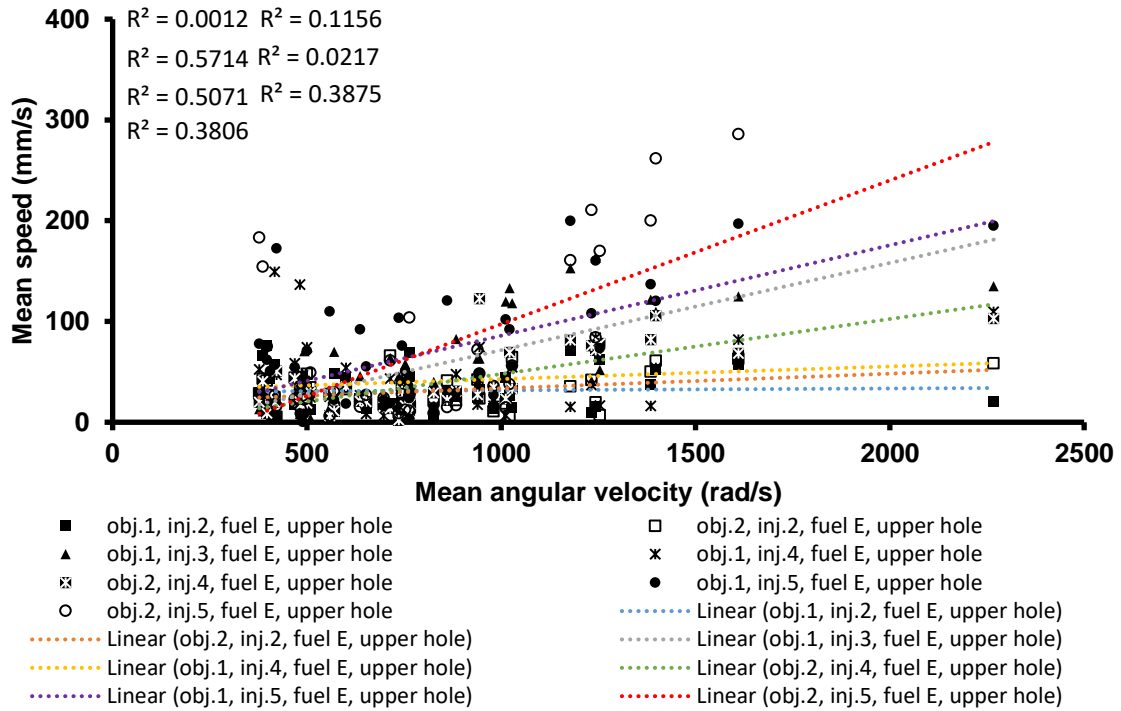
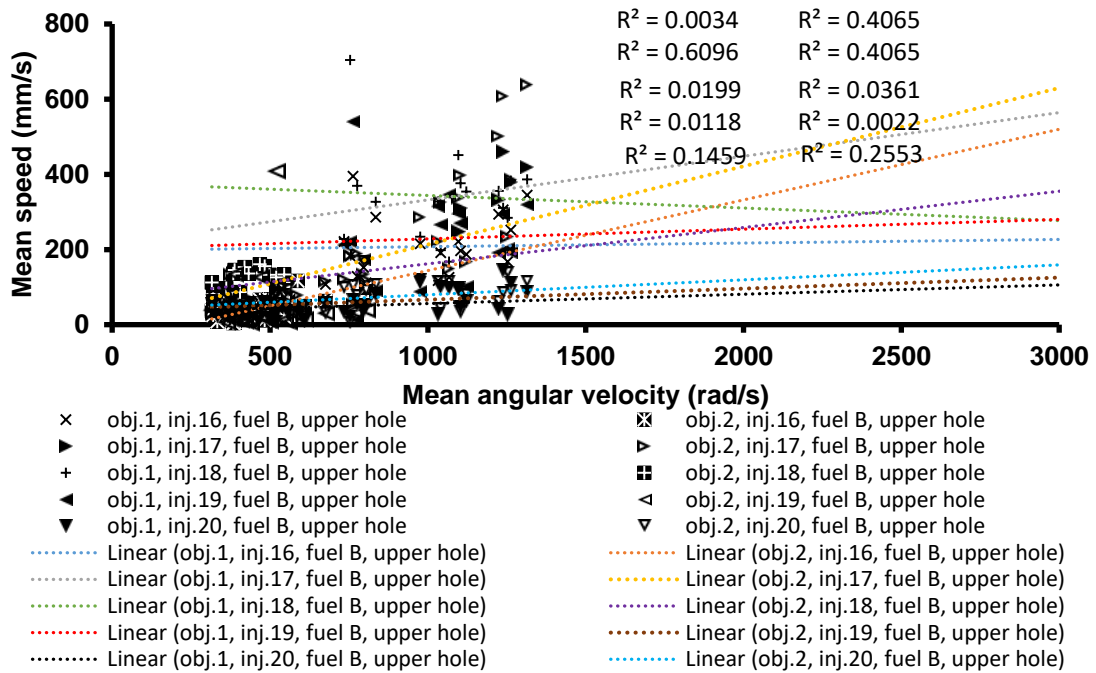Figure A2.29: Mean speed vs. mean angular speed graph, fuel E, 350bar, inj.1-5, upper hole.
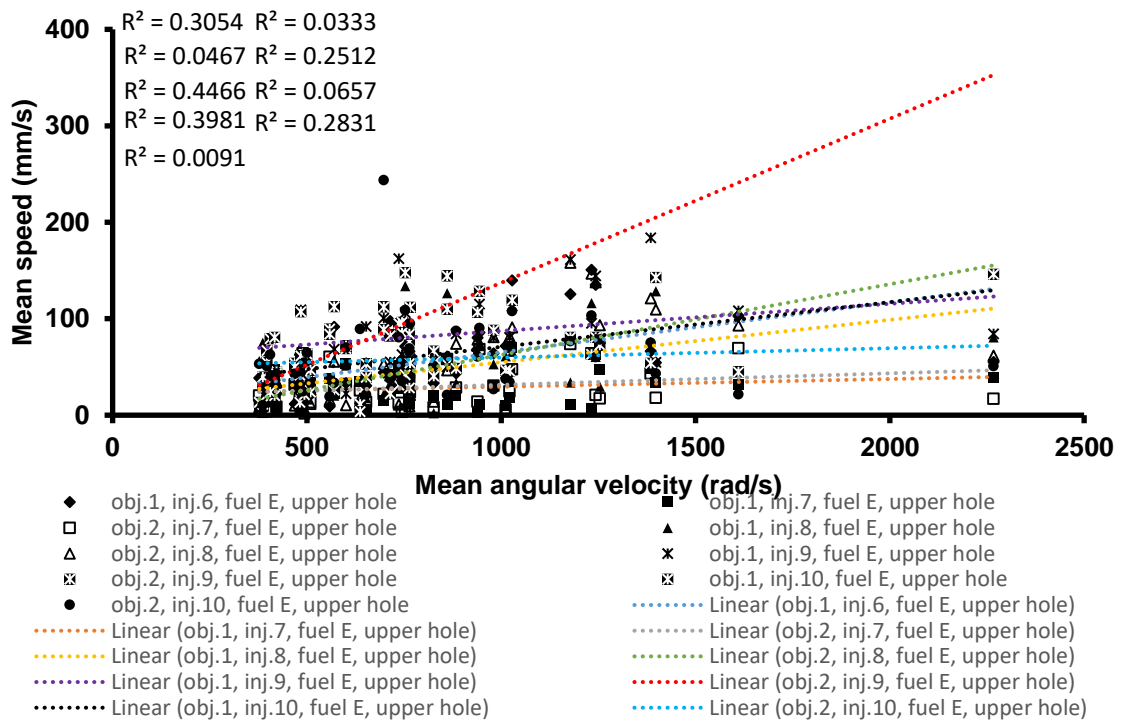
Figure A2.30: Mean speed vs. mean angular speed graph, fuel E, 350bar, inj.6-10, upper hole.

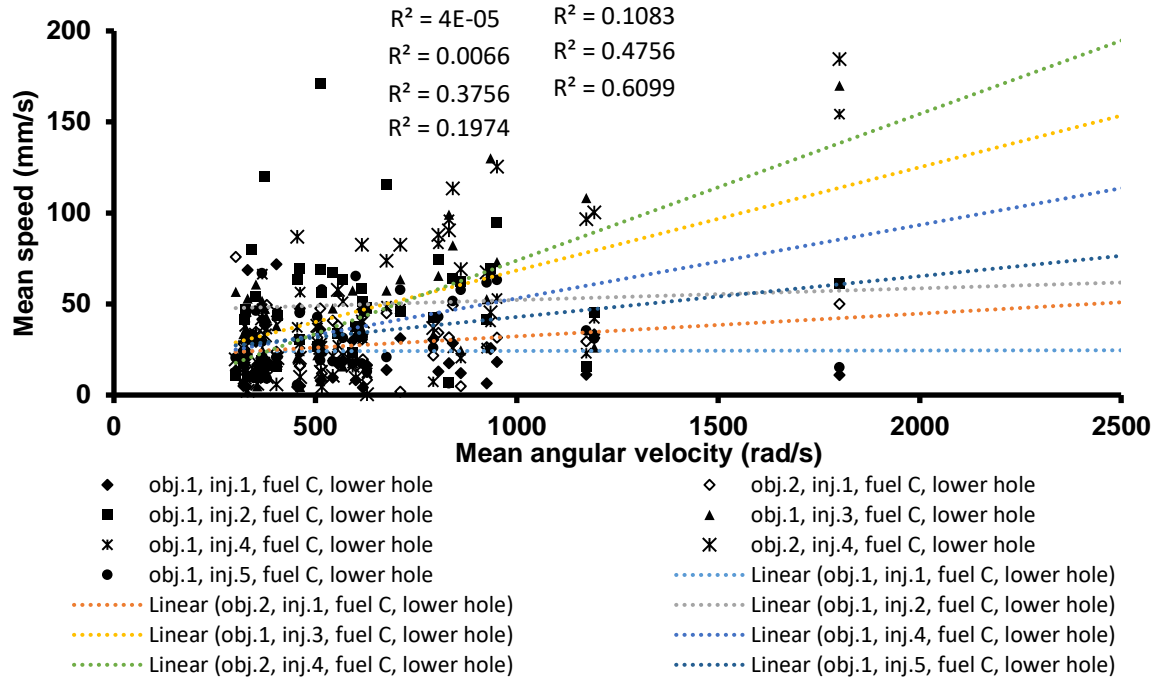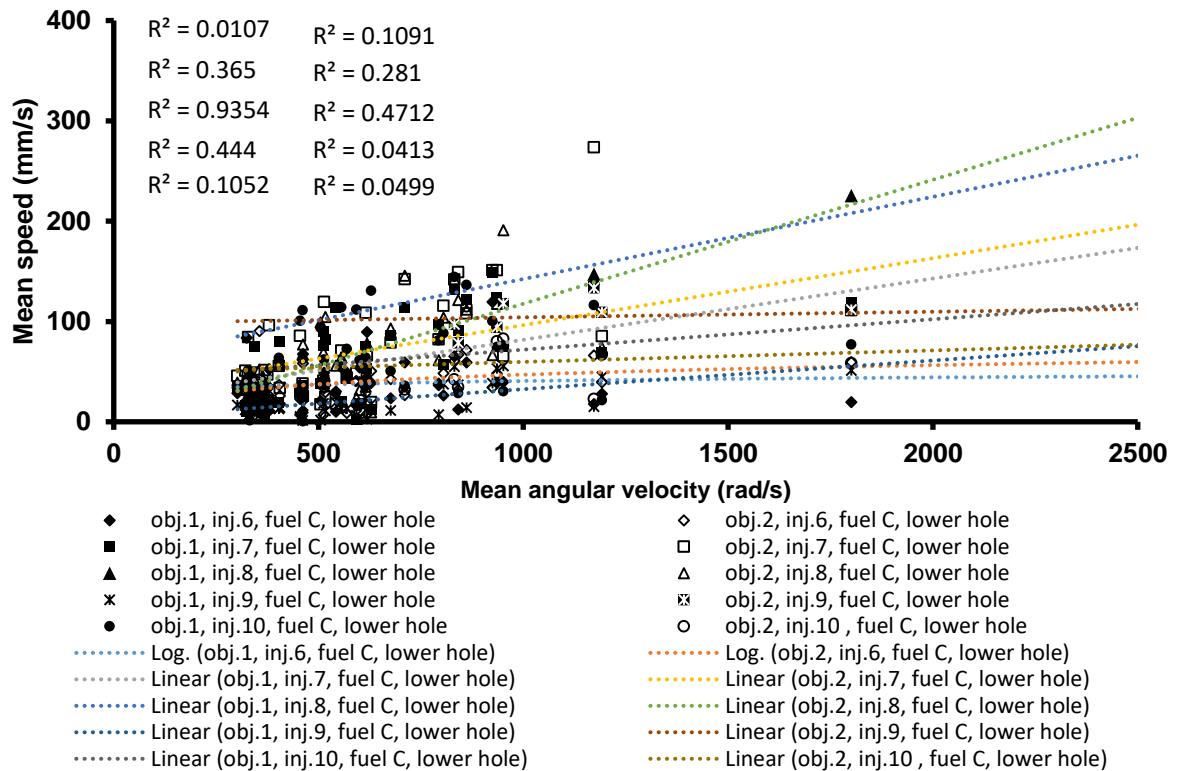# Correlation between mean in-hole speed and mean in-sac radial flow
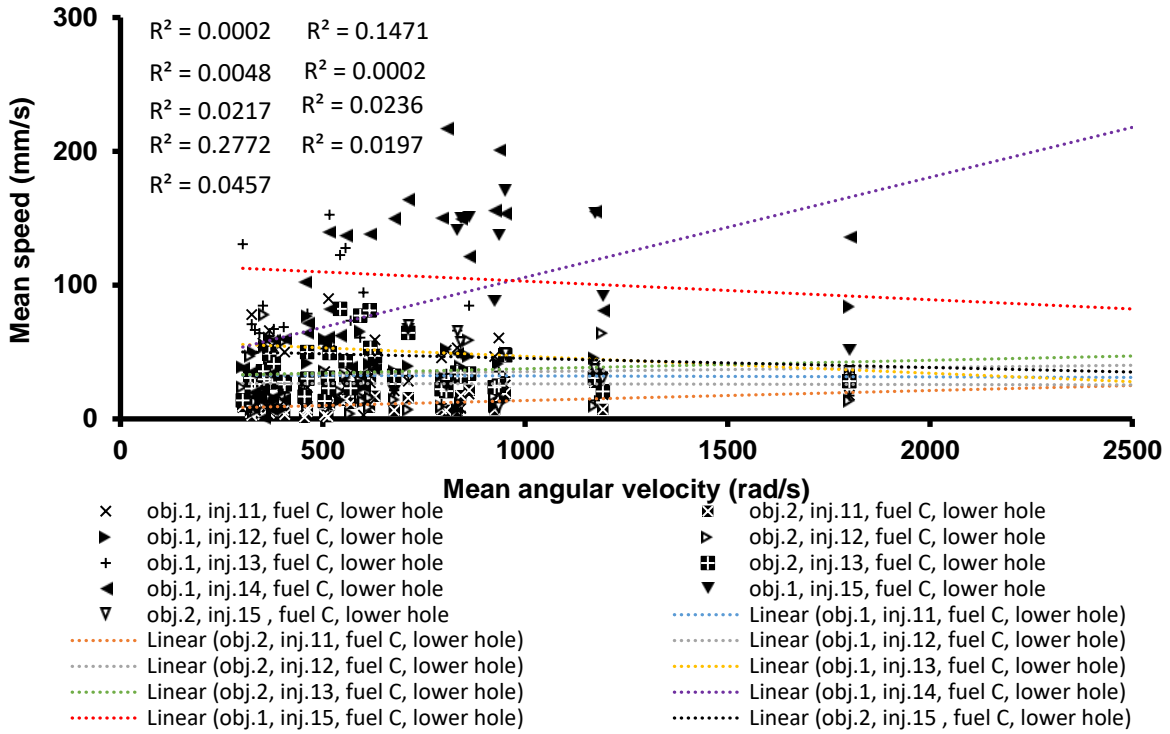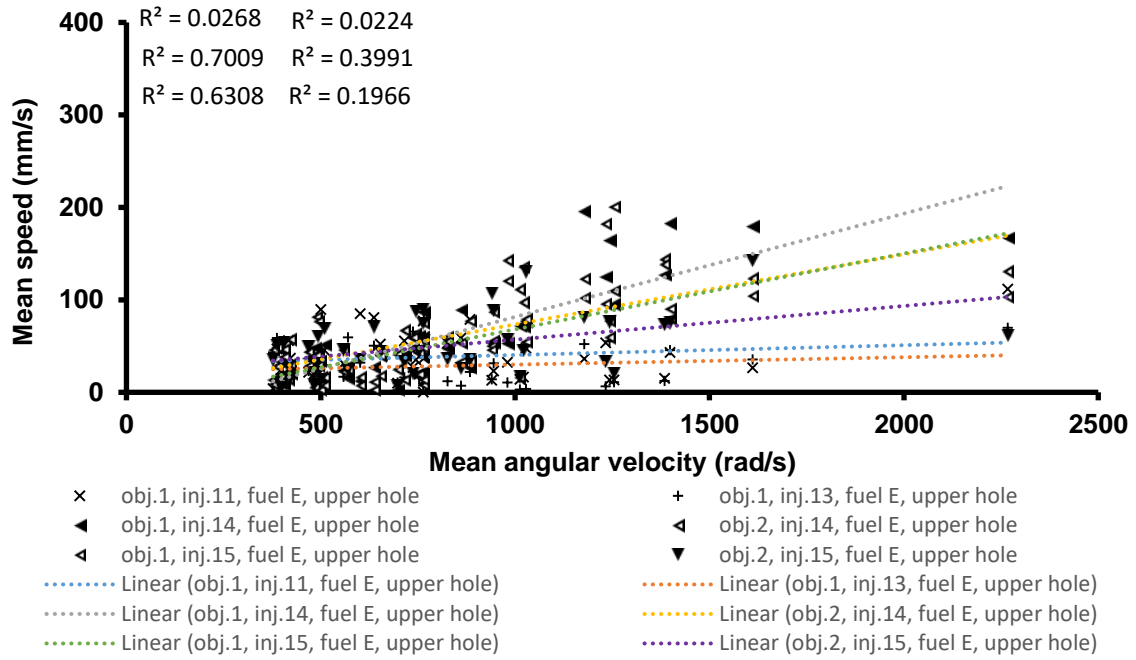

Figure A2.31: Mean speed vs. mean angular speed graph, fuel E, 350bar, inj.11-15, upper hole.
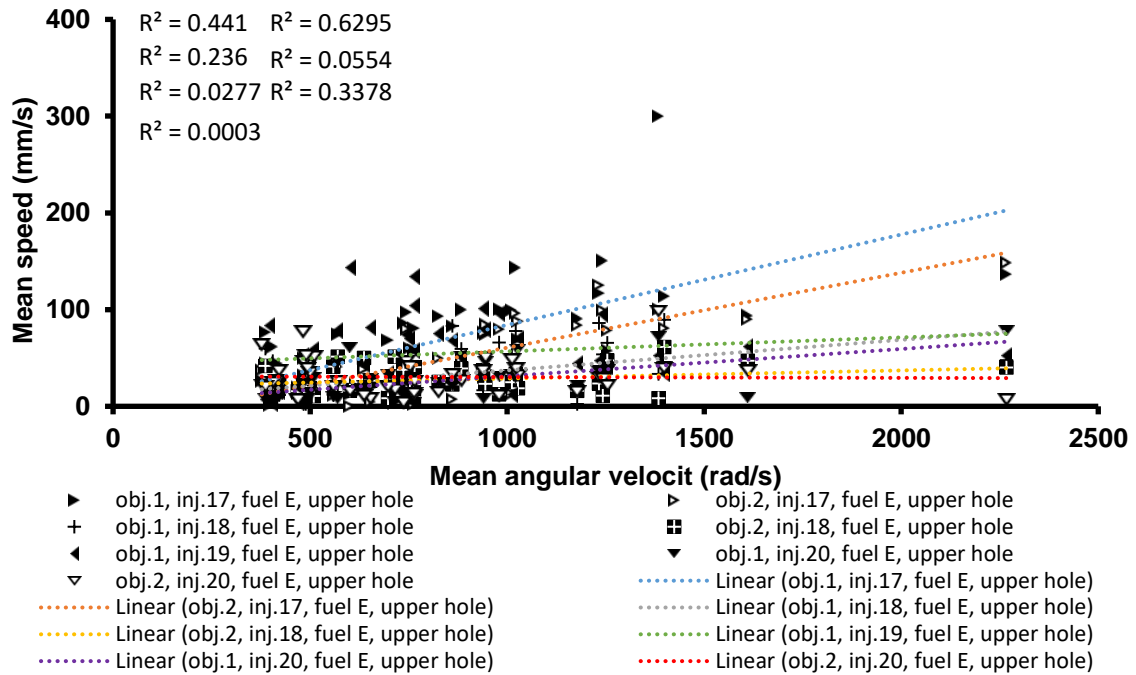
Figure A2.32: Mean speed vs. mean angular speed graph, fuel E, 350bar, inj.16-20, upper hole.

Appendix A3   Buoyant effects as a function of fuel 's physical properties.
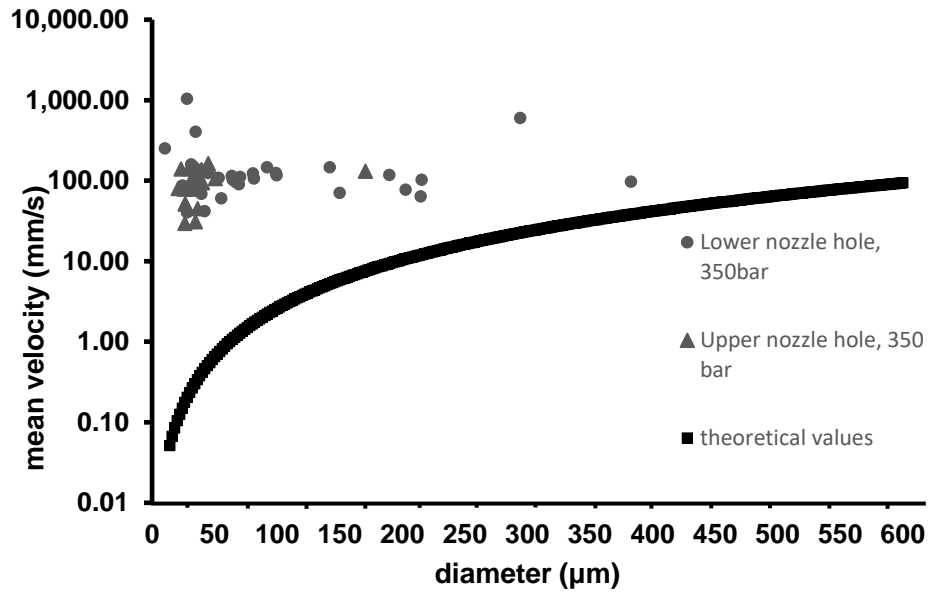
Figure A3.1: Actual bubble velocity inside the upper and lower holes versus the theoretical velocity due to buoyant forces, fuel B.
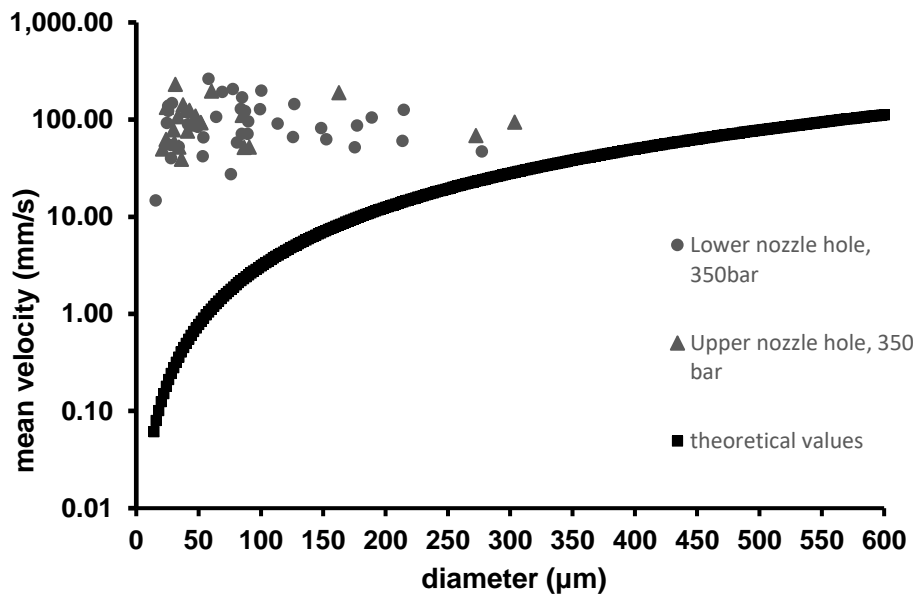
Figure A3.2: Actual bubble velocity inside the upper and lower holes versus the theoretical velocity due to buoyant forces, fuel C.

Buoyant effects as a function of fuel 's physical properties.
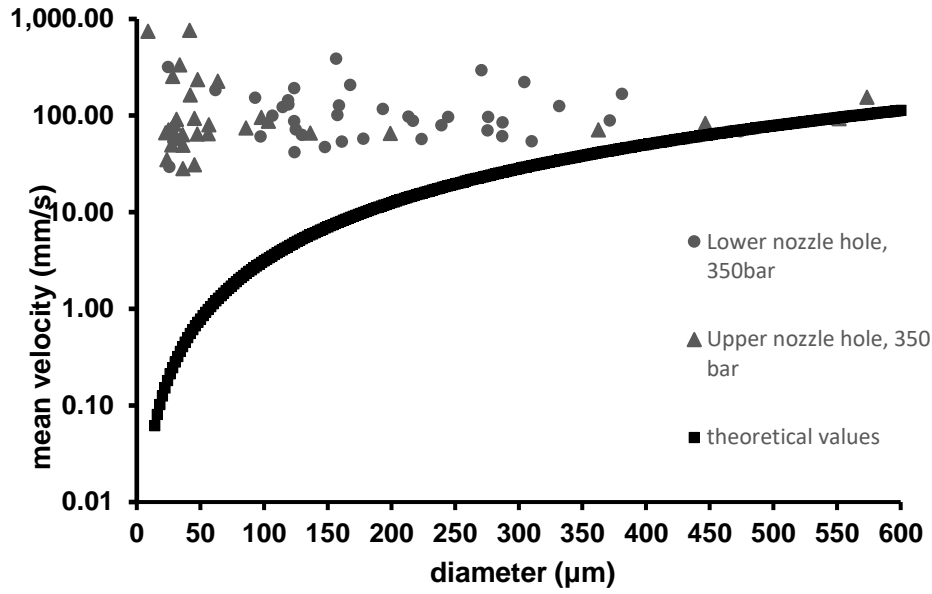
Figure A3.3: Actual bubble velocity inside the upper and lower holes versus the theoretical velocity due to buoyant forces, fuel D.
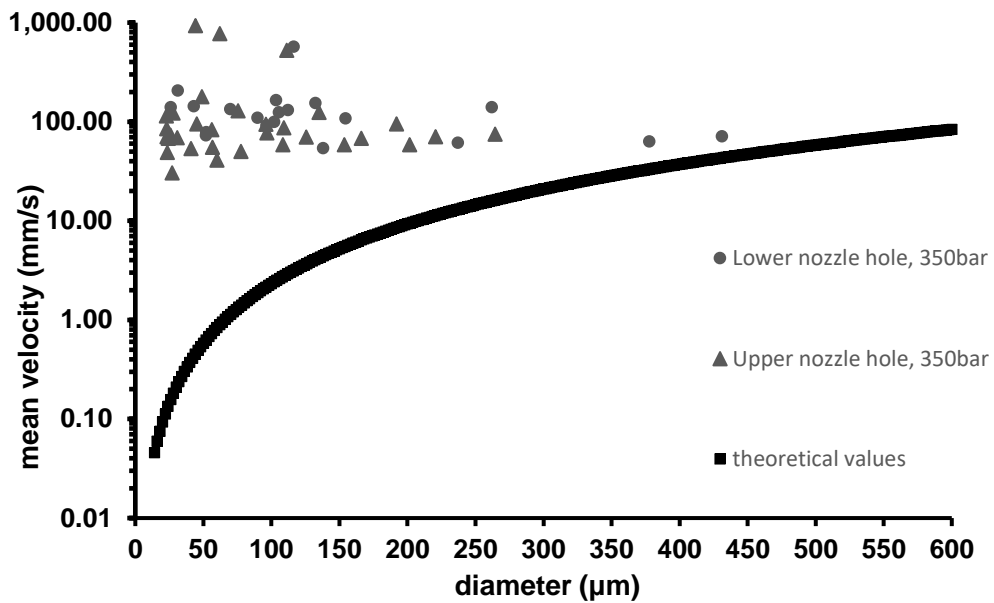
Figure A3.4: Actual bubble velocity inside the upper and lower holes versus the theoretical velocity due to buoyant forces, fuel E.

Appendix A4   Correlation between in-hole bubble displacement and radial-in sac flow

Table A4.1: Summarised results produced by fuel B showing the correlation between bubble displacement in the lower hole and radial-in sac flow.

Fuel B, lower hole			
flow direction	**In-sac flow direction**		
	Clockwise (2%)	Anti-clockwise (90%)	Irregular (8%)
Inwards (%)	0.0	0.0	0.0
Outwards (%)	0.0	8.8	0.0
In/out (%)	0.0	2.2	25.0
Out/in (%)	100.0	89.0	75.0
No movement (%)	0.0	0.0	0.0

Table A4.2: Summarised results produced by fuel B showing the correlation between bubble displacement in the upper hole and radial-in sac flow.

Fuel B, upper hole			
flow direction	**In-sac flow direction**		
	Clockwise (2%)	Anti-clockwise (90%)	Irregular (8%)
Inwards (%)	0.0	0.0	0.0
Outwards (%)	0.0	4.4	0
In/out (%)	100.0	95.6	100.0
Out/in (%)	0.0	0.0	0.0
No movement (%)	0.0	0.0	0.0

Correlation between in-hole bubble displacement and radial-in sac flow

Table A4.3: Summarised results produced by fuel C showing the correlation between bubble displacement in the lower hole and radial-in sac flow.

Fuel C, lower hole			
flow direction	**In-sac flow direction**		
	Clockwise (54%)	Anti-clockwise (12%)	Irregular (34%)
Inwards (%)	7.40	33.30	6.25
Outwards (%)	11.10	16.60	18.75
In/out (%)	3.70	16.60	18.75
Out/in (%)	77.80	33.30	62.50
No movement (%)	0.00	0.00	0.00

Table A4.4: Summarised results produced by fuel C showing the correlation between bubble displacement in the upper hole and radial-in sac flow.

Fuel C, upper hole			
flow direction	**In-sac flow direction**		
	Clockwise (54%)	Anti-clockwise (12%)	Irregular (34%)
Inwards (%)	7.40	33.30	6.25
Outwards (%)	11.10	16.60	18.75
In/out (%)	3.70	16.60	18.75
Out/in (%)	77.80	33.30	62.50
No movement (%)	0.00	0.00	0.00

Correlation between in-hole bubble displacement and radial-in sac flow

Table A4.5: Summarised results produced by fuel D showing the correlation between bubble displacement in the lower hole and radial-in sac flow.

Fuel D, lower hole			
flow direction	**In-sac flow direction**		
	Clockwise (96%)	Anti-clockwise (0%)	Irregular (4%)
Inwards (%)	16.68	0.00	0.00
Outwards (%)	6.25	0.00	0.00
In/out (%)	4.16	0.00	0.00
Out/in (%)	72.91	0.00	0.00
No movement (%)	0.00	0.00	100

Table A4.6: Summarised results produced by fuel D showing the correlation between bubble displacement in the upper hole and radial-in sac flow.

Fuel D, upper hole			
flow direction	**In-sac flow direction**		
	Clockwise (96%)	Anti-clockwise (0%)	Irregular (4%)
Inwards (%)	4.15	0.00	0.00
Outwards (%)	12.5	0.00	0.00
In/out (%)	39.60	0.00	0.00
Out/in (%)	43.75	0.00	0.00
No movement (%)	0.00	0.00	100

Correlation between in-hole bubble displacement and radial-in sac flow

Table A4.7: Summarised results produced by fuel E showing the correlation between bubble displacement in the lower hole and radial-in sac flow.

Fuel E, lower hole			
flow direction	**In-sac flow direction**		
	Clockwise (8%)	Anti-clockwise (84%)	Irregular (8%)
Inwards (%)	0.0	4.8	0.0
Outwards (%)	25.0	23.8	0.0
In/out (%)	0.0	0.0	0.0
Out/in (%)	75.0	61.9	75.0
No movement (%)	0.0	9.5	25.0

Table A4.8: Summarised results produced by fuel E showing the correlation between bubble displacement in the upper hole and radial-in sac flow.

Fuel E, upper hole			
flow direction	**In-sac flow direction**		
	Clockwise (8%)	Anti-clockwise (84%)	Irregular (8%)
Inwards (%)	0.00	2.38	0.00
Outwards (%)	25.00	16.67	25.00
In/out (%)	50.00	9.52	0.00
Out/in (%)	25.00	71.43	75.00
No movement (%)	0.00	0.00	0.00

Appendix B

Appendix B1   Filling, emptying, flushing procedures of the fuel injection system

Draining procedure of the diesel fuel injection rig

1.   Turn off the power supply to the rig (wall switch). Make sure that the room ventilation is on.

2.   Put on PPE (lab coat, gloves, glasses)

3.   Bring waste bottles, absorbing sand close to the working area

4.   Remove the nut from the filter base. Make sure that the filter valve is closed before opening it

5.   Place a large beaker under the filter valve. Open the filter valve and valve 3 to empty the rig.

6.   Close valve 3 and filter valve and measure the volume of the drained fuel. Pour the fuel into the waste bottles. Store the waste bottles into the chemical cupboard.

7.   Measure the volume of the replacing fuel to be equal to the volume of the drained fuel. Pour the fresh fuel into the rig tank.

8.   Turn on the power and water supply to the rig. Place the drain out hose into a large beaker. Open valve 2 before you start the rig. Run the HP pump and pump out ~ 1L of fuel.

9.   Measure the volume of the pumped-out fuel and pour it into the waste bottles. Replace the same volume with fresh fuel. Put the filter nut back in place. The total fuel volume removed from the rig (LP and HP loops) should be ~3.1L-3.2L.

Flushing procedure of the diesel fuel injection rig

10.   To flush the rig, run the LP pump for 1hour and then run the HP pump for 20mins.

11.   In case of a new fuel, the rig needs to be drained 2 times (draining procedure, steps 5-9) and flushed 3 times. Between each flush, the system needs to be drained (see draining procedure)

12.   After the second flush, mount the flush tip onto the injector and achieve a crude alignment of the nozzle holes against the holes of the catch (use drill bit). After the alignment, increase the compression pressure (1bar) to secure the position of the tip.

13.   After the second and the third flush, it is essential to empty the line between the CR and the injector (~250cc of fuel). Produce a square pulse of 20Hz, 50ms period using the signal generator utilised for the laser trigger data acquisition. Make sure that there is no power supply to the signal generator and the injector driver. Remove the laser sync in BNC cable and the output BNC cable from the signal generator. Disconnect the BNC cable at the back of the injector driver. Place a free end of a BNC cable to the output of the signal generator and the other end to the oscilloscope. Press the run button on the generator and turn it on. Check on the oscilloscope that the produced signal is a 20Hz signal with a 50ms period. Disconnect the cable from the oscilloscope and connect it to the injector driver. Turn on the injector driver but do **NOT** press enable button.

14.   Place the catch back in place and check whether the spray will be injected in the middle of the hose cross section (the distance from the nozzle holes and the centre of the hoses should be 30mm).

15.   Turn on the suction from the wall switch next to the door. Put on safety glasses and the breathing mask.

16.   To remove ~250cc from the system, a 30s injection is required. Start the rig, set the pressure at ~200bar. Increase the compression pressure to ~2.3 bar. Press the enable button on the injector driver unit. Press the emergency button on the rig after the 30s period to stop the fuel injection.

17.   Close the suction system and switch off the injector driver and the signal generator.

18.   Disconnect the BNC cables from the injector driver and the signal generator. Put back the laser sync in as input to the signal generator and the cable leading to the data acquisition card as output. Press the trigger button and then turn on the signal generator. Connect the cable at the back of the injector driver.

19.   Drain the rig. (After the second drain of the rig, the filter should be replaced with a new one)

20.   After the third flush, relief the compression pressure and retract the catch. Replace the flush tip with the tip under investigation.

Appendix B2   Injected mass experimental procedure

1.   Measure the mass of three condoms and fused silica cone on the high precision scale (4 significant figures). Take three measurements and calculate the mean value.

2.   Retract the catch.

3.   Place the three condoms around the acrylic bar and seal the tip onto the injector by applying a suitable compression force. Check that the radial and axial position of the tip against the acrylic cone.

4.   Unroll the condoms in a way that they cover the injector body. Seal the condoms onto the injector using a rubber band or a plastic-coated wire tie. Make sure that the condoms are loose.

5.   Set the required parameters on the control box and turn on the rig. Make sure the pressure is set at 350bar. Press enable button on the injector driver unit.

6.   Put on safety glasses, gloves and breathing mask and start the injections. Place a piece of paper of known mass underneath the injector in case of a fuel spillage. During the injection process, hold the condoms in place and check for any damages on the condoms. In case of condom failure stop the rig.

7.   After the experiment is completed, stop the rig by pressing the emergency button. Take off the breathing mask and glasses.

8.   Relief the compression pressure and carefully remove the condoms with the injected fuel and the fused silica cone.

9.   Measure the overall mass of the fuel, condoms and cone on the scale. Subtract the mass of the cone and condoms to get the net fuel mass per injection.

Appendix C

Publications

- Lockett, R., Jeshani, M., Makri, K., and Price, R., "An Optical Characterization of Atomization in Non-Evaporating Diesel Sprays," SAE Technical Paper 2016-01-0865, 2016

- Makri, K., Lockett, R., Jeshani, M. & Price, R. The effect of cavitation on atomization in non-evaporating diesel sprays. (ILASS conference, Brighton,2016).

- Makri, K., Lockett, R., Jeshani, M. & Price, R. Potential mechanisms for deposit formation inside diesel injection equipment (Part A), *Fuel* (to be published)

- Makri, K., Lockett, R., Jeshani, M. & Price, R. Potential mechanisms for deposit formation inside diesel injection equipment (Part B), *Fuel* (to be published)

- Makri, K., Lockett, R., Jeshani, M. & Price, R. Simultaneous external diesel spray and internal diesel nozzle flow imaging using Laser Sheet Dropsizing and Mie scattering techniques, Experiments in Fluids (to be published)

- Makri, K., Lockett, R., Smith A. Simultaneous Laser Sheet Drop-sizing and Laser Induced Fluorescence measurements in non-evaporating diesel sprays and internal nozzle flow, Experiments in Fluids (to be published)

References

1. Arcoumanis, C. & Kamimoto, T. *Flow and combustion in reciprocating engines*. (Springer Science \& Business Media, 2009).

2. Soteriou, C., Andrews, R. & Smith, M. Further studies of cavitation and atomization in diesel injection. *SAE Technical Paper* (1999).

3. Payri, F., Bermudez, V., Payri, R. & Salvador, F. The influence of cavitation on the internal flow and the spray characteristics in diesel injection nozzles. *Fuel* **83,** 419–431 (2004).

4. Lockett, R., Liverani, L., Thaker, D., Jeshani, M. & Tait, N. The characterisation of diesel nozzle flow using high speed imaging of elastic light scattering. *Fuel* **106,** 605–616 (2013).

5. Som, S., Ramirez, A. I., Longman, D. E. & Aggarwal, S. *Influence of nozzle orifice geometry and fuel properties on flow and cavitation characteristics of a diesel injector*. (INTECH Open Access Publisher, 2012).

6. DENSO Develops a New Diesel Common Rail System With the World's Highest Injection Pressure. at <http://www.globaldenso.com/en/newsreleases/130626-01.html>

7. Shinohara, Y., Takeuchi, K., Herrmann, O. E. & Laumen, H. J. 3000 bar common rail system. *MTZ worldwide eMagazine* **72,** 4–9 (2011).

8. Lepperhoff, G. & Houben, M. *Mechanisms of deposit formation in internal combustion engines and heat exchangers*. (1993).

9. Schwab, S. D. *et al.* Internal injector deposits in high-pressure common rail diesel engines. *SAE International Journal of Fuels and Lubricants* **3,** 865–878 (2010).

10. Barker, J., Richard, P., Snape, C. & Meredith, W. *Diesel Injector Deposits-An issue that has evolved with engine technology*. (2011).

11. Ullmann, J., Geduldig, M., Stutzenberger, H., Caprotti, R. & Balfour, G. Investigation into the formation and prevention of internal diesel injector deposits. *SAE SP* **2183,** 15 (2008).

12. Tang, J. *et al.* Coking phenomena in nozzle orifices of Dl-diesel engines. *SAE International Journal of Fuels and Lubricants* **2,** 259–272 (2009).

13. Birgel, A. *et al.* Investigations on deposit formation in the holes of diesel injector nozzles. *SAE International Journal of Fuels and Lubricants* **5,** 123–131 (2011).

14. Lockett, R., Jeshani, M., Makri, K. & Price, R. An optical characterization of atomization in non-evaporating diesel sprays. *SAE Technical Paper* (2016).

15. Chen, P.-C., Wang, W.-C., Roberts, W. L. & Fang, T. Spray and atomization of diesel fuel and its alternatives from a single-hole injector using a common rail fuel injection system. *Fuel* **103,** 850–861 (2013).

16. Jeshani, M. Optical characterisation of cavitating flows in diesel fuel injection equipment. *City University London* PhD thesis (2013).

References

17. Srivastava, S. & Hancsók, J. *Fuels from Crude Oil (Petroleum). Fuels and Fuel-Additives* 48–120 (Wiley Online Library, 2014).

18. CATOIL. REFINERY SCHEMA. (2016). at <http://www.catoil.com/site/en/refinery-schema/>

19. Marcus, A. Diesel fuel Basics-What is diesel, and where does it come from? *PassageMaker* (1999).

20. Srivastava, S. & Hancsók, J. *Properties of Motor Fuels and Their Effects on Engines and the Environment. Fuels and Fuel-Additives* 277–315 (Wiley Online Library).

21. Wilson III, G. Comparison of ASTM D613 and ASTM D6890. *US Army TARDEC Fuels and Lubricants Research Facility (SwRI) San Antonio United States* (2016).

22. Bacha, J. *et al.* Diesel fuels technical review. *Chevron Global Marketing* (2007).

23. ASTM. *Standard Test Method for Calculated Cetane Index by Four Variable Equation ASTM-D4737.* (2009).

24. Gary, J. H., Handwerk, G. E. & Kaiser, M. J. *Petroleum refining: technology and economics.* (CRC press, 2007).

25. Lefebvre, A. *Atomisation and Sprays (Combustion). An International Series, Hemisphere Publishing Corporation* (1989).

26. Chhetri, A. & Watts, K. Surface tensions of petro-diesel, canola, jatropha and soapnut biodiesel fuels at elevated temperatures and pressures. *Fuel* **104,** 704–710 (2013).

27. Ejim, C., Fleck, B. & Amirfazli, A. Analytical study for atomization of biodiesels and their blends in a typical injector: surface tension and viscosity effects. *Fuel* **86,** 1534–1544 (2007).

28. HANDBOOK, D. F. MECHANICAL SCIENCE. *DOE-HDBK-1018/1-93* (1993).

29. Kegl, B., Kegl, M., Pehan, S. & others. *Green diesel engines.* (Springer, 2013).

30. Wellington, B. F. Diesel engines and fuel systems. *5th edition* (2012).

31. Kumar, M. V., Babu, A. V. & Kumar, P. R. The impacts on combustion, performance and emissions of biodiesel by using additives in direct injection diesel engine. *Alexandria Engineering Journal* (2017).

32. Li, D., Zhen, H., Xingcai, L., Wu-gao, Z. & Jian-guang, Y. Physico-chemical properties of ethanol–diesel blend fuel and its effect on performance and emissions of diesel engines. *Renewable Energy* **30,** 967–976 (2005).

33. Kwanchareon, P., Luengnaruemitchai, A. & Jai-In, S. Solubility of a diesel-biodiesel-ethanol blend, its fuel properties, and its emission characteristics from diesel engine. *Fuel* **86,** 1053–1061 (2007).

34. Al-lwayzy Saddam H & Yusaf, T. Diesel engine performance and exhaust gas emissions using Microalgae Chlorella protothecoides biodiesel. *Renewable Energy* **101,** 690–701 (2017).

35. Wahlen, B. D. *et al.* Biodiesel from microalgae, yeast, and bacteria: engine performance and exhaust emissions. *Energy \& Fuels* **27,** 220–228 (2012).

References

36. Lapuerta, M., Armas, O. & Rodriguez-Fernandez, J. Effect of biodiesel fuels on diesel engine emissions. *Progress in energy and combustion science* **34,** 198–223 (2008).

37. Ali, Y., Hanna, M. A. & Borg, J. E. Optimization of diesel, methyl tallowate and ethanol blend for reducing emissions from diesel engine. *Bioresource Technology* **52,** 237–243 (1995).

38. Dougan, O., Çelik, M. B. & Özdalyan, B. The effect of tire derived fuel/diesel fuel blends utilization on diesel engine performance and emissions. *Fuel* **95,** 340–346 (2012).

39. Reynolds, R. *Changes in Diesel Fuel, The Service Technician's Guide to Compression Ignition Fuel Quality.* (2007).

40. Cherillo, R. A., Dahlstrom, M. A., Clark, R. & Whale, G. Assessment of Environmental Impacts of Shell GTL fuel. in *12th Diesel Engine Efficiency and Emissions Reduction Conference* (2006).

41. Maly, R. R. Effect of GTL Diesel Fuels on Emissions and Engine Performance. in *presentation at 10th Diesel Engine Emissions Reduction Conference, Coronado, Calif* (2004).

42. Gogate, P. R., Tayal, R. K. & Pandit, A. B. Cavitation: a technology on the horizon. *Current Science* **91,** 35–46 (2006).

43. Moholkar, V. S., Kumar, P. S. & Pandit, A. B. Hydrodynamic cavitation for sonochemical effects. *Ultrason Sonochem* **6,** 53–65 (1999).

44. Stinebring, D. R., Billet, M. L., Lindau, J. W. & Kunz, R. F. *Developed cavitation-cavity dynamics.* (2001).

45. Franc, J. P. & Michel, J. M. *Fundamentals of cavitation.* **76,** (Springer, 2004).

46. Rayleigh, Lord. On the pressure developed in a liquid during the collapse of a spherical cavity. *Philosophical Magazine* (1917).

47. Plesset, M. S. & Prosperetti, A. Bubble dynamics and cavitation. *Annual review of fluid mechanics* **9,** 145–185 (1977).

48. Brennen, C. E. *Cavitation and bubble dynamics.* **44,** (Oxford University Press on Demand, 1995).

49. Lorimer, J. P. & Mason, T. J. Sonochemistry. Part 1—the physical aspects. *Chemical Society Reviews* **16,** 239–274 (1987).

50. Brujan, E. *Cavitation in Non-Newtonian fluids: with biomedical and bioengineering applications.* (Springer Science \& Business Media, 2010).

51. Van Wijngaarden, L. Mechanics of collapsing cavitation bubbles. *Ultrasonics sonochemistry* **29,** 524–527 (2016).

52. Badock, C., Wirth, R., Fath, A. & Leipertz, A. Investigation of cavitation in real size diesel injection nozzles. *International journal of heat and fluid flow* **20,** 538–544 (1999).

53. Arcoumanis, C., Flora, H., Gavaises, M., Kampanis, N. & Horrocks, R. Investigation of cavitation in a vertical multi-hole injector. *SAE Technical Paper* (1999).

References

54. Soteriou, C., Andrews, R., Smith, M., Torres, N. & Sankhalpara, S. The flow patterns and sprays of variable orifice nozzle geometries for diesel injection. *SAE Technical Paper* (2000).

55. Andriotis, A., Gavaises, M. & Arcoumanis, C. Vortex flow and cavitation in diesel injector nozzles. *Journal of Fluid Mechanics* **610,** 195–215 (2008).

56. Roth, H., Gavaises, M. & Arcoumanis, C. Cavitation initiation, its development and link with flow turbulence in diesel injector nozzles. *SAE Technical Paper* (2002).

57. Lockett, R., Liverani, L., Thaker, D., Jeshani, M. & Tait, N. The characterisation of diesel nozzle flow using high speed imaging of elastic light scattering. *Fuel* **106,** 605–616 (2013).

58. Giannadakis, E., Gavaises, M. & Arcoumanis, C. Modelling of cavitation in diesel injector nozzles. *Journal of Fluid Mechanics* **616,** 153–193 (2008).

59. Payri, R., Molina, S., Salvador, F. & Gimeno, J. A study of the relation between nozzle geometry, internal flow and sprays characteristics in diesel fuel injection systems. *KSME International Journal* **18,** 1222–1235 (2004).

60. Trevena, D. Cavitation and the generation of tension in liquids. *Journal of Physics D: Applied Physics* **17,** 2139 (1984).

61. Mei, R., Chen, W. & Klausner, J. F. Vapor bubble growth in heterogeneous boiling—II. Growth rate and thermal fields. *International Journal of Heat and Mass Transfer* **38,** 921–934 (1995).

62. Arcoumanis, C., Flora, H., Gavaises, M. & Badami, M. Cavitation in real-size multi-hole diesel injector nozzles. *SAE Technical Paper* (2000).

63. Kim, J., Nishida, K. & Hiroyasu, H. Characteristics of the internal flow in a diesel injection nozzle. *International Journal of Fluid Mechanics Research* **24,** (1997).

64. Afzal, H., Arcoumanis, C., Gavaises, M. & Kampanis, N. Internal flow in diesel injector nozzles: modelling and experiments. *IMechE Paper S* **492,** 25–44 (1999).

65. Soteriou, C., Andrews, R. & Smith, M. *Direct injection diesel sprays and the effect of cavitation and hydraulic flip on atomization*. (1995).

66. Schmidt, D. P. & Corradini, M. The internal flow of diesel fuel injector nozzles: a review. *International Journal of Engine Research* **2,** 1–22 (2001).

67. Hayashi, T., Suzuki, M. & Ikemoto, M. Effects of internal flow in a diesel nozzle on spray combustion. *International Journal of Engine Research* **14,** 646–654 (2013).

68. Gavaises, M., Andriotis, A., Papoulias, D., Mitroglou, N. & Theodorakakos, A. Characterization of string cavitation in large-scale Diesel nozzles with tapered holes. *Physics of fluids* **21,** 052107 (2009).

69. Soteriou, C., Lambert, M., S., Z. & D., P. The flow characteristics of high efficiency diesel nozzles with enhanced geometry holes. *THISIEL* (2006).

70. Payri, R., Salvador, F., Gimeno, J. & De la Morena, J. Effects of nozzle geometry on direct injection diesel engine combustion process. *Applied thermal engineering* **29,** 2051–2060 (2009).

References

71. Bergwerk, W. Flow pattern in diesel nozzle spray holes. *Proceedings of the Institution of Mechanical Engineers* **173,** 655–660 (1959).

72. Hiroyasu, H. Break-up length of a liquid jet and internal flow in a nozzle. in *Proc. 5th. ICLASS* 275–282 (1991).

73. Arcoumanis, C., Nouri, J. & Andrews, R. Application of refractive index matching to a diesel nozzle internal flow. *DTIC Document* (1992).

74. Chaves, H., Knapp, M., Kubitzek, A., Obermeier, F. & Schneider, T. Experimental study of cavitation in the nozzle hole of diesel injectors using transparent nozzles. *SAE technical paper* (1995).

75. Mitroglou, N., Gavaises, M., Nouri, J. & Arcoumanis, C. Cavitation inside enlarged and real-size fully transparent injector nozzles and its effect on near nozzle spray formation. in *Proceedings of the DIPSI Workshop 2011. Droplet Impact Phenomena \& Spray Investigations* 33–45 (2011).

76. Mitroglou, N., Lorenzi, M., Santini, M. & Gavaises, M. Application of X-ray micro-computed tomography on high-speed cavitating diesel fuel flows. *Experiments in Fluids* **57,** 175 (2016).

77. Cook, S. & Richards, P. Possible influence of high injection pressure on diesel fuel stability: a review and preliminary study. *SAE Technical Paper* (2009).

78. Caprotti, R., Breakspear, A., Graupner, O., Klaua, T. & Kohnen, O. Diesel injector deposits potential in future fueling systems. *SAE Technical Paper* (2006).

79. Barker, J., Langley, G. J. & Richards, P. Insights into deposit formation in high pressure diesel fuel injection equipment. *SAE Technical Paper* (2010).

80. Lacey, P. *et al.* Fuel quality and diesel injector deposits. *SAE International Journal of Fuels and Lubricants* **5,** 1187–1198 (2012).

81. D' Ambrosio, S. & Ferrari, A. Diesel injector coking: optical-chemical analysis of deposits and influence on injected flow-rate, fuel spray and engine performance. *Journal of engineering for gas turbines and power* **134,** 062801 (2012).

82. Ikemoto, M. *et al.* Injection Nozzle Coking Mechanism in Common-rail Diesel Engine. *SAE International Journal of Fuels and Lubricants* **5,** 78–87 (2011).

83. Lacey, P., Gail, S., Kientz, J. M., Milovanovic, N. & Gris, C. Internal fuel injector deposits. *SAE International Journal of Fuels and Lubricants* **5,** 132–145 (2011).

84. Ullmann, J., Gedulding, M., Stutzenberger, H., Caprotti, R. & Balfour, G. Effects of fuel impurities and additive interactions on the formation of internal diesel injector deposits. in *TAE 7th International Colloquium Fuels, Esslingen* (2009).

85. Arters, D., Goodrich, B., Millard, A. & Gunter, G. Internal Diesel Injector Deposits. *Coordinating Reasearch Council* (2013).

86. Quigley, R. *et al.* A Study of the Internal Diesel Injector Deposit Phenomenon. in *TAE Fuels 7th Annual Colloquium* (2009).

References

87. Reid, J. & Barker, J. Understanding polyisobutylene succinimides (PIBSI) and internal diesel injector deposits. *SAE Technical Paper* (2013).

88. Katritzky, A. R., Yao, J., Qi, M. & Davis, S. Ring Opening of Succinimides. *Heterocycles* (1998).

89. Julie, G.-F. Diesel Injector Internal Deposits: Causes, Effects and Resolution. *JSAE* (2011).

90. Price, R., Blazina, D., Smith, G. C. & Davies, T. J. Understanding the impact of cavitation on hydrocarbons in the middle distillate range. *Fuel* **156,** 30–39 (2015).

91. Caprotti, R., Fowler, W., Lepperhoff, G. & Houben, M. Diesel Additive Technology Effects on Injector Hole Erosion/Corrosion, Injector Fouling and Particulate Traps. *SAE Technical Paper* (1993).

92. He, Z. *et al.* Visual experiment of transient cavitating flow characteristics in the real-size diesel injector nozzle. *International Communications in Heat and Mass Transfer* **78,** 13–20 (2016).

93. Reitz, R. D. Atomization and other breakup regimes of a liquid jet. *Princeton University* PhD thesis (1978).

94. Tafreshi, H. V. & Pourdeyhimi, B. The effects of nozzle geometry on waterjet breakup at high Reynolds numbers. *Experiments in fluids* **35,** 364–371 (2003).

95. Lin, S. & Reitz, R. Drop and spray formation from a liquid jet. *Annual Review of Fluid Mechanics* **30,** 85–105 (1998).

96. Liu, H. *Science and Engineering of Droplets: Fundamentals and Applications*. (William Andrew, 1999).

97. Dumouchel, C. On the experimental investigation on primary atomization of liquid streams. *Experiments in fluids* **45,** 371–422 (2008).

98. Faeth, G., Hsiang, L.-P. & Wu, P.-K. Structure and breakup properties of sprays. *International Journal of Multiphase Flow* **21,** 99–127 (1995).

99. Bracco, F. Modeling of engine sprays. *SAE Technical Paper* (1985).

100. Rizk, N. Studies on liquid sheet disintegration in airblast atomizers. *Cranfield University* PhD thesis (1976).

101. Yan, K., Ning, Z., Lü, M. & Sun, C. Study on droplet size and velocity distributions of a pressure swirl atomizer based on the Maximum Entropy Formalism. *Entropy* **17,** 580–593 (2015).

102. Ghurri, A., Kim, J.-D., Kim, H. G., Jung, J.-Y. & Song, K.-K. The effect of injection pressure and fuel viscosity on the spray characteristics of biodiesel blends injected into an atmospheric chamber. *Journal of mechanical science and technology* **26,** 2941–2947 (2012).

103. Jankowski, A., Sieminska-Jankowska, B., Sandel, A. & Boche'nski, C. Investigation of the fuel spray atomization spectrum in common-rail system for diesel engines. *Journal of KONES Internal Combustion Engines* **10,** (2003).

References

104. Reitz, R. & Bracco, F. Mechanism of atomization of a liquid jet. *The Physics of Fluids* **25,** 1730–1742 (1982).

105. Gulder, O. L. Views on the structure of transient diesel sprays. *Atomization and Sprays* **10,** (2000).

106. Fath, A., Fettes, C. & Leipertz, A. Investigation of the diesel spray break-up close to the nozzle at different injection conditions. in *The fourth international symposium COMODIA* **98,** 429–433 (1998).

107. Suh, H., Park, S. & Lee, C. Experimental investigation of nozzle cavitating flow characteristics for diesel and biodiesel fuels. *International Journal of Automotive Technology* **9,** 217–224 (2008).

108. Makri, K., Lockett, R., Jeshani, M. & Price, R. The effect of cavitation on atomization in non-evaporating diesel sprays. *ILASS proceedings, Brighton* (2016).

109. Leick, P. *et al.* X-ray measurements of the mass distribution in the dense primary break-up region of the spray from a standard multi-hole common-rail diesel injection system. in *21st Annual ILASS-Europe Conference, Mugla, Turkey* (2007).

110. Chehroudi, B., Chen, S.-H., Bracco, F. V. & Onuma, Y. On the intact core of full-cone sprays. *SAE Technical Paper* (1985).

111. Martinez-Martinez, S., Sanchez, F., Riesco-Avila, J. M. & Bermudez, V. *Liquid sprays characteristics in diesel engines*. (INTECH Open Access Publisher, 2010).

112. Hiroyasu, H., Kodata, T. & Arai, M. *Fuel Spray Characterization in Diesel Engines. Combustion modelling in reciprocant engines* (Plenum Press, 1980).

113. Hiroyasu, H., Shimizu, M. & Arai, M. The breakup of high speed jet in a high pressure gaseous atmosphere. *ICLASS-82, Madison, Wis* (1982).

114. Gülder, Ö. L., Smallwood, G. J. & Snelling, D. R. Diesel spray structure investigation by laser diffraction and sheet illumination. *SAE Technical Paper* (1992).

115. Yue, Y., Powell, C. F., Poola, R., Wang, J. & Schaller, J. K. Quantitative measurements of diesel fuel spray characteristics in the near-nozzle region using X-ray absorption. *Atomization and sprays* **11,** (2001).

116. Gulder, O. L. & Smallwood, G. Time-resolved structure of full cone diesel sprays. in *Proceedings of the Second International Workshop on Advanced Spray Combustion* 1–10 (1998).

117. Kosaka, H., Suzuki, T. & Kamimoto, T. Numerical simulation of turbulent dispersion of fuel droplets in an unsteady spray via discrete vortex method. *SAE Technical Paper* (1995).

118. Kuo, K. K. Recent advances in spray combustion: Spray atomization and drop burning phenomena. *American Institute of Aeronautics and Astronautics* **1,** (1996).

119. Yeh, C., Kosaka, H. & Kamimoto, T. A fluorescence/scattering imaging technique for instantaneous 2-D measurements of particle size distribution in a transient spray. *Proc. 3rd Congr. Opt. Part. Sizing, Yokohama, Japan* 355–61 (1993).

References

120. Berrocal, E., Kristensson, E., Hottenbach, P., Aldén, M. & Grünefeld, G. Quantitative imaging of a non-combusting diesel spray using structured laser illumination planar imaging. *Applied physics b* **109,** 683–694 (2012).

121. Durst, F. & Whitelaw, J. Optimization of optical anemometers. *Proceedings of the Royal Society of London A: Mathematical, Physical and Engineering Sciences* **324,** 157–181 (1971).

122. Durst, F. & Zaré, M. Laser Doppler measurements in two-phase flows. in *The accuracy of flow measurements by laser Doppler methods* **1,** 403–429 (1976).

123. Durst, F. Fluid mechanics developments and advancements in the 20th century. in *Proc. 10th Int. Symp. on Applications of Laser Techniques to Fluid Mechanics (July 2000)* (2000).

124. Dual, P. Manual. *DANTEC/invent measurement technology* (1996).

125. Naqwi, A. A. Innovative phase Doppler systems and their applications. *Particle \& particle systems characterization* **11,** 7–21 (1994).

126. Aizu Y., D. F. G. O. F. X. T.-H. PDA system without gaussian beam effects. in *Congress on Optical Particle Sizing* (1993).

127. Xu, T.-H. & Tropea, C. Improving the performance of two-component phase Doppler anemometers. *Measurement Science and Technology* **5,** 969 (1994).

128. Bachalo, W. & Houser, M. Phase/Doppler spray analyzer for simultaneous measurements of drop size and velocity distributions. *Optical Engineering* **23,** 235583–235583 (1984).

129. Bachalo, W. D. The phase doppler method: Analysis, performance evaluations, and applications. *Particle \& particle systems characterization* **11,** 73–83 (1994).

130. Sankar, S. V., Ibrahim, K. M. & Bachalo, W. D. Coherent scattering by multiple particles in phase Doppler interferometry. *Particle \& particle systems characterization* **11,** 35–42 (1994).

131. Roisman, I. & Tropea, C. Drops distribution and flux measurements in sprays using the phase Doppler technique. in *10th international symposium on applications of laser techniques to fluid mechanics* 23 (2000).

132. Berrocal, E. Multiple scattering of light in optical diagnostics of dense sprays and other complex turbid media. *Cranfield University* PhD thesis (2006).

133. Wigley, G. in *Optical diagnostics for flow processes* 175–204 (Springer, 1994).

134. Tropea, C. *et al.* Dual-Mode Phase-Doppler Anemometer. *Particle \& particle systems characterization* **13,** 165–170 (1996).

135. Mauger, C., Méès, L., Michard, M., Azouzi, A. & Valette, S. Shadowgraph, Schlieren and interferometry in a 2D cavitating channel flow. *Experiments in fluids* **53,** 1895–1913 (2012).

136. Merzkirch, W. Techniques of flow visualization. *DTIC Document* (1987).

137. Paciaroni, M. & Linne, M. Single-shot, two-dimensional ballistic imaging through scattering media. *Appl Opt* **43,** 5100–9 (2004).

<div style="text-align: center;">**References**</div>

138. Linne M., P. M. B. E. S. D. Ballistic imaging of liquid breakup processes in dense sprays. *Proceedings of Combustion Institute* **32,** 2147–2161 (2009).

139. Sedarsky, D., Paciaroni, M., Zelina, J. & Linne, M. Near field fluid structure analysis for jets in crossflow with ballistic imaging. *20th ILASS Americas, Chicago, IL* (2007).

140. Sedarsky, D. L., Paciaroni, M. E., Linne, M. A., Gord, J. R. & Meyer, T. R. Velocity imaging for the liquid-gas interface in the near field of an atomizing spray: proof of concept. *Opt Lett* **31,** 906–8 (2006).

141. KUO, K., Hsieh, K. & Char, J. Observations of breakup processes of liquid jets using real-time X-ray radiography. *Journal of Propulsion and Power* **6,** 544–551 (1990).

142. Powell, C. F., Yue, Y., Poola, R. & Wang, J. Time-resolved measurements of supersonic fuel sprays using synchrotron X-rays. *Journal of synchrotron radiation* **7,** 356–360 (2000).

143. Powell, C. F., Ciatti, S., Cheong, S., Liu, J. & Wang, J. X-Ray Characterization of Diesel Sprays and the Effects of Nozzle Geometry. in *Proceedings of the Diesel Engine Emission Reduction Conference* (2004).

144. Wang, J. *et al. X-ray visions of air-assisted sprays: from radiography to quantitative phase-contrast imaging.* (2006).

145. Hahn, D. W. Light scattering theory. *Department of Mechanical and Aerospace Engineering, Florida* (2006).

146. Van de Hulst, H. C. & Twersky, V. Light scattering by small particles. *Physics Today* **10,** 28–30 (1957).

147. Bohren, C. F. & Huffman, D. R. Absorption and scattering by a sphere. *Absorption and Scattering of Light by Small Particles* 82–129 (1983).

148. Le Gal, P., Farrugia, N. & Greenhalgh, D. Laser sheet dropsizing of dense sprays. *Optics \& Laser Technology* **31,** 75–83 (1999).

149. Jermy, M. & Greenhalgh, D. Planar dropsizing by elastic and fluorescence scattering in sprays too dense for phase Doppler measurement. *Applied Physics B: Lasers and Optics* **71,** 703–710 (2000).

150. Conwell, P. R., Barber, P. W. & Rushforth, C. K. Resonant spectra of dielectric spheres. *JOSA A* **1,** 62–67 (1984).

151. Tsang, L., Kong, J. A., Ding, K.-H. & Ao, C. O. *Scattering of electromagnetic waves, numerical simulations.* **25,** (John Wiley \& Sons, 2004).

152. Le Moyne, L. LIF&Mie spray characterization. *Universite Pierre&Marie Currie* (2012).

153. Coghe, A. & Cossali, G. Quantitative optical techniques for dense sprays investigation: A survey. *Optics and Lasers in Engineering* **50,** 46–56 (2012).

154. Domann, R. & Hardalupas, Y. Quantitative measurement of planar droplet Sauter mean diameter in sprays using planar droplet sizing. *Particle \& particle systems characterization* **20,** 209–218 (2003).

References

155. Réveillé, T. Study of fuel injection and mixture formation for a gasoline direct injection engine. *Cranfield University* Phd thesis (2005).

156. Zare, R. N. & Dagdigian, P. J. Tunable laser fluorescence method for product state analysis. *Science* **185,** 739–747 (1974).

157. Lakowicz, J. R. *Principles of Fluorescence Spectroscopy*. (Springer US, 2006).

158. Valeur, B. & Berberan-Santos, M. N. *Molecular fluorescence: principles and applications*. (John Wiley \& Sons, 2012).

159. Domman, R. & Hardalupas, Y. Evaluation of the Planar Droplet Sizing (PDS)Technique . in *10th ILASS, Pasadena,USA* (2000).

160. Charalampous, G., Hardalupas, Y. & Taylor, A. Optimisation of the droplet sizing accuracy of the combined scattering (Mie)/laser induced fluorescence (LIF) technique. in *12th Int. Symp. on Appl. of Laser Tech. to Fluid Mech* 15–6 (2004).

161. Domann, R. & Hardalupas, Y. Spatial distribution of fluorescence intensity within large droplets and its dependence on dye concentration. *Applied Optics* **40,** 3586–3597 (2001).

162. Düwel, I., Schorr, J., Wolfrum, J. & Schulz, C. Laser-induced fluorescence of tracers dissolved in evaporating droplets. *Applied Physics B: Lasers and Optics* **78,** 127–131 (2004).

163. Düwel, I. Spray combustion diagnostics with tracer-based laser-induced fluorescence imaging. *Ruprecht Karls Universität* PhD thesis (2007).

164. Schulz, C. & Sick, V. Tracer-LIF diagnostics: quantitative measurement of fuel concentration, temperature and fuel/air ratio in practical combustion systems. *Progress in Energy and Combustion Science* **31,** 75–121 (2005).

165. Payri, R., Gimeno, J., Mart'\i, P. & Manin, J. Fuel concentration in isothermal Diesel sprays through structured planar laser imaging measurements. *International Journal of Heat and Fluid Flow* **34,** 98–106 (2012).

166. Kristensson, E., Berrocal, E., Richter, M., Pettersson, S.-G. & Aldén, M. High-speed structured planar laser illumination for contrast improvement of two-phase flow images. *Optics letters* **33,** 2752–2754 (2008).

167. Berrocal, E., Kristensson, E., Richter, M., Linne, M. & Aldén, M. Application of structured illumination for multiple scattering suppression in planar laser imaging of dense sprays. *Optics express* **16,** 17870–17881 (2008).

168. Mishra, Y. N., Kristensson, E. & Berrocal, E. Reliable LIF/Mie droplet sizing in sprays using structured laser illumination planar imaging. *Optics express* **22,** 4480–4492 (2014).

169. Mishra, Y. N., Nada, F. A., Polster, S., Kristensson, E. & Berrocal, E. Thermometry in aqueous solutions and sprays using two-color LIF and structured illumination. *Optics Express* **24,** 4949–4963 (2016).

170. Kristensson, E., Berrocal, E. & Aldén, M. Extinction coefficient imaging of turbid media using dual structured laser illumination planar imaging. *Optics letters* **36,** 1656–1658 (2011).

171. Cuccia, D. J., Bevilacqua, F., Durkin, A. J. & Tromberg, B. J. Modulated imaging: quantitative analysis and tomography of turbid media in the spatial-frequency domain. *Optics letters* **30,**

References

1354–1356 (2005).

172. Berrocal, E. Structured Laser Illumination Planar Imaging: New horizons for the study of spray dynamics, thermometry and droplet sizing. in *18th ILASS, Lisbon* (2016).

173. Kristensson, E., Berrocal, E., Richter, M. & Aldén, M. Nanosecond structured laser illumination planar imaging for single-shot imaging of dense sprays. *Atomization and Sprays* **20,** (2010).

174. Kristensson, E., Ehn, A., Bood, J. & Aldén, M. Advancements in Rayleigh scattering thermometry by means of structured illumination. *Proceedings of the Combustion Institute* **35,** 3689–3696 (2015).

175. Kristensson, E. Structured Laser Illumination Planar Imaging SLIPI Applications for Spray Diagnostics. *Lund University* Phd thesis (2012).

176. Lockett, R., Richter, J. & Greenhalgh, D. The characterisation of a diesel spray using combined laser induced fluorescence and laser sheet dropsizing. in *Lasers and Electro-Optics Europe, 1998. 1998 CLEO/Europe. Conference on* 148–148 (1998).

177. Sankar, S., Maher, K., Robart, D. & Bachalo, W. Spray characterization using a planar droplet sizing technique. *International journal of fluid mechanics research* **24,** (1997).

178. Abu-Gharbieh, R. Laser sheet imaging and image analysis for combustion research. *Chalmers University of Technology, Sweden*

179. Guilbault, G. G. *Practical fluorescence*. **3,** (CRC Press, 1990).

180. Liverani, L. Cavitation in Real-Size Diesel Injector Nozzles. *City University London* PhD Thesis (2010).

181. Payri, R., Garcia, J., Salvador, F. & Gimeno, J. Using spray momentum flux measurements to understand the influence of diesel nozzle geometry on spray characteristics. *Fuel* **84,** 551–561 (2005).

182. Epstein, P. S. & Plesset, M. S. On the stability of gas bubbles in liquid-gas solutions. *The Journal of Chemical Physics* **18,** 1505–1509 (1950).

183. Wu, S. *et al.* Effects of glycerol monostearate and Tween 80 on the physical properties and stability of recombined low-fat dairy cream. *Dairy Science \& Technology* **96,** 377–390 (2016).

184. Mezger, T. G. *The rheology handbook: for users of rotational and oscillatory rheometers*. (Vincentz Network GmbH \& Co KG, 2006).

185. Yang, G., Du, B. & Fan, L. Bubble formation and dynamics in gas-liquid-solid fluidization—A review. *Chemical Engineering Science* **62,** 2–27 (2007).

186. Theodorakakos, A., Mitroglou, N. & Gavaises, M. Simulation of heating effects in cavitating flows through Diesel fuel injectors caused by extreme fuel pressurisation. *Simulation* **14,** 16 (2012).

187. Widegren, J. A. & Bruno, T. J. Vapor pressure measurements on saturated biodiesel fuel esters by the concatenated gas saturation method. *Fuel* **90,** 1833–1839 (2011).

References

188. Battino, R., Rettich, T. R. & Tominaga, T. The solubility of nitrogen and air in liquids. *Journal of physical and chemical reference data* **13,** 563–600 (1984).

189. Hartley, R. & Zisserman, A. *Multiple view geometry in computer vision*. (Cambridge university press, 2003).